A bid to reignite the only U.S. fusion lab p. 618

Rushing to develop an African swine fever vaccine p. 622

Recent climate change drives bumble bee declines pp. 626 & 685

Science

$15
7 FEBRUARY 2020
sciencemag.org

AAAS

RICE YIELD

More branches with less fertilizer p. 641

CONTENTS

7 FEBRUARY 2020 • VOLUME 367 • ISSUE 6478

622

PHOTO: BREUER WILDLIFE/MINDEN PICTURES

NEWS

IN BRIEF

606 News at a glance

IN DEPTH

610 Will novel virus go pandemic or be contained?
Modelers are trying to forecast how the coronavirus will move, but they need better data *By K. Kupferschmidt and J. Cohen*

611 Combo of two HIV vaccines fails its big test
South African trial halted early because of "futility" *By J. Cohen*

612 Climate change spurs global speedup of ocean currents
Rising winds boost flows in tropics and Southern Ocean *By P. Voosen*
SCIENCE ADVANCES RESEARCH ARTICLE BY S. HU *ET AL.* 10.1126/SCIADV.AAX7727

613 Prominent spider biologist spun a web of questionable data
Two retractions spark scrutiny of dozens of papers *By E. Pennisi*

614 Prosecutor details China probe that snared chemist
Department of Justice initiative aims to counter "corrupting" influence of foreign money on scientists
By J. Mervis

616 CRISPR takes on cancer
Gene edits appear safe in first three patients
By J. Couzin-Frankel
RESEARCH ARTICLE BY E. A. STADTMAUER *ET AL.* 10.1126/SCIENCE.ABA7365; PERSPECTIVE BY J. R. HAMILTON AND J. A. DOUDNA 10.1126/SCIENCE.ABA9844

617 Underground oil fires liberate carbon-free fuel
Company ignites heavy oil fields to make green hydrogen while leaving carbon trapped
By E. Hand

FEATURES

618 Rekindling the flame
After decades of decline, the U.S. government's fusion lab seeks a rebirth
By A. Cho

INSIGHTS

PERSPECTIVES

622 No hasty solutions for African swine fever
African swine fever vaccines could pose risk of causing disease and spreading the virus further *By D. Gavier-Widén* et al.

624 Porous crystals as membranes
Microporous crystalline membranes are designed for gas separation and potential scale-up *By M. A. Carreon*
REPORT p. 667

626 Discovering the limits of ecological resilience
Bumble bee declines reveal species pushed to the edge of their environmental tolerances
By J. Bridle and A. van Rensburg
REPORT p. 685

627 Room-temperature magnetoelastic coupling
Magnetic fields alter the ferroelectric properties of a paramagnetic ytterbium-zinc complex *By Y. Zhou and S.-T. Han*
REPORT p. 671

628 In the heat of the night
An ancestral receptor plays a key role in host detection by malaria-carrying mosquitoes *By C. R. Lazzari*
REPORT p. 681

POLICY FORUM

630 Using sewage for surveillance of antimicrobial resistance
A global system would exploit metagenomic sequencing
By Frank M. Aarestrup and M. E. J. Woolhouse

Published by AAAS

BOOKS *ET AL.*

633 Death dollhouses and the birth of forensics
A wealthy patron's vision and macabre models helped forge the field of forensic medicine *By A. Adam*

634 Hidden figures
Missing population data hinder good accounting and fair resource distribution
By W. P. O'Hare

LETTERS

635 Marine heat waves threaten kelp forests
By N. Arafeh-Dalmau et al.

635 Marine restoration projects are undervalued
By T. A. C. Gordon et al.

636 U.S. action lowers barriers to invasive species
By D. Simberloff et al.

RESEARCH

IN BRIEF

637 From *Science* and other journals

REVIEW

640 Medicine
The biology, function, and biomedical applications of exosomes *R. Kalluri and V. S. LeBleu*
REVIEW SUMMARY; FOR FULL TEXT: DX.DOI.ORG/10.1126/SCIENCE.AAU6977

RESEARCH ARTICLES

641 Plant science
Enhanced sustainable green revolution yield via nitrogen-responsive chromatin modulation in rice *K. Wu* et al.
RESEARCH ARTICLE SUMMARY; FOR FULL TEXT: DX.DOI.ORG/10.1126/SCIENCE.AAZ2046

642 Immunology
Butyrophilin 2A1 is essential for phosphoantigen reactivity by γδ T cells
M. Rigau et al.
RESEARCH ARTICLE SUMMARY; FOR FULL TEXT: DX.DOI.ORG/10.1126/SCIENCE.AAY5516

643 Signal transduction
Mechanism of homodimeric cytokine receptor activation and dysregulation by oncogenic mutations *S. Wilmes* et al.

PHOTO: ALEXANDER WILD

652 Signal transduction
An AMPK–caspase-6 axis controls liver damage in nonalcoholic steatohepatitis
P. Zhao et al.

REPORTS

661 Electrochemistry
CO_2 electrolysis to multicarbon products at activities greater than 1 A cm^{-2}
F. P. García de Arquer et al.

667 Catalysis
Na^+-gated water-conducting nanochannels for boosting CO_2 conversion to liquid fuels
H. Li et al.
PERSPECTIVE p. 624

671 Multiferroics
Room temperature magnetoelectric coupling in a molecular ferroelectric ytterbium(III) complex *J. Long* et al.
PERSPECTIVE p. 627

676 Organic chemistry
Total synthesis of the complex taxane diterpene canataxpropellane
F. Schneider et al.

681 Mosquito biology
Mosquito heat seeking is driven by an ancestral cooling receptor *C. Greppi* et al.
PERSPECTIVE p. 628

685 Pollinator decline
Climate change contributes to widespread declines among bumble bees across continents *P. Soroye* et al.
PERSPECTIVE p. 626

688 Neuroscience
Microglia mediate forgetting via complement-dependent synaptic elimination *C. Wang* et al.

694 Phase separation
Valence and patterning of aromatic residues determine the phase behavior of prion-like domains
E. W. Martin et al.

700 Structural biology
Structure of an active human histone pre-mRNA 3′-end processing machinery
Y. Sun et al.

DEPARTMENTS

605 Editorial
For science, Brexit isn't done yet
By James Wilsdon

710 Working Life
Just for fun *By Bill D. Roebuck*

ON THE COVER

Rice paddy terraces in Guangxi, China. The nitrogen fertilizers used in green revolution rice cultivation increase the number of flowering branches per plant, in turn enhancing grain yield. Researchers have now discovered the gene that promotes this branching response to nitrogen. Future breeding efforts will use natural gene variants to increase grain yield and reduce fertilizer need, thus boosting agricultural sustainability. See page 641. *Photo: Chris Stenger/Minden Pictures*

Science Staff 602
New Products 704
Science Careers 705

SCIENCE (ISSN 0036-8075) is published weekly on Friday, except last week in December, by the American Association for the Advancement of Science, 1200 New York Avenue, NW, Washington, DC 20005. Periodicals mail postage (publication No. 484460) paid at Washington, DC, and additional mailing offices. Copyright © 2020 by the American Association for the Advancement of Science. The title SCIENCE is a registered trademark of the AAAS. Domestic individual membership, including subscription (12 months): $165 ($74 allocated to subscription). Domestic institutional subscription (51 issues): $2148; Foreign postage extra: Air assist delivery: $98. First class, airmail, student, and emeritus rates on request. Canadian rates with GST available upon request, GST #125488122. Publications Mail Agreement Number 1069624. **Printed in the U.S.A.**
Change of address: Allow 4 weeks, giving old and new addresses and 8-digit account number. **Postmaster:** Send change of address to AAAS, P.O. Box 96178, Washington, DC 20090–6178. **Single-copy sales:** $15 each plus shipping and handling available from backissues.sciencemag.org; bulk rate on request. **Authorization to reproduce** material for internal or personal use under circumstances not falling within the fair use provisions of the Copyright Act can be obtained through the Copyright Clearance Center (CCC), www.copyright.com. The identification code for *Science* is 0036-8075. *Science* is indexed in the *Reader's Guide to Periodical Literature* and in several specialized indexes.

Published by AAAS

Science AAAS

Editor-in-Chief Holden Thorp, hthorp@aaas.org

Executive Editor Monica M. Bradford

Editors, Research Valda Vinson, Jake S. Yeston **Editor, Insights** Lisa D. Chong

DEPUTY EDITORS Julia Fahrenkamp-Uppenbrink (UK), Stella M. Hurtley (UK), Phillip D. Szuromi, Sacha Vignieri **SR. EDITORIAL FELLOW** Andrew M. Sugden (UK) **SR. EDITORS** Gemma Alderton (UK), Caroline Ash (UK), Brent Grocholski, Pamela J. Hines, Paula A. Kiberstis, Marc S. Lavine (Canada), Steve Mao, Ian S. Osborne (UK), Beverly A. Purnell, L. Bryan Ray, H. Jesse Smith, Keith T. Smith (UK), Jelena Stajic, Peter Stern (UK), Valerie B. Thompson, Brad Wible, Laura M. Zahn **ASSOCIATE EDITORS** Michael A. Funk, Priscilla N. Kelly, Tage S. Rai, Seth Thomas Scanlon (UK), Yury V. Suleymanov **LETTERS EDITOR** Jennifer Sills **LEAD CONTENT PRODUCTION EDITORS** Harry Jach, Lauren Kmec **CONTENT PRODUCTION EDITORS** Amelia Beyna, Jeffrey E. Cook, Chris Filiatreau, Julia Katris, Nida Masiulis, Suzanne M. White **SR. EDITORIAL COORDINATORS** Carolyn Kyle, Beverly Shields **EDITORIAL COORDINATORS** Aneera Dobbins, Joi S. Granger, Jeffrey Hearn, Lisa Johnson, Maryrose Madrid, Ope Martins, Shannon McMahon, Jerry Richardson, Alana Warnke, Alice Whaley (UK), Anita Wynn **PUBLICATIONS ASSISTANTS** Jeremy Dow, Alexander Kief, Ronmel Navas, Hilary Stewart (UK), Brian White **EXECUTIVE ASSISTANT** Jessica Slater **ASI DIRECTOR, OPERATIONS** Janet Clements (UK) **ASI SR. OFFICE ADMINISTRATOR** Jessica Waldock (UK)

News Editor Tim Appenzeller

NEWS MANAGING EDITOR John Travis **INTERNATIONAL EDITOR** Martin Enserink **DEPUTY NEWS EDITORS** Elizabeth Culotta, Lila Guterman, David Grimm, Eric Hand (Europe), David Malakoff **SR. CORRESPONDENTS** Daniel Clery (UK), Jon Cohen, Jeffrey Mervis, Elizabeth Pennisi **ASSOCIATE EDITORS** Jeffrey Brainard, Catherine Matacic **NEWS REPORTERS** Adrian Cho, Jennifer Couzin-Frankel, Jocelyn Kaiser, Kelly Servick, Robert F. Service, Erik Stokstad, Paul Voosen, Meredith Wadman **INTERNS** Eva Frederick, Rodrigo Perez Ortega **CONTRIBUTING CORRESPONDENTS** Warren Cornwall, Ann Gibbons, Mara Hvistendahl, Sam Kean, Eli Kintisch, Kai Kupferschmidt (Berlin), Andrew Lawler, Mitch Leslie, Eliot Marshall, Virginia Morell, Dennis Normile (Shanghai), Elisabeth Pain (Careers), Charles Piller, Michael Price, Tania Rabesandratana (Barcelona), Emily Underwood, Gretchen Vogel (Berlin), Lizzie Wade (Mexico City) **CAREERS** Donisha Adams, Rachel Bernstein (Editor), Katie Langin(acting editor) **COPY EDITORS** Julia Cole (Senior Copy Editor), Cyra Master (Copy Chief) **ADMINISTRATIVE SUPPORT** Meagan Weiland

Creative Director Beth Rakouskas

DESIGN MANAGING EDITOR Marcy Atarod **GRAPHICS MANAGING EDITOR** Alberto Cuadra **PHOTOGRAPHY MANAGING EDITOR** William Douthitt **WEB CONTENT STRATEGY MANAGER** Kara Estelle-Powers **SENIOR DESIGNER** Chrystal Smith **DESIGNER** Christina Aycock **GRAPHICS EDITOR** Nirja Desai **INTERACTIVE GRAPHICS EDITOR** Xing Liu **SENIOR SCIENTIFIC ILLUSTRATORS** Valerie Altounian, Chris Bickel **SCIENTIFIC ILLUSTRATOR** Alice Kitterman **SENIOR GRAPHICS SPECIALISTS** Holly Bishop, Nathalie Cary **SENIOR PHOTO EDITOR** Emily Petersen **PHOTO EDITOR** Kaitlyn Dolan

Chief Executive Officer and Executive Publisher Sudip Parikh

Publisher, Science Family of Journals Bill Moran

DIRECTOR, BUSINESS SYSTEMS AND FINANCIAL ANALYSIS Randy Yi **DIRECTOR, BUSINESS OPERATIONS & ANALYSIS** Eric Knott **DIRECTOR OF ANALYTICS** Enrique Gonzales **MANAGER, BUSINESS OPERATIONS** Jessica Tierney **SENIOR BUSINESS ANALYST** Cory Lipman, Meron Kebede **FINANCIAL ANALYST** Alexander Lee **ADVERTISING SYSTEM ADMINISTRATOR** Tina Burks **SENIOR SALES COORDINATOR** Shirley Young **DIGITAL/PRINT STRATEGY MANAGER** Jason Hillman **QUALITY TECHNICAL MANAGER** Marcus Spiegler **ASSISTANT MANAGER DIGITAL/PRINT** Rebecca Doshi **SENIOR CONTENT SPECIALISTS** Steve Forrester, Jacob Hedrick, Antoinette Hodal, Lori Murphy **DIGITAL PRODUCTION MANAGER** Lisa Stanford **CONTENT SPECIALIST** Kimberley Oster **ADVERTISING PRODUCTION OPERATIONS MANAGER** Deborah Tompkins **DESIGNER, CUSTOM PUBLISHING** Jeremy Huntsinger **SR. TRAFFIC ASSOCIATE** Christine Hall **SPECIAL PROJECTS ASSOCIATE** Sarah Dhere

ASSOCIATE DIRECTOR, BUSINESS DEVELOPMENT Justin Sawyers **GLOBAL MARKETING MANAGER** Allison Pritchard **DIGITAL MARKETING MANAGER** Aimee Aponte **JOURNALS MARKETING MANAGER** Shawana Arnold **MARKETING ASSOCIATES** Tori Velasquez, Mike Romano, Ashley Hylton **DIGITAL MARKETING SPECIALIST** Asleigh Rojanavongse **SENIOR DESIGNER** Kim Huynh

DIRECTOR AND SENIOR EDITOR, CUSTOM PUBLISHING Sean Sanders **ASSISTANT EDITOR, CUSTOM PUBLISHING** Jackie Oberst

DIRECTOR, PRODUCT & PUBLISHING DEVELOPMENT Chris Reid **DIRECTOR, BUSINESS STRATEGY AND PORTFOLIO MANAGEMENT** Sarah Whalen **ASSOCIATE DIRECTOR, PRODUCT MANAGMENT** Kris Bishop **SR. PRODUCT ASSOCIATE** Robert Koepke **DIGITAL PRODUCT STRATEGIST** Michael Hardesty **SPJ ASSOCIATE** Samantha Bruno Fuller

DIRECTOR, INSTITUTIONAL LICENSING Iquo Edim **ASSOCIATE DIRECTOR, RESEARCH & DEVELOPMENT** Elisabeth Leonard **MARKETING MANAGER** Kess Knight **SENIOR INSTITUTIONAL LICENSING MANAGER** Ryan Rexroth **INSTITUTIONAL LICENSING MANAGER** Marco Castellan **MANAGER, AGENT RELATIONS & CUSTOMER SUCCESS** Judy Lillibridge **SENIOR OPERATIONS ANALYST** Lana Guz **FULFILLMENT COORDINATOR** Melody Stringer **SALES COORDINATOR** Josh Haverlock

DIRECTOR, GLOBAL SALES Tracy Holmes **US EAST COAST AND MID WEST SALES** Stephanie O'Connor **US WEST COAST SALES** Lynne Stickrod **US SALES MANAGER, SCIENCE CAREERS** Claudia Paulsen-Young **US SALES REP, SCIENCE CAREERS** Tracy Anderson **ASSOCIATE DIRECTOR, ROW** Roger Goncalves **SALES REP, ROW** Sarah Lelarge **SALES ADMIN ASSISTANT, ROW** Bryony Cousins **DIRECTOR OF GLOBAL COLLABORATION AND ACADEMIC PUBLISHING RELATIONS, ASIA** Xiaoying Chu **ASSOCIATE DIRECTOR, INTERNATIONAL COLLABORATION** Grace Yao **SALES MANAGER** Danny Zhao **MARKETING MANAGER** Kilo Lan **ASCA CORPORATION, JAPAN** Kaoru Sasaki (Tokyo), Miyuki Tani (Osaka) **COLLABORATION/CUSTOM PUBLICATIONS/JAPAN** Adarsh Sandhu

DIRECTOR, COPYRIGHT, LICENSING AND SPECIAL PROJECTS Emilie David **RIGHTS AND LICENSING COORDINATOR** Jessica Adams **RIGHTS AND PERMISSIONS ASSOCIATE** Elizabeth Sandler **CONTRACTS AND LICENSING ASSOCIATE** Lili Catlett

---

MAIN HEADQUARTERS
Science/AAAS
1200 New York Ave. NW
Washington, DC 20005

SCIENCE INTERNATIONAL
Clarendon House
Clarendon Road
Cambridge, CB2 8FH, UK

SCIENCE CHINA
Room 1004, Culture Square
No. 59 Zhongguancun St.
Haidian District, Beijing, 100872

SCIENCE JAPAN
ASCA Corporation
Sibaura TY Bldg. 4F, 1-14-5
Shibaura Minato-ku
Tokyo, 108-0073 Japan

EDITORIAL
science_editors@aaas.org

NEWS
science_news@aaas.org

INFORMATION FOR AUTHORS
sciencemag.org/authors/science-information-authors

REPRINTS AND PERMISSIONS
sciencemag.org/help/reprints-and-permissions

MEDIA CONTACTS
scipak@aaas.org

MULTIMEDIA CONTACTS
SciencePodcast@aaas.org
ScienceVideo@aaas.org

INSTITUTIONAL SALES AND SITE LICENSES
sciencemag.org/librarian

PRODUCT ADVERTISING & CUSTOM PUBLISHING
advertising.sciencemag.org/products-services
science_advertising@aaas.org

CLASSIFIED ADVERTISING
advertising.sciencemag.org/science-careers
advertise@sciencecareers.org

JOB POSTING CUSTOMER SERVICE
employers.sciencecareers.org
support@sciencecareers.org

MEMBERSHIP AND INDIVIDUAL SUBSCRIPTIONS
sciencemag.org/subscriptions

MEMBER BENEFITS
aaas.org/membercentral

AAAS BOARD OF DIRECTORS
CHAIR Margaret A. Hamburg
PRESIDENT Steven Chu
PRESIDENT-ELECT Claire M. Fraser
TREASURER Carolyn N. Ainslie
INTERIM CHIEF EXECUTIVE OFFICER Alan Leshner
BOARD Cynthia M. Beall, May R. Berenbaum, Rosina M. Bierbaum, Ann Bostrom, Stephen P. A. Fodor, S. James Gates, Jr., Laura H. Greene, Kaye Husbands Fealing, Maria Klawe, Robert B. Millard, William D. Provine

Science serves as a forum for discussion of important issues related to the advancement of science by publishing material on which a consensus has been reached as well as including the presentation of minority or conflicting points of view. Accordingly, all articles published in *Science*—including editorials, news and comment, and book reviews—are signed and reflect the individual views of the authors and not official points of view adopted by AAAS or the institutions with which the authors are affiliated.

BOARD OF REVIEWING EDITORS (Statistics board members indicated with **S**)

Adriano Aguzzi, *U. Hospital Zürich*
Takuzo Aida, *U. of Tokyo*
Leslie Aiello, *Wenner-Gren Foundation*
Judith Allen, *U. of Manchester*
Sebastian Amigorena, *Institut Curie*
James Analytis, *U. of California, Berkeley*
Paola Arlotta, *Harvard U.*
Johan Auwerx, *EPFL*
David Awschalom, *U. of Chicago*
Clare Baker, *U. of Cambridge*
Nenad Ban, *ETH Zürich*
Franz Bauer, *Pontificia Universidad Católica de Chile*
Ray H. Baughman, *U. of Texas at Dallas*
Peter Bearman, *Columbia U.*
Carlo Beenakker, *Leiden U.*
Yasmine Belkaid, *NIAID, NIH*
Philip Benfey, *Duke U.*
Gabriele Bergers, *VIB*
Bradley Bernstein, *Mass. General Hospital*
Alessandra Biffi, *Harvard Med. School*
Peer Bork, *EMBL*
Chris Bowler, *École Normale Supérieure*
Ian Boyd, *U. of St. Andrews*
Emily Brodsky, *U. of California, Santa Cruz*
Ron Brookmeyer, *U. of California, Los Angeles* (**S**)
Christian Büchel, *UKE Hamburg*
Dennis Burton, *Scripps Research*
Carter Tribley Butts, *U. of California, Irvine*
György Buzsáki, *New York U. School of Med.*
Blanche Capel, *Duke U.*
Annmarie Carlton, *U. of California, Irvine*
Nick Chater, *U. of Warwick*
Zhijian Chen, *UT Southwestern Med. Ctr.*
Ib Chorkendorff, *Denmark TU*
James J. Collins, *MIT*
Robert Cook-Deegan, *Arizona State U.*
Alan Cowman, *Walter & Eliza Hall Inst.*
Carolyn Coyne, *U. of Pittsburgh*
Roberta Croce, *VU Amsterdam*
Jeff L. Dangl, *U. of North Carolina*
Tom Daniel, *U. of Washington*
Chiara Daraio, *Caltech*
Nicolas Dauphas, *U. of Chicago*
Frans de Waal, *Emory U.*
Claude Desplan, *New York U.*
Sandra Díaz, *Universidad Nacional de Córdoba*
Ulrike Diebold, *TU Wien*
Hong Ding, *Inst. of Physics, CAS*
Jennifer Dionne, *Stanford U.*
Dennis Discher, *U. of Penn.*
Gerald Dorn, *Washington U. in St. Louis*
Jennifer A. Doudna, *U. of California, Berkeley*
Bruce Dunn, *U. of California, Los Angeles*
William Dunphy, *Caltech*
Christopher Dye, *U. of Oxford*
Todd Ehlers, *U. of Tübingen*
Jennifer Elisseeff, *Johns Hopkins U.*
Tim Elston, *U. of North Carolina*
Andrea Encalada, *U. San Francisco de Quito*
Nader Engheta, *U. of Penn.*
Karen Ersche, *U. of Cambridge*
Barry Everitt, *U. of Cambridge*
Vanessa Ezenwa, *U. of Georgia*
Michael Feuer, *The George Washington U.*
Toren Finkel, *U. of Pittsburgh Med. Ctr.*
Gwenn Flowers, *Simon Fraser U.*
Peter Fratzl, *Max Planck Inst. Potsdam*
Elaine Fuchs, *Rockefeller U.*
Eileen Furlong, *EMBL*
Jay Gallagher, *U. of Wisconsin*
Daniel Geschwind, *U. of California, Los Angeles*
Karl-Heinz Glassmeier, *TU Braunschweig*
Ramon Gonzalez, *U. of South Florida*
Elizabeth Grove, *U. of Chicago*
Nicolas Gruber, *ETH Zürich*
Kip Guy, *U. of Kentucky College of Pharmacy*
Taekjip Ha, *Johns Hopkins U.*
Christian Haass, *Ludwig Maximilians U.*
Sharon Hammes-Schiffer, *Yale U.*
Wolf-Dietrich Hardt, *ETH Zürich*
Louise Harra, *U. College London*
Jian He, *Clemson U.*
Carl-Philipp Heisenberg, *IST Austria*
Ykä Helariutta, *U. of Cambridge*
Janet G. Hering, *Eawag*
Hans Hilgenkamp, *U. of Twente*
Kai-Uwe Hinrichs, *U. of Bremen*
David Hodell, *U. of Cambridge*
Lora Hooper, *UT Southwestern Med. Ctr.*
Fred Hughson, *Princeton U.*
Randall Hulet, *Rice U.*
Auke Ijspeert, *EPFL*
Akiko Iwasaki, *Yale U.*
Stephen Jackson, *USGS and U. of Arizona*
Kai Johnsson, *EPFL*
Peter Jonas, *IST Austria*
Matt Kaeberlein, *U. of Washington*
William Kaelin Jr., *Dana-Farber Cancer Inst.*
Daniel Kammen, *U. of California, Berkeley*
V. Narry Kim, *Seoul Nat. U.*
Robert Kingston, *Harvard Med. School*
Nancy Knowlton, *Smithsonian Institution*
Etienne Koechlin, *École Normale Supérieure*
Alexander Kolodkin, *Johns Hopkins U.*
Thomas Langer, *U. of Cologne*
Mitchell A. Lazar, *U. of Penn.*
Ottoline Leyser, *U. of Cambridge*
Wendell Lim, *U. of California, San Francisco*
Marcia C. Linn, *U. of California, Berkeley*
Jianguo Liu, *Michigan State U.*
Luis Liz-Marzán, *CIC biomaGUNE*
Jonathan Losos, *Washington U. in St. Louis*
Ke Lu, *Chinese Acad. of Sciences*
Christian Lüscher, *U. of Geneva*
Fabienne Mackay, *U. of Melbourne*
Anne Magurran, *U. of St. Andrews*
Oscar Marín, *King's College London*
Charles Marshall, *U. of California, Berkeley*
Christopher Marx, *U. of Idaho*
Geraldine Masson, *CNRS*
C. Robertson McClung, *Dartmouth College*
Rodrigo Medellín, *U. of Mexico*
Graham Medley, *London School of Hygiene & Tropical Med.*
Jane Memmott, *U. of Bristol*
Edward Miguel, *U. of California, Berkeley*
Tom Misteli, *NCI, NIH*
Yasushi Miyashita, *U. of Tokyo*
Alison Motsinger-Reif, *NC State U.* (**S**)
Daniel Nettle, *Newcastle U.*
Daniel Neumark, *U. of California, Berkeley*
Beatriz Noheda, *U. of Groningen*
Helga Nowotny, *Austrian Council*
Rachel O'Reilly, *U. of Warwick*
Harry Orr, *U. of Minnesota*
Pilar Ossorio, *U. of Wisconsin*
Andrew Oswald, *U. of Warwick*
Isabella Pagano, *Istituto Nazionale di Astrofisica*
Margaret Palmer, *U. of Maryland*
Elizabeth Levy Paluck, *Princeton U.*
Jane Parker, *Max Planck Inst. Cologne*
Giovanni Parmigiani, *Dana-Farber Cancer Inst.* (**S**)
Samuel Pfaff, *Salk Inst. for Biological Studies*
Julie Pfeiffer, *UT Southwestern Med. Ctr.*
Matthieu Piel, *Institut Curie*
Kathrin Plath, *U. of California, Los Angeles*
Martin Plenio, *Ulm U.*
Katherine Pollard, *U. of California, San Francisco*
Elvira Poloczanska, *Alfred-Wegener-Inst.*
Julia Pongratz, *Ludwig Maximilians U.*
Philippe Poulin, *CNRS*
Jonathan Pritchard, *Stanford U.*
Félix A. Rey, *Institut Pasteur*
Trevor Robbins, *U. of Cambridge*
Joeri Rogelj, *Imperial College London*
Amy Rosenzweig, *Northwestern U.*
Mike Ryan, *U. of Texas at Austin*
Mitinori Saitou, *Kyoto U.*
Shimon Sakaguchi, *Osaka U.*
Miquel Salmeron, *Lawrence Berkeley Nat. Lab*
Nitin Samarth, *Penn. State U.*
Jürgen Sandkühler, *Med. U. of Vienna*
Alexander Schier, *Harvard U.*
Wolfram Schlenker, *Columbia U.*
Susannah Scott, *U. of California, Santa Barbara*
Rebecca Sear, *London School of Hygiene & Tropical Med.*
Vladimir Shalaev, *Purdue U.*
Jie Shan, *Cornell U.*
Beth Shapiro, *U. of California, Santa Cruz*
Jay Shendure, *U. of Washington*
Steve Sherwood, *U. of New South Wales*
Brian Shoichet, *U. of California, San Francisco*
Robert Siliciano, *Johns Hopkins U. School of Med.*
Lucia Sivilotti, *U. College London*
Alison Smith, *John Innes Centre*
Richard Smith, *U. of North Carolina* (**S**)
Mark Smyth, *QIMR Berghofer*
Pam Soltis, *U. of Florida*
John Speakman, *U. of Aberdeen*
Tara Spires-Jones, *U. of Edinburgh*
Allan C. Spradling, *Carnegie Institution for Science*
V. S. Subrahmanian, *U. of Maryland*
Ira Tabas, *Columbia U.*
Sarah Teichmann, *U. of Cambridge*
Rocio Titiunik, *Princeton U.*
Shubha Tole, *Tata Inst. of Fundamental Research*
Wim van der Putten, *Netherlands Inst. of Ecology*
Reinhilde Veugelers, *KU Leuven*
Bert Vogelstein, *Johns Hopkins U.*
Kathleen Vohs, *U. of Minnesota*
David Wallach, *Weizmann Inst. of Science*
Jane-Ling Wang, *U. of California, Davis* (**S**)
David Waxman, *Fudan U.*
Jonathan Weissman, *U. of California, San Francisco*
Chris Wikle, *U. of Missouri* (**S**)
Terrie Williams, *U. of California, Santa Cruz*
Ian A. Wilson, *Scripps Research* (**S**)
Yu Xie, *Princeton U.*
Jan Zaanen, *Leiden U.*
Kenneth Zaret, *U. of Penn. School of Med.*
Jonathan Zehr, *U. of California, Santa Cruz*
Xiaowei Zhuang, *Harvard U.*
Maria Zuber, *MIT*

EDITORIAL

For science, Brexit isn't done yet

If there's one sentiment that papers over the cracks in a once-United Kingdom, it's bone-weariness over Brexit. Wherever one entered the debate back in 2016—on the side of the United Kingdom leaving or remaining in the European Union (EU)—most people simply want an end to the saga, which has spewed uncertainty and paralyzed decision-making for almost 4 years. A pre-Christmas campaign pledge to "get Brexit done" propelled Prime Minister Boris Johnson back into Downing Street with a Conservative dominance of the political landscape unseen since Margaret Thatcher's heyday. One week after its reelection, the government passed the Brexit withdrawal bill, and at midnight on 31 January, the United Kingdom departed. With the democratic die now cast, universities, scientific organizations, and individual researchers must figure out how to constructively engage with Europe. Is there a soft landing for science on the other side of the leap into the dark that has just been taken?

The United Kingdom now enters an 11-month transition period, in which scientific collaboration—and the precise form of any U.K. involvement in Horizon Europe, the EU's next 7-year, multibillion euro research program—is one of a daunting list of agenda items that need to be resolved as part of any comprehensive EU-UK agreement. Throughout this transition, which runs until 31 December 2020, the United Kingdom's scientific community will continue to make a case for collaboration and for preserving the mobility of researchers.

Buoyed by his election victory, Prime Minister Johnson is so confident that he can achieve an agreement at record-breaking speed that he included in his withdrawal bill a clause outlawing any extension to the transitional arrangements. Senior figures in the European Commission, and most trade experts, warn that negotiations will take far longer. If the experts are right, and if the United Kingdom refuses to be flexible, then the United Kingdom could be back on the precipice of a no-deal Brexit in a matter of months. "Get Brexit done" may have worked as an election slogan, but it leaves unresolved numerous policy trade-offs that have bedeviled Brexit discussions since 2016.

"...much remains at stake over the next 12 months."

Others hope that it may be possible to fast-track a bespoke deal on research, in the margins of wider trade talks. A fascinating report released late last month by the Wellcome Trust and the think-tank Bruegel, entitled "A post-Brexit agreement for research and innovation," describes in detail the results of a simulated negotiation between the United Kingdom and EU. Such textured engagement by science funders and policy-makers in the fine print of the negotiations is vital but can't ultimately predict the outcome of a deeply political process, in which science and innovation will inevitably be traded off by both sides against competing interests and priorities.

Last week, the U.K. government announced a substantially expanded category of "global talent visas," an effort to signal that it will continue to support the mobility of international researchers into the United Kingdom. Prime Minister Johnson has stated that he wishes to see ongoing UK-EU collaboration in research and has pledged an £18 billion (GBP) doubling of public spending on research by 2025, as part of a renewed commitment to boosting overall research and development investment to 2.4% of gross domestic product. He also plans to rebalance research funding toward poorer regions of the country and to create a new agency for "high-risk, high-payoff research" modeled on the U.S. Defense Advanced Research Projects Agency. Even in the depths of a British winter, such largesse would normally provoke a warm response from the research community. But trust and confidence remain in short supply.

Beyond the political grandstanding, U.K. science remains, in essence, stuck at the Brexit crossroads it arrived at some 43 months ago. The United Kingdom has now departed from the EU, but its journey's end is far from clear. In contrast to the Prime Minister's ebullience, Venki Ramakrishnan, president of the Royal Society, is one of many voices reminding us how much remains at stake over the next 12 months. "If we get it wrong, the damage could cripple the UK for at least a generation."

–James Wilsdon

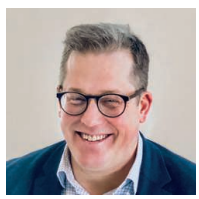

James Wilsdon is a professor of research policy at the University of Sheffield, Sheffield, UK, and director of the Research on Research Institute (RoRI), London, UK. j.wilsdon@sheffield.ac.uk

10.1126/science.abb0976

CREDITS: (PHOTO) AARTI BASNYAT; (ILLUSTRATION) MALTE MUELLER/GETTY IMAGES

Published by AAAS

NEWS

> “Employees … are questioning whether they should post potentially life-saving info or check tweets first.”
>
> **A September 2019 email by a National Weather Service official**, reported by *The Washington Post*, after superiors rebuked forecasters for contradicting the president’s inaccurate tweets about Hurricane Dorian’s path.

IN BRIEF

Edited by **Jeffrey Brainard**

Workers in Shanghai wearing makeshift protective suits help residents register to purchase face masks.

INFECTIOUS DISEASE

China virus response criticized as slow

As the novel coronavirus that emerged in Wuhan spreads worldwide (p. 610), China is facing criticism that its initial response was slow, and questions persist about officials’ openness. People in and outside of China have praised an early warning about mysterious illnesses, sounded in a message sent 30 December 2019 by Li Wenliang, an ophthalmologist at a Wuhan hospital, to his medical school classmates. On 3 January, however, local police summoned Li, chastised him for spreading socially disruptive rumors, and made him sign a letter of self-criticism. He has since become infected and was hospitalized. Last week, the country’s highest court faulted Li’s detention as overreach. China is waging a fierce battle against the virus; it built a new, 1000-bed hospital in Wuhan in just 10 days, and Chinese scientists have published several papers on the virus. But in a 30 January statement leaked on social media, China’s Ministry of Science and Technology urged researchers to pour their efforts into stopping its spread instead. “Until the task of prevention and control is completed, the focus should not be on the publication of papers,” the statement says.

Colombian science head faulted

LEADERSHIP | Some researchers in Colombia are calling for a little-known molecular biologist appointed as the country’s first ever science minister to resign. They are outraged by reports that she treated cancer patients with a fungal extract, without running a formal clinical trial. “We can only regret that the course of how to do science in our country has been left in the hands of pseudoscience,” the Colombian Association of Medical Faculties wrote in a statement. In December 2019, Mabel Gisela Torres Torres was appointed to lead the newly created Ministry of Science, Technology and Innovation. In January, she told a newspaper she did not seek formal ethical, safety, and efficacy reviews of her work with patients because she believed the fungus posed no threat to human health. Her Ph.D. adviser has defended her and notes that metabolites in the fungi Torres studied have shown potential as a cancer treatment in cell and mouse studies.

Reaping resources from sewers

ENVIRONMENTAL SCIENCE | The world’s growing flows of wastewater offer a largely untapped, potentially lucrative source of energy, agricultural fertilizers, and water for irrigation, a comprehensive study says. The opportunities will increase as the annual volume of wastewater—now 380 billion cubic meters—expands by an estimated 51% by 2050, as populations and incomes multiply, says a team led by researchers at United Nations University’s Institute for Water, Environment, and

▲ Poop’s power potential

Converting carbon in municipal wastewater to methane and burning it to generate electricity could supply power to 5% of Earth’s population, a study says.

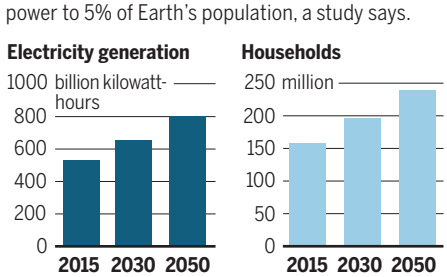

CREDITS: (PHOTO) *CHINA DAILY*/REUTERS; (GRAPHIC) J. BRAINARD/*SCIENCE*; (DATA) UNITED NATIONS UNIVERSITY INSTITUTE FOR WATER, ENVIRONMENT, AND HEALTH

Published by AAAS

A farmer tries to drive away locusts in Katitika, Kenya.

PHOTO: © FAO/SVEN TORFINN

AGRICULTURE

Locusts overrun Horn of Africa, threatening famine

The largest plague of desert locusts (*Schistocerca gregaria*) in decades is advancing across the Horn of Africa, consuming crops and threatening famine. The problem began in 2018 when unusually heavy rains on the Arabian Peninsula allowed populations to boom over several generations. In October 2019, the locusts swarmed south into Ethiopia, Eritrea, and Somalia, and in late December, they spread to Kenya, causing the worst infestation there in 70 years. Somalia—which last week declared a national emergency and asked for increased food aid—has already lost 100,000 hectares of crops and pasture. Another generation of locusts will likely hatch this month and cause more damage. The Food and Agriculture Organization of the United Nations called for $70 million to fight the outbreak with pesticides and help farmers.

Health. About 13% of global demand for fertilizer could be met by recovering nitrogen, phosphorus, and potash from wastewater; such use provides a bonus, diverting nutrients from waterways, where they can create harmful eutrophication. Sewage also offers an alternative energy source. The need to plan and finance such recovery efforts is greatest in "low- and middle-income countries, where most municipal wastewater still goes into the environment untreated," says the study, published 27 January in *Natural Resources Forum*.

Wildlife breeding plan criticized

CONSERVATION | A decision by South Africa's government to allow breeding and genetic research on more than 30 wild species—including rhinos, lions, and cheetahs—could considerably reduce their genetic diversity, scientists warned last week. The government's action has been interpreted to allow breeders to select for commercially desirable traits, such as longer horns or larger body size; that could create genetic bottlenecks by promoting a few stud lines, the researchers wrote in the *South African Journal of Science*. They added that it may prove expensive or impossible to keep the intensively bred animals from mating with wild counterparts. A handful of game ranchers requested the policy, which South Africa announced in May 2019 without consulting the public or studying potential consequences. Game ranching—for hunting, meat, and tourism—already occupies more than 15% of the country, and the government wants to expand the industry.

NSF 'big ideas' pay off

FUNDING | The U.S. National Science Foundation (NSF) announced this week seven winners in its contest for "big ideas" to address societal problems. Four winning teams will receive $26,000 each to develop ideas on topics ranging from using artificial intelligence for complex problem-solving to developing small-scale technologies that sequester carbon dioxide. Three more teams earned $10,000 as runners-up. The 2026 Idea Machine contest attracted almost 800 submissions, and although some high schoolers made it to the semifinals, all the winners work at research institutions. NSF hopes to fund workshops and exploratory grants to further develop these and other ideas from contestants.

Reproducibility tool scales up

PUBLISHING | A software company said last week it has teamed up with publishing giant Wiley to roll out in mid-2020 a tool that can signal whether findings in Wiley's scientific papers are reproducible. The software, called Scite.ai, uses artificial intelligence to examine articles that cite a paper, and determines and displays whether they provide evidence supporting or contradicting the paper's findings. Users can browse and search the relevant text of the citing articles. Scite CEO Josh Nicholson says the software allows users to home in on articles that attempted to reproduce a study; of every 100 citations analyzed, Scite has found that 94 merely

Published by AAAS

THREE QS

BRAIN Initiative gets leader

Since its launch in 2013, the U.S. Brain Research through Advancing Innovative Neurotechnologies (BRAIN) Initiative has doled out about $1.3 billion to develop tools that map and manipulate the brain. Until now, the multiagency effort has had no formal director. But last week, neurobiologist John Ngai of the University of California, Berkeley, was named to take the helm in March. (A longer version of the interview is at https://scim.ag/BRAINdirector.)

Q: Why is BRAIN getting a director?
A: The initiative has been run day to day by a terrific team of senior program directors and staff with oversight from the 10 [U.S. National Institutes of Health (NIH)] institutes and centers that are involved in BRAIN. I think as enterprises emerge from their startup phase, the question is how do you translate this into a sustainable enterprise, and yet maintain this cutting-edge innovation? ... The initiative really will benefit from somebody thinking about this 24/7.

Q: What distinguishes this second phase of BRAIN?
A: In the first phase, there was a very intentional and concentrated focus on tool development. As we learn more about how neural circuits drive behavior ... we can start implementing that knowledge, in terms of treating human diseases. I am hopeful that BRAIN, with other efforts in NIH and in partnership with industry, [can create] technology platforms that could be applied across multiple disease applications. For example: a toolkit of different types of viral delivery vectors [for gene therapy] that could be applied to different parts of the brain, different cell types in the brain, and so on.

Q: What do you see as the initiative's shortcomings?
A: We have a lot of figuring out to do in terms of how to balance the unique potential of individual investigator-initiated research versus the power of large-scale projects. ... [And] there is a diversity issue in terms of ethnic diversity as well as gender diversity [among applicants and funded investigators]. It's a hard problem. It just kills me that we're leaving all this talent on the table.

SCIENCEMAG.ORG/NEWS
Read more news from *Science* online.

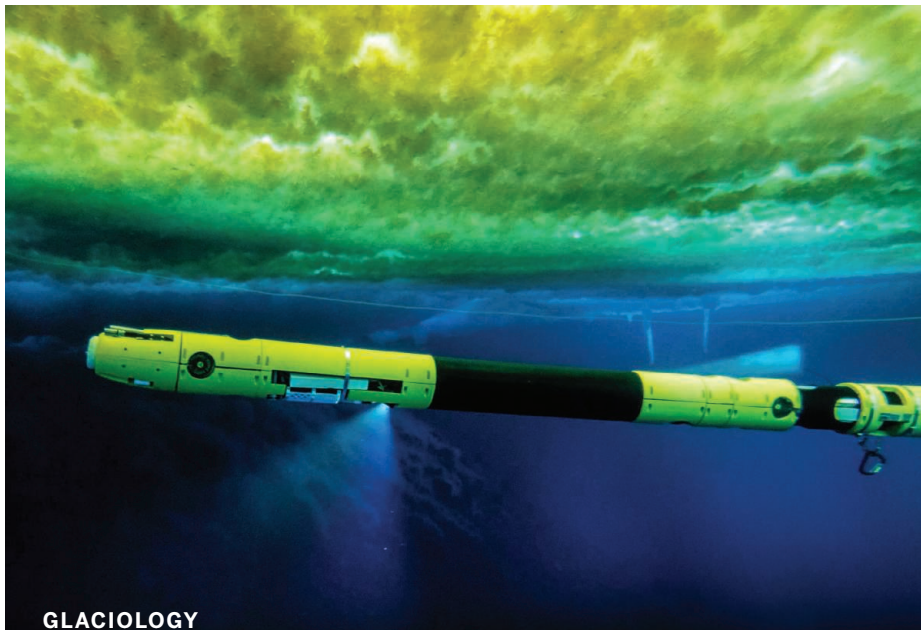

GLACIOLOGY

Warm waters revealed at base of menacing glacier

After dropping sensors and a torpedo-shaped robot through a 700-meter hole in the ice, scientists in Antarctica last week revealed the first direct evidence that warm ocean temperatures around the rapidly retreating Thwaites Glacier could destabilize the key ice sheet. Researchers are worried because Thwaites—larger than the state of Illinois—helps block the ocean from reaching and warming the even bigger, unstable West Antarctic Ice Sheet, whose melting could eventually drive meters of sea level rise. Battling 2 months of stormy conditions, the team measured ocean waters beneath Thwaites at more than 2°C above the freezing point. The robot, Icefin (above, shown operating elsewhere in Antarctica), provided the first images of the glacier's grounding zone, the mysterious boundary where the floating coastal ice sheet attaches to bedrock. The project is part of the International Thwaites Glacier Collaboration, a multiyear effort by the United States and the United Kingdom that is wrapping up its first full field season.

PHOTO: RISEUP/J. LAWRENCE

note the paper cited. The addition of Wiley's articles will expand Scite's current trove of more than 14 million papers from other publishers, most in the biomedical sciences. Nicholson expects his company to sign agreements with additional publishers to analyze their articles.

Rare disease grants awarded

BIOMEDICINE | The Chan Zuckerberg Initiative (CZI) said this week it will award $13.5 million to 30 patient advocacy groups to support their work finding treatments for rare diseases. Of an estimated 7000 rare diseases, fewer than 5% have treatments approved by the U.S. Food and Drug Administration. Each group will receive $450,000 over 2 years as well as training and mentoring as part of the foundation's Rare As One Project, launched last year to help advocates develop networks of patients, clinicians, and scientists. Most of the diseases are autoimmune, neurodegenerative, and other inherited disorders, but the list of diseases also includes rare cancers. CZI, founded by Facebook's Mark Zuckerberg and pediatrician Priscilla Chan, his wife, has made a few other awards to rare disease groups. The initiative expected to make just 10 Rare As One awards but tripled the number after receiving 275 applications.

Easing of bird fines proposed

CONSERVATION | The Trump administration proposed last week to end penalties on owners of open oil storage ponds and other industrial operations that kill birds accidentally. The administration will instead encourage voluntary efforts to protect birds. Conservation groups cried foul, saying the change to the Migratory Bird Treaty Act of 1918 will only embolden companies to take actions that threaten vulnerable species.

Published by AAAS

IN DEPTH

Travelers pass a checkpoint at the China-Russia border.

INFECTIOUS DISEASES

Will novel virus go pandemic or be contained?

Modelers are trying to forecast how the coronavirus will move, but they need better data

By **Kai Kupferschmidt** *and* **Jon Cohen**

The repatriation of 565 Japanese citizens from Wuhan, China, in late January offered scientists an unexpected opportunity to learn a bit more about the novel coronavirus (2019-nCoV) raging in that city. To avoid domestic spread of the virus, Japanese officials screened every passenger for disease symptoms and tested them for the virus after they landed. Eight tested positive, but four of those had no symptoms at all, says epidemiologist Hiroshi Nishiura of Hokkaido University, Sapporo—which is a bright red flag for epidemiologists who are trying to figure out what the fast-moving epidemic has in store for humanity. If many infections go unnoticed, as the Japanese finding suggests, that vastly complicates efforts to contain the outbreak.

Two months after 2019-nCoV emerged—and with well over 20,000 cases and 427 deaths as *Science* went to press—mathematical modelers have been racing to predict where the virus will move next, how big a toll it might ultimately take, and whether isolating patients and limiting travel will slow it. But to make confident predictions, they need to know much more about how easily the virus spreads, how sick it makes people, and whether infected people with no symptoms can still infect others.

Some of that information is coming out of China. But amid the all-out battle to control the virus, and with diagnostic capabilities in short supply, Chinese researchers cannot answer all the questions. Countries with just a handful of cases, such as Japan, can also reveal important data, says Preben Aavitsland of the Norwegian Institute of Public Health. "It's up to all countries now that receive cases to collect as much information as possible."

With the limited information so far, scientists are sketching out possible paths that the virus might take, weighing the likelihoods of each, and trying to determine the fallout. "We're at this stage where defined scenarios and the evidence for and against them are really important because it allows people to plan better," says Marc Lipsitch, an epidemiologist at the Harvard T.H. Chan School of Public Health. These scenarios break into two broad categories: The world gets the virus under control—or it doesn't.

SCENARIO 1: CONTAINMENT

The most optimistic scenario is one in which 2019-nCoV remains mostly confined to China, where 99% of the confirmed cases have occurred so far. (By 4 February, two dozen other countries had together reported 195 cases.) "There has obviously been a huge amount of spread within China, but [elsewhere], there's no evidence of any kind of substantial human-to-human transmission," says Robin Thompson, a mathematical epidemiologist at the University of Oxford. "The risk probably isn't as high as some models have been projecting."

If no other countries see sustained transmission and the quarantines and other measures taken in China start to reduce the number of infections there, the risk of spread might gradually go down, and the virus might eventually be quashed. This happened with the severe acute respiratory syndrome (SARS) outbreak in 2003, which ended after fewer than 9000 cases.

That's what the World Health Organization (WHO), which last week declared the outbreak a Public Health Emergency of International Concern, hopes for this time. In a press conference, Director-General Tedros Adhanom Ghebreyesus called for a global version of the approach his team took in the current Ebola outbreak: Fight the disease at the source and try to keep it from gaining a foothold elsewhere. "Focus on the epicenter," Tedros said. "If you have several epicenters, it is chaos."

Epidemiologist Marion Koopmans of Erasmus Medical Center says it may not be that hard to contain the virus in a new locale as long as the first cases are detected and isolated early—provided the virus is not highly transmissible. "We don't see it taking off in the 200 or so cases seeded outside of China,"

PHOTO: SVETLANA MAYOROVA/TASS/SIPA USA/NEWSCOM

Published by AAAS

Koopmans says. If that pattern holds, "there still is the possibility it will bend off."

She and others suspect the climate may help. Influenza typically only spreads during the winter months and hits northern and southern China at different times. If that is true for 2019-nCoV, its spread might start to slow down in the Northern Hemisphere within a few months. "That is a big question mark we're trying to assess at the moment," says Joseph Wu, a modeler at the University of Hong Kong.

But is containment realistic? Success will depend in part on whether infected people who don't have symptoms can spread the virus. Asymptomatic people are hard to find and isolate, so if they can spread disease, 2019-nCoV "will be very difficult to stop in China," says Alessandro Vespignani, a modeler of infectious diseases at Northeastern University. But if asymptomatic transmission is rare, he says, "isolation and social distancing can have a big impact."

So far it has been difficult to get a handle on this question. Some data from China seem to support asymptomatic transmission, but none are clear-cut. A widely reported 30 January letter in *The New England Journal of Medicine* described the case of a Chinese businesswoman who touched off a cluster of four cases in Germany before she became sick herself. But 4 days later, it became clear the researchers had not contacted the woman, who had flown back to China, before the paper was published. In a later phone interview, she said she had experienced some symptoms while in Germany.

In follow-up results announced in a 4 February press release, the researchers noted that some patients they studied shed virus even though their symptoms were mild. That's almost as bad as asymptomatic transmission, says virologist Christian Drosten of the Charité University Hospital in Berlin: Patients with mild symptoms are unlikely to seek medical care and may not even stay home, giving the virus ample opportunities to spread far and wide.

SCENARIO 2: PANDEMIC

Based on what they have seen so far, many researchers think it's probably too late to contain the virus. "As the virus continues to spread in China, the risk of exportation to other countries grows and sooner or later we will see it spread in another country," Aavitsland says. So far there has been no sustained transmission outside of China, but Lipsitch expects that to change: "I would be really shocked if in 2 or 3 weeks there wasn't ongoing transmission with hundreds of cases in several countries on several continents."

If the virus does spread to all corners of the world in a pandemic, several questions will loom large: What percentage of the population will become infected, and of those, how many will get very sick or die? More severe cases place heavier demands on health care systems—hospitals in Wuhan are already overwhelmed—and result in greater fears and disruption of daily life. A deadly pandemic might force the world to make stark choices about fair access to medicines or vaccines, if they become available. It might also lead to widespread restrictions on domestic travel akin to those already in force in China, Aavitsland says. If, on the other hand, 2019-nCoV resembles the common cold or a mild flu, the spread of the virus would be less alarming. Existing travel bans likely would be lifted.

Understanding the severity and case fatality rate is a challenge with any new pathogen. When a new influenza strain emerged in 2009—and went on to cause a pandemic—many worried it might turn out to be a nasty variety. It took months to establish that the new virus killed only about one in 10,000 patients.

So far, mortality among known 2019-nCoV cases is about 2%, and some reports say 20% of infected people suffer severe disease. But these figures may overlook tens of thousands of people with mild disease—say, a sore throat or a low-grade fever—who never seek medical care and may not even know they were infected with 2019-nCoV. Many may have no symptoms at all. "So what looks like a horrific disease may be the horrific tip of a very large iceberg," Lipsitch says.

The fact that four Japanese evacuees were asymptomatic is a case in point. Studies in China have also reported some cases with few or no symptoms. What's missing is a large study in China, Lipsitch says. He suggests some fraction of the tests that are available in a place with many cases should be set aside for that purpose. (Current recommendations in China call for testing people with clear symptoms only.)

If indeed 2019-nCoV becomes pandemic, humanity may be stuck with it indefinitely. After spreading far and wide, the virus might become endemic in the human population, just like four other coronaviruses that cause the common cold, and occasionally cause fresh outbreaks. How much death and disease it would cause is anyone's guess.

The silver lining of the epidemic is that scientists have collected and shared information at record speed. "Every day that goes by we know more and every day that goes by we can do better modeling," Vespignani says. "Unfortunately, this beast is moving very fast." ■

With reporting by Dennis Normile.

BIOMEDICINE

Combo of two HIV vaccines fails its big test

South African trial halted early because of "futility"

By **Jon Cohen**

The only HIV vaccine to show hints of working in a real-world test has failed in a $104 million trial in South Africa, which has been stopped early. "There's absolutely no evidence of efficacy," says Glenda Gray, who heads the study and is president of the South African Medical Research Council (MRC). It is another frustrating defeat in the decadeslong quest for a vaccine against the virus that causes AIDS. "Years of work went into this," Gray says. "It's a huge disappointment."

The study, which began in October 2016 and is known as HVTN 702, enrolled 5407 sexually active, HIV-uninfected men and women between 18 and 35 years of age at 14 sites across the country. Half of the participants received a pair of HIV vaccines used in a one-two punch called a prime boost, whereas the other half received placebo shots. The trial built on one from nearly 11 years ago in Thailand, which suggested a similar vaccine might deliver modest protection. HVTN 702 was supposed to last until July 2022, but on 23 January, an independent monitoring board that takes scheduled sneak peaks at the data informed study leaders it was "futile" to continue. There were 129 infections in the vaccinated group and 123 in those who received the placebo. "I was catatonic," Gray says.

Other HIV researchers say a clear verdict, even a negative one, is a step forward. "The trial was incredibly well done and we got a definitive answer, and that's what science is about," says Susan Buchbinder, an epidemiologist at the University of California, San Francisco. But the search for an HIV vaccine is far from over; Buchbinder, for example, is leading Mosaico, a large multicountry trial of a different vaccine combination.

The halted trial, funded by MRC, the U.S. National Institute of Allergy and Infectious Diseases (NIAID), and the Bill & Melinda Gates Foundation, used as "prime" a harmless canarypox virus that carries genes for HIV's surface protein and two of its other

Published by AAAS

structural proteins. Researchers hoped this mock infection with canarypox would rev up both the cell-killing and antibody-producing arms of the immune system. The boost contained a recombinant version of the surface protein mixed with an immune system booster, or adjuvant.

In the Thai study, a similar vaccine combination reduced infections by 31%. The field widely agreed that this wasn't good enough to bring the vaccine to market, but researchers were divided over whether it made sense to try to build on this vaccine strategy or abandon it.

Gray says the new trial, which used a slightly improved vaccine that was tailor-made for the HIV subtype circulating in South Africa, was worth the gamble given the severity of the epidemic there—it is home to 7.7 million of the world's 37.9 million HIV-infected people. "The epidemic is out of control here and we have to take steps to have a biomedical intervention," Gray says. NIAID Director Anthony Fauci says he has no regrets about backing the study, as no other vaccine had shown even modest promise in an efficacy study. "I don't think it was a bad choice. It was the only choice."

To this day, no one knows which immune responses can prevent an HIV infection, but many researchers have focused on creating a vaccine that can trigger antibodies capable of "neutralizing" the virus: blocking its ability to infect cells in lab studies. The vaccines in the Thai trial triggered production of antibodies that bound to HIV but did not neutralize it, Fauci notes, raising the possibility this was good enough to offer some protection. "We were struggling for years and years, and so we grabbed onto the slightest positive effect," he says. "Given the seriousness of the epidemic, if this was all we had and vaccines that stimulated neutralizing antibodies were years down the pipeline, do you do something or nothing?"

Fauci notes that the Thai study enrolled people at relatively low risk of HIV—their rate of new infections was about 0.3% per year. In the South Africa study, the rate of new infections per year was about 4% in women and 1% in men. That contrast might explain why the vaccine appeared to work in Thailand but not in South Africa. "It could be the protection was completely overwhelmed," Fauci says.

Mitchell Warren, who heads AVAC, a nonprofit HIV prevention advocacy group, says this latest failure won't slow the vaccine field. "There are other products in efficacy trials and there's a slightly larger pipeline in phase I trials than we've had in a long time," says Warren, who was on the monitoring board that recommended stopping the South African study. ■

OCEANS

Climate change spurs global speedup of ocean currents

Rising winds boost flows in tropics and Southern Ocean

By **Paul Voosen**

The oceans' great continent-wrapping currents, each one moving as much water as all the world's rivers combined, can rightly be considered the planet's circulatory system. And this circulation, it appears, has started to thump faster: For nearly 25 years the currents have been rapidly speeding up, partly because of global warming.

That's the conclusion of a new paper out this week in *Science Advances*. Based on observations combined with models, the authors claim that from 1990 to 2013, the energy of the currents increased by some 15% per decade. "This is a really huge increase," says Susan Wijffels, an oceanographer at the Woods Hole Oceanographic Institution. "It's going to stimulate a lot of other work." If the acceleration is real, it could affect jet streams, weather patterns, and the amount of heat stored in the ocean's depths.

Oceanographers have suspected that climate warming is affecting ocean circulation, but so far, observations haven't shown a trend, says Hu Shijian, an oceanographer at the Chinese Academy of Sciences's Institute of Oceanology and lead author of the study. The Kuroshio Current, running up Eastern Asia, has seemed stable, whereas the Agulhas, flowing along Africa's eastern coast, has broadened, fracturing into meandering eddies. The Atlantic Ocean's Gulf Stream may be weakening as Arctic melt slows its driver, the sinking of salty water in the North Atlantic, whereas currents in the Pacific Ocean have seen a strong uptick. Hu decided only a global view could reveal any overall trend.

No sustained, direct measurements of currents around the world are available, however. Instead, Hu's team turned to so-called reanalyses, which combine observations of the ocean and atmosphere with computer models to fill in the gaps and produce a global picture. The approach is tricky to use for time spans of decades: Changes in observations, for example when new satellites come online, can cause unknown biases.

So Hu's team combined five different reanalyses of ocean circulation, hoping their differing methods could reveal a true trend. From each one they extracted the ocean's kinetic energy month by month, at a coarse scale that would ignore the turbulence of eddies and storms. And each showed a distinct rise starting around 1990.

Was it real? A look at data from the Argo array, a fleet of nearly 4000 robotic floats deployed around the world, provided the best test. The floats have been bobbing up and down in the ocean's uppermost 2000 meters for the past 15 years, measuring temperature and salinity. They don't track velocity through the water column. But their data do indicate where winds have piled up water, helping create differences in pressure that drive large-scale flows. By combining those

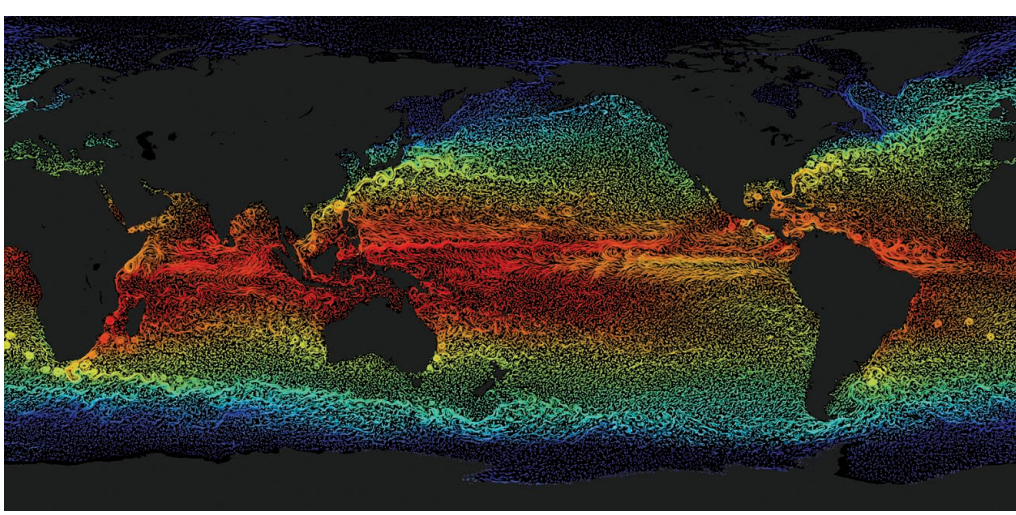

IMAGE: NASA/GODDARD SPACE FLIGHT CENTER SCIENTIFIC VISUALIZATION STUDIO

A warming climate appears to be altering global currents, reconstructed here from satellite and ship readings.

Published by AAAS

data with the floats' own current-borne trajectories, investigators can reconstruct overall currents and their speed.

The data set, compiled by oceanographer Alison Gray of the University of Washington, Seattle, covers only 6 years, from 2005 to 2010, but Hu found that it reveals an even clearer global speedup than the reanalysis models. "The evidence in the Argo data is absolutely astonishing," says Eleanor Frajka-Williams, an oceanographer at the United Kingdom's National Oceanography Centre, who was not part of the study.

Gray says she was startled by the magnitude of the acceleration. But she notes that ocean winds, which drive most currents, have steadily increased over the past 3 decades. And Hu says there's good evidence that human activity has contributed to that strengthening. For example, in the Southern Hemisphere, ozone depletion and greenhouse warming have altered atmospheric circulation to push the Southern Ocean's famed westerly winds to the south, perhaps causing a slight strengthening and spreading of the Antarctic Circumpolar Current. Meanwhile, heat from the warming tropical Atlantic has goosed the Walker Circulation, an equatorial pattern that drives the Pacific trade winds.

Still, natural fluctuations can't be ruled out, says Gerrit Lohmann, a climate scientist at the Alfred Wegener Institute. Over the past few decades, long-term cooling off western North America has caused Pacific winds to pick up—and that cooling may reflect natural oscillations in the ocean's state. Other researchers doubt these cycles exist (*Science*, 31 May 2019, p. 814). Either way, Hu thinks the oscillations could be responsible for at most one-third of the wind speedup.

The ocean acceleration could have globe-spanning effects. Stronger tropical currents could carry more warm water to higher latitudes, for example. Because carbon dioxide (CO_2) is less soluble in warm water, that could slow the ocean's uptake of CO_2 from the atmosphere. The high-latitude warming may also be shifting weather patterns. At the same time, Hu adds that by reaching deep into the ocean, the acceleration could boost the storage of heat in the depths, helping slow the warming on land. "This is the first global study," says Janet Sprintall, a co-author and oceanographer at the Scripps Institution of Oceanography. "There's a lot of uncertainty."

Oceanographers will likely fan out to test the study's findings. Perhaps the strongest confirmation could come from updated data from the Argo floats, due out later this year. Still, it will probably take another decade of observations to be sure the trend is real and driven by global warming, Wijffels says. "This paper does highlight how ill prepared we are to truly diagnose what's going on." ■

Jonathan Pruitt studies personalities of social spiders.

PHOTO: PROVIDED BY JONATHAN PRUITT

SCIENTIFIC INTEGRITY

Prominent spider biologist spun a web of questionable data

Two retractions spark scrutiny of dozens of papers

By **Elizabeth Pennisi**

In a swift rise to prominence, Jonathan Pruitt drew attention to the small field of behavioral ecology with eye-catching findings about contrasting personalities—meek and aggressive—in social spiders. But in just 2 weeks, the field has turned on its young star. What began with questions about data in one paper has flared into a scandal, with dozens of papers based on his data on spiders and other animals being scrutinized by scores of co-authors, including his former students and postdocs.

Already, two papers co-authored by Pruitt, who in 2018 was given a prestigious, well-funded Canada 150 Research Chair at McMaster University, have been retracted for data anomalies; a third journal is expected to expunge another soon. And the more Pruitt's co-authors look, the more potential data problems they find in his prolific output. Many additional retractions are expected, perhaps even an unprecedented number for behavioral ecology.

The furor has even earned a Twitter hashtag—#PruittData—where former collaborators and others are discussing how to analyze his results and debating the implications for their field. They are also voicing suspicions that the problems go beyond carelessness. "An important question that Pruitt should answer is how these data came about," says behavioral ecologist Niels Dingemanse of Ludwig Maximilian University of Munich. "We should see proof that there is nothing at fault here, because the patterns we see cannot easily be explained based on natural data collection processes."

As the storm rages, Pruitt is in the middle of 4 months of fieldwork in Australia and the South Pacific. He says he did not commit fraud and that the data issues are all mistakes. "These errors are not unheard of in data management," he told *Science* in his first interview since the retractions. But Pruitt acknowledges his career is likely over. "If a scientist can't be careful, that's as big an indictment as someone who goes around and adjusts data."

Spokespeople at McMaster and the University of California (UC), Santa Barbara, where Pruitt had a previous faculty position, acknowledged the allegations but would not say whether investigations had been launched. But Pruitt's fellow behavioral ecologists have not waited. They've launched their own investigations, hoping to control the damage to their field.

Some researchers have tweeted that the affair reflects a lack of scientific rigor in animal behavior studies, particularly those documenting distinct personalities in cognitively simple animals, but Pruitt's colleagues reject that. "It's a gross overstatement to say this is now the death of the field," Dingemanse says.

Last year, a young researcher not in Pruitt's lab came to behavioral ecologist Tom Tregenza of the University of Exeter with questions about a paper in *The American Naturalist* co-authored by Pruitt. Tregenza recruited Dingemanse and two other colleagues to probe the paper, which used social spiders as a test case to explore how social

Published by AAAS

interactions strengthen animal personalities and can help a population survive. They ran simulations of the experiments to see whether the data patterns could be real. The results were suspicious. "We were simply finding there were too many replicates of the same data points," Dingemanse says.

He then approached Pruitt's co-author, Kate Laskowski, a behavioral ecologist at UC Davis, and Daniel Bolnick, editor-in-chief of *The American Naturalist*. Laskowski found more questionable data, first in that paper and then in two others she'd co-authored with Pruitt; in each case, he had been the sole source of the animal data. Pruitt offered several explanations for these anomalies, Laskowski and Bolnick say, but ultimately, he agreed to a retraction of the initial paper, which the journal announced on 17 January.

Bolnick, a behavioral ecologist at the University of Connecticut, Storrs, then received dozens of emails, some anonymous, expressing unease with other papers involving Pruitt. He forwarded those emails to the research integrity office at McMaster and alerted other journals. He also recruited another editor at his journal and outside Pruitt's field, Jeremy Fox of the University of Calgary, to analyze the ecologist's body of work. Fox found many more data anomalies, even in Pruitt's Ph.D. thesis on spiders.

> **"Pruitt's explanation strikes me as ludicrously blasé. … The extent of the problems is hard to reconcile with accidents."**
>
> **Daniel Bolnick**, *The American Naturalist*

Bolnick then blogged on the matter and announced the creation of an online spreadsheet compiling Pruitt papers, with details about how the data in each were originally collected and how they are now being reanalyzed. So far, 23 journals are evaluating Pruitt's papers, he says. (The second retraction was in the *Proceedings of the Royal Society B. Biology Letters* may retract one next.) "I'm very concerned that people collaborating with him will be tarred with the same brush," Bolnick adds. "There are definitely papers out there [co-authored by Pruitt] where other people collected the data, and I consider those papers to be sound and trustworthy."

Noa Pinter-Wollman, a behavioral ecologist at UC Los Angeles, is among those suddenly re-evaluating her work. She teamed up with Pruitt 5 years ago to apply network analysis to Pruitt's spider data, and together they've published almost 20 papers. Pruitt alerted her to the first retraction 2 weeks ago, and she has been scrambling ever since. "We are focusing on data collected and curated by Jonathan," she says, searching for irregularities such as duplicated information or certain sequences of numbers that don't have the expected randomness. "This is the type of forensics that I never imagined I would have to do." Already, she says she's found three papers she wants to retract and has concerns about three more.

Pinter-Wollman cosigned a public statement released 29 January by Ambika Kamath, a behavioral ecologist at UC Berkeley and former Pruitt postdoc, and by some former and current Pruitt lab members and collaborators promising to get to the bottom of these problems. "We are working as a community to create a resource about which papers are reliable," Pinter-Wollman says. "But it's a tragedy for me. I lost a trusted collaborator."

Outgoing and energetic, Pruitt has won favorable press attention (including in *Science*) and generous research support: more than $600,000 in National Science Foundation funding before Canada lured him with a grant of $350,000 annually for 7 years. He is also well-liked. "I'm devastated," says his former graduate school adviser, Susan Riechert, a behavioral ecologist at the University of Tennessee, Knoxville. "He's very sharing of his work with other people and [with] credits."

Pruitt says he is puzzled by what's happening. "Each morning when I woke up, there was a different anonymous email taking issue with a different data set and a different paper," he tells *Science*. "Do they think I was just copying and pasting a spreadsheet? I don't think I would do that." But that explanation doesn't wash for Bolnick, given what he says is seen in raw data files. "Pruitt's explanation strikes me as ludicrously blasé. … The extent of the problems is hard to reconcile with accidents."

Colleagues want him to return home to address the concerns, but Pruitt says he's focusing on setting traps for insects and other invertebrates before and after cyclones hit to learn how the destruction affects different species—a follow-up on work he did examining a U.S. East Coast hurricane's effects on spiders. That work, published last year, is now being scrutinized.

The cyclone data will be useful no matter what happens, Pruitt says. "If I'm on fire and my longevity is [short], I will bequeath them to another researcher."

Even Pruitt's staunchest supporters now question his work, however. "I hope that it all turns out that he's been careless," Riechert says. "But if he has falsified data, then he has to pay the price." ■

FOREIGN INFLUENCE

Prosecutor details China probe that snared chemist

Department of Justice initiative aims to counter "corrupting" influence of foreign money on scientists

By **Jeffrey Mervis**

World-renowned inorganic chemist Charles Lieber has become the most prominent U.S. researcher to face charges stemming from undisclosed ties to Chinese research institutions. The Harvard University professor's 28 January arrest on charges of making false statements about those collaborations has also shined a spotlight on a 15-month campaign by federal prosecutors aimed at blunting China's aggressive efforts to acquire cutting-edge technologies.

In an interview last week with *Science*, Andrew Lelling, U.S. attorney for the Massachusetts district and part of a Department of Justice (DOJ) team leading its China Initiative, said Lieber's entanglements could have made him vulnerable to pressure from the Chinese government. "It was the amount of money involved that drew our attention," Lelling says, referring to a 2012 contract included in court documents that indicate Lieber received up to $50,000 a month in salary and millions of dollars in research support. "That is a corrupting level of money."

Lieber made things worse, Lelling says, by hiding that relationship from Harvard and federal agencies, including the Department of Defense, that have for decades funded his research. "When people begin to hide things, that's when law enforcement authorities get all excited."

Lieber has not been accused of transferring sensitive technology to China or economic espionage, that is, the theft of intellectual property.

Lelling and four other U.S. attorneys are managing the China Initiative, launched in November 2018. It has focused on what DOJ calls "nontraditional collaborators," and Lelling says the vast majority of the cases

Published by AAAS

U.S. Attorney Andrew Lelling helps lead the government's China Initiative, which began in 2018.

involve U.S.-based scientists working in the high-tech industry or academia, rather than someone sent by a foreign government to steal secrets.

Lieber, who was born and trained in the United States, is a member of both the U.S. national academies of sciences and medicine. He has pioneered work on the chemical synthesis of nanowires and their incorporation into devices including transistors, light emitters, and sensors, and at the time of his arrest was chair of Harvard's department of chemistry and chemical biology. In 2011, he began a collaboration with Wuhan University of Technology (WUT) in China that is at the center of his alleged violations. (WUT did not respond to requests for comment.)

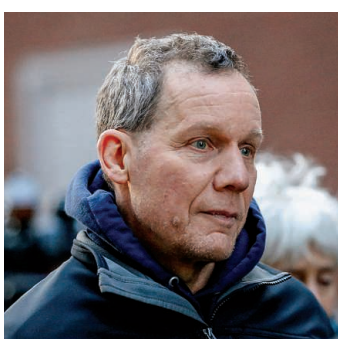

Charles Lieber is alleged to have lied about his links to China.

Lieber was released on 30 January after posting a bond of $1 million and agreeing to remain in Massachusetts. He has been suspended with pay from Harvard, which has called the charges "extremely serious" and says it is "cooperating with federal authorities." His lawyer, Peter Levitt, declined to comment on the charges.

Lelling says Lieber's stature was not a "deciding factor" in DOJ's decision to file criminal charges. "This wasn't about looking for a bigger scalp," Lelling insists. But, "The fact that Lieber is a prominent academic helps us to get out our message … that transparency works," he adds.

The DOJ team has been working closely with the National Institutes of Health (NIH), which also funded Lieber and has been much more aggressive than other federal agencies in pursuing apparent violations of federal policy requiring disclosure of foreign research support. Over the past 18 months, NIH has asked more than 60 institutions to investigate potentially questionable behavior by some 200 researchers.

Many are involved in one or more of the programs run by Chinese institutions to attract foreign talent. Lieber, for example, joined China's Thousand Talents Program in 2012, according to court documents. At least 15 scientists have resigned or been dismissed for undisclosed ties at half a dozen institutions.

"I think those [NIH] letters have had an *in terrorem* effect," Lelling says, using a legal term for how the threat of prosecution can scare people into law-abiding behavior. "And that's good, because you want a little bit of fear out there to sensitize people to the magnitude of the problem."

DOJ weighs several factors in deciding when to press charges, according to Lelling. "Is there deception?" he says. "How much money was involved? What kind of technology was transferred? And what other steps did a researcher take to develop the relationship?" The department's 89 field offices have been told "to be aggressive," he says, "because we want them to prioritize these cases."

Both DOJ and NIH are content to leave some cases to universities, he says. "There may be situations in which a professor has done something that doesn't quite reach the level of charging them with a federal felony," Lelling explains. "So maybe the federal authorities say to the university, 'You should deal with that.'"

However, he concedes that U.S. universities haven't been consistent in dealing with such cases. "The responses of universities to this kind of behavior have been all across the spectrum," Lelling told *Science*. "And obviously, we don't control what the universities do."

Lelling rejects criticism that the department has targeted ethnic Chinese people and other Asian Americans. "Dr. Lieber is probably the most prominent academic charged in this kind of case so far," Lelling says, "and he is not a Chinese national, nor is he of Chinese descent." But Lelling says many targets will inevitably be people of Chinese ancestry.

"The bottom line is that this is an effort by a rival nation state to steal U.S. technology, and that rival nation is made up almost exclusively of Han Chinese," Lelling says. "And so, unfortunately, a lot of our targets are going to be Han Chinese. If it were the French government targeting U.S. technology, we'd being looking for Frenchmen."

The two other people from the Boston area who were charged on the same day as Lieber are both ethnically Chinese. Ye Yanqing, a 29-year-old former student at Boston University, is charged with lying about her military affiliation; prosecutors allege she is a lieutenant in the Chinese military. Zheng Zaosong, a 30-year-old cancer researcher who worked at Beth Israel Deaconess Hospital, is charged with trying to smuggle 21 vials of biological material out of the country as well as lying about the contents of his suitcase to airport security agents. Ye is believed to be back in China, whereas Zheng has been detained since 30 December.

Lelling says he recognizes that international collaboration has boosted U.S. science, and he thinks that U.S.-trained scientists should be free to live and work anywhere. But he also believes that those who mingle their federal funding with support from Chinese institutions are playing a dangerous game.

"What concerns us … is that a scientist who accepts their support becomes dependent on it to the point where they are willing to accept [an assignment] from the Chinese government or a Chinese university for whatever it is they need," he says. "Those of us that work on public corruption cases develop a radar for when person or entity A is attempting to coopt or corrupt person or entity B. And a large enough amount of money can shift loyalties." ■

With reporting by Dennis Normile and Robert F. Service.

PHOTOS: (TOP TO BOTTOM) KATHERINE TAYLOR/REUTERS/NEWSCOM; KATHERINE TAYLOR/REUTERS

Published by AAAS

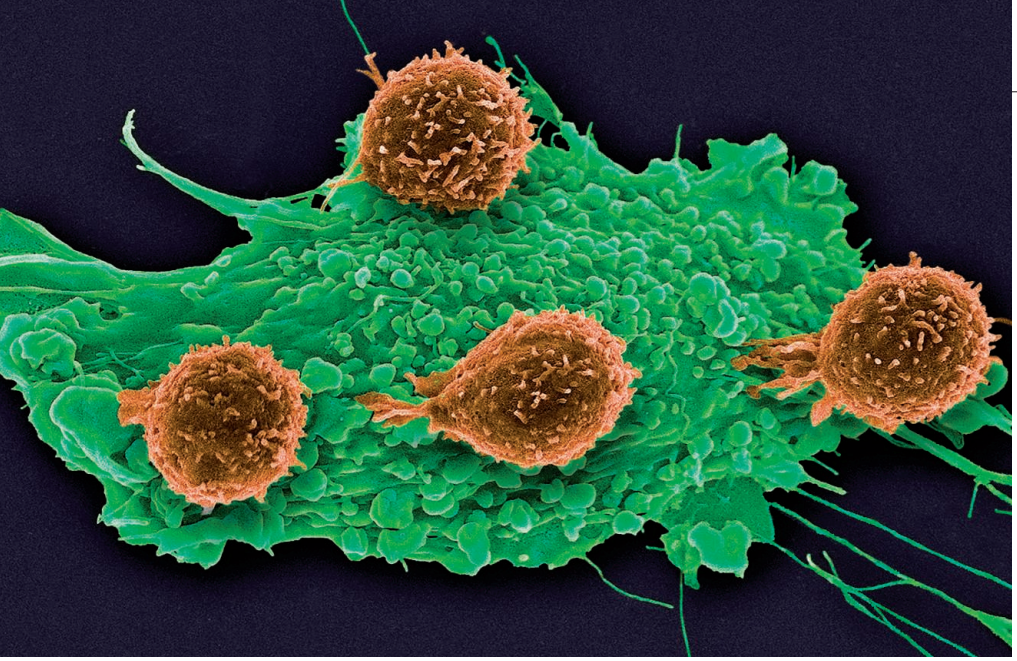

Immune cells (brown) attack a cancer cell. Using CRISPR could make the immune cells more potent.

IMAGE: STEVE GSCHMEISSNER/SCIENCE SOURCE

BIOMEDICINE

CRISPR takes on cancer

Gene edits appear safe in first three patients

By **Jennifer Couzin-Frankel**

Launching a new chapter in the fast-moving cancer immunotherapy field, scientists have blended two cutting-edge approaches: CRISPR, which edits DNA, and T cell therapy, in which sentries of the immune system are exploited to destroy tumors. Two women and one man, all in their 60s—one with sarcoma and two with the blood cancer multiple myeloma—received CRISPR-altered versions of their own cells last year, researchers report online in *Science* this week.

For these pioneers, the benefits were limited: One has since died, and the disease has worsened in the others. But the clinical trial, which underwent years of regulatory scrutiny, wasn't designed to try to cure cancer, says Carl June, a cancer researcher at the University of Pennsylvania (UPenn) who co-led the work. Rather, its goal was to show that the strategy appeared feasible and safe.

By that measure, scientists agree, it succeeded. "This is a Rubicon that has been decisively crossed," says Fyodor Urnov, a genome editor at the University of California (UC), Berkeley. The study, he says, the first of its kind in the United States, answers "questions that have frankly haunted the field."

The researchers used CRISPR alongside another strategy that incorporates new DNA into immune cells. June's team helped pioneer that strategy in 2010, when it added DNA to T cells from three men with chronic leukemia and returned those cells to the patients. The results were remarkable: Two men are still alive and healthy today. Others were testing the same approach, called CAR-T cell therapy—after the inserted chimeric antigen receptor gene that helps the infused T cells latch onto and destroy cancer cells with a specific protein on their surface. Two CAR-T cell therapies are now approved for patients with leukemia and lymphoma.

But with time, the therapy's limitations have come into focus. Not every cancer patient is helped, and even those who are can suffer a relapse, says Edward Stadtmauer, who treats blood cancers at UPenn and co-led the new study. And solid tumors like those in the brain and pancreas have proved tough to treat (*Science*, 2 September 2016, p. 983).

Using CRISPR to knock out selected genes while also adding DNA, it was hoped, might make T cells even more powerful and persistent. But CRISPR brought its own uncertainties. Lab studies have revealed "off-target" effects, in which unintended DNA gets modified. No one knew whether T cells with sliced and diced genes could even survive in the human body. Last year, Vertex Pharmaceuticals and CRISPR Therapeutics announced that two patients treated for inherited blood diseases with CRISPR-edited cells were doing well. But details were sparse.

June, Stadtmauer, and their colleagues began by hunting for patients whose tumors produced a protein called NY-ESO-1, a target for the gene the researchers would add to their T cells. The patients also needed to carry a specific version of human leukocyte antigen, an immune gene complex that could help the infused T cells flourish. The four patients who qualified were all extremely ill, as is the norm for such a novel therapy. A woman with multiple myeloma had undergone three bone marrow transplants. Another, in her late 30s with sarcoma, became too sick to treat while her cells were being prepped in the lab, a process that takes 4 to 6 weeks. She entered hospice care and died.

To try to rev up the patients' T cells against their disease, the scientists used CRISPR to knock out two genes that encode what's known as the T cell receptor. The group also crippled a third gene, for a protein called PD-1. PD-1 puts the brakes on immune responses, and eliminating its effects, June's team theorized, might enrich the T cells' powers. Then, they inserted the gene for a different T cell receptor that would target NY-ESO-1.

Intensive monitoring of the patients, including blood draws to study their altered T cells, confirmed that CRISPR had left some off-target changes. But they were few, and the number of cells with these unintended DNA changes faded over time. Encouragingly, the CRISPR-edited cells persisted at least 9 months—versus about 2 months in comparable CAR-T cell therapy studies. Imaging showed "beautiful, healthy T cells," June says, that in lab studies beat back cancer months after they'd been infused.

But in patients, outcomes were modest. The best response was in the sarcoma patient, whose primary tumor shrank, though his cancer later progressed. "It wasn't like you turned off those genes and those T cells started doing things that were amazing," says Antoni Ribas, an oncologist at UC Los Angeles. Ribas, June, and others offer potential reasons, including the small number of patients treated, possible limitations of NY-ESO-1 as a target—selected in part for its safety record—and the failure to knock out all three genes in many of the cells.

Some of the authors are working with companies to commercialize the method. But much experimentation lies ahead. "This whole area is just teeming with different ideas," Stadtmauer says. A handful of other trials, including several in China, are offering CRISPR-modified cells to patients with cancer or other diseases. A company called PACT Pharma, which Ribas helped found, is running a trial that uses CRISPR to target gene mutations within solid tumors.

What June's group offers is "a needed start" for giving patients CRISPR-edited T cells, Ribas says. From now on, he adds, "It's going to be easier—because they did it first." ■

Published by AAAS

ENERGY

Underground oil fires liberate carbon-free fuel

Company ignites heavy oil fields to make green hydrogen while leaving carbon trapped

By **Eric Hand**

This month, on the frozen plains of Saskatchewan in Canada, workers began to inject steam and air into the Superb field, a layer of sand 700 meters down that holds 200 million barrels of thick, viscous oil. Their goal was not to pump out the oil, but to set it on fire—spurring underground chemical reactions that churn out hydrogen gas, along with carbon dioxide (CO_2). Eventually the company conducting the $3 million field test plans to plug its wells with membranes that would allow only the clean-burning hydrogen to reach the surface. The CO_2, and all of its power to warm the climate, would remain sequestered deep in the earth.

"We want to launch the idea that you can get energy from petroleum resources and it can be zero carbon emissions," says Ian Gates, a chemical engineer at the University of Calgary and co-founder of the startup, called Proton Technologies.

Markets are growing for hydrogen as a fuel for power, heat, and transport, because burning it only releases water. But most hydrogen is made from natural gas, through a process that spews carbon into the air, or by electrolyzing water, which is pricey. Proton Technologies says it can cut costs by relying on oil reservoirs shunned by drillers because they are water-logged or because their oil is too thick. "Someone's abandoned liability becomes our hydrogen field," says CEO Grant Strem, who bought the Superb field out of bankruptcy.

Geoffrey Maitland, a chemical engineer at Imperial College London, says he is a "great fan" of the concept, which treats the oil reservoir as a hot, naturally pressurized reactor. "This chemistry is well-proven at the surface," he says. "The challenge is controlling these processes several kilometers underground."

Industry has experimented for decades with underground burning, also known as fire flooding. Fed by air or oxygen pumped into the ground, the fire releases gases that can push oil toward wells, and its heat can soften tarlike bitumens and other heavy oils, making them easier to pump. In the early 1980s, fire-flooding tests on an oil field called Marguerite Lake, in Canada's vast oil sands, produced substantial amounts of hydrogen as a byproduct. No one cared very much at the time, but the finding sowed "the seed of the idea," Gates says. "What if we only produce hydrogen out of the reservoir?"

In a 2011 paper in the journal *Fuel*, he and his colleagues sketched out how it could work. The first step would be to use steam to heat a reservoir to 250°C or so and add air or oxygen to touch off combustion.

Injection wells at the Superb oil field in Canada. To make hydrogen, workers heat the reservoir with steam and feed it air, setting off underground oil fires.

PHOTO: GRANT STREM

The heat "cracks" the oil's long hydrocarbon chains into smaller pieces and produces small amounts of hydrogen. But if the fire reaches temperatures above 500°C, injected steam or water vapor from the hot reservoir itself will react with the hydrocarbons to make syngas: a mixture of carbon monoxide and hydrogen. Adding more water to the syngas sets off a final reaction that produces CO_2 and more hydrogen.

The main obstacle will be raising temperatures above 500°C with in situ combustion, which is "complicated and not easy to control," says Berna Hascakir, a heavy oil reservoir engineer at Texas A&M University, College Station. Gates says the reactions can still proceed below 500°C, just less efficiently. "Ideally, we'd like to get hotter," he says. "But those temperatures are fine to produce meaningful amounts of hydrogen."

Another challenge is separating the produced hydrogen from the CO_2 and other impurities in the mix, such as toxic hydrogen sulfide. Strem says the company will use thin membranes made of palladium alloys, which will decompose hydrogen gas into individual hydrogen atoms. Those atoms will diffuse through the metal lattice, then combine to form hydrogen gas again on the other side. But palladium membranes can be fragile and finicky, even when used at the surface, notes Jennifer Wilcox, a chemical engineer at Worcester Polytechnic Institute. "When doing everything underground, it's difficult to have control."

For now, Proton Technologies will use their membranes at the surface and vent the separated CO_2. But if the company can raise roughly $50 million for the next field test, Strem would like to test the membranes deep in the wells. He also wants to buy an air separation unit and inject pure oxygen into a reservoir, which would make it a hotter and more efficient reactor. He hopes to produce commercial amounts of hydrogen in the coming months and says the company could eventually produce the gas for between 10 and 50 cents per kilogram—significantly cheaper than current sources.

The vast majority of the world's produced hydrogen is used to refine petroleum products and make ammonia fertilizer. But the market for hydrogen as a green fuel is growing, says Ken Dragoon, executive director of the Renewable Hydrogen Association. In pilot projects, utilities are injecting small amounts of hydrogen into natural gas pipelines for home heating and appliances. In transportation, he says, fleets of trains, buses, and forklifts are turning to hydrogen fuel cells, which offer a longer range and much faster refueling than the other green alternative, electric batteries.

Dragoon, an advocate for renewable hydrogen made with electrolyzers, would be happy to see a competitor like Proton Technologies. "We need everything we can," he says. "If it's safe, and it produces a climate neutral fuel, more power to them." ■

Published by AAAS

FEATURES

REKINDLING THE FLAME

After decades of decline, the U.S. government's fusion lab seeks a rebirth

By **Adrian Cho**, *in Princeton, New Jersey*

Joseph Winston, a technician here at the Princeton Plasma Physics Laboratory (PPPL), knew something was wrong with the fusion reactor just by listening. In 2016, PPPL physicists had restarted their National Spherical Torus Experiment (NSTX), after a 5-year, $94 million upgrade. During one of the machine's runs, which last just seconds, millions of amps course through NSTX's magnet coils, creating fields that squeeze an ionized gas so tightly that atomic nuclei can fuse. The currents also stress the coils, which emit a groan loud enough to be heard through more than a meter of concrete. But the sound was petering out prematurely, Winston recalls.

When Winston and his team traced the problem to a short in one coil, the 50-year PPPL veteran knew the reactor, or tokamak, would be down for a long time. The machine is "like a one-way street," he says. "If anything happens to these coils, the whole thing has to come apart just to get to it." After running for just 10 weeks, NSTX was shut down again.

It was a body blow to a lab that was already staggering. In the 1980s, PPPL ran multiple machines, employed nearly 1300 people, and led the worldwide quest to harness fusion, the energy source of the Sun. "The action was almost frantic," says Dale Meade, a PPPL physicist emeritus. "We were taking risks, building one thing before the other was finished." In 1994, PPPL's largest machine ever, the Tokamak Fusion Test Reactor (TFTR), briefly generated 10.7 megawatts of power, still the record for U.S. efforts.

The good times didn't last. Within years, Congress had slashed the Department of Energy's (DOE's) fusion budget and shut down TFTR. In 2003, the United States joined the effort to build ITER, the giant international reactor under construction near Cadarache in France—a commitment that squeezed fusion research at home even harder. In 2008, DOE canceled another unfinished fusion reactor at PPPL, leading to a reshuffling of lab leadership. Now, PPPL employs 560 people. Its one large machine, NSTX, sits idle 3 years after breaking down.

PPPL director Steven Cowley wants to grow the lab. His first task is to repair its main fusion reactor.

Yet things may be looking up for the lab. After years of DOE reviews, PPPL researchers expect to start to rebuild NSTX in April. And a year ago, a report from the National Academies of Sciences, Engineering, and Medicine (NASEM) urged the United States not only to stick with ITER—which is hugely overbudget and behind schedule—but also to prepare to build the machine after it (*Science*, 21 December 2018, p. 1343). This would be a prototype power plant, smaller and cheaper than ITER, and PPPL would likely play a leading role in building it.

Perhaps most important, in 2018 Princeton University, which runs the lab for DOE, hired a new lab director. Steven Cowley, a strapping 60-year-old Englishman with a shock of silver hair and a knighthood, makes no bones about his role as an agent of change. "My job as a director is not to be an administrator," he says in his velvety baritone. "It's about scientific vision. What should we be doing? What are the interesting questions? How do we get to fusion?" He already has a plan to diversify the lab's work, grow its staff, and start to build things again.

Physicists are watching PPPL as a bellwether for the fortunes of the U.S. fusion program, whose share of the world's public fusion research has slipped to just one-sixth. And some observers who have been critical of the lab's previous leadership and culture think PPPL is finally on the right track. "Steve is the best person on the planet for the job," says William Madia, former director of two other DOE national labs, who urged Princeton to hire Cowley. "I'm optimistic." Yet the lab still faces obstacles on the path to redemption.

NSTX RESEMBLES an extraterrestrial spaceship. The two-story orb nestles in a cocoon of pipes and cables, the red coils of its main magnet arching up out of the chaos like flying buttresses. Within the orb—the reactor's partially disassembled vacuum chamber—copper plates and graphite tiles line the silvery walls. One could imagine that some reptilian alien slumbered away the eons here while traveling to the Solar System. During

PHOTO: ELLE STARKMAN/PRINCETON PLASMA PHYSICS LABORATORY

Published by AAAS

Sun in a bottle

When it restarts in 2021, the repaired National Spherical Torus Experiment (NSTX) at Princeton Plasma Physics Laboratory (PPPL) will use magnetic fields to trap and squeeze a hot ionized gas, or plasma, coaxing atomic nuclei to fuse and generate energy the same way as in the Sun. NSTX will test how efficiently a spherical shape can squeeze the plasma. It will also test using liquid lithium to protect NSTX's chamber wall and help shunt out heat.

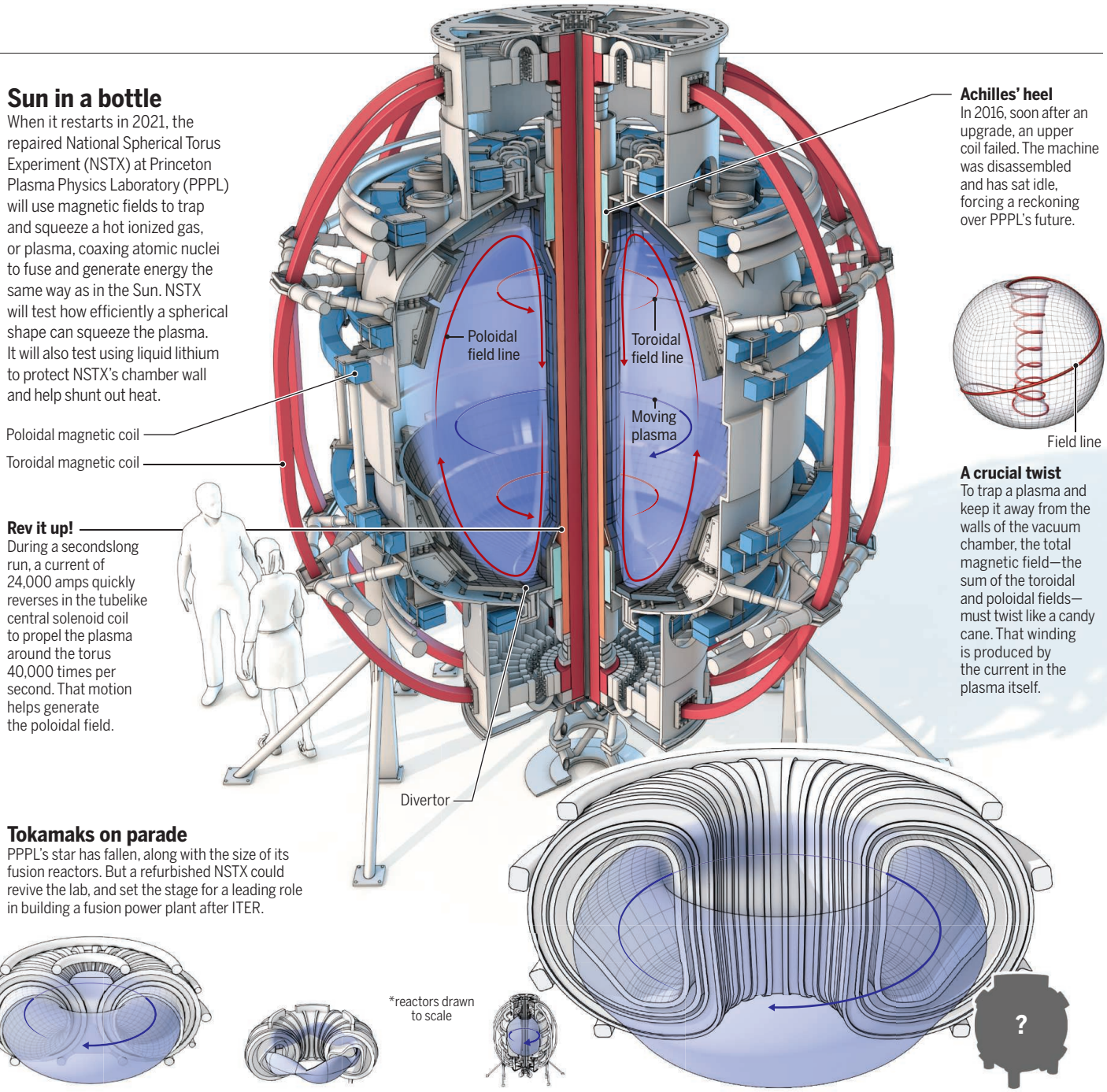

Achilles' heel
In 2016, soon after an upgrade, an upper coil failed. The machine was disassembled and has sat idle, forcing a reckoning over PPPL's future.

A crucial twist
To trap a plasma and keep it away from the walls of the vacuum chamber, the total magnetic field—the sum of the toroidal and poloidal fields—must twist like a candy cane. That winding is produced by the current in the plasma itself.

Rev it up!
During a secondslong run, a current of 24,000 amps quickly reverses in the tubelike central solenoid coil to propel the plasma around the torus 40,000 times per second. That motion helps generate the poloidal field.

Tokamaks on parade

PPPL's star has fallen, along with the size of its fusion reactors. But a refurbished NSTX could revive the lab, and set the stage for a leading role in building a fusion power plant after ITER.

*reactors drawn to scale

Tokamak Fusion Test Reactor
PPPL's biggest machine ran from 1982 to 1997. In 1994, it set a U.S. record for power produced.

National Compact Stellarator Experiment
Canceled in 2008, NCSX would have generated a twisting field with asymmetric coils, enabling it to run continuously with a stationary plasma.

National Spherical Torus Experiment
Built in 1999, NSTX tests how a spherical shape boosts plasma pressures. Tests will resume in 2021.

International Thermonuclear Experimental Reactor
The $25 billion reactor, an international effort under construction in France, aims to produce more energy than it consumes. It should begin operations in 2025.

Compact Pilot Plant
To be built in the 2030s, the prototype power plant would leverage emerging technologies and be smaller and cheaper than ITER.

GRAPHIC: C. BICKEL/*SCIENCE*

a run, something nearly as otherworldly fills the chamber: a wispy ionized gas, or plasma, heated to 100 million degrees Celsius—hotter than the core of the Sun. Injected microwaves and churning magnetic fields heat and squeeze the plasma and whirl it around the chamber 40,000 times per second.

The plasma is made of deuterium, a heavier isotope of hydrogen, and the goal is to bring it to temperatures and pressures at which colliding nuclei can fuse to form helium. The reactions release energy, carried away by free-flying neutrons. Replacing some of the deuterium with tritium, an even heavier isotope of hydrogen, could make the reactions self-sustaining. Such fusion promises abundant, carbon-free energy with little of the radioactive waste generated by fission-powered nuclear reactors. That prospect has fired PPPL for the past half-century. Yet, on a rainy Monday morning in October 2019, the lab is eerily quiet.

Nestled among pines in a technology park east of tony Princeton, PPPL grew out of the university's classified work on the hydrogen bomb and astrophysicist Lyman Spitzer's parallel effort to tame fusion as a power source. Founded in 1961, PPPL built a series of ever bigger devices that in 1982 culminated in TFTR, a reactor three times as wide

Published by AAAS

The plasma chamber of NSTX seen in 2014, before a short forced it to be disassembled.

PHOTO: ELLE STARKMAN/PRINCETON PLASMA PHYSICS LABORATORY

as NSTX that set its power record while running on deuterium and tritium. "We made a tremendous splash in the newspapers," recalls Michael Zarnstorff, PPPL's chief scientist. "People would ask, 'When are you going to have electricity from fusion?'"

That prospect has eluded physicists. ITER aims to be the first tokamak to produce more energy than it consumes. But TFTR was also supposed to do that and it came up short. Controlling a plasma turned out to be harder than anticipated, the electromagnetic equivalent of grasping an eel. After DOE shut down TFTR, PPPL researchers developed two smaller, more radical machines with different advantages.

NSTX was the more conventional design. A traditional tokamak has the shape of a doughnut. But a spherical torus like NSTX resembles a cored apple. For the same magnetic field, the rounder shape should put more pressure on the plasma, says Richard Hawryluk, a physicist at PPPL. "Basically you want to optimize the bang for the buck," he says. From 1999 to 2009, NSTX confirmed that prediction, which could make reaching the elusive break-even power point easier.

All tokamaks, including spherical ones, suffer from a limitation, however. To trap a plasma, the magnetic field going around the torus must twist like the stripes on a candy cane. To generate that twist, the plasma itself has to race around the doughnut to produce a current. And the laws of electrodynamics state that to push the plasma around, physicists need another rapidly changing magnetic field, which is generated by a coil in the doughnut hole. A run lasts as long as it takes to reverse the current in the coil—just a couple of seconds. Moreover, in a spherical torus, several different magnet coils are crammed precariously into the narrow hole.

A machine called a stellarator avoids the first limitation by generating the twist not with a moving plasma, but with twisted magnetic coils. In principle it can run steadily and more efficiently (*Science*, 23 October 2015, p. 369). In 2001, PPPL started work on one called the National Compact Stellarator Experiment (NCSX). However, by 2008—a year after it was supposed to be finished—its cost had nearly tripled to $170 million. DOE canceled the project, leaving PPPL with one machine and a black eye.

Then came the failure of NSTX after its upgrade, which aimed to double the strength of its magnetic field. An investigation revealed numerous problems in addition to the shorted coil, Hawryluk says. "We felt strongly that we really needed to understand what was going on," he says, "and not just fix one thing and then come back and say, 'Well, now something else is wrong.'" Additionally, DOE put PPPL's $199 million repair plan through the same yearslong approval process it requires for a whole new project.

That was an overreaction, says Martin Greenwald, a physicist at the Massachusetts Institute of Technology. "Instead [of fixing the problem] it's like, 'Oh, we're going have a million reviews,'" he says. But Madia says the lab brought the scrutiny on itself by failing to catch the problem and reacting slowly to it. "The problem was really leadership at the lab," he says.

If NSTX's failure strained the lab's relations with DOE, it nearly broke those with the university, Meade says. The lab's director at the time, Stewart Prager, was forced out and a few months later Princeton President Christopher Eisgruber took the staff to task in an all-hands meeting, Meade says. "He gave about a 20-minute talk admonishing the laboratory, telling them how deeply dis-

Published by AAAS

appointed and embarrassed he was about this incident," he says. Eisgruber says he simply told researchers the situation was urgent. "It's our obligation to deliver on the contracts we form with DOE," he says. "There has to be a commitment to excellence."

IN SOME WAYS, Cowley seems an odd choice to guide the beleaguered lab—a Brit who doesn't drive leading an American lab in car-clogged New Jersey. (He takes the bus to work.) For a person in the hot seat, Cowley also exudes a curious ebullience. "I'm a very lucky person because my serotonin level is pretty much always right," he says. "So I pretty much like anywhere I am."

Cowley is no stranger to PPPL. He earned his doctorate here in 1985, before going on to positions at the University of California, Los Angeles, and University College London. He also has ample leadership experience. From 2009 to 2016, he served as CEO of the UK Atomic Energy Authority and director of the Culham Centre for Fusion Energy. There he oversaw work on a competitor to NSTX, the Mega Ampere Spherical Tokamak, which was upgraded last year.

At PPPL, job No. 1 is to get NSTX running again. To do that, Cowley brought in John Galayda, an accelerator physicist who led construction of the world's first hard x-ray laser, the Linac Coherent Light Source at SLAC National Accelerator Laboratory, which in 2009 worked on the first attempt. PPPL researchers have begun to fabricate new parts and aim to have NSTX running in summer 2021. For Jessica Guttenfelder, a mechanical engineer who started at PPPL weeks before the machine conked out, it feels like a rebirth. "Everything you're exposed to is so unique," says Guttenfelder, who is in charge of a device that shoots hydrogen atoms into NSTX's plasma to help it spin.

The 20-year-old reactor still has work to do, Hawryluk says. With its stronger magnetic field, NSTX will test whether a spherical tokamak's favorable scaling of pressure with magnetic field persists at temperatures where fusion can occur. Physicists will also have to figure out how to handle unprecedented loads on the divertors, an exhaust system for the reactor's heat. They will explore whether lining the reactor with molten lithium helps stabilize the plasma and tame the exhaust.

At the same time, Cowley aims to transform PPPL into a multipurpose lab with much stronger ties to the university and industry. PPPL's nonfusion work has typically focused on the plasmas in stars and interstellar space. Cowley plans to expand into the use of cold plasmas to process materials, in particular to make ever-more-advanced microchips. "The U.S. dominates the industry that makes the machines that make the chips," he says. "If we're not careful we'll lose that to China."

Cowley plans to double the lab's staff, with the cold plasma work accounting for 30% to 50% of the total. Craig Arnold, director of the Princeton Institute for the Science and Technology of Materials, envisions close ties to PPPL. "You have these two entities that are literally next door to each other and part of the same overall organization. It's silly for us not to be working together," he says. The university and the lab are negotiating to construct a $100 million building at PPPL for the cold plasma and material science work.

> **"What's the facility after NSTX? My mission is to define that and get it to happen."**
>
> **Steven Cowley**, Princeton Plasma Physics Laboratory

In the longer term, Cowley says he wants to get PPPL back to building big machines. "What's the facility after NSTX?" he asks. "My mission is to define that and get it to happen." In particular, he would like to revisit the idea of building a stellarator. But instead of fashioning bizarrely shaped coils for the machine, Cowley envisions using conventional ones and adding high-strength permanent magnets on electronically adjustable mounts to shape the field. "It's just an idea and maybe it'll go nowhere," says Cowley, who sketches out the idea with colleagues in a paper in press at *Physical Review Letters*.

Other U.S. fusion physicists welcome his ambitions, noting that aside from parts for ITER, DOE hasn't built a major fusion machine since NSTX. "At some point we need to be building," says Erik Trask, a physicist at the fusion startup TAE Technologies. "I would love to see many midscale machines get built." Eisgruber says he is "greatly enthusiastic" about the plans for the lab. "Steve Cowley has a vision that I fully support."

THE PLAN ALSO SEEMS to dovetail with the vision outlined in the December 2018 NASEM report, which urged the United States to build a prototype power plant in the 2030s as a successor to ITER. Taking advantage of innovations such as powerful magnet coils made from high temperature superconductors, that Compact Pilot Plant (CPP) would be smaller and cheaper than ITER, a $25 billion behemoth. Such miniaturization will be vital in the U.S. energy market, Cowley predicts, as no utility will buy a plant that expensive.

The call to build the CPP might help fill PPPL's sails. PPPL wouldn't build the machine on its campus, researchers say, because it would produce too much radioactive material for a densely populated place like Princeton. But the lab would undoubtedly play a leading role in designing and building the machine. "We're enthusiastic about the report," Zarnstorff says. The first step for the CPP would be to make it into DOE's next long-range plan for fusion, which researchers and the agency aim to hash out by year's end.

But that rosy scenario faces several uncertainties. For example, even if DOE embraces the CPP, it would likely build a power plant only as part of a public-private partnership, Zarnstorff says. So the fate of the project may depend on whether companies such as TAE Technologies and Commonwealth Fusion Systems can help bear the costs and risks of the project.

The push toward a working fusion power plant also highlights a tension within DOE. Since 1998, the department's fusion energy science program has resided in its basic research wing, the Office of Science. Many U.S. fusion researchers say the basic research tag handcuffs them. "There's a lot of cutting edge research in fusion technology that we can't support that because it's not science," Greenwald says. Zarnstorff says that to pursue the CPP, DOE ultimately may have to move fusion into applied research.

Cowley says such talk is premature. "I don't think we can get to commercial fusion power without solving some really quite profound scientific problems," he says. For instance, he says, researchers still need to figure out how to deal with exhaust heat.

And then there's the question of money. The NASEM report calls for a $200-million-per-year increase in U.S. fusion research, and Congress boosted DOE's budget for fusion energy sciences from $564 million in fiscal year 2019 to $671 million this year. But all of that increase will go to ITER, and it remains to be seen whether Congress will continue to ramp up the fusion budget.

For now, Cowley is focused on rejuvenating a fallen lab and boosting its morale. Over a group lunch in a conference room, Laura Xin Zhang, a fourth-year graduate student at Princeton, says she chose fusion because she was seeking a mission in her work. "We're the generation of climate change, so everyone wants to do something with climate change," says Zhang, a native of Dalian, China. Fusion could offer an answer. "Someone has to work on this, or it will never happen," Zhang says.

"It will happen in your lifetime," Cowley interjects.

"You think?" Zhang says.

"Mine, it's touch and go," Cowley says with a smile. "I need to keep fit." ■

Published by AAAS

Wild boar in Europe, such as this male in Bavaria, Germany, help spread and maintain African swine fever virus.

PHOTO: BREUER WILDLIFE/MINDEN PICTURES

PERSPECTIVES

INFECTIOUS DISEASE

No hasty solutions for African swine fever

African swine fever vaccines could pose risk of causing disease and spreading the virus further

By **Dolores Gavier-Widén[1], Karl Ståhl[1], Linda Dixon[2]**

An epidemic of African swine fever (ASF), a lethal viral hemorrhagic disease of swine, is devastating pig production in Asia and is a global threat. The ASF virus (ASFV) reached the European Union (EU) in 2014, affecting pig production. ASFV continues to spread through wild boar (*Sus scrofa*), which form interconnected populations across Europe and which maintain the infection and can cause infection in pigs. A vaccine is not yet available and is urgently needed, both for pigs and wild boar. Live attenuated virus (LAV) vaccines are the most promising way forward in the short term (*1*), and recent advances have been made in constructing gene-deleted LAV vaccines. Naturally attenuated LAVs have also been shown to confer protection as vaccines in pigs and wild boar. However, previous experience with vaccination failures using naturally attenuated LAVs emphasizes the need for caution because of safety concerns.

ASF was first described in Kenya in 1921 (*2*) and today is endemic in most countries of sub-Saharan Africa. Local dispersion of the virus can occur through contact between animals, whereas long-distance spread results from the movement of contaminated pork products, in which the virus can survive for months or years depending on temperature. Feeding of food waste to pigs can thus establish new foci of infection. Twenty-four

[1]National Veterinary Institute (SVA), Uppsala, Sweden. [2]The Pirbright Institute, Woking, UK. Email: dolores.gavier-widen@sva.se

Published by AAAS

genotypes of ASFV have been identified. A genotype I ASFV escaped twice from West Africa into Portugal in 1957 and 1960. The later infection affected the Iberian Peninsula, where the virus persisted for more than 30 years, spreading sporadically to other countries in Europe, the Caribbean, and Brazil. ASF was eradicated from most of these countries by the mid-1990s through culling and movement bans of pigs and their products. However, genotype I ASFV still persists in the Italian island of Sardinia.

A new transcontinental spread of ASFV, this time genotype II, occurred from southeast Africa into Georgia in 2007, probably through catering waste brought by a ship (*3*). Subsequently, the virus spread to the Caucasus, the Russian Federation, Ukraine, and Belarus. It entered the EU Baltic states and Poland in 2014, where the virus is maintained in wild boar populations. Continued spread to other EU countries, including Romania and Bulgaria, has also involved the domestic pig population, with outbreaks mainly in small farms. The natural movements of infected wild boar result in local expansion of the virus; the infection front has been estimated to advance at ~1 to 2 km per month (*4*). In 2018, genotype II ASFV entered China, which contains nearly half of the world's pig population, with catastrophic socioeconomic consequences, particularly for small and underprivileged pig farmers (*5*) who comprise ~30% of the 26 million pig farmers in China (*6*). It then dispersed further to Southeast Asia. A year after its incursion into Asia, genotype II ASFV had caused the death or destruction of ~5 million pigs (*6*) and an estimated reduction of 40% of the Chinese pig herd, thus affecting global food markets (*7*).

It was not until genotype II ASFV entered the EU in 2014 that the capacity of wild boar to maintain circulation of the virus independently of outbreaks in domestic pigs was revealed (*8*). Control of ASFV in wild boar is challenging and has not been achieved in most of the affected countries. There are exceptions, however: The Czech Republic was declared officially free from ASF by the EU ~18 months after the first report, and disease spread seems to have halted in Belgium. Early detection, prompt and coordinated implementation of measures to restrict movements of potentially infected wild boar, and public-access restrictions to infected areas to prevent further ASFV spread are key factors for success. Such measures include carcass finding and removal, fencing, and strategic wild boar hunting and culling operations (*4*).

A combination of direct transmission between wild boar and indirect transmission by contact with infected wild boar carcasses or wild boar scavenging on carcasses (intraspecies scavenging) provides long-term persistence of ASFV in the environment (*8*). Thus, infection in pigs can potentially occur not only from their contact with wild boar—for example, in outdoor holdings—but also from transmission of ASFV from the environment through, for example, vehicles, shoes, and feed. High-biosecurity pig production is better protected from ASF, but it is put at risk if the environment around farms is contaminated, and even such establishments have been infected in Europe (*9*).

Populations of wild boar have been expanding throughout Europe during the past 40 years (*10*). Sustainable reduction in free-ranging wild boar populations is very difficult because wild boar have a high reproductive rate, such that culling results in compensatory growth of the population and influx from adjacent areas. In addition, intensive hunting leads to dispersion of wild boar and can result in expansion of the infected area. ASFV has also been reported in wild boar in China, Far East Russia, and the northern region of South Korea (*11*). However, information about populations of wild boar and the epidemiology of ASF in Asia is scarce.

Developing an ASFV vaccine presents many challenges. ASFV is a large, double-stranded DNA virus of the Asfarviridae family (*12*). The virus is complex; its genome is about 170 to 190 kilobases in length and encodes ~170 proteins, of which ~70 are packaged into the multilayered virus particle (*12*). Identification of antigens that might elicit vaccine-mediated protection among this very large number of proteins is difficult. Immune correlates of protection in swine to enable evaluation of vaccine candidates are insufficiently identified. Moreover, current experimental testing of vaccine candidates can only be conducted in pigs and wild boar and in high-containment facilities.

An ASFV vaccine for wild boar must also overcome the challenges of vaccinating wildlife. The approach is likely to involve oral vaccination using baits, which must be deployed in the field and thus be stable and effective in a broad range of environmental settings, including hot Iberian summers and cold Nordic winters, and similarly, but at a larger geographical and climatic scale, in Asia. Baits that are palatable, stable, safe, and inexpensive are needed.

The planning of any ASFV vaccination strategy must also consider the complex epidemiology of ASF, which will vary depending on where the vaccine is applied. For this purpose, mathematical models are essential to assess the efficacy, efficiency, and feasibility of vaccination as a single measure or as a component of an integrated disease management strategy, including, for example, zoning, movement restrictions, and culling of affected premises. However, information on domestic pig farms and their management structure as well as on wild boar populations and habitats is needed for accurate modeling.

ASFV vaccines based on inactivated virus have proven ineffective, even when used with immunogenic adjuvants, because they fail to induce cellular immunity. Subunit vaccines contain only antigenic fragments

Development of an African swine fever vaccine

Safety and efficacy of live attenuated virus (LAV) vaccine candidates and their elicited immune responses have to be tested in vivo in pigs or wild boar. Although domestic pigs can be vaccinated by injection, wild boar are more feasibly vaccinated by oral baits. Mathematical models should be used to plan the vaccination strategy and to assess the efficacy, efficiency, and feasibility of vaccination in the control of African swine fever (ASF).

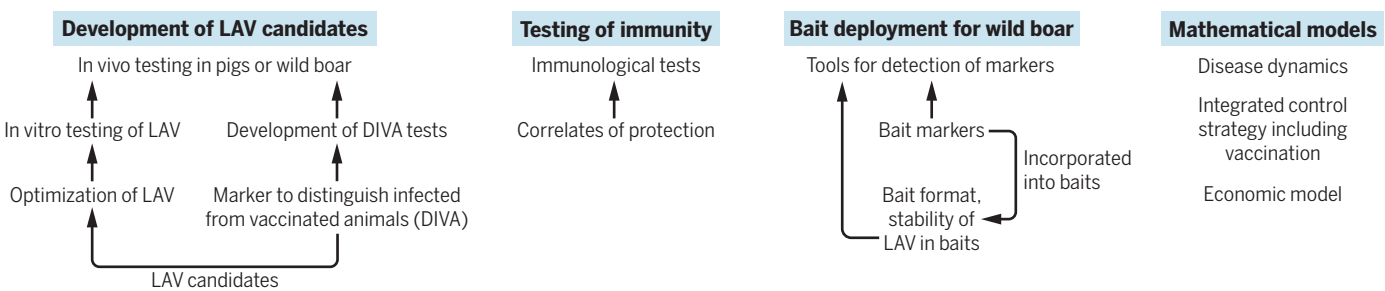

GRAPHIC: VERONICA FALCONIERI/*SCIENCE*

Published by AAAS

of the virus and are therefore safe, but their development has been hindered by the limited identification of antigens. Attempts to use either recombinant proteins or DNA vaccination have induced only partial protection or no protection.

In the 1960s, it was observed that recovery from infection with less virulent ASFV isolates protected pigs against subsequent challenge with related virulent ASFV. This is because almost all virus proteins are expressed in infected cells, thus inducing a cellular immune response against a range of virus epitopes in addition to antibody responses to the native virus particle. This demonstrated the potential for LAVs as vaccines. The introduction of ASFV to Portugal and Spain in 1960 provided impetus to produce LAVs for vaccination. LAVs are produced by selecting attenuated ASFV resulting from passage in cells, which results in genome modifications. Vaccines derived by this procedure were used for an extensive vaccination campaign (*13*). However, these vaccines were insufficiently tested and caused a debilitating chronic disease in many vaccinated pigs, resulting in vaccine withdrawal. Other naturally attenuated ASFV strains have conferred different levels of protection but also caused unacceptable postvaccination reactions (*1*).

The current status of ASFV vaccine development shows some encouraging results. The most advanced vaccine candidates are LAVs in which virulence genes are deleted, resulting in a weakened virus that still replicates (so it can trigger immunity) and can be amplified in cell culture for vaccine production. However, a licensed cell line in which a LAV can be stably grown and produced on a large scale is still required. Deletion of ASFV genes that inhibit host antiviral type I interferon responses has been an effective strategy to attenuate the virus and induce protection. These interferon inhibitory proteins include members of multigene family (MGF) 360 and MGF 505. Genetic modification allows for fine-tuning of safety and efficacy and the introduction of markers to distinguish infected from vaccinated animals (DIVA). This is needed to monitor vaccine efficacy and to confirm disease eradication. Several gene-deleted genotype I and genotype II LAV vaccine candidates have shown promising results in preliminary testing (*1*). However, these require further testing and scale-up of production before completing larger-scale safety and efficacy testing in vivo (see the figure).

Although LAVs have the potential to be effective vaccines and have been used for the eradication of smallpox and rinderpest, there are safety concerns. These include induction of ASF-like symptoms and dispersal of the vaccine virus. The vaccine may not protect enough animals to stop the epidemic. Moreover, vaccinated animals may spread the virulent virus to uninfected animals. These safety issues were also observed using a naturally attenuated ASFV strain from Latvia (Lv17/WB/Rie1) (*14*). This virus caused clinical signs of ASF in pigs, including joint swelling, which is associated with a chronic form of ASF (*15*). In addition, the vaccine replicated to high concentrations in blood and spread to pigs on contact. Replication of the virulent virus was not sufficiently controlled, and the pigs shed the virulent virus sporadically and could therefore spread ASF to other animals (*14*), potentially failing to stop the epidemic. Such safety issues should be considered during animal testing of vaccine candidates.

The race to develop an ASFV vaccine may overshadow comprehensive efficacy and safety testing, thus potentially investing in the wrong vaccine development strategy and in unnecessary use of animals for experiments. Additional caution should be taken when developing LAV vaccines to be spread in nature in oral baits. The challenge of ASFV vaccine development, including vaccination of wild boar, should not be underestimated and requires the cooperation of many disciplines in the early stages of vaccine development. ■

REFERENCES AND NOTES

1. M. Arias *et al.*, *Vaccines (Basel)* **5**, 35 (2017).
2. R. E. Montgomery, *J. Comp. Pathol. Ther.* **34**, 159 (1921).
3. D. Beltrán-Alcrudo *et al.*, *FAO EMPRES Watch* **2008**, 1 (2008).
4. European Food Safety Authority (EFSA) et al, *EFSA J.* **16**, 5494 (2018).
5. D. Smith, T. Cooper, A. Pereira, J. B. D. C. Jong, *One Health* **8**, 100109 (2019).
6. Food and Agriculture Organization of the United Nations (FAO), "One year on, close to 5 million pigs lost to Asia's swine fever outbreak," 9 August 2019; www.fao.org/news/story/en/item/1204563/icode/.
7. N. Pitts *et al.*, "Agricultural commodities report" (Australian Government Department of Agriculture, 10 March 2019); www.agriculture.gov.au/abares/research-topics/agricultural-commodities/sep-2019/african-swine-fever.
8. E. Chenais, K. Ståhl, V. Guberti, K. Depner, *Emerg. Infect. Dis.* **24**, 810 (2018).
9. I. Nurmoja *et al.*, *Prev. Vet. Med.* 10.1016/j.prevetmed.2018.10.001 (2018).
10. EFSA et al, *EFSA J.* **12**, 3616 (2014).
11. World Organization for Animal Health, World Animal Health Information Database, "African swine fever"; www.oie.int/en/animal-health-in-the-world/information-on-aquatic-and-terrestrial-animal-diseases/african-swine-fever/reports-on-asf/.
12. C. Alonso *et al.*, *J. Gen. Virol.* **99**, 613 (2018).
13. J. Manso Ribeiro *et al.*, *Bull. Off. Int. Epizoot.* **60**, 921 (1963).
14. C. Gallardo *et al.*, *Transbound. Emerg. Dis.* **66**, 1399 (2019).
15. P. J. Sánchez-Cordón, M. Montoya, A. L. Reis, L. K. Dixon, *Vet. J.* **233**, 41 (2018).

ACKNOWLEDGMENTS

The authors are supported by European Cooperation in Science and Technology (COST) Action ASF-STOP-CA15116, Biotechnology and Biological Sciences Research Council (BBSRC) (BBS/E/1/00007031), and Department for Environment, Food, & Rural Affairs (Defra) SE1516.

10.1126/science.aaz8590

MEMBRANES

Porous crystals as membranes

Microporous crystalline membranes are designed for gas separation and potential scale-up

By **Moises A. Carreon**

Chemical separations account for about half of the United States' industrial energy use and as much as 15% of total U.S. energy consumption (*1*). Most of these industrially employed separations, including distillation, evaporation, and drying, are thermally driven. Energy-efficient separation technologies require reducing heat consumption. Non–thermally driven membrane technology could play a key role in gas separations that are less energy-intensive, making them potentially economically feasible. On page 667 of this issue, Li *et al.* (*2*) illustrate a powerful example using a microporous crystalline membrane to separate water from light gases, with subsequent carbon dioxide conversion to liquid fuels by hydrogenation.

Porous crystals grown as membranes with equally sized micropores or with limiting pore apertures are highly appealing materials to effectively separate gas molecules by size exclusion. Li *et al.* designed a sodium aluminosilicate microporous crystalline molecular sieve NaA zeolite membrane displaying precise water conduction nanochannels that allow water to effectively permeate through a continuous crystalline membrane and restrict the diffusion of gas molecules. This strategy may be useful for many industrially important processes where water is present.

The precise gate effect of the membrane can be exploited for the separation of other industrially relevant gas mixtures, including ammonia separation from light gases. For instance, this zeolite composition has a pore entrance size that should be ideal to effectively sieve ammonia from hydrogen and nitrogen. Furthermore, the pore entrance of NaA zeolite promotes favorable charge-dipole interaction with polar molecules. The higher polarizability of ammo-

Chemical and Biological Engineering Department, Colorado School of Mines, Golden, CO 80401, USA.
Email: mcarreon@mines.edu

Published by AAAS

Different strategies to separate gases

Porous crystalline membranes are designed to use several different mechanisms to separate out different types of gases.

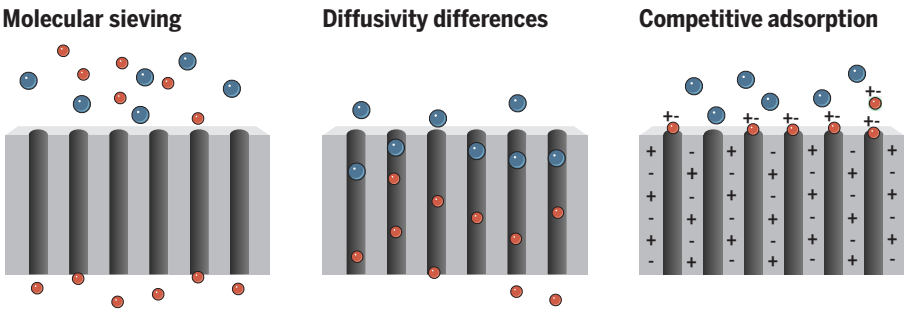

Changing the effective pore diameter will separate out the smaller gas molecules from larger ones.

The pore size and shape can affect how quickly large and small molecules move through the porous crystal membrane.

Tailoring membrane surface charge can change the relative adsorption of different molecules depending on their polarity.

nia should favor adsorption over the zeolite surface, resulting in highly selective ammonia membranes.

Microporous crystal sieves suitable for gas separations can be inorganic, organic, or a hybrid material. Zeolites are the prime example of porous inorganic crystalline molecular sieves that have been effectively used in gas separations (*3*). Metal-organic frameworks are microporous crystalline materials composed of transition metal ions linked together by organic ligands (*4*) that have shown an ability to separate gas mixtures. Covalently bonded porous organic cages can be assembled into crystalline microporous materials with three-dimensional connectivity. These materials combine highly desirable properties, such as uniform micropores, high surface area, and thermal and chemical stability. This makes them highly appealing candidates for challenging molecular gas separations (*5*).

"Porous crystals grown as membranes with... limiting pore apertures are highly appealing materials to effectively separate gas molecules by size exclusion."

The preparation of continuous porous crystalline membranes for molecular gas separations is not a trivial issue. Porous crystals displaying particular separation properties in powder or particle form may not be suitable for membrane preparation because limited adhesion to the support can lead to delamination, induced stresses at the membrane-support interface, or poor crystal intergrowth. Nonetheless, several examples of the successful synthesis of microporous crystalline membranes for gas separations are well documented. ZSM-5 (Zeolite Socony Mobil-5 with MFI topology) membranes are one example; they effectively separate gas molecules, including isomers, with very small differences in size and shape (*6*).

Over the past two decades, considerable effort has gone into developing zeolite membranes for gas separations (*7*). The successful synthesis of any metal-organic framework membrane demonstrated the feasibility for using porous crystalline compositions for hydrogen separation (*8*). This motivated the development of continuous metal-organic framework membranes (*9*) and continuous porous organic cage membranes for gas separation (*10*).

Three main separation mechanisms—molecular sieving, differences in diffusivities or kinetic contribution, and competitive adsorption or thermodynamic contribution—are observed for gas mixtures over microporous crystalline membranes (see the figure). When the effective pore aperture of the microporous crystal lies between the kinetic diameters of the molecules to be separated, molecular sieving may be possible (*11*). However, strictly speaking, true molecular sieving takes place only when molecules diffuse selectively through crystal micropores or through a single crystal. When comparing zeolites to metal-organic frameworks, we expect sharper molecular sieving for zeolites, as they have rigid pore sizes when compared to metal-organic frameworks. Smaller and lighter molecules should diffuse faster than larger and heavier molecules, promoting separation on the basis of differences in diffusivities. Preferential adsorption occurs through a variety of surface forces between the membrane and molecules with high dipole moments (*11*). Li *et al.* demonstrate that exploiting the kinetic and thermodynamic contributions could lead to highly selective water membranes.

A different separation mechanism for gases over porous organic cages was shown to effectively separate hydrogen isotopes by kinetic quantum sieving (*12*). The structure and distinctive solid-state molecular packing of porous organic cages differentiate them from other porous crystals, resulting in special transport and adsorption properties, and therefore unusual separation mechanisms.

The study by Li *et al.* represents a path toward the rational design of zeolite membranes for a highly relevant industrial separation focused on water removal from light gases, and subsequent conversion of carbon dioxide into liquid fuels. An outstanding issue is whether these high-performance NaA zeolite membranes can be scaled up. Demonstrating zeolite membranes at scale requires a testing facility; one in the United States is currently under construction. This oil field facility will allow testing of a scaled-up zeolite membrane, denoted as DDR, having uniform limiting pore apertures of 0.36 nm for carbon dioxide recovery from natural and associated gases. This field demonstration test is an exciting step toward the potential deployment of porous crystalline membranes for gas mixture separations. This should motivate focusing membrane development around cheaper supports amenable to scale-up, the assessment of membrane performance under industrial-like conditions, and stability studies. Promising membrane compositions from laboratory studies can then be scaled up and tested in the presence of impurities and the effects of pressure and temperature. This requires a true but difficult integrative connection among academia, national laboratories, and industry. ■

GRAPHIC: KELLIE HOLOSKI/*SCIENCE*

REFERENCES AND NOTES

1. D. S. Sholl, R. P. Lively, *Nature* **532**, 435 (2016).
2. H. Li *et al.*, *Science* **367**, 667 (2020).
3. M. E. Davis, *Nature* **417**, 813 (2002).
4. M. Eddaoudi *et al.*, *Science* **295**, 469 (2002).
5. T. Tozawa *et al.*, *Nat. Mater.* **8**, 973 (2009).
6. Z. Lai *et al.*, *Science* **300**, 456 (2003).
7. N. Kosinov *et al.*, *J. Membr. Sci.* **499**, 65 (2016).
8. R. Ranjan, M. Tsapatsis, *Chem. Mater.* **21**, 4920 (2009).
9. S. Qiu, M. Xue, G. Zhu, *Chem. Soc. Rev.* **43**, 6116 (2014).
10. Q. Song *et al.*, *Adv. Mater.* **28**, 2629 (2016).
11. X. Feng *et al.*, *J. Am. Chem. Soc.* **138**, 9791 (2016).
12. M. Liu *et al.*, *Science* **366**, 613 (2019).

ACKNOWLEDGMENTS

Supported by NSF grants CBET-CAREER 1054150 and CBET 1835924, U.S. Department of Energy grants ARPA-E DE-AR0001004 and NEUP DE-NE0008429, and American Chemical Society Petroleum Research Fund grant ACS-PRF49202-DNI5.

10.1126/science.aba4997

Published by AAAS

ECOLOGY

Discovering the limits of ecological resilience

Bumble bee declines reveal species pushed to the edge of their environmental tolerances

By **Jon Bridle** and **Alexandra van Rensburg**

In 1949, environmentalist Aldo Leopold wrote that "one of the penalties of an ecological education is that one lives alone in a world of wounds" (*1*). Seventy years later, biologists no longer witness such wounds in solitude. Instead, millions of people on social media share evidence every day of how the behavior of a wealthy minority (*2*) has created unsustainable rates of biodiversity loss and climate transformation (*3*). Now, on page 685 of this issue, Soroye *et al.* demonstrate widespread declines in bumble bee species that are better explained by the frequency of climate extremes than by changes in average temperatures (*4*).

Despite increasingly precise predictions of rises in average temperatures and the frequency of extreme weather events, biologists still cannot predict how ecological communities will respond to these changes. This means that scientists cannot predict where, and at what rates of climate change, ecosystems will stop providing the rainfall, decomposition, and biological productivity on which all economies depend. Another key unknown is to what extent ongoing habitat and biodiversity loss reduces the ability of ecological communities to evolve in response to the climate crisis (*3*).

To determine these critical rates of biodiversity loss and climate change as well as where they are being exceeded (*5*), scientists test for shifts in the distribution of species over time and across their geographical ranges. Such studies reveal that the warming climate leaves a footprint: The abundances of many plant, animal, and fungal species have contracted at low latitudes and elevations, and have increased at high latitudes and elevations (*6*). How these responses to environmental change vary according to species' life histories, ecologies, and their biotic interactions provides a test of which ecosystems and localities are least resilient to global change.

Soroye *et al.* used long-term datasets to assess changes in the abundance and geographical distribution of 66 bumble bee species in Europe and North America between two periods, 1901–1974 and 2000–2014. Two of their findings are especially alarming. Bumble bee populations showed substantial declines at southern (warming) ecological margins but fewer compensating population expansions at northern (cooler) margins, suggesting widespread declines in bee biodiversity across both continents. Moreover, the causes of these declines apparently depend more on the frequency of extremely warm years than on increases in average temperatures. As prevailing temperatures climb closer to species' physiological limits, extreme climate events will become increasingly associated with biodiversity loss. In addition, their effects will become more pronounced as cooler habitats, where organisms can survive unusually warm periods (e.g., deeper water, higher elevations), become increasingly rare.

Declines in *Bombus terricola* landed them on Canada's "Species at Risk" list. Climate change seems to be the cause, with population declines better explained by more frequent temperature extremes rather than by changes in average temperatures.

PHOTO: PETER SOROYE

Shifts in species' distributions in time and space vary considerably across those taxa and latitudes for which detailed data exist. For example, the physiological thermal limits of marine organisms tend to closely predict their spatial distributions, whereas those of terrestrial organisms do not. This is probably because habitat loss and fragmentation limit dispersal on land more than in the ocean (*7*). Surprisingly, however, the new study shows that bumble bee range expansions are just as rare in less intensively farmed landscapes as they are in intensively farmed ones where habitat fragmentation is higher. Why range expansions in temperate bumble bees are relatively rare, even across relatively undisturbed environments, demands further investigation.

The ability of organisms to alter their behavior or the timing of key life events such as hibernation, flowering time, and germination can minimize organisms' exposure to climate extremes. Such plasticity can slow population declines and accelerate range expansions (*8*). Also, many organisms threatened by warming persist by dispersing to locally cool microclimates (*9*). This active agency of organisms to select suitable habitats in time and space tends to increase population fragmentation at a fine spatial scale while retaining occupancy at larger spatial scales (*10*).

However, beyond a critical amount of environmental change—arguably similar to that routinely experienced during a species' history—plasticity will no longer have sufficient scope to buffer climate extremes (*11*). As climates exceed these critical limits, the widespread declines now observed for bumble bee species will manifest in more and more organisms and places. These declines also will be increasingly associated with extreme climatic events rather than average changes in temperature (*6*).

Rapid evolution could also prevent declines in population abundance and allow range shifts despite habitat fragmentation (*12*). This might result from natural selec-

School of Biological Sciences, University of Bristol, Bristol BS8 1TH, UK. Email: jon.bridle@bristol.ac.uk

Published by AAAS

tion on traits that alter organisms' physiological tolerances or their interactions with other species (*13*). However, the evolution of populations with different forms of plasticity (*14*) will be especially critical where species need to use newly informative environmental cues to decide how and when to adjust their behavior, and to coordinate their activities with those of their host and food species.

Predicting the maximum rates of such evolutionary responses demands a better understanding of genetic variation in the traits that affect fitness, as well as about how the amount of genetic variation changes with population density and with environmental shifts (*12*). Recent advances in population genomic analysis, combined with increasing access to museum collections for ecological and genetic analysis, are revolutionizing the field (*15*). For some groups of organisms, we can now integrate genomic data with environmental and demographic data to test the extent to which ecological resilience depends on evolutionary adaptation. Such data will allow researchers to estimate when and where biodiversity within a species has the power to rescue ecological communities from collapse due to climate change and habitat loss.

The new study adds to a growing body of evidence for alarming, widespread losses of biodiversity and for rates of global change that now exceed the critical limits of ecosystem resilience. However, identifying dangerous rates of climate change and biodiversity loss is only one part of the story. Political action must now follow in order to slow or mitigate these rates of global change. For how long will ecosystems continue to provide sufficient (and sufficiently predictable) rainfall, oxygen, and food, while governments ignore the economic and social costs of exceeding planetary limits? Well, we shall find out. ■

REFERENCES AND NOTES

1. A. Leopold, *A Sand County Almanac* (Oxford Univ. Press, 1949).
2. I. M. Otto, K. M. Kim, N. Dubrovsky, W. Lucht, *Nat. Clim. Change* **9**, 82 (2019).
3. S. Díaz *et al.*, *Science* **366**, 1327 (2019).
4. P. Soroye, T. Newbold, J. Kerr, *Science* **367**, 685 (2020).
5. W. Steffen *et al.*, *Science* **347**, 736 (2015).
6. I. C. Chen, J. K. Hill, R. Ohlemüller, D. B. Roy, C. D. Thomas, *Science* **333**, 1024 (2011).
7. J. M. Sunday, A. E. Bates, N. K. Dulvy, *Nat. Commun.* **2**, 686 (2012).
8. C. J. Macgregor *et al.*, *Nat. Commun.* **10**, 4455 (2019).
9. A. J. Suggitt *et al.*, *Nat. Clim. Change* **8**, 713 (2018).
10. C. P. Nadeau, M. C. Urban, J. R. Bridle, *Trends Ecol. Evol.* **32**, 786 (2017).
11. V. Radchuk *et al.*, *Nat. Commun.* **10**, 3109 (2019).
12. A. A. Hoffmann, C. M. Sgrò, *Nature* **470**, 479 (2011).
13. J. Buckley, J. R. Bridle, *Ecol. Lett.* **17**, 1316 (2014).
14. T. Bonnet *et al.*, *PLOS Biol.* **17**, 11 (2019).
15. M. W. Holmes *et al.*, *Mol. Ecol.* **25**, 864 (2016).

10.1126/science.aba6432

MULTIFERROICS

Room-temperature magnetoelastic coupling

Magnetic fields alter the ferroelectric properties of a paramagnetic ytterbium-zinc complex

By **Ye Zhou** *and* **Su-Ting Han**

Ferromagnetism, records of which date back to the 6th century BCE, is regarded as an ancient twin of ferroelectricity, which was not discovered until 1920. Ferromagnets, which have permanent magnetic moments, and ferroelectrics, which have a spontaneous electric polarization, both have domain structures and a Curie temperature, T_C, above which materials lose their ferroic orders. Magnetoelectric coupling describes the multiferroic response of the magnetization to the electric field and the polarization to the magnetic field in the same material (see the figure). On page 671 of this issue, Long *et al.* (*1*) report magnetoelectric coupling in paramagnetic molecular ferroelectrics at room temperature, in which the responses to the magnetic field and the modifications of the ferroelectricity have the same chemical origin in a chemical complex.

"...the authors demonstrated magnetoelectric coupling in a paramagnetic ferroelectric crystal..."

Since the renaissance of magnetoelectric coupling more than 20 years ago (*2*), researchers have paid particular attention to the multiferroic materials. Despite extensive exploration of materials such as inorganic oxides (*3*) and fluorides (*4*), many challenges remain, mainly that the T_C values are below room temperature (typically for the magnetic order). Also, the coupling between the two ferroic orders is weak, mainly because the magnetism and ferroelectricity have different chemical origins. These problems are unfortunately intrinsic, in that they cannot be easily solved even by state-of-the-art optimization.

Long *et al.* have demonstrated magnetic field–induced modification of the ferroelectric domains, which is realized in a single-phase material at room temperature with a relatively low operating magnetic field. The work provides an excellent molecular material for room-temperature magnetoelectric coupling; most previously reported couplings were observed at low temperatures or in otherwise multiphase composites (*5*). The finding has strong implications for the application of single-phase magnetoelectric materials from both scientific and practical points of view.

Taking advantage of molecular materials, Long *et al.* designed a chiral lanthanide complex, where the Yb^{3+} ion with a large total magnetic moment is adjacent to a chiral diamagnetic zinc center that exhibits ferroelectricity. They successfully demonstrated the magnetoelectric coupling by performing piezoresponse force microscopy measurements in the presence of a direct-current magnetic field. The redistribution of the ferroelectric domains and the increase in the electromechanical response were observed upon applying a magnetic field of only 1 kOe, which is strong evidence of magnetoelectric coupling at room temperature.

The typical value of the magnetoelectric tensor component was calculated to be ~100 mV $Oe^{-1}{\cdot}cm^{-1}$, at least one order of magnitude larger than that of $BiFeO_3$, a canonical inorganic multiferroic material. The operating field was also one order of magnitude smaller than that typically required for other molecular materials. In addition, Long *et al.* obtained six variable polarization states by switching of the electric and magnetic fields independently. The combination of a strong room-temperature magnetoelectric coupling and the small operating field, as well as the multilevel states, provides a platform for the design of new high-density memory devices (*6*).

Using a series of unconventional but consistent measurements, including both the local surface displacement and structural studies (single-crystal x-ray diffraction) in the presence of a magnetic field, Long *et al.* showed that the magnetoelectric coupling resulted from a magnetoelastic effect. By applying a magnetic field, the

Institute of Microscale Optoelectronics and Institute for Advanced Study, Shenzhen University, Shenzhen 518060, P. R. China. Email: sutinghan@szu.edu.cn

Published by AAAS

Yb^{3+} ion provided an anisotropic magnetostriction that induced a mechanical strain that in turn modified the polarization by changing the dipole configuration. The design seems simple but was powerful enough to induce a strong magnetoelectric coupling at room temperature. Instead of searching in the single-phase multiferroic family, the authors demonstrated magnetoelectric coupling in a paramagnetic ferroelectric crystal, expanding the pool of potential materials choices. The Yb^{3+} ion simultaneously responded to the magnetic field through a magnetostriction effect and accounts for the modification of polarization through the spin-lattice coupling, which overcame the aforementioned intrinsic problem in single-phase inorganic multiferroic materials.

The work of Long *et al.* provides an alternative strategy to realize magnetic field control of polarization at room temperature in molecular ferroelectrics, which removes the strict criterion that is typically required of inorganic multiferroic materials. Many different molecular materials can be designed, so this finding should also stimulate other research directions. For example, the inverse effect of electric-field control of magnetization has also been studied in inorganic materials (*7*, *8*).

Spintronics, in which the central theme is the manipulation of both the charge and spin degrees of freedom, resembles magnetoelectric coupling. The material developed by Long *et al.* is a single-molecule magnet (*9*). Such a material, which typically would have weak spin scattering as well as long spin lifetime in comparison to inorganic counterparts, could be an interesting building block for molecular spintronics. Spins can be manipulated at small size with low energy and encode computational information. These additional degrees of freedom offer unprecedented opportunities to develop entirely new devices. One of the most attractive ideas is to write the data electrically and access them magnetically (*10*), which would overcome the problems of the large writing field of magnetic and the low reading speed of ferroelectric random-access memory. These effects could be used to develop energy-efficient multibit memory, neuromorphic computing, and logic gates that may push device performance beyond current limits. ■

Molecular magnetoelectrics

Magnetoelectric effects can allow magnetic properties to be controlled by electric fields and electrical properties by magnetic fields. The latter was demonstrated by Long *et al.* for a crystal of a compound containing a rare-earth metal, ytterbium (Yb), and zinc (Zn) cations.

Ferroic properties

In these materials, polarization *P* or magnetization *M* are intrinsic and switch only if a strong enough field is applied.

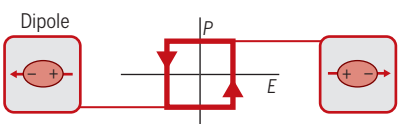

Ferroelectricity
In ferroelectrics, an applied electric field *E* aligns dipoles and results in a polarization *P*.

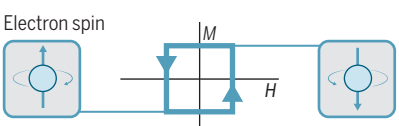

Ferromagnetism
In ferromagnets, an applied magnetic field *H* aligns electron spins and results in a magnetization *M*.

Multiferroic properties

In these materials, spins and dipoles couple so that magnetic fields can align dipoles, and electric fields can align spins.

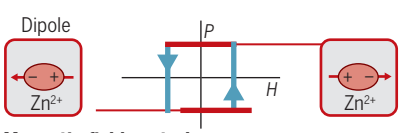

Magnetic-field control
Long *et al.* made a compound that couples Yb^{3+} spins and Zn^{2+} dipoles that enables magnetic-field control of ferroelectricity at room temperature.

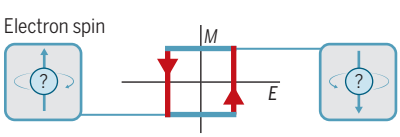

Electrical-field control
Similar control of the magnetization with an electric field was not observed. Such effects are of interest for electronic memories.

REFERENCES AND NOTES

1. J. Long *et al.*, *Science* **367**, 671 (2020).
2. S. W. Cheong, M. Mostovoy, *Nat. Mater.* **6**, 13 (2007).
3. C. Lu, W. Hu, Y. Tian, T. Wu, *Appl. Phys. Rev.* **2**, 021304 (2015).
4. J. F. Scott, R. Blinc, *J. Phys. Condens. Matter* **23**, 113202 (2011).
5. C. A. F. Vaz, J. Hoffman, C. H. Ahn, R. Ramesh, *Adv. Mater.* **22**, 2900 (2010).
6. S.-T. Han, Y. Zhou, V. A. L. Roy, *Adv. Mater.* **25**, 5425 (2013).
7. P. Wadley *et al.*, *Science* **351**, 587 (2016).
8. Y. Yamada *et al.*, *Science* **332**, 1065 (2011).
9. L. Bogani, W. Wernsdorfer, *Nat. Mater.* **7**, 179 (2008).
10. L. Zhou *et al.*, *Small* **14**, 1703126 (2018).

ACKNOWLEDGMENTS

The authors acknowledge support from the Natural Science Foundation of China (grant no. 61974093), Guangdong Province Special Support Plan for High-Level Talents (grant no. 2017TQ04X082), Guangdong Provincial Department of Science and Technology (grant no. 2018B030306028), and the Science and Technology Innovation Commission of Shenzhen (grant nos. JCYJ20180507182042530 and JCYJ20180507182000722).

10.1126/science.aba6642

INFECTIOUS DISEASE

In the heat of the night

An ancestral receptor plays a key role in host detection by malaria-carrying mosquitoes

By **Claudio R. Lazzari**

Vector-borne diseases, such as malaria caused by *Plasmodium* parasites transmitted by female *Anopheles gambiae* mosquitoes, are among the most devastating and also difficult to control problems in public health. Considerable efforts and resources are devoted to the search for effective ways to limit their transmission. An important aspect of these efforts is unravelling the biological mechanisms by which vectors find human hosts. How vectors acquire and make use of sensory information for locating potential blood sources represents a key piece of the mechanism, especially because the vector-host encounter is when pathogen infection occurs. On page 681 of this issue, Greppi *et al.* (*1*) identify the ionotropic receptor *IR21a* gene, which is conserved throughout insects, as a key mediator of heat seeking in mosquitoes carrying malaria parasites.

Mosquitoes are an important group of disease vectors. They transmit a diversity of pathogens, including viruses, bacteria, protozoans, and nematodes; they are present in most regions of the Earth; and the pathogens they transmit cause a substantial disease burden. Among these diseases, malaria claims hundreds of thousands of lives every year globally. According to the World Health Organization, in 2017 nearly half of the world's population was at risk of malaria (*2*); there were 219 million cases, and the estimated number of malaria deaths was 435,000. Children under 5 years of age are the most vulnerable to malaria parasite infection, accounting for 61% of all malaria deaths worldwide (*2*). Even though regions of Southeast Asia, Eastern Mediterranean, Western Pacific, and the Americas are also at risk, the continent of Africa has a disproportionately high share of the global malaria burden. Malaria has even influenced human evolution: The high mortality and widespread distribution of malaria

Institut de Recherche sur la Biologie de l'Insecte, UMR 7261 CNRS–University of Tours, Parc Grandmont, 37200 Tours, France. Email: claudio.lazzari@univ-tours.fr

GRPAHIC: C. BICKEL/*SCIENCE*

Published by AAAS

imposed a strong selective force for genes that confer resistance to malaria (*3*, *4*).

The complexity of the malaria parasite makes development of a malaria vaccine a difficult task. The development of resistance to chemical agents in both mosquitoes to insecticides and parasites to antiparasitic drugs make imperative the search for new tools and strategies. The rapid advance of molecular and genomic sciences represents a new hope for finding innovative solutions with low environmental impact. In recent years, several major biological mechanisms have been unraveled in mosquitoes, in particular related to their sensory systems, especially olfaction (smell). These studies revealed conceivable molecular targets for interfering with their ability to recognize and locate human hosts (*5*).

However, animals do not usually rely on just one sense for locating vital resources; rather, they exploit all available information that they can detect. Female mosquitoes are not an exception; they exploit multimodal information, such as sight, smell, heat, detection of chemicals (*6*–*8*), and probably also water vapor (*9*) for locating and recognizing potential hosts, including humans (see the figure). Thermoreception is a key sense in insects and is particularly well-developed in blood-sucking species (*10*). Thermal sensitivity is provided by temperature-dependent activation of specific molecular receptors on the membrane of specialized cells in sensory structures (sensilla) present in different parts of the insect body, particularly the antennae (*11*, *12*). These sensory cells connect to the brain, informing on temperature changes in the surrounding environment. In mosquitoes, the heat emitted by the body of warm-blooded vertebrates constitutes a major cue for short-range orientation (*13*).

Greppi *et al.* uncovered a fundamental piece of the mechanism of heat detection. They show that the *IR21a* gene is essential for the response to cooling of thermoreceptive cells in the antennae of *A. gambiae*. In mutant mosquitoes with inactivated *IR21a*, thermoreceptive cells no longer respond to temperature changes. Consequently, the ability of mutant mosquitoes to locate and land on sources of a host temperature was much reduced, as well as their responsiveness to the proximity of a human. Multimodal sensing often means that blocking one input does not completely abolish the response of an animal. Yet, the inactivation of *IR21a* significantly reduces the ability of female mosquitoes to find a food source.

Greppi *et al.* also characterized the sensory cells that express *IR21a*. Their electrical activity did not substantially vary between high and low constant temperatures but strongly reacted to temperature changes, increasing firing when temperature decreased (cooling cells). When the mosquito flies close to a host, the heat flow on its antennae increases or decreases with the distance and also the temperature of receptors. The heat flow varies nonlinearly with distance, meaning that temperature changes are more marked at the proximity of the target (*10*). That cooling cells are activated by temperature variations, but not constant temperature, raises the question of whether a mosquito could measure the distance that separates it from its host based on the activation dynamics of these cells during the final approach. Such measures seem to be taken by kissing bugs, which extend their mouthparts at the reach distance for biting, even in the absence of any chemical, visual, or mechanical cue, using only thermal information (*10*).

Another interesting question raised by the work of Greppi *et al.* is related to the evolution of haematophagy (feeding on blood), a way of life that occurs multiple times in the evolutionary history of arthropods (including mosquitoes) (*14*). That *IR21a* is conserved across insects suggests repurposing of an ancestral receptor from non–blood-sucking Diptera. This receptor is also expressed in sensory cells of the fruit fly (*Drosophila melanogaster*). However, whereas *Ir21a* mediates heat avoidance in *D. melanogaster*, *Anopheles IR21a* drives heat seeking and heat-stimulated blood feeding (*1*). Other receptors are also involved in thermal orientation, particularly transient receptor potential (TRP) channels. In mosquitoes, *TRPA1* mediates avoidance of temperatures higher than those of a host. Understanding how these different receptors contribute to thermosensation in diverse blood-sucking species could reveal how haematophagy evolved.

Thermoreception has been a relatively neglected aspect of vector biology, with research efforts focused largely on chemoreception. Odors play an important role in insect biology and could be used to manipulate vector behavior. Thus, much more work has been done on olfaction than any other sensory system of mosquitoes. Recently, however, interest for thermal sensation has increased, opening research avenues and perhaps revealing possibilities for controlling vector-borne diseases. ■

Female *Anopholes gambiae* mosquitoes are vectors of malaria parasites. They use various senses to home-in on targets, and blood-sucking allows transfer of parasites.

How mosquitoes find their hosts

Multimodal integration is essential for modulating general responsiveness, orientation, and approach. Carbon dioxide stimulates the response to other cues, and heat detection is crucial for the final approach.

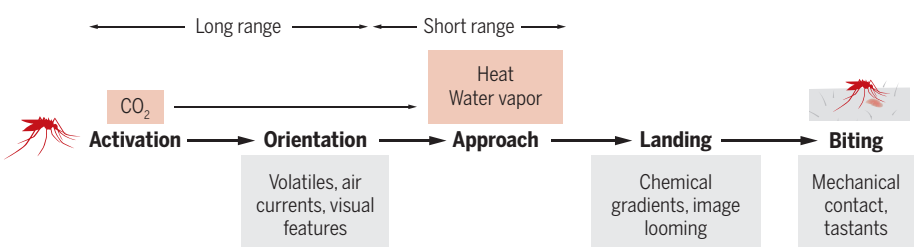

CREDITS: (PHOTO) ALEXANDER WILD; (GRAPHIC) N. DESAI/*SCIENCE*

REFERENCES AND NOTES

1. C. Greppi *et al.*, *Science* **367**, 681 (2020).
2. World Health Organization (WHO), *World Malaria Report 2018* (WHO, 2018); www.who.int/malaria/ publications/world-malaria-report-2018/en.
3. P. W. Hedrick, *Heredity* **107**, 283 92011).
4. S. Sha, *The Fever* (S. Crichton Books, 2010).
5. L. B. Duvall *et al.*, *Cell* **176**, 687 (2019).
6. C. J. McMeniman *et al.*, *Cell* **156**, 1060 (2014).
7. F. van Breugel *et al*, *Curr. Biol.* **25**, 2123 (2015).
8. R. T. Cardé, *Curr. Biol.* **25**, R793 (2015).
9. F. E. Kellogg, *J. Insect Physiol.* **16**, 99 (1970).
10. C. R. Lazzari, *Adv. Insect Physiol.* **37**, 1 (2009).
11. G. Wang *et al.*, *Eur. J. Neurosci.* **30**, 967 (2009).
12. R. A Corfas, L. B. Vosshall, *eLife* **4**, e.11750 (2015).
13. P. F. Zermoglio *et al.*, *J. Insect Physiol.* **100**, 9 (2017).
14. M. J. Lehane, *The Biology of Blood-Sucking in Insects* (Cambridge, ed. 2, 2005).

10.1126/science.aba4484

Published by AAAS

POLICY FORUM

GLOBAL HEALTH

Using sewage for surveillance of antimicrobial resistance

A global system would exploit metagenomic sequencing

By **Frank M. Aarestrup**[1] and **Mark E. J. Woolhouse**[2]

Antimicrobial resistance (AMR), a cross-cutting and increasing threat to global health (*1*–*3*), is a complex problem with multiple and interconnected drivers. Reliable surveillance data that accurately describe and characterize the global occurrence and distribution of AMR are essential for tracking changes in resistance over time, setting national and global priorities, assessing the impacts of interventions, identifying new kinds of resistance, and supporting investigation of (international) outbreaks of resistant pathogens. AMR surveillance data can also inform development of treatment guidelines. Yet it has proven difficult to achieve these objectives on a global scale, and especially in low- and middle-income countries (LMICs), largely because current surveillance systems deliver data that are extremely variable in quality and quantity and highly heterogeneous in terms of which population is sampled (usually a category of hospital patients) and what drug-bug combinations are included (*1*). Here, we outline a plan for a global AMR surveillance system based on applying next-generation sequencing (NGS) to human sewage that will be especially helpful for community AMR surveillance, which is difficult to achieve in other ways, and will provide an affordable surveillance option in resource-poor settings.

NGS is a powerful technology that has transformed the health data landscape. Among many other benefits, it has drastically improved our ability to determine the presence of AMR genes (bacterial genes known to confer resistance to an antimicrobial drug) in single isolates and to quantify them in complex microbiomes (*4*, *5*). Millions of random DNA fragments sequenced by NGS can be mapped to reference sequence databases, and the number of reads coming from any of several thousand known AMR genes can be counted to provide easily shared information on their occurrence and abundance.

Increasing numbers of people globally are connected to sewage treatment systems (*6*) and, as recently highlighted by the World Bank (*3*), metagenomics-based, near real-time quantification of AMR genes in sewage is a potentially useful surveillance tool even in remote locations without microbiology laboratories (*7*). Such an approach could quickly plug current gaps in the geographic, population, and agent coverage of AMR surveillance, especially by providing data on AMR outside hospitals (90% of antibiotic usage in humans occurs outside hospitals) (see the figure). It could also provide information on environmental transmission in populations exposed to raw sewage.

CURRENT AMR SURVEILLANCE

The relevance of local and national surveillance of AMR to inform treatment guidelines and intervention strategies has been recognized for decades. The first international AMR-surveillance program was The European Antimicrobial Resistance Surveillance Network (EARS-Net), whose predecessor (EARS) was launched in 1998. EARS-Net is based on routine clinical antimicrobial susceptibility data from clinical laboratories reported to the European Centre for Disease Control and Prevention (ECDC). Only data from invasive isolates (blood and cerebrospinal fluid) and for seven bacterial pathogens are included.

The Global Antimicrobial Resistance Surveillance System (GLASS) was launched in October 2015 by the World Health Organization (WHO) to support its global action plan on AMR. A number of local WHO surveillance networks had already been established prior to GLASS, and AMR data were also included in surveillance of single pathogens such as *Mycobacterium tuberculosis* and *Neisseria gonorrhoeae*. As of January 2020, GLASS had enrolled 90 countries covering all regions (though not all have yet provided data), each reporting on up to eight different pathogens and up to 35 drug-bug combinations considered the most clinically important (though often only a small subset of these). In addition to these formal systems, a number of more informal AMR surveillance initiatives have been established, such as ResistanceOpen that provides online maps of the occurrence of four "super-bugs" worldwide, and ResistanceMap that maps resistance data for 12 bacterial pathogens from 46 countries.

A common feature of all these initiatives is that they focus on hospitalized patients and mainly last-resort antimicrobial agents such as carbapenems (used after other agents have proven ineffective) (see the figure). This reflects the clinical perception that resistance to last-resort antibiotics is most critical for patients, and the ease of access to clinical diagnostic facilities, put in place to improve patient outcomes and not, primarily, to facilitate AMR surveillance. This emphasis on clinical settings makes it difficult to determine the global spread of resistance to first-line drugs in the wider community, a large part of the global AMR burden (*8*). Indeed, it has recently been argued that interventions to support first-line drugs (e.g., tetracyclines) might have much greater public health impact than against last-resort antimicrobial agents (*8*), the argument being that if the initial treatment works, the patients will never need a last-resort antimicrobial treatment.

Because current isolate-based surveillance greatly relies on testing already being conducted for clinical purposes, it is often based on small sample sizes and can be biased. Nor is it easily implemented in resource-poor settings where there are no laboratories to perform bacterial isolation, identification, and susceptibility testing and only a subset of the population may have access to clinical diagnostics. In addition, it has proven difficult to coordinate and harmonize both sampling and susceptibility testing results: Different definitions for clinical cases may be used, methods for identification differ, and different antimicrobial agents are tested.

SEWAGE-BASED SURVEILLANCE

Examination of sewage inlets to treatment plants is already recommended for polio surveillance and, more recently, sewage has been successfully used for quantifying the occurrence and abundance of AMR genes in human populations (*4*, *5*, *9*–*11*). These studies mostly used metagenomic sequencing (which can detect all known resistance genes), though sometimes quantitative polymerase chain reaction (which targets only selected genes). Even a single sample from one site can be representative of a large, urban population, and a complete profile

[1]Technical University of Denmark, DK-2800 Kgs. Lyngby, Denmark. [2]Usher Institute, University of Edinburgh, Edinburgh EH9 3FL, UK. Email: mark.woolhouse@ed.ac.uk

PHOTO: (OPPOSITE PAGE) JOCHEN TACK/ALAMY STOCK PHOTO

Published by AAAS

Sewage sampling is a low-tech approach that is straightforward to implement in any setting.

(occurrence and abundance) of thousands of AMR genes (the resistome) within that population can be obtained (*4*). In addition, some studies have suggested that resistance data from sewage can correlate well with data from clinical surveillance (*10*, *11*).

However, global sewage-based surveillance using metagenomics differs from conventional measures of levels and burden of AMR in several key respects. It generates pooled data from a large, non–hospital population (whereas most surveillance data refer only to hospital patients). The data are also pooled across all bacteria taxa (i.e., do not refer to a, usually cultured, subset of bacterial pathogens). Sewage-based surveillance measures AMR gene frequencies (not the prevalence of phenotypic resistance in a collection of isolates). Sewage therefore provides a different measure of AMR obtained using a different sampling frame and as such can augment current surveillance based on clinical isolates. Ideally, data from these two sources would be collected in parallel, allowing calibration and confirmation of geographic patterns and temporal trends.

We recognize certain limitations. Sewage-based AMR metagenomic surveillance, unlike isolate-based surveillance, does not link the AMR genes to specific bacterial species (though it can be argued that for surveillance purposes, it is the genes that are of interest). Also, sensitivity is likely lower than isolate-based surveillance (though this may be compensated for by not being limited to a few bacterial species).

At the same time, however, sewage-based metagenomic AMR surveillance has several important advantages. It characterizes large communities that are not routinely assessed by conventional surveillance (though only those connected to the sewage system). It is straightforward to implement, at its most basic only requiring sample collection (using inexpensive equipment that is readily available) and shipment. Sequencing and bioinformatics methods are easily standardized, especially if done by a central facility. Ethical concerns have not been raised, and there is no legal requirement for informed consent as data cannot be linked to any individual (*4*). Sewage-based surveillance is not limited to an often very restricted subset of drug-bug combinations. It can provide a baseline for future trends and to monitor the effects of interventions in any location, irrespective of whether the diagnostic capacity to isolate and identify bacterial pathogens exists. In the absence of good clinical surveillance, it can provide a comparison of

Published by AAAS

countries and regions, indicating where further actions are needed. When based on metagenomics, it allows for retrospective analyses of data should previously unknown genes subsequently be identified, providing a rapid assessment of global emergence. In addition, metagenomics provides information on all DNA and potentially RNA in the sample and can thus also be useful for surveillance of any living organisms, including enteric pathogens (*12*).

Sewage-based surveillance is also relatively cheap. For example, the World Bank has estimated the annual cost for clinical, isolate-based surveillance in one LMIC—Kenya—at approximately US$2 million (*2*). From our own experience (*4*), we estimate that the additional costs for collection, shipment, DNA purification, sequencing, and bioinformatics analysis of two sewage samples annually from two sites within the same country would be less than 0.1% of this sum. We therefore consider sewage-based surveillance to be a potentially valuable addition to current options for global AMR surveillance and monitoring. Though not a substitute for other surveillance methods, it can provide data that is otherwise hard to obtain and may sometimes be the easiest route to providing any information at all, especially in resource-poor settings.

NECESSARY STEPS

Two important considerations are the DNA-purification methodology and the choice of bioinformatics analyses, both of which can influence the outcome. Protocols for sample collection, handling, DNA purification, and sequencing are already available and evaluated (*4*, *13*), but specific choices have to be agreed on so that the process is fully standardized—ensuring balanced representation from all bacterial species, maximizing read quality, and test sensitivity are key issues. Bioinformatics methods for generating AMR gene abundance data are already available (*4*) but, again, specific choices need to be made. Unlike the sequencing step, here the choice is not irrevocable; metagenomics data, once generated, can be reanalyzed when new bioinformatics methods become available or reference sequence databases are updated (allowing, for example, retrospective study of the spread of newly identified resistance genes).

In addition, agreements are needed on sample and data sharing that comply with the Nagoya Protocol to the Convention on Biological Diversity (*14*). Agreement is needed on a standardized data reporting format, noting that gene abundance data are different in nature from isolate-based data. Competent national and global authorities must be identified. The sewage-based program must be integrated with existing isolate-based surveillance programs. Formal economic analysis is necessary, and a case for affordability and sustainability needs to be made.

It is important to ensure that global sewage-based surveillance is adopted by the right international organization(s) with the mandate to perform regional and/or global AMR surveillance, such as WHO and, for Europe, ECDC. This would also ensure direct and sustainable links to existing surveillance systems such as GLASS. This does not, however, restrict national institutions from setting up national sewage-based surveillance at any stage.

An immediate working model for global surveillance could be annual collection of sewage samples across the globe, with shipment of sewage to a central facility, perhaps a WHO Collaborating Centre, responsible for the subsequent sequencing, bioinformatics, analyses, and reporting (see the figure). As capacity builds around the world, this could transition into a system where DNA is purified and sequenced and perhaps also analyzed locally and subsequently shared globally via an international agency.

Standard reporting should at a minimum include AMR gene abundances per country over time for each antimicrobial class. Reporting frameworks will need to be adapted to accommodate this different kind of data. Though we recognize that there may be political sensitivities, we would strongly encourage global public sharing of the raw data with the global research community wherever possible, taking advantage of the global repositories for sharing sequencing data already in place.

In our opinion, the implementation of a global sewage-based AMR surveillance system would have substantial and rapid benefits, especially in resource-poor settings. It could be quickly implemented at a comparatively very low cost. By providing population-level information, it would complement and augment current AMR surveillance efforts, so contributing to meeting the key objectives of AMR surveillance at a global scale. ■

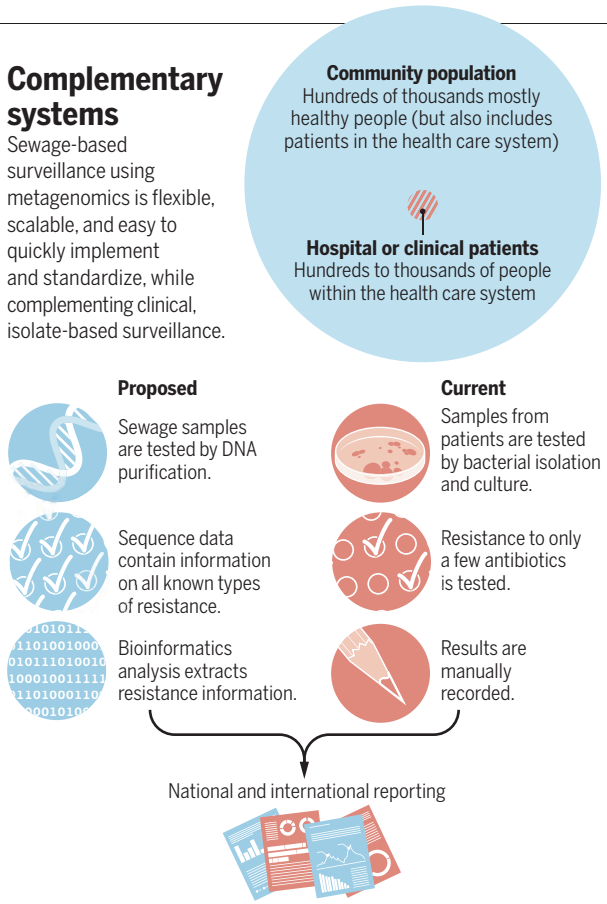

REFERENCES AND NOTES

1. World Health Organization, Antimicrobial resistance: Global report on surveillance (2014); https://apps.who.int/iris/bitstream/10665/112642/1/9789241564748_eng.pdf.
2. World Bank Group, Resistant infections; A Threat to Our Economic Future (2017); http://documents.worldbank.org/curated/en/323311493396993758/pdf/final-report.pdf.
3. World Bank Group, Pulling Together to Beat Superbugs; Knowledge and Implementation Gaps in Addressing Antimicrobial Resistance (2019); http://documents.worldbank.org/curated/en/430051570735014540/pdf/Pulling-Together-to-Beat-Superbugs-Knowledge-and-Implementation-Gaps-in-Addressing-Antimicrobial-Resistance.pdf.
4. R. S. Hendriksen *et al.*; Global Sewage Surveillance project consortium, *Nat. Commun.* **10**, 1124 (2019).
5. J. Q. Su *et al.*, *Microbiome* **5**, 84 (2017).
6. United Nations, Department of Economic and Social Affairs, Population Division, *World Urbanization Prospects: The 2018 Revision (ST/ESA/SER.A/420)* (United Nations, New York, 2019); https://population.un.org/wup/Publications/Files/WUP2018-Report.pdf (last accessed 6 January 2020).
7. K. Acharya *et al.*, *Sci. Rep.* **9**, 15726 (2019).
8. M. R. Perry *et al.*, *bioRxiv* 498329 (2018). https://doi.org/10.1101/498329
9. S. M. Joseph *et al.*, *mSystems* **4**, e00327-19 (2019).
10. K. M. M. Pärnänen *et al.*, *Sci. Adv.* **5**, eaau9124 (2019).
11. M. Hutinel *et al.*, *Euro Surveill.* **24**, 1800497 (2019).
12. R. S. Hendriksen *et al.*, *PLOS ONE* **14**, e0222531 (2019).
13. A. D. Li *et al.*, *FEMS Microbiol. Ecol.* **94**, fix189 (2018).
14. C. Dos S Ribeiro *et al.*, *Science* **362**, 404 (2018).

ACKNOWLEDGMENTS

We are grateful to the WHO GLASS team for helpful discussions and to three anonymous reviewers for constructive comments on an earlier draft. The Global Sewage Surveillance Project is supported by The Novo Nordisk Foundation (NNF16OC0021856: Global Surveillance of Antimicrobial Resistance). The authors contributed equally to this work. F.A. is the current head of a WHO Collaborating Centre for AMR.

10.1126/science.aba3432

GRAPHIC: V. ALTOUNIAN/*SCIENCE*

Published by AAAS

Frances Glessner Lee's "Attic" is among the crime scene dioramas used to train forensic scientists.

PHOTO: MANDEL NGAN/AFP/GETTY IMAGES

FORENSIC SCIENCE

Death dollhouses and the birth of forensics

A wealthy patron's vision and macabre models helped forge the field of forensic medicine

By **Alison Adam**

Frances Glessner Lee is best known for crafting a curious set of macabre dollhouses, each portraying a miniature diorama of a real crime scene in accurate and gory detail. These unusual teaching aids—referred to as "the Nutshell Studies of Unexplained Death"—are still in use in police departments and forensic training programs. Nevertheless, as Bruce Goldfarb reveals in *18 Tiny Deaths*, Glessner Lee's contribution to the development of forensic medicine and crime scene investigation was considerably wider in scope than her dollhouses of death. Goldfarb's unprecedented access to her family's papers has enabled him not only to paint a full picture of Glessner Lee's life and background but also to uncover less well-known aspects of her impact on the development of forensic science.

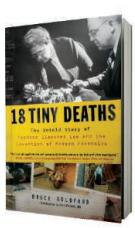

18 Tiny Deaths
Bruce Goldfarb
Sourcebooks, 2020.
368 pp.

Glessner Lee was born into a very wealthy Chicago family in 1878. She was educated at home and—like many women at the time—never attended college. Although she was aware of her educational deficiencies, she had an acute intellect and an unusual eye for detail. She also happened to be as capable with arts and crafts as she was with science and medicine.

The nutshell studies Glessner Lee created were tiny models of real crime scenes rendered with all the details needed to infer what had occurred. They were inspired by the dollhouses she made as a child. She designed all the models herself and enlisted the help of a skilled carpenter to bring them to life. Despite facing a shortage of materials—early models were produced during World War II—Glessner Lee made sure that every detail was accounted for. The first model, for example, which depicted a death by hanging in a New England barn, included such details as a 1-inch-tall hornet's nest clinging to the eaves and a horseshoe hanging with the open side down (the unlucky way, of course) over the barn door.

But Glessner Lee's impact on the field would go beyond the nutshell studies. She vigorously championed the cause of "legal" or, as it is now known, forensic medicine, compelled by the belief that the coroner system in use in the United States was prone to corruption and lacked appropriate input from those qualified in forensic medicine. She also used her fortune to endow a medicolegal library at Harvard and helped to found the university's Department of Legal Medicine, the first of its kind in the United States.

One of the goals of the Department of Legal Medicine was to act as a resource for criminal investigations throughout Massachusetts and to ultimately become a national resource for forensic medicine. To this end, Glessner Lee established and ran a series of police homicide seminars, not only arranging speakers but also paying their travel expenses and overseeing arrangements for the classroom and seminar banquets.

The seminars were an unqualified success. Indeed, their fame was such that Erle Stanley Gardner, the prolific author of the Perry Mason detective novels, wrangled a place in one. The experience prompted him to convert to the cause of legal medicine.

While the university was eager to accept Glessner Lee's money, it was sometimes reluctant to accept her advice, and the two parties frequently clashed. The lavish dinners she hosted after her seminars, for example, were criticized by some in the medical school. She argued that such events were essential for networking purposes, but the university made it clear that it would have preferred to have spent the money on other priorities.

Glessner Lee eventually grew frustrated with what she saw as "a long, discouraging struggle against petty jealousies, crass stupidities, and an obstinate unwillingness to learn that has required all the enthusiasm, patience, courage and tact that I could muster." Having initially venerated Harvard, she was ultimately disappointed with its "old fogeyish" approach and lack of gratitude. Yet, realizing that the work would not continue unless it was well funded, she left a substantial amount of money to the Department of Legal Medicine in her will, and the homicide seminars continued after her death in 1962 until 1967. (They were moved to Baltimore in 1968 and continue to be held at the State of Maryland Forensic Medical Center to this day.)

Although her career was bedeviled by setbacks, as Goldfarb ably demonstrates, Frances Glessner Lee made a real and lasting contribution to forensic science and medicine. ■

The reviewer is at the Cultural, Communication, and Computing Research Institute, Sheffield Hallam University, Sheffield S1 2NU, UK, and is the author of *A History of Forensic Science: British Beginnings in the Twentieth Century* (Routledge, 2016). Email: a.adam@shu.ac.uk

10.1126/science.aba1118

Published by AAAS

DEMOGRAPHY

Hidden figures

Missing population data hinder good accounting and fair resource distribution

By **William P. O'Hare**

In his new book, *The Uncounted*, Alex Cobham documents how shortcomings of data in two key areas—population and finances—work together to exclude certain groups from exerting political power while simultaneously conveying greater political power to other groups. Cobham, an economist and the chief executive at the Tax Justice Network in the United Kingdom, focuses on the extent to which many marginalized populations are often not counted in official statistics and the extent to which wealthy individuals and families are often able to hide their financial resources, properties, and other holdings from the government to avoid paying taxes on these assets.

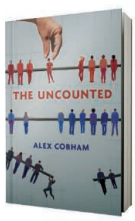

The Uncounted
Alex Cobham
Polity, 2020. 240 pp.

Cobham documents a range of situations where people are missed or undercounted in official statistics, from United Nations figures to country surveys. More often than not, the most frequently missed groups are those that are economically and socially marginalized. When such groups are not accounted for, it often leads to reduced political power as well as reduced economic well-being.

Many marginalized groups have relatively high net undercount rates in the U.S. census (*1*), and areas with high concentrations of these groups often do not receive their fair share of government aid. In addition to those noted by Cobham, there is another group that is regularly undercounted in censuses: young children (*2*–*4*).

These examples support Cobham's observation that "there may be people and groups at the bottom of distributions (e.g., income) whose 'uncounting' adds another level to their marginalization." He goes on: "Being uncounted is not generally a matter of coincidence, but reflects power: the lack of it, or its excess."

The political overtones of how power can be used to deliberately undercount marginalized groups was on full display in the buildup to the 2020 U.S. census. The Trump administration, acting through the U.S. Department of Commerce, tried to add a question to the 2020 U.S. census regarding citizenship status, knowing that it would depress participation of populations with large numbers of immigrants. This attempt—which was eventually struck down by the U.S. Supreme Court but was then the subject of an executive order with similar goals—was made despite the objections of the experts at the Census Bureau, all living former Census Bureau directors, and many other statistical experts.

Cobham next turns his attention to uncounted money and the extent to which people can hide their resources from the authorities. Hidden resources not only deprive countries of their fair share of tax revenue, they mask the real extent of economic inequality.

Here, Cobham documents efforts currently under way to make the financial world more transparent. While such efforts are still young, they appear to be having mixed success. He writes, for example, about the shortcomings of the commonly used Gini coefficient to measure income inequality, which is insensitive at higher levels of inequality, and the benefits of the more transparent Palma method, which can easily be translated into a meaningful statement for nonexpert audiences.

Throughout the book, Cobham argues that a lack of good data on population and finances is a major hindrance to good governance. Without good data, he maintains, we have little idea if a policy or program is having a positive or negative impact.

In his "Uncounted Manifesto" at the end of the book, Cobham makes the case for several changes in law and regulations that could help us get a more accurate assessment of populations and resources that currently go uncounted. Here, he highlights the promise of the international standard known as the Extractive Industries Transparency Initiative, set up to make sure multinational corporations are paying their fair share of taxes. Initially lacking in accountability, the initiative has evolved into a metric with "powerful momentum to pursue real transparency."

Ultimately, *The Uncounted* provides a good summary and overview of the extent to which official statistics are systematically biased because of uncounted populations and hidden financial resources. The book will provide a good entry point for people interested in the interplay between data, demography, and public policy. ■

The reviewer is president of O'Hare Data and Demographic Services, LLC, Cape Charles, VA 23310, USA.
Email: billohare1@gmail.com

U.S. census workers set out to count individuals experiencing homelessness in Los Angeles, California.

PHOTO: LIZ O. BAYLEN/*LOS ANGELES TIMES*/GETTY IMAGES

REFERENCES AND NOTES

1. W. P. O'Hare, *Differential Undercounts in the U.S. Census: Who Is Missed?* (Springer, 2019).
2. W. P. O'Hare, *The Undercount of Young Children in the U.S. Decennial Census* (Springer, 2015).
3. W. P. O'Hare, *Stat. J. IAOS* **33**, 289 (2017).
4. D. Goodkind, *Demography* **48**, 291 (2011).

10.1126/science.aba0447

Published by AAAS

LETTERS

Kelp forests serve as early indicators that portend climate impacts in other marine ecosystems.

PHOTO: B. FISCELLA PROYECTO/MERO GIGANTE-COBI

Edited by **Jennifer Sills**

Marine heat waves threaten kelp forests

Marine kelp forests, among the most productive ecosystems on our planet (*1*), are in danger. The increase in the frequency and intensity of extreme climatic events (*2*) such as marine heat waves is compromising kelp forests' capacity to produce goods and services (such as biomass of commercial fisheries, coastal protection, nutrient cycling, carbon sequestration, and recreational opportunities) that are worth billions of dollars to humanity (*3*). However, despite increasing climate-change advocacy and the overwhelming evidence demonstrating social and ecological impacts of climate change (*4*), political denial and inaction are jeopardizing society's ability to respond adequately to the multifaceted consequences of the accelerating pace of climate-driven loss of marine forests.

Between 2014 and 2016, extreme marine heat waves of unprecedented duration and magnitude in the northwestern Pacific Ocean decimated giant kelp forest ecosystems across the U.S. state of California and Baja California, Mexico (*5*–*7*). Three years later, the once-extensive giant kelp forests have not recovered. Many of these underwater forests are now gone, replaced by smaller kelps or by sea urchin "barrens" (*7*), which can no longer provide food and shelter to diverse ecological communities. Meanwhile, at the UN climate conference COP25, the international community lost a valuable opportunity to tackle the climate crisis, mainly due to the lack of ambitious commitments by major players who are denying scientific evidence (*8*).

Kelp forests embody the concept of "sentinel systems" (early indicators) in the face of climate change. Their loss is an emergent global conservation issue (*9*) that signals future impacts throughout the marine realm. If political authorities fail to support climate-smart strategies (*10*), substantial economic losses will follow. Alarmingly, CO_2 emissions continue a trend of increase (*11*); unless this trend is reversed, studies predict a near-permanent marine heat wave status by the end of the 21st century (*12*).

We urgently need international agreements to decrease future global CO_2 emissions as well as government policies to mitigate existing local threats. Countries need to prioritize science-based mitigation and adaptation solutions, including improved management of anthropogenic impacts unrelated to climate change, the development of sea urchin markets and ranches, the exploration of climate-safe restoration sites, and the identification of genetically resilient kelp stocks. These changes will require investment in research and environmental protection. Increased human capacity will also be needed to halt and reverse the ongoing rapid loss of ecosystems and their services to people.

Nur Arafeh-Dalmau[1,2]*, David S. Schoeman[3,4], Gabriela Montaño-Moctezuma[5], Fiorenza Micheli[6], Laura Rogers-Bennett[7,8], Carolina Olguin-Jacobson[9], Hugh P. Possingham[1,10]
[1]Centre for Biodiversity & Conservation Science, School of Biological Sciences, University of Queensland, Brisbane, Queensland 4072, Australia. [2]School of Earth and Environmental Sciences, University of Queensland, St. Lucia, QLD 4072, Australia. [3]Global-Change Ecology Research Group, School of Science and Engineering, University of the Sunshine Coast, Maroochydore, QLD, Australia. [4]Department of Zoology, Centre for African Conservation Ecology, Nelson Mandela University, Port Elizabeth, South Africa. [5]Instituto de Investigaciones Oceanológicas, Universidad Autónoma de Baja California, Ensenada, Mexico. [6]Hopkins Marine Station and Stanford Center for Ocean Solutions, Pacific Grove, CA 93950, USA. [7]Karen C. Drayer Wildlife Health Center, University of California, Davis, Bodega Marine Laboratory, Bodega Bay, CA 94923, USA. [8]California Department of Fish and Wildlife, Bodega Bay, CA 94923, USA. [9]Australian Rivers Institute, School of Environment and Science, Griffith University, Southport, QLD 4215, Australia. [10]The Nature Conservancy, Arlington, VA 22203–1606, USA.
*Corresponding author.
Email: n.arafehdalmau@uq.net.au

REFERENCES AND NOTES

1. D. R. Schiel, M. S. Foster, *The Biology and Ecology of Giant Kelp Forests* (University of California Press, Oakland, CA, 2015).
2. T. L. Frölicher *et al.*, *Nature* **560**, 360 (2018).
3. D. A. Smale, *New Phytologist* 10.1111/nph.16107 (2019).
4. IPCC, "Summary for Policymakers," in *IPCC Special Report on the Ocean and Cryosphere in a Changing Climate*, H.-O. Pörtner *et al.*, Eds. (2019).
5. K. C. Cavanaugh *et al.*, *Front. Mar. Sci.* **6**, 413. (2019).
6. N. Arafeh-Dalmau *et al.*, *Front. Mar. Sci.* **6**, 499 (2019).
7. L. Rogers-Bennett, C. A. Catton, *Sci. Rep.* **9**, 1 (2019).
8. "COP25 Climate change talks: 'We've lost an important opportunity,'" *BBC* (2019).
9. W. J. Sutherland *et al.*, *Trends Ecol. Evol.* **34**, 139 (2019).
10. D. P. Tittensor *et al.*, *Sci. Adv.* **5**, eaay9969 (2019).
11. P. Friedlingstein *et al.*, *Earth Syst. Sci. Data* **11**, 1783 (2019).
12. E. C. Oliver *et al.*, *Front. Mar. Sci.* **6**, 734 (2019).

10.1126/science.aba5244

Marine restoration projects are undervalued

Coral reefs, mangroves, and seagrass beds support the livelihoods of many millions of people worldwide. These ecosystems are rapidly degrading, leading governments and foundations to dedicate billions of dollars to their active restoration. Such initiatives are often criticized for being too small in scope and too expensive to combat the extent of anthropogenic threats driving habitat loss [e.g., (*1*, *2*)]. However, this criticism undervalues key attributes of restoration projects that are not contingent on spatial scale.

Restoration accelerates the recovery of biological communities at local scales. Although restored habitats remain vulnerable to subsequent disturbance events, their biodiversity has the potential to increase ecosystem resilience of larger areas by providing seed material for recovery (*3*). Restoration can also counter the economic, socio-cultural, and psychological impacts of habitat degradation for local communities (*4*), even if techniques are too expensive to upscale globally. The pessimistic view of marine restoration as a fruitless exercise differs from attitudes about the rehabilitation of forest habitats that suffer equivalent large-scale degradation. Generally, socio-economic, ecological, and cultural values

Published by AAAS

AAAS Travels

Members and friends of AAAS are invited to join AAAS Travels on fascinating trips to all 7 continents!

GRAND CANYON
Zion & Bryce Canyon Nat'l Parks

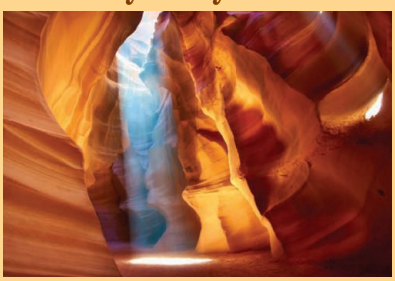

May 29 - June 6, 2020

Join naturalist and former park superintendent Ellis Richard as we explore spectacular National Parks in the canyonlands! Discover the dramatic wonderlands of ***Zion, Bryce Canyon****, and the* ***Grand Canyon****, plus Antelope Canyon. Also enjoy a half-day float trip on the Colorado River.*
$3,495 pp twin share + air

WILD ALASKA
& Denali Extension

Mt. Denali

June 26 - July 1, 2020
or July 16-21, 2020

Discover Alaska on this exciting expedition to see the region's iconic wildlife, epic landscapes, and local culture. Hike, kayak, or paddleboard and enjoy the natural wonder of this wonderland up close on board National Geographic Sea Bird.
From $4,420 pp + air.

With optional 7-day Denali extension following each cruise
$3,990 per person + air.

For a detailed brochure, please call (800) 252-4910
All prices are per person twin share + air

BETCHART EXPEDITIONS Inc.
17050 Montebello Rd
Cupertino, California 95014
Email: AAASInfo@betchartexpeditions.com
www.betchartexpeditions.com

are appreciated in tree planting, whether it involves a few saplings or millions (*5*, *6*).

Political agreements for global reductions in atmospheric carbon have been slow to emerge. Relying on their implementation as the only solution to the degradation of tropical habitats is a major gamble. In the meantime, restoration projects could help maintain species survival and ecosystem services, ultimately providing humanity with the breathing space to stabilize the climate.

Timothy A. C. Gordon[1,2]*, Andrew N. Radford[3], Stephen D. Simpson[1], Mark G. Meekan[2]
[1]University of Exeter, Exeter EX4 4PS, UK. [2]Australian Institute of Marine Science, Perth, WA 6009, Australia. [3]University of Bristol, Bristol BS8 1TQ, UK.
*Corresponding author. Email: tg333@exeter.ac.uk

REFERENCES AND NOTES

1. T. P. Hughes *et al.*, *Nature* **546**, 82 (2017).
2. D. R. Bellwood *et al.*, *Biol. Conserv.* **236**, 604 (2019).
3. E. S. Darling, I. M. Côté, *Science* **359**, 986 (2018).
4. M. Y. Hein *et al.*, *Biol. Conserv.* **239**, 14 (2019).
5. K. D. Holl, *Science* **355**, 455 (2017).
6. W. D. Newmark *et al.*, *Proc. Natl. Acad. Sci. U.S.A.* **114**, 9635 (2017).

10.1126/science.aba9141

U.S. action lowers barriers to invasive species

Invasive species can cause harm to a broad spectrum of critical needs ranging from economic, food, water, and infrastructure security to human and environmental health to military readiness (*1*). However, recent actions by the Trump Administration put national security at risk by lowering barriers to these devastating invaders. Department of the Interior officials cut the National Invasive Species Council (NISC) budget by 50% (*2*) and terminated the associated Invasive Species Advisory Committee (ISAC) (*3*), effectively crippling the ability of federal agencies to work with each other and with nonfederal stakeholders to address invasive species. The United States needs comprehensive, robust, consistent actions to minimize impacts of invasive species that already cost the nation hundreds of billions of dollars annually (*4*).

The biological invasion crisis is best addressed by using education, regulation, and border control to prevent invasive species from entering the country. Action must be taken to quickly detect and intercept nonnative species at points of entry. This responsibility largely falls to the federal government. The meager NISC budget—just $1.2 million per year (*5*)—was already grossly insufficient given the importance of its mission; invasive species have been found to be as disruptive as climate change (*6*). Prioritizing protection from invasive species is a good investment; preventing entry of a single new high-impact invasive species could save billions of dollars annually (*7*). Yet the recent cuts make clear that the U.S. government will fail to adequately prioritize prevention at ports of entry, to assess the impacts of invasive species on the economy and human health, and to implement an effective national early detection-rapid response program.

Invasive species affect every sector of the nation regardless of jurisdiction or politics. Climate change, international trade, and resource use will further facilitate invasions. The public, nongovernmental organizations (NGOs), and scientific communities must demand that the federal government build upon the vision for high-level, well-coordinated federal leadership by restoring the NISC budget, reestablishing ISAC, and increasing support for actions by NGOs and state and local governments. U.S. lands and waters face unprecedented risks from our current porous biosecurity policies.

Daniel Simberloff[1]*, Jacob N. Barney[2], Richard N. Mack[3], James T. Carlton[4], Jamie K. Reaser[5,6,7], Brent S. Stewart[8], Gary Tabor[6], Eric M. Lane[9], William Hyatt[10], Jacob W. Malcom[11,7], Lori Buchanan[12], Laura A. Meyerson[13]
[1]Department of Ecology and Evolutionary Biology, University of Tennessee, Knoxville, TN 37996, USA. [2]School of Plant and Environmental Sciences, Virginia Tech, Blacksburg, VA 24061, USA. [3]School of Biological Sciences, Washington State University, Pullman, WA 99163, USA. [4]Maritime Studies Program, Williams College–Mystic Seaport, Mystic, CT 06355, USA. [5]Giving Voice to Resilience, LLC, Stanardsville, VA 22973, USA. [6]Center for Large Landscape Conservation, Bozeman, MT 59715, USA. [7]Environmental Science and Policy, George Mason University, Fairfax, VA 22030, USA. [8]Hubbs-SeaWorld Research Institute, San Diego, CA 92109, USA. [9]Boulder County Parks & Open Space Department, Longmont, CO 80503, USA. [10]Connecticut Department of Energy and Environmental Protection, Bureau of Natural Resources, Hartford, CT 06106, USA. [11]Center for Conservation Innovation, Defenders of Wildlife, Washington, DC 20036, USA. [12]Molokai/Maui Invasive Species Committee, Kualapuu, HI 96757, USA. [13]Natural Resources Science, University of Rhode Island, Kingston, RI 02881, USA.
*Corresponding author. Email: dsimberloff@utk.edu

REFERENCES AND NOTES

1. Executive Office of the President, Executive Order 13751, 81 FR 88609-88614, 5 December 2016 (2016).
2. U.S. Department of the Interior, "Budget justifications" (2019); www.doi.gov/sites/doi.gov/files/uploads/fy2020_os_budget_justification.pdf.
3. M. Green, "White House eliminates advisory boards for marine life, invasive species," *The Hill* (2019).
4. D. Pimentel *et al.*, *Ecol. Econ.* **52**, 273 (2005).
5. U.S. Department of the Interior, "Fiscal Year 2018: The Interior budget in brief" (2017); www.doi.gov/sites/doi.gov/files/uploads/2018_highlights_book.pdf.
6. R. Early *et al.*, *Nat. Commun.* **7**, 12485 (2016).
7. R. P. Keller *et al.*, *Proc. Acad. Natl. Sci. U.S.A.* **104**, 203 (2007).

COMPETING INTERESTS

J.K.R. previously served as the National Invasive Species Council's executive director and assistant director for policy, science, and cooperation. J.K.R. also served on the Invasive Species Advisory Committee for 6 years.

10.1126/science.aba7186

Published by AAAS

RESEARCH

Water-selective zeolite nanochannels

Li et al., *p. 667*

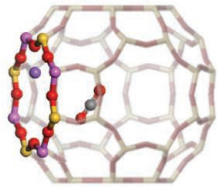

IN *SCIENCE* JOURNALS

Edited by **Michael Funk**

Wildfires scorched Amazonian forests during the 2015–2016 El Niño. Some areas of the tropics around the world are failing to recover.

ECOLOGY

Lagging recovery for tropical forests

Tropical forest aboveground carbon (AGC) stocks have yet to recover from the extremely hot and dry weather associated with the 2015–2016 El Niño event. Wigneron *et al*. used low-frequency microwave satellite data to monitor AGC changes from 2014 to 2017. By the end of 2017, AGC stocks had not reached 2014 predrought levels and continued to decline in some areas. The slow rate of recovery could be due, in part, to enhanced forest mortality and/or unaccounted deforestation and degradation, specifically in African humid forests. Such continuity in long-term records may improve understanding of climate change on ecosystems. —SN

Sci. Adv. 10.1126/sciadv.aay4603 (2020).

ORGANIC CHEMISTRY

Synthesis of Taxol's complicated cousin

Propellane molecules contain three rings that all share a common edge, thereby collectively resembling a propeller. Canataxpropellane, a yew-derived natural product related to the cancer drug Taxol, is unusual in that it has two different propellane motifs in its backbone. Schneider *et al*. report a chemical synthesis of this intricate compound in under 30 steps. Key features of the route include a Diels-Alder reaction rendered asymmetric by introduction of a chiral silyl auxiliary, followed by a photochemical cycloaddition to establish the cyclobutane core. —JSY

Science, this issue p. 676

MULTIFERROICS

Major-league magnetostriction

Magnetoelectric materials polarize in response to either electric or magnetic fields, making them attractive for data-storage applications. Long *et al*. discovered a ytterbium-based molecular magnetoelectric material with high magnetoelectric coupling (see the Perspective by Zhou and Han). An applied magnetic field strains the material, which changes its electrical properties. The required field is much lower than other magnetoelectric materials, and this work highlights the potential for using molecular materials in devices. —BG

Science, this issue p. 671; see also p. 627

POLLINATOR DECLINE

Increasing temperatures and declines

One aspect of climate change is an increasing number of days with extreme heat. Soroye *et al*. analyzed a large dataset of bumble bee occurrences across North America and Europe and found that an increasing frequency of unusually hot days is increasing local extinction rates, reducing colonization and site occupancy, and decreasing species richness within a region, independent of land-use change or condition (see the Perspective by Bridle and van Rensburg). As average temperatures continue to rise, bumble bees may be faced with an untenable increase in frequency of extreme temperatures. —SNV

Science, this issue p. 685; see also p. 626

GPCR SIGNALING

A biased position for receptors

G protein–coupled receptors (GPCRs) are the largest class of druggable receptors in the human proteome and can have multiple downstream signaling partners. Sanchez-Soto *et al.* studied how changes in the ligand-binding site of GPCRs

CREDITS: (TOP TO BOTTOM) LI *ET AL.*; ADAM RONAN/ECOFOR

Published by AAAS

can bias signaling toward one pathway versus another. They identified a specific conserved residue in the ligand-binding site for multiple class A GPCRs that modulates signaling by one partner, β-arrestin, while minimally affecting that mediated by another, G proteins. Mutations in this residue resulted in conformational changes predicted to allosterically affect the interaction of the receptor with β-arrestin. —WW

Sci. Signal. **13**, eaaw5885 (2020).

ELECTROCHEMISTRY

Graceful choreography for CO_2 and H_2O

One challenge for efficient electrochemical reduction of carbon dioxide (CO_2) is that the gas is hydrophobic, but many of its desirable reactions require water (H_2O). García de Arquer *et al*. addressed this problem by combining a copper electrocatalyst with an ionomer assembly that intersperses sulfonate-lined paths for the H_2O with fluorocarbon channels for the CO_2. The electrode architecture enables production of two-carbon products such as ethylene and ethanol at current densities just over an ampere per square centimeter. —JSY

Science, this issue p. 661

SIGNAL TRANSDUCTION

Liver disease defect identified

The energy sensor adenosine monophosphate–activated protein kinase (AMPK) is implicated in liver damage in nonalcoholic steatohepatitis (NASH), a leading cause of liver-associated death in humans. Zhao *et al*. used mouse models of NASH and samples from human NASH patients to show that AMPK, the activity of which is lost in NASH, phosphorylates the enzyme procaspase-6. In normal liver cells, this modification limits the activation of caspase-6 and the consequent caspase activation cascade that leads to apoptosis. AMPK and caspase-6 may thus provide therapeutic targets for the treatment of NASH. —LBR

Science, this issue p. 652

STRUCTURAL BIOLOGY

Architecture of an mRNA processor

The 3′-end processing of the three major classes of RNA polymerase II transcripts in metazoan cells—polyadenylated messenger RNAs (mRNAs), histone mRNAs, and small nuclear RNAs (snRNAs)—requires three distinct machineries that share common features. Sun *et al*. reconstituted the active human histone pre-mRNA 3′-end processing machinery and solved its structure at near-atomic resolution by cryo–electron microscopy. This structure provides a basis for understanding the mechanism of the shared catalytic reactions between histone pre-mRNA and canonical pre-mRNA and snRNA 3′-end processing machineries. —SYM

Science, this issue p. 700

MOSQUITO BIOLOGY

Heat seeking is cool

Mosquitoes seek hosts using several cues, one of which is body heat. Greppi *et al*. hypothesized that cooling-activated receptors could be used for locating mammalian hosts if they were rewired downstream for repulsion responses (see the Perspective by Lazzari). A gene family conserved in insects and known to be responsible for sensing changes in temperature in fruit flies was the starting point. Genome-wide analyses and labeled CRISPR-Cas9 mutants allowed visualization of the receptor in neurons of *Anopheles gambiae* mosquitoes' antennae and assessment of adult female mosquitoes with a disrupted copy of the receptor. This ancestral insect temperature regulatory system has been repurposed for host-finding by malaria mosquitoes. —CA

Science, this issue p. 681; see also p. 628

IN OTHER JOURNALS

Edited by **Caroline Ash** *and* **Jesse Smith**

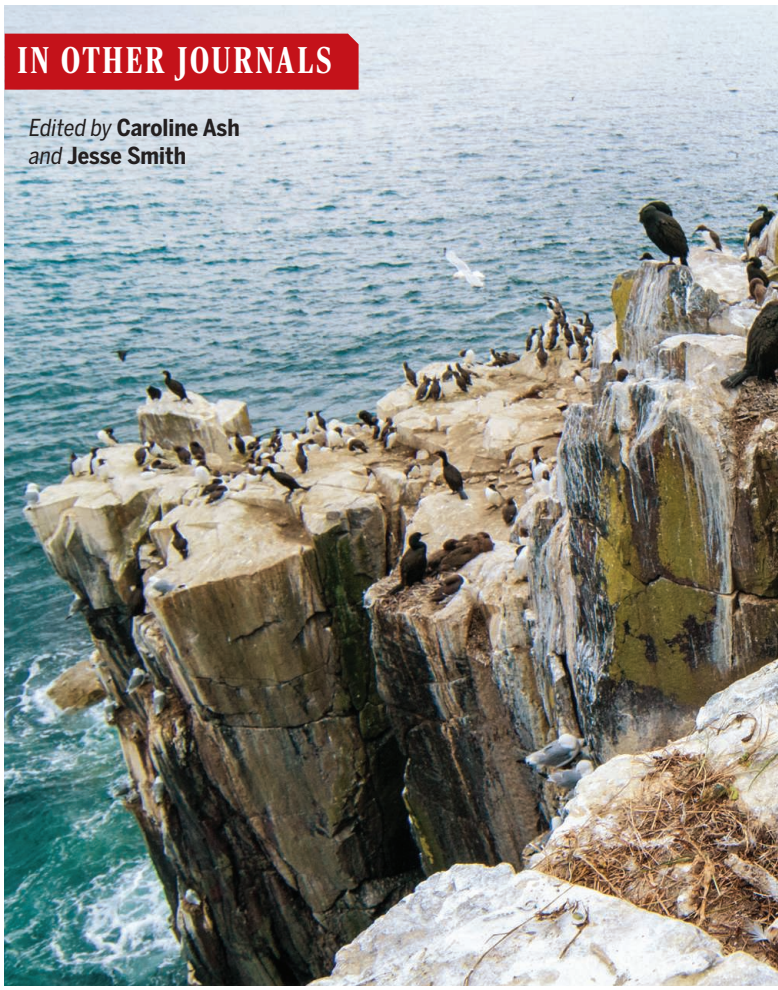

PHOTO: NATURE PICTURE LIBRARY / ALAMY STOCK PHOTO

BIOCHEMISTRY

Breaking the wall

Lysostaphin is a bacteriolytic enzyme that is active against methicillin-resistant *Staphylococcus aureus*. It targets cell wall peptidoglycan, which comprises short glycan chains that cross-link to form the bacterial cell wall. In staphylococci, the cross-link is pentaglycine, which can be cleaved by lysostaphin. Lysostaphin weakly binds to pentaglycine through the enzyme's SH3b domain. Gonzalez-Delgado *et al*. used nuclear magnetic resonance, x-ray crystallography, and mutational analysis to show that the SH3b domain has two binding sites on opposite sides of the enzyme. One site binds the pentaglycine cross-bridge, and the other site binds the peptide stem. Binding to the two sites induces clustering of lysostaphin. Weak binding, combined with high local concentration, likely allows the enzyme to rapidly and progressively degrade the peptidoglycan surface. —VV

Nat. Chem. Biol. **16**, 24 (2020).

CANCER

Active tumor penetration

Anticancer nanoparticle development has relied on the assumption that nanoparticles passively cross leaky blood vessels to enter solid tumors. Using transmission electron microscopy to analyze a glioblastoma xenograft model, Sindhwani *et al*. found that gaps between endothelial cells lining blood vessels are infrequent and do not account for observed nanoparticle accumulation in tumors. Instead, nanoparticles actively enter tumors by transendothelial extravasation. They also show

Published by AAAS

CONSERVATION

Marine mapping for saving seabirds

Seabirds are widely threatened by human activity, both at their breeding grounds and at sea. For conservation to be effective, reliable information on the birds' ranges is essential. In waters around the United Kingdom, Cleasby *et al*. used a combination of GPS electronic tracking data, species distribution modeling, and mapping techniques to identify high-density aggregations of guillemots, razorbills, kittiwakes, and shags. Their methods identified hotspots of breeding-season distributions for these birds, an improvement on previous techniques, which were solely based on foraging ranges. A combination of species distribution modeling and hotspot mapping can thus offer accurate guidance for identifying important areas for seabird protection. —AMS

Biol. Conserv. **241**, 108375 (2020).

Hotspots for breeding seabirds—such as these shags, kittiwakes, razorbills, and guillemots on the Farne Islands, UK—can now be identified by a combination of location techniques.

that the vascular architecture in human tumor samples is mostly intact, which supports the observations that nanoparticles enter tumors by means of an active process rather than by a generalized leakiness. —SYM

Nat. Mater. 10.1038/s41563-019-0566-2 (2020).

COSMIC DUST

Ages of interstellar dust in a meteorite

Some primitive meteorites contain presolar grains, which are solid particles that formed in the interstellar medium before being incorporated into the Solar System. Presolar grains were known to be older than the Sun but had not been precisely dated. Heck *et al*. examined neon isotopes in presolar silicon carbide grains extracted from the Murchison CM2 meteorite. This allowed them to calculate how long each grain had remained in the interstellar medium, a period of time ranging from 3.9 ± 1.6 million years up to 3 ± 2 billion years before the formation of the Solar System, making the grains the oldest known solid material. Most grains had presolar ages of less than 300 million years, constraining astronomers' models of how long dust survives in the interstellar medium. —KTS

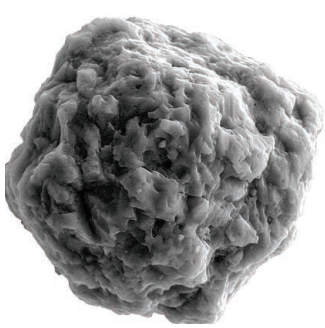

Scanning electron microscope image of a presolar silicon carbide grain from the Murchison CM2 meteorite

PHOTO: P. R. HECK *ET AL*., *PROC. NATL. ACAD. SCI. U.S.A.* **117**, 1884 (2020)

Proc. Natl. Acad. Sci. U.S.A. **117**, 1884 (2020).

ORGANIC CHEMISTRY

Machine learning for asymmetric catalysis

Catalysts can introduce asymmetry in the outcome of chemical reactions, favoring one mirror-image product over another. Many of the most effective catalysts for this application were optimized through trial and error, but more recently, parameterization and systematic analysis have played an increasing role. Singh *et al*. now showcase the predictive power of machine learning applied to the ligands used for asymmetric hydrogenation. A random forest algorithm trained on several different families of chiral binaphthyl phosphorus compounds predicted selectivity in hydrogenation of alkenes and imines with a root-mean-square error of just over 8%. —JSY

Proc. Natl. Acad. Sci. U.S.A. **117**, 1339 (2020).

MATERIALS SCIENCE

When changing is in phase

Shape memory materials can respond to stimuli like heat, light, or moisture to switch between two or more preprogrammed shapes. Spatial variation in the material can allow for complex patterns of bending, folding, buckling, or twisting to make three-dimensional shapes, but these are often one-way processes. Deng *et al*. show that a simple composite made of wax droplets in a silicone matrix can form a programmable, reversible three-dimensional shape-changing material. When the material is stretched, specific wax particles can be melted and cooled, changing their shape and leaving a residual stress. On relaxation of the matrix, it will buckle and fold into complex shapes such as a pneumatic actuator or it can be used for rewritable "paper." Similar effects can be seen with polycaprolactone particles in a polyacrylamide hydrogel. —MSL

ACS Appl. Mater. Interfaces **12**, 4014 (2020).

NEURODEVELOPMENT

The eyes have the signals

Anterior segment dysgenesis is a genetic disorder that causes errors in the development of the iris, cornea, or lens of the eye. This anterior portion of the eye develops from migrating neural crest cells. Developmental errors here can lead to complications that include glaucoma and blindness in a growing child. Portal *et al*. ablated the primary cilia of key neural crest cells in mice. Disrupting the cilia altered the hedgehog signaling pathway and impaired corneal innervation. This outcome in mice replicates defective eye development seen clinically. —PJH

eLife **8**, e52423 (2019).

Published by AAAS

ALSO IN *SCIENCE* JOURNALS

Edited by **Michael Funk**

SIGNAL TRANSDUCTION

Activated by interaction

Cytokines trigger immune responses when they bind to their cognate receptors. Class I cytokine receptors rely on the associated Janus kinase 2 (JAK2) to initiate signal transduction. There has been debate over whether activation involves ligand-induced dimerization of these receptors or ligand-induced conformational change of preformed dimers. Wilmes *et al*. imaged cytokine receptors in the plasma membranes of live human cells by single-molecule fluorescence microscopy and observed ligand-induced dimerization. They found that the JAK2 pseudokinase domains contribute to dimerization and that hyperactive JAK2 mutants promote dimerization, consistent with the model that dimerization triggers activation. —VV

Science, this issue p. 643

MEDICINE

Clinical uses of cellular communication

Exosomes are a type of extracellular vesicle that contain constituents (protein, DNA, and RNA) of the cells that secrete them. They are taken up by distant cells, where they can affect cell function and behavior. Intercellular communication through exosomes seems to be involved in the pathogenesis of various disorders, including cancer, neurodegeneration, and inflammatory diseases. In a Review, Kalluri and LeBleu discuss the biogenesis and function of exosomes in disease, highlighting areas where more research is needed. They also discuss the potential clinical applications of exosome profiling for diagnostics and exosome-mediated delivery of therapeutics to target disease cells. —GKA

Science, this issue p. 640

INFECTIOUS DISEASE

Concern about swine fever vaccines

African swine fever (ASF) is a lethal hemorrhagic disease that affects swine, including wild boar and domestic pigs. Beginning in mid-2018 with the introduction of the ASF virus to China, an outbreak of ASF has devastated pig farming in Asia. The disease is spreading into Europe and may soon become a global threat to the pig population. Efforts to prevent the spread of ASF virus are challenged by residual infection in the wild boar population and difficulties in preventing the movement of pig products. In a Perspective, Gavier-Widén *et al*. discuss strategies to develop a vaccine that can be used in bait for wild boar and be administered to farmed animals to effectively overcome ASF. However, in the rush to generate a vaccine, there are concerns that the existing options under development may make matters worse. —GKA

Science, this issue p. 622

PLANT SCIENCE

Decoupling tillering and fertilization

For rice as an agricultural crop, more tillers, or branches that carry grains, are desired, as is less demand for nitrogen fertilization. Unfortunately, for many rice varieties, the number of tillers depends on the amount of nitrogen fertilization. Wu *et al*. now show that nitrogen status affects chromatin function through modification of histones, a process in which the transcription factor NGR5 recruits polycomb repressive complex 2 to target genes. Some of these genes regulate tillering, such that with more nitrogen, the plants develop more tillers. NGR5 is regulated by proteasomal destruction and mediates hormone signaling. An increase in NGR5 levels can drive increases in rice tillering and yield without requiring increases in nitrogen-rich fertilizer. —PJH

Science, this issue p. 641

IMMUNOLOGY

A weird way to recognize phosphoantigens

In contrast to the well-studied αβ T cells, which recognize peptide antigens presented by major histocompatibility complex (MHC) and MHC-like molecules, how γδ T cells recognize antigens remains largely a mystery. One major class of γδ T cells, designated Vγ9Vδ2$^+$, is activated by small, phosphorylated nonpeptide antigens, or phosphoantigens, produced by microbes and cancer cells. Rigau *et al*. found that these cells needed the combination of two immunoglobulin superfamily members, butyrophilin 2A1 (BTN2A1) and BTN3A1, on their cell surface to recognize these phosphoantigens. BTN2A1 directly binds the Vγ9$^+$ domain of the T cell receptor (TCR), whereas a second ligand, potentially BTN3A1, binds the Vδ2 and γ-chain regions on the opposite side of the TCR. A better understanding of this unexpected form of T cell antigen recognition should inform and enhance future γδ T cell–mediated immunotherapies. —STS

Science, this issue p. 642

CATALYSIS

Water-selective zeolite membranes

The yield of many gas-phase industrial reactions is limited by the formation of water as a by-product. Li *et al*. harnessed the water-sieving properties of NaA zeolite crystals by forming them into continuous defect-free membranes within tube reactors (see the Perspective by Carreon). These membranes can let water pass but reject gases such as hydrogen, carbon monoxide, and carbon dioxide (CO_2). When these membranes were used in CO_2 hydrogenation to form methanol with water as a by-product, substantial increases were observed in both the CO_2 conversion and methanol yield. —PDS

Science, this issue p. 667; see also p. 624

NEUROSCIENCE

Microglia modulate memories

Synaptic reorganization and circuit rewiring leads to loss or weakening of connections between neurons and may result in the erasure of previously formed memories. Microglia eliminate excessive synapses in the developing brain and regulate the dynamics of synaptic connections between neurons throughout life. However, it is still unclear whether forgetting is related to microglia activity and how microglia regulate memory erasure in the adult brain. Wang *et al*. discovered that microglia eliminated synaptic components in the adult hippocampus and that depleting microglia or inhibiting phagocytosis of microglia prevented forgetting. Synapse elimination by microglia may thus lead to degradation of memory engrams and forgetting of previously learned contextual fear memory. —PRS

Science, this issue p. 688

PHASE SEPARATION

Not too sticky

There is increasing evidence for a role of liquid-liquid phase separation (LLPS) in many cellular processes. Many proteins that undergo LLPS include prion-like domains (PLDs), which are enriched in polar amino acids and often interspersed with aromatic residues. Combining experimental data with simulations, Martin *et al*. quantified concentrations of PLDs in coexisting dilute and dense phases as

Published by AAAS

a function of temperature and show that the phase behavior is determined by the number of aromatic residues and their patterning, with uniform patterning of aromatic residues promoting LLPS and inhibiting aggregation. They developed a sticker-and-spacers model that can predict the phase behavior of PLDs on the basis of their sequence. —VV

Science, this issue p. 694

PAIN

A pathway to pain in female mice

Men and women experience pain differently, but the mechanisms mediating this difference and their universality, are unclear. In female rodents, the short isoform of the prolactin receptor (PRLR-S), but not the long isoform (PRLR-L), has been shown to regulate the excitability of sensory neurons. Chen *et al*. studied opioid-induced hyperalgesia (OIH) in a mouse model and found that opioid administration, but not trauma-induced nerve injury, augmented prolactin and decreased PRLR-L in female mice, promoting the activation of PRLR-S and the development of OIH. Prolactin inhibition prevented the occurrence of OIH in female mice, and targeting prolactin signaling is an attractive direction for future research in preventing OIH in women. —MM

Sci. Transl. Med. **12**, eaay7550 (2020).

Published by AAAS

REVIEW SUMMARY

MEDICINE

The biology, function, and biomedical applications of exosomes

Raghu Kalluri* and Valerie S. LeBleu

BACKGROUND: All cells, prokaryotes and eukaryotes, release extracellular vesicles (EVs) as part of their normal physiology and during acquired abnormalities. EVs can be broadly divided into two categories, ectosomes and exosomes. Ectosomes are vesicles that pinch off the surface of the plasma membrane via outward budding, and include microvesicles, microparticles, and large vesicles in the size range of ~50 nm to 1 μm in diameter. Exosomes are EVs with a size range of ~40 to 160 nm (average ~100 nm) in diameter with an endosomal origin. Sequential invagination of the plasma membrane ultimately results in the formation of multivesicular bodies, which can intersect with other intracellular vesicles and organelles, contributing to diversity in the constituents of exosomes. Depending on the cell of origin, EVs, including exosomes, can contain many constituents of a cell, including DNA, RNA, lipids, metabolites, and cytosolic and cell-surface proteins. The physiological purpose of generating exosomes remains largely unknown and needs investigation. One speculated role is that exosomes likely remove excess and/or unnecessary constituents from cells to maintain cellular homeostasis. Recent studies reviewed here also indicate a functional, targeted, mechanism-driven accumulation of specific cellular components in exosomes, suggesting that they have a role in regulating intercellular communication.

ADVANCES: Exosomes are associated with immune responses, viral pathogenicity, pregnancy, cardiovascular diseases, central nervous system–related diseases, and cancer progression. Proteins, metabolites, and nucleic acids delivered by exosomes into recipient cells effectively alter their biological response. Such exosome-mediated responses can be disease promoting or restraining. The intrinsic properties of exosomes in regulating complex intracellular pathways has advanced their potential utility in the therapeutic control of many diseases, including neurodegenerative conditions and cancer. Exosomes can be engineered to deliver diverse therapeutic payloads, including short interfering RNAs, antisense oligonucleotides, chemotherapeutic agents, and immune modulators, with an ability to direct their delivery to a desired target. The lipid and protein composition of exosomes can affect their pharmacokinetic properties, and their natural constituents may play a role in enhanced bioavailability and in minimizing adverse reactions. In addition to their therapeutic potential, exosomes also have the potential to aid in disease diagnosis. They have been reported in all biological fluids, and the composition of the complex cargo of exosomes is readily accessible via sampling of biological fluids (liquid biopsies). Exosome-based liquid biopsy highlights their potential utility in diagnosis and determining the prognosis of patients with cancer and other diseases. Disease progression and response to therapy may also be ascertained by a multicomponent analysis of exosomes.

OUTLOOK: The study of exosomes is an active area of research. Ongoing technological and experimental advances are likely to yield valuable information regarding their heterogeneity and biological function(s), as well as enhance our ability to harness their therapeutic and diagnostic potential. As we develop more standardized purification and analytical procedures for the study of exosomes, this will likely reveal their functional heterogeneity. Nonetheless, functional readouts using EVs enriched for exosomes have already provided new insights into their contribution to various diseases. New genetic mouse models with the ability for de novo or induced generation of cell-specific exosomes in health and disease will likely show the causal role of exosomes in cell-to-cell communication locally and between organs. Whether exosome generation and content change with age needs investigation, and such information could offer new insights into tissue senescence, organ deterioration, and programmed or premature aging. Whether EVs and/or exosomes preceded the first emergence of the single-cell organism on the planet is tempting to speculate, and focused bioelectric and biochemical experiments in the future could reveal their cell-independent biological functions. Single-exosome identification and isolation and cryoelectron microscopy analyses have the potential to substantially improve our understanding of the basic biology of exosomes and their use in applied science and technology. Such knowledge will inform the therapeutic potential of exosomes for various diseases, including cancer and neurodegenerative diseases. ■

ON OUR WEBSITE

Read the full article at http://dx.doi.org/10.1126/science.aau6977

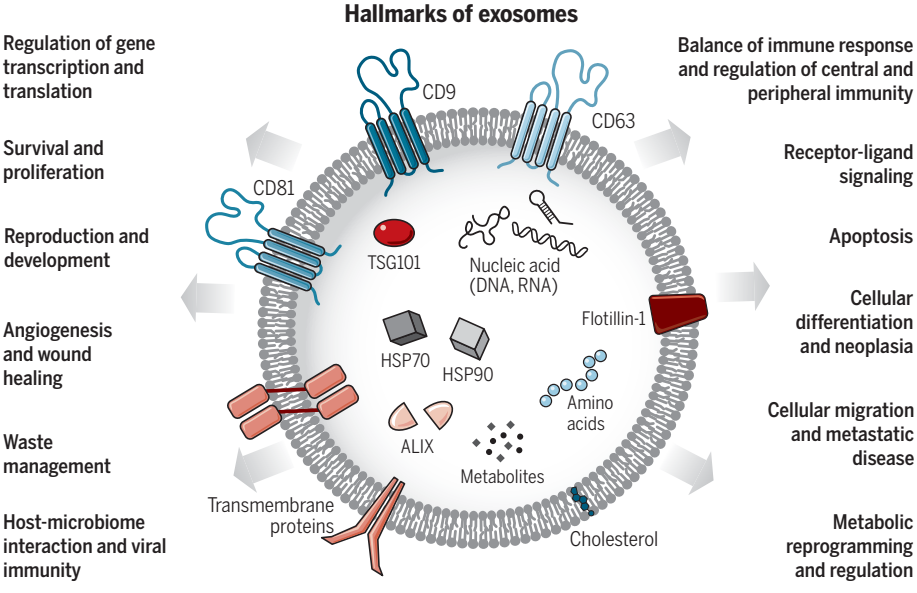

Exosomes: A cell-to-cell transit system in the human body with pleiotropic functions. Exosomes are extracellular vesicles generated by all cells and they carry nucleic acids, proteins, lipids, and metabolites. They are mediators of near and long-distance intercellular communication in health and disease and affect various aspects of cell biology.

The list of author affiliations is available in the full article online.
*Corresponding author. Email: rkalluri@mdanderson.org
Cite this article as R. Kalluri, V. S. LeBleu, *Science* **367**, eaau6977 (2020). DOI: 10.1126/science.aau6977

REVIEW

MEDICINE

The biology, function, and biomedical applications of exosomes

Raghu Kalluri[1,2,3]* and Valerie S. LeBleu[1]

The study of extracellular vesicles (EVs) has the potential to identify unknown cellular and molecular mechanisms in intercellular communication and in organ homeostasis and disease. Exosomes, with an average diameter of ~100 nanometers, are a subset of EVs. The biogenesis of exosomes involves their origin in endosomes, and subsequent interactions with other intracellular vesicles and organelles generate the final content of the exosomes. Their diverse constituents include nucleic acids, proteins, lipids, amino acids, and metabolites, which can reflect their cell of origin. In various diseases, exosomes offer a window into altered cellular or tissue states, and their detection in biological fluids potentially offers a multicomponent diagnostic readout. The efficient exchange of cellular components through exosomes can inform their applied use in designing exosome-based therapeutics.

The study of extracellular vesicles (EVs) and the mechanisms that govern their generation and function(s) in multicellular organisms spans from physiological tissue regulation to pathogenic injury and organ remodeling. Research in this field is stimulated by the potential of EVs as diagnostic and therapeutic tools for the treatment of various diseases, including neurodegeneration, cardiovascular dysfunction, and cancer. Increasingly, EV research is aimed at classification of EVs, isolation methods, and cataloging their putative functions in disease progression and therapy (*1*–*5*). Current characterization of biological activities of EVs has largely relied on tissue culture generated (and possibly amplified), nonphysiological readouts, as well as diverse EV isolation methods, which require further refinement (*6*, *7*). Therefore, it remains unclear whether some of the purported properties of EVs are physiologically relevant in whole organisms in health or disease. Nonetheless, the production of EVs by cells appears to extend beyond a simple protein-recycling function, as initially reported for the transferrin receptor in reticulocyte maturation (*8*, *9*), and varies according to cellular origin, metabolic status, and environment of the cells. EV research remains restricted by current experimental limitations in single-particle detection and isolation, and the inability to image and track exosomes in vivo at a reliable resolution. Despite such experimental caveats, exciting discoveries have emerged. The utility of EVs as liquid biopsies is particularly promising because of their presence in all biological fluids and their potential for multicomponent analyses (*2*).

Although the classification of EVs is continuously evolving (*1*), they generally fall into two major categories, ectosomes and exosomes (*10*) (Fig. 1). Ectosomes are vesicles generated by the direct outward budding of the plasma membrane, which produces microvesicles, microparticles, and large vesicles in the size range of ~50 nm to 1 μm in diameter. By contrast, exosomes are of endosomal origin and in a size range of ~40 to 160 nm in diameter (~100 nm on average). In this review, we focus on exosomes and discuss other EVs to offer contrast and comparison when relevant. Critically, challenges remain when establishing purification and analytical procedures for the study of exosomes, possibly resulting in a heterogeneous population of EVs that include exosomes. As such, some of the findings discussed may reflect those of exosomes mixed with other EVs. Exosomes are of particular interest in biology because their creation involves a distinct intracellular regulatory process that likely determines their composition, and possibly their function(s), once secreted into the extracellular space (*2*, *6*, *11*). It is important to recognize that exosome isolation methods are constantly evolving, and current biological markers may only recognize a subpopulation of exosomes with specific contents (*1*, *7*, *12*, *13*). Therefore, some findings will need to be refined as new technology is embraced.

The biogenesis of exosomes

Exosomes are generated in a process that involves double invagination of the plasma membrane and the formation of intracellular multivesicular bodies (MVBs) containing intraluminal vesicles (ILVs). ILVs are ultimately secreted as exosomes with a size range of ~40 to 160 nm in diameter through MVB fusion to the plasma membrane and exocytosis (Fig. 1). The first invagination of the plasma membrane forms a cup-shaped structure that includes cell-surface proteins and soluble proteins associated with the extracellular milieu (Fig. 2). This leads to the de novo formation of an early-sorting endosome (ESE) and in some cases may directly merge with a preexisting ESE. The trans-Golgi network and endoplasmic reticulum can also contribute to the formation and the content of the ESE (*2*, *4*–*6*, *13*, *14*). ESEs can mature into late-sorting endosomes (LSEs) and eventually generate MVBs, which are also called multivesicular endosomes. MVBs form by inward invagination of the endosomal limiting membrane (that is, double invagination of the plasma membrane). This process results in MVBs containing several ILVs (future exosomes). The MVB can either fuse with lysosomes or autophagosomes to be degraded or fuse with the plasma membrane to release the contained ILVs as exosomes (*3*, *4*).

The Ras-related protein GTPase Rab, Sytenin-1, TSG101 (tumor susceptibility gene 101), ALIX (apoptosis-linked gene 2-interacting protein X), syndecan-1, ESCRT (endosomal sorting complexes required for transport) proteins, phospholipids, tetraspanins, ceramides, sphingomyelinases, and SNARE [soluble *N*-ethylmaleimide–sensitive factor (NSF) attachment protein receptor] complex proteins are involved in the origin and biogenesis process of exosomes, although their precise rate-limiting actions and functions in exosome biogenesis require further in-depth exploration, especially in vivo (*6*, *11*, *15*). An intersection of the exosome biogenesis pathway with other molecular pathways associated with the trafficking of intracellular vesicles has confounded the interpretation of functional studies. Specifically, loss- or gain-of-function experiments involving Rab and ESCRT proteins likely interfere with other distinct vesicular activities within cells, such as autophagy and lysosomal pathways, and Golgi apparatus–derived vesicle trafficking, which may exert indirect effects on exosome biogenesis. Distinct cell types, culture conditions, and genomic health of the cells may also favor or dispense some of the putative key regulators of exosome biogenesis in vivo (*6*). The potential inconsistencies in identifying regulatory elements associated with exosome biogenesis could also result from different methods for exosome production, enrichment, and concentration (*13*).

Computing the rate of exosome production is challenged by the dynamic process associated with the de novo production and uptake of external exosomes by any given cell type. A study using time-lapse monitoring of single human cells cultured in a platform that enabled tetraspanin antibody capture of shed exosomes indicated distinct rates of net exosome production by noncancerous versus

[1]Department of Cancer Biology, Metastasis Research Center, University of Texas MD Anderson Cancer Center, Houston, TX, USA. [2]School of Bioengineering, Rice University, Houston, TX, USA. [3]Department of Molecular and Cellular Biology, Baylor College of Medicine, Houston, TX, USA.
*Corresponding author. Email: rkalluri@mdanderson.org

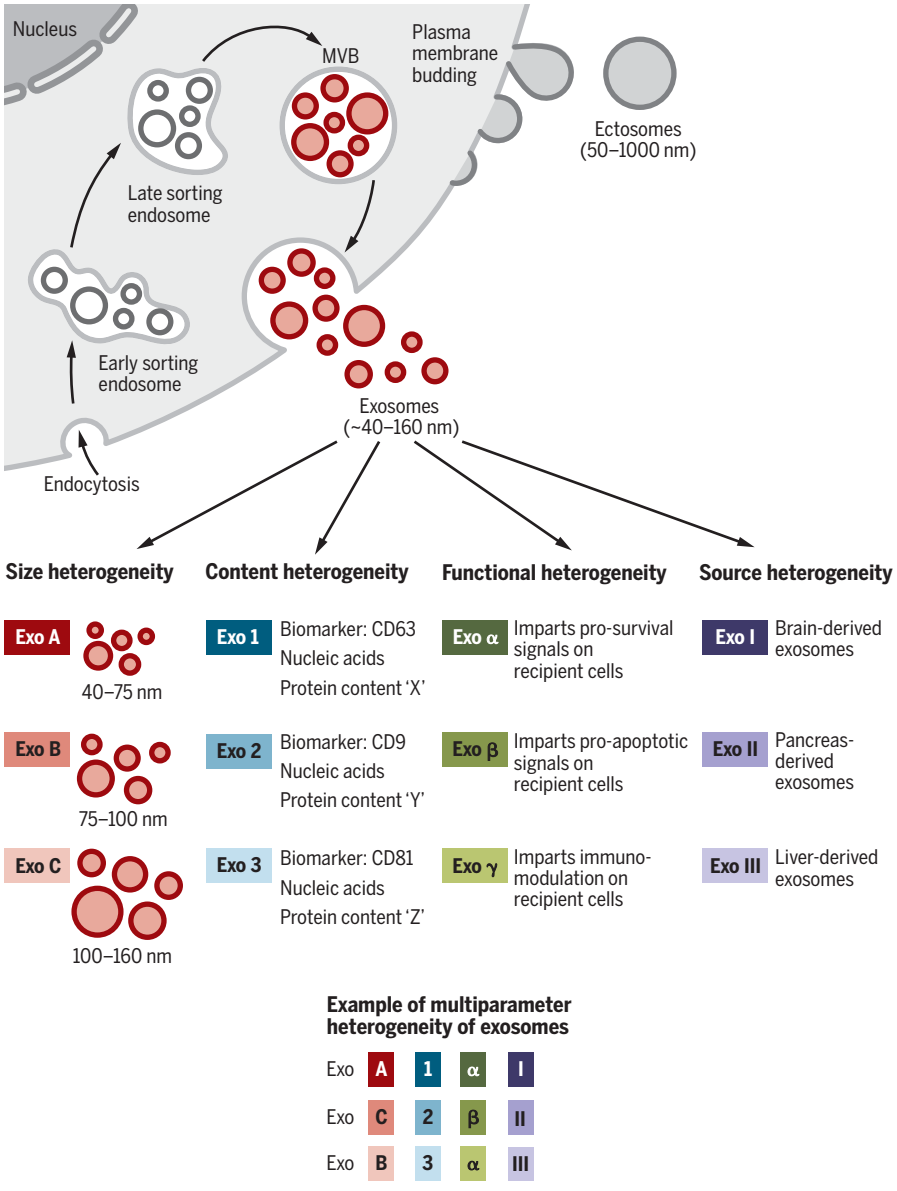

Fig. 1. Identity and the heterogeneity of extracellular vesicles and exosomes. The two major categories of EVs are ectosomes and exosomes. Ectosomes are released through plasma membrane budding and are in the size range of ~50 nm to 1 μm. Exosomes originate from the endosomal pathway by the formation of the ESEs, LSEs, and ultimately MVBs, which contain ILVs. When MVBs fuse with the plasma membrane, exosomes are released (size range ~40 to 160 nm). Exosomes can be a highly heterogeneous population and have distinct abilities to induce a complex biological response. The heterogeneity of exosomes may be conceptualized on the basis of their size, content (cargo), functional impact on recipient cells, and cell of origin (source). Distinct combinations of these characteristics give rise to a complex heterogeneity of exosomes.

cancerous breast epithelial cells. The breast cancer cells shed lower numbers of exosomes (~60 to 65 per cell per hour) compared with tissue-matched, nontumorigenic cell line–derived exosomes (*16*). In other studies, it has been suggested that cancer cells secrete more exosomes compared with normal cells from the same or other tissues [reviewed in (*2*, *11*)], but such studies relied on different isolation methods that may measure both exosomes and ectosomes of similar size.

Exosome heterogeneity

The heterogeneity of exosomes is likely reflective of their size, content, functional impact on recipient cells, and cellular origin (Fig. 1). Size inequality could be due to uneven invagination of the limiting membrane of the MVB, resulting in distinct total content of fluid and solids, or isolation methods that include other EVs (*6*, *11*, *15*). Refined fractionation methods involving EVs revealed that exosomes may contain subpopulations defined by a distinct size range (*17*). Size heterogeneity can also result in different amounts of exosomal content. The microenvironment and the inherent biology of the cells may influence the content of the exosomes and their biological markers. Exosomes can contain membrane proteins, cytosolic and nuclear proteins, extracellular matrix proteins, metabolites, and nucleic acids, namely mRNA, noncoding RNA species, and DNA (*18*–*21*) (Fig. 2). Although exosomal cargo analyses require large pools of purified exosomes, not all exosomes contain a similar abundance of a given cargo, as observed, for example, with miRNA exosomal cargo (*22*). Proteomic analyses of EVs have revealed the marker heterogeneity of exosomes, cautioning their utility in experimental design using marker-determined purification methodologies (*23*). Nonetheless, the proteome of breast cancer cells and their exosomes can show whether the cell of origin was epithelial like or mesenchymal like (*24*), and distinct proteins and nucleic acids are enriched in exosomes compared with their cell of origin, suggesting a specific protein-sorting mechanism associated with exosome biogenesis and/or content loading.

The effects of exosomes on recipient cells can be different because of their varied expression of cell surface receptors, and such functional heterogeneity can result in one set of exosomes inducing cell survival, another set inducing apoptosis, and a different set inducing immunomodulation, etc., in different target cell types (Fig. 1). Heterogeneity can also be based on the organ and tissue of origin of the exosomes, including whether they are from cancer cells (*24*), giving them distinct properties such as tropism to certain organs and uptake by specific cell types. A combination of all of these features would have the potential to give rise to a higher order of complexity and heterogeneity of exosomes.

Intercellular communication

The questions surrounding the function of exosomes are largely focused on understanding the fate of their constituents and the phenotypic and molecular alterations that they induce on recipient cells in cell-culture systems. Exosome uptake and secretion pathways may intersect, resulting in net production of a mixed population of exosomes over time for any given cell that is composed of both endogenously produced and recycled exosomes (Fig. 3). The distinct mechanisms and pathways associated with exosome uptake (*6*, *25*, *26*), and the putative specificity of exosomes for certain cell types, add complexity to the function of exosomes in intercellular communication. For example, oncogenic signals induced by mutant KRAS

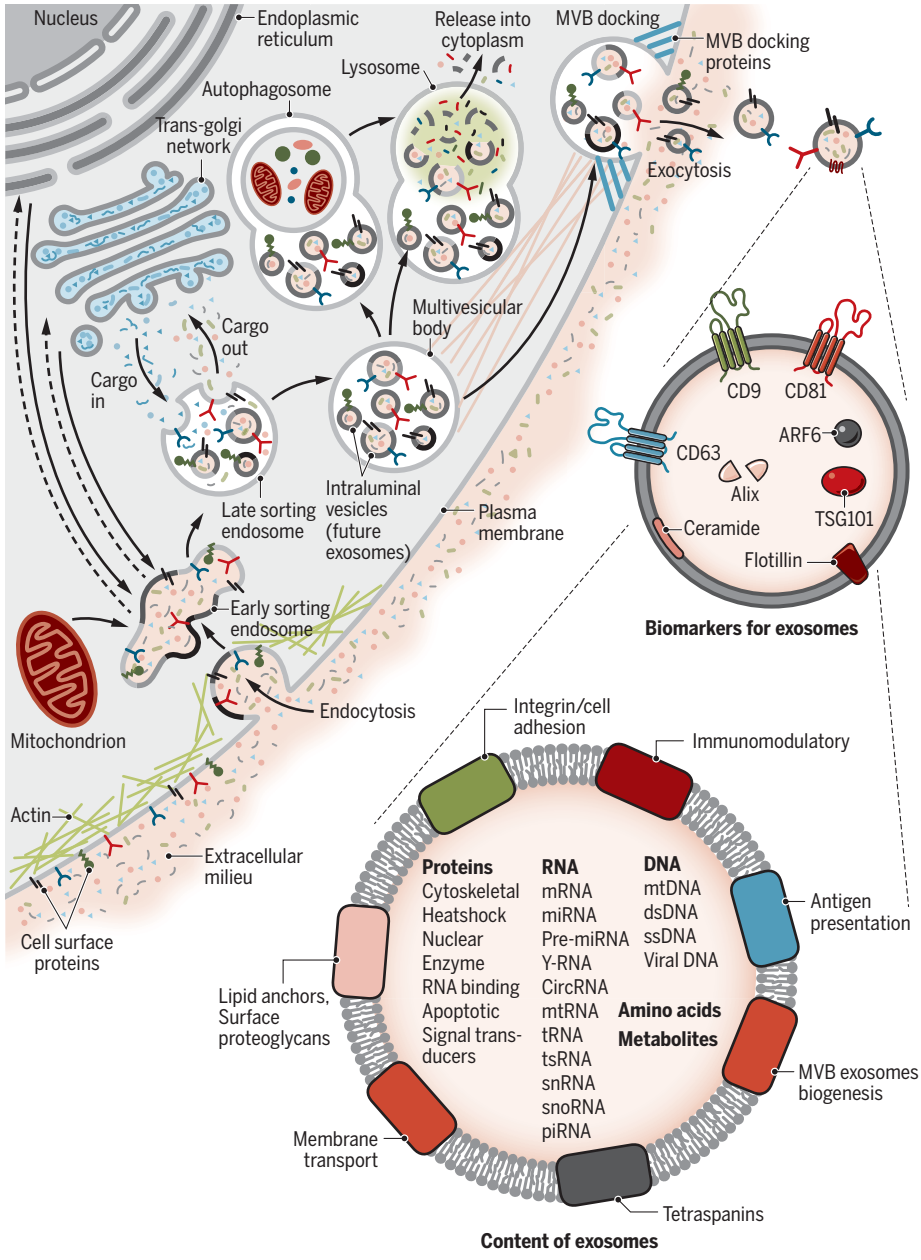

Fig. 2. Biogenesis and identification of exosomes. Fluid and extracellular constituents such as proteins, lipids, metabolites, small molecules, and ions can enter cells, along with cell surface proteins, through endocytosis and plasma membrane invagination. The resulting plasma membrane bud formation in the luminal side of the cell presents with outside-in plasma membrane orientation. This budding process leads to the formation of ESEs or possible fusion of the bud with ESEs preformed by the constituents of the endoplasmic reticulum (ER), trans-Golgi network (TGN), and mitochondria. The ESEs could also fuse with the ER and TGN, possibly explaining how the endocytic cargo reaches them. Some of the ESEs can therefore contain membrane and luminal constituents that can represent diverse origins. ESEs give rise to LSEs. Second invagination in the LSE leads to the generation of ILVs, and this step can lead to further modification of the cargo of the future exosomes, with cytoplasmic constituents entering the newly forming ILV. As part of the formation of ILVs, proteins (that were originally on the cell surface) could be distinctly distributed among ILVs. Depending on the invagination volume, the process could give rise to ILVs of different sizes with distinct content. LSEs give rise to MVBs with defined collection of ILVs (future exosomes). MVBs can fuse with autophagosomes, and ultimately the contents can undergo degradation in the lysosomes. The degradation products could be recycled by the cells. MVBs can also directly fuse with lysosomes for degradation. MVBs that do not follow this trajectory can be transported to the plasma membrane through the cytoskeletal and microtubule network of the cell and dock on the luminal side of the plasma membrane with the help of MVB-docking proteins. Exocytosis follows and results in the release of the exosomes with a similar lipid bilayer orientation as the plasma membrane. Several proteins are implicated in exosome biogenesis and include Rab GTPases, ESCRT proteins (see text), as well as others that are also used as markers for exosomes (CD9, CD81, CD63, flotillin, TSG101, ceramide, and Alix). Exosome surface proteins include tetraspanins, integrins, immunomodulatory proteins, and more. Exosomes can contain different types of cell surface proteins, intracellular protein, RNA, DNA, amino acids, and metabolites.

expression promote exosome uptake by macropinocytosis in human pancreatic cancer cells (*27*, *28*). Human melanoma cells uptake exosomal cargo through their fusion with the plasma membrane (*29*), and the neurosecretory PC12 cells (derived from rat adrenal medullary tumor) more readily rely on clathrin-dependent endocytosis for uptake (*30*). It is unknown whether a different mode of exosome uptake by recipient cells results in distinct localization, degradation, and/or functional outcomes of the exosomal constituents. Moreover, it remains poorly understood whether administration of externally generated exosomes from different cell types into mice results in different organ tropism and/or retention compared with physiological tropism by de novo–produced exosomes (*28*, *31*–*35*). It is possible that the "turnover rate" for internalized exosomal cargo varies depending on the nature of the cargo and the recipient cell's metabolic status that regulates uptake of extracellular molecules and vesicles.

To track intercellular exchange of exosomes under physiological conditions, in vivo experiments involving various genetic strategies in mice were explored (*36*–*38*). These studies demonstrate that exosomes can deliver mRNA to a recipient cell on rare occasions. Such rare events were enhanced by the activation and expansion of exosome-producing immune cells in mouse models of acute inflammation (peritonitis) or chronic inflammation (subcutaneous tumor) (*36*). Therapeutic interventions such as chemotherapy could also influence exosome uptake and subsequent biological responses of tumors. For example, inhibiting a proton pump or altering cellular pH in melanoma cells limits exosome uptake (*29*).

Although it is not surprising that the proteome of the exosomes reflects the proteome of the originating cell, exosome protein cargo from cancer cells can be altered. For example, proteomic studies have revealed that oncogenic alteration, such as constitutively active expression of EGFRvIII (epidermal growth factor receptor variant III) in glioblastoma cells, yields exosomes with a protein cargo specifically

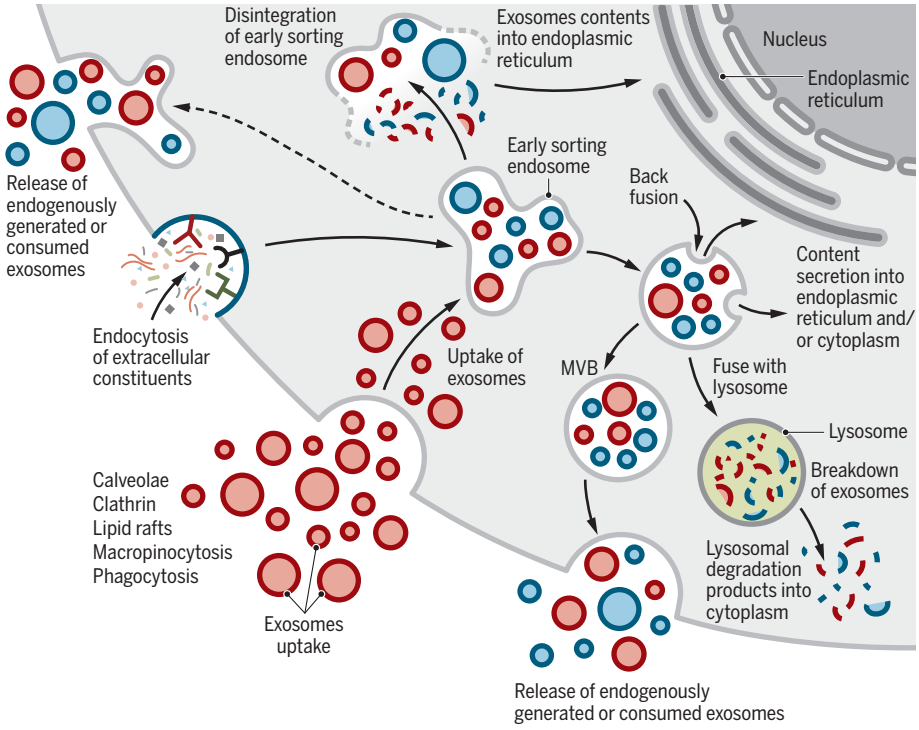

Fig. 3. Cellular journey of internalized exosomes and endogenously produced exosomes. Exosomes may directly enter cells by different mechanisms (red). Exosomes are generated de novo by cells through the endocytosis process (blue). Exosomes are continuously being generated by and taken up by cells. It is likely that they can be secreted as a mixture of the de novo–generated and consumed exosomes (red and blue). It is unknown if the release of endogenously generated or consumed exosomes occurs together or separately. Exosomes that are taken up can get degraded by lysosomes. Exosomes that enter cells may enter or fuse with preexisting ESEs and subsequently disintegrate and release their contents into the cytoplasm. Alternatively, endosomes could fuse back with the plasma membrane and release exosomes outside the cells.

enriched in many proinvasive molecules (*39*). Neural stem cells challenged with inflammatory cytokines produce exosomes with IFNγ (interferon gamma)–bound-IFNGR1 (interferon gamma receptor 1), and these specifically activate STAT1 (signal transducer and activator of transcription 1) signaling in recipient cells that also express IFNGR1 (*40*). These results support the idea that proteins are sorted into exosomes and can selectively induce specific signals in recipient cells to regulate processes such as those seen in development, immune responses, and disease.

Mammalian reproduction and development

Human reproduction, pregnancy, and embryonic development require precise, finely tuned, and dynamic intercellular communication. Semen, amniotic fluid, blood, and breast milk all contain exosomes with putative functions. Seminal plasma exosomes have been implicated in sperm maturation (*41*). Molecular profiling indicates that the microRNAs let-7a, let-7b, miR-148a, miR-375, and miR-99a are enriched in seminal plasma-derived exosomes from multiple human donors (*42*). These miRNAs are implicated in the expression of interleukins (IL-10 and IL-13), raising the possibility that exosomes play a role in genitalia-resident immunity (*42*). Seminal plasma-derived exosomes also inhibit HIV-1 infection (*43*, *44*), possibly by blocking HIV early protein transcriptional activator (Tat) recruitment and subsequent transcription of HIV-1 (*45*) (Fig. 4).

Exosomes may also help to prevent infection of the placenta by delivery of exosomal miRNA (chromosome 19 miRNA cluster, C19MC) from specialized cells of the placenta (trophoblasts) to nonplacental cells to induce autophagy and defense against viral infections such as poliovirus, human cytomegalovirus, and herpes simplex virus 1 infection (*46*). In the blood plasma of pregnant women, the exosomal miRNA and protein cargo change with respect to gestational age and when compared with preterm birth (*47*, *48*). Plasma-derived exosomes dynamically evolve during pregnancy in mice as well, and gestation-stage specific exosomes are functionally linked to labor and delivery (*49*). Specifically, late-gestation plasma-derived exosomes induce preterm birth in near-term pregnancies in mice but do not affect pregnancies at an earlier stage of gestation (*49*).

In breast milk, exosomes seem to promote postnatal health and growth. Breast milk–derived exosomes contain miRNAs with immune-related functions (*50*) and enhance the number of peripheral blood–derived T-regulatory cells ex vivo, possibly to regulate immune tolerance (*51*). Although breast milk–derived exosomes have been shown to promote the proliferation of porcine intestinal epithelial cells in culture conditions and the mouse intestinal tract in vivo (*52*), it remains unclear to what extent, if any, the transfer of nucleic acids and other exosomal cargos is preserved after ingestion, having to overcome digestive enzymes and uptake in the intestinal epithelium. The impact of different routes of administration on tissue uptake of exosomes will likely influence potential therapeutic strategies (*53*).

Immune responses and infection

The role of exosomes in immune responses has been widely documented (*54*–*56*), although it should be noted that no severe immune reaction was observed in mice repeatedly administered with a relatively low dose of mouse or human cell–derived exosomes for extended periods of time (*28*, *35*, *57*). Whole-blood and plasma transfusions, which have been performed for >50 years, do not appear to be associated with potential EV-mediated immune reactions despite no effort to match HLA (human leukocyte antigen) types and the infusion of trillions of EVs including exosomes. Exogenous administration and endogenous secretion of exosomes may thus elicit immune responses in a context- and dose-dependent manner and this remains to be elucidated.

Recent experiments with engineered exosomes have nonetheless indicated a function of exosomes in eliciting adaptive and innate immune reactions, supporting their utility for therapy development and a potential role in coordinating immune reactions in response to infectious agents or cancer (Fig. 5). The function of exosomes in immune regulation is likely due to the transfer and presentation of antigenic peptides, delivery of DNA-inducing cGAS-STING (cyclic GMP-AMP synthase stimulator of interferon genes) signaling in recipient cells (an immune pathway wherein sensing of cytosolic DNA triggers the expression of inflammatory genes and a type I IFN response), gene-expression manipulation by exosomal miRNA, and induction of different signaling pathways by surface ligands present on the exosomes.

Exosomes from antigen-presenting cells (APCs) carry p-MHC-II [major histocompatibility complex II with antigenic peptide (p)] and costimulatory signals, and directly present the peptide antigen to specific T cells to induce their activation. However, for reasons that remain to be elucidated, T cell stimulation by exosomes is less effective than that by APCs (*58*–*60*). In

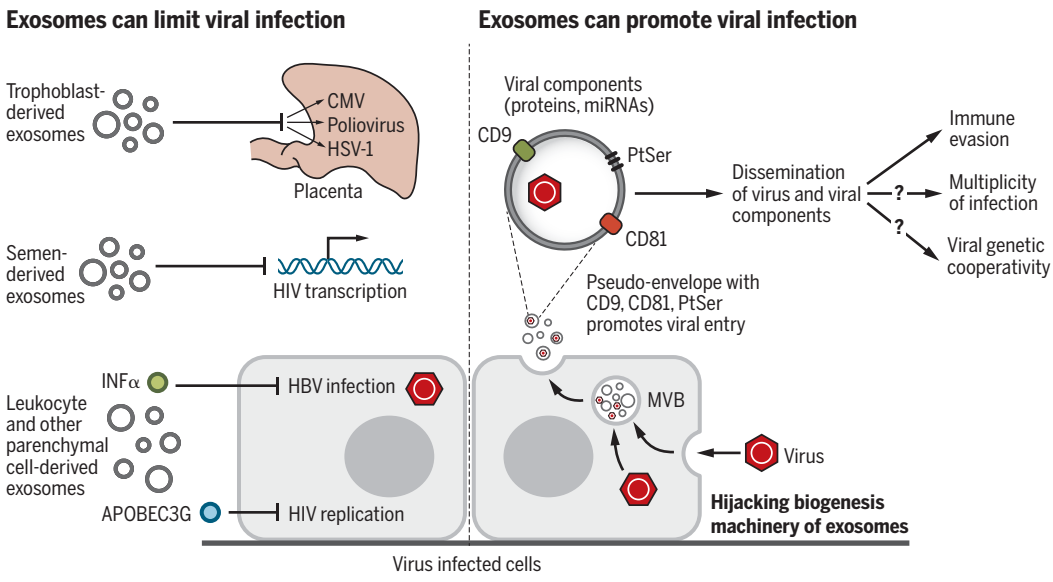

Fig. 4. Exosomes in viral infection. Exosomes can limit or promote viral infection. Exosomal cargo such as IFNα or APOBEC3G can suppress infection by limiting viral replication or enhancing antiviral immunity. Viruses can also highjack the exosome biogenesis machinery to promote viral dissemination. Exosomes may serve as a pseudoenvelope that enhances viral entry by tetraspanins (CD81, CD9) and PtSer interaction and uptake into recipient cells and aid in evading antiviral immunity. Cotransport of a viral component (proteins and miRNA) may also enhance infectivity. Exosome-mediated transfer of viruses may participate in viral genetic cooperativity and multiplicity of infection. CMV, cytomegalovirus; HSV-1, herpes simplex virus 1.

mice, tumor eradication and growth delay were observed with a single intradermal injection of APC-derived exosomes with MHC-II loaded with tumor peptide (*60*). The potency and durability of the observed $CD8^+$ cytotoxic T cell–mediated antitumor response also implied indirect antigen presentation because of the transfer of the antigenic peptide on exosomes to the APCs, which in turn prime naïve T and/or B cells for activation. Immature mouse dendritic cells activated by exosome-derived immunogenic peptides indirectly activate APCs and induce specific $CD4^+$ T cell proliferation (*61*). Exosomes shed by human dendritic cells, regardless of their maturity, promote a T helper 1 response (IFNγ production) in culture (*62*). Exosomes from ovalbumin (OVA)–pulsed dendritic cells were more efficient in eliciting antigen (OVA)-specific $CD8^+$ T cell activation than were microvesicles (*63*), supporting a potential molecular intersection between exosome biogenesis (which is distinct from microvesicle biogenesis, as discussed above) and antigen presentation. The role of exosomes in antigen presentation was also explored in the context of bacterial infection (with a focus on *Mycobacterium tuberculosis* and *Helicobacter pylori*), wherein exosomes may enhance antibacterial immune responses by promoting bacterial antigen presentation from macrophage-derived exosomes (*64*). This could subsequently influence the adaptive immune response (*64*); the production of IFNα and IFNγ, tumor necrosis factor α (TNFα), and IL-containing exosomes from macrophages to promote dendritic cell maturation and $CD4^+$ and $CD8^+$ T cell activation (*65*); and the regulation of macrophage IL expression (*66*). Bacteria-derived EVs have also been identified in humans and have implications in health and disease (*67*, *68*), and given the emerging role of exosomes in antigen presentation in the context of bacterial infection, it is plausible that exosomes would play a role in microbiota-associated inflammation.

The nucleic acid exosomal cargo, namely DNA and miRNA, has been implicated in regulating innate and adaptive immune responses. The DNA of intracellular bacteria (e.g., *Listeria*, *Legionella pneumophila*, and *Franciscella tularensis*) are sorted into exosomes with the capacity to stimulate cGAS-STING signaling in nearby cells, effectively activating innate immune responses. However, in the case of *Listeria*, this happens at the expense of suppressing T cells and thus lowering antibacterial defense (*69*). By contrast, in the context of *M. tuberculosis* infection, bacterial RNA shed from infected macrophages enhances host immunity by eliciting the RNA-sensing pathway and promoting phagosome maturation in recipient macrophages (*70*). Although the functional role of exosomes in immune responses against fungal and parasitic infections is largely unknown, some studies related to parasite-derived exosomes have indicated that exosomes may participate in disease virulence (*71*, *72*). Specifically, the malaria-causing parasite *Plasmodium falciparum* was shown to shed its DNA and small RNAs into the exosomes from the red blood cells that it infects (*73*). Instead of enhancing the STING-dependent antipathogen immune response, human monocytes that take up exosomes containing the parasitic DNA may elicit STING-dependent DNA sensing as a decoy strategy to enhance parasite survival (*73*).

The role of exosomal DNA in the immune response was also shown to be functionally relevant to cancer progression. Adaptive immune responses elicited by exosomes include the activation of dendritic cells with the uptake of breast cancer cell–derived exosomal genomic DNA and activation of cGAS-STING signaling and antitumor response in mice (*74*). In vitro, after T cell contact, the priming of dendritic cells (immune instruction that changes the activity of dendritic cells to enhance their response to future stimulation) is also associated with the uptake of exosomal genomic and mitochondrial DNA (mtDNA) from T cells, inducing type I IFN production by cGAS-STING signaling (*75*). Although exosomal DNA uptake by recipient cells alters their signaling, exosome biogenesis may also play a role in clearing cytoplasmic DNA and in preventing activation of the cytosolic DNA-sensing machinery and reactive oxygen species–dependent DNA damage response (*76*). In the context of cancer, this exosomal DNA shedding may be beneficial, such that inhibition of EGFR in cancer cells leads to increased DNA in the exosomes from those cells and could induce cGAS-STING signaling in dendritic cells and contribute to overall suppression of tumor growth (*77*). By contrast, the impact of tumor exosomal DNA on inflammatory responses can indirectly worsen cancer, and uptake of tumor-derived exosomal DNA by circulating neutrophils was shown to enhance the production of tissue factor and IL-8, which play a role in promoting tumor inflammation and paraneoplastic events (thrombosis) (*78*).

Exosomes may also regulate the immune response by influencing gene expression and signaling pathways in recipient cells, principally by the transfer of miRNAs. Exosomal miRNA can exchange between dendritic cells and repress gene expression (*79*), and such exosome-mediated intercellular communication may influence dendritic cell maturation. Tumor-derived exosomal miR-212-3p down-regulates the MHC-II transcription factor RFXAP (regulatory factor X associated protein) in dendritic cells, possibly promoting immune evasion by cancer cells (*80*). Tumor–derived exosomal miR-222-3p down-regulates SOCS3 (suppressor of cytokine signaling 3) in monocytes, which promotes STAT3-mediated M2 polarization

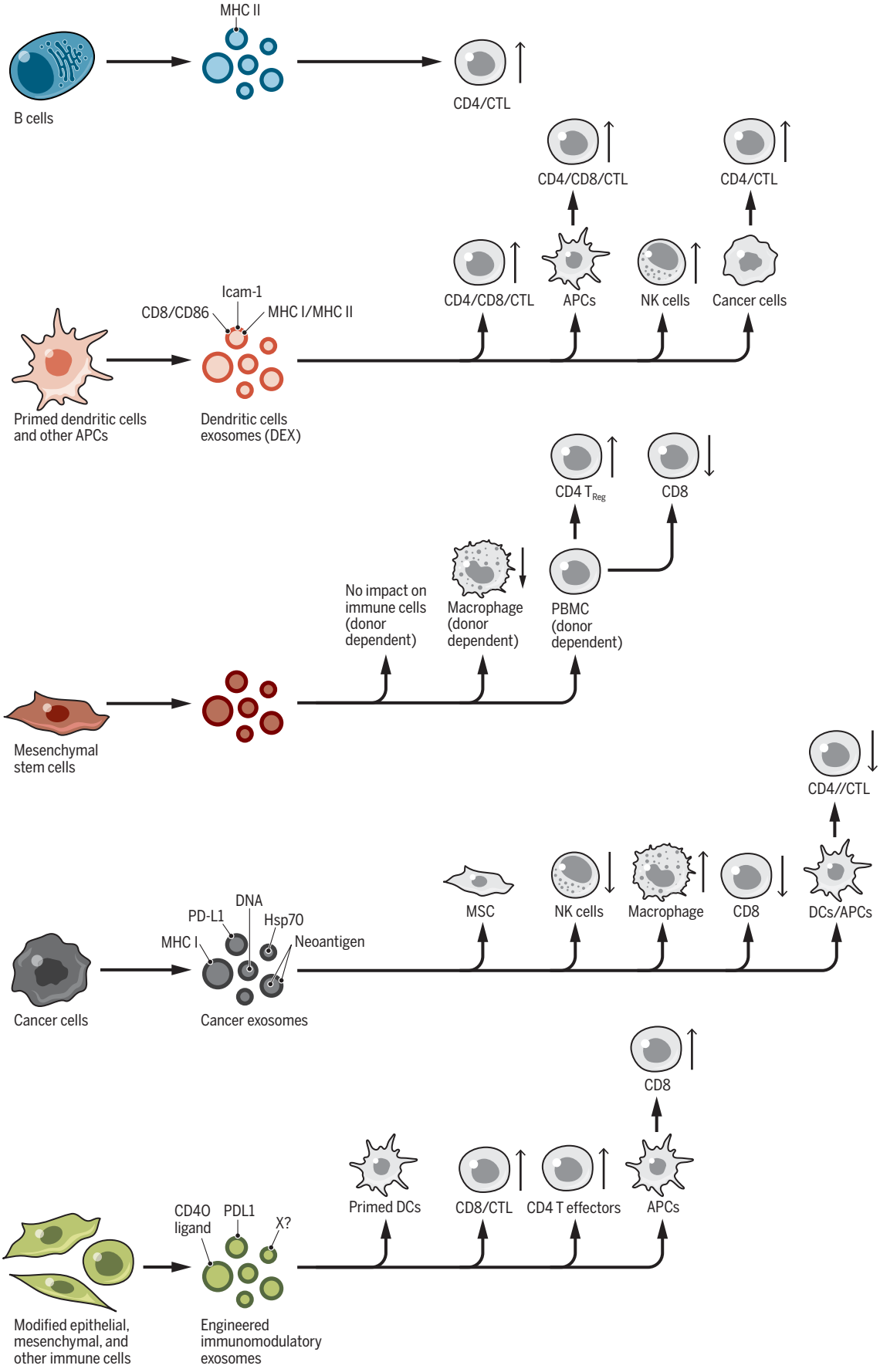

Fig. 5. Regulation of immune response by exosomes. Exosomes from distinct cellular sources, including immune cells (B cells and dendritic cells), cancer cells, epithelial, and mesenchymal cells, shed exosomes with cargos that can influence the proliferation and respective activity of recipient cells of both the innate and adaptive immune system. $CD4^+$ and $CD8^+$ T cells [cytotoxic T cells (CTL)] can be directly or indirectly influenced by exosomes, stimulating or suppressing their proliferation and function(s). PBMC, peripheral blood mononuclear cell; X?, other potential immunomodulatory proteins.

of macrophages (*81*), possibly generating an immunosuppressive microenvironment.

Modulation of immune responses by exosomes might also involve presentation of immunoregulatory molecules such as PD-L1 (programmed cell death ligand 1) and FasL (Fas cell surface death receptor ligand) on their surface. PD-L1 on melanoma-derived exosomes suppresses $CD8^+$ T cell antitumor function in vivo (*82*), and cancer cell–derived exosomes block dendritic cell maturation and migration in a PD-L1–dependent manner (*83*). Further, cancer cell–derived PD-$L1^+$ exosomes promote T cell exhaustion in the draining lymph nodes of tumor-bearing mice, promoting tumor growth (*84*). FasL on melanoma or prostate cancer-derived exosomes induces Fas-dependent apoptosis of T cells (*85*, *86*). In addition to exosomes, ligand-mediated signaling to T cells and enzymatic activities associated with exosomes derived from multiple human cancer cell types that express with CD39 (ectonucleoside triphosphate diphosphohydrolase 1) and CD73 (5′ nuleotidase) result in 5′AMP-to-adenosine conversion and adenosine signaling in T cells, effectively limiting their activation in vitro (*87*). Such actions could ultimately suppress the adaptive immune response. By contrast, mast cell–derived exosomes express MHC-II, CD86, LFA-1 (lymphocyte function-associated antigen 1), and ICAM-1 (intercellular adhesion molecule 1) and induce the proliferation of B and T cells in vitro and in vivo (*88*). Finally, cancer cell–derived exosomes engineered to overexpress CD40L (CD40 ligand or CD154, a costimulatory molecule on T cells that binds to CD40 on APCs) promotes dendritic cell maturation, resulting in increased proliferation of T cells and antitumor activity in vivo (*89*).

The role of exosomes in the innate immune response in cancer has also been reported. Exosomes from pancreatic cancer cells and plasma of pancreatic cancer patients were shown to limit complement-mediated lysis by acting as decoys, thus decreasing cytotoxicity against cancer cells (*90*). Exosomal HSP72 (heat shock protein 70 kDa protein 1) can trigger myeloid-derived suppressor cell activation by STAT3 (*91*), and exosomes derived from glioblastoma stem cells induce a STAT3-mediated immunosuppressive (M2 type) switch of macrophage phenotype (*92*), which would limit antitumoral immune response in the tumor microenvironment. Exosomal miR-21 and miR-29a from cancer cells trigger human TLR8 and mouse TLR7-mediated NF-κB (nuclear factor-κB) activation in macrophages and the production of IL-6 and TNF-α to promote melanoma lung metastasis and lung cancer in mice (*93*).

Exosomes not only play a role in immune responses related to cancer cells, but also those associated with infectious agents (bacteria, viruses, fungi, and parasites) (*71*, *94*). Exosomes might promote viral infection by enabling the dissemination of viral components, and viruses may highjack the exosome biogenesis pathway for their survival [reviewed in (*95*)] (Fig. 4). Viral infection associated with both enveloped and nonenveloped virus is regulated by exosomes. The prototypic nonenveloped hepatitis A and hepatitis E viruses (HAV and HEV, respectively) can exist in a pseudoenveloped form within exosomes (*96*, *97*). The use of the exosome biogenesis machinery by viruses and exosomes as a pseudoviral envelope evokes a "Trojan horse" ploy to favor viral entry into the cell, thereby enhancing infectivity (*98*). The similarities—in size, density, molecular cargo, and use of common components to harness the cellular proteins and vesicle-trafficking machinery—between enveloped retroviruses (in particular, HIV-1/2) and exosomes support this idea (*98*, *99*). It has been proposed that multiple viruses may package within exosomes, a process that would promote multiplicities of infection and viral genetic cooperativity (*99*). Although it remains unclear whether exosomes participate in viral immune evasion by limiting detection by neutralizing antibodies (*96*), they take part in augmenting viral entry into cells through the tetraspanins (transmembrane proteins) CD81 and CD9 present on exosomes, possibly by stabilizing the interaction of exosomes containing virus particles with the cellular plasma membrane and delivery of viral constituents (*100*–*103*). Similarly, the phosphatidylserine (PtdSer) receptor TIM-4 (T cell immunoglobulin and mucin domain containing 4) on exosomes may facilitate the cellular entry of HIV-1 because of its PtdSer-rich envelope (*104*).

A postulated advantage of viruses using exosomes to exit cells could be to evade inflammation and prevent virus-induced cell lysis. Tumor-derived transfer of EGFR-associated exosomes to macrophages weakens their antiviral response in a MEKK2 (mitogen-activated protein kinase kinase 2)- and IRF3 (interferon regulatory factor 3)–dependent manner, suggesting that cancer may enhance viral infection (*105*). Although exosomes shed from virus- infected cells can promote infection (see above), exosomes also participate in antiviral immunity. For example, IFNα-stimulated human macrophages shed exosomes that deliver antiviral mediators, including the single-stranded DNA cytidine deaminase APOBEC3G (apolipoprotein B mRNA editing enzyme, catalytic polypeptide-like 3G), protecting human hepatocytes from HBV (hepatitis B virus) infection (*106*). Exosomal APOBEC3G from exosomes also impairs HIV-1 infection of T cells (*107*). The HIV-1 receptor CD4 on exosomes from $CD4^+$ T cells was shown to reduce HIV-1 infection in vitro, and the HIV-1 accessory protein Nef in infected T cells reduced the expression of exosomal CD4, effectively enhancing HIV-1 infection (*108*). Future studies will hopefully further clarify the opposing roles of exosomes in HIV-1 infection in vivo.

Metabolic and cardiovascular diseases

Exosomes may play a role in the emergence of metabolic diseases as well as in cardiovascular fitness. They have been found to transfer metabolites and to facilitate intercellular communication through exosomal miRNA exchange among pancreatic β-cells, adipose tissue, skeletal muscles, and the liver of mice and humans (*109*). Reciprocal signaling between adipocytes and macrophages mediated by exosomes in the *Leptin* gene-knockout spontaneous mouse model of obesity implicates RBP4 (retinol binding protein 4) in stimulation of macrophages and insulin resistance (*110*). Obese mice fed a high-fat diet display distinct circulating exosomal miRNAs, which are sufficient to promote insulin resistance in lean mice, possibly through down-regulation of *Ppara* (peroxisome proliferator-activated receptor alpha) expression in white adipose tissue (*111*). Cachexia, a condition of severe weight loss and muscle wasting associated with chronic disease such as cancer, as well as other metabolic paraneoplastic syndromes (e.g., new-onset diabetes in pancreatic cancer), may be exacerbated by cancer cell–derived exosomal cargo acting on mouse and human adipocytes and muscle cells (*112*). Adrenomedullin, a peptide hormone inducing lipolysis, was found in exosomes generated by human pancreatic cancer cells and induced lipolysis in mouse and human adipocytes (*113*) and inhibited insulin secretion in rat and human islet cells (*114*). Mouse and human cancer cell derived–exosomes, which are rich in heat shock proteins (HSP70 and HSP90), are also functionally implicated in muscle wasting in mice (*115*). These findings support that cancer cell–derived exosomes can change the metabolism of noncancer cells, including adipocytes and pancreatic islet cells, thus functionally contributing to the development of cachexia and paraneoplastic syndrome.

Exosomes from mouse and human cell culture supernatant (endothelial cells, cardiac progenitor cells, cardiac fibroblasts, cardiomyocytes) have been associated with metabolic disease, including atherosclerosis, diabetes-related cardiovascular disease (CVD), and metabolic adaptation associated with heart failure (*116*). The functions of exosomes in preventing atherosclerosis was demonstrated in mice, where platelet-derived exosomes reduced macrophage scavenger receptor CD36 expression and consequently reduced the uptake of harmful cholesterol [oxidized low-density lipoprotein (LDL)] (*117*). By contrast, human smooth muscle cell–derived exosomes may promote thrombogenesis, as shown by in vitro assays (*118*). The use of stem cell (bone marrow–derived stem cells and embryonic stem cells)–derived exosomes in cardiovascular protection (*119*) has emerged as a potential therapeutic approach in mice

and rats despite limited knowledge on how exosomes potentiate these effects. Exosomal microRNAs, including miR-19a, miR-21 [from murine cardiac progenitor cells targeting PDCD4 (programmed cell death 4) in rat myoblasts in vitro (*120*)], miR-22 [from mouse bone marrow–derived mesenchymal stromal cells (MSCs) targeting MECP2 (methyl CpG binding protein 2) in ischemic mouse heart (*121*)], and miR-21-5p [from human bone marrow–derived MSCs targeting SERCA2a (sarcoendoplasmic reticulum Ca^{2+}) adenosine triphosphatase (ATPase) and L-type calcium channels in human cardiac myocytes derived from pluripotent stem cells in vitro (*122*)], mediate cardiovascular protective effects, possibly by limiting cardiomyocyte apoptosis, promoting mitochondrial function, and preserving cardiac contractility.

Neurodegeneration

The intersection between exosomal biogenesis and the regulation of secretory vesicles in neuronal cells offered new insight into the putative connection between exosomes and the pathogenesis of neurodegenerative diseases. Exosomes may promote or limit aggregation of unfolded and abnormally folded proteins in the brain (*123*–*128*). Exosomes could participate in the clearing of misfolded proteins, thereby exerting detoxifying and neuroprotective functions, or participate in the propagation and aggregation of misfolded proteins, effectively promoting the "infectivity" of protein aggregates and contributing to disease progression. Such opposing functions of exosomes might not be mutually exclusive and are described below.

Pharmacological blocking using GW4869 (which inhibits inward budding of MVBs) or enhancement of exosome production using monensin (which increases intracellular Ca^{2+} and MVB generation) results in a decrease or increase, respectively, of the transmission of the infectious prion protein PrP^{sc}, which is associated with Creutzfeldt–Jakob disease in vitro (*129*). Both Tau and Aβ (β-amyloid generated by the cleavage of amyloid precursor protein [APP]), implicated in Alzheimer's disease, are found in exosomes, including patients' cerebrospinal fluid–derived exosomes (Tau), mouse microglial cell culture supernatant-derived exosomes (Tau), and exosomes of supernatant from the culture of mouse and human cell lines (Aβ). Pathological propagation of Tau aggregation by exosomes was noted in vitro and in vivo (*130*, *131*). Using a simple circuit of neurons in a microfluidic device, exosomal transfer of Tau between neurons was proposed to include takeover of the endosomal pathway (*131*). The cleavage of APP was observed in early endosomes, and Aβ accumulated in MVBs of N2a (mouse neuroblastoma) and HeLa cells modified to express fluorescent APP (*132*); however, whether exosomes promote neurotoxic Aβ oligomerization in vivo is unknown.

The exosome biogenesis machinery may also be neuroprotective. Exosomes may impair neurotoxic oligomer formation (*133*) or exosomes may carry them out of cells (*134*). More recently, exosomal secretion of Aβ from the brains of mice engineered to overexpress APP was implicated in the initiation and propagation of toxic amyloid. This process involves the deregulation of ECE1/2 (endothelin-converting enzyme 1/2), effectively resulting in an increase in oligomerized Aβ in exosomes from the brains of APP-transgenic mice (*135*).

Similar observations were made in distinct proteinopathies such as Parkinson's disease (PD) and amyotrophic lateral sclerosis (ALS). The pathological protein α-synuclein is found in cerebrospinal fluid–derived exosomes of patients with PD or dementia with Lewy bodies (*136*), and the exosome biogenesis machinery is implicated in the accumulation α-synuclein, with α-synuclein downregulating ESCRT and limiting its intracellular degradation (*137*). SOD1 (superoxide dismutase 1) and TDP-43 (transactive response DNA binding protein 43 kDa), two misfolded proteins associated with ALS, have been identified in exosomes (*138*–*140*). Exosomes containing SOD1 from mouse astrocytes resulted in the death of mouse spinal cord–derived motor neurons in culture (*138*), mutant SOD1 could be transferred between human mesenchymal cells in vitro (*139*), and TDP-43 was found in exosomes from the culture supernatant of mouse neuroblast cells (*140*). However, in vivo suppression of exosome secretion using GW4869 in TDP-43^{A325T}-transgenic mice was detrimental because this appeared to limit the clearance of pathological TDP-43 from neurons (*140*). Although exosomes containing neurotoxic proteins could be transferred to distinct cell types in vitro (see above), possibly promoting disease progression, it remains unknown whether exosome-mediated exchange of such proteins affects—either positively or negatively—disease progression in vivo.

Although the function of exosomes in neurodegenerative disorders has focused on exosome control of misfolded protein accumulation, nucleic acids and other constituents may be implicated in worsening or ameliorating other neurological disorders. In a study evaluating the serum-derived exosomes of children with autism spectrum disorder (ASD), mtDNA exosomal cargo was proposed to illicit microglia IL-1β secretion, possibly contributing to the inflammation associated with ASD (*141*). The role of exosomes in the pathophysiology of neurodegenerative disorder and ASD requires more study, but this has not hindered efforts to use them in therapy development. Such effort is largely encouraged by the intrinsic properties of exosomes to efficiently pass through the blood–brain barrier, a vascular network functioning as a selective filter to keep drugs or toxins from reaching the brain (*28*, *142*–*144*).

Cancer

The study of exosomes in cancer has progressed at a rapid pace compared with research into their role in other diseases (*2*, *145*), and exosomes have been associated with several hallmark features of cancer (*146*). Exosomes influence neoplasia, tumor growth and metastasis, paraneoplastic syndromes, and resistance to therapy. The role of exosomes in cancer progression is likely dynamic and specific to cancer type, genetics, and stage.

Exosomes may induce or promote neoplasia. Exosomes from pancreatic cancer cells were shown to initiate cell transformation by inducing mutations in NIH/3T3 recipient cells (*147*). Exosomes derived from breast cancer and prostate cancer cells induce neoplasia through transfer of their miRNA cargo (*148*, *149*). miR-125b, miR-130, miR-155, as well as HRas and Kras mRNAs in exosomes from prostate cancer cells, participate in neoplastic reprogramming and tumor formation of adipose stem cells (*149*). The plasticity of cancer cells may also be attributed in part to exosomes, with exosomal miR-200 from metastatic breast cancer cells enhancing the epithelial to mesenchymal transition (EMT) and metastasis of otherwise weakly metastatic breast cancer cells (*150*). Although more work is needed to decipher the rate-limiting role of exosomes in neoplasia and EMT, research has focused on the exchange of exosomal cargo between cancer cells and stromal cells in the tumor microenvironment and on defining the functional outcome of such exchange on tumor growth and metastasis. These studies have explored cancer in mouse models and often rely on exogenously administered exosomes in mice.

In most studies, the stromal cell recipients of cancer cell–derived exosomes are cancer-associated fibroblasts (CAFs) and immune cells, which dynamically regulate one another in the tumor microenvironment. Distinct cancer cell–derived exosomal cargo, such as nucleic acids, signaling proteins, and metabolites, can exert protumorigenic effects on stromal cells. For example, breast cancer exosome–derived miR-122 suppresses pyruvate kinase and subsequent glucose uptake in the lungs, which promotes metastasis (*151*). Although RNA shielded by proteins prevents their recognition as pathological RNAs that would otherwise elicit inflammatory responses, breast cancer cells induce the accumulation of unshielded RN7SL1 (RNA component of signal recognition particle 7SL1) RNA in exosomes from CAFs, which ultimately produces a proinflammatory response when delivered to immune cells and results in increased tumor growth and metastasis in mice (*152*).

Examples of exosomes from cancer cells eliciting a parenchymal signaling response at metastatic sites, effectively remodeling distant microenvironments to enhance metastasis, have

been reported in multiple cancer types. For example, TGFβ (transforming growth factor-β) expressed on the surface of cancer cell–derived exosomes induces fibroblast activation by gain of αSMA (α-smooth muscle actin) and FGF2 (fibroblast growth factor 2) expression (*153*). The recruitment of bone marrow progenitor cells and macrophages to metastatic sites by cancer cell–derived exosomes has been reported in melanoma (*154*) and pancreatic cancer (*155*) and implicated in metastasis. PEDF (pigment epithelium-derived factor) on the surface of exosomes from mouse and human nonmetastatic melanoma cells elicits the expansion of patrolling monocytes by NR4A1 (nuclear receptor subfamily 4 group A member 1) induction, which suppresses metastasis in the lungs of mice (*156*). Cancer cell–derived exosomes are also proposed to play a role in organotropic metastasis of breast and pancreatic cancers, in part through integrin expression on exosomes and organ-specific proinflammatory responses (*157*), and the delivery of exosomal EGFR from gastric cancer cells to Kupffer cells and hepatic stellate cells promotes liver-specific metastasis through enhanced HGF (hepatocyte growth factor) signaling in the liver (*158*). These results are among the growing body of evidence that support a complex exosome-mediated cell-to-cell communication in the tumor microenvironment.

A reciprocal exosome exchange from the stroma to cancer cells also modulates cancer progression and metastasis. For example, mtDNA in exosomes from CAFs induces oxidative phosphorylation (with expression of mtRNA) in breast cancer cells, promoting their survival and exit from metabolic dormancy in mice (*159*). Another example of stromal exosomal cargo promoting cancer cell progression includes astrocyte-derived miR-19a delivered to breast cancer cells, which results in PTEN (phosphatase and tensin homolog) suppression and contributed to metastasis (*160*). Fibroblast-derived exosomes also stimulate the migration of breast cancer cells by inducing Wnt-PCP (planar cell polarity) autocrine signaling (*161*). In addition, exosomes encapsulate metabolites, including lactate, glutamate, acetate, stearate, palmitate, and amino acids (*162*, *163*). ^{13}C-labeled CAF–derived exosomes fuel the tricarboxylic acid cycle of recipient cancer cells through metabolite transfer, and exosomes from prostate and pancreatic CAFs also replenish lipids in cancer cells, enhancing their fitness during tumor growth (*163*). Plasma-derived exosomes contain metabolic enzymes, including hexokinase 1, pyruvate kinase, lactate dehydrogenase, enolase, and glyceraldehyde 3-phospate dehydrogenase, and these enzymes mediate the production of adenosine 5′-triphosphate (ATP) in exosomes (*164*). CAF-derived exosomes suppress oxidative phosphorylation in prostate and pancreas cancer cells by transferring miR-22, let7a, and miR-125b, and promote glycolysis and glutamine-dependent reductive carboxylation by metabolite transfer (*163*). The cancer stroma–derived exosomes thus promote the metabolic fitness of cancer cells growing as tumors in mice.

Exosomes have also been implicated in the angiogenic and extracellular matrix remodeling of the tumor microenvironment, a critical step in tumor growth and metastatic dissemination. miR-105 from breast cancer cell–derived exosomes suppresses endothelial tight junction ZO-1 (zonular occludens 1) expression, resulting in increased metastasis by impairing the integrity of blood vessels and enhancing vascular permeability (*165*). Exosomes from hypoxic glioblastoma (GBM) cells induce proangiogenic programming of endothelial cells and GBM cell proliferation (*166*). Recent findings implicate neutrophil-derived exosomes in proteolytic degradation of the lung extracellular matrix associated with chronic obstructive pulmonary disease (*167*). In the context of cancer, MMP1 (matrix metalloprotease 1) in exosomes from ovarian cancer cells may play a role in compromising the mesothelium and promoting peritoneal dissemination of cancer cells (*168*).

Exosomes shed by cancer cells are reported to promote resistance to various chemotherapeutic agents and antibodies. CD20$^+$ exosomes from B cell lymphoma act as a decoy for the binding of anti-CD20 to B cells (*169*), and HER2 (human epidermal growth factor receptor 2)–positive exosomes from breast cancer cells act as a decoy for anti-HER2 therapy (*170*), thus limiting their activity toward cancer cells. CAF-derived exosomes promote colorectal cancer chemoresistance by enhancing the growth of cancer stem cells (*171*) and aid in the spread of drug-resistance properties between cancer cell populations. This process may be mediated by horizontal transfer of exosomal miRNAs (observed in breast cancer cells) (*172*). Specifically, an exosomal long noncoding RNA (lncRNA) called lncARSR [lncRNA activated in renal cell carcinoma (RCC) with sunitinib resistance] binds competitively to miR-34 and miR-449 and enhances expression of the tyrosine kinases AXL and MET, overcoming the effect of sunitinib (*173*). When tumors are treated with radiation therapy or gamma secretase inhibitor, the expansion of tumor-initiating cells resistant to radiation therapy emerges through CAF-derived exosomal RNA and transposable elements transfer to cancer cells (*174*). CAF-derived exosomal miR-21 binding to APAF1 (apoptotic protease activating factor 1) in ovarian cancer cells confers resistance to paclitaxel (*175*), and macrophage-derived exosomal miR-385 induces cytidine deaminase activity in pancreatic cancer cells and confers resistance to gemcitabine (*176*). Chemotherapy and radiation therapy could also directly affect exosome biogenesis and the content of exosomes with potential implications on therapy outcome (*177*). Radiation therapy enhances exosomal miR-7-5p production by cancer cells, which induces bystander cell autophagy (*178*). These findings capture the distinct role of exosomes in promoting resistance to therapy, which results from exosomes directly interacting with therapeutic agents and decreasing their efficacy against cancer cells, or from exosomes (mainly from CAFs) changing the transcriptome of cancer cells to promote their survival.

Clinical applications of exosomes

The biology of exosomes in disease is still emerging, and the number of studies addressing their utility in the diagnosis and treatment of various pathologies has increased substantially. This takes advantage of the complex cargo of exosomes, allowing for a multicomponent diagnostic window into disease detection and monitoring. The characteristic properties of exosomes in delivering functional cargos to diseased cells also favor their use as therapeutic vehicles, both at the basic and applied levels.

Diagnostic potential of exosomes

Exosomes are found in all biological fluids and are secreted by all cells, rendering them attractive as minimally invasive liquid biopsies with the potential for longitudinal sampling to follow disease progression. Exosome biogenesis enables the capture of a complex extracellular and intracellular molecular cargo for comprehensive, multiparameter diagnostic testing (Fig. 2). Surface proteins on exosomes also facilitate their immune capture and enrichment. Diseases that have been the focus of diagnostic application of exosomes include CVDs (*116*, *179*), diseases affecting the central nervous system (CNS) (*180*), and cancer (*2*, *181*). This effort is rapidly expanding to other diseases involving the liver (*182*), kidney (*183*), and lung (*184*).

Some studies have suggested that small amounts of DNA can be found in exosomes and that this DNA can be of value in detecting cancer-associated mutations in serum exosomes (*185*–*188*). Although some studies suggest that exosomes from human cell lines and serum do not contain DNA, this remains contentious and quantitative studies are required. One study did not specify the quantity of exosomes used in its analytical assays, leading to ambitious conclusions (*12*). Should exosomal DNA reflect larger fragments of DNA than circulating free DNA, this may be beneficial in detecting mutations, including in *KRAS* and *TP53*, in the circulating exosomes of patients with pancreatic cancer (*186*–*192*). Specific miRNAs or groups of miRNAs in exosomes may provide diagnostic or prognostic potential in the detection of cancer (*193*). Oncogenic and tumor-suppressor miRNAs in exosomes may be of high diagnostic value because of their differential expression between cancer cells and normal cells, possibly enhancing

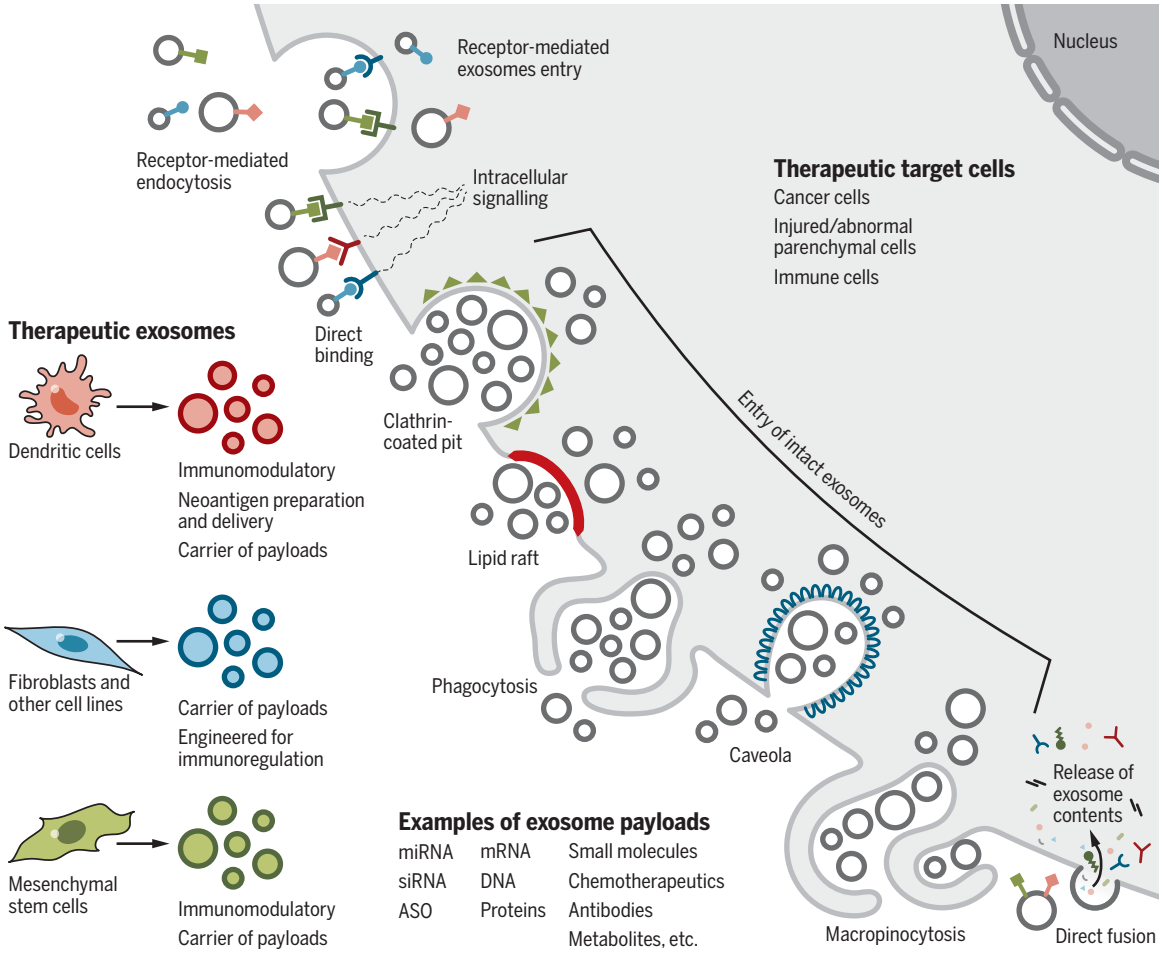

Fig. 6. Cellular uptake of therapeutic exosomes. Therapeutic exosomes isolated from dendritic cells, fibroblasts, and mesenchymal cells can impart specific effects on the target cells, including neoantigen presentation, immunomodulation, and drug payload delivery. The impact of therapeutic exosomes on target cells may be controlled by the different mechanisms of entry or interaction. Entry of intact exosomes can involve receptor-mediated endocytosis, clathrin-coated pits, lipid rafts, phagocytosis, caveolae, and macropinocytosis. Entry of the content of the exosomes, or induction of signals by exosomes, can involve ligand-receptor–induced intracellular signaling or fusion to deposit the contents of the exosomes into the cytoplasm. Examples of therapeutic payload are listed. Target cells include cancer cells, injured parenchymal cells, and immune cells. ASO, antisense oligonucleotide (a DNA oligo-binding RNA target).

their usefulness in early diagnosis (*193*). This may be in part driven by the genomic landscape of cancer cells, with oncogenic Kras reported to differentially enrich for miR-100 in exosomes (*194*). Elevated circulating exosomal miR-21 has been associated with glioblastomas and pancreatic, colorectal, colon, liver, breast, ovarian, and esophageal cancers, and elevated urine-derived exosomal miR-21 has been associated with bladder and prostate cancer [reviewed in (*193*, *195*)]. Other exosomal oncogenic microRNAs associated with multiple cancer types include miR-155, the miR-17-92 cluster, and miR-1246 (*196*–*199*). These are noted to be up-regulated in cancers of the brain, pancreas, colorectum, colon, liver, breast, prostate, and esophagus; in oral squamous cell cancer; as well as in lymphoma and leukemia (*193*). Tumor-suppressor miRNAs, including miR-146a and miR-34a, are associated with liver, breast, colon, pancreatic, and hematologic malignancies (*193*). The combination of multiple microRNAs may enhance the diagnostic and prognostic potential of exosomal miRNA, and exosomal miR signatures are continuously emerging in association with cancer diagnosis and prognosis (*195*, *200*–*204*). The diagnostic potential of phosphoprotein in circulating exosomes from breast cancer patients has also been reported (*205*), as well as exosome surface protein analyses (*206*). Several independent laboratories have reported the utility of GPC1 (glypican 1)–positive exosomes in the diagnosis of pancreatic, breast, and colon cancer, with GPC1 being enriched in cancer cell–derived exosomes, thus enabling the detection of cancer and possibly response to therapy (decrease in exosome numbers and thus tumor burden) (*207*–*216*). Immunocapture strategies are also under investigation to detect circulating cancer exosomes using surface CD147 expression in patients with colorectal cancer (*217*). The relative PtdSer composition of exosomes may also prove useful for the early detection of cancer in mice, as evaluated from the serum of mice bearing breast or pancreatic tumors (*218*). The possibility of combining protein, lipid, RNA, and miRNA exosomal cargos in cancer diagnosis and prognostic evaluation is currently being considered. A multicomponent, combinatorial approach using a combination of markers that reflect distinct aspects of disease-generating exosomes (e.g., metabolite, RNA, and protein content) could potentially enhance the specificity and sensitivity of an exosome-based diagnostic. Such efforts would be more likely to identify collective disease-specific changes, and lipid bilayer encapsulation could preserve enzyme-sensitive molecular cargos.

Therapeutic potential of exosomes

Exosomes by themselves or as vehicles for the delivery of drug payload(s) are being actively explored as therapeutic agents (Fig. 6). In contrast to liposomes, injected exosomes are efficient at entering other cells and can deliver a functional cargo with minimal immune clearance upon exogenous administration in mice (*2*, *181*, *219*–*221*). In addition, the therapeutic application of exosomes is promising because they have been demonstrated to be well tolerated. Exosomes from mesenchymal

cells and epithelial cells do not induce toxicity when repeatedly injected in mice (*35*, *57*). MSC-derived exosomes have been proposed to be therapeutic by themselves (*222*), and the use of MSC-derived exosomes in the treatment of a patient with graft versus host disease showed that repeated injections were well tolerated, were not associated with substantial side effects, and resulted in patient response (*223*).

Enrichment of exosomes on the basis of their surface ligand presentation may also enable the development of receptor-mediated tissue targeting. Ligand enrichment on engineered exosomes may also be used to induce or inhibit signaling events in recipient cells or to target exosomes to specific cell types. For example, αv integrin-specific RGD (R, arginine; G, glycine; D, aspartic acid)–modified peptide (a modified tumor-homing peptide sequence that acts as a recognition sequence for integrins) on immature dendritic cell–derived exosomes loaded with doxorubicin showed therapeutic response in mammary tumor–bearing mice (*224*). Other chemotherapeutic compounds have also been loaded into exosomes for cancer therapy and tested in mice, and antitumor efficacy and reduced toxicity were reported. For example, macrophage-derived exosomes loaded with paclitaxel induced lung tumor responses in mice (*225*).

Building on the observation that exosomal microRNAs effectively engage target mRNA and suppress gene expression in recipient cells, engineering of exosomes to deliver a specific miRNA or small interfering RNA (siRNA) payload has been developed for CNS diseases and cancer. The exosomal RNAs may be protected from degradation by blood-derived ribonucleases (*226*) and, combined with superior systemic retention compared with liposomes, this could allow exosomes to exert their function at distant sites. Preclinical testing with the delivery of miRNA or siRNA payload using exosomes has focused on anticancer treatment in rodents with mammary carcinoma (*227*), glioma (*228*), and pancreatic cancer (*28*, *35*), as well as exploratory brain targeting. $EGFR^+$ breast cancer cell targeting using exosomes modified with GE11 synthetic peptide and delivery of microRNA let-7a to the cancer cells limited their growth in vivo (*227*). MSC-derived exosomes enabled miR-146b delivery and EGFR targeting in glioma in rats (*228*). Clinical-grade MSC-derived exosomes with $Kras^{G12D}$ siRNA payload (iExosomes) have been used to treat pancreatic cancer in multiple animal models (*28*, *35*). These studies demonstrated that iExosomes, administered as a single agent, yield a robust increase in overall survival of mice and enable specific target engagement without any obvious toxicity (*28*, *35*). It was shown that CD47 on exosomes results in a "don't eat me" signal, protecting them from phagocytosis and limiting their clearance form circulation (*28*). Further, macropinocytosis associated with cancer cells enhanced the entry of exogenously administered iExosomes (*28*). Further development of iExosome-based therapy has led to a phase I clinical trial for the treatment of patients with $Kras^{G12D}$ mutation–associated pancreatic cancer (ClinicalTrials.gov identifier: NCT03608631).

In the context of neurological diseases, intranasal administration of human MSC–derived exosomes resulted in amelioration of autistic-like behavior in mice (BTBR mouse model), although the precise mechanisms are unknown (*229*). Intravenous administration of human MSC–derived exosomes supports neuroprotection, as shown by a swine model of traumatic brain injury (*230*). RVG (rabies virus glycoprotein)–modified dendritic cell–derived exosomes with therapeutic *Bace1*-targeting siRNA were intravenously administrated to mice and the results showed suppression of BACE1 expression in the brain, a potential target for the treatment of Alzheimer's disease (*142*). RVG-modified exosomes with siRNA targeting α-synuclein reduced aggregate formation in the brains of S129D α-synuclein mice and improved brain pathology (*143*). Macrophage-derived exosomes show the capacity to effectively negotiate the blood–brain barrier and deliver protein cargo (*231*), supporting the idea that minimal modification of exosomes is required to reach the brain parenchyma. Macrophage-derived exosomes loaded with catalase showed therapeutic benefit (neuroprotective effect) when administered intranasally in a mouse model of PD (*232*). Finally, blood-derived exosomes loaded with dopamine reached the brain after intravenous injection and, compared with free dopamine, exhibited improved therapeutic efficacy with decreased toxicity in a PD mouse model (*233*). These findings support the potential of therapeutic cargo in exosomes reaching clinically challenging targets in the brain, in part because of engineered exosomal cargo (siRNA)–targeting genes for which there are no effective pharmacological agents, and in part because of their ability to pass through the blood-brain barrier.

The role of exosomes in polarizing the tumor immune microenvironment (discussed above) has also prompted the design of therapeutic exosomes aimed at enhancing antitumor immune responses (*54*). The antitumor action of exosomes from dendritic cells potentially caused by antigen presentation was tested in a clinical setting (*234*). The engineered exosomes, called "dexosomes," were obtained from IFN-γ–matured dendritic cells and loaded with MART1 (melanoma antigen recognized by T cells 1) peptides. Although the approach did not yield a measurable cancer-specific T cell response, dexosomes induced increased cytolytic activity associated with natural killer cells in patients with stage IIIB/IV non–small-cell lung cancer (*234*). Only one among the 22 patients treated with dexosomes showed substantial liver toxicity, and 7 out of 22 patients exhibited disease stabilization exceeding 4 months (*234*), although the response could not be attributed specifically to the dexosomes. Together, these early clinical data and the numerous preclinical studies offer encouragement for the development of exosomes as therapeutic agents.

Conclusions

Although interesting exosome biology is being unraveled largely using cell-culture systems, there is a need for experiments using mouse models and physiologically relevant experimental conditions. Exosomes are reported to induce molecular alteration in cells but the question remains whether such observations are of relevance because of the use of supraphysiological numbers of cell culture–derived exosomes, which often also need more precise isolation and characterization procedures (*1*). The need for precise and accurate characterization of exosomes will continue to grow as our knowledge of the heterogeneity of EVs, their cargo, and functions evolve. Exogenous bolus doses of supraphysiological levels of exosomes into mice were associated with a penetrant cellular phenotype, including modulation of cancer progression (*144*, *151*, *165*, *235*), induction of neoplasia (*148*), and regeneration of tissue (*236*). It remains unclear whether unmanipulated, physiological levels of exosomes exert regulatory homeostatic or pathological functions (or neither) in vivo. The field is in urgent need of animal models with which to study biogenesis, trafficking, and cellular entry of exosomes. *Drosophila*, *C. elegans*, *Xenopus*, and zebrafish models may offer additional insights (*237*–*239*).

Exosomes are generated by cells, but it is tempting to wonder whether they are reminiscent of early primordial particles that contributed to the generation of the first protocell (*240*, *241*). It remains to be determined whether exosomes can grow and divide and, given the right environment, participate in signaling events and autonomous biochemical reactions. The similarities between exosomes and retrovirus (*242*) also raise the possibility that exosomes may have functioned as primordial particles that preceded single-cell organisms.

REFERENCES AND NOTES

1. C. Théry *et al.*, Minimal information for studies of extracellular vesicles 2018 (MISEV2018): A position statement of the International Society for Extracellular Vesicles and update of the MISEV2014 guidelines. *J. Extracell. Vesicles* **7**, 1535750 (2018). doi: 10.1080/20013078.2018.1535750; pmid: 30637094
2. R. Kalluri, The biology and function of exosomes in cancer. *J. Clin. Invest.* **126**, 1208–1215 (2016). doi: 10.1172/JCI81135; pmid: 27035812
3. C. Kahlert, R. Kalluri, Exosomes in tumor microenvironment influence cancer progression and metastasis. *J. Mol. Med.* **91**, 431–437 (2013). doi: 10.1007/s00109-013-1020-6; pmid: 23519402

4. G. van Niel, G. D'Angelo, G. Raposo, Shedding light on the cell biology of extracellular vesicles. *Nat. Rev. Mol. Cell Biol.* **19**, 213–228 (2018). doi: 10.1038/nrm.2017.125; pmid: 29339798
5. K. M. McAndrews, R. Kalluri, Mechanisms associated with biogenesis of exosomes in cancer. *Mol. Cancer* **18**, 52 (2019). doi: 10.1186/s12943-019-0963-9; pmid: 30925917
6. M. Mathieu, L. Martin-Jaular, G. Lavieu, C. Théry, Specificities of secretion and uptake of exosomes and other extracellular vesicles for cell-to-cell communication. *Nat. Cell Biol.* **21**, 9–17 (2019). doi: 10.1038/s41556-018-0250-9; pmid: 30602770
7. M. J. Shurtleff, M. M. Temoche-Diaz, R. Schekman, Extracellular vesicles and cancer: Caveat lector. *Annu. Rev. Cancer Biol.* **2**, 395–411 (2018). doi: 10.1146/annurev-cancerbio-030617-050519
8. C. Harding, J. Heuser, P. Stahl, Receptor-mediated endocytosis of transferrin and recycling of the transferrin receptor in rat reticulocytes. *J. Cell Biol.* **97**, 329–339 (1983). doi: 10.1083/jcb.97.2.329; pmid: 6309857
9. B. T. Pan, K. Teng, C. Wu, M. Adam, R. M. Johnstone, Electron microscopic evidence for externalization of the transferrin receptor in vesicular form in sheep reticulocytes. *J. Cell Biol.* **101**, 942–948 (1985). doi: 10.1083/jcb.101.3.942; pmid: 2993317
10. E. Cocucci, J. Meldolesi, Ectosomes and exosomes: Shedding the confusion between extracellular vesicles. *Trends Cell Biol.* **25**, 364–372 (2015). doi: 10.1016/j.tcb.2015.01.004; pmid: 25683921
11. M. P. Bebelman, M. J. Smit, D. M. Pegtel, S. R. Baglio, Biogenesis and function of extracellular vesicles in cancer. *Pharmacol. Ther.* **188**, 1–11 (2018). doi: 10.1016/j.pharmthera.2018.02.013; pmid: 29476772
12. D. K. Jeppesen *et al*., Reassessment of exosome composition. *Cell* **177**, 428–445.e18 (2019). doi: 10.1016/j.cell.2019.02.029; pmid: 30951670
13. E. Willms, C. Cabañas, I. Mäger, M. J. A. Wood, P. Vader, Extracellular vesicle heterogeneity: subpopulations, isolation techniques, and diverse functions in cancer progression. *Front. Immunol.* **9**, 738 (2018). doi: 10.3389/fimmu.2018.00738; pmid: 29760691
14. N. P. Hessvik, A. Llorente, Current knowledge on exosome biogenesis and release. *Cell. Mol. Life Sci.* **75**, 193–208 (2018). doi: 10.1007/s00018-017-2595-9; pmid: 28733901
15. C. Ciardiello *et al*., Focus on extracellular vesicles: New frontiers of cell-to-cell communication in cancer. *Int. J. Mol. Sci.* **17**, 175 (2016). doi: 10.3390/ijms17020175; pmid: 26861306
16. Y. J. Chiu, W. Cai, Y. R. Shih, I. Lian, Y. H. Lo, A single-cell assay for time lapse studies of exosome secretion and cell behaviors. *Small* **12**, 3658–3666 (2016). doi: 10.1002/smll.201600725; pmid: 27254278
17. H. Zhang *et al*., Identification of distinct nanoparticles and subsets of extracellular vesicles by asymmetric flow field-flow fractionation. *Nat. Cell Biol.* **20**, 332–343 (2018). doi: 10.1038/s41556-018-0040-4; pmid: 29459780
18. S. Keerthikumar *et al*., ExoCarta: A web-based compendium of exosomal cargo. *J. Mol. Biol.* **428**, 688–692 (2016). doi: 10.1016/j.jmb.2015.09.019; pmid: 26434508
19. M. Pathan *et al*., Vesiclepedia 2019: A compendium of RNA, proteins, lipids and metabolites in extracellular vesicles. *Nucleic Acids Res.* **47**, D516–D519 (2019). doi: 10.1093/nar/gky1029; pmid: 30395310
20. B. W. van Balkom, A. S. Eisele, D. M. Pegtel, S. Bervoets, M. C. Verhaar, Quantitative and qualitative analysis of small RNAs in human endothelial cells and exosomes provides insights into localized RNA processing, degradation and sorting. *J. Extracell. Vesicles* **4**, 26760 (2015). doi: 10.3402/jev.v4.26760; pmid: 26027894
21. E. Lasda, R. Parker, Circular RNAs co-precipitate with extracellular vesicles: A possible mechanism for circRNA clearance. *PLOS ONE* **11**, e0148407 (2016). doi: 10.1371/journal.pone.0148407; pmid: 26848835
22. J. R. Chevillet *et al*., Quantitative and stoichiometric analysis of the microRNA content of exosomes. *Proc. Natl. Acad. Sci. U.S.A.* **111**, 14888–14893 (2014). doi: 10.1073/pnas.1408301111; pmid: 25267620
23. J. Kowal *et al*., Proteomic comparison defines novel markers to characterize heterogeneous populations of extracellular vesicle subtypes. *Proc. Natl. Acad. Sci. U.S.A.* **113**, E968–E977 (2016). doi: 10.1073/pnas.1521230113; pmid: 26858453
24. S. W. Wen *et al*., Breast cancer-derived exosomes reflect the cell-of-origin phenotype. *Proteomics* **19**, e1800180 (2019). doi: 10.1002/pmic.201800180; pmid: 30672117
25. L. A. Mulcahy, R. C. Pink, D. R. Carter, Routes and mechanisms of extracellular vesicle uptake. *J. Extracell. Vesicles* **3**, 24641 (2014). doi: 10.3402/jev.v3.24641; pmid: 25143819
26. K. J. McKelvey, K. L. Powell, A. W. Ashton, J. M. Morris, S. A. McCracken, Exosomes: Mechanisms of uptake. *J Circ Biomark* **4**, 7 (2015). doi: 10.5772/61186; pmid: 28936243
27. C. Commisso *et al*., Macropinocytosis of protein is an amino acid supply route in Ras-transformed cells. *Nature* **497**, 633–637 (2013). doi: 10.1038/nature12138; pmid: 23665962
28. S. Kamerkar *et al*., Exosomes facilitate therapeutic targeting of oncogenic KRAS in pancreatic cancer. *Nature* **546**, 498–503 (2017). doi: 10.1038/nature22341; pmid: 28607485
29. I. Parolini *et al*., Microenvironmental pH is a key factor for exosome traffic in tumor cells. *J. Biol. Chem.* **284**, 34211–34222 (2009). doi: 10.1074/jbc.M109.041152; pmid: 19801663
30. T. Tian *et al*., Exosome uptake through clathrin-mediated endocytosis and macropinocytosis and mediating miR-21 delivery. *J. Biol. Chem.* **289**, 22258–22267 (2014). doi: 10.1074/jbc.M114.588046; pmid: 24951588
31. P. Gangadaran, C. M. Hong, B. C. Ahn, An update on *in vivo* imaging of extracellular vesicles as drug delivery vehicles. *Front. Pharmacol.* **9**, 169 (2018). doi: 10.3389/fphar.2018.00169; pmid: 29541030
32. P. Gangadaran *et al*., A new bioluminescent reporter system to study the biodistribution of systematically injected tumor-derived bioluminescent extracellular vesicles in mice. *Oncotarget* **8**, 109894–109914 (2017). doi: 10.18632/oncotarget.22493; pmid: 29299117
33. C. P. Lai *et al*., Dynamic biodistribution of extracellular vesicles in vivo using a multimodal imaging reporter. *ACS Nano* **8**, 483–494 (2014). doi: 10.1021/nn404945r; pmid: 24383518
34. M. Morishita, Y. Takahashi, M. Nishikawa, Y. Takakura, Pharmacokinetics of exosomes: An important factor for elucidating the biological roles of exosomes and for the development of exosome-based therapeutics. *J. Pharm. Sci.* **106**, 2265–2269 (2017). doi: 10.1016/j.xphs.2017.02.030; pmid: 28283433
35. M. Mendt *et al*., Generation and testing of clinical-grade exosomes for pancreatic cancer. *JCI Insight* **3**, e99263 (2018). doi: 10.1172/jci.insight.99263; pmid: 29669940
36. K. Ridder *et al*., Extracellular vesicle-mediated transfer of genetic information between the hematopoietic system and the brain in response to inflammation. *PLOS Biol.* **12**, e1001874 (2014). doi: 10.1371/journal.pbio.1001874; pmid: 24893313
37. A. Zomer *et al*., In Vivo imaging reveals extracellular vesicle-mediated phenocopying of metastatic behavior. *Cell* **161**, 1046–1057 (2015). doi: 10.1016/j.cell.2015.04.042; pmid: 26000481
38. M. Tkach, C. Théry, Communication by extracellular vesicles: Where we are and where we need to go. *Cell* **164**, 1226–1232 (2016). doi: 10.1016/j.cell.2016.01.043; pmid: 26967288
39. D. Choi *et al*., The impact of oncogenic EGFRvIII on the proteome of extracellular vesicles released from glioblastoma cells. *Mol. Cell. Proteomics* **17**, 1948–1964 (2018). doi: 10.1074/mcp.RA118.000644; pmid: 30006486
40. C. Cossetti *et al*., Extracellular vesicles from neural stem cells transfer IFN-γ via Ifngr1 to activate Stat1 signaling in target cells. *Mol. Cell* **56**, 193–204 (2014). doi: 10.1016/j.molcel.2014.08.020; pmid: 25242146
41. R. Sullivan, F. Saez, J. Girouard, G. Frenette, Role of exosomes in sperm maturation during the transit along the male reproductive tract. *Blood Cells Mol. Dis.* **35**, 1–10 (2005). doi: 10.1016/j.bcmd.2005.03.005; pmid: 15893944
42. L. Vojtech *et al*., Exosomes in human semen carry a distinctive repertoire of small non-coding RNAs with potential regulatory functions. *Nucleic Acids Res.* **42**, 7290–7304 (2014). doi: 10.1093/nar/gku347; pmid: 24838567
43. M. N. Madison, P. H. Jones, C. M. Okeoma, Exosomes in human semen restrict HIV-1 transmission by vaginal cells and block intravaginal replication of LP-BM5 murine AIDS virus complex. *Virology* **482**, 189–201 (2015). doi: 10.1016/j.virol.2015.03.040; pmid: 25880110
44. J. L. Welch *et al*., Effect of prolonged freezing of semen on exosome recovery and biologic activity. *Sci. Rep.* **7**, 45034 (2017). doi: 10.1038/srep45034; pmid: 28338013
45. J. L. Welch, H. Kaddour, P. M. Schlievert, J. T. Stapleton, C. M. Okeoma, Semen exosomes promote transcriptional silencing of HIV-1 by disrupting NF-kB/Sp1/Tat circuitry. *J. Virol.* **92**, e00731-18 (2018). doi: 10.1128/JVI.00731-18; pmid: 30111566
46. E. Delorme-Axford *et al*., Human placental trophoblasts confer viral resistance to recipient cells. *Proc. Natl. Acad. Sci. U.S.A.* **110**, 12048–12053 (2013). doi: 10.1073/pnas.1304718110; pmid: 23818581
47. R. Menon *et al*., Circulating exosomal miRNA profile during term and preterm birth pregnancies: A longitudinal study. *Endocrinology* **160**, 249–275 (2019). doi: 10.1210/en.2018-00836; pmid: 30358826
48. R. Menon *et al*., Quantitative proteomics by SWATH-MS of maternal plasma exosomes determine pathways associated with term and preterm birth. *Endocrinology* **160**, 639–650 (2019). doi: 10.1210/en.2018-00820; pmid: 30668697
49. S. Sheller-Miller, J. Trivedi, S. M. Yellon, R. Menon, Exosomes cause preterm birth in mice: Evidence for paracrine signaling in pregnancy. *Sci. Rep.* **9**, 608 (2019). doi: 10.1038/s41598-018-37002-x; pmid: 30679631
50. B. P. Foster *et al*., Extracellular vesicles in blood, milk and body fluids of the female and male urogenital tract and with special regard to reproduction. *Crit. Rev. Clin. Lab. Sci.* **53**, 379–395 (2016). doi: 10.1080/10408363.2016.1190682; pmid: 27191915
51. C. Admyre *et al*., Exosomes with immune modulatory features are present in human breast milk. *J. Immunol.* **179**, 1969–1978 (2007). doi: 10.4049/jimmunol.179.3.1969; pmid: 17641064
52. T. Chen *et al*., Porcine milk-derived exosomes promote proliferation of intestinal epithelial cells. *Sci. Rep.* **6**, 33862 (2016). doi: 10.1038/srep33862; pmid: 27646050
53. O. P. Wiklander *et al*., Extracellular vesicle in vivo biodistribution is determined by cell source, route of administration and targeting. *J. Extracell. Vesicles* **4**, 26316 (2015). doi: 10.3402/jev.v4.26316; pmid: 25899407
54. U. Gehrmann, T. I. Näslund, S. Hiltbrunner, P. Larssen, S. Gabrielsson, Harnessing the exosome-induced immune response for cancer immunotherapy. *Semin. Cancer Biol.* **28**, 58–67 (2014). doi: 10.1016/j.semcancer.2014.05.003; pmid: 24859748
55. P. Kurywchak, J. Tavormina, R. Kalluri, The emerging roles of exosomes in the modulation of immune responses in cancer. *Genome Med.* **10**, 23 (2018). doi: 10.1186/s13073-018-0535-4; pmid: 29580275
56. P. D. Robbins, A. E. Morelli, Regulation of immune responses by extracellular vesicles. *Nat. Rev. Immunol.* **14**, 195–208 (2014). doi: 10.1038/nri3622; pmid: 24566916
57. X. Zhu *et al*., Comprehensive toxicity and immunogenicity studies reveal minimal effects in mice following sustained dosing of extracellular vesicles derived from HEK293T cells. *J. Extracell. Vesicles* **6**, 1324730 (2017). doi: 10.1080/20013078.2017.1324730; pmid: 28717420
58. G. Raposo *et al*., B lymphocytes secrete antigen-presenting vesicles. *J. Exp. Med.* **183**, 1161–1172 (1996). doi: 10.1084/jem.183.3.1161; pmid: 8642258
59. H. Vincent-Schneider *et al*., Exosomes bearing HLA-DR1 molecules need dendritic cells to efficiently stimulate specific T cells. *Int. Immunol.* **14**, 713–722 (2002). doi: 10.1093/intimm/dxf048; pmid: 12096030
60. L. Zitvogel *et al*., Eradication of established murine tumors using a novel cell-free vaccine: Dendritic cell-derived exosomes. *Nat. Med.* **4**, 594–600 (1998). doi: 10.1038/nm0598-594; pmid: 9585234
61. A. Montecalvo *et al*., Exosomes as a short-range mechanism to spread alloantigen between dendritic cells during T cell allorecognition. *J. Immunol.* **180**, 3081–3090 (2008). doi: 10.4049/jimmunol.180.5.3081; pmid: 18292531
62. M. Tkach *et al*., Qualitative differences in T-cell activation by dendritic cell-derived extracellular vesicle subtypes. *EMBO J.* **36**, 3012–3028 (2017). doi: 10.15252/embj.201696003; pmid: 28923825
63. C. J. E. Wahlund *et al*., Exosomes from antigen-pulsed dendritic cells induce stronger antigen-specific immune responses than microvesicles in vivo. *Sci. Rep.* **7**, 17095 (2017). doi: 10.1038/s41598-017-16609-6; pmid: 29213052
64. Y. Cheng, J. S. Schorey, Exosomes carrying mycobacterial antigens can protect mice against *Mycobacterium tuberculosis* infection. *Eur. J. Immunol.* **43**, 3279–3290 (2013). doi: 10.1002/eji.201343727; pmid: 23943377
65. P. K. Giri, J. S. Schorey, Exosomes derived from *M. bovis* BCG infected macrophages activate antigen-specific CD4+ and CD8+ T cells in vitro and in vivo. *PLOS ONE* **3**, e2461 (2008). doi: 10.1371/journal.pone.0002461; pmid: 18560543
66. J. Wang *et al*., MicroRNA-155 in exosomes secreted from *Helicobacter pylori* infection macrophages immunomodulates inflammatory response. *Am. J. Transl. Res.* **8**, 3700–3709 (2016). pmid: 27725852

67. S. Ahmadi Badi *et al*., Microbiota-derived extracellular vesicles as new systemic regulators. *Front. Microbiol.* **8**, 1610 (2017). doi: 10.3389/fmicb.2017.01610; pmid: 28883815
68. L. E. Smythies, J. R. Smythies, Exosomes in the gut. *Front. Immunol.* **5**, 104 (2014). doi: 10.3389/fimmu.2014.00104; pmid: 24672525
69. R. Nandakumar *et al*., Intracellular bacteria engage a STING-TBK1-MVB12b pathway to enable paracrine cGAS-STING signalling. *Nat. Microbiol.* **4**, 701–713 (2019). doi: 10.1038/s41564-019-0367-z; pmid: 30804548
70. Y. Cheng, J. S. Schorey, Extracellular vesicles deliver *Mycobacterium* RNA to promote host immunity and bacterial killing. *EMBO Rep.* **20**, e46613 (2019). doi: 10.15252/embr.201846613; pmid: 30683680
71. J. Wang *et al*., Host derived exosomes-pathogens interactions: Potential functions of exosomes in pathogen infection. *Biomed. Pharmacother.* **108**, 1451–1459 (2018). doi: 10.1016/j.biopha.2018.09.174; pmid: 30372847
72. A. Marcilla *et al*., Extracellular vesicles in parasitic diseases. *J. Extracell. Vesicles* **3**, 25040 (2014). doi: 10.3402/jev.v3.25040; pmid: 25536932
73. X. Sisquella *et al*., Malaria parasite DNA-harbouring vesicles activate cytosolic immune sensors. *Nat. Commun.* **8**, 1985 (2017). doi: 10.1038/s41467-017-02083-1; pmid: 29215015
74. Y. Kitai *et al*., DNA-containing exosomes derived from cancer cells treated with topotecan activate a STING-dependent pathway and reinforce antitumor immunity. *J. Immunol.* **198**, 1649–1659 (2017). doi: 10.4049/jimmunol.1601694; pmid: 28069806
75. D. Torralba *et al*., Priming of dendritic cells by DNA-containing extracellular vesicles from activated T cells through antigen-driven contacts. *Nat. Commun.* **9**, 2658 (2018). doi: 10.1038/s41467-018-05077-9; pmid: 29985392
76. A. Takahashi *et al*., Exosomes maintain cellular homeostasis by excreting harmful DNA from cells. *Nat. Commun.* **8**, 15287 (2017). doi: 10.1038/ncomms15287; pmid: 28508895
77. L. Montermini *et al*., Inhibition of oncogenic epidermal growth factor receptor kinase triggers release of exosome-like extracellular vesicles and impacts their phosphoprotein and DNA content. *J. Biol. Chem.* **290**, 24534–24546 (2015). doi: 10.1074/jbc.M115.679217; pmid: 26272609
78. S. Chennakrishnaiah *et al*., Leukocytes as a reservoir of circulating oncogenic DNA and regulatory targets of tumor-derived extracellular vesicles. *J. Thromb. Haemost.* **16**, 1800–1813 (2018). doi: 10.1111/jth.14222; pmid: 29971917
79. A. Montecalvo *et al*., Mechanism of transfer of functional microRNAs between mouse dendritic cells via exosomes. *Blood* **119**, 756–766 (2012). doi: 10.1182/blood-2011-02-338004; pmid: 22031862
80. G. Ding *et al*., Pancreatic cancer-derived exosomes transfer miRNAs to dendritic cells and inhibit RFXAP expression via miR-212-3p. *Oncotarget* **6**, 29877–29888 (2015). doi: 10.18632/oncotarget.4924; pmid: 26337469
81. X. Ying *et al*., Epithelial ovarian cancer-secreted exosomal miR-222-3p induces polarization of tumor-associated macrophages. *Oncotarget* **7**, 43076–43087 (2016). doi: 10.18632/oncotarget.9246; pmid: 27172798
82. G. Chen *et al*., Exosomal PD-L1 contributes to immunosuppression and is associated with anti-PD-1 response. *Nature* **560**, 382–386 (2018). doi: 10.1038/s41586-018-0392-8; pmid: 30089911
83. Y. Ning *et al*., Tumor exosomes block dendritic cells maturation to decrease the T cell immune response. *Immunol. Lett.* **199**, 36–43 (2018). doi: 10.1016/j.imlet.2018.05.002; pmid: 29800589
84. M. Poggio *et al*., Suppression of exosomal PD-L1 induces systemic anti-tumor immunity and memory. *Cell* **177**, 414–427. e13 (2019). doi: 10.1016/j.cell.2019.02.016; pmid: 30951669
85. G. Andreola *et al*., Induction of lymphocyte apoptosis by tumor cell secretion of FasL-bearing microvesicles. *J. Exp. Med.* **195**, 1303–1316 (2002). doi: 10.1084/jem.20011624; pmid: 12021310
86. A. J. Abusamra *et al*., Tumor exosomes expressing Fas ligand mediate CD8+ T-cell apoptosis. *Blood Cells Mol. Dis.* **35**, 169–173 (2005). doi: 10.1016/j.bcmd.2005.07.001; pmid: 16081306
87. A. Clayton, S. Al-Taei, J. Webber, M. D. Mason, Z. Tabi, Cancer exosomes express CD39 and CD73, which suppress T cells through adenosine production. *J. Immunol.* **187**, 676–683 (2011). doi: 10.4049/jimmunol.1003884; pmid: 21677139
88. D. Skokos *et al*., Mast cell-dependent B and T lymphocyte activation is mediated by the secretion of immunologically active exosomes. *J. Immunol.* **166**, 868–876 (2001). doi: 10.4049/jimmunol.166.2.868; pmid: 11145662
89. J. Wang, L. Wang, Z. Lin, L. Tao, M. Chen, More efficient induction of antitumor T cell immunity by exosomes from CD40L gene-modified lung tumor cells. *Mol. Med. Rep.* **9**, 125–131 (2014). doi: 10.3892/mmr.2013.1759; pmid: 24173626
90. M. Capello *et al*., Exosomes harbor B cell targets in pancreatic adenocarcinoma and exert decoy function against complement-mediated cytotoxicity. *Nat. Commun.* **10**, 254 (2019). doi: 10.1038/s41467-018-08109-6; pmid: 30651550
91. F. Chalmin *et al*., Membrane-associated Hsp72 from tumor-derived exosomes mediates STAT3-dependent immunosuppressive function of mouse and human myeloid-derived suppressor cells. *J. Clin. Invest.* **120**, 457–471 (2010). doi: 10.1172/JCI40483; pmid: 20093776
92. K. Gabrusiewicz *et al*., Glioblastoma stem cell-derived exosomes induce M2 macrophages and PD-L1 expression on human monocytes. *Oncoimmunology* **7**, e1412909 (2018). doi: 10.1080/2162402X.2017.1412909; pmid: 29632728
93. M. Fabbri *et al*., MicroRNAs bind to Toll-like receptors to induce prometastatic inflammatory response. *Proc. Natl. Acad. Sci. U.S.A.* **109**, E2110–E2116 (2012). doi: 10.1073/pnas.1209414109; pmid: 22753494
94. S. G. van der Grein, K. A. Y. Defourny, E. F. J. Slot, E. N. M. Nolte-'t Hoen, Intricate relationships between naked viruses and extracellular vesicles in the crosstalk between pathogen and host. *Semin. Immunopathol.* **40**, 491–504 (2018). doi: 10.1007/s00281-018-0678-9; pmid: 29789863
95. B. J. Crenshaw, L. Gu, B. Sims, Q. L. Matthews, Exosome biogenesis and biological function in response to viral infections. *Open Virol. J.* **12**, 134–148 (2018). doi: 10.2174/1874357901812010134; pmid: 30416610
96. Z. Feng *et al*., A pathogenic picornavirus acquires an envelope by hijacking cellular membranes. *Nature* **496**, 367–371 (2013). doi: 10.1038/nature12029; pmid: 23542590
97. S. Nagashima *et al*., Hepatitis E virus egress depends on the exosomal pathway, with secretory exosomes derived from multivesicular bodies. *J. Gen. Virol.* **95**, 2166–2175 (2014). doi: 10.1099/vir.0.066910-0; pmid: 24970738
98. S. J. Gould, A. M. Booth, J. E. Hildreth, The Trojan exosome hypothesis. *Proc. Natl. Acad. Sci. U.S.A.* **100**, 10592–10597 (2003). doi: 10.1073/pnas.1831413100; pmid: 12947040
99. N. Altan-Bonnet, Extracellular vesicles are the Trojan horses of viral infection. *Curr. Opin. Microbiol.* **32**, 77–81 (2016). doi: 10.1016/j.mib.2016.05.004; pmid: 27232382
100. V. Ramakrishnaiah *et al*., Exosome-mediated transmission of hepatitis C virus between human hepatoma Huh7.5 cells. *Proc. Natl. Acad. Sci. U.S.A.* **110**, 13109–13113 (2013). doi: 10.1073/pnas.1221899110; pmid: 23878230
101. B. Sims *et al*., Tetraspanin blockage reduces exosome-mediated HIV-1 entry. *Arch. Virol.* **163**, 1683–1689 (2018). doi: 10.1007/s00705-018-3737-6; pmid: 29429034
102. M. Lenassi *et al*., HIV Nef is secreted in exosomes and triggers apoptosis in bystander CD4+ T cells. *Traffic* **11**, 110–122 (2010). doi: 10.1111/j.1600-0854.2009.01006.x; pmid: 19912576
103. D. M. Pegtel *et al*., Functional delivery of viral miRNAs via exosomes. *Proc. Natl. Acad. Sci. U.S.A.* **107**, 6328–6333 (2010). doi: 10.1073/pnas.0914843107; pmid: 20304794
104. B. Sims *et al*., Role of TIM-4 in exosome-dependent entry of HIV-1 into human immune cells. *Int. J. Nanomedicine* **12**, 4823–4833 (2017). doi: 10.2147/IJN.S132762; pmid: 28740388
105. L. Gao *et al*., Tumor-derived exosomes antagonize innate antiviral immunity. *Nat. Immunol.* **19**, 233–245 (2018). doi: 10.1038/s41590-017-0043-5; pmid: 29358709
106. J. Li *et al*., Exosomes mediate the cell-to-cell transmission of IFN-α-induced antiviral activity. *Nat. Immunol.* **14**, 793–803 (2013). doi: 10.1038/ni.2647; pmid: 23832071
107. A. K. Khatua, H. E. Taylor, J. E. Hildreth, W. Popik, Exosomes packaging APOBEC3G confer human immunodeficiency virus resistance to recipient cells. *J. Virol.* **83**, 512–521 (2009). doi: 10.1128/JVI.01658-08; pmid: 18987139
108. J. V. de Carvalho *et al*., Nef neutralizes the ability of exosomes from CD4+ T cells to act as decoys during HIV-1 infection. *PLOS ONE* **9**, e113691 (2014). doi: 10.1371/journal.pone.0113691; pmid: 25423108
109. C. Guay, R. Regazzi, Exosomes as new players in metabolic organ cross-talk. *Diabetes Obes. Metab.* **19** (Suppl 1), 137–146 (2017). doi: 10.1111/dom.13027; pmid: 28880477
110. Z. B. Deng *et al*., Adipose tissue exosome-like vesicles mediate activation of macrophage-induced insulin resistance. *Diabetes* **58**, 2498–2505 (2009). doi: 10.2337/db09-0216; pmid: 19675137
111. C. Castaño, S. Kalko, A. Novials, M. Párrizas, Obesity-associated exosomal miRNAs modulate glucose and lipid metabolism in mice. *Proc. Natl. Acad. Sci. U.S.A.* **115**, 12158–12163 (2018). doi: 10.1073/pnas.1808855115; pmid: 30429322
112. S. V. Chitti, P. Fonseka, S. Mathivanan, Emerging role of extracellular vesicles in mediating cancer cachexia. *Biochem. Soc. Trans.* **46**, 1129–1136 (2018). doi: 10.1042/BST20180213; pmid: 30242118
113. G. Sagar *et al*., Pathogenesis of pancreatic cancer exosome-induced lipolysis in adipose tissue. *Gut* **65**, 1165–1174 (2016). doi: 10.1136/gutjnl-2014-308350; pmid: 26061593
114. N. Javeed *et al*., Pancreatic cancer-derived exosomes cause paraneoplastic β-cell dysfunction. *Clin. Cancer Res.* **21**, 1722–1733 (2015). doi: 10.1158/1078-0432.CCR-14-2022; pmid: 25355928
115. G. Zhang *et al*., Tumor induces muscle wasting in mice through releasing extracellular Hsp70 and Hsp90. *Nat. Commun.* **8**, 589 (2017). doi: 10.1038/s41467-017-00726-x; pmid: 28928431
116. Y. Zhang, Y. W. Hu, L. Zheng, Q. Wang, Characteristics and roles of exosomes in cardiovascular disease. *DNA Cell Biol.* **36**, 202–211 (2017). doi: 10.1089/dna.2016.3496; pmid: 28112546
117. S. Srikanthan, W. Li, R. L. Silverstein, T. M. McIntyre, Exosome poly-ubiquitin inhibits platelet activation, downregulates CD36 and inhibits pro-atherothombotic cellular functions. *J. Thromb. Haemost.* **12**, 1906–1917 (2014). doi: 10.1111/jth.12712; pmid: 25163645
118. A. N. Kapustin *et al*., Prothrombin loading of vascular smooth muscle cell-derived exosomes regulates coagulation and calcification. *Arterioscler. Thromb. Vasc. Biol.* **37**, e22–e32 (2017). doi: 10.1161/ATVBAHA.116.308886; pmid: 28104608
119. Y. Yuan *et al*., Stem cell-derived exosome in cardiovascular diseases: Macro roles of micro particles. *Front. Pharmacol.* **9**, 547 (2018). doi: 10.3389/fphar.2018.00547; pmid: 29904347
120. J. Xiao *et al*., Cardiac progenitor cell-derived exosomes prevent cardiomyocytes apoptosis through exosomal miR-21 by targeting PDCD4. *Cell Death Dis.* **7**, e2277 (2016). doi: 10.1038/cddis.2016.181; pmid: 27336721
121. Y. Feng, W. Huang, M. Wani, X. Yu, M. Ashraf, Ischemic preconditioning potentiates the protective effect of stem cells through secretion of exosomes by targeting Mecp2 via miR-22. *PLOS ONE* **9**, e88685 (2014). doi: 10.1371/journal.pone.0088685; pmid: 24558412
122. J. Mayourian *et al*., Exosomal microRNA-21-5p mediates mesenchymal stem cell paracrine effects on human cardiac tissue contractility. *Circ. Res.* **122**, 933–944 (2018). doi: 10.1161/CIRCRESAHA.118.312420; pmid: 29449318
123. V. Budnik, C. Ruiz-Cañada, F. Wendler, Extracellular vesicles round off communication in the nervous system. *Nat. Rev. Neurosci.* **17**, 160–172 (2016). doi: 10.1038/nrn.2015.29; pmid: 26891626
124. C. Quek, A. F. Hill, The role of extracellular vesicles in neurodegenerative diseases. *Biochem. Biophys. Res. Commun.* **483**, 1178–1186 (2017). doi: 10.1016/j.bbrc.2016.09.090; pmid: 27659705
125. L. Yuan, J. Y. Li, Exosomes in Parkinson's disease: Current perspectives and future challenges. *ACS Chem. Neurosci.* **10**, 964–972 (2019). doi: 10.1021/acschemneuro.8b00469; pmid: 30664350
126. J. Howitt, A. F. Hill, Exosomes in the pathology of neurodegenerative diseases. *J. Biol. Chem.* **291**, 26589–26597 (2016). doi: 10.1074/jbc.R116.757955; pmid: 27852825
127. F. N. Soria *et al*., Exosomes, an unmasked culprit in neurodegenerative diseases. *Front. Neurosci.* **11**, 26 (2017). doi: 10.3389/fnins.2017.00026; pmid: 28197068
128. E. Levy, Exosomes in the diseased brain: First insights from *in vivo* studies. *Front. Neurosci.* **11**, 142 (2017). doi: 10.3389/fnins.2017.00142; pmid: 28386213
129. B. B. Guo, S. A. Bellingham, A. F. Hill, Stimulating the release of exosomes increases the intercellular transfer of prions. *J. Biol. Chem.* **291**, 5128–5137 (2016). doi: 10.1074/jbc.M115.684258; pmid: 26769968
130. H. Asai *et al*., Depletion of microglia and inhibition of exosome synthesis halt tau propagation. *Nat. Neurosci.* **18**, 1584–1593 (2015). doi: 10.1038/nn.4132; pmid: 26436904
131. S. Baker, J. C. Polanco, J. Götz, Extracellular vesicles containing P301L mutant tau accelerate pathological tau phosphorylation and oligomer formation but do not seed

mature neurofibrillary tangles in ALZ17 mice. *J. Alzheimers Dis.* **54**, 1207–1217 (2016). doi: 10.3233/JAD-160371; pmid: 27567840

132. L. Rajendran *et al*., Alzheimer's disease beta-amyloid peptides are released in association with exosomes. *Proc. Natl. Acad. Sci. U.S.A.* **103**, 11172–11177 (2006). doi: 10.1073/pnas.0603838103; pmid: 16837572
133. C. Falker *et al*., Exosomal cellular prion protein drives fibrillization of amyloid beta and counteracts amyloid beta-mediated neurotoxicity. *J. Neurochem.* **137**, 88–100 (2016). doi: 10.1111/jnc.13514; pmid: 26710111
134. K. Yuyama *et al*., A potential function for neuronal exosomes: Sequestering intracerebral amyloid-β peptide. *FEBS Lett.* **589**, 84–88 (2015). doi: 10.1016/j.febslet.2014.11.027; pmid: 25436414
135. J. Pacheco-Quinto *et al*., Intracellular metalloprotease activity controls intraneuronal Abeta aggregation and limits secretion of Abeta via exosomes. *FASEB J.* **33**, 3758–3771 (2019). doi: 10.1096/fj.201801319R; pmid: 30481490
136. A. Stuendl *et al*., Induction of α-synuclein aggregate formation by CSF exosomes from patients with Parkinson's disease and dementia with Lewy bodies. *Brain* **139**, 481–494 (2016). doi: 10.1093/brain/awv346; pmid: 26647156
137. B. Spencer *et al*., α-Synuclein interferes with the ESCRT-III complex contributing to the pathogenesis of Lewy body disease. *Hum. Mol. Genet.* **25**, 1100–1115 (2016). doi: 10.1093/hmg/ddv633; pmid: 26740557
138. M. Basso *et al*., Mutant copper-zinc superoxide dismutase (SOD1) induces protein secretion pathway alterations and exosome release in astrocytes: Implications for disease spreading and motor neuron pathology in amyotrophic lateral sclerosis. *J. Biol. Chem.* **288**, 15699–15711 (2013). doi: 10.1074/jbc.M112.425066; pmid: 23592792
139. L. I. Grad *et al*., Intercellular propagated misfolding of wild-type Cu/Zn superoxide dismutase occurs via exosome-dependent and -independent mechanisms. *Proc. Natl. Acad. Sci. U.S.A.* **111**, 3620–3625 (2014). doi: 10.1073/pnas.1312245111; pmid: 24550511
140. Y. Iguchi *et al*., Exosome secretion is a key pathway for clearance of pathological TDP-43. *Brain* **139**, 3187–3201 (2016). doi: 10.1093/brain/aww237; pmid: 27679482
141. I. Tsilioni, T. C. Theoharides, Extracellular vesicles are increased in the serum of children with autism spectrum disorder, contain mitochondrial DNA, and stimulate human microglia to secrete IL-1β. *J. Neuroinflammation* **15**, 239 (2018). doi: 10.1186/s12974-018-1275-5; pmid: 30149804
142. L. Alvarez-Erviti *et al*., Delivery of siRNA to the mouse brain by systemic injection of targeted exosomes. *Nat. Biotechnol.* **29**, 341–345 (2011). doi: 10.1038/nbt.1807; pmid: 21423189
143. J. M. Cooper *et al*., Systemic exosomal siRNA delivery reduced alpha-synuclein aggregates in brains of transgenic mice. *Mov. Disord.* **29**, 1476–1485 (2014). doi: 10.1002/mds.25978; pmid: 25112864
144. J. Skog *et al*., Glioblastoma microvesicles transport RNA and proteins that promote tumour growth and provide diagnostic biomarkers. *Nat. Cell Biol.* **10**, 1470–1476 (2008). doi: 10.1038/ncb1800; pmid: 19011622
145. C. Rajagopal, K. B. Harikumar, The origin and functions of exosomes in cancer. *Front. Oncol.* **8**, 66 (2018). doi: 10.3389/fonc.2018.00066; pmid: 29616188
146. D. Hanahan, R. A. Weinberg, Hallmarks of cancer: The next generation. *Cell* **144**, 646–674 (2011). doi: 10.1016/j.cell.2011.02.013; pmid: 21376230
147. K. Stefanius *et al*., Human pancreatic cancer cell exosomes, but not human normal cell exosomes, act as an initiator in cell transformation. *eLife* **8**, e40226 (2019). doi: 10.7554/eLife.40226; pmid: 31134894
148. S. A. Melo *et al*., Cancer exosomes perform cell-independent microRNA biogenesis and promote tumorigenesis. *Cancer Cell* **26**, 707–721 (2014). doi: 10.1016/j.ccell.2014.09.005; pmid: 25446899
149. Z. Y. Abd Elmageed *et al*., Neoplastic reprogramming of patient-derived adipose stem cells by prostate cancer cell-associated exosomes. *Stem Cells* **32**, 983–997 (2014). doi: 10.1002/stem.1619; pmid: 24715691
150. M. T. Le *et al*., miR-200-containing extracellular vesicles promote breast cancer cell metastasis. *J. Clin. Invest.* **124**, 5109–5128 (2014). doi: 10.1172/JCI75695; pmid: 25401471
151. M. Y. Fong *et al*., Breast-cancer-secreted miR-122 reprograms glucose metabolism in premetastatic niche to promote metastasis. *Nat. Cell Biol.* **17**, 183–194 (2015). doi: 10.1038/ncb3094; pmid: 25621950
152. B. Y. Nabet *et al*., Exosome RNA unshielding couples stromal activation to pattern recognition receptor signaling in cancer. *Cell* **170**, 352–366.e13 (2017). doi: 10.1016/j.cell.2017.06.031; pmid: 28709002
153. J. Webber, R. Steadman, M. D. Mason, Z. Tabi, A. Clayton, Cancer exosomes trigger fibroblast to myofibroblast differentiation. *Cancer Res.* **70**, 9621–9630 (2010). doi: 10.1158/0008-5472.CAN-10-1722; pmid: 21098712
154. H. Peinado *et al*., Melanoma exosomes educate bone marrow progenitor cells toward a pro-metastatic phenotype through MET. *Nat. Med.* **18**, 883–891 (2012). doi: 10.1038/nm.2753; pmid: 22635005
155. B. Costa-Silva *et al*., Pancreatic cancer exosomes initiate pre-metastatic niche formation in the liver. *Nat. Cell Biol.* **17**, 816–826 (2015). doi: 10.1038/ncb3169; pmid: 25985394
156. M. P. Plebanek *et al*., Pre-metastatic cancer exosomes induce immune surveillance by patrolling monocytes at the metastatic niche. *Nat. Commun.* **8**, 1319 (2017). doi: 10.1038/s41467-017-01433-3; pmid: 29105655
157. A. Hoshino *et al*., Tumour exosome integrins determine organotropic metastasis. *Nature* **527**, 329–335 (2015). doi: 10.1038/nature15756; pmid: 26524530
158. H. Zhang *et al*., Exosome-delivered EGFR regulates liver microenvironment to promote gastric cancer liver metastasis. *Nat. Commun.* **8**, 15016 (2017). doi: 10.1038/ncomms15016; pmid: 28393839
159. P. Sansone *et al*., Packaging and transfer of mitochondrial DNA via exosomes regulate escape from dormancy in hormonal therapy-resistant breast cancer. *Proc. Natl. Acad. Sci. U.S.A.* **114**, E9066–E9075 (2017). doi: 10.1073/pnas.1704862114; pmid: 29073103
160. L. Zhang *et al*., Microenvironment-induced PTEN loss by exosomal microRNA primes brain metastasis outgrowth. *Nature* **527**, 100–104 (2015). doi: 10.1038/nature15376; pmid: 26479035
161. V. Luga *et al*., Exosomes mediate stromal mobilization of autocrine Wnt-PCP signaling in breast cancer cell migration. *Cell* **151**, 1542–1556 (2012). doi: 10.1016/j.cell.2012.11.024; pmid: 23260141
162. K. C. Vallabhaneni *et al*., Extracellular vesicles from bone marrow mesenchymal stem/stromal cells transport tumor regulatory microRNA, proteins, and metabolites. *Oncotarget* **6**, 4953–4967 (2015). doi: 10.18632/oncotarget.3211; pmid: 25669974
163. H. Zhao *et al*., Tumor microenvironment derived exosomes pleiotropically modulate cancer cell metabolism. *eLife* **5**, e10250 (2016). doi: 10.7554/eLife.10250; pmid: 26920219
164. K. G. Ronquist, B. Ek, A. Stavreus-Evers, A. Larsson, G. Ronquist, Human prostasomes express glycolytic enzymes with capacity for ATP production. *Am. J. Physiol. Endocrinol. Metab.* **304**, E576–E582 (2013). doi: 10.1152/ajpendo.00511.2012; pmid: 23341497
165. W. Zhou *et al*., Cancer-secreted miR-105 destroys vascular endothelial barriers to promote metastasis. *Cancer Cell* **25**, 501–515 (2014). doi: 10.1016/j.ccr.2014.03.007; pmid: 24735924
166. P. Kucharzewska *et al*., Exosomes reflect the hypoxic status of glioma cells and mediate hypoxia-dependent activation of vascular cells during tumor development. *Proc. Natl. Acad. Sci. U.S.A.* **110**, 7312–7317 (2013). doi: 10.1073/pnas.1220998110; pmid: 23589885
167. K. R. Genschmer *et al*., Activated PMN exosomes: Pathogenic entities causing matrix destruction and disease in the lung. *Cell* **176**, 113–126.e15 (2019). doi: 10.1016/j.cell.2018.12.002; pmid: 30633902
168. A. Yokoi *et al*., Malignant extracellular vesicles carrying MMP1 mRNA facilitate peritoneal dissemination in ovarian cancer. *Nat. Commun.* **8**, 14470 (2017). doi: 10.1038/ncomms14470; pmid: 28262727
169. T. Aung *et al*., Exosomal evasion of humoral immunotherapy in aggressive B-cell lymphoma modulated by ATP-binding cassette transporter A3. *Proc. Natl. Acad. Sci. U.S.A.* **108**, 15336–15341 (2011). doi: 10.1073/pnas.1102855108; pmid: 21873242
170. V. Ciravolo *et al*., Potential role of HER2-overexpressing exosomes in countering trastuzumab-based therapy. *J. Cell. Physiol.* **227**, 658–667 (2012). doi: 10.1002/jcp.22773; pmid: 21465472
171. Y. Hu *et al*., Fibroblast-derived exosomes contribute to chemoresistance through priming cancer stem cells in colorectal cancer. *PLOS ONE* **10**, e0125625 (2015). doi: 10.1371/journal.pone.0125625; pmid: 25938772
172. W. X. Chen *et al*., Exosomes from drug-resistant breast cancer cells transmit chemoresistance by a horizontal transfer of microRNAs. *PLOS ONE* **9**, e95240 (2014). doi: 10.1371/journal.pone.0095240; pmid: 24740415
173. L. Qu *et al*., Exosome-transmitted lncARSR promotes sunitinib resistance in renal cancer by acting as a competing endogenous RNA. *Cancer Cell* **29**, 653–668 (2016). doi: 10.1016/j.ccell.2016.03.004; pmid: 27117758
174. M. C. Boelens *et al*., Exosome transfer from stromal to breast cancer cells regulates therapy resistance pathways. *Cell* **159**, 499–513 (2014). doi: 10.1016/j.cell.2014.09.051; pmid: 25417103
175. C. L. Au Yeung *et al*., Exosomal transfer of stroma-derived miR21 confers paclitaxel resistance in ovarian cancer cells through targeting APAF1. *Nat. Commun.* **7**, 11150 (2016). doi: 10.1038/ncomms11150; pmid: 27021436
176. Y. Binenbaum *et al*., Transfer of miRNA in macrophage-derived exosomes induces drug resistance in pancreatic adenocarcinoma. *Cancer Res.* **78**, 5287–5299 (2018). doi: 10.1158/0008-5472.CAN-18-0124; pmid: 30042153
177. D. Cesselli *et al*., Extracellular vesicles: How drug and pathology interfere with their biogenesis and function. *Front. Physiol.* **9**, 1394 (2018). doi: 10.3389/fphys.2018.01394; pmid: 30327618
178. M. Song *et al*., Bystander autophagy mediated by radiation-induced exosomal miR-7-5p in non-targeted human bronchial epithelial cells. *Sci. Rep.* **6**, 30165 (2016). doi: 10.1038/srep30165; pmid: 27417393
179. F. Jansen, Q. Li, Exosomes as diagnostic biomarkers in cardiovascular diseases. *Adv. Exp. Med. Biol.* **998**, 61–70 (2017). doi: 10.1007/978-981-10-4397-0_4; pmid: 28936732
180. K. M. Kanninen, N. Bister, J. Koistinaho, T. Malm, Exosomes as new diagnostic tools in CNS diseases. *Biochim. Biophys. Acta* **1862**, 403–410 (2016). doi: 10.1016/j.bbadis.2015.09.020; pmid: 26432482
181. C. A. Fitts, N. Ji, Y. Li, C. Tan, Exploiting exosomes in cancer liquid biopsies and drug delivery. *Adv. Healthc. Mater.* **8**, e1801268 (2019). doi: 10.1002/adhm.201801268; pmid: 30663276
182. A. I. Masyuk, T. V. Masyuk, N. F. Larusso, Exosomes in the pathogenesis, diagnostics and therapeutics of liver diseases. *J. Hepatol.* **59**, 621–625 (2013). doi: 10.1016/j.jhep.2013.03.028; pmid: 23557871
183. W. Zhang *et al*., Extracellular vesicles in diagnosis and therapy of kidney diseases. *Am. J. Physiol. Renal Physiol.* **311**, F844–F851 (2016). doi: 10.1152/ajprenal.00429.2016; pmid: 27582107
184. S. D. Alipoor *et al*., Exosomes and exosomal miRNA in respiratory diseases. *Mediators Inflamm.* **2016**, 5628404 (2016). doi: 10.1155/2016/5628404; pmid: 27738390
185. J. Cai *et al*., Extracellular vesicle-mediated transfer of donor genomic DNA to recipient cells is a novel mechanism for genetic influence between cells. *J. Mol. Cell Biol.* **5**, 227–238 (2013). doi: 10.1093/jmcb/mjt011; pmid: 23580760
186. C. Kahlert *et al*., Identification of double-stranded genomic DNA spanning all chromosomes with mutated KRAS and p53 DNA in the serum exosomes of patients with pancreatic cancer. *J. Biol. Chem.* **289**, 3869–3875 (2014). doi: 10.1074/jbc.C113.532267; pmid: 24398677
187. R. Kalluri, V. S. LeBleu, Discovery of double-stranded genomic DNA in circulating exosomes. *Cold Spring Harb. Symp. Quant. Biol.* **81**, 275–280 (2016). doi: 10.1101/sqb.2016.81.030932; pmid: 28424339
188. B. K. Thakur *et al*., Double-stranded DNA in exosomes: A novel biomarker in cancer detection. *Cell Res.* **24**, 766–769 (2014). doi: 10.1038/cr.2014.44; pmid: 24710597
189. K. Allenson *et al*., High prevalence of mutant KRAS in circulating exosome-derived DNA from early-stage pancreatic cancer patients. *Ann. Oncol.* **28**, 741–747 (2017). doi: 10.1093/annonc/mdx004; pmid: 28104621
190. V. Bernard *et al*., Circulating nucleic acids are associated with outcomes of patients with pancreatic cancer. *Gastroenterology* **156**, 108–118.e4 (2019). doi: 10.1053/j.gastro.2018.09.022; pmid: 30240661
191. M. R. Fernando, C. Jiang, G. D. Krzyzanowski, W. L. Ryan, New evidence that a large proportion of human blood plasma cell-free DNA is localized in exosomes. *PLOS ONE* **12**, e0183915 (2017). doi: 10.1371/journal.pone.0183915; pmid: 28850588
192. S. Yang *et al*., Detection of mutant KRAS and TP53 DNA in circulating exosomes from healthy individuals and patients with pancreatic cancer. *Cancer Biol. Ther.* **18**, 158–165 (2017). doi: 10.1080/15384047.2017.1281499; pmid: 28121262
193. M. Salehi, M. Sharifi, Exosomal miRNAs as novel cancer biomarkers: Challenges and opportunities. *J. Cell. Physiol.* **233**, 6370–6380 (2018). doi: 10.1002/jcp.26481; pmid: 29323722

194. D. J. Cha *et al*., KRAS-dependent sorting of miRNA to exosomes. *eLife* **4**, e07197 (2015). doi: 10.7554/eLife.07197; pmid: 26132860
195. A. Thind, C. Wilson, Exosomal miRNAs as cancer biomarkers and therapeutic targets. *J. Extracell. Vesicles* **5**, 31292 (2016). doi: 10.3402/jev.v5.31292; pmid: 27440105
196. D. Bhagirath *et al*., microRNA-1246 is an exosomal biomarker for aggressive prostate cancer. *Cancer Res.* **78**, 1833–1844 (2018). doi: 10.1158/0008-5472.CAN-17-2069; pmid: 29437039
197. X. J. Li, Z. J. Ren, J. H. Tang, Q. Yu, R. N. A. Exosomal Micro, Exosomal microRNA MiR-1246 promotes cell proliferation, invasion and drug resistance by targeting CCNG2 in breast cancer. *Cell. Physiol. Biochem.* **44**, 1741–1748 (2017). doi: 10.1159/000485780; pmid: 29216623
198. L. Pigati *et al*., Selective release of microRNA species from normal and malignant mammary epithelial cells. *PLOS ONE* **5**, e13515 (2010). doi: 10.1371/journal.pone.0013515; pmid: 20976003
199. S. Sakha, T. Muramatsu, K. Ueda, J. Inazawa, Exosomal microRNA miR-1246 induces cell motility and invasion through the regulation of DENND2D in oral squamous cell carcinoma. *Sci. Rep.* **6**, 38750 (2016). doi: 10.1038/srep38750; pmid: 27929118
200. A. H. Alhasan *et al*., Circulating microRNA signature for the diagnosis of very high-risk prostate cancer. *Proc. Natl. Acad. Sci. U.S.A.* **113**, 10655–10660 (2016). doi: 10.1073/pnas.1611596113; pmid: 27601638
201. S. Ebrahimkhani *et al*., Deep sequencing of circulating exosomal microRNA allows non-invasive glioblastoma diagnosis. *NPJ Precis Oncol* **2**, 28 (2018). doi: 10.1038/s41698-018-0071-0; pmid: 30564636
202. S. Halvaei *et al*., Exosomes in Cancer Liquid Biopsy: A Focus on Breast Cancer. *Mol. Ther. Nucleic Acids* **10**, 131–141 (2018). doi: 10.1016/j.omtn.2017.11.014; pmid: 29499928
203. I. Stevic *et al*., Specific microRNA signatures in exosomes of triple-negative and HER2-positive breast cancer patients undergoing neoadjuvant therapy within the GeparSixto trial. *BMC Med.* **16**, 179 (2018). doi: 10.1186/s12916-018-1163-y; pmid: 30301470
204. X. Zhou *et al*., Diagnostic value of a plasma microRNA signature in gastric cancer: A microRNA expression analysis. *Sci. Rep.* **5**, 11251 (2015). doi: 10.1038/srep11251; pmid: 26059512
205. I. H. Chen *et al*., Phosphoproteins in extracellular vesicles as candidate markers for breast cancer. *Proc. Natl. Acad. Sci. U.S.A.* **114**, 3175–3180 (2017). doi: 10.1073/pnas.1618088114; pmid: 28270605
206. J. Castillo *et al*., Surfaceome profiling enables isolation of cancer-specific exosomal cargo in liquid biopsies from pancreatic cancer patients. *Ann. Oncol.* **29**, 223–229 (2018). doi: 10.1093/annonc/mdx542; pmid: 29045505
207. H. Etayash, A. R. McGee, K. Kaur, T. Thundat, Nanomechanical sandwich assay for multiple cancer biomarkers in breast cancer cell-derived exosomes. *Nanoscale* **8**, 15137–15141 (2016). doi: 10.1039/C6NR03478K; pmid: 27492928
208. A. E. Frampton *et al*., Glypican-1 is enriched in circulating-exosomes in pancreatic cancer and correlates with tumor burden. *Oncotarget* **9**, 19006–19013 (2018). doi: 10.18632/oncotarget.24873; pmid: 29721179
209. J. Hu *et al*., A signal-amplifiable biochip quantifies extracellular vesicle-associated RNAs for early cancer detection. *Nat. Commun.* **8**, 1683 (2017). doi: 10.1038/s41467-017-01942-1; pmid: 29162835
210. X. Lai *et al*., A microRNA signature in circulating exosomes is superior to exosomal glypican-1 levels for diagnosing pancreatic cancer. *Cancer Lett.* **393**, 86–93 (2017). doi: 10.1016/j.canlet.2017.02.019; pmid: 28232049
211. J. M. Lewis *et al*., Integrated analysis of exosomal protein biomarkers on alternating current electrokinetic chips enables rapid detection of pancreatic cancer in patient blood. *ACS Nano* **12**, 3311–3320 (2018). doi: 10.1021/acsnano.7b08199; pmid: 29570265
212. J. Li *et al*., GPC1 exosome and its regulatory miRNAs are specific markers for the detection and target therapy of colorectal cancer. *J. Cell. Mol. Med.* **21**, 838–847 (2017). doi: 10.1111/jcmm.12941; pmid: 28233416
213. J. Li *et al*., The clinical significance of circulating GPC1 positive exosomes and its regulative miRNAs in colon cancer patients. *Oncotarget* **8**, 101189–101202 (2017). doi: 10.18632/oncotarget.20516; pmid: 29254156
214. S. A. Melo *et al*., Glypican-1 identifies cancer exosomes and detects early pancreatic cancer. *Nature* **523**, 177–182 (2015). doi: 10.1038/nature14581; pmid: 26106858
215. J. Y. Qian, Y. L. Tan, Y. Zhang, Y. F. Yang, X. Q. Li, Prognostic value of glypican-1 for patients with advanced pancreatic cancer following regional intra-arterial chemotherapy. *Oncol. Lett.* **16**, 1253–1258 (2018). doi: 10.3892/ol.2018.8701; pmid: 29963198
216. K. S. Yang *et al*., Multiparametric plasma EV profiling facilitates diagnosis of pancreatic malignancy. *Sci. Transl. Med.* **9**, eaal3226 (2017). doi: 10.1126/scitranslmed.aal3226; pmid: 28539469
217. Y. Yoshioka *et al*., Ultra-sensitive liquid biopsy of circulating extracellular vesicles using ExoScreen. *Nat. Commun.* **5**, 3591 (2014). doi: 10.1038/ncomms4591; pmid: 24710016
218. R. Sharma, X. Huang, R. A. Brekken, A. J. Schroit, Detection of phosphatidylserine-positive exosomes for the diagnosis of early-stage malignancies. *Br. J. Cancer* **117**, 545–552 (2017). doi: 10.1038/bjc.2017.183; pmid: 28641308
219. L. Barile, G. Vassalli, Exosomes: Therapy delivery tools and biomarkers of diseases. *Pharmacol. Ther.* **174**, 63–78 (2017). doi: 10.1016/j.pharmthera.2017.02.020; pmid: 28202367
220. S. W. Ferguson, J. Nguyen, Exosomes as therapeutics: The implications of molecular composition and exosomal heterogeneity. *J. Control. Release* **228**, 179–190 (2016). doi: 10.1016/j.jconrel.2016.02.037; pmid: 26941033
221. W. Liao *et al*., Exosomes: The next generation of endogenous nanomaterials for advanced drug delivery and therapy. *Acta Biomater.* (2018). pmid: 30597259
222. R. W. Yeo *et al*., Mesenchymal stem cell: An efficient mass producer of exosomes for drug delivery. *Adv. Drug Deliv. Rev.* **65**, 336–341 (2013). doi: 10.1016/j.addr.2012.07.001; pmid: 22780955
223. L. Kordelas *et al*., MSC-derived exosomes: A novel tool to treat therapy-refractory graft-versus-host disease. *Leukemia* **28**, 970–973 (2014). doi: 10.1038/leu.2014.41; pmid: 24445866
224. Y. Tian *et al*., A doxorubicin delivery platform using engineered natural membrane vesicle exosomes for targeted tumor therapy. *Biomaterials* **35**, 2383–2390 (2014). doi: 10.1016/j.biomaterials.2013.11.083; pmid: 24345736
225. M. S. Kim *et al*., Development of exosome-encapsulated paclitaxel to overcome MDR in cancer cells. *Nanomedicine (Lond.)* **12**, 655–664 (2016). doi: 10.1016/j.nano.2015.10.012; pmid: 26586551
226. L. Cheng, R. A. Sharples, B. J. Scicluna, A. F. Hill, Exosomes provide a protective and enriched source of miRNA for biomarker profiling compared to intracellular and cell-free blood. *J. Extracell. Vesicles* **3**, 23743 (2014). doi: 10.3402/jev.v3.23743; pmid: 24683445
227. S. Ohno *et al*., Systemically injected exosomes targeted to EGFR deliver antitumor microRNA to breast cancer cells. *Mol. Ther.* **21**, 185–191 (2013). doi: 10.1038/mt.2012.180; pmid: 23032975
228. M. Katakowski *et al*., Exosomes from marrow stromal cells expressing miR-146b inhibit glioma growth. *Cancer Lett.* **335**, 201–204 (2013). doi: 10.1016/j.canlet.2013.02.019; pmid: 23419525
229. N. Perets, S. Hertz, M. London, D. Offen, Intranasal administration of exosomes derived from mesenchymal stem cells ameliorates autistic-like behaviors of BTBR mice. *Mol. Autism* **9**, 57 (2018). doi: 10.1186/s13229-018-0240-6; pmid: 30479733
230. A. M. Williams *et al*., Mesenchymal stem cell-derived exosomes provide neuroprotection and improve long-term neurologic outcomes in a swine model of traumatic brain injury and hemorrhagic shock. *J. Neurotrauma* **36**, 54–60 (2019). doi: 10.1089/neu.2018.5711; pmid: 29690826
231. D. Yuan *et al*., Macrophage exosomes as natural nanocarriers for protein delivery to inflamed brain. *Biomaterials* **142**, 1–12 (2017). doi: 10.1016/j.biomaterials.2017.07.011; pmid: 28715655
232. M. J. Haney *et al*., Exosomes as drug delivery vehicles for Parkinson's disease therapy. *J. Control. Release* **207**, 18–30 (2015). doi: 10.1016/j.jconrel.2015.03.033; pmid: 25836593
233. M. Qu *et al*., Dopamine-loaded blood exosomes targeted to brain for better treatment of Parkinson's disease. *J. Control. Release* **287**, 156–166 (2018). doi: 10.1016/j.jconrel.2018.08.035; pmid: 30165139
234. B. Besse *et al*., Dendritic cell-derived exosomes as maintenance immunotherapy after first line chemotherapy in NSCLC. *OncoImmunology* **5**, e1071008 (2015). doi: 10.1080/2162402X.2015.1071008; pmid: 27141373
235. Y. Liu *et al*., Tumor exosomal RNAs promote lung pre-metastatic niche formation by activating alveolar epithelial TLR3 to recruit neutrophils. *Cancer Cell* **30**, 243–256 (2016). doi: 10.1016/j.ccell.2016.06.021; pmid: 27505671
236. G. Mao *et al*., Exosomes derived from miR-92a-3p-overexpressing human mesenchymal stem cells enhance chondrogenesis and suppress cartilage degradation via targeting WNT5A. *Stem Cell Res. Ther.* **9**, 247 (2018). doi: 10.1186/s13287-018-1004-0; pmid: 30257711
237. K. B. Beer, A. M. Wehman, Mechanisms and functions of extracellular vesicle release in vivo: What we can learn from flies and worms. *Cell Adhes. Migr.* **11**, 135–150 (2017). doi: 10.1080/19336918.2016.1236899; pmid: 27689411
238. M. Danilchik, T. Tumarkin, Exosomal trafficking in *Xenopus* development. *Genesis* **55**, e23011 (2017). doi: 10.1002/dvg.23011; pmid: 28095652
239. F. J. Verweij *et al*., Live tracking of inter-organ communication by endogenous exosomes in vivo. *Dev. Cell* **48**, 573–589.e4 (2019). doi: 10.1016/j.devcel.2019.01.004; pmid: 30745143
240. I. Budin, A. Debnath, J. W. Szostak, Concentration-driven growth of model protocell membranes. *J. Am. Chem. Soc.* **134**, 20812–20819 (2012). doi: 10.1021/ja310382d; pmid: 23198690
241. G. F. Joyce, J. W. Szostak, Protocells and RNA self-replication. *Cold Spring Harb. Perspect. Biol.* **10**, a034801 (2018). doi: 10.1101/cshperspect.a034801; pmid: 30181195
242. E. Nolte-'t Hoen, T. Cremer, R. C. Gallo, L. B. Margolis, Extracellular vesicles and viruses: Are they close relatives? *Proc. Natl. Acad. Sci. U.S.A.* **113**, 9155–9161 (2016). doi: 10.1073/pnas.1605146113; pmid: 27432966

ACKNOWLEDGMENTS

The authors apologize to the investigators and research laboratories whose original studies were not cited because of space limitations. **Funding:** The authors acknowledge support by research funds from MD Anderson Cancer Center. The exosome-related research in the Kalluri laboratory is funded by NCI RO1 CA213233, NCI RO1 CA195733, and NCI CA 231465. **Competing interests:** MD Anderson Cancer Center and R.K. hold patents in the area of exosome biology and are licensed to Codiak Biosciences, Inc. MD Anderson Cancer Center and R.K. are stock equity holders in Codiak Biosciences, Inc. R.K. is a consultant and scientific adviser for Codiak Biosciences, Inc. V.S.L. is a paid consultant for Codiak Biosciences, Inc.

10.1126/science.aau6977

RESEARCH ARTICLE SUMMARY

PLANT SCIENCE

Enhanced sustainable green revolution yield via nitrogen-responsive chromatin modulation in rice

Kun Wu*, Shuansuo Wang*, Wenzhen Song, Jianqing Zhang, Yun Wang, Qian Liu, Jianping Yu, Yafeng Ye, Shan Li, Jianfeng Chen, Ying Zhao, Jing Wang, Xiaokang Wu, Meiyue Wang, Yijing Zhang, Binmei Liu, Yuejin Wu, Nicholas P. Harberd†, Xiangdong Fu†

INTRODUCTION: The green revolution of the 1960s boosted cereal crop yields in part through widespread adoption of semi-dwarf plant varieties. The beneficial semi-dwarfism is respectively conferred in wheat and rice green revolution varieties by mutant *Reduced height-1* (*Rht-1*) and *semi-dwarf1* (*sd1*) alleles. These alleles cause accumulation of growth-repressing DELLA proteins, the normal forms of which are characterized by the presence of an Asp-Glu-Leu-Leu-Ala amino acid motif. Resultant semi-dwarf plants resisted lodging but required high nitrogen fertilizer inputs to maximize yield. Normally, gibberellin promotes growth by stimulating DELLA degradation as regulated by the gibberellin receptor GID1 (GIBBERELLIN INSENSITIVE DWARF1), the F-box protein GID2 (GIBBERELLIN INSENSITIVE DWARF2), and the SCF (Skp, Cullin, F-box–containing) ubiquitin ligase complex. Nitrogen fertilization–induced increase in grain yield is determined by the integration of three components (tiller number, grain number, and grain weight), but exogenous application of gibberellin reduces tiller number in rice. Here, we asked how nitrogen fertilization affects the gibberellin signaling that regulates rice tillering. Nitrogen fertilization promotes crop yield, but overuse in agriculture degrades the environment. A future of sustainable agriculture demands improved nitrogen use efficiency.

RATIONALE: Increased tillering, nitrogen fertilization, and high-density planting all contribute to the high yield typical of green revolution rice varieties. Increases in tiller number despite reduced nitrogen fertilization could help to sustain yield while reducing the environmental impact of agriculture. To investigate the effect of gibberellin on nitrogen-promoted rice tillering, we used genetic screening to identify a mutation in the *ngr5* (*nitrogen-mediated tiller growth response 5*) gene. Plants carrying the *ngr5* mutant displayed fewer tillers; tiller number was insensitive to nitrogen supply. Further genetic and biochemical studies defined the mechanisms underlying the interaction between nitrogen- and gibberellin-mediated effects on tiller number.

RESULTS: We found that increased nitrogen supply enhanced transcription and abundance of the rice APETALA2-domain transcription factor encoded by an *NGR5* (*NITROGEN-MEDIATED TILLER GROWTH RESPONSE 5*) allele. NGR5 interacts with a component of the polycomb repressive complex 2 (PRC2) and alters the genome-wide histone H3 lysine 27 trimethylation (H3K27me3) pattern response to changes in nitrogen availability. The extent of this alteration was reduced in *ngr5* plants or by gibberellin treatment. RNA sequencing and chromatin immunoprecipitation (ChIP)–polymerase chain reaction analysis showed that an increase in nitrogen supply reduced the abundance of mRNAs specified by strigolactone signaling and other branching-inhibitory genes [such as *Dwarf14* (*D14*) and *squamosa promoter binding protein-like–14* (*OsSPL14*)] in a dosage-dependent manner. Lack of *D14* or *OsSPL14* function was epistatic to *ngr5* in regulating rice tillering. We next found that the DELLA-mediated enhancement of nitrogen-induced tiller number, typical of green revolution rice varieties, was abolished in plants with the *ngr5* mutation.

ON OUR WEBSITE

Read the full article at http://dx.doi.org/10.1126/science.aaz2046

These observations suggest that NGR5-driven recruitment of PRC2 promotes repressive H3K27me3 modification of target branching-inhibitory genes, thus causing an increase in tiller number. On the other hand, a nitrogen-induced NGR5-dependent increase in tiller number is enhanced in green revolution rice varieties, and this effect is inhibited by gibberellin treatment. Although NGR5 abundance is negatively associated with gibberellin amount, gibberellin-promoted destabilization of NGR5 is neither dependent on nor downstream of gibberellin-induced DELLA destruction. Moreover, NGR5 interacts with the gibberellin receptor GID1 and DELLA proteins; this suggests that gibberellin-promoted proteasomal destruction of NGR5 is not due to gibberellin-promoted destruction of DELLAs, but is due to a gibberellin-potentiated interaction of NGR5-GID1, leading to polyubiquitination of NGR5 and subsequent destruction in the proteasome. Accumulation of DELLA proteins competitively inhibited the GID1-NGR5 interaction, thus stabilizing NGR5 by reducing its gibberellin-GID1–mediated destruction.

CONCLUSION: We conclude that nitrogen fertilization alters genome-wide reprogramming of H3K27me3 methylation via NGR5-dependent recruitment of PRC2. In rice, methylation represses genes that inhibit tillering and consequently promotes an increase in tiller number. NGR5 is a target of gibberellin-GID1–promoted proteasomal destruction. Modulation of competitive interactions among NGR5, DELLA proteins, and GID1 enables enhanced grain yield in elite rice varieties despite reduced nitrogen fertilizer inputs. Such shifts in yield and input use could promote agricultural sustainability and food security. ■

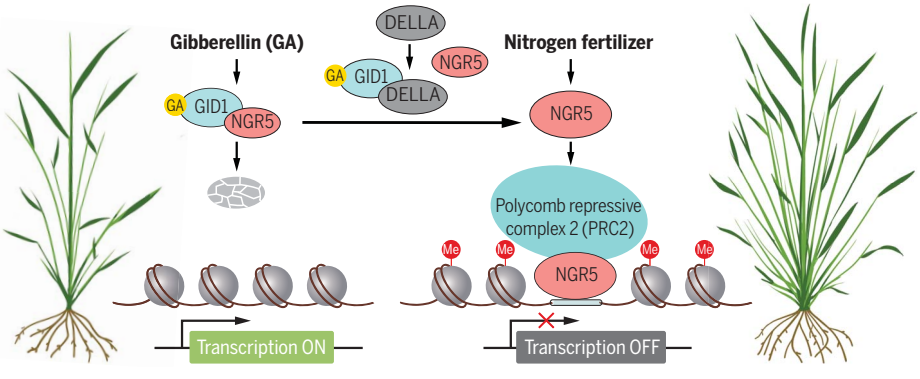

Nitrogen-responsive chromatin modulation enhances rice tillering. The rice transcription factor NGR5 facilitates nitrogen-dependent recruitment of PRC2 to repress expression of shoot branching-inhibitory genes, thus promoting tillering in response to increasing nitrogen supply. NGR5 interacts with the gibberellin receptor GID1 and with growth-repressing DELLA proteins. DELLA accumulation competitively inhibits the GID1-NGR5 interaction, thus stabilizing NGR5 by reducing gibberellin- and GID1-promoted proteasomal destruction.

The list of author affiliations is available in the full article online.
*These authors contributed equally to this work.
†Corresponding author. Email: nicholas.harberd@plants.ox.ac.uk (N.P.H.); xdfu@genetics.ac.cn (X.F.)
Cite this article as K. Wu *et al.*, *Science* **367**, eaaz2046 (2020). DOI: 10.1126/science.aaz2046

RESEARCH ARTICLE

PLANT SCIENCE

Enhanced sustainable green revolution yield via nitrogen-responsive chromatin modulation in rice

Kun Wu[1]*, Shuansuo Wang[1]*, Wenzhen Song[1,2], Jianqing Zhang[1,2], Yun Wang[1,2], Qian Liu[1], Jianping Yu[1], Yafeng Ye[1,3], Shan Li[1,2], Jianfeng Chen[1,2], Ying Zhao[1,2], Jing Wang[1,2], Xiaokang Wu[1,2], Meiyue Wang[4], Yijing Zhang[4], Binmei Liu[3], Yuejin Wu[3], Nicholas P. Harberd[5]†, Xiangdong Fu[1,2]†

Because environmentally degrading inorganic fertilizer use underlies current worldwide cereal yields, future agricultural sustainability demands enhanced nitrogen use efficiency. We found that genome-wide promotion of histone H3 lysine 27 trimethylation (H3K27me3) enables nitrogen-induced stimulation of rice tillering: APETALA2-domain transcription factor NGR5 (NITROGEN-MEDIATED TILLER GROWTH RESPONSE 5) facilitates nitrogen-dependent recruitment of polycomb repressive complex 2 to repress branching-inhibitory genes via H3K27me3 modification. NGR5 is a target of gibberellin receptor GIBBERELLIN INSENSITIVE DWARF1 (GID1)–promoted proteasomal destruction. DELLA proteins (characterized by the presence of a conserved aspartate-glutamate-leucine-leucine-alanine motif) competitively inhibit the GID1-NGR5 interaction and explain increased tillering of green revolution varieties. Increased NGR5 activity consequently uncouples tillering from nitrogen regulation, boosting rice yield at low nitrogen fertilization levels. NGR5 thus enables enhanced nitrogen use efficiency for improved future agricultural sustainability and food security.

The agricultural green revolution of the 1960s enhanced cereal crop yields, fed a growing world population, and was in part due to increased cultivation of semi-dwarf green revolution varieties (*1*–*4*). The beneficial semi-dwarfism is conferred by mutant alleles at the wheat *Reduced height-1* (*Rht-1*) (*5*, *6*) and rice *Semi-dwarf1* (*SD1*) (*7*, *8*) loci that enhance the activity of growth-repressing DELLA proteins (DELLAs). Normally, the phytohormone gibberellin stimulates the destruction of DELLAs (*9*, *10*), thus promoting plant growth. However, the mutant wheat DELLA protein Rht-1 likely resists gibberellin-stimulated destruction (*5*), whereas the rice *sd1* allele reduces gibberellin abundance (*11*, *12*) and increases accumulation of the rice DELLA protein SLR1 (SLENDER RICE1) (*13*). The result is plants that are shorter than normal, which, because they are shorter, are more resistant to lodging (the flattening of plants by wind and rain) (*4*). However, green revolution rice varieties require a high-nitrogen fertilizer supply to achieve maximum yield potential, and the drive toward increased agricultural sustainability necessitates reduced nitrogen fertilizer use (*13*). Grain yield is the sum of the multiplicative integration of three major components [tiller numbers per plant, grain numbers per panicle, and 1000-grain weight (*14*)], and an increased tillering ability in high-density planting conditions contributes to the high-yield properties of green revolution rice varieties (*1*, *15*). Further increase in tiller (lateral branch) numbers at low nitrogen supply is therefore important for future agricultural sustainability and is a key cereal breeding goal. Here, we first define the mechanisms underlying the promotive effects of nitrogen on tiller bud outgrowth. We then show how genetic modulation of these mechanisms can enable increased grain yield of green revolution varieties despite reduced nitrogen input, thus advancing agricultural sustainability.

Nitrogen promotes rice tillering via NGR5

We found that the tiller number per plant of *indica* rice variety Nanjing6 (NJ6) increased with increasing nitrogen supply (Fig. 1A). Additional effects of increased nitrogen on NJ6 included increases in grain number (per panicle) and yield (per plant) (*13*) (fig. S1, A to C). NJ6-*sd1* (a NJ6 isogenic line containing the *sd1* allele) also displayed nitrogen-dependent tiller number increases: increased tiller numbers per plant under different nitrogen fertilization levels, with tiller numbers being consistently higher in NJ6-*sd1* than in NJ6 (Fig. 1A). The *Rht-B1b* (formerly termed *Rht-1*) allele conferred similar properties on wheat

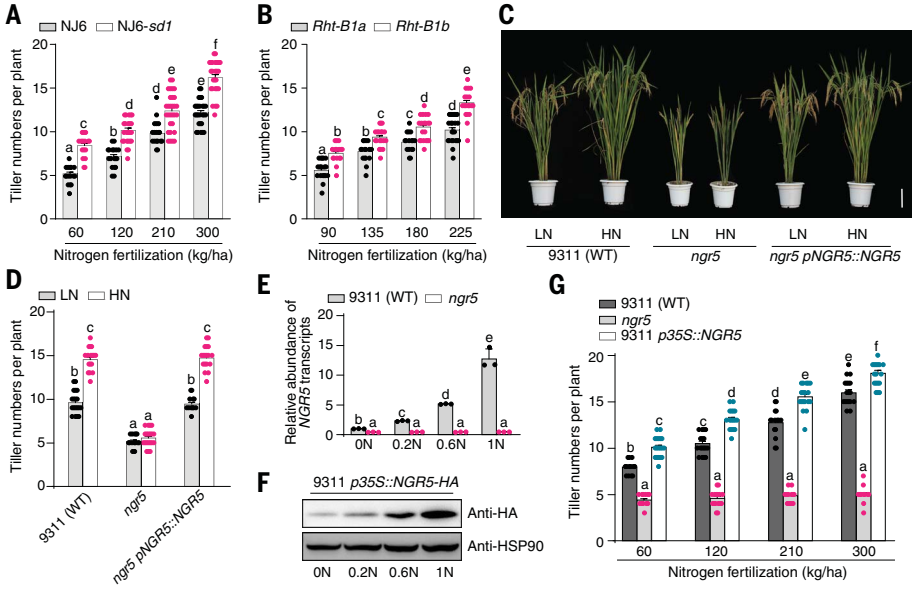

Fig. 1. NGR5 mediates nitrogen-dependent promotion of tillering. (**A** and **B**) Tiller numbers of field-grown rice and wheat plants in response to nitrogen supply. (A) NJ6 versus NJ6-*sd1*. (B) *Rht-B1a* versus *Rht-B1b*. Data are means ± SE (n = 30). (**C**) Mature plants grown in low (90 kg/ha; LN) versus high (180 kg/ha; HN) nitrogen supply. Scale bar, 20 cm. (**D**) Tiller numbers at LN (90 kg/ha) versus HN (180 kg/ha). Data are means ± SE (n = 20). (**E**) *NGR5* mRNA abundance in tiller buds. Three-week-old plants were grown hydroponically with varying nitrogen supply (0.2N, 0.25 mM NH_4NO_3; 0.6N, 0.75 mM NH_4NO_3; 1N, 1.25 mM NH_4NO_3), mRNA abundance values are relative to that of 0N (set to 1). Data are means ± SE (n = 3). (**F**) Accumulation of NGR5-HA in tiller buds of 3-week-old plants [as shown in (E)]. Heat shock protein 90 (HSP90) serves as loading control. (**G**) Tiller numbers of field-grown rice plants under increasing nitrogen supply. Data are means ± SE (n = 20). In (A), (B), (D), (E), and (G), different letters denote significant differences (P < 0.05, Duncan multiple-range test).

[1]State Key Laboratory of Plant Cell and Chromosome Engineering, Institute of Genetics and Developmental Biology, Innovation Academy for Seed Design, Chinese Academy of Sciences, Beijing 100101, China. [2]College of Life Sciences, University of Chinese Academy of Sciences, Beijing 100049, China. [3]Key Laboratory of High Magnetic Field and Ion Beam Physical Biology, Hefei Institutes of Physical Science, Chinese Academy of Sciences, Hefei, Anhui 230031, China. [4]National Key Laboratory of Plant Molecular Genetics, CAS Center for Excellence in Molecular Plant Sciences, Shanghai Institute of Plant Physiology and Ecology, Shanghai Institutes for Biological Sciences, Chinese Academy of Sciences, Shanghai 200032, China. [5]Department of Plant Sciences, University of Oxford, Oxford OX1 3RB, UK.
*These authors contributed equally to this work.
†Corresponding author. Email: nicholas.harberd@plants.ox.ac.uk (N.P.H.); xdfu@genetics.ac.cn (X.F.)

(versus the *Rht-B1a* control allele; Fig. 1B and fig. S1, D to F). In contrast, either exogenous gibberellin treatment or overexpression of the rice gibberellin receptor GID1 (*16*) inhibited nitrogen-promoted tillering (fig. S2). Thus, the enhanced DELLA function typical of green revolution varieties increases nitrogen-induced promotion of tiller number. Further analysis showed that nitrogen-induced increases in tiller number in the elite *sd1*-containing *indica* rice variety 9311 (fig. S3, A and B) were not due to nitrogen-responsive increases in numbers of lateral buds, but rather to increased numbers of buds initiating outgrowth and tiller branch extension (*17*) (fig. S3, C to E).

We next screened an ethyl methane sulfonate (EMS)–mutagenized 9311 population for mutants displaying an altered tiller number nitrogen response. Among such mutants, *ngr5* (*nitrogen-mediated tiller growth response 5*) displayed a reduced tiller number that was insensitive to changes in nitrogen supply (Fig. 1, C and D). Map-based cloning (fig. S4, A and B) and genetic complementation (Fig. 1, C and D, and fig. S4, C and D) revealed the *NGR5* allele to encode an APETALA2 (AP2)–domain transcription factor [NGR5, previously known as SMOS1 (SMALL ORGAN SIZE1) and RLA1 (REDUCED LEAF ANGLE1)] (*18*–*20*), thus identifying an unknown function for NGR5 in nitrogen-responsive tillering regulation. The *ngr5* allele carries a G → A nucleotide substitution conferring a Gly → Arg mutant protein (fig. S4B), which fails to complement *ngr5* phenotypes (fig. S4, C to F). In addition to its effect on tiller number (Fig. 1, C and D, and fig. S4D), *NGR5* is required for nitrogen-induced promotion of panicle branching and grain number (fig. S4, E and F). Accordingly, whereas 9311 grain yield per plot increased progressively with increasing nitrogen supply (*13*), this effect was abolished in *ngr5* plants (fig. S4G). Further analysis showed that lack of NGR5 (in *ngr5* plants) had no effect on the formation of tiller buds (lateral bud initials; fig. S3C) but reduced the number of buds initiating lateral outgrowth and tiller branch extension (fig. S3, D and E), thus confirming that nitrogen-responsive regulation of tillering is dependent on *NGR5*.

We next found that an increasing nitrogen supply increased NGR5 abundance at both mRNA and protein levels (Fig. 1, E and F). First, increasing nitrogen supply increased *NGR5* mRNA abundance, and this effect was abolished in *ngr5* plants (Fig. 1E). Second, although nitrogen supply had no effect on *NGR5-HA* (hemagglutinin-tagged fusion gene) mRNA abundance in plants transgenically expressing *p35S::NGR5-HA* (fig. S5), accumulation of NGR5-HA fusion protein increased with increasing nitrogen supply (Fig. 1F). Furthermore, NGR5 positively regulated tillering over a wide expression range, because the *p35S::NGR5* transgene increased 9311 tiller number (thus mimicking the effect of increasing nitrogen supply on tillering capacity; Fig. 1G). We conclude that nitrogen promotes increased NGR5 abundance, which in turn promotes tiller bud outgrowth. In addition, because *ngr5* suppressed the *sd1*-conferred tillering phenotype of 9311 (Fig. 1D), NGR5 is necessary for the DELLA-promoted increase in tiller number characteristic of green revolution varieties.

NGR5 represses branching-inhibitory genes

RNA sequencing (RNA-seq) analysis next revealed that lack of *NGR5* causes genome-wide change in mRNA abundance, with multiple differentially expressed genes displaying an increase in mRNA abundance in *ngr5* (fig. S6A). Further gene set enrichment analysis revealed a correlation between genes up-regulated in *ngr5* and the set of H3K27me3 (histone H3 lysine 27 trimethylation)–marked genes already known to be normally repressed by histone modification (fig. S6B), with H3K27me3 marks occurring at both TSS (transcription start site) and gene body regions of *ngr5*–up-regulated genes (fig. S6C). These results suggest that NGR5 may be involved in PRC2 (polycomb repressive complex 2)–mediated epigenetic repression. Among genes up-regulated in *ngr5* (table S1), we identified *D14* [*Dwarf14*, encoding the receptor for the phytohormone strigolactone (SL)] (*21*), *D3* [*Dwarf3*, encoding the F-box component of the Skp, Cullin, F-box–containing (SCF) ubiquitin ligase that targets the DWARF53 repressor of SL signaling for proteasomal destruction] (*22*–*24*), *OsTB1* (*TEOSINTE BRANCHED1*, encoding a TCP domain transcription factor) (*25*), and *OsSPL14* (*squamosa promoter binding protein-like–14*, encoding an SBP-domain transcription factor) (*26*, *27*) genes, all of which are already known to inhibit lateral branching and tiller number. Quantitative real-time polymerase chain reaction (qRT-PCR) analysis showed that high nitrogen supply reduced the abundances of mRNAs specified by these shoot branching-inhibitory genes, and this effect was abolished by lack of *NGR5* function (in *ngr5*; fig. S6D). In addition, we found that lack of *D14* or *OsSPL14* function (conferred by *d14* or *osspl14* alleles) (*28*, *29*) is epistatic to *ngr5* in regulating lateral branching (fig. S7). Thus, *D14* and *OsSPL14* function downstream of *NGR5*, and NGR5 mediates nitrogen-promoted increase in tiller number by repressing the inhibitory functions of *D14* and *OsSPL14* (and likely of other) branching-regulatory genes.

Chromatin immunoprecipitation–PCR (ChIP-PCR) experiments revealed binding of NGR5-HA to gene body and promoter regions of *D14* and *OsSPL14* [fig. S6E; confirmed in EMSA (electrophoretic mobility shift assays), fig. S6F]. Furthermore, the extent and effect of binding on NGR5-target gene repression correlated with increasing nitrogen supply (fig. S6, G and H). *D14* mRNA abundance decreased with increasing nitrogen supply in *NGR5* (but not in *ngr5*; fig. S6G), and the extent of NGR5 binding and the level of H3K27me3 modification at *D14* were correspondingly increased in a nitrogen-dependent manner (but not in *ngr5*; fig. S6G). Similar effects were observed for *OsSPL14* (fig. S6H), which suggests that NGR5 promotes tillering in response to increasing nitrogen supply by binding to target branching-inhibitory genes, thus causing their repression through regulation of H3K27me3 modification.

NGR5 recruits PRC2 for H3K27me3 deposition

To determine how NGR5 regulates nitrogen-promoted H3K27me3 modification, we first performed a yeast two-hybrid screen for NGR5 interactors, identifying LC2 (leaf inclination2, a component of the PRC2 complex) (*30*) among many others (table S2). NGR5-LC2 interactions were confirmed in bimolecular fluorescence complementation (BiFC; Fig. 2A) and coimmunoprecipitation (Co-IP; Fig. 2B) experiments. Furthermore, a CRISPR/Cas9-generated *LC2* reduced-function allele (*lc2*; fig. S8A) was shown, like *ngr5*, to abolish nitrogen-promoted increase in tiller number (Fig. 2, C and D). *lc2* also suppressed the increased tiller number conferred by *p35S::NGR5* (Fig. 1G and Fig. 2, C and D), whereas lack of *D14* or *OsSPL14* function (conferred by *d14* or *osspl14*) was epistatic to *lc2* (fig. S9). Taken together, these results suggest that NGR5-dependent nitrogen-promoted increase in tiller number depends on LC2 (PRC2 complex) function. Because PRC2 regulates genome-wide patterns of H3K27me3 methylation, we next conducted genome-wide surveys of H3K27me3 methylation in response to varying nitrogen supply. Although increasing nitrogen supply altered the genome-wide H3K27me3 methylation pattern, the extent of this alteration was reduced in *ngr5* (Fig. 2E), which suggests that nitrogen-mediated genome-wide reprogramming of H3K27me3 methylation is NGR5-dependent.

We next performed ChIP-sequencing experiments and identified a total of 453 binding sites shared in common by NGR5 and LC2 (Fig. 2F and tables S3 and S4). Further analysis identified potential target-site recognition motifs shared by NGR5 and LC2 (Fig. 2, G and H), with a predominant shared GCCGCC motif being common in the gene body regions of both *ngr5*–up-regulated and nitrogen-induced genes (Fig. 2E). Accordingly, increasing nitrogen supply progressively reduced *D14* and *OsSPL14* mRNA abundance in wild-type plants, and these effects were abolished in *lc2* plants (Fig. 2, I and J, top), just as they were in *ngr5* plants (fig. S6, G and H). Furthermore, increasing nitrogen

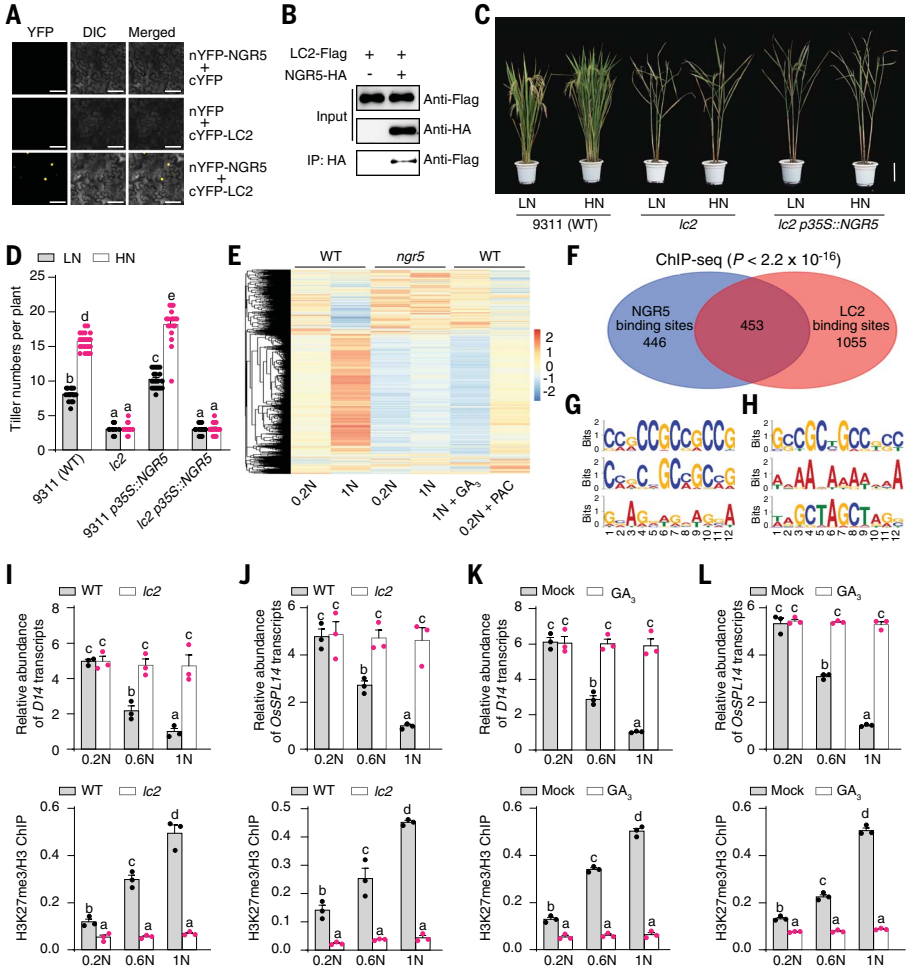

Fig. 2. Nitrogen regulates tillering via H3K27me3 reprogramming. (**A**) BiFC assays. Scale bar, 60 μm. (**B**) Co-IP assays. (**C**) Mature plants grown in low (90 kg/ha; LN) versus high (180 kg/ha; HN) nitrogen supply. Scale bar, 20 cm. (**D**) Tiller number. Data are means ± SE (n = 20). (**E**) Genome-wide surveys of H3K27me3 enrichment density. Each peak was normalized to zero mean and unit of energy (z-score). (**F**) Overlap of H3K27me3 ChIP-seq peaks. (**G** and **H**) Sequence motifs enriched during ChIP-seq with NGR5-HA (G) and LC2-HA (H). (**I** and **J**) Comparisons of mRNA abundance and H3K27me3 modification of *D14* (I) and *OsSPL14* (J) between 9311 [wild type (WT)] and *lc2*. (**K** and **L**) Transcript abundance and H3K27me3 modification of *D14* (K) and *OsSPL14* (L) in 9311 with or without 100 μM GA_3 treatment. RT-PCR and ChIP experiments [(F), (I) to (L)] were performed using tiller buds of 3-week-old plants grown in increasing nitrogen supply (0.2N, 0.25 mM NH_4NO_3; 0.6N, 0.75 mM NH_4NO_3; 1N, 1.25 mM NH_4NO_3); mRNA abundance values are relative to that of WT in 1N (set to 1). Data in (I) to (L) are means ± SE (n = 3). In (D) and (I) to (L), different letters denote significant differences (P < 0.05, Duncan multiple range test).

supply progressively increased H3K27me3 modification of both *D14* and *OsSPL14* in wild-type plants, and these effects were also abolished in *lc2* plants (Fig. 2, I and J, bottom). Taken together, these observations suggest that NGR5-driven recruitment of the PRC2 complex (of which LC2 is a component) to *D14* and *OsSPL14* results in repressive H3K27me3 modification of these genes in response to increased nitrogen supply, thereby promoting bud outgrowth and increasing tiller number.

NGR5 is a target of gibberellin receptor GID1

As shown above, nitrogen-induced increase in tiller number was enhanced in green revolution varieties (Fig. 1, A and B), and this effect was inhibited by exogenous gibberellin treatment (fig. S2A). Analysis of both RNA-seq and ChIP sequencing revealed multiple common gene targets to be co-regulated by NGR5 and gibberellin treatment (tables S5 and S6). Furthermore, gibberellin treatment altered the change in genome-wide H3K27me3 modification pattern due to increasing nitrogen supply in a manner similar to the alteration conferred by *ngr5*, whereas a partially restored H3K27me3 modification pattern was induced by treatment with paclobutrazol (PAC, an inhibitor of gibberellin biosynthesis; Fig. 2E). In addition, gibberellic acid (GA_3), like *ngr5* and *lc2*, inhibited the nitrogen-dependent increase in H3K27me3 modification and consequent repression of expression of shoot branching inhibitor genes such as *D14* (Fig. 2K) and *OsSPL14* (Fig. 2L). These observations suggest the existence of a mechanistic link between nitrogen- and gibberellin-mediated effects on tiller number.

In canonical gibberellin signaling, gibberellin binds its receptor GID1, thus recruiting DELLAs for polyubiquitination by the F-box protein GIBBERELLIN INSENSITIVE DWARF2 (GID2) and the Skp, Cullin, F-box–containing (SCF) ubiquitin ligase complex (SCF^{GID2}) and subsequent destruction in the 26*S* proteasome, thus promoting plant growth (*9*, *10*, *16*, *31*–*34*). We next found that reduced GID1 function in a NJ6-*gid1-10* mutant (*gid1* loss-of-function mutant; fig. S8B) led to an increased tiller number above that of NJ6 controls in both high and low nitrogen supply (similar to NJ6-*sd1*; Fig. 3, A and B). Conversely, transgenic NJ6-*sd1* plants overexpressing *GID1* under the control of the cauliflower mosaic virus (CaMV) *35S* promoter exhibited nitrogen-insensitive responses, with lower tiller number than in nontransgenic controls (Fig. 3B). Although gibberellin repressed tiller number in both NJ6 and NJ6-*sd1* plants, it had no effect on tiller number in NJ6-*gid1-10* or NJ6-*sd1-ngr5* plants, nor in NJ6-*sd1* plants overexpressing *GID1* (Fig. 3B). Furthermore, either gibberellin-induced inhibition or GID1-mediated repression of tillering mimicked the effect of *ngr5* (Fig. 3B). These results suggest that gibberellin-GID1–mediated repression of tiller number is dependent on the nitrogen-regulated function of NGR5.

We next found that NGR5 abundance is negatively associated with gibberellin level: NGR5-HA accumulation was increased in relatively gibberellin-deficient NJ6-*sd1* plants (versus NJ6), whereas it was reduced by exogenous gibberellin treatment (Fig. 3C). Conversely, a gibberellin-mediated decrease in NGR5-HA abundance was inhibited by treatment with the proteasome inhibitor MG132 (carbobenzoxy-Leu-Leu-leucinal), such that NGR5-HA accumulation was increased above that of NJ6-*sd1* plants (Fig. 3C). Accordingly, Western blot analysis detected the accumulation of polyubiquitinated NGR5-HA in the presence of MG132 (Fig. 3D), which suggests that gibberellin promotes polyubiquitination and subsequent proteolysis of NGR5 in the 26*S* proteasome. In addition, gibberellin-induced degradation of NGR5-HA was inhibited in the NJ6-*gid1-10* mutant (Fig. 3E), indicating that gibberellin-induced promotion of NGR5 polyubiquitination and proteasome destruction is dependent on the *GID1* function.

Gibberellin responses are conventionally considered to be activated by GID1-mediated destruction of DELLAs (*9*, *10*). However, we found that gibberellin-mediated degradation of NGR5-HA occurs either in the absence of

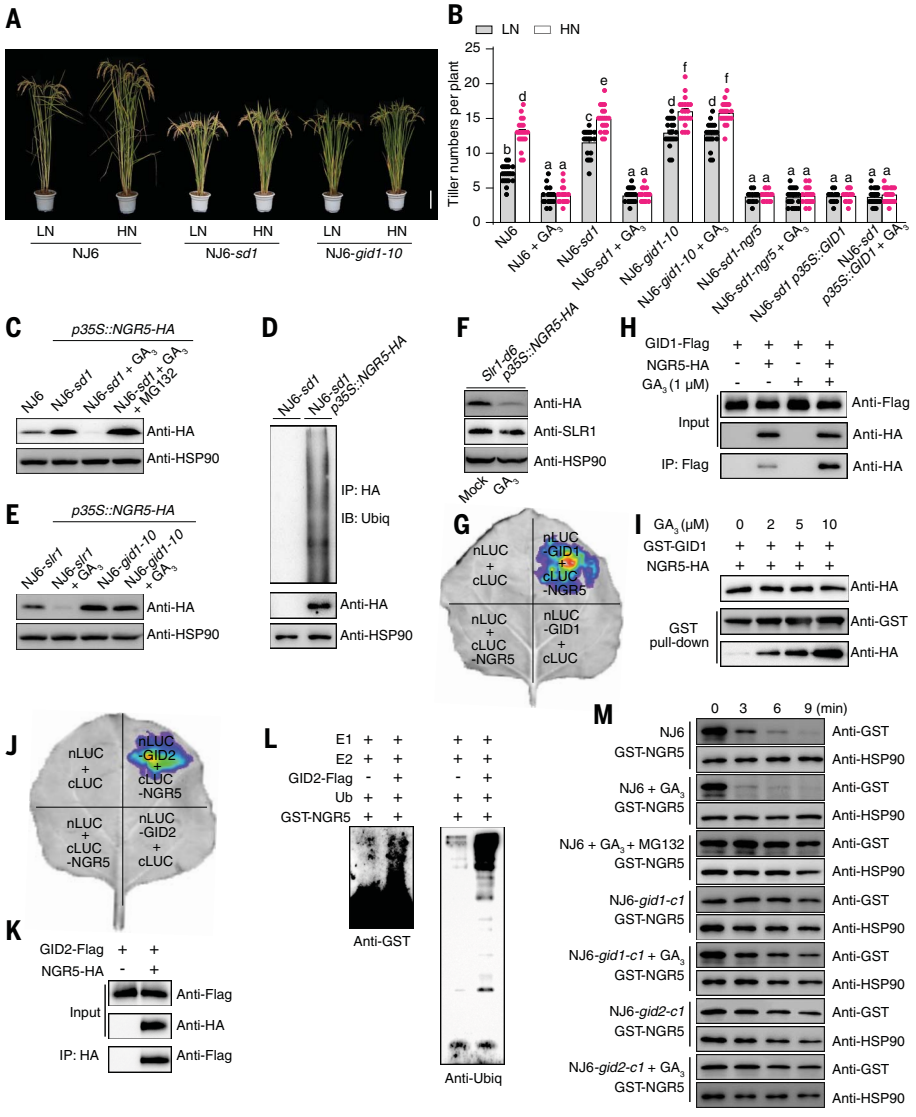

Fig. 3. Gibberellin-GID1-SCF^{GID2} targets NGR5 for destruction. (**A**) Mature plants grown in low (90 kg/ha; LN) versus high (180 kg/ha; HN) nitrogen supply. Scale bar, 20 cm. (**B**) Tiller number. Data are means ± SE (n = 20). (**C**) Immunodetection of NGR5-HA. (**D**) Immunodetection of poly-ubiquitinated NGR5-HA. (**E**) Accumulation of NGR5-HA. (**F**) Effects of gibberellin on NGR5-HA and SLR1 accumulation. In (C) to (F), total protein was extracted from tiller buds of 3-week-old plants treated for 4 hours with 1 μM GA_3 and/or 100 μM MG132; HSP90 serves as loading control. (**G** and **J**) SFLC assays. nLUC-tagged GID1 (G) or nLUC-tagged GID2 (J) was co-transformed into tobacco leaves along with cLUC-targeted NGR5. (**H** and **K**) Co-IP assays. Flag-tagged GID1 (H) or Flag-tagged GID2 (K) was co-transformed into rice protoplasts along with HA-targeted NGR5. (**I**) Pull-down assays. (**L**) In vitro ubiquitination assay. The immunoprecipitated GID2-Flag proteins transiently expressed in rice protoplasts were used in an in vitro ubiquitination reaction in the presence of E1, E2 (UbcH5B), His-Ub, and GST-NGR5. (**M**) Gibberellin-GID1-SCF^{GID2} destabilizes GST-NGR5. Lysates from NJ6, NJ6-*gid1-c1*, and NJ6-*gid2-c1* plants were co-incubated with GST-NGR5 in the presence or absence of 100 μM GA_3 and 100 μM MG132. The lysates were harvested at various incubation times and immunoblotted to assess the accumulation of NGR5 and HSP90.

DELLAs in a loss-of-function *slr1* mutant (Fig. 3E) (*11*) or in the presence of the high-level DELLA accumulation conferred by the *Slr1-d6* gain-of-function mutation (Fig. 3F) (*35*). Although the mutant SLR1 DELLA encoded by *Slr1-d6* was relatively resistant to gibberellin-mediated destruction, NGR5-HA was still destabilized by exogenous gibberellin treatment (Fig. 3F). Thus, gibberellin-promoted destabilization of NGR5, although dependent on GID1, is neither dependent on nor downstream of gibberellin-induced destruction of DELLAs. We therefore explored the possibility of an alternative, previously unknown, DELLA-independent mechanism whereby the SCF^{GID2} E3 ubiquitin ligase directly mediates gibberellin-promoted destruction of NGR5, finding that GID1 interacts directly with NGR5 [as assayed by both split firefly luciferase complementation (SFLC) and Co-IP; Fig. 3, G and H] and that the strength of this interaction is potentiated by increasing concentrations of gibberellin (Fig. 3, H and I). Thus, as with the DELLAs, gibberellin enhances the interaction between NGR5 and GID1, thereby identifying NGR5 as a potential alternative substrate for GID1-promoted polyubiquitination.

Although NGR5 lacks the specific DELLA motif that enables the GID1-DELLA interaction (*33*, *34*), we found a motif within the AP2-R2 (repeated units 2) (*18*) domain of NGR5 to enable the GID1-NGR5 interaction (fig. S10). Furthermore, NGR5 also interacted with the GID2 F-box component of the SCF^{GID2} E3 ubiquitin ligase that normally targets SLR1 for destruction in the 26*S* proteasome (Fig. 3, J and K). Accordingly, an in vitro ubiquitination assay showed that GST (glutathione *S*-transferase)–NGR5 fusion protein is polyubiquitinated by GID2-Flag (Asp-Tyr-Lys-Asp-Asp-Asp-Asp-Lys peptide) fusion protein in the presence of ubiquitin-activating enzyme E1, ubiquitin-conjugating enzyme E2, and ubiquitin, but not in the absence of GID2-Flag (Fig. 3L), which suggests that NGR5 is a substrate of the SCF^{GID2} E3 ubiquitin ligase. Additional time-course experiments showed that gibberellin promotes the progressive degradation of GST-NGR5 but that this degradation is inhibited both by MG132 and in *gid1-c1*, a CRISPR/Cas9-generated *GID1* loss-of-function mutant (Fig. 3M and fig. S8B). Finally, lack of GID2 function (in a *gid2-c1* mutant; fig. S8C) also inhibits gibberellin-mediated degradation of GST-NGR5 (Fig. 3M). We conclude that the gibberellin-mediated regulation of NGR5 is not due to gibberellin-promoted destruction of DELLAs, but is due to a previously unknown direct and gibberellin-potentiated interaction of NGR5-GID1, leading to polyubiquitination of NGR5 by the SCF^{GID2} E3 ubiquitin ligase and subsequent destruction in the proteasome.

DELLA-NGR5 modulation of tiller N response

We next found that NGR5 interacts directly with SLR1 [in yeast two-hybrid screens (table S2) and in BiFC and Co-IP assays (fig. S11, A and B)]. Nonetheless, we additionally found that the LC2-NGR5 interaction is not inhibited by the presence of SLR1 (fig. S12), which suggests that the SLR1-NGR5 interaction does not directly interfere with the LC2-NGR5 interaction that determines NGR5 function. Further experiments showed that the LHR1 (leucine heptad repeat 1) motif of the DELLA protein is necessary for the NGR5-SLR1 interaction

(fig. S11C). Thus, in addition to both being substrates of gibberellin-GID1-SCF^{GID2}, SLR1 and NGR5 interact directly with one another. With the LHR1 motif being conserved in all the GRAS [derived from three initially identified members, GAI (gibberellin-insensitive), RGA (repressor of ga1-3), and SCARECROW] proteins, we next found that NGR5 interacts with two additional GRAS proteins [DWARF AND LOW-TILLERING (DLT) and MONOCULM1 (MOC1)] previously shown to regulate tiller number (*17*, *19*, *36*) (fig. S13A). The competitive nature of the SLR1-NGR5 relationship with respect to GID1 (and hence with respect to GID1-promoted destruction) (fig. S13B) caused accumulation of NGR5-HA (conferred by *p35S::NGR5-HA*) to further increase the accumulation of SLR1 in 9311 (fig. S13C).

We next determined whether competitive SLR1-NGR5-GID1 relationships also condition gibberellin and nitrogen effects on tiller number. As shown in Fig. 1B, the enhanced DELLA function conferred by the *Rht-B1b* allele results in increased tiller number. We therefore tested the possibility that the effect of *Rht-B1b* on tiller number might be due to differential effects on NGR5 stability. Accordingly, using FRET (Förster resonance energy transfer) analysis, we found that the extent of the interaction between GID1 and NGR5 is reduced by the presence of Rht-B1b (Fig. 4, A and B). We then confirmed the expectation that a reduced GID1-NGR5 interaction in the presence of Rht-B1b reduces the rate of proteasome-dependent GST-NGR5 destruction (Fig. 4C), and we found similar reductions to be conferred by accumulation of wild-type Rht-B1a or SLR1 proteins (Fig. 4, A to C). Further comparative studies showed His-NGR5 (His-tagged fusion protein) destruction to be more rapid than that of His-SLR1 (His-tagged fusion protein; Fig. 4D). Thus, although gibberellin-promoted NGR5 destruction was DELLA-independent (Fig. 3, E and F), competition between NGR5 and SLR1 for GID1 interaction reduced the extent of NGR5-GID1 interaction (fig. S13B). Moreover, the abundance of NGR5-GFP (green fluorescent protein) fusion protein (conferred by *p35S::NGR5-GFP*) was increased with PAC treatment but was reduced in response to combined gibberellin and PAC treatments (fig. S13, D and E). This is also consistent with the observations that *ngr5* exhibits a higher ratio of gibberellin-induced leaf sheath growth, whereas transgenic plants overexpressing *NGR5-HA* display reduced sensitivity to PAC treatment relative to wild-type controls (fig. S14). We conclude that the enhanced DELLA function characteristic of both wheat and rice green revolution varieties competitively inhibits the GID1-NGR5 interaction, thus stabilizing NGR5 by reducing gibberellin-GID1–mediated destruction.

To determine whether DELLA promotion of rice tillering is NGR5-dependent, we generated 9311 NILs (near-isogenic lines) carrying various combinations of different *SD1*, *GID1*, and *NGR5* alleles. Although the increased SLR1 accumulations in both 9311-*NGR5-gid1-10* and 9311-*NGR5-sd1* increased the tiller numbers of plants grown in either low or high nitrogen supply (versus 9311-*NGR5-SD1*), there was almost no difference in tiller number when 9311-*ngr5-sd1*, 9311-*ngr5-SD1*, and 9311-*ngr5-gid1-10* were compared (Fig. 4E). Thus, the DELLA-mediated enhancement of nitrogen-induced tiller number increase typical of green revolution rice varieties is dependent on NGR5 function. Accordingly, comparisons of NGR5-regulated mRNA abundance and H3K27me3 modification of branching-inhibitory *D14* (Fig. 4F) and *OsSPL14* (Fig. 4G) genes in 9311 (containing *sd1*) versus 9311-*SD1* revealed mRNA abundance and modification status at 0.6N in 9311-*SD1* to be roughly equivalent to that at 0.2N in

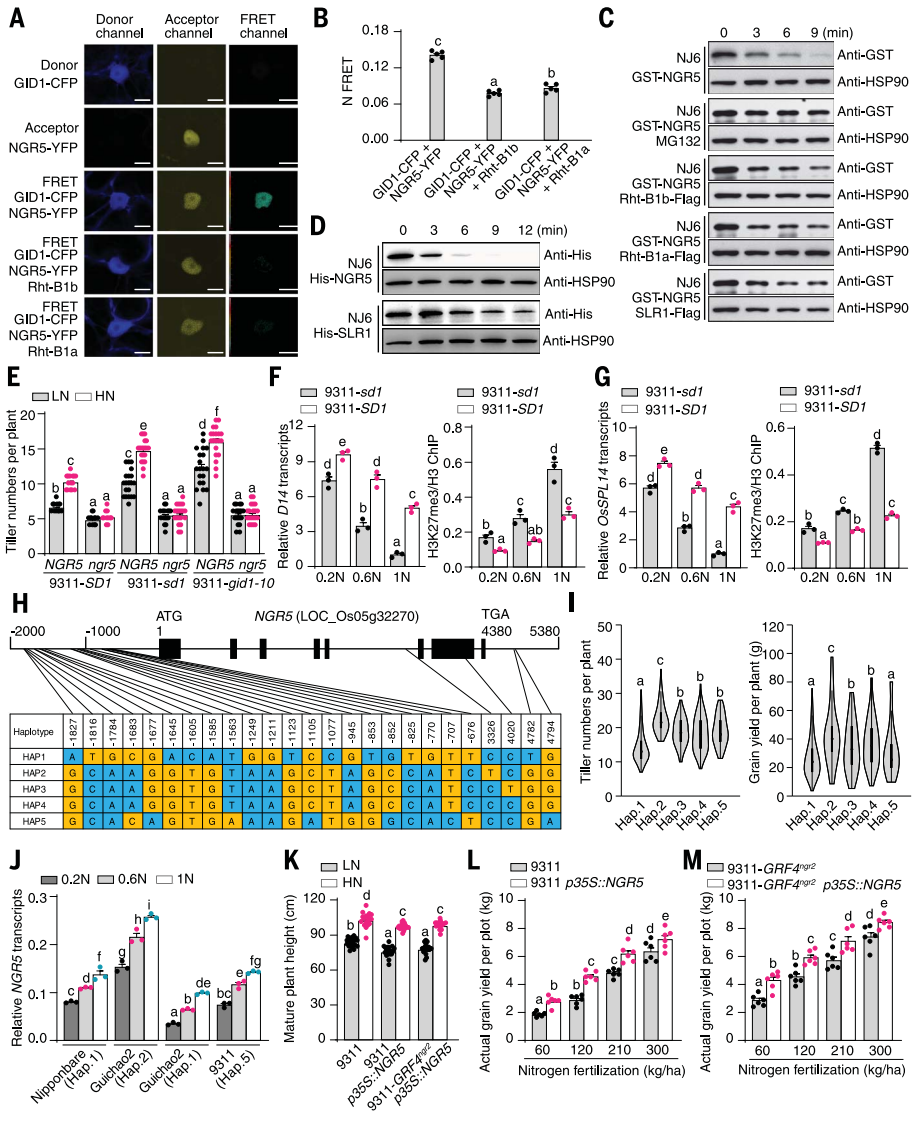

Fig. 4. Balanced DELLA-NGR5 interactions improve nitrogen use efficiency. (**A**) FRET images. Scale bars, 200 μm. (**B**) Mean N-FRET data for GID1-CFP and NGR5-YFP channels. Data are means ± SE (n = 5). (**C**) Time-course analysis of GST-NGR5 degradation. HSP90 serves as loading control. (**D**) Degradation rate of His-NGR5 and His-SLR1. (**E**) Tiller number. (**F** and **G**) Relative mRNA abundance and H3K27me3 modification of *D14* (F) and *OsSPL14* (G). Transcript abundance values are relative to that of 9311-*sd1* in 1N (set to 1). Data are means ± SE (n = 3). (**H**) Natural allelic variation at *NGR5*. (**I**) Tiller number and grain yield. Data are means ± SE (Hap.1, n = 305; Hap.2, n = 84; Hap.3, n = 62; Hap.4, n = 138; Hap.5, n = 97). (**J**) Relative mRNA abundance of *NGR5*. Abundance shown is relative to that of *OsActin1*. (**K**) Plant height. Data in (E) to (K) are means ± SE (n = 20). (**L** and **M**) Grain yield per plot. Data are means ± SE of six plots (each plot contained 220 plants) per line per nitrogen level. In (B), (E) to (G), and (I) to (M), different letters denote significant differences (P < 0.05, Duncan multiple range test).

9311-*sd1*. Thus, the enhanced DELLA function of *sd1* increases tiller number in response to nitrogen supply by increasing the stability of NGR5 (Fig. 3, C and E), which in turn inhibits the expression of shoot branching inhibitor genes, thereby promoting tiller number.

NGR5 improves yield and nitrogen use efficiency

We next determined whether an increase in NGR5 abundance beyond that seen in elite rice varieties (e.g., *sd1*-containing 9311) could further increase tiller number and yield in reduced nitrogen fertilizer inputs. First, we surveyed publicly available rice varietal genome sequence data for natural genetic variation at *NGR5* (*37*), distinguished five distinct haplotypes (Hap.1 to Hap.5; Fig. 4H), and found that Hap.2 was associated with increased *NGR5* mRNA abundances in both low and high nitrogen conditions (fig. S15), together with increases in tiller number and field-grown grain yield of 686 diverse Asian cultivated rice accessions (Fig. 4I). Further analysis showed that Hap.2-containing Guichao2 [Guichao2(Hap.2), one of the highest-yielding of *indica* varieties cultivated in China since the 1980s] displayed a greater *NGR5* mRNA abundance than did Guichao2(Hap.1) (a NIL carrying Hap.1 in the Guichao2 genetic background) and other lines (including Hap.5-containing 9311), even at low and moderate nitrogen supply (Fig. 4J). In addition, we showed that a transgenic mimic of Hap.2 (expression from a *p35S::NGR5* transgene) enhanced 9311 grain yield in a range of nitrogen supply conditions, without affecting the characteristic and beneficial semi-dwarfism of 9311 (Fig. 4, K and L); this suggests that breeding with Hap.2 is a feasible future strategy toward improving nitrogen use efficiency of the elite rice varieties. Finally, having recently shown that allelic variation at *GRF4* (encoding the rice GROWTH-REGULATING FACTOR 4 transcription factor) enhances grain yield and nitrogen use efficiency through coordinating effects on carbon and nitrogen metabolic regulation (*13*), we investigated the genetic interaction between *GRF4* and *NGR5*. We found that increased abundances of both *GRF4* and *NGR5* further enhanced 9311 yield and nitrogen use efficiency, particularly at relatively low levels of nitrogen supply (Fig. 4M).

We have shown that nitrogen determines genome-wide chromatin status (specific H3K27me3 histone modification) via NGR5-dependent recruitment of the polycomb complex PRC2 to target genes, among which are tiller branch-repressing genes. In consequence, repression of tiller outgrowth is reduced in increasing nitrogen supply, causing increased tillering. We have also shown that NGR5 is a non-DELLA target of gibberellin-GID1-SCF^{GID2}–mediated proteasomal destruction and that competitive NGR5-DELLA-GID1 interactions cause the NGR5-dependent yield-enhancing tillering increases typical of green revolution rice varieties. Because NGR5 is already known to be involved in the cross-talk between auxin and brassinosteroid signaling (*19*, *20*), our discoveries add to a growing understanding of how diverse modes of molecular and functional cross-talk between multiple phytohormonal signaling and fertilizer use responses function in the environmentally adaptive regulation of plant growth and development. Finally, we have shown that increasing NGR5 expression or activity provides a breeding strategy to reduce nitrogen fertilizer use while boosting grain yield above what is currently sustainably achievable.

Materials and methods

Plant materials and growth conditions

A nitrogen-insensitive rice mutant, designated *ngr5* (*nitrogen-mediated tiller growth response 5*), was isolated from the progeny of EMS-mutagenized *indica* cultivar 9311. NILs carrying allelic combinations of the *NGR5*, *SD1*, and *GID1* loci were obtained by backcrossing to recurrent parent 9311 (or NJ6) six times. Details of the germplasm used for the positional cloning and haplotype analysis are described in (*13*, *37*–*39*). Paddy-grown rice plants, including 686 diverse Asian cultivated rice accessions (*37*), were planted in rows 20 cm apart and raised in standard paddy conditions at two experimental stations, one in Lingshui (Hainan Province), the other in Hefei (Anhui Province).

Hydroponic culture conditions

Hydroponic culture conditions were as described (*13*). Rice seeds were surface-sterilized with 20% sodium hypochlorite solution for 30 min, then rinsed and soaked in water for 3 days to allow the seeds to germinate. Surface-sterilized seeds were then germinated in moist Perlite. Seven-day-old seedlings were transplanted to PVC pots containing 40 liters of nutrient solution (1.25 mM NH_4NO_3, 0.5 mM $NaH_2PO_4{\cdot}2H_2O$, 0.75 mM K_2SO_4, 1 mM $CaCl_2$, 1.667 mM $MgSO_4{\cdot}7H_2O$, 40 μM Fe-EDTA (Na), 19 μM H_3BO_3, 9.1 μM $MnSO_4{\cdot}H_2O$, 0.15 μM $ZnSO_4{\cdot}7H_2O$, 0.16 μM $CuSO_4$, and 0.52 μM $(NH_4)_3Mo_7O_{24}{\cdot}4H_2O$, pH 5.5), and growth was continued in a greenhouse. Compositions of nutrient solutions containing different levels of supplied nitrogen were as follows: 1N, 1.25 mM NH_4NO_3; 0.6N, 0.75 mM NH_4NO_3; 0.2N, 0.25 mM NH_4NO_3; 0N, 0 mM NH_4NO_3. All nutrient solutions were changed twice per week; pH was adjusted to 5.5 every day. The temperature was maintained at 30°C day and 22°C night, and the relative humidity was 70%.

Map-based cloning of NGR5

Fine-scale mapping of *ngr5* was based on 600 F_2 plants and 1256 BC_1F_2 plants derived from a cross between the *ngr5* mutant and the *japonica* rice cultivar Lansheng (recurrent parent). Genomic DNA sequences in the candidate region were compared between 9311, Nipponbare, and Lansheng. Primer sequences used for map-based cloning and genotyping assays are given in table S7.

Transgene constructs

Wild-type *NGR5* and *ngr5* mRNA-encoding sequences (together with intron sequences and/or promoter regions lying 3 kbp upstream of the transcription start site) were amplified from 9311 and *ngr5* mutant plants, respectively. These amplified genomic DNA fragments were inserted into the *p35S::HA-nos* (*40*) and *pCAMBIA1300* (CAMBIA, www.cambia.org) vectors to respectively generate *pNGR5::NGR5*, *pNGR5::ngr5*, *pNGR5::NGR5-HA*, and *p35S::NGR5* constructs. Full-length cDNAs of *NGR5*, *GID1*, and *LC2* cDNAs were amplified from 9311 plants and inserted into *p35S::HA-nos* (*40*) or *p35::GFP-nos* (*39*–*41*) vector to respectively generate *p35S::GID1*, *p35S::LC2-HA*, *p35S::NGR5-HA*, and *p35S::NGR5-GFP* constructs. gRNA constructs required for CRISPR/Cas9-mediated generation of *GID1*, *GID2*, and *LC2* mutant alleles were made as described (*13*, *41*). The transgenic rice plants were generated by *Agrobacterium*-mediated transformation as described (*42*). Relevant primer sequences are given in table S8.

qRT-PCR analysis

Total RNAs were extracted from tiller buds of 3-week-old rice plants using the TRIzol reagent (Invitrogen) according to the manufacturer's protocol, and treated with RNase-free DNase I (Invitrogen) to remove contaminating genomic DNAs. The full-length cDNAs were then reverse-transcribed using a cDNA synthesis kit (TRANSGEN, AE311-02). Subsequent qRT-PCR processing steps were performed according to the manufacturer's instructions (TRANSGEN, AQ101), with each qRT-PCR assay being replicated at least three times with three independent RNA preparations. Rice *Actin1* gene (*OsActin1*, LOC_Os03 g50885) transcripts were used as an internal reference. Relevant primer sequences are given in table S9.

Yeast two-hybrid assays

Yeast two-hybrid screening was performed as described (*38*). The full length *NGR5* cDNA was amplified and subcloned into *pGBKT7* (Takara Bio Inc.), then transformed into yeast strain AH109. The NGR5 protein was used as a bait to screen a cDNA library prepared from equal amounts of poly(A)-containing RNA sampled from various rice tissues/organs, including tiller buds, roots, leaves, shoot apical meristem (SAM), young panicles, etc. Experimental procedures for screening and plasmid isolation were performed according to the

manufacturer's user guide. cDNAs encoding various deleted and nondeleted versions of SLR1 were amplified and then subcloned into the *pGBKT7* vector (Takara Bio Inc.). Bait and prey vectors were co-transformed into yeast strain AH109, and experimental procedures were performed according to the manufacturer's instructions (Takara Bio Inc.). Relevant primer sequences are given in table S8.

Bimolecular fluorescence complementation (BiFC) assays

As described (*13*), full-length cDNAs of *NGR5*, *LC2*, *SLR1*, *DLT*, and *MOC1* were amplified from 9311 and inserted into *pSY-735-35S-cYFP-HA* or *pSY-736-35S-nYFP-EE* vectors (YFP, yellow fluorescent protein) to generate fusion constructs. Cotransfection of constructs (e.g., nYFP-NGR5 and cYFP-LC2) into tobacco leaf epidermal cells by *Agrobacterium*-mediated infiltration enabled testing for protein-protein interaction. After 48 hours of incubation in the dark, the YFP signal was captured using a confocal microscope (Zeiss LSM710). Each BiFC assay was repeated at least three times. Relevant primer sequences are given in table S8.

Split firefly luciferase complementation (SFLC) assays

Full-length cDNAs of *GID1* and *GID2* and cDNAs encoding various deleted and nondeleted versions of *NGR5* were amplified from 9311, and then inserted into *pCAMBIA1300-35S-Cluc-RBS* or *pCAMBIA1300-35S-HA-Nluc-RBS* vectors (*39*) to generate fusion constructs. Two different vectors (e.g., nLUC-GID1 and cLUC-NGR5) enabling testing of protein-protein interaction, together with the p19 silencing plasmid, were cotransfected into tobacco leaf epidermal cells by *Agrobacterium*-mediated infiltration. After 48 hours of incubation in the dark, the injected leaves were sprayed with 1 mM luciferin (Promega, E1605) and the LUC signal was captured using a cooled CCD imaging apparatus (Berthold, LB985). Each assay was repeated at least three times. Relevant primer sequences are given in table S8.

FRET (Förster resonance energy transfer) assays

FRET assays were performed as described (*13*). Cauliflower mosaic virus (CaMV) *35S* promoter-driven fusion constructs with C-terminal tagging CFP (cyan fluorescent protein) or YFP were created to generate the donor vectors *p35S::GID1-CFP* (or *p35S::LC2-CFP*), and the acceptor vector *p35S::NGR5-YFP*. Donor and acceptor vectors, with or without *p35S::Rht-B1a* (*p35S::Rht-B1b*, or *p35S::SLR1*) vector, were cotransformed into tobacco leaf epidermis cells by *Agrobacterium*-mediated vacuum infiltration to provide the FRET measurements. Transformation with the *p35S::GID1-CFP* vector provided only the donor channel, and with the *p35S::NGR5-YFP* vector only the acceptor channel. The FRET signal was detected and photographed using a confocal microscope (Zeiss LSM710). Relevant primer sequences are given in table S8.

Western blotting and coimmunoprecipitation (Co-IP) assays

Protein extracts were electrophoretically separated by SDS-PAGE and transferred to a nitrocellulose membrane (GE Healthcare). Proteins were detected by immunoblot using the following antibodies: anti-SLR1 (ABclonal Technology), anti-HA (MBL, M180-7), anti-Ubiquitin (Abcam, ab134953), anti-GST (Santa Cruz, sc-138), anti-GFP (Abcam, ab6673), and anti-HSP90 (BGI), respectively. For Co-IP experiments, full-length *NGR5*, *LC2*, *SLR1*, *GID1*, and *GID2* cDNAs were amplified, then inserted into either the *pUC-35S-HA-RBS* or the *pUC-35S-Flag-RBS* vector as described (*13*, *39*). Rice protoplasts were transfected with 100 μg of plasmid DNA and then incubated overnight in the dark. Total protein was extracted from harvested protoplasts with a lysis buffer [50 mM HEPES (pH 7.5), 150 mM KCl, 1 mM EDTA, 0.5% Triton X-100, 1 mM DTT, proteinase inhibitor cocktail (Roche LifeScience)]. Lysates were incubated with magnetic beads conjugated with an anti-DDDDK-tag antibody (MBL, M185-11) or anti-HA-tag antibody (MBL, M180-11) at 4°C for 4 hours. The magnetic beads were then washed 5 times with TBS-T buffer [500 mM NaCl, 20 mM Tris-HCl (pH 8.0), 0.1% Tween 20] and eluted with 3×Flag peptide (Sigma-Aldrich, F4709). Immunoprecipitates were electrophoretically separated and specific proteins detected by immunoblotting with anti-HA (MBL, M180-7) or anti-DDDDK (MBL, M185-7) antibodies. Relevant primer sequences are given in table S8.

In vivo pull-down

A full-length rice *GID1* cDNA was amplified and then inserted into the *pGEX-4T-1* vector (GE Healthcare). The recombinant GST-GID1 protein was expressed in *Escherichia coli* BL21 (DE3) (Transgen, CD701-01), and then purified and immobilized on Glutathione Sepharose 4B beads (GE Healthcare, 17-0756) following the manufacturer's instructions. The beads were divided into four equal aliquots and incubated with the same amount of NGR5-HA (or NGR5-Flag) protein lysate, together with His-SLR1 or with different concentrations of GA_3 (0, 2, 5, 10 μM) and/or MG132 (50 μM) for 2 hours at 4°C. The beads were subsequently washed five times with TBS-T buffer, followed by elution with 50 μl of elution buffer (50 mM Tris-HCl, 10 mM reduced glutathione, pH 8.0). Supernatants were resolved by 12% SDS-PAGE and subjected to immunoblotting using anti-GST (Santa Cruz, sc-138) and anti-HA (MBL, M180-7) antibodies. Relevant primer sequences are given in table S8.

EMSA assays

EMSA assays were performed as described (*39*). A full-length *NGR5* cDNA was amplified and inserted into the *pGEX-4T-1* vector (GE Healthcare). Recombinant GST-NGR5 protein was expressed in *E. coli* BL21 (DE3) strain and purified using Glutathione Sepharose 4B (GE Healthcare, 17-0756) following the manufacturer's instructions. DNA probes (D5 fragment for the *D14* gene, S3 fragment for the *OsSPL14* gene) were amplified and labeled using a biotin label kit (Biosune). DNA gel shift assays were performed using the LightShift Chemiluminescent EMSA kit (Thermo Fisher Scientific, 20148). Relevant primer sequences are given in table S10.

Cell-free protein degradation assays

Three-week-old NJ6-*gid1-c1* and NJ6-*gid2-c1* seedlings (together with NJ6) were harvested and ground into a fine powder in liquid nitrogen. Lysates were subsequently extracted with lysis buffer [25 mM Tris-HCl (pH 7.5), 10 mM NaCl, 10 mM $MgCl_2$, 4 mM PMSF, 5 mM DTT, and 10 mM ATP] as described (*43*); total protein extracts were adjusted to be at equal concentration in the lysis buffer for each assay. Rice cell lysates (200 μl) were incubated with 100 ng of purified GST-NGR5 (or His-NGR5) fusion protein in the presence or absence of the recombinant Rht-B1b-Flag, Rht-B1a-Flag, SLR1-Flag, or His-SLR1 proteins. Proteins were extracted from lysates that had or had not been exposed to treatments with 100 μM GA_3 and/or 100 μM MG132 for a series of incubation times and then subjected to SDS-PAGE and Western blotting using an anti-GST antibody (Santa Cruz, sc-138). HSP90 was used as a loading control.

In vitro protein ubiquitination assays

Full-length *GID2* cDNA was amplified and inserted into *PUC-35S-flag-RBS* vector (*39*). Rice protoplasts were transfected with 100 μg of plasmid and incubated for 24 hours. Total protein was extracted from harvested protoplasts in the lysis buffer [50 mM HEPES (pH 7.5), 150 mM KCl, 1 mM EDTA, 0.5% Triton X-100, 1 mM DTT, and proteinase inhibitor cocktail (Roche LifeScience)]. Lysates were incubated with agarose-conjugated anti-Flag antibodies (Sigma-Aldrich, A2220) at 4°C for 2 hours, rinsed 6 times in the PBS-T buffer, and then eluted with 3×Flag peptide (Sigma-Aldrich). Purified GID2-Flag proteins were used for in vitro ubiquitination assays as described (*44*). Crude extracts containing recombinant GST-NGR5, purified E3 (GID2-Flag), 6×His-tagged Ubiquitin (Ub), E1 and E2 (Ubiquitinylation kit; Enzo Life Science, BML-UW9920-0001) were used. Buffer at a final concentration of 50 mM Tris-HCl (pH 7.4), 5 mM $MgCl_2$, and 2 mM ATP was also added to the system. The reactions were incubated at 30°C for 2 hours,

and terminated by adding SDS sample buffer with β-mercaptoethanol. Reaction products were separated with 12% SDS-PAGE and subjected to immunoblotting using anti-ubiquitin antibody (Abcam, ab134953) and anti-GST antibody (Santa Cruz, sc-138). Relevant primer sequences are given in table S8.

ChIP-PCR assay

ChIP assays were performed as described (*13*). A 2-g sample of 2-week-old rice plants was collected and immediately fixed with 1% (v/v) formaldehyde under vacuum for 15 min at 25°C, and then homogenized in liquid nitrogen. After the nuclei were isolated and lysed, the chromatin was ultrasonically fragmented on ice to an average size of 500 bp. Immunoprecipitations were performed with an anti-HA antibody (Santa Cruz, sc-7932x) and an anti-H3K27me3 antibody (Millipore, 07-449) overnight at 4°C. At the same time, an equal volume of the supernatant was prepared without any antibody as a mock sample. The bound DNA fragments were then reversely released and amplified by real-time quantitative PCR. Relevant primer sequences are listed in table S11.

RNA-seq

Total RNAs were extracted from tiller buds of 3-week-old 9311 plants treated with and without gibberellin and *ngr5* mutants grown in high N (1.25 mM NH_4NO_3) supply conditions using the TRIzol reagent (Invitrogen) according to the manufacturer's instructions. Libraries were constructed and sequenced using the BGISEQ-500 sequencer. Raw sequencing reads were cleaned by removing adaptor sequences, reads containing poly-N sequences, and low-quality reads, and clean reads were then mapped to the Nipponbare reference genome as described (*13*).

ChIP-seq

ChIP-Seq analysis was performed as described (*13*). Approximately 2 g of 2-week-old transgenic plants carrying the *p35S::LC2-HA* and *pNGR5::NGR5-HA* constructs grown in high N (1N, 1.25 mM NH_4NO_3) supply conditions, and of *ngr5* and wild-type plants grown in low (0.2N, 0.25 mM NH_4NO_3) or high nitrogen (1N, 1.25 mM NH_4NO_3) supply conditions with or without 100 μM GA_3 (Sigma-Aldrich, G1025) and 10 μM PAC (Sigma-Aldrich, 19847) treatments, were fixed with 1% (v/v) formaldehyde under vacuum for 15 min at 25°C, and then homogenized in liquid nitrogen. After cell lysis and nucleic acid isolation, cross-linked chromatin fibers were ultrasonically fragmented into fragments of an average size of 500 bp. Immunoprecipitations were performed with anti-HA antibodies (Santa Cruz, sc-7932) and anti-H3K27me3 antibodies (Millipore, 07-449) overnight at 4°C. The precipitated DNA was recovered by centrifugation (13,000*g*, 5 min, 25°C) and dissolved in sterile distilled water. Illumina sequencing libraries were constructed according to the manufacturer's instructions, and then sequenced on the BGISEQ-500 platform. Sequencing reads were mapped to the reference genome as described (*13*). The precipitated DNA samples also served as template for quantitative real-time PCR. Relevant primer sequences are given in table S11.

Processing of ChIP- and RNA-sequencing data

Sequencing reads were cleaned with Trimmomatic (version 0.36) (*45*) and Sickle, including elimination of bases with low-quality scores (< 25) and irregular GC contents, as well as removal of sequencing adapters and short reads. The remaining clean reads were mapped to the genome of japonica rice (MSU7.0 release) with the Burrows-Wheeler Aligner-backtrack (version 0.7.16a-r1181) (*46*) for ChIP-sequencing data and HISAT2 2.1.0 (*47*) for RNA-seq data. MACS (version 1.3.7) (*48*) was used to identify read-enriched regions (peaks) of ChIP-sequencing databased on the following combined criteria: P value < 0.00001 and fold-change > 32. Target genes were defined as genes with a peak within or near the gene body (±2 kb). DESeq (*49*) was applied to determine the significance of the differential expression between samples with the combined criteria: fold change > 2 and adj. P < 0.05.

Gene set enrichment analysis

To determine the enrichment of H3K27me3 targets in *NGR5*-regulated genes (i.e., differentially expressed genes in ngr5), we performed gene set enrichment analysis (GSEA), which is a robust computational method that determines whether an a priori gene set shows statistically significant and concordant differences between two samples (*50*). Briefly, *NGR5* regulated genes were ranked by the quantitative expression change in *ngr5*, followed by calculation of the fraction of regulated genes that are targeted by H3K27me3. The enrichment score is normalized by the size of the gene set (NES). P value is estimated by permutating genes.

Statistical analysis

Data were statistically analyzed and multiple comparisons were made using Duncan's multiple range test as described (*13*). P values of less than 0.05 were considered to indicate statistical significance. Statistical calculations were performed using Microsoft Excel 2010.

REFERENCES AND NOTES

1. G. S. Khush, Green revolution: Preparing for the 21st century. *Genome* **42**, 646–655 (1999). doi: 10.1139/g99-044; pmid: 10464789
2. P. L. Pingali, Green revolution: Impacts, limits, and the path ahead. *Proc. Natl. Acad. Sci. U.S.A.* **109**, 12302–12308 (2012). doi: 10.1073/pnas.0912953109; pmid: 22826253
3. R. E. Evenson, D. Gollin, Assessing the impact of the green revolution, 1960 to 2000. *Science* **300**, 758–762 (2003). doi: 10.1126/science.1078710; pmid: 12730592
4. P. Hedden, The genes of the Green Revolution. *Trends Genet.* **19**, 5–9 (2003). doi: 10.1016/S0168-9525(02)00009-4; pmid: 12493241
5. J. Peng *et al*., 'Green revolution' genes encode mutant gibberellin response modulators. *Nature* **400**, 256–261 (1999). doi: 10.1038/22307; pmid: 10421366
6. C. Zhang, L. Gao, J. Sun, J. Jia, Z. Ren, Haplotype variation of Green Revolution gene *Rht-D1* during wheat domestication and improvement. *J. Integr. Plant Biol.* **56**, 774–780 (2014). doi: 10.1111/jipb.12197; pmid: 24645900
7. A. Sasaki *et al*., A mutant gibberellin-synthesis gene in rice. *Nature* **416**, 701–702 (2002). doi: 10.1038/416701a; pmid: 11961544
8. W. Spielmeyer, M. H. Ellis, P. M. Chandler, Semidwarf (*sd-1*), "green revolution" rice, contains a defective gibberellin 20-oxidase gene. *Proc. Natl. Acad. Sci. U.S.A.* **99**, 9043–9048 (2002). doi: 10.1073/pnas.132266399; pmid: 12077303
9. N. P. Harberd, E. Belfield, Y. Yasumura, The angiosperm gibberellin-GID1-DELLA growth regulatory mechanism: How an "inhibitor of an inhibitor" enables flexible response to fluctuating environments. *Plant Cell* **21**, 1328–1339 (2009). doi: 10.1105/tpc.109.066969; pmid: 19470587
10. H. Xu, Q. Liu, T. Yao, X. Fu, Shedding light on integrative GA signaling. *Curr. Opin. Plant Biol.* **21**, 89–95 (2014). doi: 10.1016/j.pbi.2014.06.010; pmid: 25061896
11. H. Itoh, M. Ueguchi-Tanaka, Y. Sato, M. Ashikari, M. Matsuoka, The gibberellin signaling pathway is regulated by the appearance and disappearance of SLENDER RICE1 in nuclei. *Plant Cell* **14**, 57–70 (2002). doi: 10.1105/tpc.010319; pmid: 11826299
12. K. Asano *et al*., Artificial selection for a green revolution gene during *japonica* rice domestication. *Proc. Natl. Acad. Sci. U.S.A.* **108**, 11034–11039 (2011). doi: 10.1073/pnas.1019490108; pmid: 21646530
13. S. Li *et al*., Modulating plant growth-metabolism coordination for sustainable agriculture. *Nature* **560**, 595–600 (2018). doi: 10.1038/s41586-018-0415-5; pmid: 30111841
14. H. Sun *et al*., Heterotrimeric G proteins regulate nitrogen-use efficiency in rice. *Nat. Genet.* **46**, 652–656 (2014). doi: 10.1038/ng.2958; pmid: 24777451
15. G. W. Wu, L. T. Wilson, A. M. McClung, Contribution of rice tillers to dry matter accumulation and yield. *Agron. J.* **90**, 317–323 (1998). doi: 10.2134/agronj1998.00021962009000030001x
16. M. Ueguchi-Tanaka *et al*., GIBBERELLIN INSENSITIVE DWARF1 encodes a soluble receptor for gibberellin. *Nature* **437**, 693–698 (2005). doi: 10.1038/nature04028; pmid: 16193045
17. Z. Liao *et al*., SLR1 inhibits MOC1 degradation to coordinate tiller number and plant height in rice. *Nat. Commun.* **10**, 2738 (2019). doi: 10.1038/s41467-019-10667-2; pmid: 31227696
18. K. Aya *et al*., A novel AP2-type transcription factor, SMALL ORGAN SIZE1, controls organ size downstream of an auxin signaling pathway. *Plant Cell Physiol.* **55**, 897–912 (2014). doi: 10.1093/pcp/pcu023; pmid: 24486766
19. K. Hirano *et al*., SMALL ORGAN SIZE 1 and SMALL ORGAN SIZE 2/DWARF AND LOW-TILLERING form a complex to integrate auxin and brassinosteroid signaling in rice. *Mol. Plant* **10**, 590–604 (2017). doi: 10.1016/j.molp.2016.12.013; pmid: 28069545
20. S. Qiao *et al*., The RLA1/SMOS1 transcription factor functions with OsBZR1 to regulate brassinosteroid signaling and rice architecture. *Plant Cell* **29**, 292–309 (2017). doi: 10.1105/tpc.16.00611; pmid: 28100707
21. R. Yao *et al*., DWARF14 is a non-canonical hormone receptor for strigolactone. *Nature* **536**, 469–473 (2016). doi: 10.1038/nature19073; pmid: 27479325
22. L. Jiang *et al*., DWARF 53 acts as a repressor of strigolactone signalling in rice. *Nature* **504**, 401–405 (2013). doi: 10.1038/nature12870; pmid: 24336200
23. F. Zhou *et al*., D14-SCF(D3)-dependent degradation of D53 regulates strigolactone signalling. *Nature* **504**, 406–410 (2013). doi: 10.1038/nature12878; pmid: 24336215
24. S. Ishikawa *et al*., Suppression of tiller bud activity in tillering dwarf mutants of rice. *Plant Cell Physiol.* **46**, 79–86 (2005). doi: 10.1093/pcp/pci022; pmid: 15659436
25. T. Takeda *et al*., The OsTB1 gene negatively regulates lateral branching in rice. *Plant J.* **33**, 513–520 (2003). doi: 10.1046/j.1365-313X.2003.01648.x; pmid: 12581309
26. Y. Jiao *et al*., Regulation of OsSPL14 by OsmiR156 defines ideal plant architecture in rice. *Nat. Genet.* **42**, 541–544 (2010). doi: 10.1038/ng.591; pmid: 20495565
27. K. Miura *et al*., OsSPL14 promotes panicle branching and higher grain productivity in rice. *Nat. Genet.* **42**, 545–549 (2010). doi: 10.1038/ng.592; pmid: 20495564

28. S. Wang *et al*., Non-canonical regulation of SPL transcription factors by a human OTUB1-like deubiquitinase defines a new plant type rice associated with higher grain yield. *Cell Res.* **27**, 1142–1156 (2017). doi: 10.1038/cr.2017.98; pmid: 28776570
29. T. Arite *et al*., d14, a strigolactone-insensitive mutant of rice, shows an accelerated outgrowth of tillers. *Plant Cell Physiol.* **50**, 1416–1424 (2009). doi: 10.1093/pcp/pcp091; pmid: 19542179
30. J. Wang, J. Hu, Q. Qian, H. W. Xue, LC2 and OsVIL2 promote rice flowering by photoperoid-induced epigenetic silencing of *OsLF*. *Mol. Plant* **6**, 514–527 (2013). doi: 10.1093/mp/sss096; pmid: 22973062
31. A. Sasaki *et al*., Accumulation of phosphorylated repressor for gibberellin signaling in an F-box mutant. *Science* **299**, 1896–1898 (2003). doi: 10.1126/science.1081077; pmid: 12649483
32. X. Fu *et al*., The Arabidopsis mutant sleepy1gar2-1 protein promotes plant growth by increasing the affinity of the SCF^{SLY1} E3 ubiquitin ligase for DELLA protein substrates. *Plant Cell* **16**, 1406–1418 (2004). doi: 10.1105/tpc.021386; pmid: 15161962
33. K. Murase, Y. Hirano, T. P. Sun, T. Hakoshima, Gibberellin-induced DELLA recognition by the gibberellin receptor GID1. *Nature* **456**, 459–463 (2008). doi: 10.1038/nature07519; pmid: 19037309
34. A. Shimada *et al*., Structural basis for gibberellin recognition by its receptor GID1. *Nature* **456**, 520–523 (2008). doi: 10.1038/nature07546; pmid: 19037316
35. Z. Wu *et al*., Characterization of a new semi-dominant dwarf allele of SLR1 and its potential application in hybrid rice breeding. *J. Exp. Bot.* **69**, 4703–4713 (2018). doi: 10.1093/jxb/ery243; pmid: 29955878
36. H. Tong *et al*., DWARF AND LOW-TILLERING, a new member of the GRAS family, plays positive roles in brassinosteroid signaling in rice. *Plant J.* **58**, 803–816 (2009). doi: 10.1111/j.1365-313X.2009.03825.x; pmid: 19220793
37. W. Wang *et al*., Genomic variation in 3,010 diverse accessions of Asian cultivated rice. *Nature* **557**, 43–49 (2018). doi: 10.1038/s41586-018-0063-9; pmid: 29695866
38. S. Wang *et al*., The *OsSPL16-GW7* regulatory module determines grain shape and simultaneously improves rice yield and grain quality. *Nat. Genet.* **47**, 949–954 (2015). doi: 10.1038/ng.3352; pmid: 26147620
39. Q. Liu *et al*., G-protein βγ subunits determine grain size through interaction with MADS-domain transcription factors in rice. *Nat. Commun.* **9**, 852 (2018). doi: 10.1038/s41467-018-03047-9; pmid: 29487282
40. S. Wang *et al*., Control of grain size, shape and quality by OsSPL16 in rice. *Nat. Genet.* **44**, 950–954 (2012). doi: 10.1038/ng.2327; pmid: 22729225
41. X. Ma *et al*., A robust CRISPR/Cas9 system for convenient, high-efficiency multiplex genome editing in monocot and dicot plants. *Mol. Plant* **8**, 1274–1284 (2015). doi: 10.1016/j.molp.2015.04.007; pmid: 25917172
42. X. Huang *et al*., Natural variation at the *DEP1* locus enhances grain yield in rice. *Nat. Genet.* **41**, 494–497 (2009). doi: 10.1038/ng.352; pmid: 19305410
43. F. Wang *et al*., Biochemical insights on degradation of Arabidopsis DELLA proteins gained from a cell-free assay system. *Plant Cell* **21**, 2378–2390 (2009). doi: 10.1105/tpc.108.065433; pmid: 19717618
44. Q. Zhao *et al*., A plant-specific in vitro ubiquitination analysis system. *Plant J.* **74**, 524–533 (2013). doi: 10.1111/tpj.12127; pmid: 24695404
45. A. M. Bolger, M. Lohse, B. Usadel, Trimmomatic: A flexible trimmer for Illumina sequence data. *Bioinformatics* **30**, 2114–2120 (2014). doi: 10.1093/bioinformatics/btu170; pmid: 24695404
46. H. Li, R. Durbin, Fast and accurate short read alignment with Burrows-Wheeler transform. *Bioinformatics* **25**, 1754–1760 (2009). doi: 10.1093/bioinformatics/btp324; pmid: 19451168
47. D. Kim, B. Langmead, S. L. Salzberg, HISAT: A fast spliced aligner with low memory requirements. *Nat. Methods* **12**, 357–360 (2015). doi: 10.1038/nmeth.3317; pmid: 25751142
48. Y. Zhang *et al*., Model-based analysis of ChIP-Seq (MACS). *Genome Biol.* **9**, R137 (2008). doi: 10.1186/gb-2008-9-9-r137; pmid: 18798982
49. S. Anders, W. Huber, Differential expression analysis for sequence count data. *Genome Biol.* **11**, R106 (2010). doi: 10.1186/gb-2010-11-10-r106; pmid: 20979621
50. A. Subramanian *et al*., Gene set enrichment analysis: A knowledge-based approach for interpreting genome-wide expression profiles. *Proc. Natl. Acad. Sci. U.S.A.* **102**, 15545–15550 (2005). doi: 10.1073/pnas.0506580102; pmid: 16199517

ACKNOWLEDGMENTS

We thank C. Sun for providing the CSSLs, Q. Qian for providing *d14*, Z. Cheng for providing *Slr1-d6*, and M. Matsuoka for critical comments on the manuscript. **Funding:** Supported by the National Key Research and Development Program of China (2016YFD0100401, 2016YFD0100706), the National Key Program on Transgenic Research from the Ministry of Agriculture of China (2016ZX08009-001, 2016ZX08009-003), the National Natural Science Foundation of China (31830082, 31921005, 91935301, 31970304), the Strategic Priority Research Program of the Chinese Academy of Sciences (XDB27010000), and the Biological and Biotechnological Sciences Research Council (UK) "Newton Fund" Rice Research Initiative grant BB/N013611/1. **Author contributions:** K.W. performed most of the experiments; K.W., B.L., and Y.W. conducted the *NGR5* mutation screening; S.W. and K.W. performed map-based cloning and genetic complementation; K.W., W.S., J.C., and J.Z. constructed NILs and mutant plants; K.W., S.W., S.L., and Q.L. characterized the phenotypes of transgenic plants; W.S., X.W., and K.W. conducted protein-protein interactions; K.W., Y.Z., and J.W. performed field experiments; M.W., K.W., and Y.J.Z. performed analysis of ChIP-seq and RNA-seq; Y.W. and J.Y. performed haplotype analysis; K.W., N.P.H., and X.F. designed experiments; N.P.H. and X.F. wrote the manuscript; and all authors discussed and commented on the manuscript. **Competing interests:** The authors declare no competing interests. **Data and materials availability:** The raw sequence data reported in this paper have been deposited in the Genome Sequence Archive in BIG Data Center of CRA002108 that are publicly accessible at https://bigd.big.ac.cn/gsa. Requests for materials should be addressed to X.F. All of the data pertaining to the work are contained within the figures and supplementary materials.

SUPPLEMENTARY MATERIALS

science.sciencemag.org/content/367/6478/eaaz2046/suppl/DC1
Materials and Methods
Figs. S1 to S15
Tables S1 to S11

20 August 2019; accepted 18 December 2019
10.1126/science.aaz2046

RESEARCH ARTICLE SUMMARY

IMMUNOLOGY

Butyrophilin 2A1 is essential for phosphoantigen reactivity by γδ T cells

Marc Rigau, Simone Ostrouska, Thomas S. Fulford, Darryl N. Johnson, Katherine Woods, Zheng Ruan, Hamish E.G. McWilliam, Christopher Hudson, Candani Tutuka, Adam K. Wheatley, Stephen J. Kent, Jose A. Villadangos, Bhupinder Pal, Christian Kurts, Jason Simmonds, Matthias Pelzing, Andrew D. Nash, Andrew Hammet, Anne M. Verhagen, Gino Vairo, Eugene Maraskovsky, Con Panousis, Nicholas A. Gherardin, Jonathan Cebon, Dale I. Godfrey*†, Andreas Behren*†, Adam P. Uldrich*†

INTRODUCTION: T cells represent a key component of the immune system that can recognize foreign molecules (antigens) via cognate cell surface receptors termed T cell receptors (TCRs). The two main families of T cells, known as αβ and γδ T cells, are defined by the different gene loci that they use to generate their respective TCRs. αβ T cells typically recognize antigens displayed on the surface of target cells in association with antigen-presenting molecules known as major histocompatibility complex (MHC) molecules. Much less is known about how γδ T cells recognize antigen, although it is clear they are also essential to protective immunity. In humans, many γδ T cells (classified as Vγ9Vδ2 T cells) respond to small phosphorylated nonpeptide antigens, called phosphoantigens (pAgs), which are produced by cellular pathogens and cancers. In turn, γδ T cells become activated, proliferate, rapidly produce proinflammatory cytokines such as IFN-γ, and exert cytotoxic activity. pAg recognition appears to involve a cell surface molecule, butyrophilin 3A1 (BTN3A1), which plays a necessary, but not sufficient, role in this process. Therefore, the molecular basis that underpins pAg recognition by Vγ9Vδ2 T cells remains unclear and represents a long-standing conundrum, which has impeded the study of these important immune cells.

RATIONALE: In contrast to αβ T cells, Vγ9Vδ2 T cells are not MHC-restricted and can recognize pAg expressed by multiple cancers and infectious diseases. Thus, they represent an attractive target for the development of new immunotherapy treatments. A much clearer understanding of the molecular basis for pAg recognition is required to optimally harness these cells for immunotherapy. We undertook a multipronged approach to investigate which molecules are necessary for pAg detection by γδ T cells. We used a genome-wide screen to identify molecules that mediate pAg-driven γδ T cell activation. Furthermore, we asked if these molecules directly bind to the Vγ9Vδ2 TCR and how they work in conjunction with BTN3A1.

RESULTS: The top candidate molecule identified in our genome-wide screen was butyrophilin 2A1 (BTN2A1), a molecule distinct from, but related to, BTN3A1. We show that without BTN2A1, Vγ9Vδ2 T cells cannot be activated by either bacterial or mammalian pAgs, and that BTN2A1 expression was required for Vγ9Vδ2 T cell–mediated tumor cell killing. Neither BTN3A1 nor the other butyrophilin family members tested can compensate for loss of BTN2A1. BTN2A1 can bind directly to the Vγ9Vδ2 TCR and associates closely with BTN3A1 on the surface of target cells. We also identify an important role for the transmembrane and/or intracellular domain of BTN2A1. Furthermore, pAg-mediated activation of γδ T cells requires coexpression of both BTN2A1 and BTN3A1, which together appear to convey pAg recognition and responsiveness by Vγ9Vδ2 T cells. Lastly, we show that BTN2A1 binds to the side of the Vγ9 domain of the TCR, and also reveal the existence of a critical putative second ligand-binding domain on a separate region of the TCR that incorporates Vδ2. Disruption of either of these binding sites abrogated the ability of Vγ9Vδ2 T cells to respond to pAg.

ON OUR WEBSITE

Read the full article at http://dx.doi.org/10.1126/science.aay5516

CONCLUSION: Our findings suggest that γδ T cells recognize pAg in an entirely different way to how any other immune cell recognizes antigen. We propose a model whereby BTN2A1 and BTN3A1 co-bind the Vγ9Vδ2 TCR in response to pAg. This pAg likely modifies the BTN2A1–BTN3A1 complex to make it stimulatory, which may occur through BTN molecule remodeling and/or conformational changes. Targeting these molecules will create new opportunities for the development of γδ T cell–based immunotherapies for diseases in which pAgs are produced, including infections, autoimmunity, and cancer. ■

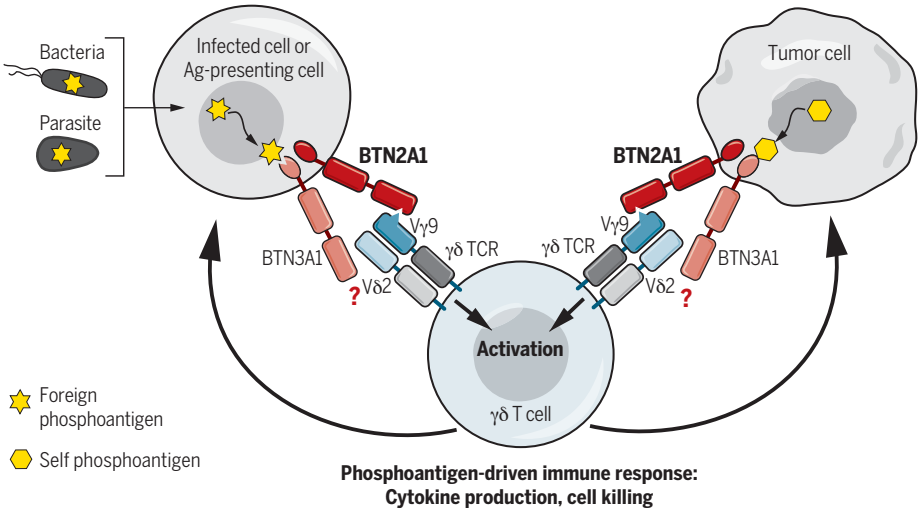

Butyrophilin 2A1 plays a critical role in phosphoantigen recognition by human T cells. Human γδ T cells become activated in response to microbial and cancer-derived phosphoantigens, but the molecular mechanism for phosphoantigen recognition remained unclear. We show that a critical component of this recognition is the cell-surface molecule butyrophilin 2A1 (BTN2A1), which binds to the γδ TCR and in conjunction with BTN3A1, signals the presence of phosphoantigens to γδ T cells.

The list of author affiliations is available in the full article online.
*These authors contributed equally to this work.
†Corresponding author. Email: auldrich@unimelb.edu.au (A.P.U.); andreas.behren@onjcri.org.au (A.B.); godfrey@unimelb.edu.au (D.I.G.)
Cite this article as M. Rigau *et al.*, *Science* **367**, eaay5516 (2020). DOI: 10.1126/science.aay5516

RESEARCH ARTICLE

IMMUNOLOGY

Butyrophilin 2A1 is essential for phosphoantigen reactivity by γδ T cells

Marc Rigau[1,2,3], Simone Ostrouska[4,5], Thomas S. Fulford[1], Darryl N. Johnson[1,3], Katherine Woods[4,5,6], Zheng Ruan[1,3], Hamish E.G. McWilliam[1,7], Christopher Hudson[6], Candani Tutuka[4,5], Adam K. Wheatley[1,8], Stephen J. Kent[1,8], Jose A. Villadangos[1,7], Bhupinder Pal[4,5], Christian Kurts[2], Jason Simmonds[9], Matthias Pelzing[9], Andrew D. Nash[9], Andrew Hammet[9], Anne M. Verhagen[9], Gino Vairo[9], Eugene Maraskovsky[9], Con Panousis[9], Nicholas A. Gherardin[1], Jonathan Cebon[4,5,6,10,11], Dale I. Godfrey[1,3]*†, Andreas Behren[4,5,6,10]*†, Adam P. Uldrich[1,3]*†

Gamma delta (γδ) T cells are essential to protective immunity. In humans, most γδ T cells express Vγ9Vδ2$^+$ T cell receptors (TCRs) that respond to phosphoantigens (pAgs) produced by cellular pathogens and overexpressed by cancers. However, the molecular targets recognized by these γδTCRs are unknown. Here, we identify butyrophilin 2A1 (BTN2A1) as a key ligand that binds to the Vγ9$^+$ TCR γ chain. BTN2A1 associates with another butyrophilin, BTN3A1, and these act together to initiate responses to pAg. Furthermore, binding of a second ligand, possibly BTN3A1, to a separate TCR domain incorporating Vδ2 is also required. This distinctive mode of Ag-dependent T cell activation advances our understanding of diseases involving pAg recognition and creates opportunities for the development of γδ T cell–based immunotherapies.

Alpha beta (αβ) T cells recognize antigens (Ags) via T cell receptors (TCRs), encoded by *TRA* and *TRB* gene loci, which bind to Ags displayed by Ag-presenting molecules. This fundamental principle applies to αβ T cells that recognize peptide Ags presented by major histocompatibility complex (MHC) molecules, natural killer T (NKT) cells that recognize lipid Ags presented by CD1d, and mucosal-associated invariant T (MAIT) cells that recognize vitamin B metabolites presented by MR1 (*1*). γδ T cells are a specialized lineage that express TCRs derived from separate variable (V), diversity (D), joining (J) and constant (C) *TRG* and *TRD* gene loci. Most circulating human γδ T cells express Vγ9Vδ2$^+$ TCRs that react to a distinct class of Ag, termed phosphoantigens (pAgs) (*2*, *3*). pAgs are intermediates in the biosynthesis of isoprenoids and are present in virtually all cellular organisms. Vertebrates produce isoprenoids via the mevalonate pathway, whereas microbes utilize the nonmevalonate pathway, and these pathways yield chemically distinct pAg intermediates (*4*). Vγ9Vδ2$^+$ T cells sense pAgs produced via either pathway, including isopentenyl pyrophosphate (IPP) from the mevalonate pathway and 4-hydroxy-3-methyl-but-2-enyl pyrophosphate (HMBPP) from the nonmevalonate pathway. However, these cells show roughly 1000-fold higher sensitivity to microbial HMBPP than to vertebrate IPP pAgs (*5*). Thus, Vγ9Vδ2$^+$ T cells can respond to HMBPP derived from microbial infection, but also to accumulated IPP in abnormal cells such as cancer cells. During bacterial and parasitic infections, pAg drives Vγ9Vδ2$^+$ T cells to produce cytokines and expand to represent ~10 to 50% of peripheral blood mononuclear cells (PBMCs) (*6*, *7*). The important role that Vγ9Vδ2$^+$ T cells play in antibacterial immunity was demonstrated by human PBMC transfer into immune-deficient mice, which led to Vγ9Vδ2$^+$ T cell–dependent protection against bacterial infection (*8*). They can also kill diverse tumor cell lines in vitro in a pAg-dependent manner, and numerous clinical trials have examined their anticancer potential, with some encouraging results (*9*).

The molecular mechanisms governing pAg recognition by γδ T cells are unclear. Cell contact and Vγ9Vδ2$^+$ TCR expression are required, but classical Ag-presenting molecules such as MHC or MHC-like molecules are dispensable, suggesting a mechanism that is distinct from αβ T cell Ag recognition (*10*, *11*). Butyrophilin (BTN) surface protein BTN3A1 expression on Ag-presenting cells (APCs) plays a key role in pAg recognition (*12*), binding pAg via its intracellular B30.2 domain (*5*, *13*, *14*). After pAg binding, BTN3A1 intracellular (*15*, *16*) and extracellular (*17*) domains may undergo a conformational change that is important for γδTCR-mediated responses. This may be mimicked by an agonist anti-BTN3A1 monoclonal antibody (mAb) that stimulates Vγ9Vδ2$^+$ T cells without requiring exogenous pAg (*12*, *18*). However, a simplistic 1:1 interaction model between BTN3A1 and the γδTCR is unlikely because there is little evidence for a direct interaction between these molecules (*5*), and *BTN3A1* transfection into rodent APCs fails to restore pAg-presenting capability, unless an extra, undefined gene or genes on human chromosome 6 are included (*5*, *19*). Thus, other ligands in addition to BTN3A1 appear to be required for the γδ T cell response to pAg.

Here, we identify BTN2A1 as a direct ligand for the Vγ9Vδ2$^+$ TCR, and furthermore, we show that this ligand plays a critical role in pAg recognition by γδ T cells. BTN2A1 closely associates with BTN3A1 on the surface of APCs, and this complex can transmit pAg-mediated activation of Vγ9Vδ2$^+$ T cells. Accordingly, we propose a model whereby BTN2A1 acts in unison with BTN3A1 to license γδ T cell responses to pAg.

Results

BTN2A1 is a ligand for Vγ9$^+$ γδTCRs

To identify candidate ligands for Vγ9Vδ2$^+$ γδ TCRs, we generated soluble Vγ9Vδ2$^+$ TCR tetramers derived from pAg-reactive γδ T cells (fig. S1) and used them to stain a diverse panel of human cell lines. This revealed clear staining of some lines, including HEK-293T, but not others, including the B cell line C1R (Fig. 1A). In particular, a melanoma cell line, LM-MEL-62, was strongly stained (*20*) (Fig. 1A). Using a genome-wide knockdown screen on the LM-MEL-62 cell line, we found that the most significant guide RNA (gRNA) responsible for Vγ9Vδ2$^+$ TCR tetramer reactivity was *BTN2A1*, with a >13-fold enrichment compared to the controls (Fig. 1B and fig. S2). BTN2A1 is a poorly characterized member of the butyrophilin family, found in humans but not mice. Like BTN3A1, it consists of two extracellular domains (IgV and IgC) and an intracellular B30.2 domain. Apart from one study suggesting that it may interact with the C-type lectin receptor CD209 (DC-SIGN) in a glycosylation-dependent manner (*21*), BTN2A1 is generally considered an orphan receptor. To further investigate the relevance of this finding, we confirmed a loss of reactivity to Vγ9Vδ2$^+$ TCR tetramers in two independent LM-MEL-62 *BTN2A1*-mutant lines (*BTN2A1*^{null}

[1]Department of Microbiology and Immunology at the Peter Doherty Institute for Infection and Immunity, The University of Melbourne, Parkville, Victoria 3010, Australia. [2]University of Bonn, Bonn, Germany. [3]Australian Research Council Centre of Excellence for Advanced Molecular Imaging at the University of Melbourne, Victoria 3010, Australia. [4]Olivia Newton-John Cancer Research Institute, Heidelberg, Victoria 3084, Australia. [5]School of Cancer Medicine, La Trobe University, Heidelberg, Victoria 3084, Australia. [6]Ludwig Institute for Cancer Research, Melbourne -Austin Branch, Victoria 3084, Australia. [7]Department of Biochemistry and Molecular Biology at the Bio21 Molecular Science and Biotechnology Institute, The University of Melbourne, Parkville, Victoria 3010, Australia. [8]Australian Research Council Centre of Excellence for Convergent Bio-Nano Science and Technology at the University of Melbourne, Victoria 3010, Australia. [9]CSL Limited at the Bio21 Molecular Science and Biotechnology Institute, The University of Melbourne, Parkville, Victoria 3010, Australia. [10]Department of Medicine, The University of Melbourne, Melbourne, Victoria 3010, Australia. [11]Austin Health, Heidelberg, Victoria 3084, Australia.
*These authors contributed equally to this work.
†Corresponding author. Email: auldrich@unimelb.edu.au (A.P.U.); andreas.behren@onjcri.org.au (A.B.); godfrey@unimelb.edu.au (D.I.G.)

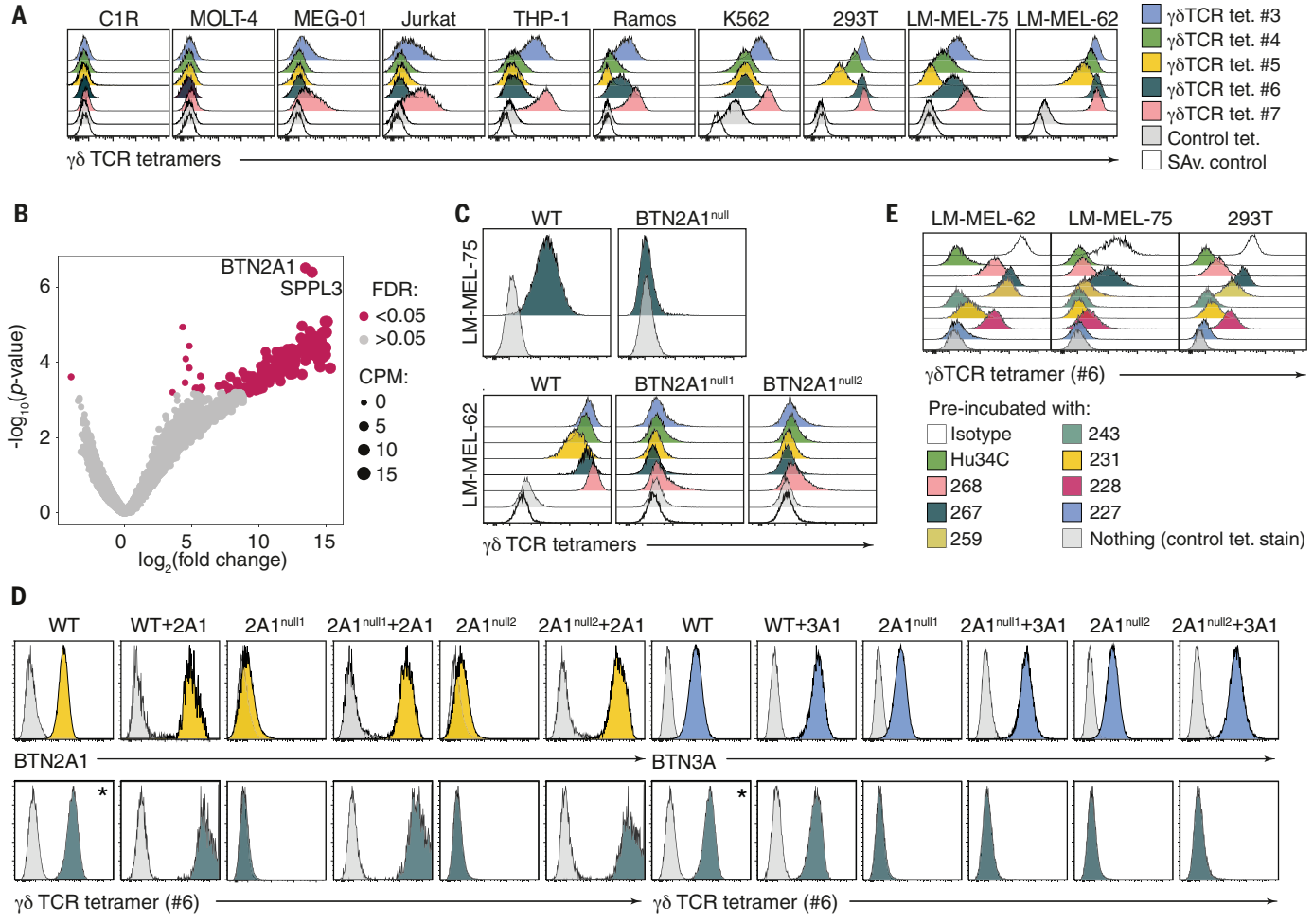

Fig. 1. Vγ9Vδ2$^+$ γδ T cell receptor tetramer staining is dependent on BTN2A1. (**A**) Vγ9Vδ2$^+$ TCR tetramer staining of various cell lines. Colored histograms depict γδTCR tetramers #3 to #7; gray, irrelevant control (mouse CD1d–α-GalCer) tetramer; unfilled, streptavidin (SAv)–PE control. (**B**) Volcano plot depicting $\log_2$ (fold-change) versus $-\log_{10}$ (*p* value) for each gRNA, between unsorted and Vγ9Vδ2 TCR tetramer #6^{lo} LM-MEL-62 cells, where magenta depicts significant differences [false discovery rate (FDR) < 0.05]. CPM, counts per million. (**C**) Vγ9Vδ2$^+$ TCR tetramer staining of LM-MEL-62 *BTN2A1*^{null} and LM-MEL-75 *BTN2A1*^{null} cells compared to parental (wild type, WT) cells. Color scheme as in (A). (**D**) Anti-BTN2A1 mAb (clone 231, yellow), anti-BTN3A1/3A2/3A3 mAb (clone 103.2, blue), and Vγ9Vδ2$^+$ TCR tetramer (#6) staining (dark green) on parental and *BTN2A1*$^{null1\ or\ null2}$ LM-MEL-62 cells transfected with either *BTN2A1* or *BTN3A1*. *γδTCR tetramer staining is depicted twice. (**E**) Vγ9Vδ2$^+$ TCR tetramer #6 staining of LM-MEL-62, LM-MEL-75, and HEK-293T cells, after preincubation of cells with a panel of anti-BTN2A1 mAb (colored histograms), compared to isotype control unfilled. Lower histograms (gray) depict control staining with irrelevant mouse CD1d–α-GalCer tetramer. tet, tetramer. Data in (A), (C), (D), and (E) are representative of two independent experiments 293T, HEK-293T.

and *BTN2A1*^{null2}), with similar results also from a distinct LM-MEL-75 *BTN2A1*-mutant cell line (Fig. 1C and fig. S3). This was independent of BTN3A1 expression, which was essentially unchanged between parental LM-MEL-62 and *BTN2A1*^{null} lines (Fig. 1D and fig. S3A). Additionally, Vγ9Vδ2$^+$ TCR tetramer reactivity of *BTN3A1*^{null} lines was comparable to that of parental lines (fig. S3B). Reintroduction of *BTN2A1* into either LM-MEL-62 *BTN2A1*^{null1} or *BTN2A1*^{null2} cells restored Vγ9Vδ2$^+$ TCR tetramer reactivity, whereas transfection with *BTN3A1* had no effect (Fig. 1D). Thus, BTN2A1 expression is essential for Vγ9Vδ2$^+$ TCR tetramer reactivity.

We next generated a panel of BTN2A1-reactive mAbs, which exhibited varying degrees of cross-reactivity to BTN2A2 (87% ectodomain homology) but not to BTN3A2 (45% ectodomain homology) (fig. S4, A to C). These mAbs stained parental LM-MEL-62, but most failed to bind to LM-MEL-62 *BTN2A1*^{null} lines, confirming their reactivity to BTN2A1 (fig. S4, D and E). Most of the anti-BTN2A1 mAbs fully or partially blocked Vγ9Vδ2$^+$ TCR tetramer staining on LM-MEL-62, LM-MEL-75, and 293T cells (Fig. 1E), suggesting that BTN2A1 is a ligand for the Vγ9Vδ2$^+$ γδTCR.

To explore whether BTN2A1 selectively binds to Vγ9Vδ2$^+$ γδ T cells, we produced fluorescent BTN2A1 ectodomain tetramers (fig. S5), which stained a subset of CD3$^+$ T cells within PBMCs, but no other cell type (Fig. 2A). The BTN2A1 tetramer$^+$ cells were γδTCR$^+$, but not αβTCR$^+$ (Fig. 2A). BTN2A1 tetramer labeled essentially all Vγ9$^+$Vδ2$^+$ and Vγ9$^+$Vδ1$^+$ γδ T cells, but no Vγ9$^-$Vδ1$^+$ γδ T cells, suggesting that the Vγ9 domain of the TCR γ chain is associated with reactivity (Fig. 2B). Furthermore, Förster resonance energy transfer (FRET) between fluorescent BTN2A1 tetramer and anti-CD3ε mAb (*22*) indicated that BTN2A1 tetramer was binding within ~10 nm of the γδTCR (Fig. 2C). To directly assess whether BTN2A1 binds Vγ9$^+$ γδTCR, we performed surface plasmon resonance (SPR) to measure interactions between soluble BTN2A1 and γδTCR ectodomains. Consistent with the pattern of BTN2A1 tetramer reactivity among primary γδ T cells, soluble BTN2A1 bound Vγ9Vδ2$^+$ TCR (TCR #6) with an affinity of K_D = 40 μM, similar to what is observed

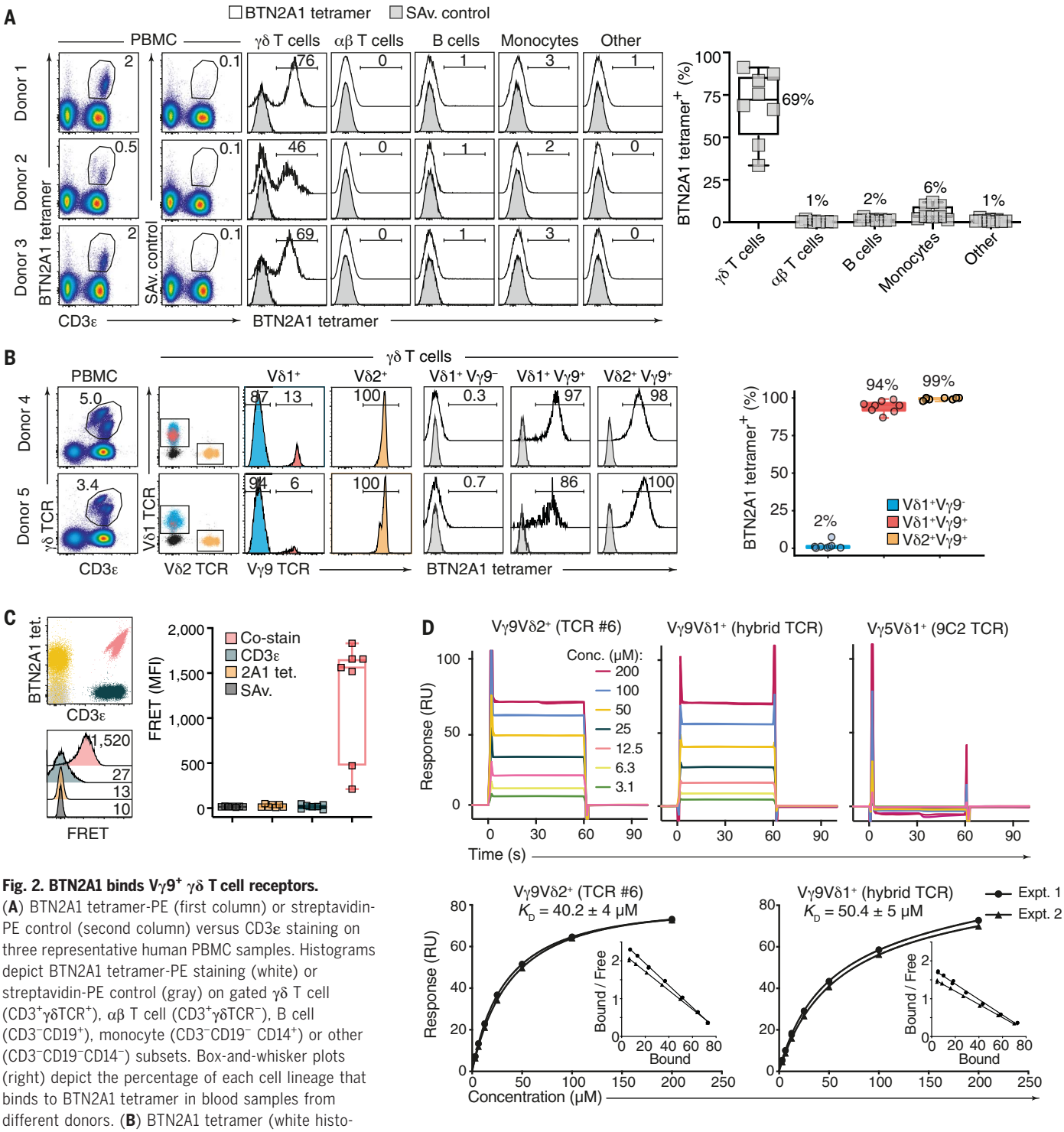

Fig. 2. BTN2A1 binds Vγ9+ γδ T cell receptors.
(**A**) BTN2A1 tetramer-PE (first column) or streptavidin-PE control (second column) versus CD3ε staining on three representative human PBMC samples. Histograms depict BTN2A1 tetramer-PE staining (white) or streptavidin-PE control (gray) on gated γδ T cell ($CD3^+\gamma\delta TCR^+$), αβ T cell ($CD3^+\gamma\delta TCR^-$), B cell ($CD3^-CD19^+$), monocyte ($CD3^-CD19^-$ $CD14^+$) or other ($CD3^-CD19^-CD14^-$) subsets. Box-and-whisker plots (right) depict the percentage of each cell lineage that binds to BTN2A1 tetramer in blood samples from different donors. (**B**) BTN2A1 tetramer (white histograms) overlaid with streptavidin-PE alone control (gray histograms) staining, on $V\gamma9^+V\delta2^+$ (orange), $V\gamma9^+V\delta1^+$ (pink), or $V\gamma9^-V\delta1^+$ (blue) T cells, with parent gating shown to the left. Box-and-whisker plots (right) depict the percentage of each γδ T cell subset that binds to BTN2A1 tetramer-PE in different donors. (**C**) FRET fluorescence (histogram overlays) between BTN2A1 tetramer-PE and CD3ε-APC on dual-stained (pink) or single-stained controls (orange and dark green, respectively), using purified in vitro–expanded $V\delta2^+$ T cells. Box-and-whisker plots depict FRET median fluorescence intensity (MFI) in γδ T cell subsets from different human donors. (**D**) Binding of soluble BTN2A1 (200 to 3.1 μM) to immobilized $V\gamma9^+V\delta2^+$ ("TCR #6," left), $V\gamma9^+V\delta1^+$ ("hybrid," middle), and $V\gamma5^+V\delta1^+$ ("9C2," right) γδTCRs, as measured by surface plasmon resonance. Saturation plots (below) depict binding at equilibrium, and Scatchard plots. K_D, dissociation constant at equilibrium ± SEM; SAv, streptavidin. Data represent (A) $n = 8$ donors pooled from two independent experiments; (B) $n = 8$ donors from two experiments; (C) $n = 7$ donors pooled from three independent experiments; (D) $n = 2$ separate experiments, one of which (Expt. 2) was performed in duplicate and averaged.

for classical αβ T cells (*23*). It also bound a "hybrid" γδTCR that coexpressed the TCR #6 γ chain paired with an irrelevant Vδ1$^+$ δ chain with comparable affinity (50 μM). However, BTN2A1 did not bind to a γδTCR comprising a Vγ5$^+$ γ chain paired with the Vδ1$^+$ δ chain (Fig. 2D). Lastly, we tested whether cells transfected with other butyrophilin family members could bind to Vγ9Vδ2$^+$ TCR. BTN2A2 exhibited only very weak binding, and BTN3A1+BTN3A2 and BTNL3+BTNL8 did not bind Vγ9Vδ2$^+$ TCR tetramers (fig. S6). Thus, BTN2A1 is a ligand for Vγ9$^+$ γδTCR.

BTN2A1 is important for γδ T cell responses to pAg

We next determined if BTN2A1 is important in pAg-mediated γδ T cell responses. As expected, PBMCs cultured with the aminobisphosphonate compound zoledronate, which induces accumulation of the pAg IPP (*24*), resulted in Vδ2$^+$ but not Vδ1$^+$ γδ T cell induction of CD25 and down-regulation of surface CD3 (Fig. 3A), and production of interferon-γ (IFN-γ) and tumor necrosis factor (TNF) (Fig. 3B). These indicators of TCR-dependent activation were significantly inhibited by anti-BTN2A1 mAb clone Hu34C and, to a lesser extent, by clones 259 and 267, compared to isotype control mAb-treated samples. Next, purified in vitro pre-expanded Vδ2$^+$ γδ T cells were cultured with parental or *BTN2A1*^{null} LM-MEL-62 cells as APCs. Robust Vδ2$^+$ γδ T cell responses to zoledronate, in terms of CD25 up-regulation and CD3 down-regulation, were observed in the presence of parental LM-MEL-62 APCs. However, both *BTN2A1*^{null1} and *BTN2A1*^{null2} APCs failed to promote γδ T cell activation above the level of control cultures without APCs (Fig. 3C). Similarly, the proliferative expansion of Vδ2$^+$ γδ cells was diminished when *BTN2A1*^{null1} APCs were used (Fig. 3D). There was also γδ T cell–mediated, zoledronate-dependent, killing of parental LM-MEL-62 tumor cells, which was not observed with *BTN2A1*^{null1} cells, suggesting that BTN2A1 is important for Vγ9Vδ2$^+$ γδ T cell cytotoxicity of tumor targets (Fig. 3E). Thus, BTN2A1 is important for γδ T cell responses to endogenous forms of pAg.

Vγ9Vδ2$^+$ γδ T cells can self-present high-affinity foreign forms of pAg such as microbial HMBPP in the absence of APCs (*11*). BTN2A1 was also indispensable in this setting because purified in vitro pre-expanded Vδ2$^+$ γδ T cells failed to up-regulate CD25 and produce IFN-γ in the presence of neutralizing anti-BTN2A1 mAb (clones Hu34C, 227, 236, and 266) (Fig. 3F). Clone 267 was only a partial inhibitor of HMBPP-induced activation (Fig. 3F). Notably, these mAbs did not inhibit anti-CD3– plus anti-CD28–mediated activation (Fig. 3F) nor did they block primary CD8$^+$ αβ T cell activation mediated by a mixture of viral peptides derived from cytomegalovirus, Epstein–Barr virus, and influenza epitopes ("CEF" peptide, fig. S7). Thus, these BTN2A1 mAbs are specific antagonists of both self and foreign forms of pAg-driven T cell immunity. Taken together, BTN2A1 plays an important role in pAg-mediated Vγ9Vδ2$^+$ γδ T cell activation and resultant cytokine production, proliferation, and antitumor cytotoxicity by these cells.

BTN2A1 cooperates with BTN3A1 to elicit pAg responses by γδ T cells

We next determined if BTN2A1-dependent pAg responses are specifically mediated via γδTCR signaling. After coculture with either parental LM-MEL-75 or LM-MEL-62 APCs, J.RT3-T3.5 (Jurkat) T cells expressing the prototypical "G115" Vγ9Vδ2$^+$ TCR clonotype (*25*) up-regulated CD69 in response to zoledronate. By contrast, *BTN2A1*^{null} and *BTN3A1*^{null} APCs largely failed to induce pAg reactivity (Fig. 4A). Untransduced (parental) Jurkat cells or those expressing an irrelevant γδTCR (clone 9C2 (*26*)) also failed to respond to pAg. Similar results were obtained with HMBPP and IPP (fig. S8, A to C). Thus, BTN2A1 and BTN3A1 are both required to specifically mediate pAg responses in a Vγ9Vδ2$^+$ TCR-dependent manner.

Although BTN3A1 is essential for pAg-mediated responses, forced BTN3A1 overexpression fails to confer pAg-driven γδ T cell–stimulatory capacity to hamster and mouse APCs, indicating a requirement for other factors (*5*, *19*). We found that both hamster and mouse APCs transfected with *BTN2A1* and *BTN3A1* in combination, but not singly, were capable of pAg-dependent activation of γδ T cells (Fig. 4B and fig. S9, A and B). Although another butyrophilin molecule, BTN3A2, was not necessary for this response, it moderately enhanced activation of γδ T cells when combined with BTN2A1 and BTN3A1, consistent with its potential role in increasing BTN3A1 activity (*27*). A modified *BTN2A1* construct with irrelevant transmembrane and intracellular domains derived from mouse paired immunoglobulin-like type 2 receptor beta, termed BTN2A1ΔB30, was also tested. This was still expressed on the cell surface and bound Vγ9Vδ2$^+$ TCR tetramer (fig. S9C), but it did not confer pAg-mediated activation (Fig. 4C). Thus, in addition to the role of its extracellular domain in binding Vγ9$^+$ γδTCR, the intracellular or transmembrane domain of BTN2A1 may also be important for pAg-mediated activation of Vγ9Vδ2$^+$ γδ T cells. This did not appear to be due to the intracellular B30.2 domain of BTN2A1 directly binding purified pAgs (HMBPP or IPP) because no clear interaction between these molecules was detected by isothermal titration calorimetry (fig. S10). This was in contrast to the clear interaction between the BTN3A1 B30.2 domain with pAg, as expected (*5*, *15*, *16*).

Lastly, we tested whether BTN2A1 and BTN3A1 induce pAg-mediated activation when expressed on the same cell (in cis) or on separate cells (in trans). BTN2A1$^+$ APCs mixed with either BTN3A1$^+$ APCs or BTN3A1$^+$BTN3A2$^+$ APCs failed to elicit γδ T cell responses to pAg (Fig. 4D), suggesting that these molecules must be expressed on the same APC to mediate pAg-induced activation of γδ T cells.

BTN2A1 associates with BTN3A molecules on the cell surface

The requirement for BTN2A1 and BTN3A1 coexpression in cis raised the possibility that they associate with each other. Parental LM-MEL-75 cells stained with anti-BTN2A1 and anti-BTN3A1/3A2/3A3 ("BTN3A molecules") mAbs showed a similar staining pattern for BTN2A1 and BTN3A molecules on the cell surface (Fig. 5, A to C). Pearson correlation coefficients indicated a significant overlap between the staining of BTN2A1 and BTN3A molecules, compared to the overlap of either with an irrelevant control (pan-HLA-A,B,C). Thus, BTN2A1 and BTN3A molecules appear to associate with one another on the plasma membrane (Fig. 5B). Furthermore, costaining of LM-MEL-75 cells with anti-BTN2A1 (clone 259) and anti-BTN3A (clone 103.2) resulted in a clear FRET signal (Fig. 5C), indicative of colocalization on the cell surface. Costaining with anti-BTN3A (clone 20.1) failed to cause FRET. Likewise, other anti-BTN2A1 clones (Hu34C and 267) resulted in only weak FRET. This may be because some mAb combinations yield spatially segregated donor and acceptor fluorochromes beyond the 10-nm limit for FRET detection. Similar results were derived with mouse NIH-3T3 fibroblasts transfected with different combinations of BTN molecules (fig. S11). Staining of BTN2A1ΔB30$^+$BTN3A1$^+$ or BTN2A1ΔB30$^+$BTN3A2$^+$ NIH-3T3 cells with anti-BTN2A1 and anti-BTN3A also resulted in FRET. The latter findings suggest that the association between these molecules is independent of the B30.2 domains, because BTN3A2 also lacks a B30.2 domain (fig. S11).

We next determined whether the intracellular domains of BTN2A1 and BTN3A1 are also in close proximity to each other, by generating cyan fluorescent protein (CFP)– or yellow fluorescent protein (YFP)–conjugated butyrophilin constructs (fig. S12). Cotransfection of mouse NIH-3T3 fibroblasts with BTN2A1^{CFP}+BTN3A1^{YFP} or BTN2A1^{YFP}+BTN3A1^{CFP} resulted in clear FRET signals, similar to the positive controls that are known to associate [butyrophilin-like molecule 3 (BTNL3)^{CFP}+BTNL8^{YFP}] (*27*). Little to no FRET occurred in BTN3A1^{CFP}+BTNL8^{YFP} or BTNL3^{CFP}+BTN2A1^{YFP} or single-transfectant controls (Fig. 5D and fig. S13A). We also tested whether pAg modulated the FRET signal between BTN2A1 and BTN3A1 but did not detect any major changes (fig. S13, B and C). However, anti-BTN2A1 mAb clones with antagonist activity (from Fig. 3D) all strongly disrupted their

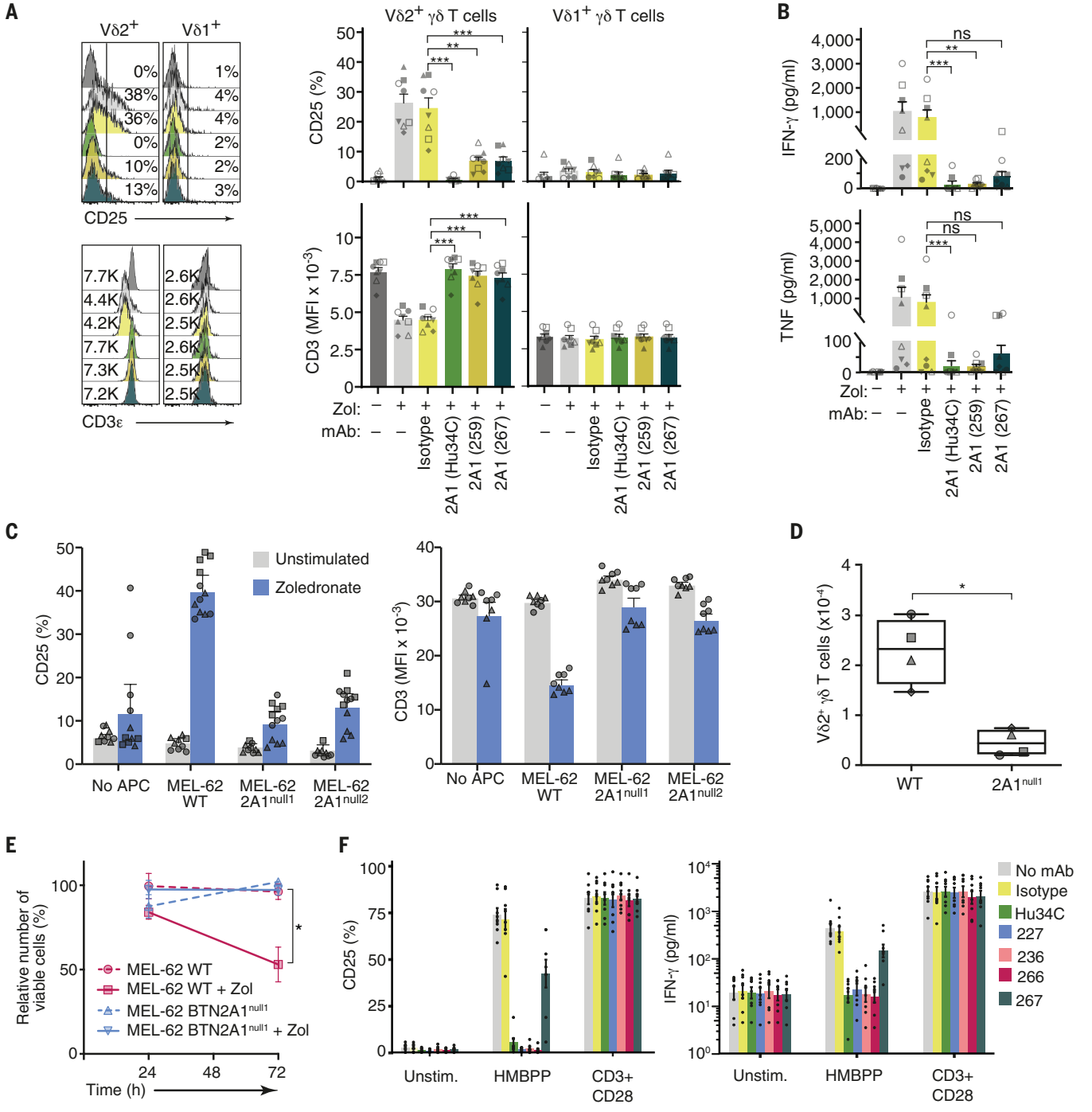

Fig. 3. γδ T cell functional responses to pAg depend on BTN2A1. (**A**) CD25 expression and CD3ε mean fluorescence intensity (MFI) on Vδ2$^+$ and control Vδ1$^+$ T cells gated among PBMCs cultured for 24 hours ± 4 μM zoledronate and ± 10 μg/ml neutralizing anti-BTN2A1 mAb as indicated. $^{**}p < 0.01$, $^{***}p < 0.001$, by ANOVA. (**B**) IFN-γ and TNF concentration in the culture supernatants from (A). $^{**}p < 0.01$, $^{***}p < 0.001$, by Friedman test. (**C**) CD3 MFI and CD25 expression on purified in vitro–expanded Vδ2$^+$ T cells cocultured with parental or *BTN2A1*^{null} LM-MEL-62 APCs without (gray) or with (blue) 4 μM zoledronate. Each symbol represents a different donor. Bar graphs depict mean ± SEM of the donors, each averaged from the technical replicates. (**D**) Number of Vδ2$^+$ γδ T cells in cocultures of PBMCs with parental or *BTN2A1*^{null1} LM-MEL-62 APC after a 2-day challenge with 1 μM zoledronate followed by maintenance of nonadherent PBMCs for an additional 7 days in media containing IL-2. $^*p < 0.05$ using a Mann–Whitney test. (**E**) Cell viability (mean ± SEM) as determined using the metabolic dye MTS, normalized against input cell number, of cocultures of parental (WT) or BTN2A1^{null} LM-MEL-62 targets with in vitro–expanded Vδ2$^+$ T cells, at the indicated time points ± 1 μM zoledronate. $^*p < 0.05$ using a Mann–Whitney test between zoledronate-treated groups. (**F**) CD25 expression (left) and IFN-γ concentration (right) after culture of purified in vitro–expanded Vδ2$^+$ T cells with HMBPP (0.5 ng/ml) or plate-bound anti-CD3 plus anti-CD28 (10 μg/ml each) ± 10 μg/ml neutralizing anti-BTN2A1 mAb. Data represent [(A) and (B)] $n = 8$ donors pooled from two independent experiments; (C) $n = 2$ to 3 donors pooled from three independent experiments, each performed with $n = 1$ to 4 technical replicates indicated by different symbols; (D) $n = 4$ donors, each averaged from one to five technical replicates across five independent experiments; (E) $n = 4$ donors, each averaged from two to six technical replicates across six independent experiments; (F) $n = 8$ donors pooled from two independent experiments. Zol, zoledronate.

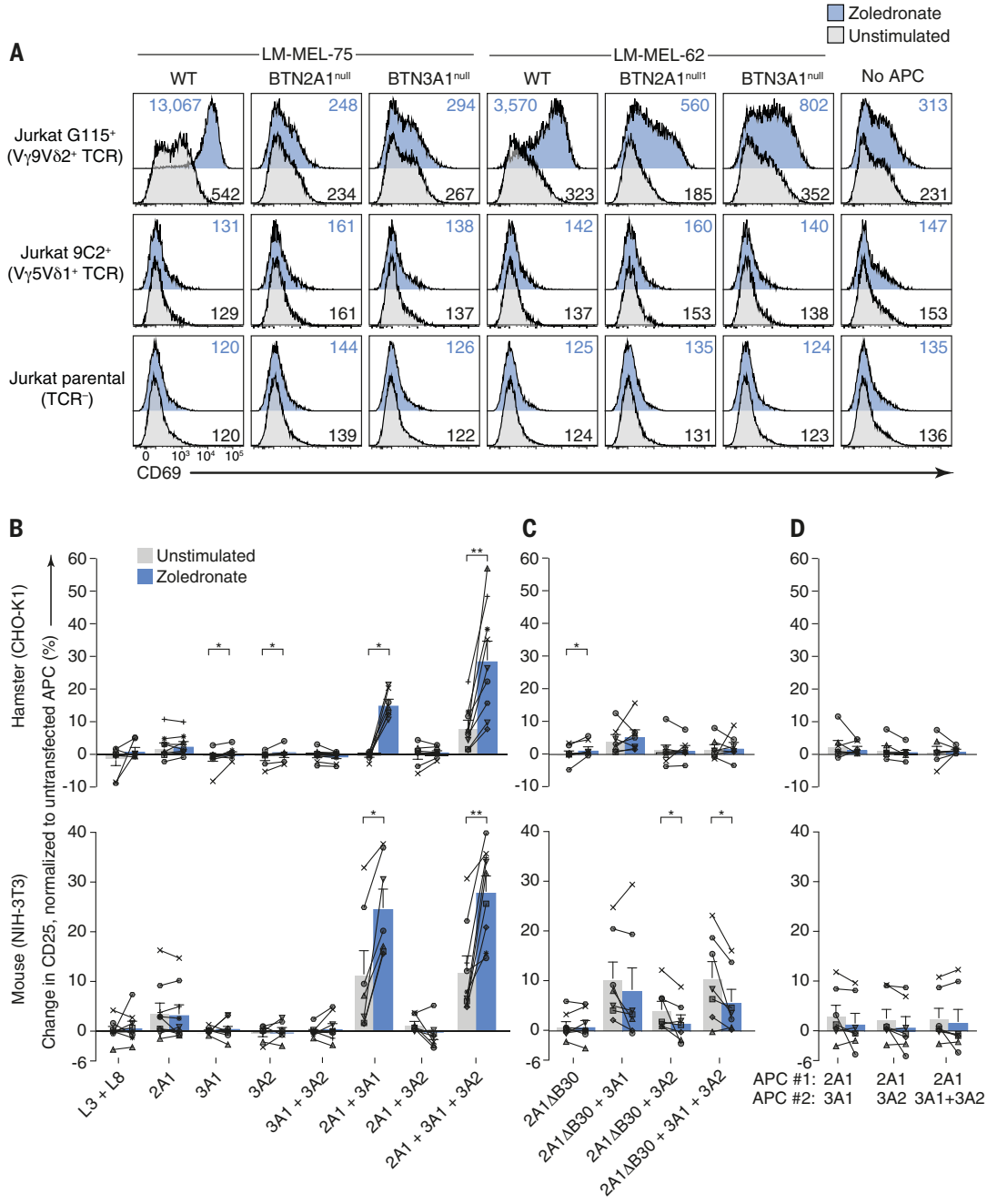

Fig. 4. BTN2A1 and BTN3A1 are both necessary for pAg presentation. (**A**) CD69 expression on G115 Vγ9Vδ2$^+$ TCR (top row), control 9C2 Vγ5Vδ1$^+$ TCR (middle), and parental (TCR$^-$) J.RT3-T3.5 (bottom row) Jurkat cells after overnight coculture with the indicated APCs, in the presence (blue) or absence (gray) of 40 μM zoledronate. Numbers indicate the median fluorescence intensity. (**B**) Change in CD25 expression (normalized to unstimulated control for each sample) on purified in vitro–expanded γδ T cells cocultured for 24 hours in the presence (blue) or absence (gray) of 4 μM zoledronate with CHO-K1 (hamster origin) or NIH-3T3 (mouse origin) APCs transfected with the indicated combinations of (B) *BTNL3*, *BTNL8*, *BTN2A1*, *BTN3A1*, and *BTN3A2* or (**C**) BTN2A1ΔB30, *BTN3A1*, and *BTN3A2*. (**D**) γδ T cells cocultured as in (B), except in the presence of a 1:1 mixture of two populations of APCs, each transfected separately with combinations of *BTN2A1*, *BTN3A1*, and *BTN3A2*. Each symbol and connecting line represents a different donor. *p < 0.05, **p < 0.01 (Wilcoxon paired test). Bar graphs depict mean ± SEM. Data in (A) are representative of one of three similar experiments; data in (B) to (D) represent n = 7 to 9 donors per group pooled from 3 to 5 independent experiments.

association (fig. S14). Thus, both the extracellular and intracellular domains of BTN2A1 and BTN3A1 are closely associated.

Vγ9Vδ2$^+$ TCR recognizes at least two ligands

Given that BTN2A1 binds all Vγ9$^+$ γδTCRs yet only Vγ9Vδ2$^+$ γδ T cells are pAg-reactive, we hypothesized that Vδ2 is also involved in this interaction. A corollary of this hypothesis could be that separate binding domains exist on the Vγ9Vδ2$^+$ TCR: one responsible for binding BTN2A1, located within the germline-encoded region of Vγ9, and another that is also responsible for pAg reactivity, incorporating Vδ2 specificity. Mutations of Vγ9 residues Arg^{20}, Glu^{70}, and His^{85} (and to a lesser extent Glu^{22}) to Ala all resulted in complete loss of BTN2A1 tetramer reactivity, whereas none of the Vδ2 mutations had this effect (Fig. 6A). The side chains of these Vγ9 residues were in close proximity to one another (Glu^{70} to His^{85} distance, 2.8 Å; His^{85} to Arg^{20} distance, 5.1 Å) and located on the outer faces of the B, D, and E strands, respectively, of the ABED antiparallel β sheet of Vγ9. Together they formed a polar triad within the framework region of Vγ9 (Fig. 6B), consistent with BTN2A1 binding to the vast majority of Vγ9$^+$ γδ T cells (Fig. 2B). Thus, BTN2A1 appears to bind to the side of Vγ9, distal to the δ chain and not in the vicinity of the complementarity-determining region (CDR) loops that are typically associated with Ag recognition.

We next examined which residues were important for mediating functional responses to pAg. Jurkat cells transduced with γδTCR mutants expressed similar amounts of CD3–γδTCR complex on their surface and responded equivalently to immobilized anti-CD3 mAb (fig. S15). Mutations in each of the BTN2A1-binding triad of γ-chain mutants abrogated pAg-mediated Jurkat cell activation (Fig. 6B). However, mutations in two additional residues, Arg^{51} of the Vδ2-encoded CDR2 loop and Lys^{108} of the CDR3 loop of the TCR γ chain, also abrogated

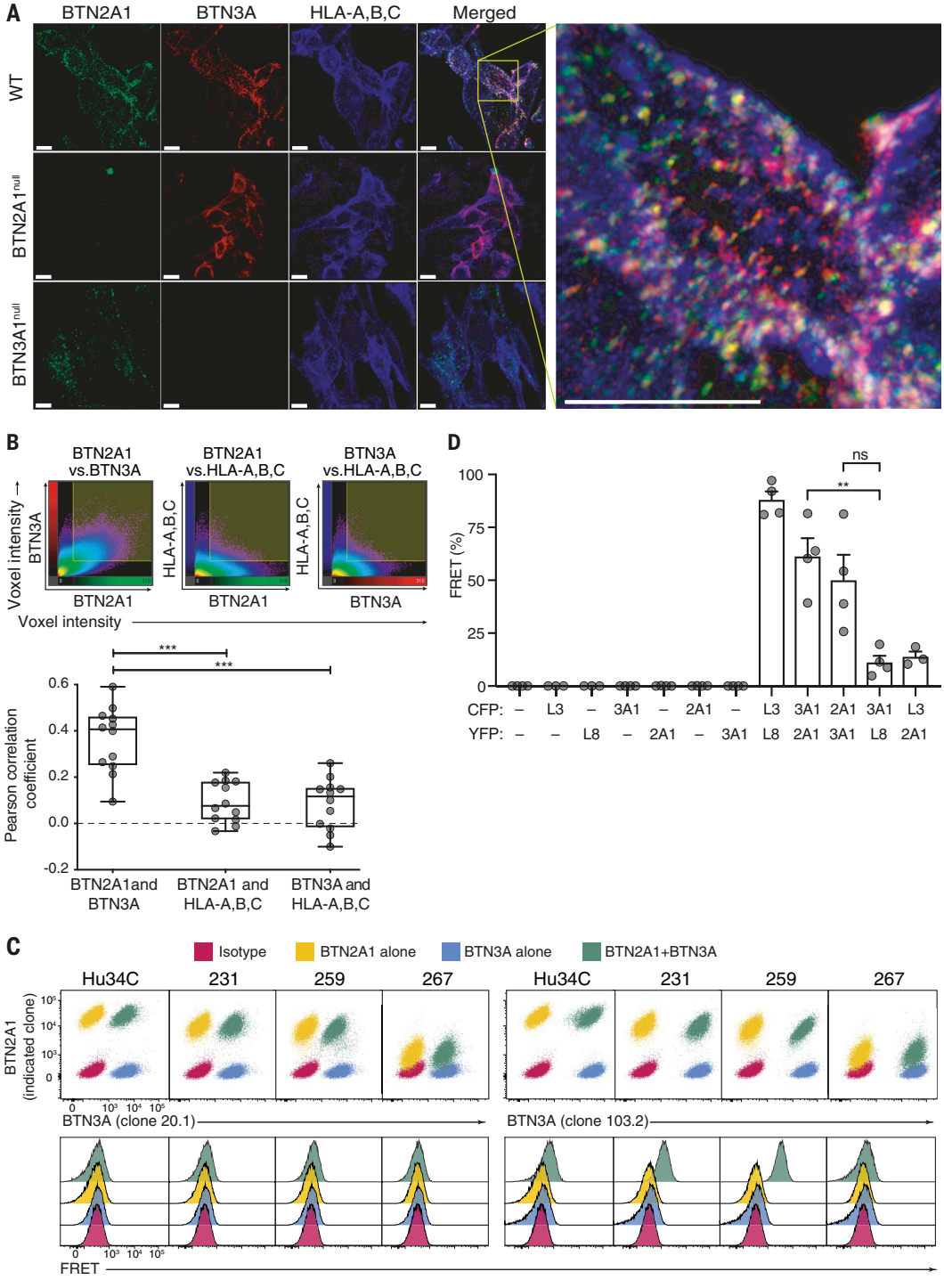

Fig. 5. BTN2A1 associates with BTN3A1 on the cell surface. (**A**) Z-stack confocal microscopy of surface BTN2A1 (green, clone 259), BTN3A (red, clone 103.2), and pan-HLA (human leukocyte antigen) class I (blue, clone W6/32) on parental LM-MEL-75 ("WT", top row), *BTN2A1*^{null} (middle row), and *BTN3A1*^{null} (bottom row) cells. Scale bars, 10 μm. (**B**) Graph depicts Pearson correlation coefficients for individual fields of view. Representative voxel density plots depicting correlation between anti-BTN2A1 versus anti-BTN3A1/3A2/3A3 ("BTN3A") (left); anti-BTN2A1 versus anti- HLA-A,B,C (middle); and anti-BTN3A versus anti-HLA-A,B,C (right). ***$p < 0.001$ using a Kruskal–Wallis with Dunn's post-test. (**C**) Anti-BTN2A1 versus BTN3A costaining (green), or single staining (yellow and blue, respectively), or mouse IgG1 versus mouse IgG2a isotype control staining (*x* and *y* axis respectively, magenta) on LM-MEL-75 cells using the indicated mAb clones (top row). Histograms (second row) depict FRET fluorescence. (**D**) Percentage of FRET^{+} cells between butyrophilin$^{CFP/YFP}$-transfected NIH-3T3 cells. Data are representative of [(A) and (B)] two pooled independent experiments; (C) one experiment; (D) three to four independent experiments.

pAg-mediated activation (Fig. 6C) (*10*). These residues had no effect on BTN2A1 binding (Fig. 6B) and were located on the opposite side of the TCR to the putative BTN2A1 footprint (~30 to 40 Å separation). However, they were in close proximity to one another (~11 Å) (Fig. 6D), thereby potentially representing a separate binding interface necessary for pAg-mediated activation via the Vγ9Vδ2^{+} TCR, but not for BTN2A1 binding. This second binding interface explains the importance of (i) the Vδ2^{+} TCR δ chain through involvement of germline-encoded residues and (ii) the invariant nature of the CDR3γ motif among pAg-reactive γδ T cells, through engagement of specific residues within this loop.

Finally, we tested agonist BTN3A1 mAb (clone 20.1)–mediated activation, which is thought to mimic pAg-mediated signaling by conformational modulation or cross-linking of BTN3A1 (*12*). Agonist BTN3A1 mAb–pulsed parental APCs induced Vγ9Vδ2 TCR^{+} Jurkat cell activation (Fig. 7), an effect that was not observed with agonist BTN3A1 mAb–pulsed *BTN2A1*^{null} APCs, suggesting that BTN2A1 is critical for BTN3A1-mediated activation of γδ T cells. Furthermore, Jurkat cells expressing TCR γ-chain Ala mutants of the BTN2A1-binding residues His^{85}, Arg^{20}, and Glu^{70}, as well as BTN2A1-independent mutants of Arg^{51}

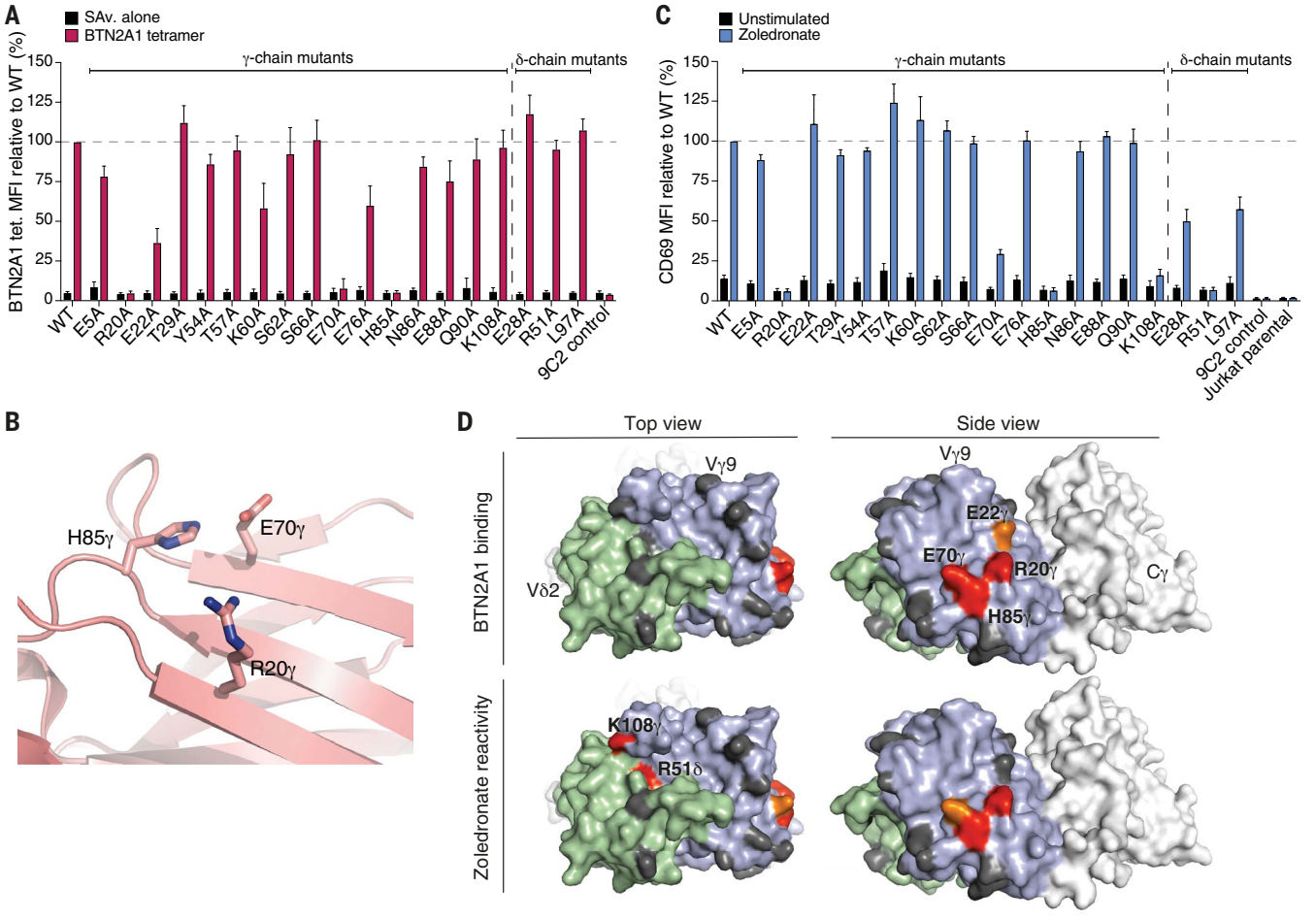

Fig. 6. Vγ9Vδ2$^+$ T cell receptors contain two distinct ligand-binding domains. (**A**) BTN2A1 tetramer-PE (red) and control streptavidin-PE alone (black) staining of gated GFP$^+$CD3$^+$ HEK-293T cells transfected with single-residue G115 γδTCR alanine mutants (or control Jurkat 9C2 γδTCR), normalized to BTN2A1 tetramer staining of G115 WT γδTCR. (**B**) Cartoon view of the G115 γδTCR [Protein Data Bank (PDB) code 1HXM (*25*)] Vγ9 ABED β sheet depicting the side chains of R20, E70, and H85. (**C**) CD69 expression on Jurkat cells expressing G115 γδTCR alanine mutants (or 9C2 γδTCR$^+$ or parental γδTCR$^-$ Jurkat cells), normalized to the activation levels of G115 WT γδTCR$^+$ Jurkat cells, after overnight culture with LM-MEL-75 APCs in the presence (blue) or absence (black) of 40 μM zoledronate. (**D**) Surface of G115 γδTCR [PDB code 1HXM (*25*)] depicting the residues important for BTN2A1 tetramer binding (top row) and zoledronate reactivity (bottom row). Side chains of tested residues with >75% loss of BTN2A1 binding or CD69 induction are shown in red; 50 to 75% reduction in orange; <50% reduction in gray; Vδ2, green; Vγ9, blue; constant regions, white. MFI, median fluorescence intensity; SAv, streptavidin alone control; Unstimulated, unstimulated control. Data in (A) and (C) represent the mean ± SEM of n = 3 separate experiments. Single-letter abbreviations for the amino acid residues are as follows: A, Ala; C, Cys; D, Asp; E, Glu; F, Phe; G, Gly; H, His; I, Ile; K, Lys; L, Leu; M, Met; N, Asn; P, Pro; Q, Gln; R, Arg; S, Ser; T, Thr; V, Val; W, Trp; and Y, Tyr.

(δ chain) and Lys^{108} (γ chain), all failed to respond to parental APCs pulsed with agonist anti-BTN3A1 mAb (Fig. 7). Thus, an interaction between BTN2A1 and the Vγ9$^+$ TCR γ chain is essential, but not sufficient, for BTN3A1-driven γδ T cell responses. This may explain why, in earlier studies, the agonist anti-BTN3A1 mAb failed to induce activation of γδ T cells in co-cultures with mouse-derived APCs transfected with human BTN3A1 alone (*5*), because mice do not express BTN2A1.

Accordingly, these mutant studies indicate the existence of two separate interaction sites on Vγ9Vδ2$^+$ TCRs necessary for pAg- and BTN3A1-mediated activation. One site on the side of the Vγ9 domain is essential for both BTN2A1 binding and for activation, whereas the other site, incorporating both the Vδ2-encoded CDR2 and γ-chain–encoded CDR3 loops, is required for pAg- and BTN3A1-mediated activation. Thus, Vγ9Vδ2$^+$ γδ T cells appear to be selectively activated by pAg through a distinct, dual-ligand interaction whereby BTN2A1 binds to the Vγ9 domain and another ligand, potentially BTN3A1, binds to a separate interface incorporating both the Vγ9 and Vδ2 domains.

Concluding remarks

Our findings support a model whereby BTN2A1 and BTN3A1 associate on the cell surface and are both required for pAg-mediated γδ T cell activation. This model also suggests that after pAg binds BTN3A1 through its intracellular B30.2 domain, the BTN2A1–BTN3A1 complex engages the γδTCR via two distinct binding sites: BTN2A1 binds to Vγ9 framework regions, whereas another ligand—possibly BTN3A1—binds to the Vδ2-encoded CDR2 and γ-chain–encoded CDR3 loops on the opposite side of the TCR. This represents a distinct model of Ag sensing that is highly divergent from canonical MHC-Ag complex recognition by αβ T cells.

A previous study, using short hairpin RNA knockdown, found no apparent role for BTN2A1 in pAg presentation (*28*). However, as the knockdown efficiency was only 81% and BTN2A1 protein was not measured, residual BTN2A1 may have retained functionality. Until now, BTN2A1 has been poorly characterized, with only one earlier study identifying a glycosylation-dependent receptor, CD209 (*21*). We found that N-linked glycans were dispensable for BTN2A1 binding to the γδTCR (fig. S16), making

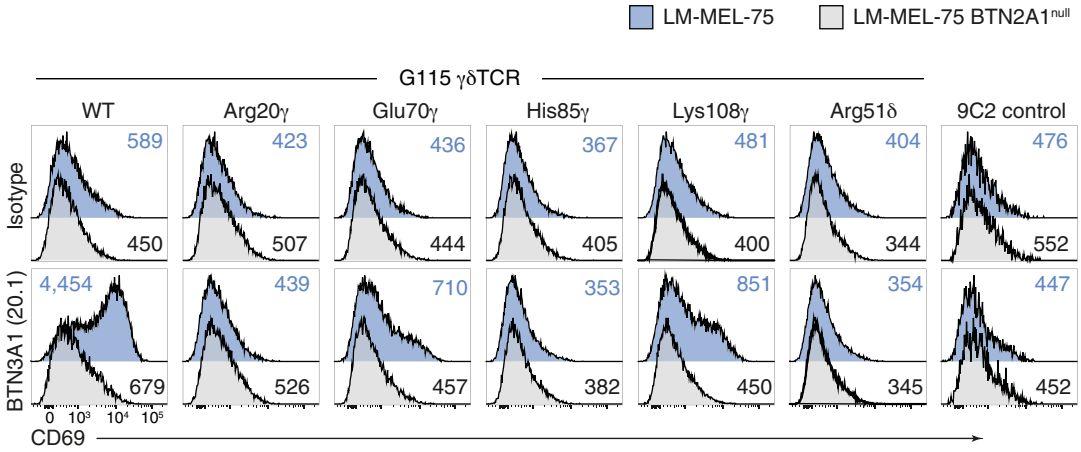

Fig. 7. Agonistic activity of anti-BTN3A1 mAb clone 20.1 depends on BTN2A1. CD69 expression on Jurkat cells expressing Vγ9Vδ2$^+$ TCR (clone G115), or the indicated G115 γδTCR mutants, or control Vγ5Vδ1$^+$ TCR (clone 9C2) after coculture with either parental LM-MEL-75 ("WT") or *BTN2A1*^{null} APCs preincubated with anti-BTN3A (clone 20.1, 10 μg/ml, blue histograms) or isotype control (mouse IgG1, 10 μg/ml, gray). Data are representative of one of two separate experiments.

it unlikely that CD209 plays a role in this interaction. Although little is known about the expression pattern of BTN2A1, RNA analysis predicts broad expression on immune cells. We confirmed that BTN2A1 is expressed on circulating B, T, and NK cells, as well as monocytes and Vγ9Vδ2$^+$ γδ T cells (fig. S17), potentially explaining how γδ T cells can present pAg to themselves (*11*).

Recent studies revealed that human BTNL3 and BTNL8 coassociate and are stimulatory to human Vγ4$^+$ γδ T cells, with BTNL3 interacting with a germline-encoded region of the γ-chain variable domain termed the HV4 loop (*29*–*31*). Likewise, mouse BTNL1 and BTNL6 are linked and important for intestinal Vγ7$^+$ γδ T cell function and appear to bind to a similar region of the γδTCR (*29*–*31*), and a similar ligand-binding domain was also recently identified within Vγ9 (*31*). The BTN2A1–Vγ9 binding interface encompasses a similar docking site, although it exhibits greater dependency on the outer face of the ABED β sheet of the Vγ9 TCR that extends beyond the HV4 loop. This suggests that the BTN2A1-binding footprint on Vγ9 may be located farther away from the CDR loops and closer to the Cγ domain. Given the tendency of butyrophilin molecules to dimerize [e.g., BTN3A1 can form stable V-shaped homodimers, and also heterodimers with BTN3A2 (*15*), and BTNL3–BTNL8 heterodimers (*30*)], it is possible that the association between BTN2A1 and BTN3A1 represents a direct interaction, although the molecular basis for this remains to be determined.

Compared to other Ag-presenting molecules (MHC and MHC-like molecules), the recognition of heteromeric butyrophilin complexes represents a fundamentally distinct class of immune recognition. It is not yet known how pAg alters this complex to induce antigenicity, but it may involve butyrophilin dimer or multimer remodeling and/or conformational changes to BTN2A1 and BTN3A1. Other associated molecules such as ABCA1 (*32*) may be directly required, although on the basis of our data, these would need to be conserved across humans, mice, and hamsters.

In conclusion, this study substantially advances our understanding of how pAgs are sensed by γδ T cells. In light of the mixed outcomes in numerous clinical trials that have utilized γδ T cells for anticancer therapy through pAg stimulation (*9*), it will be important to reexamine those data to determine whether BTN2A1 expression holds prognostic and/or therapeutic value. Our findings also suggest that BTN2A1 may represent a direct target for agonistic and/or antagonistic intervention in γδ T cell–mediated immunotherapy for infectious disease, cancer, and autoimmunity.

Methods

Human samples

Healthy donor-derived human PBMCs were obtained from the Australian Red Cross Lifeblood under ethics approval 17-08VIC-16 or 16-12VIC-03, with ethics approval from University of Melbourne Human Ethics Sub-Committee (1035100) or Olivia Newton John Cancer Research Institute (ONJCRI) Austin Health Human Research Ethics Committee (H2012-04446) and isolated by density gradient centrifugation (Ficoll-Paque PLUS GE Health care) and red blood cell lysis (ACK buffer, produced in-house). Established cell lines were routinely verified as *Mycoplasma*-negative using the MycoAlert test (Lonza).

Flow cytometry

Human cells were pelleted (400*g*), washed, and incubated at 4°C with phosphate-buffered saline (PBS) supplemented with 2% fetal calf serum (FCS) containing human Fc receptor block (Miltenyi Biotec). Mouse NIH-3T3 cells were incubated with anti-CD16/CD32 (clone 2.4G2, produced in-house). Cells were then incubated with 7-aminoactinomycin D (7-AAD, Sigma) or LIVE/DEAD viability markers (Thermo Fisher) plus antibodies (table S1). BTN2A1 and BTN3A were detected using monoclonal antibodies generated in-house (see below). Anti-BTN2A1 mAb or matched isotype control (clone BM4, produced in house) were conjugated to Alexa Fluor-647 by amine coupling (Thermo Fisher), and anti-BTN3A (clone 103.2) was conjugated to R-phycoerythrin (PE) (Prozyme) using sulfo-SMCC heterobifunctional crosslinker. In some experiments, unconjugated anti-BTN2A1 mAbs were detected with goat anti-mouse polyclonal secondary antibody BV421 or PE (BD-Pharmingen), with a subsequent blocking step (5% normal mouse serum). Cells were also stained with tetrameric Vγ9Vδ2$^+$ TCR, BTN2A1, MR1–5-OP-RU, or mouse CD1d–α-GalCer ectodomains (produced in house, see below), or equivalent amounts of streptavidin conjugate alone (BD). Each reagent was titrated to determine the optimal dilution factor. All data were acquired on an LSRFortessa II, FACSCanto (BD), or CytoFLEX LX (Beckman Coulter) and analyzed with FACSDiva and FlowJo (BD) software. All samples were gated to exclude unstable events, doublets, and dead cells using time, forward-scatter area versus height, and viability dye parameters, respectively.

γδ T cell isolation and expansion

In some experiments, γδ T cells were enriched by magnetic-activated cell sorting (MACS) using PE-Cy7-conjugated anti-γδTCR followed by anti-phycoerythrin–mediated magnetic bead purification (Miltenyi Biotec). After enrichment, CD3$^+$Vδ2$^+$ γδ T cells were further purified by sorting with an Aria III (BD). Enriched γδ T cells were stimulated in vitro for 48 hours with plate-bound anti-CD3ε (OKT3, 10 μg/ml, Bio-X-Cell), soluble anti-CD28 (CD28.2, 1 μg/ml, BD Pharmingen), phytohemagglutinin (0.5 μg/ml, Sigma), IL-15 (50 ng/ml, PeproTech), and recombinant human IL-2 (100 U/ml, PeproTech), followed by maintenance with IL-2 and IL-15 for 14 to 21 days. Cells were cultured in complete medium consisting of a 50:50 (v/v) mixture of

RPMI-1640 and AIM-V (Invitrogen) supplemented with 10% (v/v) FCS (JRH Biosciences), penicillin (100 U/ml), streptomycin (100 μg/ml), Glutamax (2 mM), sodium pyruvate (1 mM), nonessential amino acids (0.1 mM), and HEPES buffer (15 mM), pH 7.2 to 7.5 (all from Invitrogen Life Technologies), plus 50 μM 2-mercaptoethanol (Sigma-Aldrich).

Transfections

BTN2A1, *BTN2A2*, *BTN3A1*, *BTN3A2*, *BTNL3* and *BTNL8* (all isoform 1) were cloned into pMIG II mammalian expression vector (a gift from D. Vignali, Addgene plasmid # 52107) (*33*) and verified by Sanger sequencing. Mouse NIH-3T3, hamster CHO-K1, and human LM-MEL-62 cells were plated out the day before and transfected using FuGene HD or Viafect in OptiMEM, according to the manufacturer's instructions. After 48 hours (72 hours with LM-MEL-62 cells) to enable gene expression, cells were tested for green fluorescent protein (GFP) and gene expression and subsequently used in phenotyping or functional assays.

γδ T cell functional assays

Fresh PBMCs (2×10^6) were cultured in 24-well plates ± zoledronate (4 μM, Sigma) and purified mAb against BTN2A1, BTN3A1, or isotype control immunoglobulin G1, κ (IgG1, κ) (MOPC-21, BioLegend) (10 μg/ml). After 24 hours, $CD3\varepsilon^+$ $\gamma\delta TCR^+V\delta2^{+/-}$ γδ T cell activation was assessed by flow cytometry, and cytokine production was determined by cytometric bead array according to the manufacturer's instructions (BD). For the assays in fig. S7, PBMCs were cultured in 24-well plates and blocked for 30 min with mAb against BTN2A1, BTN3A1, or isotype control (10 μg/ml). Cells were then stimulated for 18 hours with combinations of HMBPP (0.5 ng/ml, Sigma), zoledronate (4 μM, Sigma), and CEF (1 μg/ml, Miltenyi) in addition to IL-2 (25 U/ml, Miltenyi), and Golgiplug protein transport inhibitor (BD Biosciences). Cells were surface-stained and then fixed and permeabilized with Foxp3/Transcription Factor Staining Buffer Set (Invitrogen) according to the manufacturer's protocol followed by staining with anti-IFN-γ (Biolegend). For coculture assays, purified and in vitro–expanded γδ T cells (5×10^5) were incubated in 96-well plates with APCs (3×10^5) for 24 hours ± zoledronate (4 μM), and γδ T cell activation was determined by flow cytometry as above. Alternatively (in Fig. 3C), 4×10^4 primary γδ T cells purified from PBMC donors by using a γδ T cell magnetic bead isolation kit (Miltenyi) were cultured at a 2:1 ratio with either LM-MEL-62 WT or $BTN2A1^{null1}$ APC in the presence of 1 μM zoledronate for 2 days. Nonadherent cells were subsequently washed and cultured in fresh plates without APC for an additional 7 days in media plus IL-2 (100 U/ml). $V\delta2^+$ γδ T cells were then enumerated by flow cytometry.

FRET assays

For detection of FRET between BTN2A1 and BTN3A1 ectodomains, cells were stained with PE-conjugated anti-BTN3A (donor), and Alexa 647-conjugated BTN2A1 (acceptor). FRET was detected in a compensated yellow 670/30 channel. CFP (mTurquoise2, donor) and YFP (mVenus, acceptor) constructs containing either a long (used for BTN3A1 and BTNL3) or short (used for BTN2A1 and BTNL8) flexible N-terminal linker (fig. S12B) were synthesized (Thermo Fisher) and cloned into the C terminus of butyrophilin constructs between an in-frame MfeI site that was introduced by site-directed mutagenesis, and a 3′ Sal I site, which also removed the pMIG IRES-GFP motif. CFP was detected in a violet 450/50 channel, YFP using blue 530/30, and FRET using a violet 530/30 channel from which CFP and YFP spillover had been removed by compensation. The frequency of cells identified as $FRET^+$ was examined on gated CFP^+YFP^+ NIH-3T3 cells for dual transfectants, and either CFP^+ or YFP^+ for single transfectants.

Tumor viability assays

Tumor (10^4) cells were plated out in 96-well plates in RF-10. The next day, 2×10^4 γδ T cells were added with IL-2 (100 U/ml) (Miltenyi) ± 1 μM zoledronate (Sigma). After a 1- or 3-day incubation, viability was assessed by an MTS assay, with absorbance measured at 490 nm on a SpectroStar Nano plate reader (BMG Labtech) and corrected for background and normalized against wells containing APCs alone at each time point.

Single-cell γδTCR sequencing

$CD3\varepsilon^+\gamma\delta TCR^+V\delta2^+$ T cells derived from healthy donor PBMCs were individually sorted. The γδTCR was then amplified from cDNA with primers listed in table S2. Polymerase chain reaction (PCR) amplicons were then cloned into pHL-sec containing either γ- or δ-chain ectodomains (fig. S1C) for expression.

Whole-genome CRISPR-Cas9 knockout screen

The CRISPR-Cas9 knockout screen was performed essentially as described (*34*). Briefly, a pooled lentiviral human gRNA knockout library containing $n = 6$ gRNAs per gene (GeCKOv2, a gift from F. Zhang, Addgene #1000000048) was transformed into Endura ElectroCompetent cells (Lucigen) at >500× coverage and grown in 1-liter liquid Luria Broth cultures for 16 hours at 37°C. Plasmid DNA was purified (PureLink gigaprep, Thermo Fisher) and gRNA abundance in pre- and postamplified libraries was validated by sequencing of PCR-amplified libraries (Illumina HiSeq, 60×10^6 reads per sample), with <0.2% gRNA dropout. Lentiviral particles were produced by transient transfection of HEK-293T cells with the gRNA library DNA plus packaging plasmids using FuGENE (Promega), and culture supernatant was titrated on LM-MEL-62 cells to determine the viral titer using puromycin (1 μg/ml, Thermo Fisher). Four biological replicates of LM-MEL-62 cells (2×10^8 each) were transduced with the lentiviral library at a multiplicity of infection of ~0.3. Transduced cells were then selected with puromycin for an additional 5 days, after which $V\gamma9V\delta2^+$ γδTCR tetramer $\#6^{lo}$ cells were sorted from half of each replicate (~6×10^7), and the remaining half was used as the unsorted control. The sorted cells were re-expanded for ~2 weeks and subsequently re-sorted. This was repeated an additional two times to adequately enrich for a clear $V\gamma9V\delta2$ TCR tetramer $\#6^{lo}$ population of LM-MEL-62 cells (fig. S2A). Genomic DNA was then extracted as previously described (*35*), including an additional phenol–chloroform purification step. gRNA from ~6×10^7 unsorted and ~3×10^7 sorted cells was amplified from genomic DNA by PCR (33 cycles) with *Pfu*-based DNA polymerase (Herculase II Fusion, Agilent Technologies) and one-step primers containing index and adaptor sequences (IDT Ultramer oligos) as previously described (*34*). Amplicons were gel-extracted after electrophoresis (Wizard SV Gel Clean-Up System, Promega), quantified with PicoGreen (Thermo Fisher), and sequenced with a NovaSeq (Illumina). Sample data were demultiplexed using a combination of the forward primer stagger motifs and the reverse eight-oligomer barcodes using Cutadapt (*36*) and analyzed using the EdgeR software package in R studio (*37*). Guides were enumerated using the *processAmplicons* function, allowing for a single–base-pair mismatch or shifted guide position. Guides with fewer than 0.5 counts/10^6 in at least five samples were excluded from the analysis. After dispersion estimation, differential gRNA expression between unsorted and sorted samples was determined using the *exactTest* function, where a false discovery rate (FDR) of <0.05 was considered statistically significant. The raw count files and analysis script are available in database S1.

Production of soluble proteins

Soluble human γδTCRs, BTN2A1 and mouse CD1d ectodomains were expressed by transient transfection of mammalian Expi293F or GNTI-defective HEK-293S cells using ExpiFectamine or PEI, respectively, with pHL-sec vector DNA encoding constructs with C-terminal biotin ligase (AviTag) and His_6 tags (*38*). MR1-5-OP-RU tetramer was produced as previously described (*39*). Protein was purified from culture supernatant using immobilized metal affinity chromatography (IMAC) and gel filtration, and enzymatically biotinylated using BirA (produced in-house). Proteins were repurified by size exclusion chromatography and stored at −80°C. Biotinylated proteins were tetramerized

with streptavidin-PE (BD) at a 4:1 molar ratio. DNA constructs encoding butyrophilin B30.2 intracellular domains with C-terminal His_6 tags were synthesized de novo (Thermo Fisher) and cloned into pET-30 bacterial expression vectors. BL21 DE3 (pLysS) *Escherichia coli* were used for overnight expressions at 30°C after induction with isopropyl-β-D-thiogalactopyranoside (IPTG, 1 mM). Cell pellets were washed and lysed using a sonicator in PBS–1 mM dithiothreitol and B30.2 proteins were purified from clarified lysate using IMAC and gel filtration.

Generation of anti-BTN2A1 mAb

A human antibody phage display library was used to screen for antibody clones with specificity for BTN2A1. Screening consisted of three rounds of selection for binding to 50 nM recombinant soluble C-terminally His-tagged BTN2A1 ectodomain immobilized on streptavidin-coated paramagnetic beads (Dynal), with preadsorption of nonspecific binders on an unrelated control His-tagged protein also immobilized on streptavidin-coated beads. After extensive washing, bound phage were eluted and amplified overnight by infection of exponentially growing bacterial cultures (TG1; Stratagene). Purified phage were then used for a subsequent round of panning. After three rounds, bound phage were eluted and 190 clones were randomly picked and tested by enzyme-linked immunosorbent assay for binding to BTN2A1 immobilized in a microplate. Sequencing of positive clones revealed a total of 52 individual antibody clones, of which 45 were then subcloned into a mammalian expression vector for expression in Expi293F cells (Thermo Fisher) and purification on MabSelect SuRe resin (GE Lifesciences) as full-length IgG molecules, which comprised a human IgG4 Fab region and murine IgG2a Fc region. Isotype control clone BM4 contained the same Fc region, except for a mouse Fab region with irrelevant specificity.

Production of anti-BTN3A antibodies

DNA constructs encoding anti-BTN3A antibody variable domains (clones 20.1 and 103.2) were synthesized (Thermo Fisher) and cloned into mammalian expression vectors containing a mouse IGHV signal peptide and IgG1 constant regions. Antibodies were expressed in Expi293F cells as above and purified by Protein G column chromatography (GE), followed by buffer-exchange into PBS.

Enzyme-linked immunosorbent assay

Purified recombinant proteins (0.2 to 20 μg/ml) were immobilized in microplate wells in PBS buffer overnight at 4°C. Nonspecific binding was then blocked by incubation in PBS containing 0.05% Tween 20 plus 5% skim milk powder or 0.5% (w/v) bovine serum albumin (BSA). The wells were then incubated for 60 min at room temperature in the presence of antibodies at 2 to 5 μg/ml in a solution of PBS, 0.05% Tween 20, and 2% skim milk powder or 0.5% BSA, followed by washing in PBS–0.05% Tween 20. Plates were then incubated with horseradish peroxidase–labeled sheep anti-mouse IgG secondary antibody (Chemicon), or goat anti-mouse IgG secondary antibody (Millipore) followed by detection with 3,3′,5,5′-tetramethylbenzidine substrate (Sigma), and absorbance was measured at 450 nm by a plate reader.

Generation of CRISPR-Cas9–mediated knockout cell lines

For BTN2A1 knockout lines, two gRNAs (*BTN2A1*^{null1}: 5′-TCACAAAGGTGGTTCTTCCT-3′; and *BTN2A1*^{null2}: 5′-CAATAGATGCATACGGCAAT-3′) were cloned into GeneArt CRISPR Nuclease Vector Kit (Life Technologies) according to the manufacturer's protocol and sequence-verified by Sanger sequencing. Cells were transfected using Lipofectamine 2000 and sorted after 48 hours on the basis of orange fluorescent protein expression. Cells were cultured and stained with anti-BTN2A1 (clone Hu34C) and the negative fraction sorted. For *BTN3A1*-knockout lines, a *BTN3A1* CRISPR-Cas9 KO Plasmid kit (Santa Cruz Biotechnology) containing three specific gRNA sequences was used (5′-GGCACTTACGAGATGCATAC-3′, 5′-GAGAGACATTCAGCCTATAA-3′, and 5′-ACCATCAGAAGTTCCCTCCT-3′). Cells were transfected using Lipofectamine 3000 (Thermo Fisher) and sorted after 48 hours on the basis of GFP. Sorted cells were cultured and stained with anti-BTN3A (clone 103.2), and the negative fraction was sorted and cultured.

Jurkat assays

LM-MEL-62 or LM-MEL-75 APCs at 2.5×10^4 cells/well in a 96-well plate were incubated overnight. Then, 2×10^4 G115 mutant γδTCR-expressing J.RT3-T3.5 (ATCC TIB-153) Jurkat cells ± zoledronate, HMBPP, or IPP were added for 20 hours. CD69 expression was then measured by flow cytometry on GFP$^+$ Jurkat cells. A panel of 19 single-residue alanine (Ala) mutants, each in the Vγ9 or Vδ2 domains of the Vγ9Vδ2$^+$ G115 TCR, were generated by site-directed mutagenesis using the primers listed in table S2. Primers (IDT) were phosphorylated (PNK, NEB) followed by 25 cycles of PCR using KAPA HiFi master mix (KAPA Biosystems) with WT G115 in pMIG as template, and PCR product was digested with Dpn I (NEB) and ligated with T4 DNA ligase (NEB). Construct sequences were then verified by Sanger sequencing prior to transfections. To examine the capacity of G115 TCR mutants to bind to BTN2A1 tetramer, we transfected HEK-293T cells with individual γ-chain or δ-chain mutants, plus the corresponding WT δ or γ chain, respectively, as well as a pMIG construct encoding 2A-linked human CD3γδεζ, at a 1:3 ratio with FuGENE HD (Promega) in OptiMEM (Gibco, Thermo Fisher). Forty-eight hours after transfection, HEK-293T cells were resuspended by pipetting and stained for CD3ε expression and PE-labeled BTN2A1 tetramer or control PE-conjugated streptavidin. The median fluorescence intensity (MFI) of BTN2A1 tetramer interacting with mutant G115 TCRs was examined on gated CD3$^+$GFP$^+$ HEK-293T cells by flow cytometry.

Jurkat cell lines used in pAg stimulation assays were produced by transducing J.RT3-T3.5 Jurkat cells with G115 mutant TCRs. HEK-293T cells were transfected with each particular γ-chain or δ-chain mutant, plus the corresponding wild-type δ or γ chain, respectively, along with human CD3, pVSV (-G), and pEQ-Pam3(-E), and mixed at a 1:3 ratio with FuGENE HD in OptiMEM. After 24 hours, viral supernatants were collected and filtered through a 0.45-μm CA syringe filter, then incubated with JRT3-T3.5 Jurkat cells for 12 hours. This process was repeated twice a day for 4 days. CD3$^+$GFP$^+$ Jurkat cells were purified by fluorescence-activated cell sorting (BD FACSAria III) and examined for their capacity to respond to pAg presented by wild-type LM-MEL-75 APCs as described above.

To measure G115 γδTCR-expressing Jurkat cell reactivity to anti-BTN3A (clone 20.1) mAb, we preincubated 2.5×10^4 LM-MEL-75 APC cells with functional grade 20.1 (10 μg/ml, Biolegend) or matched isotype control for 30 min at room temperature and later plated the cells in a flat-bottom 96-well plate. Once the APCs had adhered, 2.5×10^4 Jurkat cells were added, giving a final antibody concentration of 5 μg/ml. After 24 hours of coculture, cell-surface CD69 expression by CD3$^+$GFP$^+$ Jurkat cells was determined by flow cytometry.

Surface plasmon resonance

SPR experiments were conducted at 25°C on a Biacore T200 instrument (GE Healthcare) using 10 mM HEPES-HCl (pH 7.4), 150 mM NaCl, 3 mM EDTA, and 0.05% Tween 20 buffer. γδTCR ectodomains were directly immobilized to 260 resonance units (RU) on a Biacore sensor chip SA preimmobilized with streptavidin. Soluble butyrophilins were serially diluted (200 to 3.1 μM) and simultaneously injected over test and control surfaces at a rate of 30 μl/min. After subtraction of data from the control flow cell (streptavidin alone) and blank injections, interactions were analyzed with Biacore T200 evaluation software (GE Healthcare) and Prism version 8 (GraphPad), and equilibrium dissociation constants (K_D's) were derived at equilibrium.

Isothermal titration calorimetry

ITC experiments were conducted on a MicroCal ITC200 instrument (GE Healthcare) at 25°C.

BTN2A1 or BTN3A1 B30.2 domains were buffer exchanged into PBS and adjusted to a final concentration of 100 μM. HMBPP (Cayman Chemical) and IPP were adjusted to final concentrations of 1.9 and 2 mM, respectively, and serially injected into the cell in 2-μl increments, after an initial 0.4-μl injection that was discarded from the analysis. Data were analyzed with Microcal Origin software.

Confocal microscopy

LM-MEL-75 WT, *BTN2A1*^{null}, *BTN3A1*^{null} cells were cultured overnight in RPMI-1640 (Thermo Fisher) supplemented with 10% (v/v) FCS (JRH Biosciences), penicillin (100 U/ml), streptomycin (100 μg/ml), Glutamax (2 mM), sodium pyruvate (1 mM), nonessential amino acids (0.1 mM), and HEPES buffer (15 mM), pH 7.2 to 7.5 (all from Invitrogen Life Technologies), plus 50 μM 2-mercaptoethanol (Sigma-Aldrich) and allowed to adhere to chamber well slides (Lab-Tek, Thermo Fisher). The next day, cells were washed and incubated with human Fc receptor block (Miltenyi Biotec) diluted with Opti-MEM (Thermo Fisher) on ice for 20 min. Cells were washed and stained with anti-BTN2A1-AF647 (clone 259), anti-BTN3A-PE (clone 103.2), and anti-pan-HLA class I-AF488 (clone W6/32, BioLegend) diluted in Opti-MEM on ice for 20 min. Cells were fixed with 1% paraformaldehyde (Electron Microscopy Sciences) in PBS for 20 min, then mounted with ProLong Gold AntiFade (Thermo Fisher) and covered with a #1 coverslip (Menzel-Gläser) overnight. Each reagent was titrated to determine the optimal dilution factor. Z-stack, single-tile images with 76.9 nm lateral and 400 nm axial voxel size and 1024 × 1024 voxel density were acquired on a LSM780 laser scanning confocal microscope with an inverted 20× (0.8 numerical aperture) objective, PMT detectors, and Zen software (Zeiss). Fluorochromes were excited with 488-, 561-, and 633-nm laser lines. Images were deconvoluted with Huygens Professional (Scientific Volume Imaging) and analyzed with Imaris (Oxford Instruments) software. Regions of interest defining the imaged cells were made on the basis of the brightfield channel, and the Imaris Coloc module was used to calculate Pearson correlation coefficients of voxels with intensity thresholds set for each analyzed channel on the basis of negative controls for each stain.

Immunoblotting

Cells were washed in PBS and lysed in Pierce RIPA buffer (Thermo fisher) in the presence of complete protease inhibitor cocktail (Roche). Protein quantification in cell lysates was performed with Pierce BCA protein assay kit (Thermo fisher). Samples were run on NuPAGE 4 to 12% Bis-Tris protein gels (Invitrogen Life Technologies), and proteins were resolved by immunoblotting with the iBlot system (Invitrogen Life Technologies). Primary antibodies anti-BTN2A1 (0.2 μg/ml, Sigma Prestige) and GAPDH (0.04 μg/ml, Cell Signaling Technology) were detected with IRDye 680RD goat anti-rabbit IgG secondary antibody (0.1 μg/ml, Licor). Polyvinylidene difluoride (PVDF) membrane was scanned with an Odyssey scanner.

Statistical analyses

For comparison of two independent groups, a nonparametric Mann–Whitney *U* test was used. For the comparison of more than two independent groups, a Kruskal–Wallis test with a Dunn's post-test was used. For comparison of two paired groups, a Wilcoxon test was used. For comparison of more than two paired groups that were normally distributed (determined by a Kolmogorov–Smirnov test), a repeated-measures ANOVA and Dunnett's multiple comparison test were performed with individual variances computed for each comparison; otherwise, a Friedman test with a Dunn's post-test was used. All p values (or FDR values for Fig. 1B) less than 0.05 were considered statistically significant.

REFERENCES AND NOTES

1. J. Rossjohn *et al*., T cell antigen receptor recognition of antigen-presenting molecules. *Annu. Rev. Immunol.* **33**, 169–200 (2015). doi: 10.1146/annurev-immunol-032414-112334; pmid: 25493333
2. P. Constant *et al*., Stimulation of human gamma delta T cells by nonpeptidic mycobacterial ligands. *Science* **264**, 267–270 (1994). doi: 10.1126/science.8146660; pmid: 8146660
3. Y. Tanaka *et al*., Natural and synthetic non-peptide antigens recognized by human gamma delta T cells. *Nature* **375**, 155–158 (1995). doi: 10.1038/375155a0; pmid: 7753173
4. L. Zhao, W. C. Chang, Y. Xiao, H. W. Liu, P. Liu, Methylerythritol phosphate pathway of isoprenoid biosynthesis. *Annu. Rev. Biochem.* **82**, 497–530 (2013). doi: 10.1146/annurev-biochem-052010-100934; pmid: 23746261
5. A. Sandstrom *et al*., The intracellular B30.2 domain of butyrophilin 3A1 binds phosphoantigens to mediate activation of human Vγ9Vδ2 T cells. *Immunity* **40**, 490–500 (2014). doi: 10.1016/j.immuni.2014.03.003; pmid: 24703779
6. Y. L. Wu *et al*., γδ T cells and their potential for immunotherapy. *Int. J. Biol. Sci.* **10**, 119–135 (2014). doi: 10.7150/ijbs.7823; pmid: 24520210
7. J. Zheng, Y. Liu, Y. L. Lau, W. Tu, γδ-T cells: An unpolished sword in human anti-infection immunity. *Cell. Mol. Immunol.* **10**, 50–57 (2013). doi: 10.1038/cmi.2012.43; pmid: 23064104
8. L. Wang, A. Kamath, H. Das, L. Li, J. F. Bukowski, Antibacterial effect of human V gamma 2V delta 2 T cells in vivo. *J. Clin. Invest.* **108**, 1349–1357 (2001). doi: 10.1172/JCI200113584; pmid: 11696580
9. D. I. Godfrey, J. Le Nours, D. M. Andrews, A. P. Uldrich, J. Rossjohn, Unconventional T Cell Targets for Cancer Immunotherapy. *Immunity* **48**, 453–473 (2018). doi: 10.1016/j.immuni.2018.03.009; pmid: 29562195
10. H. Wang, Z. Fang, C. T. Morita, Vgamma2Vdelta2 T Cell Receptor recognition of prenyl pyrophosphates is dependent on all CDRs. *J. Immunol.* **184**, 6209–6222 (2010). doi: 10.4049/jimmunol.1000231; pmid: 20483784
11. C. T. Morita *et al*., Direct presentation of nonpeptide prenyl pyrophosphate antigens to human gamma delta T cells. *Immunity* **3**, 495–507 (1995). doi: 10.1016/1074-7613(95)90178-7; pmid: 7584140
12. C. Harly *et al*., Key implication of CD277/butyrophilin-3 (BTN3A) in cellular stress sensing by a major human γδ T-cell subset. *Blood* **120**, 2269–2279 (2012). doi: 10.1182/blood-2012-05-430470; pmid: 22767497
13. D. A. Rhodes *et al*., Activation of human γδ T cells by cytosolic interactions of BTN3A1 with soluble phosphoantigens and the cytoskeletal adaptor periplakin. *J. Immunol.* **194**, 2390–2398 (2015). doi: 10.4049/jimmunol.1401064; pmid: 25637025
14. Z. Sebestyen *et al*., RhoB Mediates Phosphoantigen Recognition by Vγ9Vδ2 T Cell Receptor. *Cell Reports* **15**, 1973–1985 (2016). doi: 10.1016/j.celrep.2016.04.081; pmid: 27210746
15. S. Gu *et al*., Phosphoantigen-induced conformational change of butyrophilin 3A1 (BTN3A1) and its implication on Vγ9Vδ2 T cell activation. *Proc. Natl. Acad. Sci. U.S.A.* **114**, E7311–E7320 (2017). doi: 10.1073/pnas.1707547114; pmid: 28807997
16. M. Salim *et al*., BTN3A1 Discriminates γδ T Cell Phosphoantigens from Nonantigenic Small Molecules via a Conformational Sensor in Its B30.2 Domain. *ACS Chem. Biol.* **12**, 2631–2643 (2017). doi: 10.1021/acschembio.7b00694; pmid: 28862425
17. Y. Yang *et al*., A Structural Change in Butyrophilin upon Phosphoantigen Binding Underlies Phosphoantigen-Mediated Vγ9Vδ2 T Cell Activation. *Immunity* **50**, 1043–1053.e5 (2019). doi: 10.1016/j.immuni.2019.02.016; pmid: 30902636
18. L. Starick *et al*., Butyrophilin 3A (BTN3A, CD277)-specific antibody 20.1 differentially activates Vγ9Vδ2 TCR clonotypes and interferes with phosphoantigen activation. *Eur. J. Immunol.* **47**, 982–992 (2017). doi: 10.1002/eji.201646818; pmid: 28386905
19. F. Riaño *et al*., Vγ9Vδ2 TCR-activation by phosphorylated antigens requires butyrophilin 3 A1 (BTN3A1) and additional genes on human chromosome 6. *Eur. J. Immunol.* **44**, 2571–2576 (2014). doi: 10.1002/eji.201444712; pmid: 24890657
20. A. Behren *et al*., The Ludwig institute for cancer research Melbourne melanoma cell line panel. *Pigment Cell Melanoma Res.* **26**, 597–600 (2013). doi: 10.1111/pcmr.12097; pmid: 23527996
21. G. Malcherek *et al*., The B7 homolog butyrophilin BTN2A1 is a novel ligand for DC-SIGN. *J. Immunol.* **179**, 3804–3811 (2007). doi: 10.4049/jimmunol.179.6.3804; pmid: 17785817
22. P. Batard *et al*., Use of phycoerythrin and allophycocyanin for fluorescence resonance energy transfer analyzed by flow cytometry: Advantages and limitations. *Cytometry* **48**, 97–105 (2002). doi: 10.1002/cyto.10106; pmid: 12116371
23. M. E. Birnbaum *et al*., Deconstructing the peptide-MHC specificity of T cell recognition. *Cell* **157**, 1073–1087 (2014). doi: 10.1016/j.cell.2014.03.047; pmid: 24855945
24. A. J. Roelofs *et al*., Peripheral blood monocytes are responsible for gammadelta T cell activation induced by zoledronic acid through accumulation of IPP/DMAPP. *Br. J. Haematol.* **144**, 245–250 (2009). doi: 10.1111/j.1365-2141.2008.07435.x; pmid: 19016713
25. T. J. Allison, C. C. Winter, J. J. Fournié, M. Bonneville, D. N. Garboczi, Structure of a human gammadelta T-cell antigen receptor. *Nature* **411**, 820–824 (2001). doi: 10.1038/35081115; pmid: 11459064
26. A. P. Uldrich *et al*., CD1d-lipid antigen recognition by the γδ TCR. *Nat. Immunol.* **14**, 1137–1145 (2013). doi: 10.1038/ni.2713; pmid: 24076636
27. P. Vantourout *et al*., Heteromeric interactions regulate butyrophilin (BTN) and BTN-like molecules governing γδ T cell biology. *Proc. Natl. Acad. Sci. U.S.A.* **115**, 1039–1044 (2018). doi: 10.1073/pnas.1701237115; pmid: 29339503
28. S. Vavassori *et al*., Butyrophilin 3A1 binds phosphorylated antigens and stimulates human γδ T cells. *Nat. Immunol.* **14**, 908–916 (2013). doi: 10.1038/ni.2665; pmid: 23872678
29. R. Di Marco Barros *et al*., Epithelia Use Butyrophilin-like Molecules to Shape Organ-Specific γδ T Cell Compartments. *Cell* **167**, 203–218.e17 (2016). doi: 10.1016/j.cell.2016.08.030; pmid: 27641500
30. D. Melandri *et al*., The γδTCR combines innate immunity with adaptive immunity by utilizing spatially distinct regions for agonist selection and antigen responsiveness. *Nat. Immunol.* **19**, 1352–1365 (2018). doi: 10.1038/s41590-018-0253-5; pmid: 30420626
31. C. R. Willcox *et al*., Butyrophilin-like 3 directly binds a human Vγ4^{+} T cell receptor using a modality distinct from clonally-restricted antigen. *Immunity* **51**, 813–825.e4 (2019). doi: 10.1016/j.immuni.2019.09.006; pmid: 31628053
32. B. Castella *et al*., The ATP-binding cassette transporter A1 regulates phosphoantigen release and Vγ9Vδ2 T cell activation by dendritic cells. *Nat. Commun.* **8**, 15663 (2017). doi: 10.1038/ncomms15663; pmid: 28580927
33. J. Holst *et al*., Generation of T-cell receptor retrogenic mice. *Nat. Protoc.* **1**, 406–417 (2006). doi: 10.1038/nprot.2006.61; pmid: 17406263
34. J. Joung *et al*., Genome-scale CRISPR-Cas9 knockout and transcriptional activation screening. *Nat. Protoc.* **12**, 828–863 (2017). doi: 10.1038/nprot.2017.016; pmid: 28333914

35. S. Chen *et al*., Genome-wide CRISPR screen in a mouse model of tumor growth and metastasis. *Cell* **160**, 1246–1260 (2015). doi: 10.1016/j.cell.2015.02.038; pmid: 25748654
36. M. Martin, Cutadapt removes adapter sequences from high-throughput sequencing reads. *EMBnet J.* **17**, 10–12 (2011). doi: 10.14806/ej.17.1.200
37. M. D. Robinson, D. J. McCarthy, G. K. Smyth, edgeR: A Bioconductor package for differential expression analysis of digital gene expression data. *Bioinformatics* **26**, 139–140 (2010). doi: 10.1093/bioinformatics/btp616; pmid: 19910308
38. A. R. Aricescu, W. Lu, E. Y. Jones, A time- and cost-efficient system for high-level protein production in mammalian cells. *Acta Crystallogr. D Biol. Crystallogr.* **62**, 1243–1250 (2006). doi: 10.1107/S0907444906029799; pmid: 17001101
39. H. F. Koay *et al*., Diverse MR1-restricted T cells in mice and humans. *Nat. Commun.* **10**, 2243 (2019). doi: 10.1038/s41467-019-10198-w; pmid: 31113973

ACKNOWLEDGMENTS

We thank Z. Chen and L. Kjer-Nielsen for providing parental J.RT3-T3.5 cells and P. Neeson for providing zoledronic acid. The authors thank Z. Tian for technical assistance. We also thank T. Luke and staff at the Doherty Institute Flow Cytometry Facility, V. Jameson and staff at the Melbourne Brain Centre Flow Cytometry Facility, A. Gonzalez from the Melbourne Cytometry Platform, and D. Baloyan at the Olivia Newton-John Cancer Research Institute for flow cytometry support. We thank P. McMillan and staff at the Biological Optical Microscopy Platform for microscopy support. We thank staff at AGRF for DNA sequencing support, and Y. Mok from the Melbourne Protein Characterisation Platform for ITC support. **Funding:** This work was supported by the Cancer Council of Victoria (1126866), the Australian Research Council (ARC; CE140100011, DP170102471), the National Health and Medical Research Council of Australia (NHMRC; 1165467, 1113293), and the Operational Infrastructure Support Program provided by the Victorian Government, Australia. A.P.U. was supported by an ARC Future Fellowship (FT140100278); A.B. is supported by a fellowship from the Department of Health and Human Services acting through the Victorian Cancer Agency; D.I.G. is supported by an NHMRC Senior Principal Research Fellowship (1117766); M.R. is supported by the Deutsche Forschungsgemeinschaft (GRK2168) and the University of Melbourne through the International Research and Research Training Fund; J.A.V. is supported by an NHMRC Principal Research Fellowship (1154502); H.E.G.M. is supported by an ARC Discovery Early Career Researcher Award (DE170100575) and the AMP Tomorrow Fund. **Author contributions:** Conceptualization, A.P.U., A.B., D.I.G., J.C.; methodology, A.P.U., A.B., D.G., M.R., S.O.; investigation, M.R., S.O., T.S.F., D.J., A.B., A.P.U.; resources, K.W., Z.R., H.E.G.M., C.H., C.T., A.K.W., S.J.K., J.A.V., B.P., J.S., M.P., A.D.N., A.H., A.M.V., G.V., E.M., C.P., N.A.G., J.C., D.I.G., A.B., A.P.U.; writing – original draft, A.P.U., A.B., D.I.G., M.R.; writing – reviewing and editing, A.P.U., A.B., D.I.G., M.R., T.S.F., D.N.J., H.E.G.M., S.J.K., N.A.G.; supervision, A.P.U., A.B., D.I.G., J.C., N.A.G., C.K.; funding acquisition, A.P.U., A.B., D.I.G. **Competing interests:** A.D.N., J.S., M.P., A.H., A.M.V., G.V., E.M., and C.P. are employees of CSL Limited and are able to partake in employee share schemes. Some of the authors, including M.R., S.O., T.F., C.H., K.W., A.H., A.M.V., E.M., C.P., J.C., D.I.G., A.B., and A.P.U. are listed as inventors on patent applications related to the use of BTN2A1 to influence immune reactions. A.B. and J.C. received research funding from CSL Limited. All other authors declare no competing interests. **Data and materials availability:** Raw data and analysis scripts associated with the whole-genome screen depicted in Fig. 1B are available in database S1. Anti-BTN Abs are available from G.V. at CSL Limited upon request. All data necessary to understand and evaluate the conclusions of this paper are provided in the manuscript and supplementary materials.

SUPPLEMENTARY MATERIALS

science.sciencemag.org/content/367/6478/eaay5516/suppl/DC1
Figs. S1 to S17
Tables S1 and S2
Database S1

View/request a protocol for this paper from *Bio-protocol*.

28 June 2019; accepted 23 December 2019
Published online 9 January 2020
10.1126/science.aay5516

RESEARCH ARTICLE

SIGNAL TRANSDUCTION

Mechanism of homodimeric cytokine receptor activation and dysregulation by oncogenic mutations

Stephan Wilmes[1,2]*, Maximillian Hafer[1]*, Joni Vuorio[3,4], Julie A. Tucker[5], Hauke Winkelmann[1], Sara Löchte[1], Tess A. Stanly[5], Katiuska D. Pulgar Prieto[5], Chetan Poojari[3], Vivek Sharma[3,6], Christian P. Richter[1], Rainer Kurre[1], Stevan R. Hubbard[7], K. Christopher Garcia[8,9], Ignacio Moraga[2], Ilpo Vattulainen[3,4]†, Ian S. Hitchcock[5]†, Jacob Piehler[1]†

Homodimeric class I cytokine receptors are assumed to exist as preformed dimers that are activated by ligand-induced conformational changes. We quantified the dimerization of three prototypic class I cytokine receptors in the plasma membrane of living cells by single-molecule fluorescence microscopy. Spatial and spatiotemporal correlation of individual receptor subunits showed ligand-induced dimerization and revealed that the associated Janus kinase 2 (JAK2) dimerizes through its pseudokinase domain. Oncogenic receptor and hyperactive JAK2 mutants promoted ligand-independent dimerization, highlighting the formation of receptor dimers as the switch responsible for signal activation. Atomistic modeling and molecular dynamics simulations based on a detailed energetic analysis of the interactions involved in dimerization yielded a mechanistic blueprint for homodimeric class I cytokine receptor activation and its dysregulation by individual mutations.

Cytokines bind their cognate receptors to regulate hematopoiesis and immunological homeostasis. Consequently, imbalances in levels of circulating cytokines, or mutations that alter cytokine receptor function, can lead to severe pathological effects, ranging from aberrant immune responses to hematological malignancies. Therefore, a complete understanding of the dynamics and mechanisms underpinning cytokine receptor activation is critical.

The class I cytokine receptor family includes receptors for interleukins, colony-stimulating factors, and hormones. These receptors lack intrinsic kinase activity, relying instead on associated Janus kinase (JAK) proteins to initiate signal transduction. The precise activation mechanism of class I cytokine receptors, however, remains unclear (*1*). Originally, ligand-induced receptor dimerization was assumed to trigger signal activation (*2*). However, this model has been replaced by more complex concepts that propose ligand-induced conformational changes of pre-dimerized receptor subunits (Fig. 1A) (*1*, *3*, *4*). Supported by extensive structural and biochemical studies, homodimeric class I cytokine receptors such as the erythropoietin (Epo) and growth hormone (GH) receptors have become a paradigm for pre-assembled receptor dimers (*1*, *5*–*7*). Moreover, pre-dimerization has also been reported for numerous heterodimeric class I and class II cytokine receptors (*8*–*12*), which suggests that receptor pre-dimerization may be a generic feature of this receptor family (*1*, *4*). However, the molecular mechanism responsible for triggering JAK activation by preformed receptor dimers has remained rather speculative. Current models cannot convincingly explain receptor dysregulation by constitutively activating, oncogenic JAK mutations. Notably, hyperactivity of JAK2 caused by somatic mutations such as $Val^{617} \rightarrow Phe$ (JAK2 V617F) is the most common cause of the Philadelphia chromosome–negative myeloproliferative neoplasms (Ph^- MPNs) (*13*, *14*). Gaining a mechanistic understanding of pathway activation could inspire more specific strategies to target the aberrant signaling that underlies such MPNs.

Directly observing the spatiotemporal organization of cytokine receptors in the plasma membrane of living cells under physiological conditions has been hindered by their very low cell surface expression levels, which are below the detection limit of conventional fluorescence microscopy (*15*, *16*). We devised a method for quantifying the monomer-dimer equilibrium of homodimeric class I cytokine receptors at physiological densities in the plasma membrane by dual-color single-molecule fluorescence imaging in combination with posttranslational cell surface labeling. We found that thrombopoietin receptor (TpoR), Epo receptor (EpoR), and GH receptor (GHR) are monomeric and randomly distributed in the plasma membrane in the resting state, yet efficiently dimerize upon ligand binding. By quantifying the monomer-dimer equilibrium for various receptor and JAK variants, we obtained a comprehensive energetic landscape of ligand- and oncogene-induced receptor dimerization, revealing finely tuned, additive interactions involving JAK and receptor domains. On the basis of these quantitative insights in conjunction with atomistic molecular dynamics (MD) simulations, we suggest a mechanism of homodimeric class I cytokine receptor activation by ligand-induced dimerization, which can explain their dysregulation by individual mutations.

Random distribution and diffusion of TpoR in the plasma membrane

For time-lapse dual-color single-molecule imaging at the plasma membrane of live HeLa cells by total internal reflection fluorescence microscopy (TIRFM), receptor subunits were stochastically labeled with photostable fluorescent dyes by using equal concentrations of anti-GFP (green fluorescent protein) nanobodies conjugated to either Rho11 (^{Rho11}NB) or DY647 (^{DY647}NB) (Fig. 1A). To this end, EpoR, TpoR, and GHR were N-terminally fused to monomeric enhanced GFP (mEGFP) that had been rendered nonfluorescent by the mutation $Tyr^{66} \rightarrow Phe$ (mXFP). Because the endogenous JAK2 levels in HeLa cells are negligibly low, JAK2 fused to mEGFP (JAK2-mEGFP) was coexpressed with the receptor subunit to verify functional integrity at the single-cell level. Efficient association of JAK2-mEGFP with the receptor (fig. S1), as well as uncompromised activity of mXFP-tagged receptor and JAK2-mEGFP (figs. S2 and S3A), were confirmed. Representative results of dual-color single-molecule imaging experiments obtained for mXFP-TpoR expressed in HeLa cells are summarized in Fig. 1, B to F. After labeling with ^{Rho11}NB and ^{DY647}NB, individual TpoR subunits randomly diffusing in the plasma membrane could be discerned (Fig. 1B and movie S1). The presence of individual receptor subunits was confirmed by single-step photobleaching at elevated laser power (movie S2 and fig. S4A). Long–time scale single-molecule localization microscopy of TpoR confirmed largely homogeneous spatiotemporal distribution across the plasma membrane (fig. S4B). Despite coexpression of JAK2, a low cell surface receptor density was obtained, with typically 0.4 to 0.5 molecules/μm^2 in each spectral channel and a Rho11/Dy647 ratio close to unity

[1]Department of Biology and Center of Cellular Nanoanalytics, University of Osnabrück, 49076 Osnabrück, Germany. [2]Division of Cell Signalling and Immunology, School of Life Sciences, University of Dundee, Dundee, UK. [3]Department of Physics, University of Helsinki, Helsinki, Finland. [4]Computational Physics Laboratory, Tampere University, Tampere, Finland. [5]York Biomedical Research Institute and Department of Biology, University of York, Heslington, York YO10 5DD, UK. [6]Institute of Biotechnology, University of Helsinki, Helsinki, Finland. [7]Skirball Institute and Department of Biochemistry and Molecular Pharmacology, New York University School of Medicine, New York, NY, USA. [8]Howard Hughes Medical Institute, Stanford University School of Medicine, Stanford, CA, USA. [9]Department of Molecular and Cellular Physiology and Department of Structural Biology, Stanford University School of Medicine, Stanford, CA, USA.
*These authors contributed equally to this work.
†Corresponding author. Email: ilpo.vattulainen@helsinki.fi (I.V.); ian.hitchcock@york.ac.uk (I.S.H.); piehler@uos.de (J.P.)

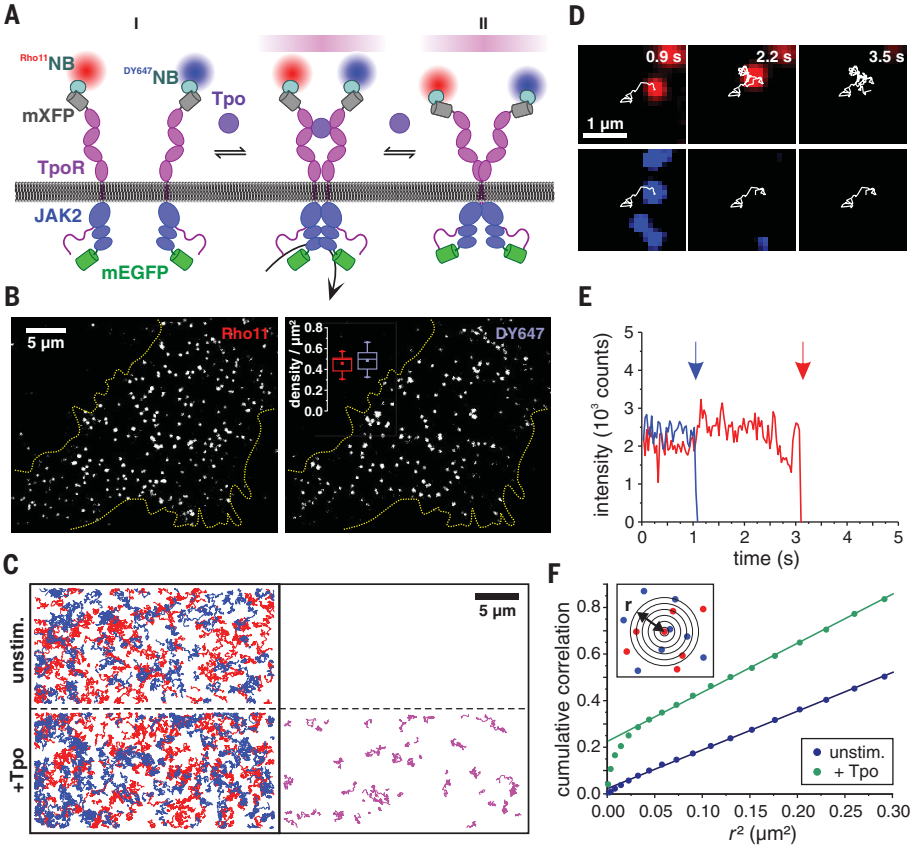

Fig. 1. Receptor monomer-dimer equilibrium quantified by dual-color single-molecule imaging. (**A**) Cytokine receptor activation by ligand-induced dimerization (I) versus ligand-induced conformational change of pre-formed dimers (II) schematically depicted for TpoR. Receptor subunits fused to mXFP were labeled with anti-GFP nanobodies (NB) conjugated to Rho11 (^{Rho11}NB) and DY647 (^{Dy647}NB) at equal concentrations. Receptor homodimers carrying both Rho11 and DY647 are identified by co-tracking analysis (stochastically only 50% of the entire dimer population). Coexpression of JAK2 wild-type and JAK2 variants fused to mEGFP ensures unambiguous detection at the single-cell level. (**B**) Individual mXFP-TpoR subunits in the plasma membrane of HeLa cells after labeling with ^{Rho11}NB and ^{Dy647}NB. The densities of molecules in each channel are depicted in the inset (calculated from 15 cells). In this and later figures, box plots indicate the data distribution of the second and third quartiles (box), median (line), mean (square), and 1.5× interquartile range (whiskers). (**C**) TpoR tracking and co-tracking analysis shown for representative cells. Left: Trajectories (150 frames, ~4.8 s) of individual Rho11-labeled (red) and DY647-labeled (blue) TpoR subunits before (top) and after (bottom) addition of Tpo. Right: Receptor dimers identified by co-locomotion analysis. (**D** and **E**) Single-step photobleaching observed for an individual TpoR dimer (red, Rho11; blue, Dy647) in the presence of Tpo (D) and intensity-time traces with bleaching events indicated by arrows (E). (**F**) Spatial correlation of TpoR at single-molecule level by PICCS as schematically indicated in the inset. Representative results for a cell in the absence (blue) and presence of Tpo (green), respectively, are shown.

(Fig. 1B). Taking into account an effective labeling degree of ~70% achieved by both ^{Rho11}NB and ^{DY647}NB (fig. S4C), the total cell surface concentration of receptor subunits was ~1 to 1.5 molecules/µm^2. Very similar cell surface densities of endogenous TpoR were found in UT-7/Tpo cells, a megakaryocytic cell line commonly used for functional studies on TpoR (*17*), as quantified by flow cytometry experiments with fluorescence-labeled Tpo (fig. S4D). These observations confirm the physiological relevance of low cell surface expression in our model system and suggest that TpoR cell surface densities are under tight control.

Ligand-induced TpoR dimerization revealed by single-molecule co-tracking

Receptor dimerization was quantified by co-localization and co-tracking of individual receptor subunits detected in both spectral channels. We recognized that, statistically, only half of the dimerized receptors would be labeled with two different colors (*18*). This method was calibrated on the basis of negative and positive control experiments with a model transmembrane protein that was dimerized via a monoclonal antibody (movie S3 and fig. S5A). For TpoR coexpressed with JAK2, very few (on average less than one per cell) co-trajectories of ^{Rho11}NB- and ^{DY647}NB-labeled receptors could be detected in the absence of ligand (Fig. 1C and movie S4). By contrast, strong TpoR dimerization was observed upon addition of Tpo, yielding a large number of single-molecule co-trajectories (Fig. 1C and movie S4). The stoichiometry of TpoR homodimers was confirmed by single- and dual-color photobleaching experiments (Fig. 1, D and E, and fig. S5B). The significant increase in Rho11 fluorescence upon photobleaching of DY647 indicated FRET within co-locomoting TpoR dimers, confirming molecular proximity within ligand-induced TpoR dimers (Fig. 1E and fig. S5C). TpoR dimerization levels increased up to a concentration of 10 nM Tpo and then decreased at elevated concentrations, yielding a bell-shaped dose-dimerization curve that essentially matched the bell-shaped dose-response curve of STAT5 phosphorylation (fig. S3, A and B). This concentration-dependent self-inhibition can be explained by a gradual shift from a 1:2 to a 1:1 Tpo:TpoR stoichiometry. Ligand-induced receptor dimerization was accompanied by a small yet significant decrease of ~25% in the overall diffusion constant (fig. S5D and table S1) that can be ascribed to the increased friction within the membrane for receptor dimers relative to monomers (*19*, *20*). Furthermore, the fraction of immobile receptors increased after addition of ligand (table S1), which is in line with receptor endocytosis upon activation (*21*, *22*). Very similar diffusion properties in the absence and presence of Tpo were obtained for TpoR labeled via the 21–amino acid E3 tag (*23*) (fig. S5D and table S1), confirming minimal bias of receptor diffusion and interaction by the mXFP tag. Significantly lower levels of ligand-induced dimerization were observed in the absence of JAK2 (Fig. 2A). The diffusion constants of TpoR monomers and dimers were ~15% lower when JAK2 was coexpressed (fig. S5E and table S1).

Dissociation of ligand-induced TpoR dimers was observed very rarely within the experimental time frame. A reliable determination of complex lifetimes was therefore not possible because of a lack of co-tracking fidelity as well as photobleaching. These observations suggest that the stability of ligand-induced TpoR dimers is high relative to the imaging time resolution. To exclude the possibility that TpoR pre-dimerization was missed by co-tracking analysis because of very short dimer lifetimes in the absence of ligand, we quantified the spatial organization of receptor subunits in the plasma membrane by particle image cross-correlation spectroscopy (PICCS) (*24*) of individual TpoR subunits detected in both channels.

Spatial cross-correlation above the background was observed only after adding the ligand (Fig. 1F, fig. S6, C and D, and table S2), yielding dimerization levels similar to those determined by co-locomotion analysis. Quantification of the relative number of co-trajectories yielded ligand-induced dimerization levels that were 75% of those of a positive control based on a model transmembrane protein that was dimerized by a high-affinity monoclonal antibody (Fig. 2A and movie S3). Antibody-induced dimerization of the model transmembrane protein reduced its diffusion constant in a way similar to that observed for ligand stimulation of TpoR (table S1).

Comparable spatiotemporal dynamics of TpoR, EpoR, and GHR dimerization

For EpoR and GHR, very similar properties with respect to diffusion and interaction in the plasma membrane were observed: The receptor cell surface expression was low, as previously found for EpoR in erythroid cell types (*15*) and in binding experiments with labeled GH bound to endogenous GHR in GH-responsive (*25*) HuH7 cells (figs. S7 and S8). Uncorrelated receptor diffusion was observed in the absence of ligand, and efficient dimerization occurred in the presence of ligand with a bell-shaped concentration dependence (Fig. 2A, movies S5 and S6, and figs. S3B, S7, A and B, and S8, A and B). Similar levels of ligand-induced dimerization (50% and 60% for EpoR and GHR, respectively) were observed, which depended on the presence of JAK2, as well as similar changes in the diffusion properties (Fig. 2A, figs. S7C and S8C, and table S1). However, assays with GHR using cells cultured in the presence of fetal calf serum were strongly biased by traces of bovine GH (fig. S8D). For this reason, dimerization was quantified after serum starving and scavenging of residual bovine GH by adding purified soluble GHR ectodomain. Under these conditions, ligand-induced dimerization was unambiguously confirmed for GHR. By contrast, antagonistic Epo (Ser^{126} → Glu) and GH (Gly^{146} → Arg) mutants (*26*, *27*) did not dimerize their receptors in the plasma membrane (figs. S7D and S8E).

JAK2 PK domains contribute to receptor dimerization

The increased levels of ligand-induced dimerization that were obtained for all three receptors in the presence of JAK2 (Fig. 2A) suggest that the associated JAKs energetically contribute to receptor dimerization. To exclude the possibility that dimerization was enhanced by downstream signal activation, we compared TpoR dimerization in the absence and presence of the JAK2 inhibitor ruxolitinib, which remained unchanged (Fig. 2B). These observations suggested stabilizing interactions between the associated JAKs, which have been implicated in regulating the activation of receptor tyrosine kinases (*28*). JAKs comprise four domains: The intimately connected N-terminal FERM and SH2-like (FS) domains bind the receptor through its membrane proximal box 1 and box 2 motifs (Fig. 2, C and D), whereas the C-terminal tyrosine kinase (TK) domain is regulated by the adjacent pseudokinase (PK) domain, which lacks tyrosine kinase activity. To identify the role played by the TK and PK domains in contributing to the additional binding energy, we quantified TpoR dimerization in the presence of JAK2 variants in which the TK domain (JAK2 ΔTK) or both TK and PK domains (JAK2 ΔPK-TK) were truncated (Fig. 2C). These experiments established that stabilization of ligand-induced dimers was maintained in the absence of the TK domain but was abrogated for JAK2 ΔPK-TK (Fig. 2E).

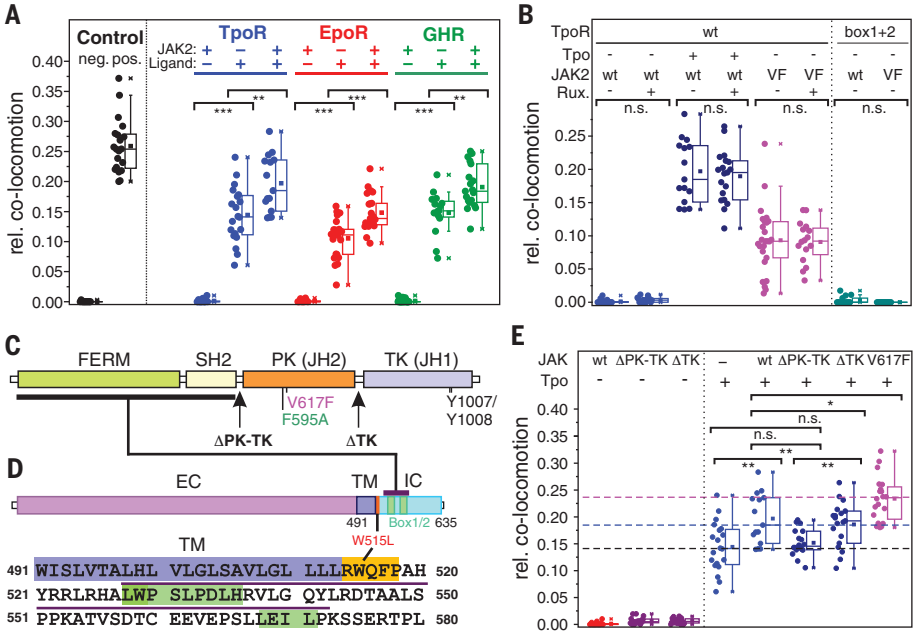

Fig. 2. JAK2 regulates ligand-induced dimerization of TpoR, EpoR, and GHR. (**A**) Relative number of co-trajectories observed for positive and negative control proteins as well as for unstimulated TpoR, EpoR, and GHR and after stimulation with the respective ligand with and without coexpression of JAK2. (**B**) Comparison of dimerization levels in the absence and presence of the JAK2 inhibitor ruxolitinib (left) and dimerization levels of TpoR Box1+2 mutant (right) coexpressed with JAK2 wild-type (wt) or V617F (VF). (**C**) Primary structure of JAK2 comprising FERM-SH2 (FS), pseudokinase (PK), and tyrosine kinase (TK) domains. Positions of the C-terminal truncations ΔTK and ΔPK-TK as well as key residues and mutations are highlighted. (**D**) Primary structure of TpoR including extracellular (EC), transmembrane (TM), and intracellular (IC) domains. The primary sequence of the TM domain (blue) followed by a functionally critical amphipathic motif (orange) and the intracellular domain (ICD) including the Box motifs (green) is shown below. The putative JAK2 binding sequence is indicated by a purple overline. Amino acid abbreviations: A, Ala; C, Cys; D, Asp; E, Glu; F, Phe; G, Gly; H, His; I, Ile; K, Lys; L, Leu; M, Met; N, Asn; P, Pro; Q, Gln; R, Arg; S, Ser; T, Thr; V, Val; W, Trp; Y, Tyr. (**E**) Ligand-induced dimerization of TpoR coexpressed with different JAK2 variants as identified in (C). Dashed lines mark the mean dimerization levels in the absence (black) and presence of JAK2 wt (blue) or JAK2 V617F (magenta), respectively. In (A), (B), and (E), each data point represents the analysis from one cell with a minimum of 10 cells measured for each condition. $*P < 0.05$, $**P \leq 0.01$, $***P \leq 0.001$; n.s., not significant.

The oncogenic JAK2 V617F mutation induces ligand-independent receptor dimerization

These data suggest that intermolecular JAK2 interactions involving the PK domains may be important for JAK activation. The JAK2 PK domain is the primary site of somatic mutations in Ph^- MPNs (*14*, *29*). For example, JAK2 V617F is hyperactive (fig. S2C), and the consequent factor-independent proliferation relies on the coexpression of a homodimeric class I cytokine receptor, usually either EpoR or TpoR, at the cell surface (*30*, *31*). However, the mechanisms underlying JAK2 V617F activation remain elusive. Strikingly, coexpression of JAK2 V617F yielded substantial ligand-independent dimerization of TpoR, EpoR, and GHR (Fig. 3A and movies S4 to S6). Relative to ligand-induced dimerization, ligand-independent dimerization in the presence of JAK2 V617F reached ~50% of the maximum level for TpoR, ~25% for EpoR, and ~10% for GHR, respectively.

Single-molecule photobleaching confirmed that JAK2 V617F induced formation of TpoR dimers, and single-molecule FRET (smFRET) confirmed the molecular proximity of both subunits (fig. S9A). Ligand-independent JAK2 V617F–induced receptor dimers showed diffusion properties that were very similar to those of the corresponding ligand-induced receptor dimers in the presence of wild-type JAK2 (table S1 and figs. S5E, S7E, and S8G). Somewhat higher FRET efficiencies were observed for ligand-independent dimerization of TpoR in the presence of V617F relative to TpoR dimers formed in the presence of Tpo (fig. S9A), suggesting differences in the structural organization of the receptor ectodomains in these dimers. Ligand-independent dimerization of TpoR in the presence of JAK2 V617F did not rely on JAK2 TK activity, as confirmed by treatment with ruxolitinib (Fig. 2B). Moreover, no dimerization of TpoR by JAK2 V617F was found for a box 1/box 2 mutant (TpoR Box 1+2) that is defective in JAK recruitment to the receptor (Fig. 2B).

Additional molecular determinants contribute to JAK2 V617F–mediated dimerization

These results support our hypothesis that JAK2 V617F short-circuits ligand-induced receptor dimerization and highlight the critical role of the PK domain. We therefore explored in more detail the molecular determinants of JAK2 V617F–induced dimerization of TpoR. Combination of V617F with the mutation Phe^{595} → Ala (F595A), which effectively abolishes constitutive activation by V617F (*32*), largely neutralized ligand-independent dimerization of TpoR by JAK2 V617F (Fig. 3B). In the absence of the tyrosine kinase domain (ΔTK), JAK2 V617F dimerized TpoR in a ligand-independent manner and remained sensitive to the combination with F595A (Fig. 3B). Strikingly, dimerization and activation of TpoR by JAK2 V617F occurred independently of the receptor ectodomain (Fig. 3B, movie S7, and fig. S9, B and C). Taken together, these results suggest that the V617F mutation enhances interactions between the PK domains. Further enhanced dimerization levels of TpoR were observed in the presence of Tpo and JAK2 V617F (Fig. 2E). The substantial differences observed between JAK2 V617F–induced dimerization of EpoR, TpoR, and GHR, however, suggested that the receptor itself also contributes to dimerization. We therefore explored whether JAK2 V617F was capable of driving homodimerization of the interferon-γ receptor subunit IFNGR2. Significant dimerization, although much lower than with EpoR, TpoR, and GHR, was observed for IFNGR2 (Fig. 3C), confirming the critical role of the receptor in JAK2 V617F–mediated dimerization. JAK2 V617F was even capable of driving substantial heterodimerization between mXFP-TpoR and SNAPf-EpoR (Fig. 3C and movie S8); this result served to corroborate that ligand-independent dimerization was largely driven by JAK2 V617F.

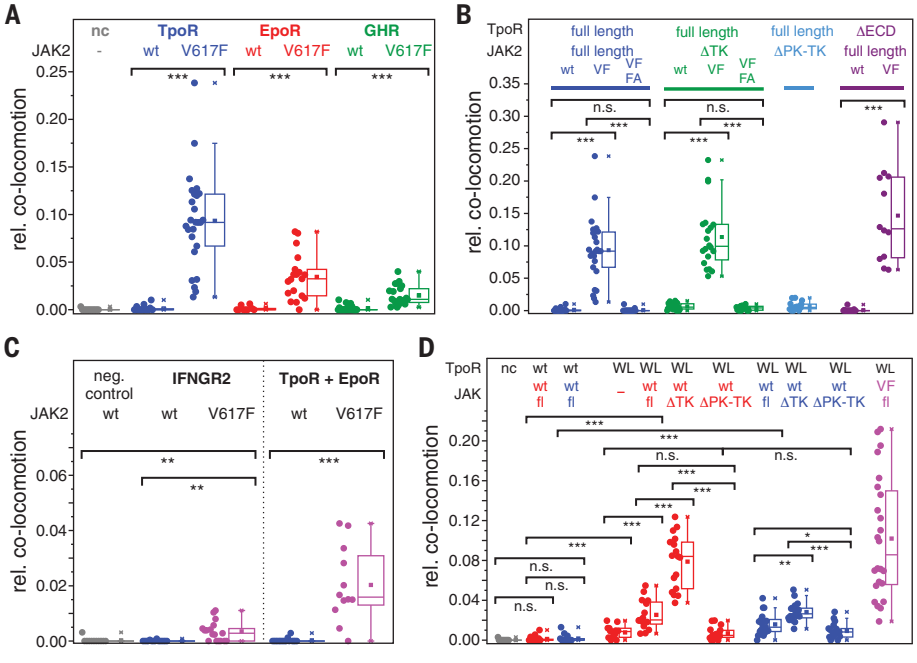

Fig. 3. Oncogenic JAK2 and TpoR mutants drive ligand-independent receptor dimerization. (**A**) Ligand-independent dimerization of TpoR, EpoR, and GHR by JAK2 V617F. Co-locomotion was quantified for TpoR, EpoR, and GHR coexpressed with either JAK2 or JAK2 V617F, compared to a negative control (nc). (**B**) Ligand-independent dimerization by JAK2 V617F is driven by the pseudokinase domain. Co-locomotion was analyzed for the indicated receptor and JAK2 variants. For ΔECD-TpoR, dimerization by JAK2 V617F was quantified by single-molecule FRET (see movie S7). (**C**) Homo- and heterodimerization of cytokine receptors by JAK2 V617F. Left: Homodimerization of IFNGR2. Right: Heterodimerization of EpoR and TpoR, which were orthogonally labeled via mXFP and SNAPf-tag, respectively (see movie S8). (**D**) Ligand-independent dimerization of TpoR W515L (WL) in the absence and presence of different JAK2 (red) and TYK2 (blue) variants and JAK2 V617F (VF, magenta). In (A) to (D), each data point represents the analysis from one cell with a minimum of 10 cells measured for each condition. *P < 0.05, **P ≤ 0.01, ***P ≤ 0.001.

Membrane-proximal amphipathic segment is involved in receptor dimerization

To shed light on potential interactions directly mediated by the receptor, we focused on the juxtamembrane (JM) amphipathic motif of TpoR (Fig. 2D), which is critical in regulating TpoR activation (*33*). Most prominently, the mutation Trp^{515} → Leu (W515L) is an oncogenic mutation that constitutively activates TpoR signaling (*34*). Structural studies on the transmembrane (TM) and JM domains of TpoR by solid-state nuclear magnetic resonance have suggested that W515L enhances interaction of the TM domains (*35*). Similar weak interactions between the TM domains have been reported for EpoR (*36*) and GHR (*6*, *7*). Strikingly, we observed substantial dimerization of TpoR W515L in the absence of ligand (Fig. 3D). Although ligand-independent dimerization of TpoR W515L in the absence of JAK2 was weak and transient, stronger and more stable dimerization was observed upon coexpression of JAK2 (Fig. 3D and movie S9), confirming cooperative interactions mediated by TpoR TM-JM and JAK2 PK domains. Likewise, a significant (but lesser) increase in ligand-independent dimerization was observed for TpoR W515L when coexpressing TYK2 instead of JAK2. TYK2 complements the activity of TpoR in the absence of JAK2, although with lower potency (*37*). Whereas deletion of the TK domains further increased ligand-independent TpoR W515L dimerization (Fig. 3D), truncation of the PK domain decreased dimerization to the level in the absence of JAK2/TYK2 (Fig. 3D), confirming productive PK-PK interactions in W515L-induced dimers. Ligand-independent dimerization was enhanced upon coexpression of TpoR W515L with JAK2 V617F (Fig. 3D), highlighting the additive nature of these interactions, in line with their additivity in ligand-independent signaling activities (*38*).

Additive interactions control the assembly of the signaling complex

To quantify the different energetic contributions involved in the assembly of the TpoR

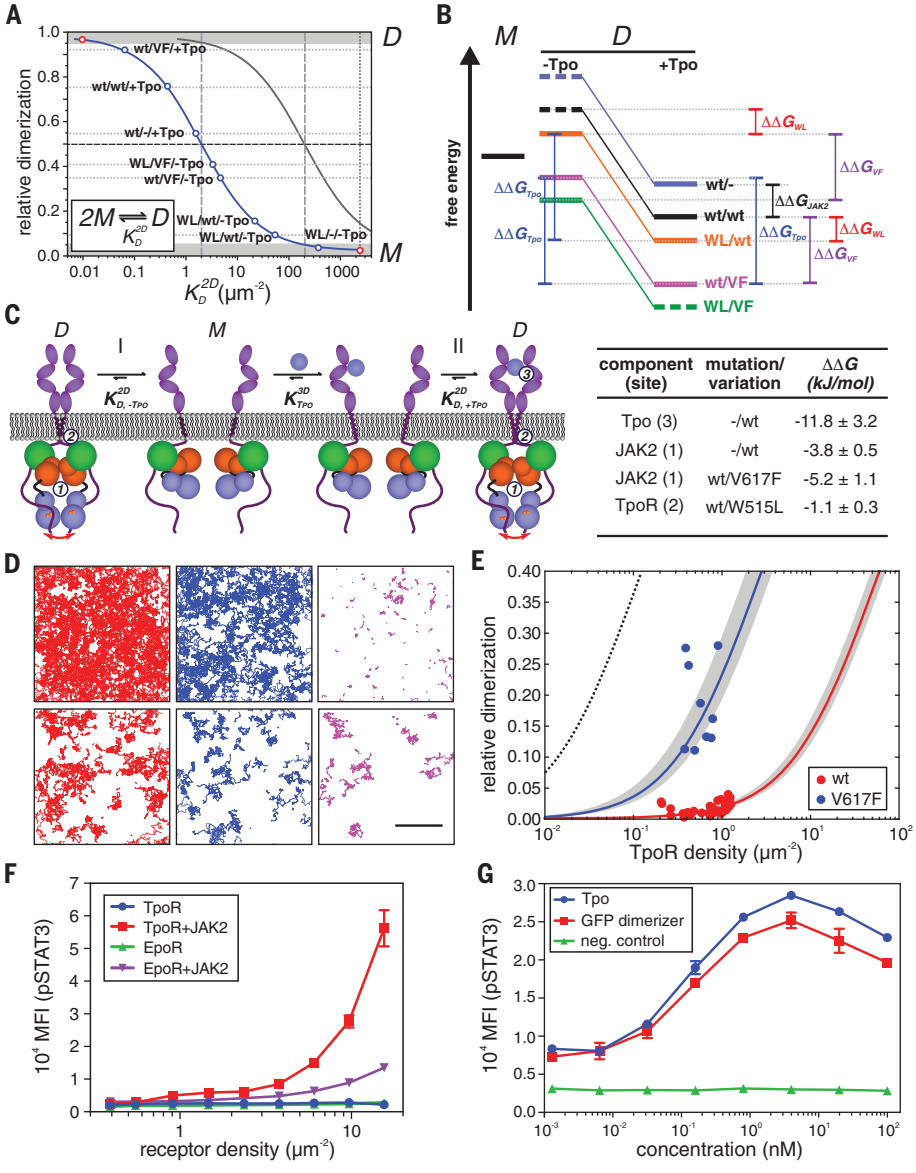

Fig. 4. Energy landscape of TpoR dimerization and its mechanistic interpretation. (**A**) Determination of 2D equilibrium dissociation constants from the dimerization levels observed under different conditions. Each dot corresponds to a dimerization experiment where the label denotes TpoR [wt or W515L (WL)]/JAK2 [wt or V617F (VF)]/ligand (+/−Tpo). The 2D law of mass action is depicted for a monomer-dimer (*M-D*) equilibrium at a total receptor surface concentration of 2 μm^{-2} (blue) and 200 μm^{-2} (gray). Dimerization levels that cannot be unambiguously quantified by co-tracking are indicated by gray zones. (**B**) Semi-quantitative energy diagram of the *M-D* equilibrium in the absence (−Tpo) and presence (+Tpo) of ligand as derived from (A). Experiments involving different TpoR/JAK2 combinations are depicted in different colors; energy levels for determining different values of ΔΔ*G* are indicated. Energetic contributions ΔΔ*G* obtained for different combinations of components and mutations are listed in the table below. (**C**) Proposed mechanism of homodimeric cytokine receptor activation deduced from live-cell dimerization assays: In the absence of ligand (I), the basal level of dimerization caused by interactions mediated via the JAK2 PK domains (1) and TM/JM domains (2) is negligible because K_D^{2D} substantially exceeds the receptor surface concentration in the plasma membrane. Ligand binding provides the additional binding energy (3) required to shift the equilibrium toward the dimeric state. Oncogenic mutations enhancing interactions 1 or 2 shift the equilibrium toward the dimeric state in a ligand-independent manner (II). (**D** to **F**) Intrinsic dimerization and activation of TpoR and EpoR. (D) Representative smFRET experiments with TpoR coexpressed with JAK2-mEGFP wt (top) and V617F (bottom) showing single-molecule trajectories of the donor (red) as well as the acceptor upon direct excitation (blue) and via smFRET (magenta) detected within 150 frames (5 s). Total receptor densities were 1.2/μm^2 for JAK2 wt and 0.4/μm^2 for JAK2 V617F. Scale bar, 5 μm. (E) Relative ligand-independent dimerization levels as a function of receptor density for full-length TpoR in the presence of JAK2 wt and V617F and fit by the law of mass action for a monomer-dimer equilibrium (solid lines). Confidence intervals of the fit are indicated as gray zones. The dimerization curve in the presence of Tpo calculated from the corresponding K_D^{2D} is shown for comparison (black dotted line). (F) Ligand-independent activation of STAT3 phosphorylation upon overexpression of TpoR and EpoR, respectively, together with JAK2 wt in HeLa cells. pSTAT3 and receptor cell surface densities were quantified by phospho-flow analysis. As a negative control, coexpression of JAK2 was omitted. (**G**) Activation of mXFP-TpoR by dimerization with an NB-based cross-linker that binds the mXFP-tag. For comparison, activation by Tpo in the presence and absence of TpoR (neg. control) is shown. In (F) and (G), error bars denote SEM.

signaling complex, we converted dimerization levels into two-dimensional equilibrium dissociation constants (K_D^{2D}) according to the law of mass action for a monomer-dimer equilibrium (Fig. 4A and table S3). These were used to estimate the energetic contributions, ΔΔ*G*, of the different interaction sites within the receptor, as schematically outlined in Fig. 4B. The ΔΔ*G* values were determined under the assumption that ligand-mediated dimerization, as well as the interactions mediated by the JAK2 PK domains and by the TM/JM domains, additively contribute to the total binding energy (Fig. 4C). Exploiting the availability of the constitutively dimerizing mutants TpoR W515L and JAK2 V617F, we obtained a comprehensive energetic picture for the different interactions (Fig. 4B). These moderate binding energies highlight the cooperativity of fine-tuned subtle interactions regulating receptor dimerization. Our results indicate a low intrinsic dimerization affinity of the TpoR/JAK2 subunits, which is attributed to interactions between the JAK PK domains and the TM/JM region of the receptor (sites 1 and 2, respectively, in Fig. 4C). At physiological receptor densities at the plasma membrane, the total binding energy of these interactions is not sufficient to yield significant dimerization in the absence of ligand (Fig. 4C). Thus, the additional binding energy provided by ligand-mediated receptor cross-linking effectively shifts the equilibrium toward receptor dimers (Fig. 4C). Likewise, a small increase in the binding energy of the intrinsic interactions upon single point mutations in the constitutive interacting sites

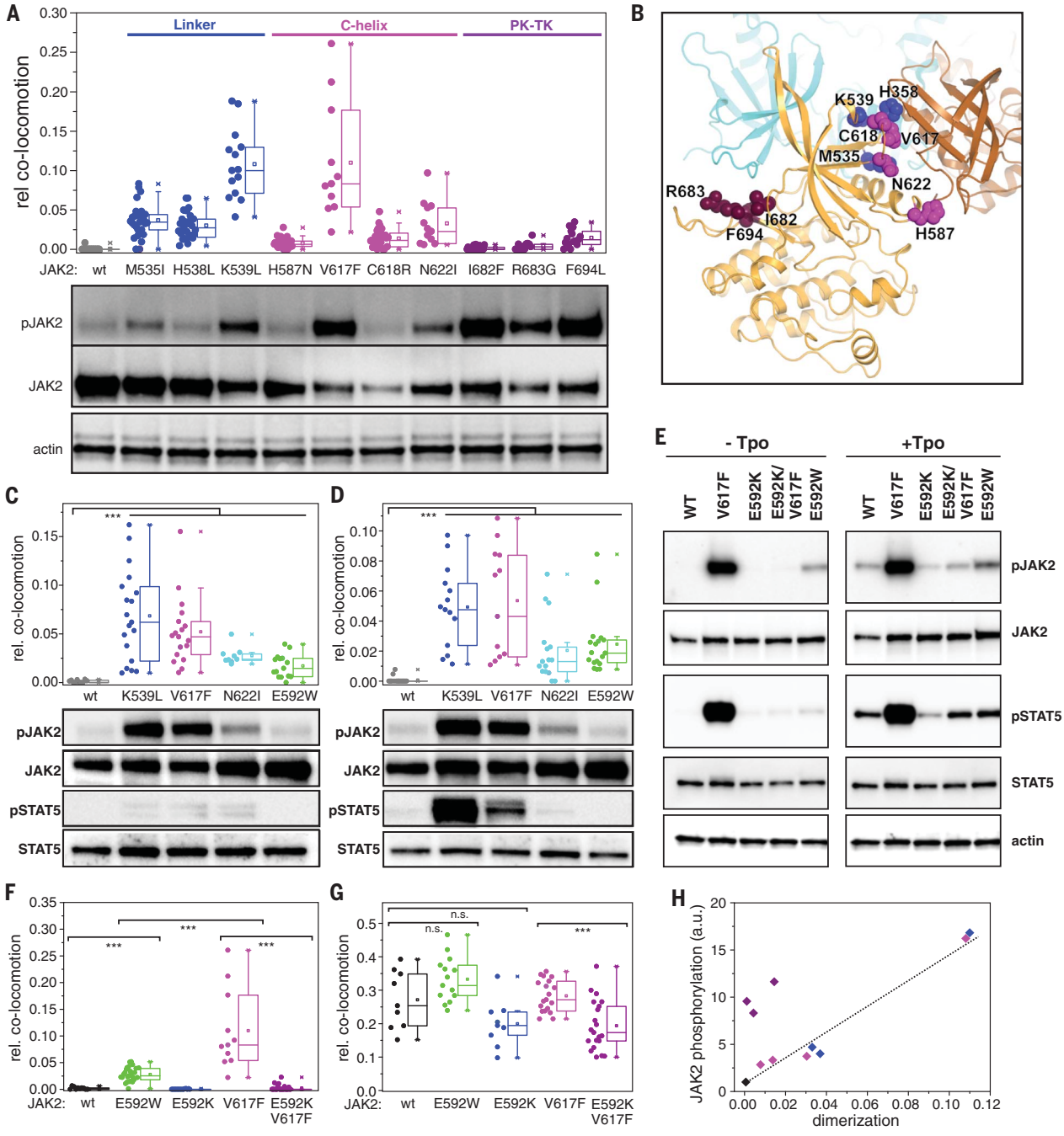

Fig. 5. Dimerization interface of JAK2 PK domains. (**A**) Ligand-independent dimerization of TpoR (top) and associated JAK2 phosphorylation (bottom) in the presence of oncogenic mutations within the JAK2 PK domain. Residues are grouped and colored according to their location within the PK structure: FS-PK linker (blue); αC helix (magenta), and PK-TK interface (purple). (**B**) Putative intermolecular PK-PK interface derived from the MD simulations, with one PK domain colored orange and the other brown. The positions of the residues mutated in (A) are mapped onto the orange PK domain. Superimposed in cyan is the TK domain in its autoinhibitory configuration (intramolecular) relative to the orange PK domain; the TK domain would clash with the second (brown) PK domain. (**C** and **D**) Ligand-independent dimerization of EpoR (C) and GHR (D) (top) and associated JAK2 phosphorylation (bottom) for selected constitutively active JAK2 mutants. (**E** to **G**) Altering dimerization and activation by perturbation of the putative PK-PK interface via mutagenesis of Glu^{592}. (E) Activity of different JAK2 mutants in HeLa cells stably expressing mXFP-TpoR. Phosphorylation of JAK2 and STAT5 in the absence of ligand (left) and after stimulation with Tpo (right) was probed by Western blot. [(F) and (G)] Dimerization of TpoR associated with different JAK2 mutants in the absence (F) and presence (G) of Tpo. (**H**) Correlation of receptor dimerization with activation for constitutively active JAK2 mutants [same color coding as in (A)]. Error bars are omitted for clarity. In (A), (C), (D), (F), and (G), each data point represents the analysis from one cell with a minimum of nine cells measured for each condition. ***$P \leq 0.001$.

can shift the equilibrium toward receptor dimers, as observed for TpoR W515L and JAK2 V617F.

Weak intrinsic receptor dimerization correlates with constitutive activation

These analyses predict a low intrinsic dimerization affinity for homodimeric class I cytokine receptors. To experimentally quantify the K_D^{2D} of ligand-independent receptor dimerization, we used single-molecule FRET (smFRET) for direct detection of dimer formation via sensitized fluorescence. Thus, ligand-independent interaction of the receptors could be reliably detected and quantified even at relatively high receptor densities, which were not compatible with robust co-tracking analysis. Under these conditions, ligand-independent TpoR dimers could be observed in the presence of wild-type JAK2, whereas much higher levels were observed in the presence of JAK2 V617F even at much lower receptor densities (Fig. 4D, fig. S9D, and movie S10). Substantially shorter smFRET trajectories were found for TpoR dimers in the presence of wild-type JAK2 compared to JAK2 V617F, suggesting rather transient dimerization under wild-type conditions. These observations support our hypothesis that the V617F mutation promotes receptor dimerization by stabilizing inter-JAK2 interactions. Relative dimerization increased in a receptor density–dependent manner (Fig. 4E). By fitting the law of mass action, a two-dimensional K_D^{2D} of 110 (±60)/μm^2 was determined for TpoR in the presence of wild-type JAK2 compared to 5 (±2)/μm^2 for JAK2 V617F, in good agreement with the values determined from co-locomotion analysis (table S3). Similar results were observed with variants of EpoR and TpoR lacking the extracellular domains (EpoR-ΔECD and TpoR-ΔECD, respectively) (fig. S9, E and F, and table S3). These observations are in line with the activation of EpoR via synthetic cross-linkers (*19*, *39*). Likewise, efficient activation of TpoR was achieved by dimerization through binding of a flexible cross-linker based on the NB against the mXFP-tag (Fig. 4G).

Dimerizing and nondimerizing oncogenic JAK2 mutations

To further investigate the mechanism of signal activation, we compared various oncogenic mutations in the JAK2 PK domain (Fig. 5, A to D) (*40*). Three groups of mutations were chosen covering the FS-PK linker region (M535I, H538L, and K539L; group I), residues in the proximity of the αC helix (H587N, C618R, N622I; group II), and a hotspot at the autoinhibitory PK-TK interface (*41*, *42*) (I682F, R683G, F694L; group III) (Fig. 5, A and B). Whereas ligand-independent activation was confirmed for all these JAK2 mutants, consistent TpoR dimerization was observed only for mutations within the first two groups (Fig. 5, A and B, and fig. S10). In contrast, JAK2 mutations at the PK-TK interface (group III) yielded very low dimerization levels relative to their potent constitutive activation. This disconnect suggests that gain-of-function mutations in the PK cause JAK2 hyperactivity via distinct mechanisms: (i) loss of PK-mediated autoinhibition, facilitating trans-autophosphorylation of the TK domains

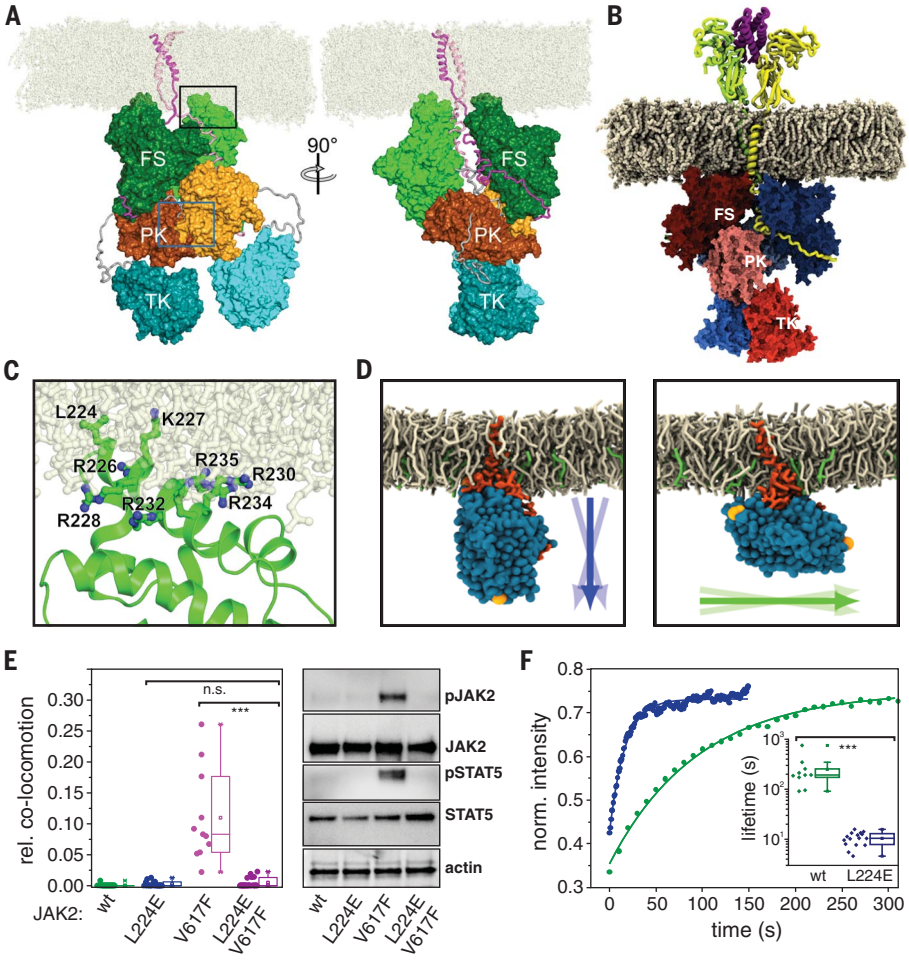

Fig. 6. Structural organization of homodimeric cytokine receptor signaling complexes in the membrane. (**A**) Snapshot (t = 1 μs) from all-atom MD simulations of JAK2 bound to TpoR (TM and IC domains) forming a homodimeric complex (system $S1_{AA}$; movie S11). JAK2 is colored green (FS), orange (PK), and cyan (TK). Protomer 1 is in dark colors with domains labeled; protomer 2 is in light colors and unlabeled. The FS-PK and PK-TK linkers are colored gray. TpoR is colored magenta (bound to JAK2 protomer 1) and pink (bound to JAK2 protomer 2). POPC lipid molecules are colored off-white. The PK-PK interface region highlighted by the green rectangle is shown in Fig. 5B. (**B**) Snapshot (t = 1 μs) from an all-atom MD simulation of a homodimeric complex of JAK2 bound to EpoR (residues Pro^{31} to Ser^{335}, system $S4_{AA}$) in the presence of Epo (movie S12). (**C**) Membrane binding of the F2 subdomain of FS stabilizes the orientation of JAK2 relative to the membrane [enlarged view of the region indicated by the black rectangle in (A)]. The side chains of Lys^{224} and the seven Lys and Arg residues in α3 that change orientation and flexibility upon interaction with the membrane are highlighted. (**D** to **F**) Functional role of Lys^{224} in TpoR dimerization and activation. (D) Representative orientation of JAK2 FS wt (left) and L224E (right) observed in MD simulations (systems $S14_{CG}$ and $S16_{CG}$, respectively). Arrows indicate the orientation of the FS domain and its variation during the simulations. (E) Ligand-independent dimerization of TpoR (left) as well as JAK2 and STAT5 phosphorylation (right) observed for JAK2 wt and V617F upon combination with L224E. (F) Stability of JAK2 FS wt and L224E binding to TpoR probed by live-cell micropatterning (fig. S14C) in combination with FRAP. Representative FRAP curves are shown for JAK2 wt (green) and L224E (blue); the inset, using the same colors, shows a statistical analysis of dissociation rate constants. Each data point represents the analysis from one cell with a minimum of 10 cells measured for each condition. ***$P \leq 0.001$.

in the context of receptor-JAK2 monomers (group III), and (ii) stabilization of receptor-JAK2 dimers (groups I and II). Similar dimerization and activation patterns were observed for EpoR and GHR upon expression of selected mutants from groups I and II (Fig. 5, C and D), supporting the common mechanistic basis for mutational hyperactivation of different receptors.

Putative PK-PK interface mediates receptor dimerization and activation

Interestingly, groups I and II both localize to a putative PK-PK interface (*43*, *44*), which has been proposed based on the JAK1 PK crystal structure (*45*). This interaction is mediated by the N lobe of the PK domain, predominantly the αC-helix, and the linker connecting the FS and PK domains (*43*, *45*, *46*). We focused on residue Glu^{592}, which is located at the center of the interface (Fig. 5B). In the context of TpoR, the mutation $Glu^{592} \rightarrow$ Ala did not alter basal (non–cytokine-mediated) JAK2 activation (*33*); however, activity increased upon introduction of a large hydrophobic residue [$Glu^{592} \rightarrow$ Trp (E592W); Fig. 5E and fig. S11A], and this correlated with ligand-independent dimerization of TpoR (Fig. 5F). In contrast, switching charge at this position [$Glu^{592} \rightarrow$ Lys (E592K)] led to slightly reduced levels of activation and dimerization in the presence of Tpo (Fig. 5, E and G) and substantially suppressed the hyperactivity of V617F (E592K/V617F) by reducing dimerization (Fig. 5, E and F, and fig. S11A).

TpoR density–dependent activation assays with JAK2 Glu^{592} mutants showed that E592W shifted the onset of constitutive activation to lower receptor densities relative to the wild type, whereas no constitutive activation was detectable for E592K (fig. S11B). These results highlight the changes in the intrinsic dimerization affinities resulting from mutation of the PK-PK interface. JAK2 E592W also constitutively dimerized and activated EpoR and GHR (Fig. 5, C and D). Very similar patterns of dimerization and activation were found for the combination of JAK2 Glu^{592} mutants with EpoR using pSTAT5 as a functional readout (fig. S11, C and D), highlighting the generic relevance of this JAK2 interaction site for homodimeric cytokine receptors. Overall, constitutive receptor dimerization and activation showed a striking correlation for all mutants located in close proximity to the PK-PK interface (Fig. 5H), thereby confirming the relevance of the PK-PK interface for JAK2 activation and dysregulation.

Atomistic model of a transmembrane signaling complex

On the basis of existing structural data and our experimental validation of a JAK2 PK-PK interface, we generated atomistic models of TpoR and EpoR dimers within membranes. Ligand-independent dimerization was modeled for JAK2 in complex with TpoR-ΔECD (Fig. 3B; Fig. 4, E and F; and fig. S9, B and C). We performed multiple independent 1-μs all-atom MD simulations for this system integrated into a 1-palmitoyl-2-oleoyl-*sn*-glycero-3-phosphocholine (POPC) membrane (simulation system $S1_{AA}$; table S4) [see (*18*) for model system construction]. For comparison, we generated a corresponding model of JAK2 bound to EpoR including the ectodomains dimerized by Epo (simulation systems 4_{AA} and 5_{AA}; table S4) [see (*18*) for an independent construction of this model system]. These systems represent very high receptor densities (~5000 receptors/μm^2), and therefore we expect the equilibrium to be fully shifted toward the dimer even in the absence of the ligand. Despite starting with different complex geometries (*18*), these MD simulations converged into similar structural organization of JAK2 homodimers (Fig. 6, A and B, movies S11 and S12, and fig. S12, A to C). In both cases, JAK2 adopts a stable extended orientation perpendicular to the membrane normal, with a slightly more tilted orientation in the EpoR complex (fig. S12B). The FERM domains were found to strongly interact with the inner leaflet of the lipid bilayer through the hydrophobic residue Lys^{224} and several positively charged residues from helix α3 in the F2 subdomain (Fig. 6C and fig. S13, A to C), which may account for the decreased receptor diffusion constants in the presence of JAK2 (figs. S5E, S7E, and S8G). These JAK2-lipid interactions stabilize the orientation of the complex with respect to the membrane. In contrast to the crystal structure of the JAK2 FS domains (used here as the starting geometry), which suggested that EpoR dimerization is mediated by FS domains (*47*), we observed no stable contacts between the FS domains during our simulations. The contacts observed in the crystal structure predominantly dissociated during the simulations of the EpoR-JAK2 complex (fig. S13, D to F), and the residues involved in these contacts were found anchored into the membrane (fig. S13G). Structural organization of JAK2 at the membrane was largely independent of the lipid composition, as confirmed by atomistic MD simulations with lipid mixtures comprising cholesterol and phosphatidylinositides in addition to POPC (simulation system $S3_{AA}$; table S4 and figs. S12, A to C, and S13, B and C). The tight coupling of the FS domains with the membrane enforces an appropriate orientation for optimal intermolecular PK-PK interaction of JAKs within the receptor dimers (Fig. 6A, left) involving several residues that we experimentally found to be implicated in dimerization (Fig. 5B). The TK domains were the most mobile parts of the otherwise stable complex (Fig. 6, A and B, fig. S12, and movies S11 and S12). The simulation results support the schematic model shown in Fig. 4C, in which receptor dimerization shifts the cis PK-TK autoinhibitory interaction to a trans PK-PK interaction and thus liberates the TK domains.

Membrane anchoring of the FERM domain regulates dimerization affinity

MD simulations predicted an important role for FERM domain anchoring into the membrane via Lys^{224}, a conserved hydrophobic residue within the JAK family (Leu in JAK1 and TYK2, Val in JAK3), which is surface-exposed in all FERM domain structures. To functionally test this prediction, we introduced a negative charge in this position [$Lys^{224} \rightarrow$ Glu (L224E)]. MD simulations confirmed a pronounced reorientation of JAK2 L224E relative to the wild type (simulation systems $S14_{CG}$ and $S16_{CG}$; Fig. 6D, table S4, and fig. S14, A and B). Strikingly, introduction of L224E led to markedly reduced ligand-independent TpoR, EpoR, and GHR dimerization and activation by JAK2 V617F (Fig. 6E and fig. S14, C and D); this finding supports the key role of Lys^{224} in orienting JAK2 at the membrane to allow productive PK-PK interactions. Cell micropatterning experiments revealed that the L224E mutation diminished without completely abrogating JAK2 binding to the receptors (fig. S14E). The binding stability of the FS interaction with TpoR at the plasma membrane was reduced by a factor of ~20, as quantified by FRAP experiments (Fig. 6F). Ligand-induced receptor dimerization and activation were still observed for JAK2 L224E, although with reduced potency relative to wild-type JAK2 (fig. S14, F and G), which was also observed for the mutation E592K that directly compromised the PK-PK interface. Likewise, JAK2 L224E abrogated ligand-independent TpoR activation at elevated receptor densities (fig. S14H). JAK2 L224E also strongly reduced ligand-stimulated activation of EpoR and GHR (fig. S14G), which supports the key role of membrane anchoring across the homodimeric class I cytokine receptor family. Taken together, these results confirm that the L224E mutation does not compromise the structural integrity of JAK2; rather, it destabilizes the intermolecular interaction between JAK2 monomers by altering the orientation of the receptor complex, as predicted by our MD simulations.

Oncogenic mutations alter and stabilize the receptor dimerization interface

The PK-PK interaction in the signaling complex remained highly stable during the dimer simulations (systems $S1_{AA}$ to $S5_{AA}$), corroborating the relevance of this interaction for the structural organization of the signaling complex. This stability arises from a combination

of hydrophobic and polar interactions at the interface (tables S5 and S6). Interactions of certain key residues, such as Glu^{592} and Phe^{595}, were found to be very stable, as exemplified by persistent contacts with their counterparts in the other monomer (table S5). These results are consistent with a previous suggestion that the JAK2 V617F mutation promotes activation by forming an intramolecular pi-stacking network between Phe^{617}, Phe^{594}, and Phe^{595} (*46*, *48*). This hypothesis was tested by atomistic MD simulations for the isolated V617F mutant PK-PK dimer (systems $S6_{AA}$ and $S7_{AA}$; table S4). Comparison of the interacting residue pairs in these two cases (table S6) highlights that some of the interactions at the interface are strikingly reorganized. Many of these interaction pairs involve a residue from the N-terminal linker (residues 526 to 539) connecting the PK domain to the FS domain. This linker has been shown to play a role in JAK2 activation (*49*). The reorganization of the interface leads to an increase in the number of intermolecular contacts for JAK2 V617F relative to the wild type in systems $S6_{AA}$ and $S7_{AA}$ (table S6). Free energy calculations conducted on JAK2 wild-type (simulation $S6_{AA}$) and V617F (simulation $S7_{AA}$) systems using the MM-PBSA (Molecular Mechanics Poisson-Boltzmann Surface Area) scheme (*50*) displayed consistently lower binding free energy values for the mutated PK dimer relative to the wild type ($\Delta\Delta G_{wt\text{-}VF}$ = −32.7 ± 16.2 kJ/mol). Such free energy differences indicate stabilization of the V617F dimer over the wild type, as also observed in our experiments (see Fig. 4).

To assess the role of the TpoR TM/JM segment, we simulated the receptor TM/JM helices (system $S8_{AA}$ and $S9_{AA}$; table S4). They were found to align in a rather tilted orientation (helix tilt angle 37° ± 2°), with W491 and W515 partitioning into the water/membrane interface, as is typical for Trp residues. The W515L mutation increased the helix tilt to 41° ± 1°, likely imposing constraints on the TM domain that favor dimerization. Such involvement of the amphipathic JM segment in regulating TM interactions via tilting is qualitatively supported by spectroscopic studies on reconstituted TM-JM peptides (*35*). Coarse-grained simulations (systems $S10_{CG}$ to $S13_{CG}$; table S4) corroborate this result, showing a highly tilted X-shape to be the most stable TM dimer structure (figs. S15 and S16) (*18*).

Discussion

Our live-cell single-molecule imaging experiments establish that the prototypic homodimeric class I cytokine receptors EpoR, TpoR, and GHR are monomeric in the basal state and are dimerized by their ligand. We therefore propose a molecular mechanism with ligand-induced dimerization as the fundamental switch initiating activation of these receptors, as originally proposed by Wells and co-workers (*2*). This mechanism contradicts the current view of pre-dimerized, inactive receptors that are activated by a ligand-induced conformational change (*4*). Although we confirmed weak intrinsic receptor dimerization affinities that involve multiple interaction interfaces, we also found that receptor predimerization is negligible at physiological expression levels yet accounts for a basal signaling activity. Thus, our quantitative studies did not provide any evidence for inactive receptor dimers but rather revealed a strict correlation of receptor dimerization and activation. The weak intrinsic dimerization affinities, however, explain the observation of pre-dimerized receptors by techniques such as protein fragment complementation or cysteine cross-linking (*7*, *51*, *52*), which irreversibly form cross-links between weakly interacting subunits and thus shift the equilibrium toward receptor dimers. By contrast, the single-molecule assays used in this study allow direct visualization and quantification of the monomer-dimer equilibrium at physiological receptor expression levels in living cells. Moreover, TIRF imaging in combination with extracellular posttranslational labeling ensures selective detection of receptor dimerization at the plasma membrane. The large fraction of the receptor that resides in endosomal vesicles may bias other methods of interaction analysis because of increased local concentrations during endocytic trafficking. Despite overexpression, we observed low cell surface densities for these cytokine receptors, indicating that receptor cell surface concentrations are highly regulated so as to minimize ligand-independent dimerization and activation.

In addition to identifying ligand-induced dimerization as the key step of receptor activation, we have established the importance of the interaction between JAK PK domains within receptor dimers at the plasma membrane. So far, the critical regulatory function of the PK domain has been appreciated at the level of intramolecular inhibition of TK activity (*41*, *42*), and the numerous constitutively JAK-activating mutations have been interpreted accordingly. Here, we have shown that a substantial proportion of constitutively activating PK mutations, including JAK2 V617F, act by altering and strengthening the intermolecular interactions involving the PK-PK dimerization interface. These mutations drive cytoplasmic stabilization of receptor-JAK dimers, bypassing stabilization of dimers via extracellular cytokine binding. Our insights suggest that the design of agents that interfere with dimerization by direct or allosteric targeting of the PK-PK interface could improve therapeutic intervention for MPNs and potentially other hematological malignancies and immunological disorders. Equally, our work demonstrates that although the extracellular domain is not required for oncogenic signaling, antagonism of receptor dimerization at the extracellular interface could be exploited to destabilize the active dimer, using a strategy similar to that used for the modulation of EpoR signaling by engineered dimerizers (*19*, *39*).

REFERENCES AND NOTES

1. M. Atanasova, A. Whitty, *Crit. Rev. Biochem. Mol. Biol.* **47**, 502–530 (2012).
2. B. C. Cunningham *et al.*, *Science* **254**, 821–825 (1991).
3. R. M. Stroud, J. A. Wells, *Sci. STKE* **2004**, re7 (2004).
4. M. J. Waters, A. J. Brooks, *Biochem. J.* **466**, 1–11 (2015).
5. J. Gent, P. van Kerkhof, M. Roza, G. Bu, G. J. Strous, *Proc. Natl. Acad. Sci. U.S.A.* **99**, 9858–9863 (2002).
6. R. J. Brown *et al.*, *Nat. Struct. Mol. Biol.* **12**, 814–821 (2005).
7. A. J. Brooks *et al.*, *Science* **344**, 1249783 (2014).
8. S. Tenhumberg *et al.*, *Biochem. Biophys. Res. Commun.* **346**, 649–657 (2006).
9. M. Zaks-Zilberman, A. E. Harrington, T. Ishino, I. M. Chaiken, *J. Biol. Chem.* **283**, 13398–13406 (2008).
10. C. D. Krause *et al.*, *Cell Res.* **16**, 55–69 (2006).
11. C. D. Krause *et al.*, *Mol. Cell. Proteomics* **1**, 805–815 (2002).
12. C. D. Krause *et al.*, *Biochem. Biophys. Res. Commun.* **340**, 377–385 (2006).
13. R. L. Levine *et al.*, *Cancer Cell* **7**, 387–397 (2005).
14. W. Vainchenker, S. N. Constantinescu, *Oncogene* **32**, 2601–2613 (2013).
15. V. C. Broudy, N. Lin, M. Brice, B. Nakamoto, T. Papayannopoulou, *Blood* **77**, 2583–2590 (1991).
16. W. J. McKinstry *et al.*, *Blood* **89**, 65–71 (1997).
17. N. Komatsu *et al.*, *Blood* **87**, 4552–4560 (1996).
18. See supplementary materials.
19. I. Moraga *et al.*, *Cell* **160**, 1196–1208 (2015).
20. I. Chung *et al.*, *Nature* **464**, 783–787 (2010).
21. I. S. Hitchcock, M. M. Chen, J. R. King, K. Kaushansky, *Blood* **112**, 2222–2231 (2008).
22. G. B. Bulut, R. Sulahian, H. Yao, L. J. S. Huang, *Blood* **122**, 3964–3972 (2013).
23. Y. Yano *et al.*, *ACS Chem. Biol.* **3**, 341–345 (2008).
24. S. Semrau, L. Holtzer, M. González-Gaitán, T. Schmidt, *Biophys. J.* **100**, 1810–1818 (2011).
25. K. C. Leung, N. Doyle, M. Ballesteros, M. J. Waters, K. K. Ho, *J. Clin. Endocrinol. Metab.* **85**, 4712–4720 (2000).
26. G. Fuh *et al.*, *Science* **256**, 1677–1680 (1992).
27. S. Elliott, T. Lorenzini, D. Chang, J. Barzilay, E. Delorme, *Blood* **89**, 493–502 (1997).
28. N. F. Endres *et al.*, *Cell* **152**, 543–556 (2013).
29. O. Silvennoinen, S. R. Hubbard, *Blood* **125**, 3388–3392 (2015).
30. X. Lu *et al.*, *Proc. Natl. Acad. Sci. U.S.A.* **102**, 18962–18967 (2005).
31. X. Lu, L. J. Huang, H. F. Lodish, *J. Biol. Chem.* **283**, 5258–5266 (2008).
32. A. Dusa, C. Mouton, C. Pecquet, M. Herman, S. N. Constantinescu, *PLOS ONE* **5**, e11157 (2010).
33. J. Staerk *et al.*, *Blood* **107**, 1864–1871 (2006).
34. Y. Pikman *et al.*, *PLOS Med.* **3**, e270 (2006).
35. J. P. Defour *et al.*, *Proc. Natl. Acad. Sci. U.S.A.* **110**, 2540–2545 (2013).
36. S. N. Constantinescu *et al.*, *Proc. Natl. Acad. Sci. U.S.A.* **98**, 4379–4384 (2001).
37. Y. Royer, J. Staerk, M. Costuleanu, P. J. Courtoy, S. N. Constantinescu, *J. Biol. Chem.* **280**, 27251–27261 (2005).
38. C. Pecquet *et al.*, *Blood* **115**, 1037–1048 (2010).
39. K. Mohan *et al.*, *Science* **364**, eaav7532 (2019).
40. H. M. Hammarén, A. T. Virtanen, J. Raivola, O. Silvennoinen, *Cytokine* **118**, 48–63 (2019).
41. Y. Shan *et al.*, *Nat. Struct. Mol. Biol.* **21**, 579–584 (2014).
42. P. J. Lupardus *et al.*, *Proc. Natl. Acad. Sci. U.S.A.* **111**, 8025–8030 (2014).
43. S. R. Hubbard, *Front. Endocrinol.* **8**, 361 (2018).
44. H. M. Hammarén *et al.*, *J. Allergy Clin. Immunol.* **143**, 1549–1559.e6 (2019).

45. A. V. Toms *et al*., *Nat. Struct. Mol. Biol.* **20**, 1221–1223 (2013).
46. R. M. Bandaranayake *et al*., *Nat. Struct. Mol. Biol.* **19**, 754–759 (2012).
47. R. D. Ferrao, H. J. Wallweber, P. J. Lupardus, *eLife* **7**, e38089 (2018).
48. K. Gnanasambandan, A. Magis, P. P. Sayeski, *Biochemistry* **49**, 9972–9984 (2010).
49. L. Zhao *et al*., *J. Biol. Chem.* **284**, 26988–26998 (2009).
50. R. Kumari, R. Kumar, Open Source Drug Discovery Consortium, A. Lynn, *J. Chem. Inf. Model.* **54**, 1951–1962 (2014).
51. I. Remy, I. A. Wilson, S. W. Michnick, *Science* **283**, 990–993 (1999).
52. E. E. Matthews *et al*., *FASEB J.* **25**, 2234–2244 (2011).

ACKNOWLEDGMENTS

We thank G. Hikade, H. Kenneweg, W. Kohl, L. Roberts, and the University of York Technology Facility for technical support; J. van der Heyden (Ghent University) for providing rabbit GHR cDNA; D. Richter and P. Selenschik for providing evaluation tools; and the Center for Scientific Computing (CSC)–IT Center for Science (Espoo, Finland) for computing resources. **Funding:** Supported by Deutsche Forschungsgemeinschaft grants SFB 944 P8/Z, PI 405/14-1, and PI 405/15-1 (J.P. and R.K.); long-term EMBO fellowship ALTF 454-2017 (S.W.); NIH grant 5R01AI101256 (S.R.H.); the Academy of Finland Center of Excellence program, the Sigrid Jusélius Foundation, the European Research Council (CROWDED-PRO-LIPIDS), and the Helsinki Institute of Life Science (HiLIFE) Fellow project (I.V.); the Academy of Finland, the Sigrid Jusélius Foundation, and the University of Helsinki (V.S.); NIH grant R01-AI51321, the Ludwig and Mathers Foundations, and HHMI (K.C.G.); CRUK grant A24593 (I.S.H.); and Horizon 2020 Framework program grant 714680, the Wellcome Trust, and Royal Society Sir Henry Dale Fellowship 202323/Z/16/z (I.M.). **Author contributions:** I.S.H. and J.P. conceived the project with contributions from S.W., S.R.H., I.V., and K.C.G.; S.W., M.H., and H.W. performed single-molecule imaging experiments and analyses; S.L. performed cell micropatterning assays; C.P.R. and R.K. developed single-molecule microscopy and image analysis techniques; I.M., I.S.H., and J.A.T. provided proteins; S.W., M.H., J.A.T., H.W., S.L., and I.M. cloned expression constructs and generated mutants; S.W., M.H., I.M., T.A.S., K.D.P.P., and I.S.H. carried out binding and activity assays; K.C.G., I.S.H., and J.P. supervised experimental work and data evaluation; J.V., C.P., V.S., and I.V. performed and supervised molecular modeling and MD simulations; I.M., K.C.G., I.S.H., I.V., and J.P. acquired funding; and S.W., I.S.H., and J.P. wrote the manuscript with input from all authors. **Competing interests:** The authors declare no competing interests. **Data and materials availability:** Results from single-molecule imaging and phospho-flow cytometry experiments are available at DOI:10.5281/zenodo.3588316. The single-molecule evaluation software used for tracking and co-tracking analysis has been archived via GitHub (DOI:10.5281/zenodo.3588413). Final structures of the simulated systems, as well as all simulation files and protein structures needed to carry out the simulations are available at DOI:10.5281/zenodo.3555291. Materials are available from the authors upon request.

SUPPLEMENTARY MATERIALS

science.sciencemag.org/content/367/6478/643/suppl/DC1
Materials and Methods
Figs. S1 to S16
Tables S1 to S6
Movies S1 to S13
References (*53*–*89*)

12 December 2018; resubmitted 8 October 2019
Accepted 20 December 2019
10.1126/science.aaw3242

SIGNAL TRANSDUCTION

An AMPK–caspase-6 axis controls liver damage in nonalcoholic steatohepatitis

Peng Zhao[1]*†, Xiaoli Sun[1]†, Cynthia Chaggan[1], Zhongji Liao[1], Kai in Wong[1], Feng He[2], Seema Singh[3], Rohit Loomba[3], Michael Karin[2], Joseph L. Witztum[1], Alan R. Saltiel[1,2]*

Liver cell death has an essential role in nonalcoholic steatohepatitis (NASH). The activity of the energy sensor adenosine monophosphate (AMP)–activated protein kinase (AMPK) is repressed in NASH. Liver-specific AMPK knockout aggravated liver damage in mouse NASH models. AMPK phosphorylated proapoptotic caspase-6 protein to inhibit its activation, keeping hepatocyte apoptosis in check. Suppression of AMPK activity relieved this inhibition, rendering caspase-6 activated in human and mouse NASH. AMPK activation or caspase-6 inhibition, even after the onset of NASH, improved liver damage and fibrosis. Once phosphorylation was decreased, caspase-6 was activated by caspase-3 or -7. Active caspase-6 cleaved Bid to induce cytochrome c release, generating a feedforward loop that leads to hepatocyte death. Thus, the AMPK–caspase-6 axis regulates liver damage in NASH, implicating AMPK and caspase-6 as therapeutic targets.

Nonalcoholic steatohepatitis (NASH)—characterized by hepatic steatosis, inflammation, and liver damage—has become a leading cause of liver transplant and liver-associated death. Hepatocellular death, characterized by swollen hepatocytes on liver biopsy, is a cardinal feature of NASH (*1*, *2*). In healthy liver, hepatocyte apoptosis has a key role in liver homeostasis, maintaining equilibrium between hepatocyte loss and replacement (*3*). However, pathological conditions such as viral infection, alcoholic or nonalcoholic steatohepatitis, and physical injury lead to extensive hepatocyte apoptosis and liver damage (*4*), which cause progressive fibrosis and cirrhosis (*1*, *5*). Improving liver damage and preventing fibrosis are major goals of NASH therapy (*2*). Moreover, liver cell death is a major contributor to the pathogenesis of hepatocellular carcinoma (*2*). Therefore, understanding the molecular mechanisms that control hepatocellular death may lead to new treatments for liver diseases.

Adenosine monophosphate (AMP)–activated protein kinase (AMPK) is a key metabolic regulator that senses energy status and controls energy expenditure and storage (*6*). AMPK is allosterically activated by AMP and repressed by adenosine triphosphate (ATP) (*6*). Its activity is increased during undernutrition (*7*) and decreased during obesity (*8*, *9*) and hyperglycemia (*9*) and by inhibitory phosphorylation driven by hyperinsulinemia and inflammation (*10*–*12*). Although activation of hepatic AMPK attenuates high-fat diet (HFD)–induced nonalcoholic fatty liver (NAFL), reducing AMPK activity does not cause or further worsen it (*13*). Whether the pathogenic repression of AMPK activity in obesity contributes to the occurrence of NASH and NASH-associated liver damage remains unknown.

Caspases are related aspartic-serine proteases that regulate inflammation and cell death. Apoptotic caspases are classified as "initiator," such as caspase-8 and -9, or "executioner," including caspase-3, -6, and -7 (*14*). Apoptotic cell death occurs through extrinsic and intrinsic pathways (*15*). The extrinsic pathway is driven by extracellular death receptor ligands, such as the tumor necrosis factor (TNF) superfamily and Fas ligand, and mediated by caspase-8. The intrinsic pathway is triggered by intracellular stress-induced cytochrome c release from mitochondria, leading to activation of the Apaf1–caspase-9 apoptosome. Both pathways converge in cleavage and activation of caspase-3 and -7 to execute programmed cell death (*15*). Although classified as an executioner, the mechanisms of activation and cleavage and the function of caspase-6 remain uncertain (*14*). We found that caspase-6 functions in steatosis-induced hepatocyte death and integrates signals from both inflammation and energy metabolism through direct phosphorylation by AMPK. Steatosis-induced decline in AMPK-catalyzed phosphorylation permits caspase-6 activation, leading to hepatocyte death. This link to obesity suggests that the AMPK–caspase-6 axis has a key role in NASH and might represent a new therapy.

Liver-specific AMPK knockout exaggerates liver damage in NASH

Hepatic AMPK activity is suppressed in diet-induced NAFL (*9*, *13*). Although AMPK activation attenuates steatosis, loss of AMPK does not induce steatosis (*13*). Moreover, the role of AMPK in the pathogenesis of NASH remains uncertain. We generated liver-specific AMPKα1/α2 (*Prkaa1*/*Prkaa2*) double-knockout (LAKO) mice that are devoid of hepatocyte expression of AMPKα1 and -α2, the catalytic subunits of AMPK (Fig. 1A). Liver-specific AMPK ablation did not affect body weight, liver weight, or triglycerides (TGs) in mice fed normal chow diet (ND) (fig. S1, A to C). ND-fed LAKO mice had normal serum alanine aminotransferase (ALT), aspartate aminotransferase (AST), and alkaline phosphatase (ALP) activities and liver morphology (fig. S1, D to G).

We fed Flox and LAKO mice with a choline-deficient HFD (CD-HFD) to rapidly induce hepatic steatosis, liver damage, and fibrosis, which are characteristics of NASH (*16*). CD-HFD decreased AMPK Thr^{172} phosphorylation in livers of C57BL/6J mice, indicating repression of AMPK activity (Fig. 1B). LAKO mice were identical to Flox mice with respect to body weight, liver weight, or hepatic TGs (Fig. 1, C to E). However, a significant increase of serum ALT, AST, and ALP activities suggested exaggerated liver damage in CD-HFD–fed LAKO mice (Fig. 1, F to H). Increased liver terminal deoxynucleotidyl transferase–mediated deoxyuridine triphosphate nick end labeling (TUNEL) staining demonstrated that knockout of AMPK substantially increased the number of apoptotic cells, without affecting necroptotic cells identified by staining with phosphorylated mixed lineage kinase domain-like protein (phospho-MLKL) (Fig. 1, I and J). LAKO mice showed no changes in liver macrophage infiltration, as evidenced by similar macrophage marker F4/80 staining in Flox and LAKO mice (Fig. 1K). Nonetheless, hepatic fibrosis as measured with Sirius red staining and abundance of hydroxyproline was increased in LAKO mice, correlating with enhanced scarring from exaggerated liver damage (Fig. 1, K to M). LAKO did not affect the expression of the macrophage marker adhesion G protein–coupled receptor E1 (*Adgre1*, F4/80), the chemotactic cytokine C-C motif chemokine ligand 2 (*Ccl2*) and its receptor *Ccr2*, or pro-inflammatory cytokines tumor necrosis factor–α (*Tnfa*) and interleukin-1β (*Il1b*) (Fig. 1N). Although LAKO increased cell death and liver damage, the expression of cell death mediators caspase-3 (*Casp3*), *Casp8*, receptor-interacting serine/threonine protein kinase 1 (*Ripk1*), and *Ripk3* was not affected (Fig. 1O). Consistent with increased fibrosis, LAKO increased the expression of the fibrosis marker gene actin α2 (*Acta2*), collagen genes collagen type I α1 (*Col1a1*) and *Col3a1*, as well as hepatic stellate cell (HSC)–activating growth factor platelet-derived growth factor subunit B (*Pdgfb*) (Fig. 1P). LAKO mice showed no differences in the expression of transforming growth factor–β (*Tgfb*), the major macrophage-derived fibrogenic

[1]Department of Medicine, School of Medicine, University of California, San Diego, La Jolla, CA 92093, USA. [2]Department of Pharmacology, School of Medicine, University of California, San Diego, La Jolla, CA 92093, USA. [3]NAFLD Research Center, Division of Gastroenterology, Department of Medicine, University of California, San Diego, La Jolla, CA 92093, USA.
†These authors contributed equally to this work.
*Corresponding author. Email: asaltiel@ucsd.edu (A.R.S.); pez021@ucsd.edu (P.Z.)

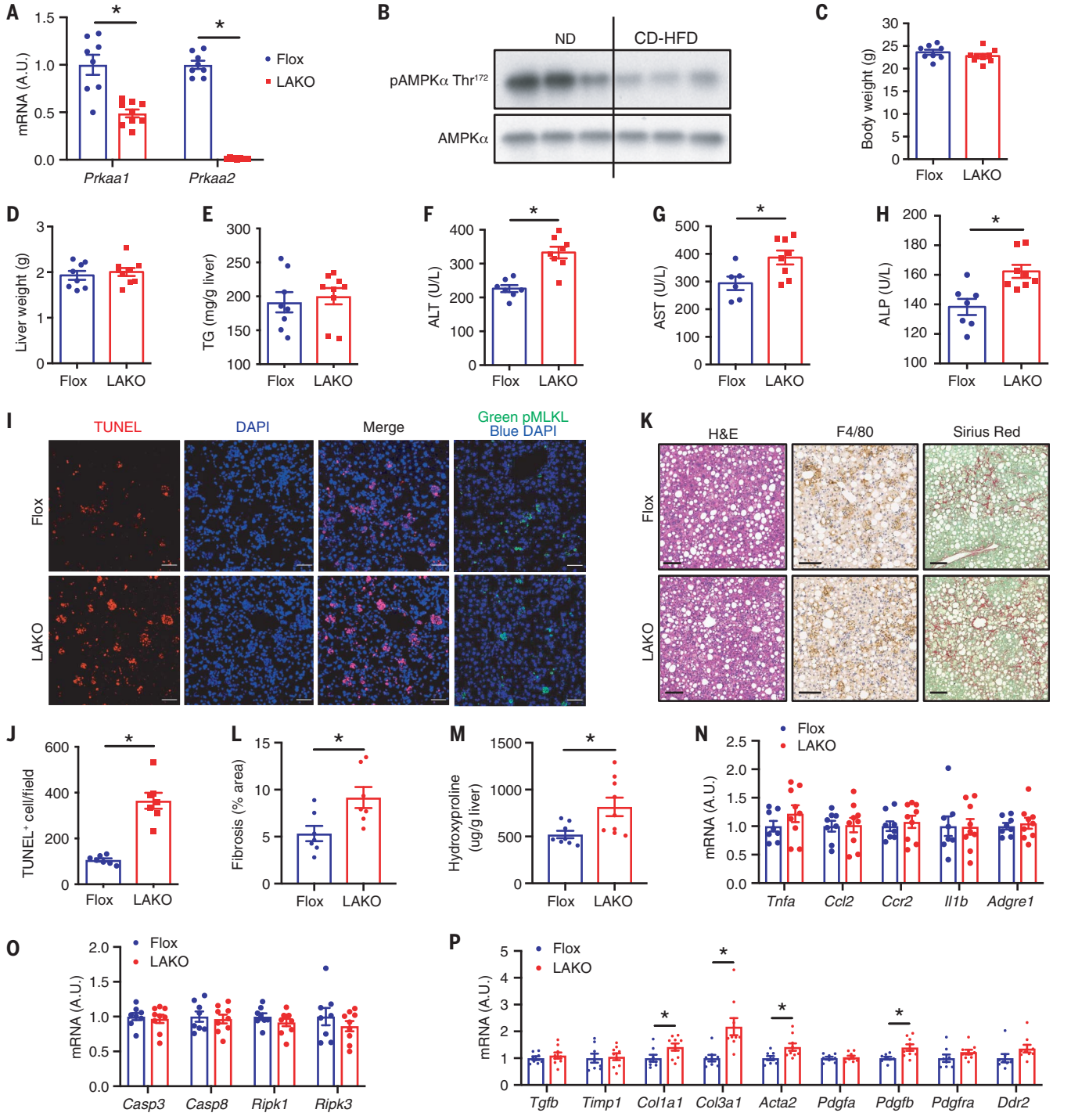

Fig. 1. Liver-specific AMPK knockout exaggerates liver damage in NASH. (**A**) Expression of *Prkaa1* and *Prkaa2* in liver; *n* = 8 to 9 mice. A.U., arbitrary units. (**B**) Immunoblot of liver lysate from ND or CD-HFD–fed mice; *n* = 3 mice. (**C** to **P**) Flox and LAKO mice fed CD-HFD for 11 weeks. (C) Body weight. (D) liver weight. (E) Liver TG. [(F) to (H)] Serum ALT (F), AST (G), ALP (H); *n* = 8 to 9 mice. (I) Liver sections stained TUNEL (red) and 4′,6-diamidino-2-phenylindole (DAPI) (blue) or pMLKL (Green). Scale bar, 50 μm. (J) Quantification of TUNEL-positive nuclei per field in (I); *n* = 7 mice. (K) H&E, F4/80, and Sirius red staining of liver sections. Scale bar, 100 μm; *n* = 7 mice. (L) Quantification of fibrosis area (percent of total area) shown in (K); *n* = 7 mice. (M) Liver hydroxyproline; *n* = 8 to 9 mice. (N) Expression of *Tnfa*, *Ccl2*, *Ccr2*, *Il1b*, and *Adgre1* in liver; *n* = 8 to 9 mice. (O) Expression of *Casp3*, *Casp8*, *Ripk1*, and *Ripk3* in liver; *n* = 8 to 9 mice. (P) Expression of *Tgfb*, *Timp1*, *Col1a1*, *Col3a1*, *Acta2*, *Pdgfa*, *Pdgfb*, *Pdgfra*, and *Ddr2* in liver; *n* = 8 to 9 mice. Mean ± SEM; **P* < 0.05, Student's unpaired *t* test.

cytokine, which is consistent with similar macrophage infiltration in Flox and LAKO mice. Likewise, LAKO mice showed no difference in growth factor *Pdgfa* and receptor *Pdgfra* expression or matrix remodeling genes tissue inhibitor matrix metalloproteinase 1 (*Timp1*) and discoidin domain receptor tyrosine kinase 2 (*Ddr2*) (Fig. 1P).

We also fed mice with the Amylin (AMLN) diet, which is used to mimic human NASH in preclinical studies (*2*, *17*). AMLN also repressed AMPK activation in C57BL/6J mice (fig. S2A).

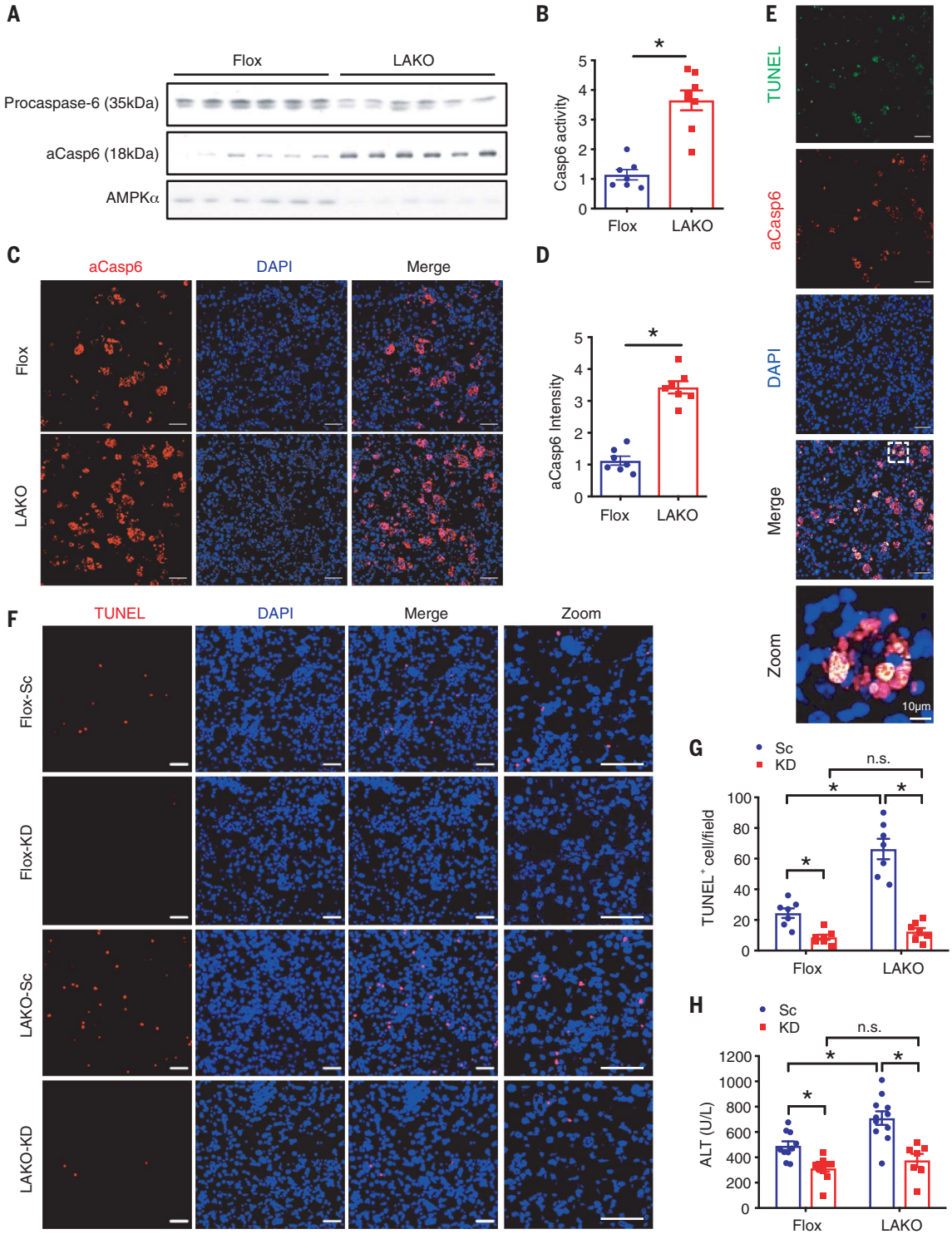

Fig. 2. AMPK deficiency increases caspase-6 cleavage to promote liver damage in NASH. (**A** to **E**) Flox and LAKO mice fed CD-HFD for 11 weeks. (A) Immunoblot analysis of liver lysate; $n = 6$ mice. (B) Casp6 activity in liver lysate; $n = 7$ to 8 mice. (C) Liver sections stained active Caspase-6 (aCasp6, red) and DAPI (blue). Scale bar, 50 μm. (D) Quantification of aCasp6 staining in (C); $n = 7$ mice. (E) Liver sections stained TUNEL (green), aCasp6 (red), and DAPI (blue). Scale bar, 50 μm. *$P <$ 0.05, Student's unpaired t test. (**F** to **H**) Flox and LAKO mice fed with CD-HFD for 3 weeks, followed by intravenous injection of 1.5 mg/kg caspase-6 siRNA (KD) or scrambled RNA (Sc) twice per week for 3 weeks while fed continuous CD-HFD. (F) Liver sections stained TUNEL (red) and DAPI (blue). Scale bar, 50 μm. (G) Quantification of TUNEL-positive nuclei per field in (F); $n = 7$ mice. (H) Serum ALT; $n = 7$ to 10 mice. Mean ± SEM; *$P < 0.05$, two-way analysis of variance (ANOVA).

LAKO had no effect on body weight, liver weight, liver-to–body weight ratio, hepatic TG, fasting glucose, glucose tolerance, or insulin resistance (fig. S2, B to H). LAKO did not affect the expression of *Adgre1*, gluconeogenic genes glucose-6-phosphatase catalytic subunit (*G6pc*) and phosphoenolpyruvate carboxykinase 1 (*Pck1*), lipogenic genes sterol regulatory element binding transcription factor 1 (*Srebf1*) and fatty acid synthase (*Fasn*), or mitochondria and lipid oxidation regulation genes peroxisome proliferator activated receptor γ coactivator 1 α (*Ppargc1a*) and carnitine palmitoyltransferase 1a (*Cpt1a*) (fig. S2, I to L) in AMLN-fed mice. However, LAKO significantly increased serum ALT, AST, and ALP activities, suggesting enhanced liver damage (fig. S2, M to O). LAKO mice had increased numbers of apoptotic liver cells (fig. S2, P and Q). Furthermore, exaggerated liver damage in LAKO mice led to increased fibrosis (fig. S2, R to T). Similar to the results from CD-HFD–fed mice, LAKO increased the expression of fibrosis markers *Acta2*, *Col1a1*, and *Col3a1* and fibrogenic growth factors *Pdgfa* and *Pdgfb*, with no effect on *Tgfb*, *Timp1*, *Pdgfra*, or *Ddr2* in AMLN-fed mice (fig. S2U). Thus, although LAKO did not

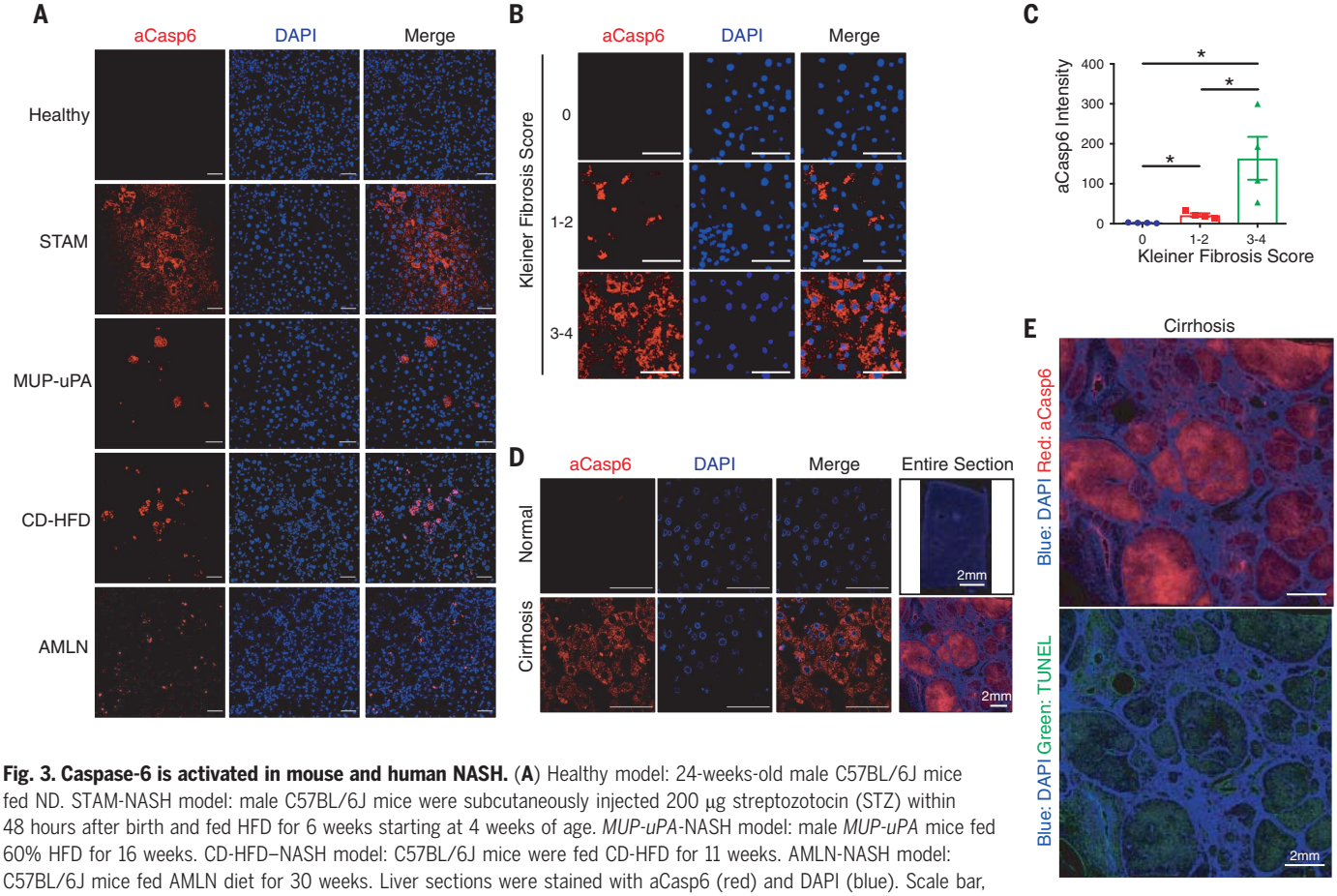

Fig. 3. Caspase-6 is activated in mouse and human NASH. (**A**) Healthy model: 24-weeks-old male C57BL/6J mice fed ND. STAM-NASH model: male C57BL/6J mice were subcutaneously injected 200 μg streptozotocin (STZ) within 48 hours after birth and fed HFD for 6 weeks starting at 4 weeks of age. *MUP-uPA*-NASH model: male *MUP-uPA* mice fed 60% HFD for 16 weeks. CD-HFD–NASH model: C57BL/6J mice were fed CD-HFD for 11 weeks. AMLN-NASH model: C57BL/6J mice fed AMLN diet for 30 weeks. Liver sections were stained with aCasp6 (red) and DAPI (blue). Scale bar, 50 μm. (**B**) Human liver sections were classified blindly by liver pathologist and stained with aCasp6 (Kleiner fibrosis score 0, 1 to 2, and 3 to 4). Scale bar, 50 μm. (**C**) Quantification of aCasp6 staining in (B), plotted against Kleiner fibrosis scores; n = 4 human subjects. (**D**) Human liver sections were stained aCasp6 to compare caspase-6 activation in healthy and cirrhotic donors. Scale bar, 50 μm. (**E**) Scanning of human liver section stained aCasp6 (red), TUNEL (green), and DAPI. Scale bar, 2 mm. Mean ± SEM; *P < 0.05, Student's unpaired t test.

further exaggerate steatosis or inflammation during NASH, hepatocellular death and fibrosis were enhanced.

AMPK deficiency increases caspase-6 activation to promote liver damage in NASH

To investigate the mechanism of exacerbated liver damage in NASH, we focused on proapoptotic caspases because necroptosis was not affected by LAKO. Cleavage of procaspase-6 and caspase-6 activity were increased in livers of LAKO mice on both CD-HFD (Fig. 2, A and B) and AMLN diets (fig. S3A). *Casp6* mRNA was not regulated by either diet (fig. S3B). LAKO significantly increased active caspase-6 (aCasp6) in livers of mice on CD-HFD (Fig. 2, C and D) or AMLN diet (fig. S3, C and D). Costaining of TUNEL and aCasp6 revealed TUNEL-stained nuclei located within cells with aCasp6 (Fig. 2E), correlating caspase-6 activation with hepatocellular death in NASH.

We examined the temporal relationship of caspase-6 activation and NASH development. Symptoms of NASH were apparent by 3 weeks of CD-HFD feeding, as evidenced by development of steatosis; TUNEL staining; and increased activities of ALT, AST, and ALP in serum. After 6 weeks, the mice developed extensive steatosis and substantial TUNEL staining, indicating well-established NASH (fig. S4, A to E). After 3 weeks of CD-HFD to develop NASH, Flox and LAKO mice were intravenously injected with control or caspase-6 small interfering RNA (siRNA) for 3 weeks during continuous CD-HFD (fig. S5A). Caspase-6 siRNA reduced hepatic *Casp6* mRNA by more than 80%. LAKO did not affect *Casp6* expression (fig. S5B). Caspase-6 depletion did not affect body or liver weight in CD-HFD–fed mice of either genotype (fig. S5, C and D). However, caspase-6 depletion reduced the number of apoptotic hepatocytes and serum ALT activity in both Flox and LAKO mice to a similar extent (Fig. 2, F to H). Depletion of caspase-6 significantly attenuated fibrosis in Flox and LAKO mice and nullified the deleterious effects of LAKO (fig. S5, E to G).

Caspase-6 is activated in mouse and human NASH

Because depleting caspase-6 attenuated liver damage in CD-HFD–induced NASH, we examined whether the activation of caspase-6 might occur in other NASH models, including HFD-fed streptozotocin-administered neonatal mice (*18*), HFD-fed major urinary protein-urokinase-type plasminogen activator (*MUP-uPA*) transgenic mice (*19*), or even human NASH. Caspase-6 was activated in livers of all mouse NASH models but not in healthy livers (Fig. 3A). The presence of NASH was validated with hematoxylin and eosin (H&E) staining (fig. S6A). To determine whether caspase-6 is activated in human NASH, we blindly assessed aCasp6 in liver sections of NASH patients, in whom liver status had been diagnosed. Caspase-6 was activated in livers from patients with NASH and cirrhosis (Fig. 3, B to D). Active caspase-6 significantly increased with Kleiner fibrosis score and positively correlated with severity of NASH (Fig. 3, B and C). Furthermore, whereas sections from normal livers had almost no

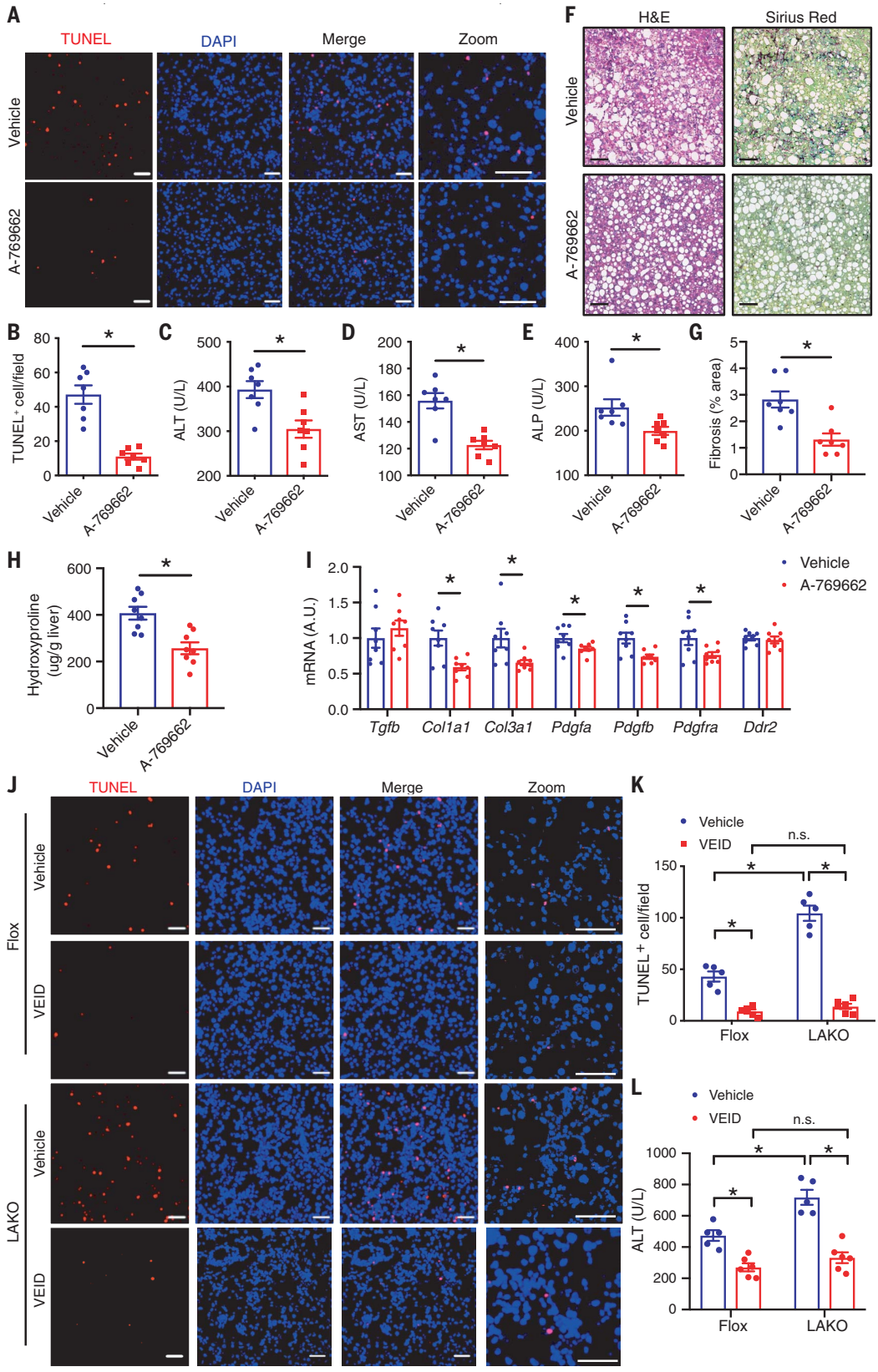

Fig. 4. Both an AMPK agonist and a caspase-6 inhibitor therapeutically improve liver damage. (**A** to **I**) C57BL/6J mice were fed CD-HFD for 6 weeks, followed by intraperitoneal injection of 25 mg/kg A-769662 or vehicle daily for 2 weeks while fed continuous CD-HFD. (A) Liver sections stained TUNEL (red) and DAPI (blue). Scale bar, 50 μm. (B) Quantification of TUNEL-positive nuclei per field in (A); *n* = 7 mice. [(C) to (E)] Serum ALT (C), AST (D), and ALP (E); *n* = 7 mice. (F) H&E and Sirius red staining of liver sections. Scale bar, 100 μm. (G) Quantification of liver fibrosis area (percent of total area) in (F); *n* = 7 mice. (H) Liver hydroxyproline; *n* = 8 mice. (I) Expression of *Tgfb*, *Timp1*, *Col1a1*, *Col3a1*, *Pdgfa*, *Pdgfb*, *Pdgfra*, and *Ddr2* in livers; *n* = 8 mice. **P* < 0.05, Student's unpaired *t* test. (**J** to **L**) Flox and LAKO mice were fed CD-HFD for 6 weeks, followed by intraperitoneal injection of 5 mg/kg VEID or vehicle every other day for 2 weeks while continuously feeding. (J) Liver sections stained TUNEL (red) and DAPI (blue). Scale bar, 50 μm. (K) Quantification of TUNEL-positive nuclei per field in (J); *n* = 5 to 6 mice. (L) Serum ALT; *n* = 5 to 6 mice. Mean ± SEM; **P* < 0.05, two-way ANOVA.

active caspase-6 staining, the degree of active caspase-6 was increased in cirrhosis (Fig. 3D). Moreover, whole-section scanning showed that both active caspase-6 and TUNEL staining were located within the cirrhotic nodule, indicating that caspase-6 might activate apoptosis of hepatocytes in human cirrhosis (Fig. 3E).

An AMPK agonist and a caspase-6 inhibitor therapeutically improve liver damage

To test the potential of AMPK as a therapeutic target, we fed C57BL/6J mice with CD-HFD

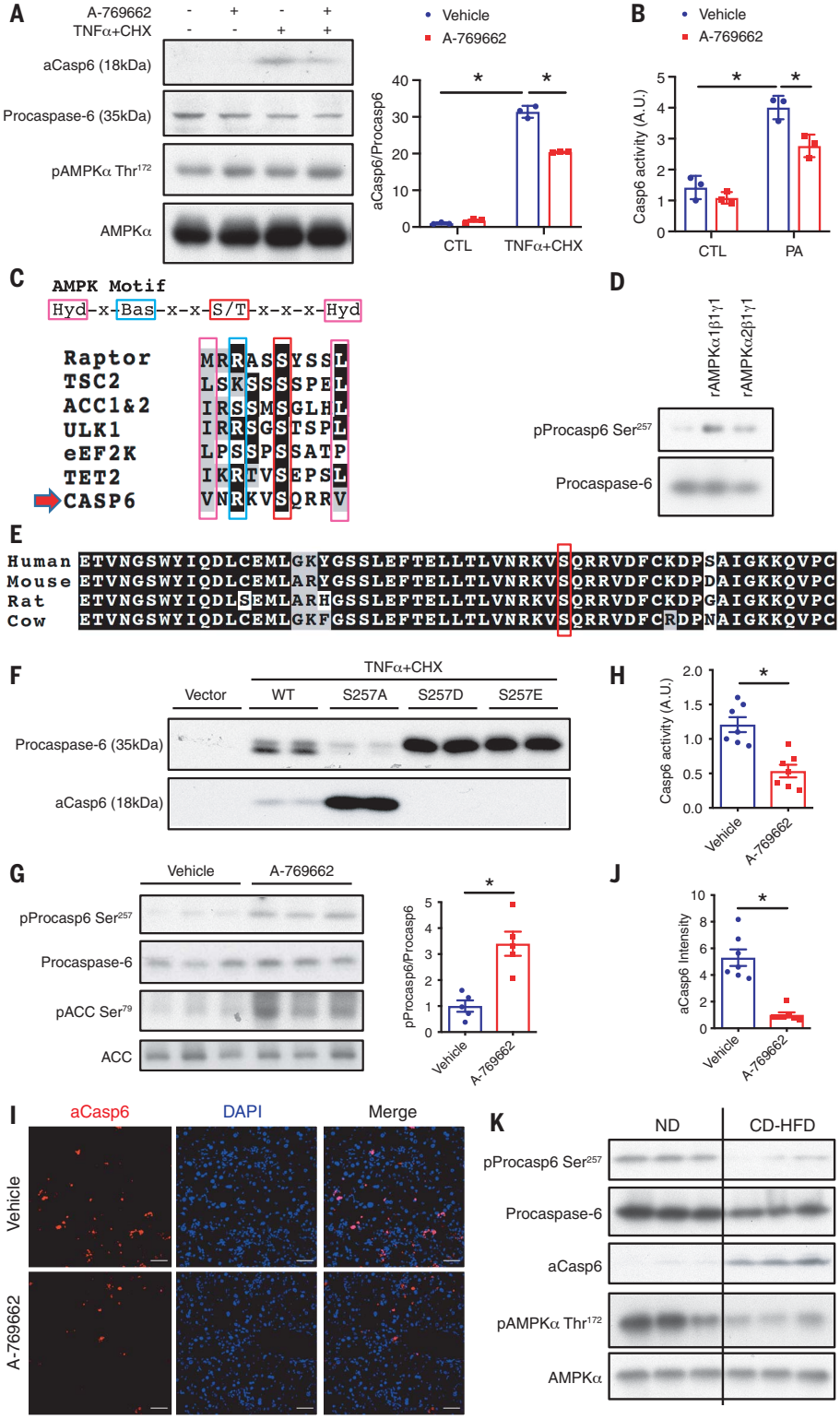

Fig. 5. AMPK phosphorylates caspase-6 to inhibit its cleavage and activation. (**A**) Primary hepatocytes were pretreated with 40 μM A-769662 for 1 hour then treated with 30 μg/ml CHX and 50 ng/ml TNFα for 2 hours. Shown is immunoblot analysis of cell lysates; $n = 3$ independent experiments. Mean ± SD; $^*P < 0.05$, two-way ANOVA. (**B**) Primary hepatocytes were pretreated with 40 μM A-769662 for 1 hour then treated with 250 μM bovine serum albumin (BSA)–conjugated PA for 2 hours. Cell lysates were subject to caspase-6 activity assay. Mean ± SD; $^*P < 0.05$. (**C**) Caspase-6 Ser^{257} locates within AMPK substrate motif. (**D**) In vitro kinase assay using recombinant caspase-6 and recombinant AMPKα1β1γ1 or AMPKα2β1γ1 active kinase. (**E**) Alignment of caspase-6 sequence. (**F**) HEK293T cells overexpressing caspase-6-myc wild type, S257A, S257D, or S257E mutant were treated with 10 μg/ml CHX and 25 ng/ml TNFα for 2 hours. Shown is immunoblot analysis of cell lysates. (Single-letter abbreviations for the amino acid residues are as follows: A, Ala; D, Asp; E, Glu; S, Ser. In the mutants, other amino acids were substituted at certain locations; for example, S257A indicates that serine at position 257 was replaced by alanine.) (**G** to **J**) C57BL/6J mice were fed CD-HFD for 6 weeks, followed by intraperitoneal injection of 25 mg/kg A-769662 or vehicle daily for 2 weeks while fed continuous CD-HFD. Mice were euthanized 6 hours after the last injection. (G) Immunoblot analysis of liver lysates; $n = 5$ mice. (H) Liver lysates were subject to caspase-6 activity assay; $n = 7$ mice. (I) Liver sections stained with aCasp6 (red) and DAPI (blue). Scale bar, 50 μm. (J) Quantification of aCasp6 staining per field in (I); $n = 7$ mice. Mean ± SEM; $^*P < 0.05$, Student's unpaired t test. (**K**) Immunoblot analysis of liver lysates from C57BL/6J mice fed ND or CD-HFD. AMPK and pAMPK blots are the same as in Fig. 1B.

for 6 weeks to establish NASH and then intraperitoneally injected mice with vehicle or AMPK agonist (A-769662) for 2 weeks while continuing CD-HFD (fig. S7A). In mice, AMPKβ1 is expressed in liver but not skeletal muscle (*20*). Thus, as an AMPKβ1 agonist, A-769662 activates AMPK in liver but not skeletal muscle. A previous study showed that injection of 30 mg/kg A-769662 twice per day for 7 days reduced hepatic TGs in C57BL/6J mice fed 45% HFD (*13*). In our study, injection of 25 mg/kg A-769662 once per day for 2 weeks in CD-HFD–fed mice had no effect on body weight, liver weight, or hepatic TG (fig. S7, B to D) but significantly reduced the number of apoptotic cells (Fig. 4, A and B, and fig. S7E) and improved liver damage (Fig. 4, C to E). A-769662 injection did not decrease the number of apoptotic cells nor reduce serum ALT activity in LAKO mice, indicating that A-769662 specifically targeted AMPK in hepatocytes to improve

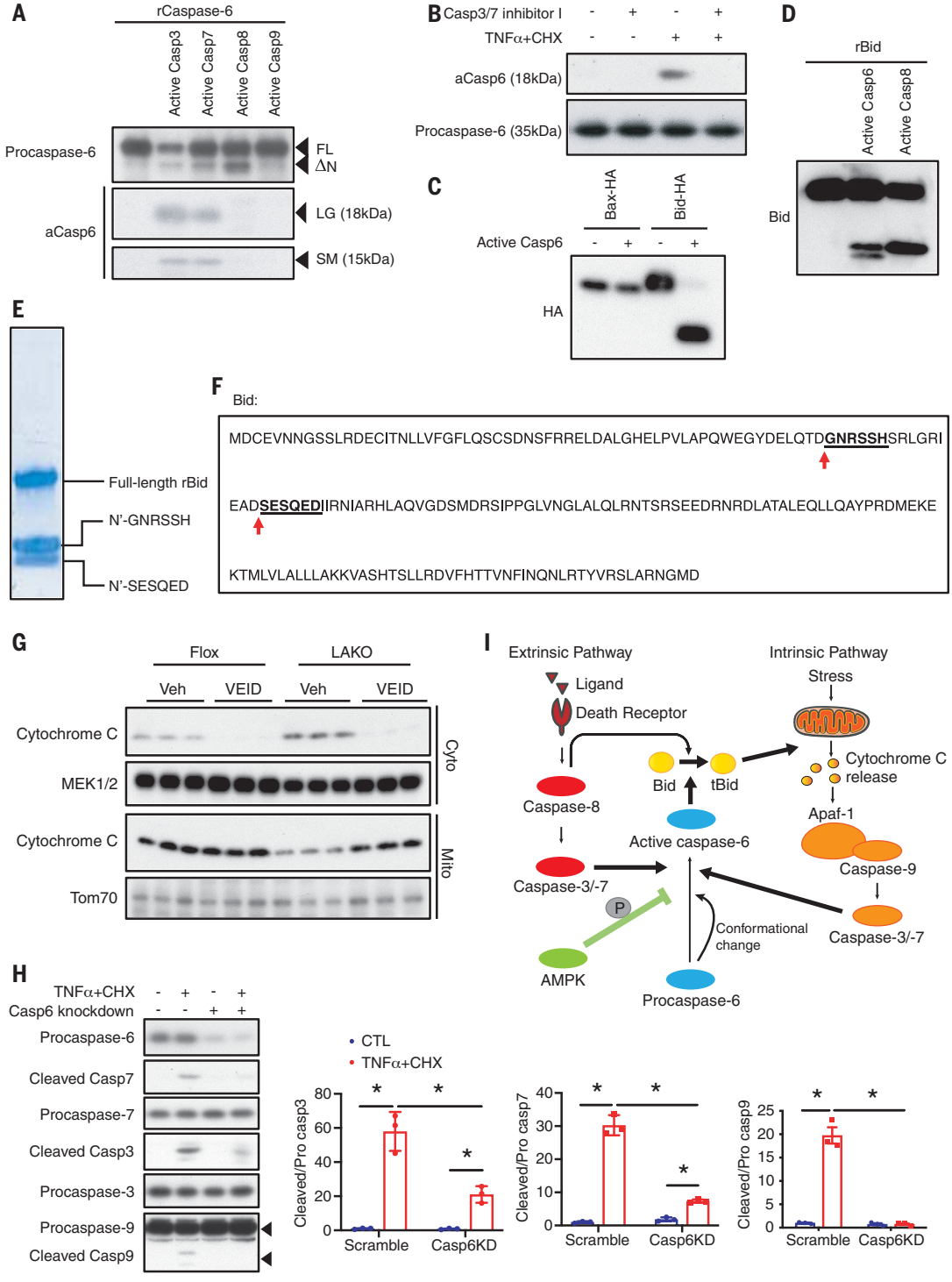

Fig. 6. Caspase-6 mediates a feedforward loop to sustain the caspase cascade. (**A**) In vitro cleavage assay using recombinant procaspase-6 with active caspase-3, -7, -8, or -9. FL, full-length; ΔN, *n* terminus deleted form; LG, large; SM, small. (**B**) Primary hepatocytes were pretreated with 10 μM caspase-3/7 inhibitor I for 1 hour then treated with 30 μg/ml CHX and 50 ng/ml TNFα for 2 hours. Immunoblot analysis of cell lysates. (**C**) In vitro cleavage assay using purified Bid-HA or Bax-HA expressed in HEK293T cells, and active caspase-6. (**D**) In vitro cleavage assay using recombinant Bid with active caspase-6 or -8. (**E**) In vitro cleavage assay using recombinant Bid with active caspase-6. Bands for cleaved Bid were subject to Edman degradation. (**F**) Bid sequence and sites cleaved by active caspase-6. (**G**) Flox and LAKO mice were fed CD-HFD for 6 weeks, followed by intraperitoneal injection of 5 mg/kg VEID or vehicle every other day for 2 weeks while fed continuous CD-HFD. Livers were fractionated to separate cytosolic and mitochondrial extract for immunoblot analysis. (**H**) HepG2 cells transfected scrambled RNA or Caspase-6 siRNA were treated with vehicle or 30 μg/ml CHX and 50 ng/ml TNFα for 2 hours. Medium was changed to remove treatment for 5 hours. Cell lysates were subject to immunoblot analysis; $n = 3$ independent experiments. Mean ± SD; $^*P < 0.05$, two-way ANOVA. (**I**) Proposed model for roles of AMPK–caspase-6 axis in apoptotic caspase cascade.

liver damage (fig. S7, F to H). A-769662 attenuated hepatic fibrosis (Fig. 4, F to H) and significantly reduced the expression of fibrotic genes *Col1a1*, *Col3a1*, *Pdgfa*, *Pdgfb*, and *Pdgfra*, without effect on *Tgfb*, *Ddr2*, or inflammation marker genes *Adgre1* or *Ccl2* (Fig. 4I and fig. S7I).

To examine whether caspase-6 inhibition might also improve liver damage and decrease the effects of AMPK deficiency, we fed Flox and LAKO mice with CD-HFD for 6 weeks to establish NASH and then intraperitoneally injected vehicle or the caspase-6 inhibitor Z-VEID-FMK (VEID) for 2 weeks while continuing CD-HFD (fig. S8A). VEID did not affect body or liver weight (fig. S8, B and C) but significantly reduced the number of apoptotic hepatocytes and decreased serum ALT activity in both Flox and LAKO mice (Fig. 4, J to L, and fig. S8D). VEID abrogated the difference in liver damage between Flox and LAKO mice. VEID reduced liver fibrosis in both Flox and LAKO mice and abolished the effect of AMPK deficiency (fig. S8, E to G), further suggesting that AMPK–caspase-6 axis critically controls liver damage.

AMPK phosphorylates procaspase-6 to inhibit its cleavage and activation

To explore the regulation of caspase-6, we treated primary hepatocytes with TNFα and

palmitic acid (PA) to mimic inflammation and lipotoxicity-induced hepatocellular death. Both induced caspase-6 activation (fig. S9A). To determine whether the AMPK agonist directly inhibited procaspase-6 cleavage in a cell-autonomous manner, we treated primary hepatocytes or HepG2 cells with A-769662 and then, to induce procaspase-6 cleavage, with TNFα and cycloheximide (CHX). In both cells, A-769662 significantly inhibited procaspase-6 cleavage (Fig. 5A and fig. S9B). The induction of caspase-6 activity by PA was also inhibited in cells pretreated with A-769662 (Fig. 5B). In silico analysis revealed one AMPK substrate motif site on procaspase-6 Ser^{257} (Fig. 5C) (*21*). Procaspase-6 Ser^{257} is phosphorylated by AMPK-related protein kinase 5 (ARK5) in colorectal adenocarcinoma cells (*22*). Phosphorylation of Ser^{257} represses procaspase-6 cleavage and activation (*23*). Both recombinant AMPKα1 and AMPKα2 directly phosphorylated procaspase-6 at Ser^{257} in vitro (Fig. 5D and fig. S9C). The Ser^{257} site and the surrounding sequence in caspase-6 are conserved across species (Fig. 5E). We overexpressed wild-type procaspase-6, or its S257A non–phospho-mimetic mutant, or S257D/S257E phospho-mimetic mutants in human embryonic kidney (HEK) 293T cells and subsequently treated the cells with low doses of TNFα and CHX to induce procaspase-6 cleavage. The S257A mutant was more sensitive to cleavage, whereas both the S257D and S257E mutants were completely resistant (Fig. 5F). Moreover, A-769662 significantly increased procaspase-6 Ser^{257} phosphorylation (Fig. 5G) and decreased caspase-6 activity in vivo (Fig. 5H). AMPK activation decreased aCasp6 in CD-HFD–induced NASH (Fig. 5, I and J). Analysis of liver lysates from CD-HFD–fed Flox and LAKO mice administered vehicle or A-769662 revealed that A-769662 significantly increased procaspase-6 phosphorylation and decreased procaspase-6 cleavage in Flox but not in LAKO mice (fig. S9, D and E). AMPK deficiency itself decreased procaspase-6 phosphorylation and increased procaspase-6 cleavage (fig. S9, D and E). Moreover, CD-HFD decreased procaspase-6 phosphorylation, correlating with the increased procaspase-6 cleavage and decreased AMPK phosphorylation (Figs. 1B and 5K and fig. S9F).

Caspase-6 mediates a feedforward loop to sustain the caspase cascade

To understand how caspase-6 controls the pathogenesis of NASH, we investigated its role in the apoptotic pathways. Depletion of caspase-6 in HepG2 cells significantly increased cell viability after 20 hours of treatment with TNFα and CHX (fig. S10A). An in vitro cleavage assay showed that procaspase-6 was directly cleaved by caspase-3 and -7 but not caspase-8 or -9 (Fig. 6A). Pretreatment with a caspase-3 and -7 inhibitor largely attenuated procaspase-6 cleavage caused by TNFα and CHX (Fig. 6B). These data suggest that caspase-6 is activated by executioner caspases but not initiators.

We searched for a relevant substrate and found that active caspase-6 cleaved purified Bcl2 family protein Bid (BH3 interacting-domain death agonist) but not Bax (Bcl2-associated X) in vitro (Fig. 6C). Both of these proteins contribute to cytochrome c release and subsequent cell damage (*24*, *25*). Active caspase-6 cleaves Bid to generate two cleaved peptide fragments (Fig. 6D), one with a size similar to that of caspase-8–cleaved Bid (*26*) and another that was smaller. N-terminal sequencing showed that active caspase-6 cleaved Bid at both Asp^{59} and Asp^{75} (Fig. 6, E and F); both cleavages activate Bid to induce cytochrome c release (*26*, *27*). Because cleavage of Bid induces mitochondrial cytochrome c release into the cytoplasm (*24*, *25*), we fractionated liver from vehicle or VEID-treated Flox and LAKO mice to isolate cytosolic (Cyto) and mitochondrial (Mito) fractions. Cytosolic cytochrome c was increased in LAKO mice. VEID treatment decreased cytosolic cytochrome c in both Flox and LAKO mice and completely abrogated the effect of LAKO (Fig. 6G).

We wondered whether caspase-6 might mediate a feedforward loop of the caspase cascade because it is cleaved by the executioner caspases-3 and -7 and in turn induces cytochrome c release. HepG2 cells were transfected with scrambled control or caspase-6 siRNA and treated with vehicle or CHX plus TNFα for 2 hours to induce caspase activation. Two hours after the medium change, amounts of cleaved caspase-9, -3, and -7 were similar in control or caspase-6–depleted cells. However, after 5 hours, caspase-6–depleted cells had significantly less cleaved caspase-9, -3, and -7 (Fig. 6H and fig. S10B). Thus, activation of the caspase cascade appears to diminish faster in caspase-6–depleted cells. Inhibition of caspase-6 with VEID also led to a substantial decrease of cleaved caspase-3 and -7 in primary hepatocytes (fig. S10C). Caspase-6 may mediate a feedforward loop to sustain activation of the caspase cascade, in which cytochrome c can potentiate the activation of the upstream caspases, and this sustained activation may be necessary for extensive apoptosis (Fig. 6I). This process is only activated under conditions of excess energy accumulation due to reduced AMPK activity.

Discussion

Overnutrition-induced hepatic steatosis and inflammation lead to liver damage in NASH (*2*). We describe here an AMPK–caspase-6 axis that regulates hepatocellular apoptosis and may shed new light on the "two-hit" or "multiple-hit" hypothesis of NASH. Inflammation in NAFL disease (NAFLD) leads to caspase-6 activation by the increased activity of upstream executioners caspase-3 and -7. Active caspase-6 in turn cleaves Bid to increase mitochondrial cytochrome c release in a feedforward loop, in which activation of upstream caspases is persistent, so that the apoptotic caspase cascade is sustained in hepatocytes. However, in the metabolically healthy liver, AMPK activity is maintained to allow phosphorylation of procaspase-6, which inhibits its activation, thus preventing this feedforward loop (Fig. 6I and fig. S10D). When AMPK activity is reduced through overnutrition, hyperglycemia, hyperinsulinemia, and inflammation in obesity, diabetes, and NAFL, caspase-6 is derepressed, leading to activation of the feedforward loop, priming hepatocytes for caspase-mediated apoptosis (fig. S10D) (*28*). AMPK inhibition may thus serve as a point of convergence by which overnutrition, steatosis, hyperinsulinemia, and inflammation contribute to liver damage. If so, pharmaceutical interventions that specifically activate AMPK or block caspase-6 in livers may represent approaches to treat NASH.

Caspase-2 triggers de novo lipogenesis and steatosis during NAFL (*19*). By contrast, caspase-6 does not contribute to the development of steatosis but specifically mediates NASH-associated liver damage. Although knockout of caspase-3 and -8 also protects against hepatocyte apoptosis (*29*, *30*), global knockout of caspase-8 is embryonically lethal, whereas caspase-3 whole-body knockout leads to multiple developmental defects (*31*, *32*). By contrast, caspase-6–deficient mice exhibit no developmental defects (*14*). It is possible that specifically targeting caspase-6 could be an effective therapeutic strategy with fewer side effects.

In AMLN- and CD-HFD–fed mice, both of which exhibit characteristics of human NASH, LAKO exaggerates liver damage without affecting steatosis and inflammation. Exacerbation of liver damage leads to increased scarring and fibrosis. Two weeks treatment with both AMPK activator and caspase-6 inhibitor substantially reduced hepatocellular death and hepatic fibrosis. Activation of AMPK inhibits proliferation of HSCs (*33*). Thus, the effects of the AMPK activator reported here on hepatic fibrosis could be attributed to both reduction of liver damage and inhibition of HSCs.

We measured caspase-6 activity with the VEID-pNA substrate, and Z-VEID-FMK was used as a caspase-6 inhibitor. Although VEID is a preferred substrate of caspase-6, it cross-reacts to a lesser extent with caspase-3 (*34*, *35*). To ensure specificity, we used multiple methodologies to determine activation of caspase-6, including Western blot and immunofluorescent staining of aCasp6. We also used siRNA to specifically deplete caspase-6, resulting in attenuation of liver damage in NASH. Taken

together, our data support the conclusion that caspase-6 is activated and participates in the pathogenesis of liver damage in NASH. Moreover, depletion of caspase-6 abrogated the exaggerated liver damage in LAKO mice, indicating that the AMPK–caspase-6 axis regulates liver damage.

A previous study showed that inhibition of caspase-3 and -7 attenuates Bid cleavage, suggesting the existence of a feedforward loop that acts downstream of the executioner caspases (*36*). We elaborated the role of caspase-6 in sustaining activation of the caspase cascade in this feedforward loop. A previous study demonstrated that caspase-6 cleaves lamin A to induce nuclear and chromatin condensation in apoptosis (*37*). Although we observed some nuclear localization of active caspase-6 in our human and mouse NASH samples, most of active caspase-6 appeared to locate within the cytoplasm, suggesting that cleavage of Bid could be a dominant function of caspase-6. However, because caspase-6 does not participate in the initiating activation of the caspase cascade, it may play a role in mediating apoptosis only in chronic diseases. Caspase-6 has been proposed as an important target in Alzheimer's disease (*38*, *39*), which is also characterized by reduced AMPK activity (*40*). Thus, the AMPK–caspase-6 axis might have a role in other chronic inflammatory pathogenic processes.

REFERENCES AND NOTES

1. V. Hernandez-Gea, S. L. Friedman, *Annu. Rev. Pathol.* **6**, 425–456 (2011).
2. S. L. Friedman, B. A. Neuschwander-Tetri, M. Rinella, A. J. Sanyal, *Nat. Med.* **24**, 908–922 (2018).
3. G. K. Michalopoulos, M. DeFrances, *Adv. Biochem. Eng. Biotechnol.* **93**, 101–134 (2005).
4. M. E. Guicciardi, G. J. Gores, *Gut* **54**, 1024–1033 (2005).
5. T. Luedde, N. Kaplowitz, R. F. Schwabe, *Gastroenterology* **147**, 765–783.e4 (2014).
6. D. G. Hardie, *Genes Dev.* **25**, 1895–1908 (2011).
7. D. G. Hardie, F. A. Ross, S. A. Hawley, *Nat. Rev. Mol. Cell Biol.* **13**, 251–262 (2012).
8. T. L. Martin *et al.*, *J. Biol. Chem.* **281**, 18933–18941 (2006).
9. B. Viollet *et al.*, *Crit. Rev. Biochem. Mol. Biol.* **45**, 276–295 (2010).
10. R. J. Valentine, K. A. Coughlan, N. B. Ruderman, A. K. Saha, *Arch. Biochem. Biophys.* **562**, 62–69 (2014).
11. P. Zhao *et al.*, *Cell* **172**, 731–743.e12 (2018).
12. G. R. Steinberg *et al.*, *Cell Metab.* **4**, 465–474 (2006).
13. N. Boudaba *et al.*, *EBioMedicine* **28**, 194–209 (2018).
14. D. R. McIlwain, T. Berger, T. W. Mak, *Cold Spring Harb. Perspect. Biol.* **5**, a008656 (2013).
15. I. Budihardjo, H. Oliver, M. Lutter, X. Luo, X. Wang, *Annu. Rev. Cell Dev. Biol.* **15**, 269–290 (1999).
16. M. Matsumoto *et al.*, *Int. J. Exp. Pathol.* **94**, 93–103 (2013).
17. J. R. Clapper *et al.*, *Am. J. Physiol. Gastrointest. Liver Physiol.* **305**, G483–G495 (2013).
18. M. Fujii *et al.*, *Med. Mol. Morphol.* **46**, 141–152 (2013).
19. J. Y. Kim *et al.*, *Cell* **175**, 133–145.e15 (2018).
20. E. C. Cokorinos *et al.*, *Cell Metab.* **25**, 1147–1159.e10 (2017).
21. D. Wu *et al.*, *Nature* **559**, 637–641 (2018).
22. A. Suzuki *et al.*, *Oncogene* **23**, 7067–7075 (2004).
23. E. M. Velázquez-Delgado, J. A. Hardy, *Structure* **20**, 742–751 (2012).
24. R. Eskes, S. Desagher, B. Antonsson, J. C. Martinou, *Mol. Cell. Biol.* **20**, 929–935 (2000).
25. M. C. Wei *et al.*, *Genes Dev.* **14**, 2060–2071 (2000).
26. H. Li, H. Zhu, C. J. Xu, J. Yuan, *Cell* **94**, 491–501 (1998).
27. V. R. Sutton *et al.*, *J. Exp. Med.* **192**, 1403–1414 (2000).
28. L. Drew, *Nature* **550**, S102–S103 (2017).
29. M. Hatting *et al.*, *Hepatology* **57**, 2189–2201 (2013).
30. S. Thapaliya *et al.*, *Dig. Dis. Sci.* **59**, 1197–1206 (2014).
31. W. J. Kaiser *et al.*, *Nature* **471**, 368–372 (2011).
32. K. Kuida *et al.*, *Nature* **384**, 368–372 (1996).
33. A. da Silva Morais *et al.*, *Clin. Sci. (Lond.)* **118**, 411–420 (2009).
34. D. E. Ehrnhoefer *et al.*, *PLOS ONE* **6**, e27680 (2011).
35. C. E. Heise *et al.*, *PLOS ONE* **7**, e50864 (2012).
36. S. N. Shelton, M. E. Shawgo, J. D. Robertson, *J. Biol. Chem.* **284**, 11247–11255 (2009).
37. S. Ruchaud *et al.*, *EMBO J.* **21**, 1967–1977 (2002).
38. A. C. LeBlanc, *Eur. J. Neurosci.* **37**, 2005–2018 (2013).
39. X. J. Wang, Q. Cao, Y. Zhang, X. D. Su, *Annu. Rev. Pharmacol. Toxicol.* **55**, 553–572 (2015).
40. A. Salminen, K. Kaarniranta, A. Haapasalo, H. Soininen, M. Hiltunen, *J. Neurochem.* **118**, 460–474 (2011).

ACKNOWLEDGMENTS

We thank S. J. Morrison at the University of Texas Southwestern and K. Inoki at the University of Michigan for sharing AMPKα1 and α2 floxed mice and University of California, San Diego (UCSD) histology core for histology study. **Funding:** This work was supported by NIH P30DK063491, R01DK076906, and R01DK117551 to A.R.S.; NIH K99HL143277 to P.Z.; AHA 18POST34060088 to X.S.; NIH P01HL088093 to J.L.W.; NIH R01DK120714 to M.K.; NIH P42ES010337, UL1TR001442, R01DK106419, and P30DK120515 and U.S. Department of Defense (DOD) CA170674P2 to R.L.; and National Institute of Neurological Disorders and Stroke P30NS047101 to the UCSD microscopy core. F.H. was supported by the Eli Lilly LIFA program. **Author contributions:** P.Z. conceived the project. A.R.S. supervised the project. P.Z. and X.S. designed and performed experiments. C.C., K.i.W., and Z.L. assisted with experiments. S.S. and R.L. provided patient biopsy samples. F.H. and M.K. provided STAM and *MUP-uPA* mouse samples. J.L.W., M.K., and R.L. provided critique. P.Z., X.S., and A.R.S. wrote the manuscript. **Competing interests:** A.R.S. and P.Z. are named inventors of a patent application related to the use of AMPK and caspase-6 as therapeutic targets for NASH. J.L.W. is a founding member of Oxitope. M.K. and A.R.S. are founders of Elgia Therapeutics. Other authors declare no competing interests. **Data availability:** All data are available in the main text or supplementary materials.

SUPPLEMENTARY MATERIALS

science.sciencemag.org/content/367/6478/652/suppl/DC1
Materials and Methods
Figs. S1 to S10
Reference (*41*)

19 May 2019; accepted 23 December 2019
10.1126/science.aay0542

REPORT

ELECTROCHEMISTRY

CO_2 electrolysis to multicarbon products at activities greater than 1 A cm^{-2}

F. Pelayo García de Arquer[1]*, Cao-Thang Dinh[1]*, Adnan Ozden[2]*, Joshua Wicks[1,3]*, Christopher McCallum[2], Ahmad R. Kirmani[4], Dae-Hyun Nam[1], Christine Gabardo[2], Ali Seifitokaldani[1], Xue Wang[1], Yuguang C. Li[1], Fengwang Li[1], Jonathan Edwards[2], Lee J. Richter[4], Steven J. Thorpe[3], David Sinton[2]†, Edward H. Sargent[1]†

Electrolysis offers an attractive route to upgrade greenhouse gases such as carbon dioxide (CO_2) to valuable fuels and feedstocks; however, productivity is often limited by gas diffusion through a liquid electrolyte to the surface of the catalyst. Here, we present a catalyst:ionomer bulk heterojunction (CIBH) architecture that decouples gas, ion, and electron transport. The CIBH comprises a metal and a superfine ionomer layer with hydrophobic and hydrophilic functionalities that extend gas and ion transport from tens of nanometers to the micrometer scale. By applying this design strategy, we achieved CO_2 electroreduction on copper in 7 M potassium hydroxide electrolyte (pH ≈ 15) with an ethylene partial current density of 1.3 amperes per square centimeter at 45% cathodic energy efficiency.

The electrochemical transformation of gases into value-added products using renewable energy is an attractive route to upgrade CO_2 and CO into fuels and chemical feedstocks (*1*–*4*) based on hydrocarbons. The success of the approach will rely on continued improvements in energy efficiency to minimize operating costs and on increasing current density to minimize capital costs (*5*, *6*). This will require catalysts that facilitate adsorption, coupling, and hydrogenation via proton-coupled electron transfer steps (*7*–*9*).

In these reactions, water-based electrolytes act both as a proton source and as the ion conductive medium (*10*). However, the solubility of these gases in water is limited, leading to constrained gas diffusion as gas molecules collide or react with their environment (*11*). The diffusion length of CO_2 can be as low as tens of nanometers in alkaline aqueous environments (*12*). This has limited the productivity of catalysts in aqueous cells to current densities in the range of tens of milliamperes per square centimeter due to mass transport (*13*–*16*).

In a gas-phase electrolyzer, catalyst layers are deposited onto hydrophobic gas-diffusion layers so that gas reactants need to diffuse only short distances to reach electroactive sites on the catalyst surface (Fig. 1A) (*17*–*19*). Gas reactant diffusion in the catalyst layer becomes the mass transport–limiting step in the cathode, as observed in the oxygen reduction reaction (ORR) in fuel cells. To improve ORR performance, fuel-cell catalyst layers are designed to balance hydrophobicity to help expel water and hydrophilicity to maintain sufficient ion conductivity.

In contrast with oxygen reduction, which generates water as a product, CO_2 reduction requires water as a proton source for hydrocarbon production. Thus, the catalyst layer is hydrophilic and fully hydrated during the reaction. In this configuration, CO_2 electrochemical reactions occur within a gas-liquid-solid three-phase reaction interface (Fig. 1B) (*20*). This volume, in which gaseous reactants and electrolytes coexist at catalyst electroactive sites, decays rapidly into the electrolyte, particularly at the high pH used in alkaline electrolysis. The decay is further increased at high current densities because of local OH^- generation (*21*). A large fraction of the catalyst is in contact with electrolyte in which CO_2 availability is limited by its solubility (<2 mM at pH 15). Because hydrogen evolution is a competing reaction with CO_2 reduction in a similar applied potential range, the large fraction of catalyst surface area exposed to CO_2-depleted electrolyte promotes undesired H_2 generation (Fig. 1C). Whereas recent advances in gas-phase CO_2 reduction have led to partial current densities for CO_2 reduction of ≈100 mA cm^{-2} (*12*, *22*, *23*), other liquid-phase electrochemical technologies such as water electrolysis achieve multi-amperes per square centimeter (*24*, *25*).

High-temperature solid oxide electrolysis offers a strategy to achieve CO_2 reduction at high current density: CO_2 diffuses directly to the surface of the catalyst, in the absence of liquid electrolyte, thus overcoming the gas diffusion limitations of low-temperature systems. However, high-temperature conditions and the absence of liquid electrolyte have thus far limited CO_2 reduction to the production to CO (*26*).

Here, we present a hybrid catalyst design that, by decoupling gas, ion, and electron transport, enables efficient CO_2 and CO gas-phase electrolysis at current densities in the >1–A cm^{-2} regime to generate multicarbon products. We exploit an ionomer layer that, with hydrophobic and hydrophilic functionalities, assembles into a morphology with differentiated domains that favor gas and ion transport routes, conformally, over the metal surface: Gas transport is promoted through a side chain of hydrophobic domains, leading to extended gas diffusion, whereas water uptake and ion transport occur through hydrated hydrophilic domains (Fig. 1D). As a result, the reaction interface at which these three components come together—gaseous reactants, ions, and electrons—all at catalytically active sites, is increased from the submicrometer regime to the several micrometer length scale.

We began by modeling the available gaseous reactant in different gas-phase electrolysis scenarios (Fig. 1, E and F), building on previously established models (*27*) (see methods for more details). We explored how catalyst performance toward gas electroreduction would be modified as the availability of the gas reactant varied at the gas-electrolyte interface. To do so, we introduced an intermediate surface channel of 20-nm thickness between the catalyst and the electrolyte with an in-plane gas diffusion coefficient (D) appreciably different from that of bulk electrolyte (D_0). As D/D_0 increases, gas flow is promoted through this layer until the gas is converted at the catalyst surface or diffuses into the electrolyte (Fig. 1F), potentially enabling CO_2 diffusion on the scale of several micrometers; whereas, for a standard catalyst configuration, CO_2 is available only within about 1 μm (Fig. 1E). As the diffusion in the layer increases, so too does the current available for the electrochemical conversion of the gas reactant (Fig. 1G). A similar trend holds for other reactant gases such as O_2 (fig. S5).

We sought to design and implement such an enhanced transport system experimentally. We turned our attention to perfluorinated sulfonic acid (PFSA) ionomers, which combine hydrophobic and hydrophilic functionalities along with ion transport (*28*–*30*). We hypothesized that their controlled assembly into distinct hydrophobic and hydrophilic layered domains would offer differentiated pathways whereby gas transport is promoted through the hydrophobic domains and water and ion transport are facilitated by the hydrophilic domains (*31*–*36*) (Fig. 2A).

PFSA ionomers such as Nafion contain $-SO_3^-$ (hydrophilic) and $-CF_2$ (hydrophobic) groups.

[1]Department of Electrical and Computer Engineering, University of Toronto, 35 St. George St., Toronto, Ontario M5S 1A4, Canada. [2]Department of Mechanical and Industrial Engineering, University of Toronto, 5 King's College Rd., Toronto, Ontario M5S 3G8, Canada. [3]Department of Materials Science & Engineering (MSE), University of Toronto, 184 College St., Toronto, Ontario M5S 3E4, Canada. [4]Materials Science and Engineering Division, National Institute of Standards and Technology (NIST), Gaithersburg, MD 20899, USA.
*These authors contributed equally to this work.
†Corresponding author. Email: ted.sargent@utoronto.ca (E.H.S.); sinton@mie.utoronto.ca (D.S.)

Nafion, a widely used material in fuel cells as a catalyst binder and membrane material, exhibits strong structure-function–dependent properties (*28*, *37*). In a polar solvent (i.e., methanol), PFSA ionomers form colloids with hydrophilic $-SO_3^-$ groups exposed to solvent (*28*). When this PFSA ionomer solution is coated on the metallic catalyst surface, we expect a configuration in which $-SO_3^-$ is preferentially exposed to hydrophilic polycrystalline metal surfaces and electrolyte provides continuous percolating hydrophobic paths through $-CF_2$ hydrophobic domains (Fig. 2B).

Seeking to promote the exposure of SO_3^- groups toward catalyst and electrolyte surfaces, we prepared ionomer solutions in polar solvents, which we then spray-coated onto hydrophilic metal catalysts deposited on a porous polytetrafluoroethylene (PTFE) substrate at different loadings (*36*, *38*, *39*). The hydrophobicity of the catalysts before and after ionomer modification was characterized using static contact angles: These yielded similar values of ≈121° to 122° (fig. S8). Scanning electron microscopy (SEM) images revealed a homogeneous, conformal ionomer coating over the entire catalyst (Fig. 2, C and D). Cryo-microtomed cross-sectional transmission electron microscopy (TEM) images revealed the presence of a 5- to 10-nm continuous and conformal ionomer layer (Fig. 2, E to G), establishing a catalyst:ionomer planar heterojunction (CIPH).

To characterize the CIPH structural configuration, we carried out wide-angle x-ray scattering (WAXS) measurements on PTFE/Cu/ionomer samples (Fig. 2H and fig. S9). Both reference and CIPH samples exhibited a similar contribution of the different Cu planes and PTFE backbone support. CIPH samples, in addition, revealed weak scattering at 1.2 $Å^{-1}$ from the amorphous PFSA phase. The crystalline PFSA is masked by the PTFE support at 1.28 $Å^{-1}$ (*28*). Attempts to quantify ≈10-nm thin-film ionomers using grazing-incidence WAXS were unsuccessful. Neutron scattering has revealed lamellar arrangements in comparably thin PFSA layers (*37*, *40*, *41*).

Seeking to characterize the CIPH and the ionomer configuration in its hydrated condition, we designed a suite of ex situ and in situ surface-enhanced Raman spectroscopy (SERS) experiments (Fig. 2I and fig. S10). As-deposited ionomers on Ag catalysts exhibited strong characteristic signals at 733 cm^{-1} (characteristic of $-CF_2$ and C–C vibrations, table S5) and at

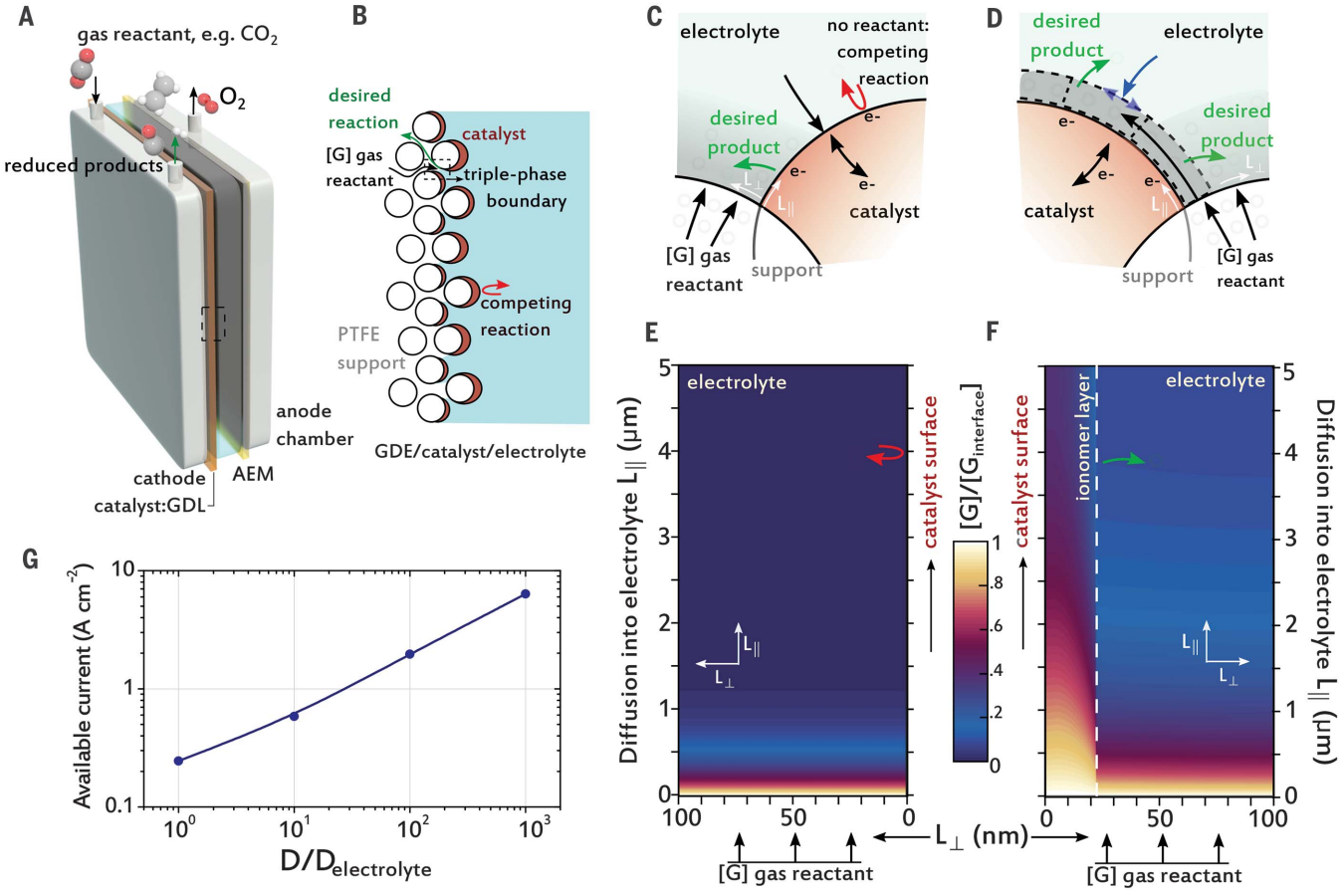

Fig. 1. Limiting current in gas-phase electrocatalysis and ionomer gas-liquid decoupled transport channels. (**A**) Flow-cell schematic. Reactant gases are fed through the back of a gas diffusion–electrode catalyst, facing an aqueous electrolyte. An anion-exchange membrane (AEM) facilitates OH^- transport from cathode to anode. GDL, gas-diffusion layer. (**B**) In a gas-diffusion electrode (GDE), catalysts are deposited onto a hydrophobic support from which gas reactants [G] diffuse. (**C**) The volume in which gas reactants, active sites, and water and ions coexist determines the maximum available current for gas electrolysis. Catalyst regions with limited reactant concentration promote by-product reactions such as hydrogen evolution. (**D**) When gas and electrolyte (water and ion source) transport is decoupled, the three-phase reaction interface can be extended so that all electrons participate in the desired electrochemical reaction. (**E** and **F**) Modeled gas reactant availability along the catalyst's surface for standard (E) and decoupled (F) gas transport into a 5 M KOH electrolyte, assuming an in-plane laminar gas diffusivity of $D_{||}/D_{KOH}$ = 1000 for the latter, where $D_{||}$ is gas diffusivity parallel to catalyst surface. Depending on the gas diffusivity within the gas transport channel, gas availability dramatically increases. $L_{||}$, distance parallel to catalyst surface; $L_\perp$, distance perpendicular to catalyst surface. (**G**) Modeled maximum available current density for CO_2 reduction. D/D_{KOH} manipulation enables entrance into the >1–A cm^{-2} regime for CO_2R. See methods for details on gas transport and reaction simulations.

1005 and 1130 cm^{-1} (associated with $-SO_3^-$ modes) as well as a complex background set of features arising from other C–C (1386 cm^{-1}), C–F (1182 and 1300 cm^{-1}), and S=O (1446 cm^{-1}) modes (*42*, *43*). Hydrated samples retain characteristic $-CF_2$, C–C and $-SO_3^-$ spectral features but a notably increased relative contribution of $-SO_3^-$ groups (1009 and 1131 cm^{-1}) compared with $-CF_2$ (730 cm^{-1}). This trend is maintained during operation in 1 M KOH electrolyte at −2 V versus Ag or AgCl reducing potentials and is also retained with the use of other catalyst metals such as Cu (fig. S11), suggesting that hydrated $-SO_3^-$ groups tend to face the electrocatalyst surface.

To assess the impact of the ionomer on gas availability, we evaluated the electrochemical performance of the CIPH for different metals and reactions in 5 M KOH electrolyte (Fig. 3). In the ORR, oxygen is reduced into water (*2*). The lack of a competing reaction to the ORR at potentials more positive than the hydrogen evolution reaction (HER) can be used to identify gas-reactant depletion and its impact on the limiting current. We built CIPH structures consisting of spray-cast ionomer coatings over PTFE/Ag substrates at different loadings, and we monitored the ORR current (fig. S12) using a 5 M KOH water electrolyte and air as reactants. Unmodified Ag catalysts showed a current density limited to less than 30 mA cm^{-2}. CIPH catalysts, on the other hand, exhibited a considerably enlarged current density that peaks at 250 mA cm^{-2} under the same conditions (Fig. 3A), with no H_2 production observed. In situ Raman measurements showed a consistent increase in the presence of O_2 near the catalyst surface at operating conditions (fig. S13). The observed enhancement can be explained as being due to ≈600× increased diffusion of O_2 relative to bulk electrolyte based on Knudsen diffusion of the reacting gas through CIPH hydrophobic domains (see methods).

To assess whether ion transport was modified in metal-ionomer catalysts, we compared the ORR and HER performance of standard Ag and Ag-CIPH samples for various electrolytes. Because the reactant in HER is in the aqueous phase (water or hydrated proton), the performance of the catalyst is not affected by the gas-diffusion properties of the PFSA ionomer layer; instead, catalyst performance is determined by water availability and ion transport. We found that CIPH samples exhibit similar hydrogen evolution activity to bare catalysts and increased ORR current across a wide range of electrolytes and pH (figs. S14 to S17). This result supports the notion that the enhanced ORR performance of the CIPH samples stems from extended gas transport.

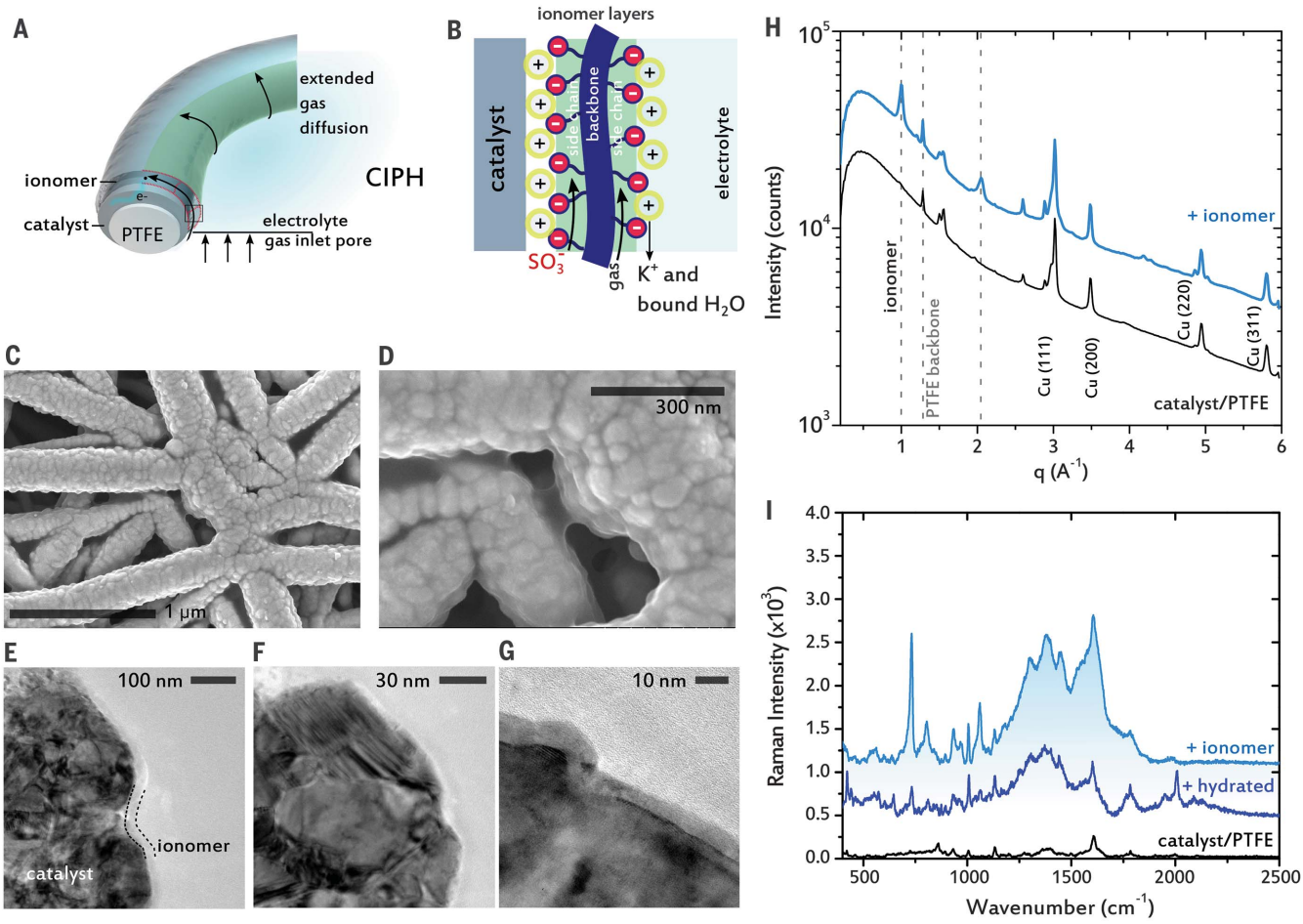

Fig. 2. The catalyst:ionomer planar heterojunction. (**A**) Schematic of metal catalyst deposited onto a PTFE hydrophobic fiber support. A flat ionomer layer conformally coats the metal. (**B**) Perfluorinated ionomers such as Nafion exhibit differentiated hydrophilic and hydrophobic characteristics endowed by $-SO_3^-$ and $-CF_2$ functionalities, respectively. Laminar Nafion arrangements have been reported depending on its thickness and substrate (*37*, *40*). (**C** and **D**) SEM images of ionomer-coated copper catalysts. (**E** to **G**) Cryo-microtomed TEM cross-sections of catalyst and ionomer revealing a laminar conformal overcoating. (**H**) WAXS spectra for reference and ionomer-modified catalysts. These reveal features at 1, 1.28, and 2 A^{-1}, associated with various PFSA and PTFE-support phases. (**I**) Raman spectra of reference and ionomer-modified catalysts revealing distinctive features of ionomer $-CF_2$ and $-SO_3^-$ groups (table S5).

We then focused on studying the performance of CIPH samples for CO_2 and CO reactants, investigating their reduction toward different products. We first screened Ag-CIPH samples for a CO_2 reduction reaction (CO_2RR) targeting CO production (*7*, *44*) and observed a CO_2RR partial current density of 400 mA cm^{-2} (Fig. 3B and fig. S18). By contrast, Ag reference samples, limited by CO_2 availability, exhibited a maximum CO_2RR partial current density of ≈54 mA cm^{-2}. This trend is maintained across different electrolytes (figs. S19 and S20).

These observations translate as well to Cu-CIPH catalysts targeting hydrocarbon generation (Fig. 3C and fig. S21) (*45*). Cu-CIPH catalysts exhibited a notable increase of CO_2RR current. At 800 mA cm^{-2}, H_2 generation remained below 10% Faradaic efficiency (FE), whereas the FE toward ethylene (C_2H_4) surpassed 60%. A CO_2 partial current density toward CO and ethylene of 510 mA cm^{-2} was achieved (Fig. 3C). Bare Cu catalysts, on the other hand, exhibited a limited CO_2RR current of 50 mA cm^{-2}. This performance is consistent with the increased presence of adsorbed CO intermediates, as observed using in situ Raman spectroscopy at similar conditions (fig. S13) (*46*). Based on the model presented herein, the observed enhancement can be explained by ≈400× increased diffusion of CO_2 relative to bulk electrolyte.

The electrochemical surface areas of reference and CIPH samples, as well as cell resistances, were comparable (see methods), indicating that these were not causes of the observed enhancement. These conclusions are further supported by the similar hydrophobicity of the catalysts before and after addition of the ionomer (fig. S8), consistent with the view that the enhanced gas reduction in CIPH samples originates from the extended gas diffusion through the ionomer layer, rather than from a redistribution of the gas or electrolyte in the PTFE substrate pores. Postreaction SEM revealed the unmodified presence of the PFSA ionomer in the CIPH after reaction (fig. S22).

To query the impact of CIPH when applied to other gas reactants, we monitored the CO reduction reaction (CORR) on Cu under similar reaction conditions—a system with activity limited by the poor solubility of CO in the electrolyte (Fig. 3D and fig. S23). Cu-CIPH samples yielded a CORR to ethylene partial current density of up to 340 mA cm^{-2}. Bare Cu samples, by contrast, showed a CORR limiting current of 64 mA cm^{-2}.

To study the effect of the ionomer on the kinetics of the reaction, which could lead to the difference in partial current densities observed, we carried out both ORR and CO_2RR in aqueous H-cell reactors. In this configuration, gas transport to the entire surface of the catalyst takes place through the electrolyte. In ORR, we observed a slight improvement in reaction kinetics, as indicated by a higher current density at low overpotential for CIPH

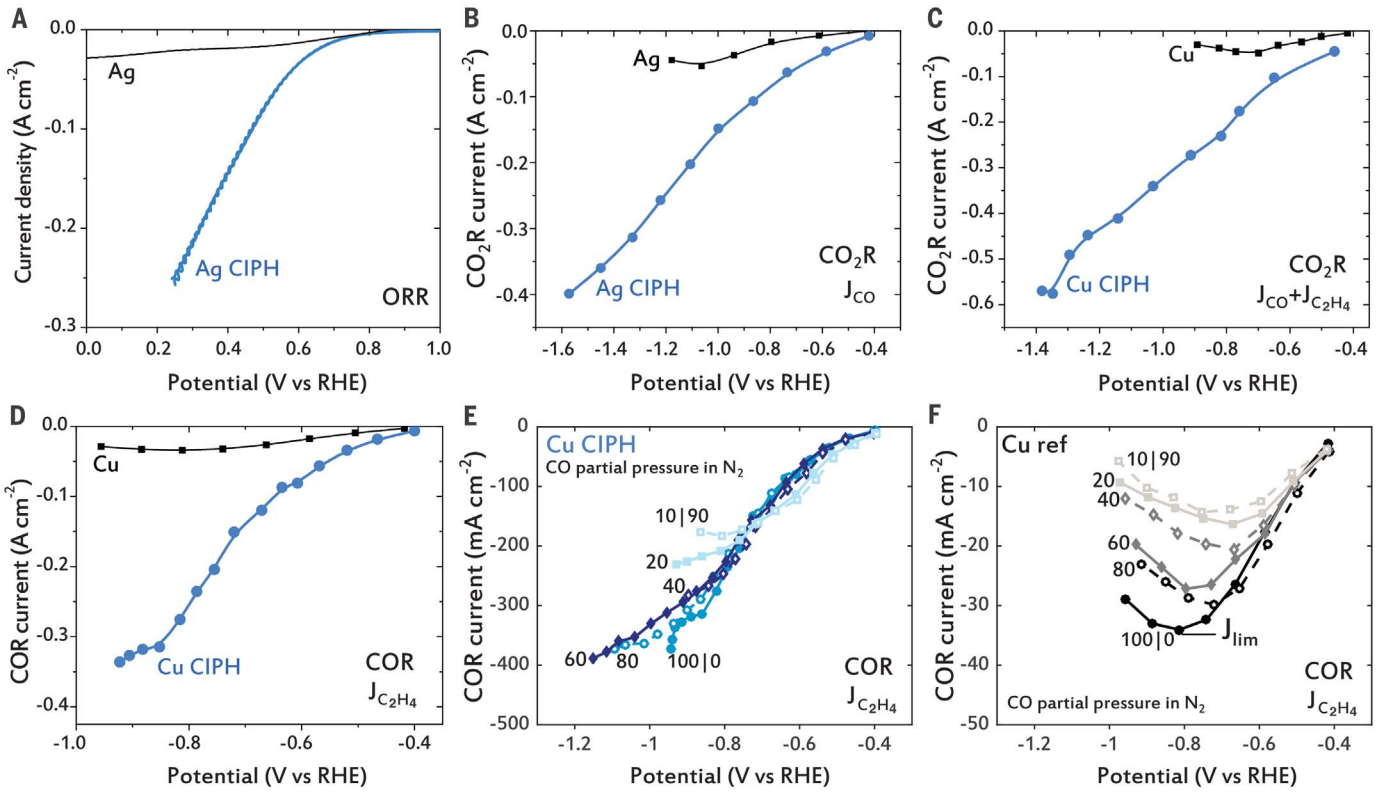

Fig. 3. Increased limiting current and underlying mechanisms for CIPH catalysts. (**A**) ORR showing a 30–mA cm^{-2} limiting current (J_{lim}) for Ag reference catalysts as opposed to 250 mA cm^{-2} for a CIPH configuration. RHE, reversible hydrogen electrode. (**B**) For CO_2RR, standard Ag catalysts yield a J_{lim} of ≈54 mA cm^{-2} (remaining current used for hydrogen evolution). This is in stark contrast with CIPH samples, which retain a FE above 85% for CO_2 reduction (CO_2R) to CO up to ≈500 mA cm^{-2}. (**C**) This trend is maintained for Cu CIPH catalysts and hydrocarbon production: J_{lim} toward ethylene (dominant product) is 50 mA cm^{-2} at −0.7 V versus RHE for bare Cu but increases beyond 0.5 A cm^{-2} for CIPH (peak FE of 61% at 835 mA cm^{-2}). (**D**) For CO reduction (COR), J_{lim} ≈ 64 mA cm^{-2} for standard Cu, whereas CIPH achieves a maximum 340–mA cm^{-2} current for the same reaction; H_2 by-product generation is restrained below 15% FE at all currents. (**E** and **F**) Partial pressure COR studies in $CO|N_2$ mixes for CIPH (E) and standard (F) catalyst show that only at partial pressures below 60% is J_{lim} observed for CIPH, whereas a sharp, steady decrease is observed for reference samples. At all partial pressures, CIPH exhibits an order of magnitude larger J_{lim}. Both reference and CIPH samples exhibit comparable resistance and double-layer capacitance. Electrochemical experiments were carried out in 5 M KOH electrolyte with a 50–cm^3 min^{-1} CO or CO_2 feedstock (in the case of 100% partial pressure).

samples (fig. S24). In CO_2RR on Ag-based catalyst, both bare Ag and Ag-CIPH showed comparable current densities (fig. S25), with a slight increase in CO FE (≈5%) for Ag-CIPH samples at low current density (<40 mA cm^{-2}), a finding attributable to a change in local environment induced by the Nafion layer. No change in oxidation or coordination number of the metal active sites was observed during in situ x-ray absorption spectroscopy (XAS) (fig. S26).

In the H-cell configuration, we observed similar limiting current densities for bare and CIPH samples in ORR and CO_2RR. These results indicate that although the presence of Nafion on the surface can change the reaction kinetics (*47*), it is its extended gas-transport properties that enable overcoming the limiting current density in gas-phase electrolysis.

To explore further the role of gas availability in the limiting current, we varied the gas availability by tuning the partial pressure of the reactant in N_2 mixtures (Fig. 3, E and F). A steep partial pressure dependence of limiting current density for ethylene was observed in CORR on Cu. Only at partial pressures below 60% was a limiting current observed for CIPH. At all CO partial pressures, Cu-CIPH exhibited an order of magnitude higher partial current density compared with bare Cu. We observed a similar trend in CO_2RR with varying CO_2 partial pressure (figs. S27 and S28). These results further confirm the role of the ionomer in enhancing reactant availability and thereby increasing current density.

In light of these findings, we sought to develop a catalyst design that took advantage of the gas-electrolyte segregated transport beyond two dimensions. Ideally, such a catalyst would maximize the triple-phase reaction interface across an extended three-dimensional (3D) morphology, enabling efficient operation in higher current regimes. We implemented a 3D catalyst:ionomer bulk heterojunction (CIBH) consisting of Cu nanoparticles and PFSA blended and spray-cast on a PTFE/Cu/ionomer (CIPH) gas-diffusion layer support, forming a 3D morphology with metal and ionomer percolation paths (Fig. 4A). Cross-sectional SEM

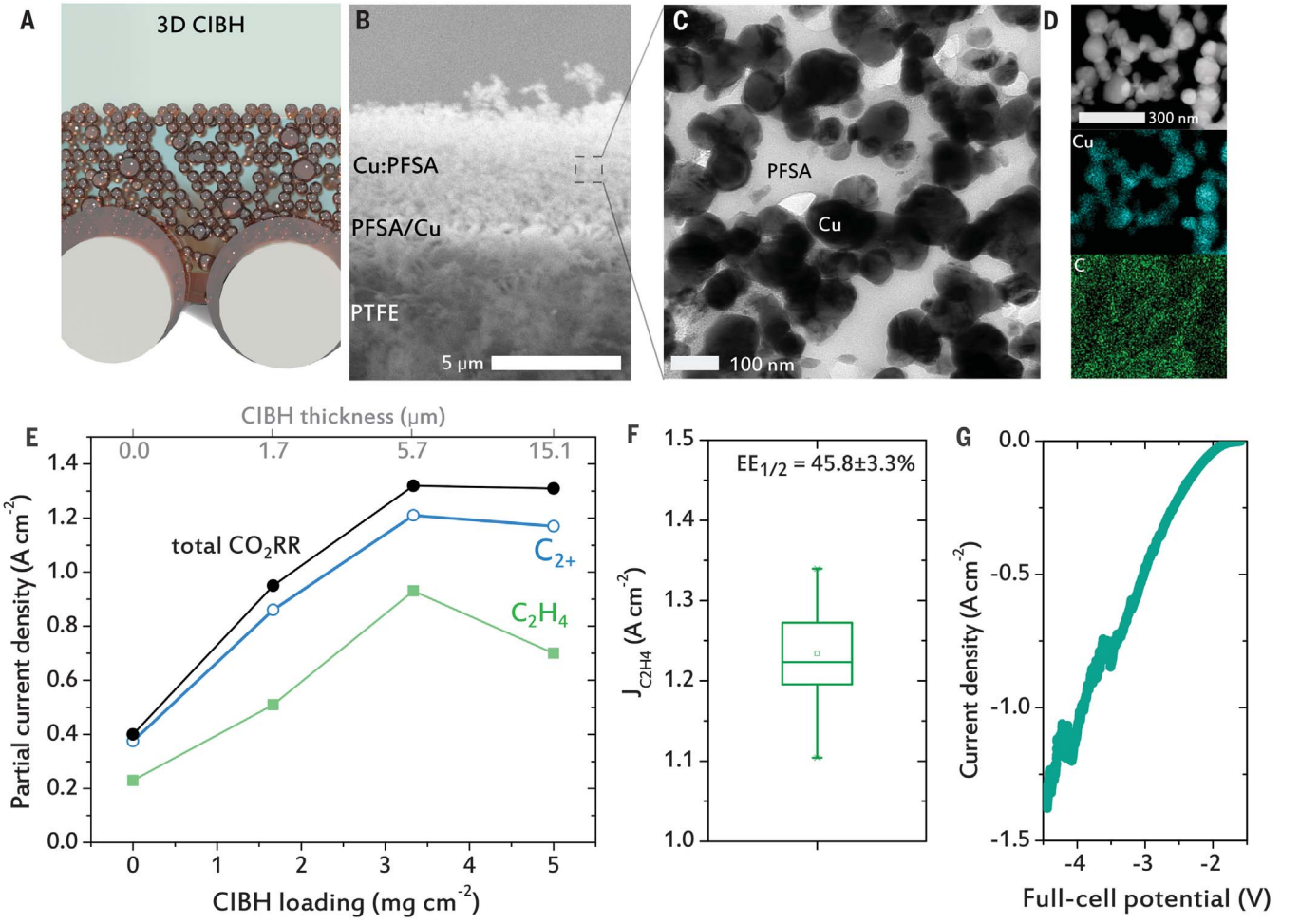

Fig. 4. 3D catalyst:ionomer bulk heterojunction for efficient gas-phase electrochemistry beyond 1 A cm^{-2}. (**A**) Schematic representation of metal-ionomer bulk heterojunction catalysts on a PTFE support. (**B**) Cross-sectional SEM of the CIBH catalyst. (**C** and **D**) TEM image of a cryo-microtomed CIBH (C) and elemental mapping of Cu and C revealing CIBH nanomorphology (D). (**E**) Partial current density for total CO_2RR reactions, with C_{2+} and C_2H_4 at maximum cathodic energy efficiency. The total CO_2R current saturates at 1.3 A cm^{-2} before cathodic energy efficiency drops for CIBH thicknesses beyond 6 µm. CIBH samples achieve more than a sixfold increase in partial current density at cathodic energy efficiencies >40% (fig. S30). Each sample and operating condition ran for at least 30 min. (**F**) Performance statistics of the highest partial current configuration for eight Cu CIBH catalysts. The box plot corresponds to Q1 to Q3 interquartile range, median, and average. The error bar represents ≈5.4 standard deviations. $EE_{1/2}$, half-cell (cathodic) energy efficiency. (**G**) Performance of the best CIBH catalyst in an ultraslim flow cell consisting of a 3-mm-wide catholyte channel. A full-cell energy efficiency of 20% for C_{2+} products is estimated at 1.1–A cm^{-2} operating current. All CIBH electrochemical experiments were carried out in 7 M KOH with a 50–cm^3 min^{-1} CO_2 feedstock.

images revealed the different layers in the CIBH catalyst (Fig. 4B). High-resolution cryomicrotomed cross-section images obtained using TEM and elemental energy-dispersive x-ray spectroscopy mapping further revealed the presence of continuous Cu nanoparticle and ionomer domains (Fig. 4, C and D).

We first optimized CIBH morphology by tuning the deposition conditions as well as the Cu:ionomer blend ratio, which we found optimized for a 4:3 weight/ by weight configuration. Using this configuration, with 7 M KOH electrolyte and 50 cm^3 min^{-1} of CO_2 flow, we then explored the effect of catalyst layer thickness. In an effective CIBH catalyst, CO_2RR current is expected to increase with catalyst loading until the length of the gas percolation paths through the ionomer phase reaches the gas reactant diffusion length. As we increased catalyst loading and corresponding thickness, we observed a monotonic increase in the total CO_2RR current, which surpassed 1 A cm^{-2} for a loading of 3.33 mg cm^{-2} (5.7 μm thickness) and which saturated at 1.32 A cm^{-2} for higher loadings before energy efficiency dropped (Fig. 4E). The total partial current for C_{2+} products (ethylene, ethanol, acetate, and propanol) reached 1.21 A cm^{-2} (fig. S29), which was achieved at a 45 ± 2% cathodic energy efficiency. The achieved C_{2+} partial current density represents a sixfold increase compared with previous best reports at similar energy efficiencies (*12*, *22*, *23*) (fig. S30 and tables S6 to S9).

The product distribution for optimal CIBH catalysts at different current densities in 7 M KOH electrolyte reveals that H_2 generation remains below 10% from 0.2 to 1.5 A cm^{-2} (fig. S29). At the highest current operation, optimized catalysts exhibited a maximum productivity toward ethylene with a FE in the 65 to 75% range, a peak partial current density of 1.34 A cm^{-2} at a cathodic energy efficiency of 46 ± 3% (Fig. 4F and figs. S31 and S32). We implemented the best CIBH catalyst in an ultraslim flow cell (with no reference electrode and a minimized catholyte channel of ≈3 mm, with water oxidized at a Ni foam anode), leading to an estimated full-cell energy efficiency toward C_{2+} products of 20% at 1.1 A cm^{-2} without the benefit of *iR* compensation (*i*, current; *R*, resistance) (Fig. 4G). CIBH catalyst current and FE remained stable over the course of a 60-hour initial study implemented in a membrane electrode assembly configuration (fig. S33).

Although CO_2 reduction kinetics improve with increasing temperature, alkaline electrolyzers manifest worsened CO_2 availability as temperature increases, and this fact curtails reaction productivity. We explored the effect of temperature on planar CIPH metal:ionomer catalysts and observed that CIPH catalysts require lower overpotentials to attain similar FE, in contrast with planar reference catalysts (fig. S34), when operated at 60°C. This effect translates into 3D CIBH catalysts, which show improved performance arising from the combination of accelerated CO_2 reduction kinetics and extended mass transport through the ionomer layer with increasing temperature (fig. S35). As a result, CIBH catalysts achieve ≈1 V reduced overpotential and more than a 50% increase in C_2 productivity when operated at industrial electrolyzer-relevant temperatures of 60°C in a full-cell configuration, compared with the case of room temperature operation (fig. S36).

The phenomena described herein showcase catalyst design principles that are not constrained by prior gas-ion-electron transport restrictions. The CIBH catalyst paves the way to the realization of renewable electrochemistry for hydrocarbon production at operating currents needed for industrial applications, as has been achieved with syngas for solid oxide electrolyzers (*48*, *49*).

REFERENCES AND NOTES

1. S. I. Seneviratne, M. G. Donat, A. J. Pitman, R. Knutti, R. L. Wilby, *Nature* **529**, 477–483 (2016).
2. Z. W. Seh *et al*., *Science* **355**, eaad4998 (2017).
3. S. Lin *et al*., *Science* **349**, 1208–1213 (2015).
4. C. Liu, B. C. Colón, M. Ziesack, P. A. Silver, D. G. Nocera, *Science* **352**, 1210–1213 (2016).
5. S. Verma, B. Kim, H.-R. M. Jhong, S. Ma, P. J. A. Kenis, *ChemSusChem* **9**, 1972–1979 (2016).
6. M. Jouny, W. Luc, F. Jiao, *Ind. Eng. Chem. Res.* **57**, 2165–2177 (2018).
7. Y. Hori, in *Modern Aspects of Electrochemistry* (Springer, 2008), pp. 89–189.
8. R. Kortlever, J. Shen, K. J. P. Schouten, F. Calle-Vallejo, M. T. M. Koper, *J. Phys. Chem. Lett.* **6**, 4073–4082 (2015).
9. Y. Zhang *et al*., *ACS Catal.* **7**, 4846–4853 (2017).
10. V. R. Stamenkovic, D. Strmcnik, P. P. Lopes, N. M. Markovic, *Nat. Mater.* **16**, 57–69 (2017).
11. M. L. Perry, J. Newman, E. J. Cairns, *J. Electrochem. Soc.* **145**, 5 (1998).
12. C.-T. Dinh *et al*., *Science* **360**, 783–787 (2018).
13. Y. Chen, C. W. Li, M. W. Kanan, *J. Am. Chem. Soc.* **134**, 19969–19972 (2012).
14. C. W. Li, J. Ciston, M. W. Kanan, *Nature* **508**, 504–507 (2014).
15. M. Liu *et al*., *Nature* **537**, 382–386 (2016).
16. Y. Lum, B. Yue, P. Lobaccaro, A. T. Bell, J. W. Ager, *J. Phys. Chem. C* **121**, 14191–14203 (2017).
17. S. Verma, X. Lu, S. Ma, R. I. Masel, P. J. A. Kenis, *Phys. Chem. Chem. Phys.* **18**, 7075–7084 (2016).
18. D. M. Weekes, D. A. Salvatore, A. Reyes, A. Huang, C. P. Berlinguette, *Acc. Chem. Res.* **51**, 910–918 (2018).
19. D. Higgins, C. Hahn, C. Xiang, T. F. Jaramillo, A. Z. Weber, *ACS Energy Lett.* **4**, 317–324 (2019).
20. M. Jouny, W. Luc, F. Jiao, *Nat. Catal.* **1**, 748–755 (2018).
21. K. Yang, R. Kas, W. A. Smith, *J. Am. Chem. Soc.* **141**, 15891–15900 (2019).
22. S. Ma *et al*., *J. Am. Chem. Soc.* **139**, 47–50 (2017).
23. J.-J. Lv *et al*., *Adv. Mater.* **30**, e1803111 (2018).
24. A. J. Martín, G. O. Larrazábal, J. Pérez-Ramírez, *Green Chem.* **17**, 5114–5130 (2015).
25. Z. Liu *et al*., *J. CO2 Util.* **15**, 50–56 (2016).
26. Y. Song, X. Zhang, K. Xie, G. Wang, X. Bao, *Adv. Mater.* **31**, 1902033 (2019).
27. T. Burdyny *et al*., *ACS Sustain. Chem.& Eng.* **5**, 4031–4040 (2017).
28. A. Kusoglu, A. Z. Weber, *Chem. Rev.* **117**, 987–1104 (2017).
29. T. D. Gierke, G. E. Munn, F. C. Wilson, *J. Polym. Sci., Polym. Phys. Ed.* **19**, 1687–1704 (1981).
30. K.-D. Kreuer, *Chem. Mater.* **8**, 610–641 (1996).
31. F. I. Allen *et al*., *ACS Macro Lett.* **4**, 1–5 (2015).
32. J.-P. Melchior, T. Bräuniger, A. Wohlfarth, G. Portale, K.-D. Kreuer, *Macromolecules* **48**, 8534–8545 (2015).
33. K.-D. Kreuer, G. Portale, *Adv. Funct. Mater.* **23**, 5390–5397 (2013).
34. M. Schalenbach *et al*., *J. Phys. Chem. C* **119**, 25145–25155 (2015).
35. L.-C. Weng, A. T. Bell, A. Z. Weber, *Phys. Chem. Chem. Phys.* **20**, 16973–16984 (2018).
36. R. Subbaraman, D. Strmcnik, V. Stamenkovic, N. M. Markovic, *J. Phys. Chem. C* **114**, 8414–8422 (2010).
37. S. C. DeCaluwe, A. M. Baker, P. Bhargava, J. E. Fischer, J. A. Dura, *Nano Energy* **46**, 91–100 (2018).
38. C.-H. Ma *et al*., *Polymer (Guildf.)* **50**, 1764–1777 (2009).
39. J. H. Lee *et al*., *Sci. Rep.* **8**, 10739 (2018).
40. S. C. DeCaluwe, P. A. Kienzle, P. Bhargava, A. M. Baker, J. A. Dura, *Soft Matter* **10**, 5763–5776 (2014).
41. A. Kusoglu *et al*., *Adv. Funct. Mater.* **24**, 4763–4774 (2014).
42. J. Zeng, D. I. Jean, C. Ji, S. Zou, *Langmuir* **28**, 957–964 (2012).
43. X. Ling, M. Bonn, S. H. Parekh, K. F. Domke, *Angew. Chem. Int. Ed.* **55**, 4011–4015 (2016).
44. C.-T. Dinh, F. P. García de Arquer, D. Sinton, E. H. Sargent, *ACS Energy Lett.* **3**, 2835–2840 (2018).
45. Y. Lum, J. W. Ager, *Nat. Catal.* **2**, 86–93 (2019).
46. M. C. Figueiredo, I. Ledezma-Yanez, M. T. M. Koper, *ACS Catal.* **6**, 2382–2392 (2016).
47. J. H. Lee *et al*., *Adv. Funct. Mater.* **28**, 1804762 (2018).
48. T. Burdyny, W. A. Smith, *Energy Environ. Sci.* **12**, 1442–1453 (2019).
49. J. Lu *et al*., *Sci. Adv.* **4**, eaar5100 (2018).
50. F. P. García de Arquer, Arquer_et_al_microscopies_aay4217.zip, figshare (2020); doi: 10.6084/m9.figshare.11406927.

ACKNOWLEDGMENTS

The authors thank D. Kopilovic and R. Wolowiec for electrochemical cell design and setup; Z. Wang and Y. Lum for assistance and useful discussions; the Ontario Centre for the Characterization of Advanced Materials (OCCAM) for sample preparation and characterization facilities; and T. P. Wu, Y. Z. Finfrock, G. Sterbinsky, and L. Ma for technical support at 9-BM beamline of APS. J.W. gratefully acknowledges financial support from the Ontario Graduate Scholarship (OGS) program. A.S. thanks Fonds de Recherche du Quebec–Nature et Technologies (FRQNT) for support in the form of a postdoctoral fellowship award. C.-T.D. and A.S. are currently affiliated with Queen's University and McGill University, respectively. Certain commercial equipment, instruments, or materials are identified in this paper in order to specify the experimental procedure adequately. Such identification is not intended to imply recommendation or endorsement by the National Institute of Standards and Technology, nor is it intended to imply that the materials or equipment identified are necessarily the best available for the purpose. **Funding:** This work was financially supported by the Ontario Research Foundation, Research Excellence Program; the Natural Sciences and Engineering Research Council (NSERC) of Canada; the CIFAR Bio-Inspired Solar Energy program; and TOTAL S.A. This research used resources of the National Synchrotron Light Source II, which is a U.S. Department of Energy (DOE) Office of Science Facility, operated at Brookhaven National Laboratory under contract no. DESC0012704, and synchrotron resources of the Advanced Photon Source (APS) (XAS measurements), an Office of Science User Facility operated for the U.S. DOE Office of Science by Argonne National Laboratory, and was supported by the U.S. DOE under contract no. DE-AC02-06CH11357 and the Canadian Light Source and its funding partners. **Author contributions:** A.R.K. is a guest researcher. F.P.G.d.A., C.-T.D., A.O., and J.W. designed and carried out all electrochemical experiments. F.P.G.d.A. and C.-T.D. designed all remaining experiments and characterizations. C.M. carried out diffusion-reaction simulations. C.G. and F.P.G.d.A. carried out Raman spectroscopies. A.S. carried out SEM imaging. A.R.K. performed WAXS measurements. J.E. carried out contact angle measurements. All authors discussed the results and assisted during manuscript preparation. F.P.G.d.A., C.-T.D., D.S., and E.H.S. supervised the project. **Competing interests:** F.P.G.d.A., C.-T.D., A.O., J.W., D.S., and E.H.S. have filed provisional patent application no. 62930229 regarding catalyst:ionomer devices. **Data and materials availability:** All data are reported in the main text and supplementary materials. Raw microscopy images are available at figshare (*50*).

SUPPLEMENTARY MATERIALS

science.sciencemag.org/content/367/6478/661/suppl/DC1
Materials and Methods
Figs. S1 to S36
Tables S1 to S9
References (*51*–*75*)

17 June 2019; resubmitted 22 September 2019
Accepted 23 December 2019
10.1126/science.aay4217

CATALYSIS

Na^+-gated water-conducting nanochannels for boosting CO_2 conversion to liquid fuels

Huazheng Li[1], Chenglong Qiu[2], Shoujie Ren[1,3], Qiaobei Dong[1], Shenxiang Zhang[1], Fanglei Zhou[1], Xinhua Liang[3], Jianguo Wang[2], Shiguang Li[4], Miao Yu[1]*

Robust, gas-impeding water-conduction nanochannels that can sieve water from small gas molecules such as hydrogen (H_2), particularly at high temperature and pressure, are desirable for boosting many important reactions severely restricted by water (the major by-product) both thermodynamically and kinetically. Identifying and constructing such nanochannels into large-area separation membranes without introducing extra defects is challenging. We found that sodium ion (Na^+)–gated water-conduction nanochannels could be created by assembling NaA zeolite crystals into a continuous, defect-free separation membrane through a rationally designed method. Highly efficient in situ water removal through water-conduction nanochannels led to a substantial increase in carbon dioxide (CO_2) conversion and methanol yield in CO_2 hydrogenation for methanol production.

Protein-constructed water channels (*1*) or ion channels (*2*) exist in all living organisms and allow fast permeation of water or specific ions while rejecting other ionic species on the basis of size exclusion and electrostatic repulsion. These attributes have led scientists to attempt to create similar channels as a means of increasing the efficiency of industrial processes. Experimental strategies to obtain high water permeability while rejecting hydrated ions in artificial systems have included the incorporation of protein-based (*3*) or polymer-based artificial water channels (*4*, *5*) into a polymer matrix or lipid layers, as well as packing of graphene-based laminates (*6*–*9*). Very promising results in terms of ion rejection for desalination have been successfully demonstrated (*6*, *7*).

We explored whether nanochannels could be fabricated that reject small gas molecules approximately half the size of the hydrated ions (for example, Na^+, 6.6 Å) at high temperatures and pressures for applications in catalysis. For example, by-product water strongly inhibits the kinetics and thermodynamics of CO_2 hydrogenation to liquid fuels such as methanol (*10*–*12*). Gas-rejecting water-conduction nanochannels could boost the reaction rate and shift the equilibrium toward product formation by removing water while retaining reactant gases and products (*13*). However, angstrom-scale nanochannels that can distinguish water molecules (kinetic diameter 2.6 Å) from gas molecules as small as H_2 (kinetic diameter 2.9 Å) are very challenging to precisely engineer. Further, the nanochannel would need to be assembled without defects into a practical separation membrane that could operate at >200°C and >20 bar.

We report gas-impeding water conduction of NaA zeolitic nanochannels assembled into a centimeter-scale membrane with negligible defects through a rationally designed method (Fig. 1, A and B). Water conduction, which was confirmed by experimental gas dehydration at high temperatures and pressures, was likely the result of a gating effect of Na^+ located in the 8-oxygen ring apertures that regulated their effective size, as supported by theoretical simulations (Fig. 2). The exceptional benefits of such a water-conduction membrane (WCM) were demonstrated for catalytic methanol synthesis from CO_2 hydrogenation at elevated temperatures (200° to 250°C) and pressures (21 to 35 bar).

We designed a rational and effective process (Fig. 1A, route a) to prepare WCMs. We dip-coated a ceramic hollow-fiber support (length 300 mm, inner diameter 0.75 mm, outer diameter 1.5 mm, pore size 400 nm; fig. S1) with 50- to 200-nm NaA crystals (fig. S2) and then dried the support at 80°C for at least 3 hours. Prior to membrane synthesis, the coated support was subjected to thermal annealing at 200°C overnight. During annealing, physically loaded nanocrystals were chemically bonded to the support surface and inside the pores through dehydration of surface hydroxyl groups of the zeolite and the support (*14*) to ensure stable and adequate nuclei for inducing membrane growth. After a single cycle of hydrothermal growth, membranes without visible surface defects grew on the support (fig. S3). The penetration of small crystals, also called seeds, inside the 400-nm support pores also induced membrane growth within the pores and resulted in an indistinguishable boundary between the membrane layer and the support. The membrane thickness was 3 to 4 μm, as indicated by energy-dispersive x-ray spectroscopy (EDX) (fig. S3).

We investigated the separation performance of our WCM for a $H_2O/CO_2/CO/H_2$/MeOH gas mixture (MeOH, methanol) with composition of 1.77 ± 0.14% / 23.52% / 0.98% / 73.50% / 0.23 ± 0.02% in our homemade apparatus (fig. S4) at 250°C and 21 bar. The mixture was generated by bubbling a 75% H_2 / 1% CO / 24% CO_2 gas mixture through a liquid tank containing 1.5 wt % MeOH in H_2O at 70°C. The selectivity (permeance ratio) of H_2O/CO_2 for this mixture (Fig. 1D and table S1) was ~551 ± 33. The minimum selectivities of H_2O/H_2, H_2O/CO, and H_2O/MeOH were 190, 170, and 80, respectively, as estimated from the detection limits of gas chromatography (GC), because no H_2, CO, and MeOH were detected on the permeate side. Relative to previously reported separation results (fig. S5 and table S2), our membrane showed two to three orders of magnitude lower gas permeances but comparable water permeance, and thus considerably higher H_2O/gas selectivity, suggesting effective gas-permeation blockage by the membrane layer (Fig. 1B).

At higher pressures (up to 38 bar), different temperatures (200° and 250°C), and various water concentrations (1 to 4.2 mol %), the WCM maintained excellent mixture separation performance (fig. S6). When a binary H_2O/gas mixture was used as feed, the selectivity of H_2O/CO_2 was as high as 10,722 ± 222 at 250°C and 21 bar (table S1). The much higher CO_2 partial pressure in the binary mixture did not lead to a proportional increase of its flux and thus drastically decreased CO_2 permeance (1.39×10^{-11} mol m^{-2} s^{-1} Pa^{-1}), whereas water permeance was almost the same (1.49×10^{-7} mol m^{-2} s^{-1} Pa^{-1}). No obvious selectivity decline (fig. S7) was detected throughout 12-hour tests, suggesting high membrane stability.

High-density small seeds (50 to 200 nm) that had been bonded to the support by annealing were critical for high membrane quality, as evidenced by the results of a series of comparative experiments (Fig. 1D and table S1). Water/gas selectivities near the as-reported values (fig. S5 and table S2) were obtained after the elimination of the annealing step (Fig. 1A, route b), highlighting the importance of annealing treatment. A marked decrease of water/gas selectivities occurred when the 50- to 200-nm seed suspensions were diluted by factors of 2 and 10 (Fig. 1A, route c), indicating that the initial high-density loading of seeds was essential. When 300- to 400-nm or 400- to 700-nm seeds were applied, the accumulated selectivities were a factor of 5 to 8 lower than with the 50- to 200-nm seeds (Fig. 1A, route d).

The decrease of water/gas selectivity was mainly the result of the increase of gas permeances (by factors of 60 to 300) because the

[1]Department of Chemical and Biological Engineering, Rensselaer Polytechnic Institute, Troy, NY 12180, USA. [2]Institute of Industrial Catalysis, State Key Laboratory Breeding Base of Green-Chemical Synthesis Technology, College of Chemical Engineering, Zhejiang University of Technology, Hangzhou 310032, P.R. China. [3]Department of Chemical and Biochemical Engineering, Missouri University of Science and Technology, Rolla, MO 65409, USA. [4]Gas Technology Institute, Des Plaines, IL 60018, USA.
*Corresponding author. Email: yum5@rpi.edu

water permeance did not exhibit large variation (less than a factor of 3). Relatively high gas permeances can be attributed to the presence of nonselective defects that allow water and gases to pass at comparable rates (Fig. 1C). High-density, stabilized seeds on the surface resulted in the growth of a continuous membrane layer on the support surface, whereas the penetrated small seeds in the support pores facilitated the growth of the crystals in the pores and subsequent seamless merging. These two intergrown layers ensure the high quality of the WCM with negligible defects and thus high water/gas selectivities.

To further understand the mechanism of gas blockage by the WCM, we performed single-gas permeation measurements for gas molecules with different sizes after membrane degassing at 200°C for at least 3 days to exclude the influence of adsorbed water in the zeolitic nanochannels. Even without adsorbed water in NaA nanochannels, gas permeances in single-gas permeation (fig. S8 and table S3) were in the same range (10^{-10} to 10^{-9} mol m^{-2} s^{-1} Pa^{-1}) as those in the mixture separation (Fig. 1D and table S1); this finding suggested that adsorbed water in mixture separation had negligible influence on gas permeation and that NaA zeolite nanochannels effectively blocked gas permeation.

We then conducted a thorough comparison of pure gas and water permeabilities with results on NaA zeolite membranes reported within the past 20 years (Fig. 1E). To have a fair comparison, we used gas permeability, calculated as the product of gas permeance and membrane thickness. The pure gas permeabilities of the WCM were two to three orders of magnitude lower than the reported results and completely dropped out of their respective permeability zones. However, the water permeability of the WCM was two to three orders of magnitude higher than that of gases and was well within the water permeability zone, comparable to the reported results. These findings, combined with mixture separation results, indicate that the WCM has very high quality and negligible defects. Moreover, the WCM also exhibited good thermal stability in dry gas up to 400°C (table S4) and good water stability up to 300°C (fig. S9).

The accepted channel diameter of the NaA structure, dominated by the 8-oxygen ring (Fig. 2A), is 4.2 Å, as calculated from the interatomic distance of two opposing oxygen atoms across the ring (*15*). However, Na^+, by neutralizing the negatively charged NaA framework (*Fm*$\bar{3}$*c* space group with a = 24.555 Å, unit cell composition of $Na_{96}Si_{96}Al_{96}O_{384}$) and positioning inside zeolite nanocavities with three locations (Fig. 2A), partially blocks the nanochannels and decreases the effective aperture size (*16*, *17*). We further speculate, on the basis of our permeation results, that molecules entering these nanochannels can be influenced strongly by Na^+. The passage of small, polar water molecules to the zeolitic nanochannel could be facilitated by Na^+, whereas the passage of larger and less polar molecules, such as H_2 and CO_2, would be hindered,

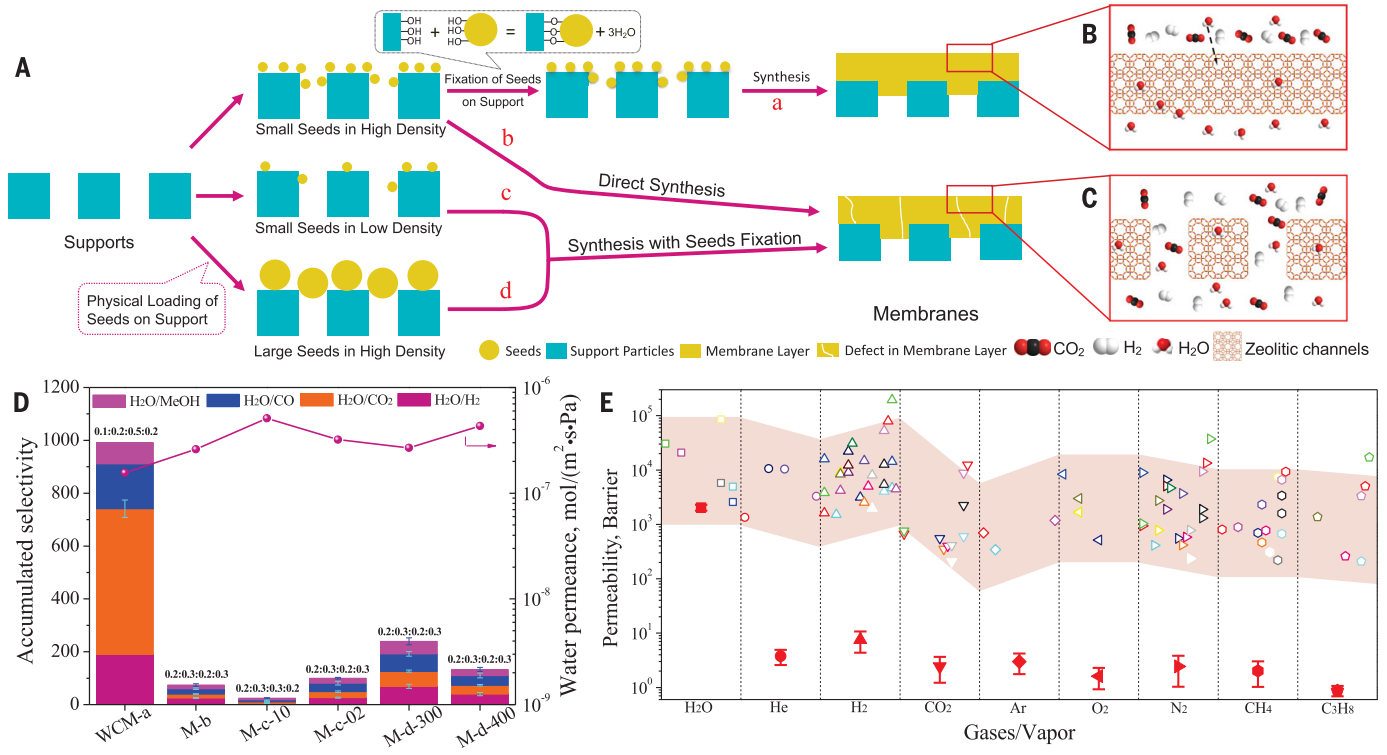

Fig. 1. Rationally designed preparation strategy and separation/permeation properties of water-conduction membrane (WCM). (**A**) Schematics of different preparation routes. In route a, 50- to 200-nm seeds are fixed at high loading density onto and into the support through dehydration of surface hydroxyl groups as illustrated, for growth of WCM-a with defects largely suppressed, whereas in route b, these seeds are used directly for growth of membrane (M-b) with defects. In route c, the seeds are diluted by a factor of 2 or 10 relative to route a for growth of M-c-02 and M-c-10, respectively. In route d, larger seeds (300 to 400 nm and 400 to 700 nm) are fixed onto and into the support through dehydration for growth of M-d-300 and M-d-400, respectively. (**B** and **C**) Molecular transport pathway through WCM-a (B) and through membranes prepared by routes b to d (C). (**D**) Separation performance of membranes prepared by different routes for $H_2O/CO_2/CO/H_2$/MeOH mixture with composition of 1.77 ± 0.14% / 23.52% / 0.98% / 73.50% / 0.23 ± 0.02% at 250°C and 21 bar. The minimum H_2O/H_2, H_2O/CO, and H_2O/MeOH selectivities of the WCM are estimated from the detection limits of GC. The fraction ratio at the top of each column represents the selectivity ratio from top to bottom. Error bars denote SD. (**E**) Permeability of pure gases and water through the WCM at 25° to 200°C and 2 to 8 bar (solid red symbols) and comparison with previous results (open symbols) (*23*–*44*). The shaded area is the permeability zone of gases and water, based on reported results. Error bars denote SD.

leading to much faster transport of water molecules through the zeolitic nanochannel.

To better understand the potential gating effect of Na^+, we performed density functional theory (DFT) simulations to mimic the process of molecules passing the 8-oxygen ring aperture (Fig. 2B). We consider the passage of a molecule through the 8-oxygen ring as a three-step process with four defined states of a molecule (Fig. 2B): (i) approaching the surface of the 8-oxygen ring; (ii) entering the ring, referred to as admission of a molecule to the ring; and (iii) moving out of the ring and entering the α-cage of the NaA zeolite. Our result suggests that the most stable Na^+ location in NaA zeolite

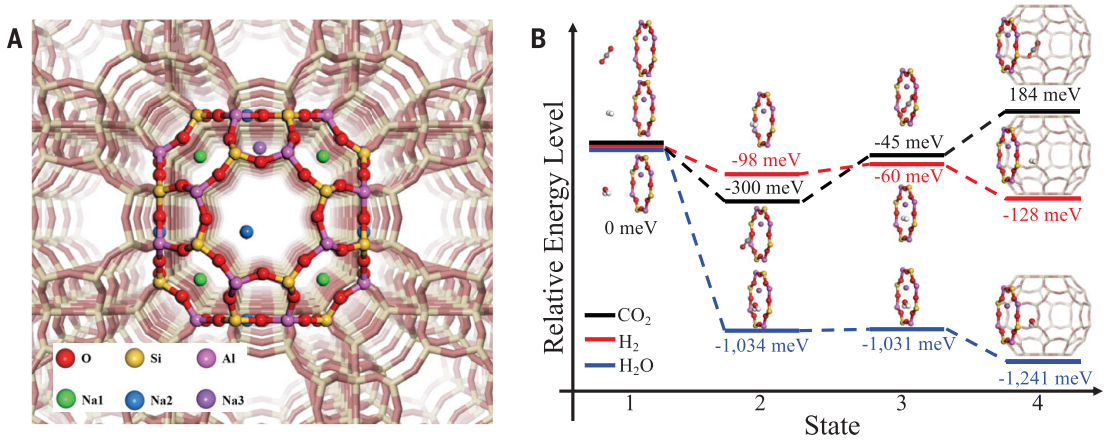

Fig. 2. DFT simulation of the passage of molecules through NaA zeolitic channels. (**A**) Top view of the structural framework of NaA zeolite with three Na^+ sites in the dehydrated crystal structure. (**B**) The passage of molecules through the zeolitic channels of NaA. In state 1, the gas molecule is away from the 8-oxygen ring. In state 2, the gas molecule is adsorbed onto the ring. In state 3, the gas molecule is in the ring. In state 4, the gas molecule is in the α-cage of the NaA zeolite. Numbers are energy levels calculated by DFT for three molecules moving into the α-cage of NaA zeolite through the 8-oxygen ring.

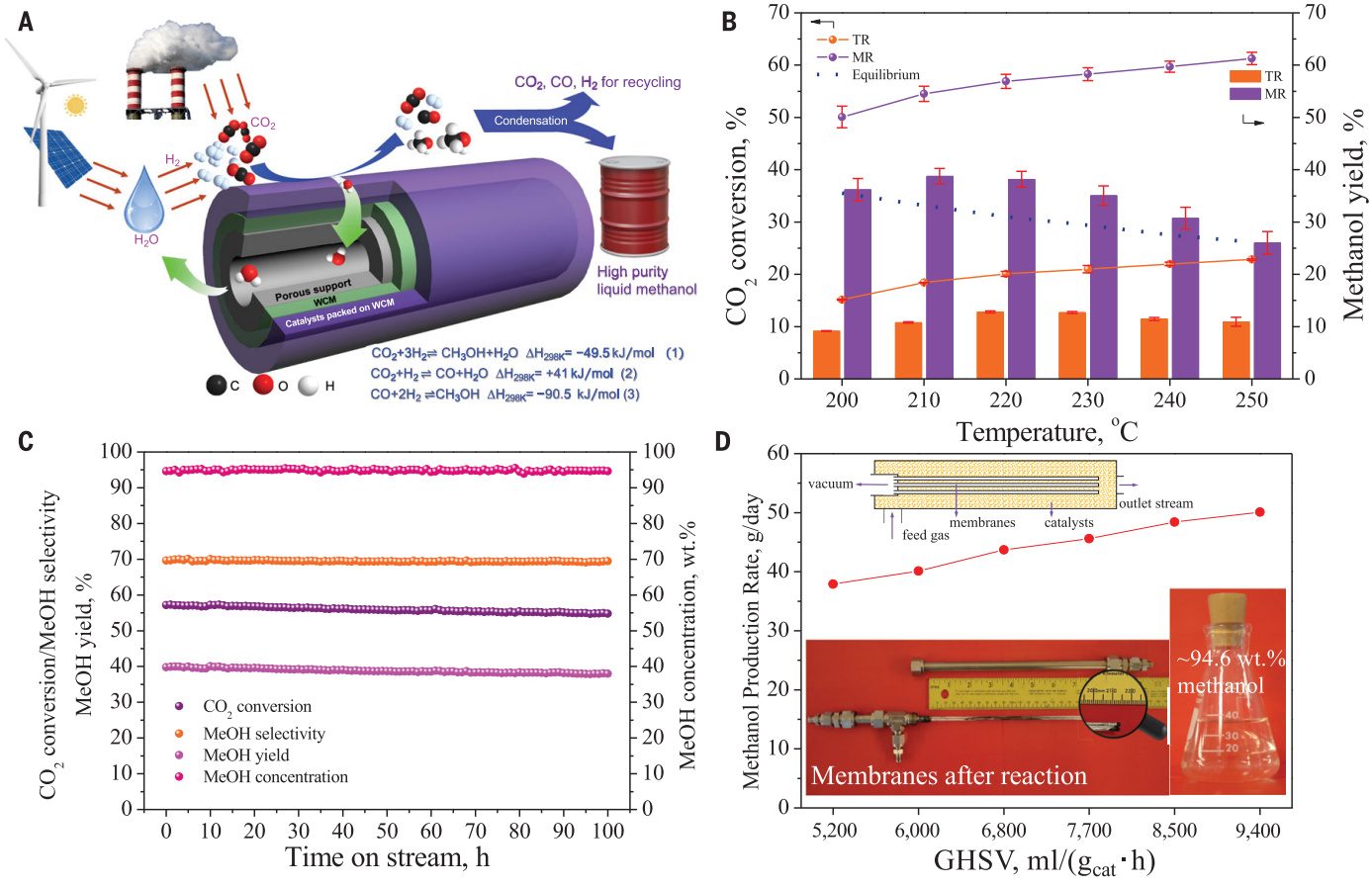

Fig. 3. Schematics of the membrane reactor (MR) concept and catalytic performance of the MR. (**A**) Schematics of WCM-incorporated dehydration MR for high-purity methanol direct synthesis from renewable resources. (**B**) Catalytic CO_2 conversion (points) and methanol yield (columns) obtained in the traditional reactor (TR; orange) and in the MR (purple) as a function of temperature at 35 bar and feed (CO_2/H_2 = 1/3) gas hourly space velocity (GHSV) of 5100 ml g_{cat}^{-1} $hour^{-1}$. Membrane length is 45 mm. Error bars denote SD. (**C**) Catalytic performance of methanol synthesis from CO_2 hydrogenation over 100 hours in the MR at 220°C and 35 bar. The feed (CO_2/H_2 = 1/3) GHSV is 4200 ml g_{cat}^{-1} $hour^{-1}$; membrane length is 45 mm. (**D**) Demonstration of high-purity methanol direct synthesis in the MR at different feed GHSVs at 220°C and 35 bar with three hollow-fiber WCMs 210 mm in length.

is 1.27 Å away from the center, which is consistent with previous reports (*17*, *18*); in the presence of H_2O, H_2, and CO_2, respectively, stable Na^+ positions are ~1.33 Å away from the center (fig. S10). At its stable positions, in contrast to the case without Na^+ in the 8-oxygen ring, the introduction of Na^+ decreases the admission energy barrier for H_2O but increases the barrier for CO_2 and H_2 (fig. S11 and table S5), supporting our hypothesis. Specifically, in Fig. 2B, the DFT calculation shows a substantial energy decrease (1034 meV) when a polar H_2O molecule adsorbs onto the aperture. The corresponding decreases were 300 meV for the less polar CO_2 molecule and 98 meV for nonpolar H_2, indicating a much more favorable interaction between Na^+ and H_2O than with CO_2 and H_2.

The admission energy barriers ΔE are 255 meV for CO_2, 38 meV for H_2, and 3 meV for H_2O. Whereas H_2O encounters a negligible energy barrier when entering the aperture, apparently resulting from the favorable interaction between polar H_2O and Na^+ and its small size, H_2 and CO_2 must overcome higher energy barriers, especially for larger CO_2, to enter the aperture. When further entering the α-cage, H_2O shows the largest energy drop (200 meV), followed by H_2 (68 meV); for CO_2, energy input (229 meV) is needed to enter the cage. The favorable interaction between H_2O and the α-cage also facilitates its fast passage of the 8-oxygen ring. Overall, both the admission into the 8-oxygen ring and subsequent entry into the α-cage energetically favor the H_2O molecule.

We applied a WCM to a reaction for the production of liquid fuels (Fig. 3A). We loaded copper-zinc-alumina (CZA) catalysts (fig. S12), which have been commercialized for methanol production, on the outer surface of a WCM to catalyze CO_2 hydrogenation for methanol production at 21 to 35 bar and 200° to 250°C and gas hourly space velocity (GHSV) between 5100 and 10,500 ml g_{cat}^{-1} $hour^{-1}$. The CZA catalyst was reduced in pure H_2 in situ at 250°C and atmospheric pressure for 10 hours with a ramping rate of 2°C/min in a homemade apparatus [membrane reactor (MR); fig. S13]. For comparison, the performance of the same catalysts without incorporation of the WCM [traditional reactor (TR)] was also evaluated with the same catalyst packed in a nonpermeable dense tube with the same dimensions as the WCM. Among all results obtained (Fig. 3B and figs. S14 and S15), CO_2 conversion (up to 61.4%) exceeded the equilibrium conversion (*19*) after incorporation of the WCM and was 2.6 to 3.0 times that obtained without the WCM.

Because NaA zeolite has no catalytic activity for CO_2 hydrogenation (*20*) and only CO_2 and H_2 were detected with only the WCM in the reactor at 35 bar and 250°C, effective in situ water removal by the WCM was the only reason for the drastically increased CO_2 conversion; moreover, it was the only reason why the thermodynamic equilibrium limitation on CO_2 hydrogenation was overcome. The adsorption of water on the catalyst was greatly inhibited by the low water concentration (less than 2 mol %) inside the MR, which should have enhanced the kinetics of the reaction and catalyst activity. Indeed, the methanol yield (25.1% to 38.9%) in the MR was 2.8 to 3.5 times that in the TR, with no obvious difference in product selectivity (figs. S16 and S17). Correspondingly, the space-time yield (STY) of methanol was highly promoted, for example, from 339 mg g_{cat}^{-1} $hour^{-1}$ in the TR to 809 mg g_{cat}^{-1} $hour^{-1}$ in the MR with GHSV of 10,500 ml g_{cat}^{-1} $hour^{-1}$ at 250°C and 35 bar (fig. S18), the highest value ever reported under similar conditions.

Moreover, because of the in situ water removal (by 95%) from methanol, very-high-purity methanol was directly obtained by simply condensing liquid products after the reactor—for example, 95.9 wt % in the MR versus 54.3 wt % in the TR at 230°C and 35 bar (figs. S19 and S20). The purity can be further increased by optimizing the MR (see detailed analysis in supplementary materials). This process could be expected to save a considerable amount of energy in purification processes such as distillation. The selectivities of H_2O over other components during the reaction (fig. S21) were consistent with the mixture separation results (fig. S6).

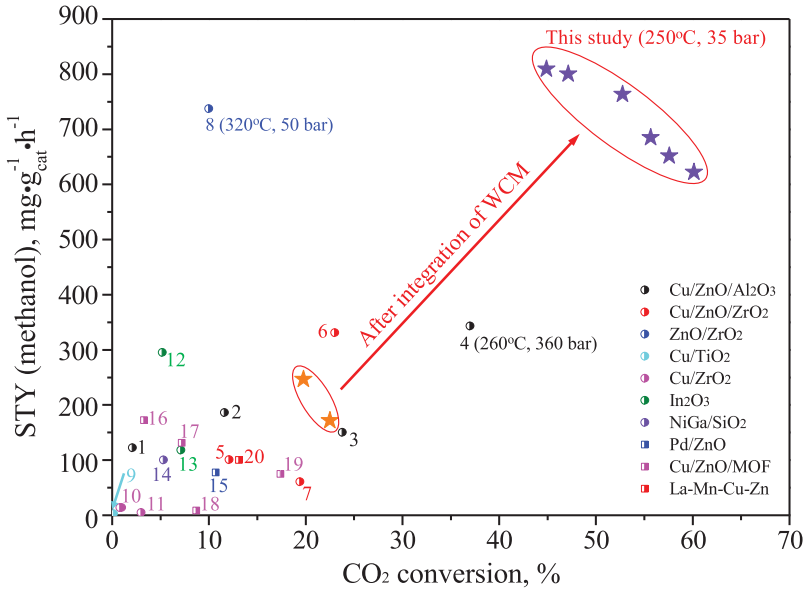

Fig. 4. Comparisons of catalytic results in the MR using WCMs in this study with TR results from literature in terms of CO_2 conversion and methanol space-time yield. Data points 1 and 12 are from (*45*); 2, (*46*); 3, (*47*); 4, (*48*); 5, (*49*); 6, (*50*); 7, (*51*); 8, (*52*); 9, (*53*); 10 and 11, (*54*); 13, (*55*); 14, (*56*); 15, (*57*); 16 to 19, (*58*); 20, (*59*). Orange stars, TR in this study; purple stars, MR in this study.

We performed stability tests at the highest methanol yield (TR, 14.0%; MR, 39.8%) under conditions of 220°C and 35 bar. We obtained a minor decrease (4%) of CO_2 conversion (57.2% to 54.8%) and methanol yield (39.8% to 38.1%) in the MR, as well as very stable high-purity methanol (~95 wt %) production for more than 100 hours (Fig. 3C); by contrast, in the TR, in which catalysts were exposed to large amounts of product water, we obtained a 10% decrease of CO_2 conversion (22.7% to 20.4%) and a 20% decrease of methanol yield (14.0% to 11.2%) (fig. S22). These results suggest excellent stability of our WCM under reaction conditions and effective protection of catalysts from water poisoning and catalyst sintering. Moreover, no obvious difference between SEM images of the WCM (fig. S23) and Brunauer-Emmett-Teller (BET) surface areas of catalysts (table S6) before and after reaction supported the above observation.

We tested our WCM for potential use at larger scale by assembling three 210-mm-long membranes (Fig. 3D, lower left inset) and loading ~2.8 g of catalysts in one reactor. We ran bench-scale methanol synthesis by drawing vacuum on the permeate side (Fig. 3D, upper inset) to generate driving force for water permeation at 250°C and 35 bar (movie S1). CO_2 conversion of 41.0% to 57.6% and methanol yield of 21.9% to 30.3% were achieved with the long MR comparable to those for the short MR; the methanol production rate of the long MR approached 50 g/day with an average

purity of 94.6 wt % (Fig. 3D, lower right inset, and fig. S24).

We compared our catalytic reaction results with those previously reported (Fig. 4 and table S7) in terms of CO_2 conversion and STY of methanol. With only CZA catalysts, the TR showed only moderate CO_2 conversion (23.0%) and methanol STY (339 mg g_{cat}^{-1} $hour^{-1}$). After the incorporation of the WCM, both CO_2 conversion and methanol STY were greatly boosted (61.4% and 809 mg g_{cat}^{-1} $hour^{-1}$, respectively). Our results obtained in the MR represent the highest values reported to date under similar reaction conditions and are even higher than those obtained at much higher temperatures and pressures. It may be possible to use WCMs for other reactions that are kinetically or thermodynamically restricted by water—such as CO_2 hydrogenation to dimethyl ether (*21*) and Fischer-Tropsch synthesis (*22*)—by loading corresponding catalysts onto the outer surface of the WCM.

REFERENCES AND NOTES

1. G. M. Preston, T. P. Carroll, W. B. Guggino, P. Agre, *Science* **256**, 385–387 (1992).
2. R. MacKinnon, *Nature* **350**, 232–235 (1991).
3. M. Kumar, M. Grzelakowski, J. Zilles, M. Clark, W. Meier, *Proc. Natl. Acad. Sci. U.S.A.* **104**, 20719–20724 (2007).
4. R. H. Tunuguntla *et al*., *Science* **357**, 792–796 (2017).
5. Y. X. Shen *et al*., *Proc. Natl. Acad. Sci. U.S.A.* **112**, 9810–9815 (2015).
6. K. Gopinadhan *et al*., *Science* **363**, 145–148 (2019).
7. L. Chen *et al*., *Nature* **550**, 380–383 (2017).
8. B. Radha *et al*., *Nature* **538**, 222–225 (2016).
9. A. Esfandiar *et al*., *Science* **358**, 511–513 (2017).
10. J. Graciani *et al*., *Science* **345**, 546–550 (2014).
11. C. F. Shih, T. Zhang, J. Li, C. Bai, *Joule* **2**, 1925–1949 (2018).
12. B. M. Tackett, E. Gomez, J. G. Chen, *Nat. Catal.* **2**, 381–386 (2019).
13. N. Diban, A. T. Aguayo, J. Bilbao, A. Urtiaga, I. Ortiz, *Ind. Eng. Chem. Res.* **52**, 10342–10354 (2013).
14. H. Li *et al*., *J. Membr. Sci.* **444**, 513–522 (2013).
15. D. W. Breck, *Zeolite Molecular Sieves: Structure, Chemistry, and Use* (Wiley, 1974).
16. D. Breck, W. Eversole, R. Milton, T. Reed, T. Thomas, *J. Am. Chem. Soc.* **78**, 5963–5972 (1956).
17. J. J. Pluth, J. V. Smith, *J. Am. Chem. Soc.* **102**, 4704–4708 (1980).
18. E. Csányi, Z. Ható, T. Kristóf, *J. Mol. Model.* **18**, 2349–2356 (2012).
19. W.-J. Shen, K.-W. Jun, H.-S. Choi, K.-W. Lee, *Korean J. Chem. Eng.* **17**, 210–216 (2000).
20. I. Makertiharta, P. Dharmawijaya, I. Wenten, in *AIP Conference Proceedings* (American Institute of Physics, 2017), vol. 1788, p. 040001.
21. A. Álvarez *et al*., *Chem. Rev.* **117**, 9804–9838 (2017).
22. M. Rohde, G. Schaub, S. Khajavi, J. Jansen, F. Kapteijn, *Micropor. Mesopor. Mater.* **115**, 123–136 (2008).
23. Y. H. Ma, Y. J. Zhou, R. Poladi, E. Engwall, *Separ. Purif. Tech.* **25**, 235–240 (2001).
24. K. Okamoto, H. Kita, K. Horii, K. Tanaka, M. Kondo, *Ind. Eng. Chem. Res.* **40**, 163–175 (2001).
25. X. Xu, W. Yang, J. Liu, L. Lin, *Separ. Purif. Tech.* **25**, 241–249 (2001).
26. X. Xu *et al*., *J. Membr. Sci.* **229**, 81–85 (2004).
27. W. Zhu *et al*., *J. Membr. Sci.* **253**, 57–66 (2005).
28. X. Xu *et al*., *J. Membr. Sci.* **249**, 51–64 (2005).
29. X. Chen, W. Yang, J. Liu, L. Lin, *J. Membr. Sci.* **255**, 201–211 (2005).
30. A. Tavolaro, P. Tavolaro, *Catal. Commun.* **8**, 789–794 (2007).
31. A. Huang, W. Yang, *Separ. Purif. Tech.* **61**, 175–181 (2008).
32. A. Huang, F. Liang, F. Steinbach, J. Caro, *J. Membr. Sci.* **350**, 5–9 (2010).
33. A. Huang, J. Caro, *J. Mater. Chem.* **21**, 11424–11429 (2011).
34. S. G. Sorenson *et al*., *J. Membr. Sci.* **366**, 413–420 (2011).
35. A. Huang, N. Wang, J. Caro, *Micropor. Mesopor. Mater.* **164**, 294–301 (2012).
36. A. Huang *et al*., *J. Membr. Sci.* **437**, 57–64 (2013).
37. K. P. Dey, D. Kundu, M. Chatterjee, M. K. Naskar, *J. Am. Ceram. Soc.* **96**, 68–72 (2013).
38. S. Shirazian, S. N. Ashrafizadeh, *Fuel* **148**, 112–119 (2015).
39. S. Shirazian, S. N. Ashrafizadeh, *J. Ind. Eng. Chem.* **22**, 132–137 (2015).
40. K. Xu, C. Yuan, J. Caro, A. Huang, *J. Membr. Sci.* **511**, 1–8 (2016).
41. X.-L. Wei *et al*., *RSC Adv.* **6**, 71863–71866 (2016).
42. X.-L. Wei *et al*., *J. Membr. Sci.* **530**, 240–249 (2017).
43. X.-L. Wei, H. Liu, Y.-Y. Xu, Y.-L. Sun, Z.-S. Chao, *CrystEngComm* **20**, 7195–7205 (2018).
44. S. M. Lee *et al*., *J. Porous Mater.* **26**, 1121–1129 (2019).
45. O. Martin *et al*., *Angew. Chem. Int. Ed.* **55**, 6261–6265 (2016).
46. F. Gallucci, L. Paturzo, A. Basile, *Chem. Eng. Process. Process Intensif.* **43**, 1029–1036 (2004).
47. R. Gaikwad, A. Bansode, A. Urakawa, *J. Catal.* **343**, 127–132 (2016).
48. A. Bansode, A. Urakawa, *J. Catal.* **309**, 66–70 (2014).
49. L. Li, D. Mao, J. Yu, X. Guo, *J. Power Sources* **279**, 394–404 (2015).
50. L. Angelo *et al*., *C. R. Chim.* **18**, 250–260 (2015).
51. R. Raudaskoski, M. V. Niemelä, R. L. Keiski, *Top. Catal.* **45**, 57–60 (2007).
52. J. Wang *et al*., *Sci. Adv.* **3**, e1701290 (2017).
53. S. Kattel, B. Yan, Y. Yang, J. G. Chen, P. Liu, *J. Am. Chem. Soc.* **138**, 12440–12450 (2016).
54. K. Larmier *et al*., *Angew. Chem. Int. Ed.* **56**, 2318–2323 (2017).
55. K. Sun *et al*., *J. CO_2 Utiliz.* **12**, 1–6 (2015).
56. F. Studt *et al*., *Nat. Chem.* **6**, 320–324 (2014).
57. H. Bahruji *et al*., *J. Catal.* **343**, 133–146 (2016).
58. B. An *et al*., *J. Am. Chem. Soc.* **139**, 3834–3840 (2017).
59. H. Zhan *et al*., *Catal. Lett.* **145**, 1177–1185 (2015).

ACKNOWLEDGMENTS

Funding: Supported by Advanced Research Projects Agency–Energy (ARPA-E), U.S. Department of Energy, award DE-AR0000806; Rensselaer Polytechnic Institute (RPI) startup funds; and National Natural Science Foundation of China grant NSFC-21625604 (J.W.). **Author contributions:** M.Y. and H.L. conceived the project; H.L. prepared and evaluated the membranes and membrane reactors; S.R. and X.L. supplied and characterized the catalysts; Q.D. conducted the BET test; S.Z. and S.L. drew and discussed some figures; F.Z. performed the XRD; C.Q. and J.W. performed the DFT calculation; M.Y. directed all aspects of the project; and M.Y. and H.L. wrote the manuscript. **Competing interests:** A U.S. provisional patent (application number 62/795,082), with M.Y. and H.L. as co-inventors, has been filed by RPI. **Data and materials availability:** All data are available in the main text or the supplementary materials.

SUPPLEMENTARY MATERIALS

science.sciencemag.org/content/367/6478/667/suppl/DC1
Materials and Methods
Figs. S1 to S24
Tables S1 to S7
Movie S1
References (*60*–*75*)

2 October 2019; accepted 10 December 2019
10.1126/science.aaz6053

MULTIFERROICS

Room temperature magnetoelectric coupling in a molecular ferroelectric ytterbium(III) complex

Jérôme Long[1]*, Maxim S. Ivanov[2], Vladimir A. Khomchenko[2], Ekaterina Mamontova[1], Jean-Marc Thibaud[1], Jérôme Rouquette[1], Mickaël Beaudhuin[1], Dominique Granier[1], Rute A. S. Ferreira[3], Luis D. Carlos[3], Bruno Donnadieu[4], Marta S. C. Henriques[2], José António Paixão[2], Yannick Guari[1], Joulia Larionova[1]

Magnetoelectric (ME) materials combine magnetic and electric polarizabilities in the same phase, offering a basis for developing high-density data storage and spintronic or low-consumption devices owing to the possibility of triggering one property with the other. Such applications require strong interaction between the constitutive properties, a criterion that is rarely met in classical inorganic ME materials at room temperature. We provide evidence of a strong ME coupling in a paramagnetic ferroelectric lanthanide coordination complex with magnetostrictive phenomenon. The properties of this molecular material suggest that it may be competitive with inorganic magnetoelectrics.

A ferroelectric material exhibits a permanent electrical polarization that can be switched by an electric field (*1*, *2*). Such electroactive materials have a wide range of applications, including temperature sensing, data storage, piezoelectric devices, and electro-optics. The association of electrical and magnetic polarizabilities gives rise to multifunctional systems called magnetoelectrics. The term describes the influence of a magnetic (electric) field on the polarization (magnetization), allowing the constitutive properties to be simultaneously triggered (*3*, *4*). For computing, modifying the polarization or magnetization using a low-magnitude magnetic or electric field may reduce the energy needed and speed up the processing rate of nonvolatile memory devices (*3*, *5*, *6*). Conventional approaches to designing single-phase magnetoelectrics are widely based on inorganic materials, such as oxides or fluorides (*6*–*8*). However, if the origins of ferroelectricity and magnetism are associated with different carriers, we should expect only a moderate magnetoelectric (ME) coupling (*9*). For instance, only a few examples exist of ME coupling at room temperature (*6*, *10*, *11*). In contrast, large ME coupling has been found in strain-mediated multiphase materials, such as composites or multilayers, by combining piezoelectricity with the magnetostrictive effect (*3*).

Molecular materials exhibit numerous advantages over inorganic ones, such as structural diversity, soft chemistry routes, environmentally friendly processing and shaping, optical transparency, and light density (*12*). For these reasons, molecular ferroelectrics (*13*, *14*) are often considered an alternative to traditional metal oxides (*15*, *16*). Although most molecular materials exhibit a magnetic ordering temperature below room temperature, important ME coupling may be expected from the association of paramagnetism and ferroelectricity (fig. S1) (*7*), as both these properties could involve the same chemical element. Although ME coupling in nonferroelectric molecular materials has been reported (*17*, *18*), the interaction between magnetism and ferroelectricity has not been extensively studied (*19*–*26*). For the few examples that exist, the ferroelectric ordering temperatures are typically lower than room temperature. Moreover, the modification of the polarization or magnetization by applying magnetic or electric fields, respectively—which also remains challenging in pure inorganic materials—requires a large magnitude operating field (*27*).

We designed a chiral lanthanide complex exhibiting an above–room temperature ferroelectricity that, in association with a strong magnetostriction, gives rise to a distinctive ME coupling. This allowed tuning of the ferroelectric domains at the nanometric scale by applying a relatively low magnetic field at room temperature. Our molecular approach to designing ME materials relied on the association of paramagnetic lanthanide ions, such as Yb^{3+}, with a chiral diamagnetic zinc complex in order to favor the crystallization in 1 of the 10 polar point groups compatible with ferroelectricity. We chose the Yb^{3+} ion because it has a large total magnetic moment, which, being oriented along a magnetic field, can provide an anisotropic magnetostriction underlying the coupling between magnetic and structural subsystems.

The stoichiometric reaction of *R*,*R*-H_2L [6,6'-((1E,1'E)-(((1R,2R)-1,2-diphenylethane-1,2-diyl)bis(azaneylylidene))bis(methaneylylidene))bis(2-methoxyphenol)] or *S*,*S*-H_2L [6,6'-((1E,1'E)-(((1S,2S)-1,2-diphenylethane-1,2-diyl)bis(azaneylylidene))bis(methaneylylidene))bis(2-methoxyphenol)], $Zn(OAc)_2{\cdot}2H_2O$, and $Yb(NO_3)_3{\cdot}5H_2O$ in methanol yielded to a yellow solution, which, upon slow diffusion of diethylether, resulted in the crystallization of *R*,*R*-[Zn(OAc)(L)Yb$(NO_3)_2$] (*R*,*R*-**1**) or *S*,*S*-[Zn(OAc)(L)Yb$(NO_3)_2$] (*S*,*S*-**2**). Using single

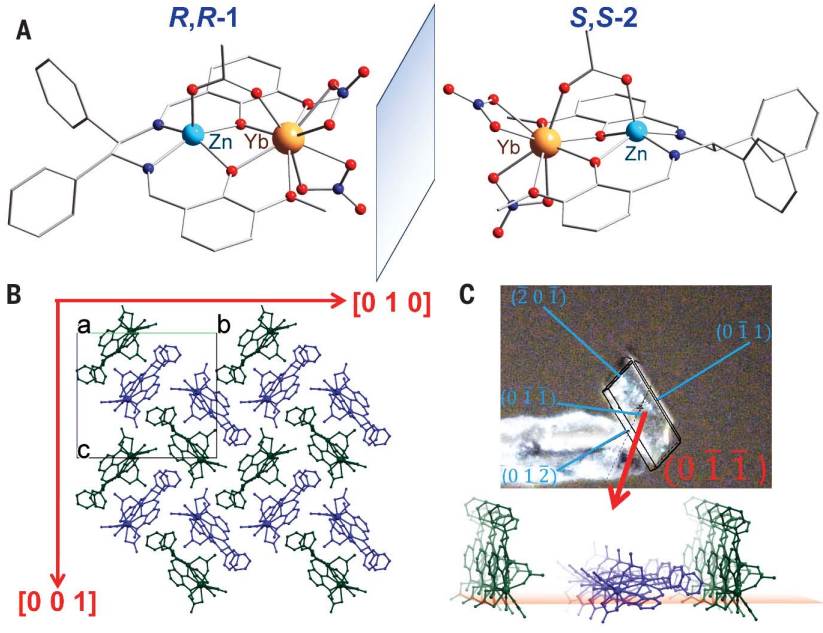

Fig. 1. Crystal structures of *R*,*R*-1 and *S*,*S*-2. (**A**) Molecular structure of the dinuclear Zn^{2+}-Yb^{3+} complexes *R*,*R*-**1** and *S*,*S*-**2** and their enantiomeric relationship. Orange, Yb^{3+}; light blue, Zn^{2+}; blue, N; red, O; gray, C. Hydrogen atoms have been omitted for clarity. (**B**) View of the crystal packing arrangement of *R*,*R*-**1** along the *a* axis, emphasizing the two homochiral complexes. (**C**) Single-crystal facets assignment and view of the slice in the crystallographic $(0\bar{1}\bar{1})$ plane.

[1]Institut Charles Gerhardt Montpellier, UMR 5253, Université de Montpellier, ENSCM, CNRS, Place E. Bataillon, 34095 Montpellier Cedex 5, France. [2]CFisUC, Department of Physics, University of Coimbra, 3004-516 Coimbra, Portugal. [3]Physics Department and CICECO–Aveiro Institute of Materials, University of Aveiro, 3810-193 Aveiro, Portugal. [4]Fédération de Recherche Chimie Balard–FR3105, Université de Montpellier, Place E. Bataillon, 34095 Montpellier Cedex 5, France.
*Corresponding author. Email: jerome.long@umontpellier.fr

crystal x-ray diffraction, we found that *R*,*R*-**1** and *S*,*S*-**2** are isostructural to the dysprosium analog (*28*). The two enantiomers crystallized in the polar space group $P2_1$ with two independent homochiral dinuclear complexes within the asymmetric unit (Fig. 1 and figs. S2 and S3). These two complexes exhibit differences in the crystallographic distances and geometries (tables S1 and S2) that give rise to uncompensated dipolar moments along the *b* axis. We confirmed this by analyzing the location of the ions in the unit cell (table S3) (*29*–*31*).

We corroborated the enantiomeric nature of *R*,*R*-**1** and *S*,*S*-**2** using solid-state circular dichroism (CD) (fig. S4), with the mirror-symmetrical CD spectra showing Cotton effects of opposite signs at maximum wavelengths (λ_{max}) of 261, 303, and 386 nm. The presence of the zinc complex also acted as a sensitizer toward lanthanide ions. Hence, the complexes *R*,*R*-**1** and *S*,*S*-**2** showed the typical Yb^{3+} luminescence in the 925- to 1075-nm near-infrared region at both room and low temperatures (figs. S5 to S11) (*32*).

We verified the absence of solvent molecules with thermogravimetric analysis, which also indicated that both enantiomers remain stable up to 550 K (fig. S12). We used single-crystal x-ray diffraction at 400 K and differential scanning calorimetry to confirm the absence of a phase transition up to the decomposition temperature (fig. S13). This demonstrated that the material remains crystallized in the $P2_1$ polar space group. We investigated the magnetic properties of *R*,*R*-**1** and *S*,*S*-**2** using SQUID (superconducting quantum interference device) magnetometry. We confirmed the paramagnetic behavior expected for a single Yb^{3+} ion with a $^2F_{7/2}$ ground state (total angular moment $J = 7/2$; orbital moment $L = 3$; spin moment $S = 1/2$) and a room-temperature magnetic moment close to 4.32 bohr magnetons (fig. S14). We also observed a typical slow relaxation of the magnetization at

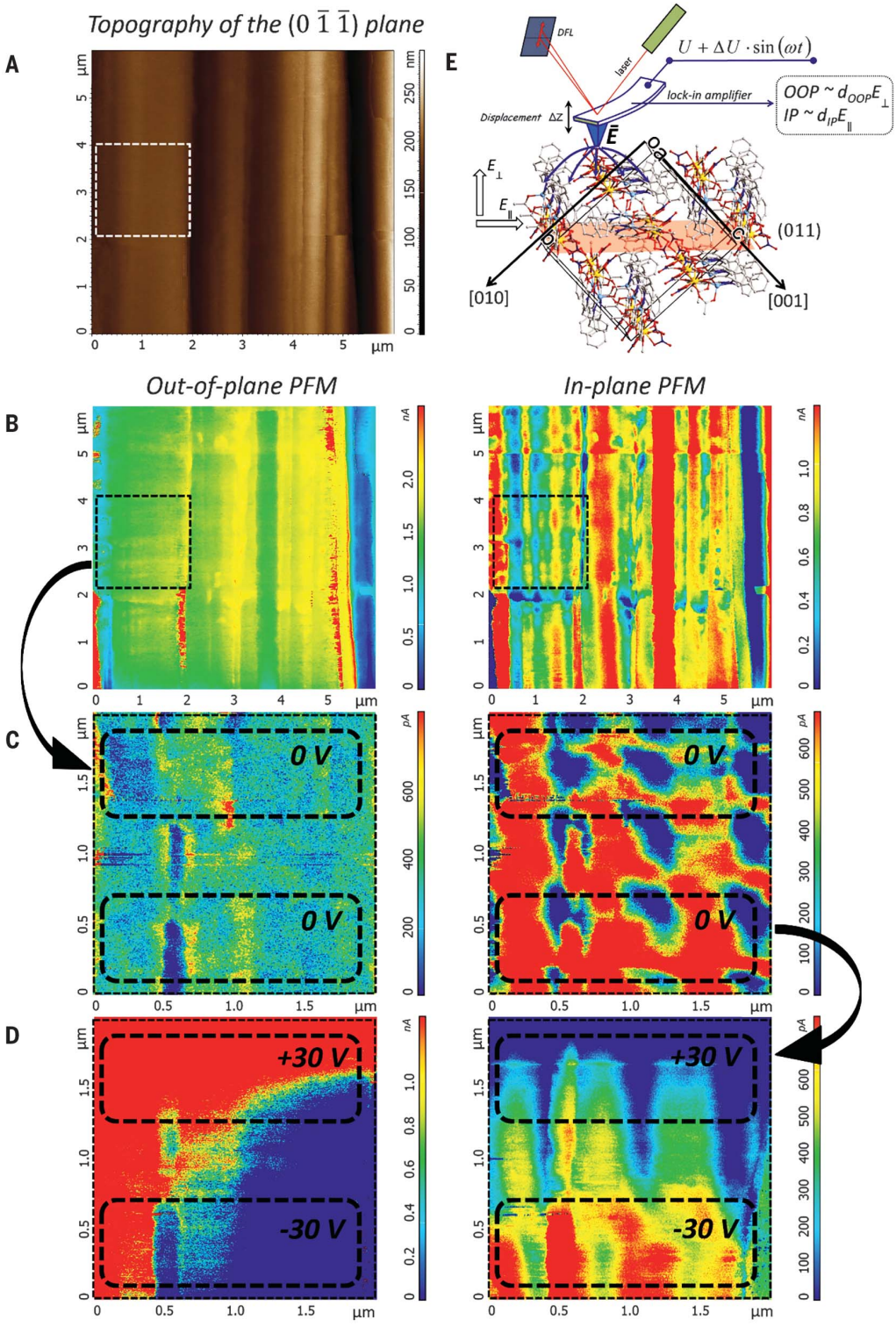

Fig. 2. Scanning probe microscopy (SPM) measurements of the (0$\bar{1}\bar{1}$)-oriented *R*,*R*-1 single crystal. (**A**) AFM topography of the (0$\bar{1}\bar{1}$) plane. (**B**) OOP (left) and IP (right) PFM responses without electrical bias. The color mapping reveals a distinctive organization demonstrating the presence of spontaneously polarized domains of opposite polarization states (shown in red and blue). (**C**) Magnified (×3) part of the scanned area [marked with a dashed square in (A) and (B)] with the OOP (left) and IP (right) PFM responses at 0 V. (**D**) OOP (left) and IP (right) PFM responses measured for the same area after the direct current (dc) bias voltage (±30 V) poling. (**E**) Schematic of the PFM experiment. DFL, deflection; *E*, electric field.

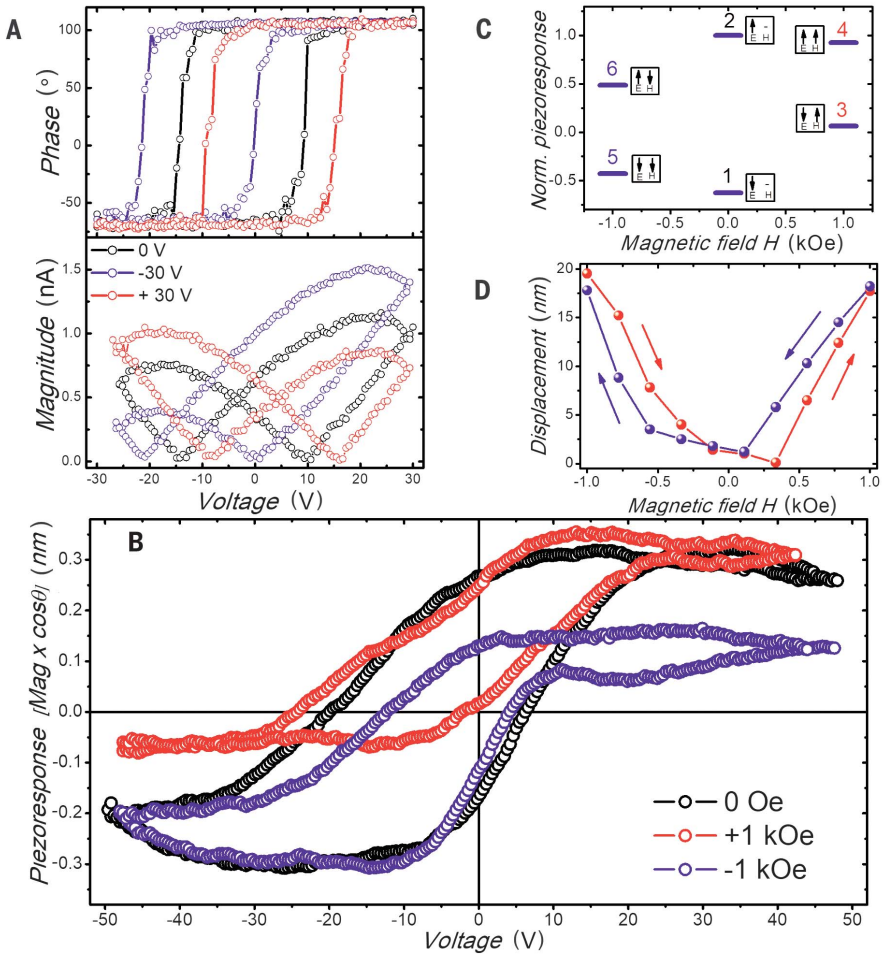

Fig. 3. SS-PFM hysteresis loops, multilevel states, and magnetostriction. (**A**) SS-PFM hysteresis loops obtained for the virgin (0 V) area and the areas polished by dc bias voltage (± 30 V): phase and displacement components as a function of the voltage. (**B**) SS-PFM hysteresis loops obtained at zero and under applied magnetic field of ±1 kOe. (**C**) Normalized piezoresponse as a function of the magnetic field enlightening the six remanent polarization states that could be actuated by applying magnetic and/or electric fields. (**D**) Magnetostriction measured on a single crystal of *R,R*-**1** at ±1 kOe (averaged on 5 loops). The lines are guides for the eye.

low temperature (figs. S15 to S20 and tables S4 to S6) (*32*).

Both enantiomers crystallized in the acentric space group $P2_1$, giving a 2 point group. We confirmed ferroelectric behavior of *R,R*-**1** (figs. S21 and S22) (*32*), which also applies to *S,S*-**2** because the ferroelectric properties of pairs of enantiomers are known to be identical (*33*, *34*). The absence of phase transition up to the decomposition of the material (550 K) indicates that the ferroelectric Curie point (T_c) will be located at a higher temperature, as observed in ferroelectrics such as $[(CH_3)_4N]HgCl_3$ and $[C(NH_2)_3][Al(H_2O)_6](SO_4)_2$ (*14*).

We carried out piezoresponse force microscopy (PFM) measurements to investigate the polar behavior and ME coupling (*32*, *35*). We measured the vertical and lateral responses, both of which consisted of amplitude and phase signals directly related to the magnitude of the polarization and to its orientation, respectively. This method provided sufficient spatial resolution for the detailed study of in-plane (IP; lateral PFM amplitude × phase) and out-of-plane (OOP; vertical PFM amplitude × phase) piezoelectric behavior at the nanoscale (*35*, *36*). Because additional contributions having ionic transport or electrostatic nature could affect the PFM signals, we carried out the measurements taking into account the protocol described by Vasudevan *et al.* (*37*) and Balke *et al.* (*38*) (figs. S23 and S24) (*32*). Hence, the PFM responses we observed reflected the polarization state of the material. We obtained a clear piezoresponse coming from several planes of *R,R*-**1** single crystal (fig. S25), but we detected the strongest simultaneous OOP and IP responses for the largest crystal facet accounting for the $(0\bar{1}\bar{1})$ plane (fig. S26). The atomic force microscopy (AFM) for the $(0\bar{1}\bar{1})$ plane reveals a stripe-like morphology (Fig. 2A). We found a peculiar organization in the OOP and IP PFM responses that demonstrated the presence of spontaneously polarized domains of opposite polarization states (shown in red and blue in Fig. 2B). Such striped organization was previously observed in other molecular or metal oxide ferroelectrics, such as $BiFeO_3$ (*35*, *39*–*41*). The crystal symmetry predicts that the ferroelectric domain structure visualized by the IP and OOP components of the piezoresponse must be consistent. However, the resulting PFM response depends on the azimuthal angle between the scanning direction and the polar axis and contains different tensile and shear piezoelectric strain components (as described in the "PFM Measurements" subsection of the supplementary materials). This situation is reminiscent of that observed in the benchmark molecular ferroelectric diisopropylammonium bromide (*40*). According to the initial work of Aizu (*42*), which was recently applied to molecular ferroelectrics (*13*, *43*, *44*), the number of polarization directions in the ferroelectric phase depends on the symmetry of the paraelectric phase. Although the structure of the paraelectric phase cannot be examined (T_c is higher than the decomposition temperature)—thus precluding the determination of the uniaxial or multiaxial character of the polarization—a clear correlation between the IP and OOP responses can be observed in some other PFM experiments (fig. S27).

We investigated the polarization switchability using direct current (dc) bias voltage of ±30 V applied to different areas (dashed rectangles in Fig. 2, C and D). In these areas, we achieved uniform (monodomain-like) polarization states, visible on both IP and OOP images (Fig. 2D). Taking advantage of the absence of a phase transition, we performed PFM measurements at 450 K (fig. S24) (*32*). We found a notable decrease in the electromechanical response, directly related to the polarization, which reflected the temperature-dependent behavior for a ferroelectric material. The switchable character of the electric polarization was further demonstrated by applying opposite dc bias to generate box-in-box patterns that showed clear 180° phase contrast and domain walls (fig. S28). Moreover, the piezoresponse hysteresis loops obtained by switching spectroscopy (SS)–PFM were found to exhibit a centered square-like shape with a 180° switching for the phase component (Fig. 3A). We also measured the typical butterfly loops of the displacement signal, which confirmed the ferroelectric character (*37*). Previously switched areas (±30 V) revealed a shift of the phase and amplitude component toward either positive or negative voltage, owing to the formation of coherent remnant polarization states that caused a strong depolarization

field (Fig. 3A). We determined a maximum local longitudinal piezoelectric coefficient d_{OOP} = 73 pm V^{-1} at room temperature, which corresponded to a polarization of the order of magnitude of 10 μC cm^{-2}. The theoretical spontaneous polarization that we estimated from the point charge model (*29*–*31*) along the *b* axis by considering only the metal ions and some atoms of the ligand (Zn^{2+}, Yb^{3+}, O^{-}, and N^{+}) gives 3.32 μC cm^{-2} along the $[0\bar{1}\bar{1}]$ direction (table S3) (*32*). We can rationalize this value, which was weaker than the experimental one, by pointing out the complexity of the structure. Also, we did not take into account the effect of additional molecular dipoles constituting the coordination complexes as well as covalency. Thus, the experimental value of the polarization could be positively compared with that of Rochelle salt (0.25 μC cm^{-2}) and was found in the same order of magnitude as the better-performing molecular ferroelectrics (*14*, *15*, *40*, *41*).

The ferroelectric character of *R*,*R*-**1** crystals suggests the possibility of a ME coupling at room temperature. We performed PFM measurements on the same single crystal in the presence of a dc magnetic field of ±1 kOe applied along the $(0\bar{1}\bar{1})$ plane. We observed the stripe-like morphology obtained by AFM (Fig. 4A). We found ferroelectric polarization redistribution with a low-magnitude magnetic field of ±1 kOe, similar to that produced by an electrical bias voltage (Fig. 4, B and C). The change of the polarization states and enhancement of the response make the effect easy to see. The ferroelectric domain's modification appears only in some parts of the region, as has been systematically observed in the rare examples of materials investigated by PFM (*27*, *45*–*47*). The typical magnitude of the magnetoelectric tensor component $\alpha_{31} = \frac{\Delta u}{d_{OOP}\Delta H D}$, where *D* is the thickness of the $(0\bar{1}\bar{1})$-oriented crystal and Δu is the change in vertical surface displacement induced by the change in lateral magnetic field ΔH, attains the order of 100 mV $Oe^{-1}{\cdot}cm^{-1}$. Although this value reflects the polarization change for a given magnetic field, it greatly exceeds (by at least one order of magnitude) those observed in the bulk $BiFeO_3$ multiferroics (ranging from 0.6 to 7 mV $Oe^{-1}{\cdot}cm^{-1}$) (*48*) and is comparable to those of ferroelectric and ferro(ferri)magnetic composites with strain-mediated ME coupling (*49*). Additional confirmation of the change in responses comes from our in situ PFM measurements performed on other crystal facets and with various magnetic fields (figs. S29 to S32) (*32*).

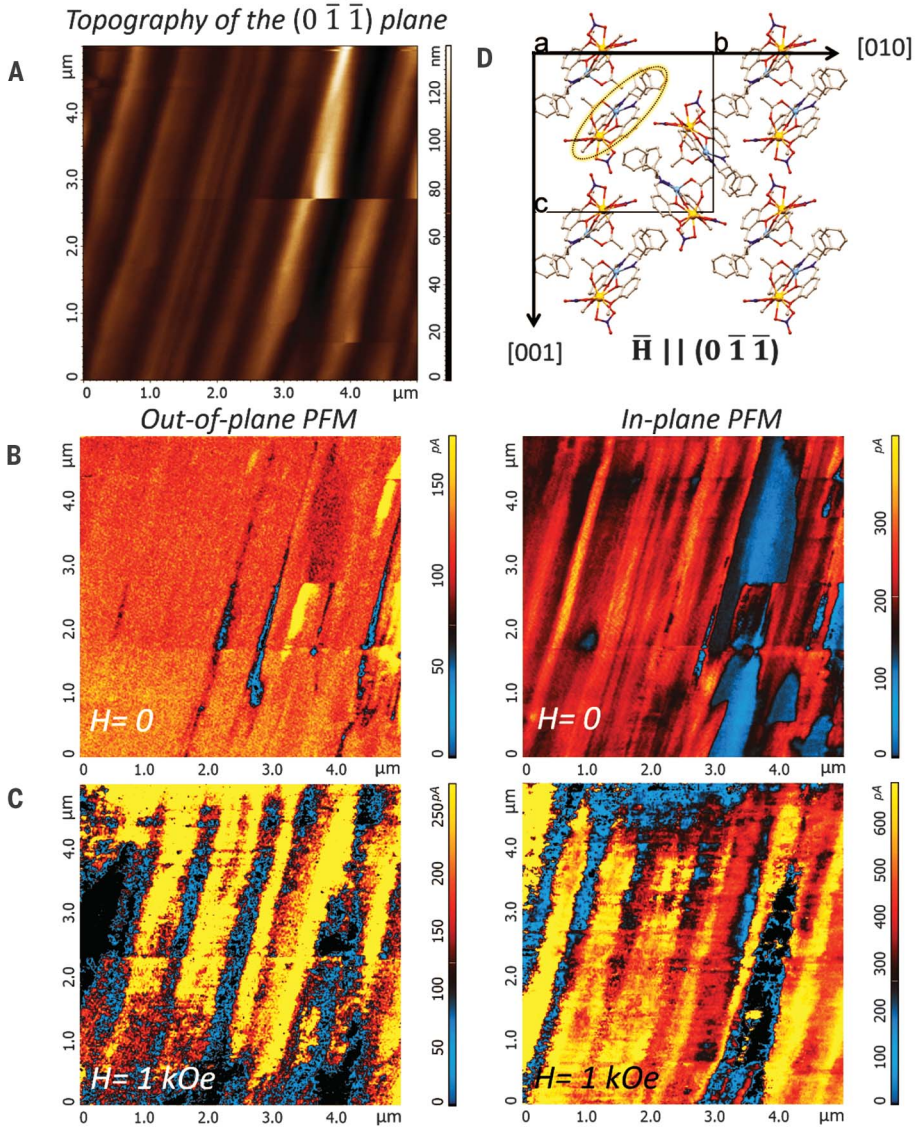

Fig. 4. Room-temperature PFM studies under magnetic field evidencing the ME coupling. (**A**) AFM topography of the $(0\bar{1}\bar{1})$ plane for *R*,*R*-**1**. (**B**) OOP and IP PFM responses at *H* = 0 Oe. (**C**) OOP and IP PFM responses at *H* = 1 kOe evidencing the ME coupling as redistribution in the ferroelectric domains (change in colors) and increase in the electromechanical response. (**D**) Sketch illustrating the possible deformation of the individual complex under an applied magnetic field.

We found additional evidence of the ME interaction in the SS-PFM local hysteresis loop measurements that we performed under dc magnetic field. These loops were strongly affected by a magnetic field, specifically in their asymmetry and height, as well as in the coercive fields (Fig. 3B). Taking advantage of this ME coupling, we actuated variable polarization states via the dc electric and magnetic fields (Fig. 3C). This feature may be suitable for multilevel polarization state devices designed for high-density data systems (*50*). Notably, this interaction occurs in the paramagnetic state at room temperature using a moderate magnetic field (1 kOe). The low magnetic field we used clearly contrasts with other molecule-based materials that required fields of several tesla to induce a change in the pyroelectric currents (*23*). Such room-temperature low-field switching is also quite rare in metal oxides (*11*, *26*, *27*).

The strong ME effect we observed is because the same chemical element, Yb^{3+}, is implicated in the two functionalities. Lanthanide ions present a larger spin-orbit coupling with respect to transition metal ions in classical inorganic magnetic ferroelectrics. Applying a magnetic field to a material containing anisotropic Yb^{3+} (nonzero orbital angular momentum, $L = 3$, spin-orbit coupling) should affect the crystal lattice producing magnetostriction. To confirm this, we investigated the magnetostriction, λ, at the microscopic and macroscopic levels. We measured the local surface displacement using contact AFM mode (no electric field applied) and evaluated it as a function of the applied magnetic field. We found a large room-temperature field-induced mechanical deformation (parastriction) (Fig. 3D). The displacement increased

with magnetic field and reached ~10^{-4} (1 kOe). The magnetostriction value we found was consistent with the macroscopic data we obtained from a single-crystal x-ray diffraction experiment we conducted under a magnetic field of ~0.8 kOe applied with a deviation angle of 10 ± 5° along the $[01\bar{1}]$ direction and yielding λ value of up to 1×10^{-3} (table S7) (*32*). We confirmed this effect on a different single crystal and by collecting three datasets to provide a statistical analysis (table S8). Reversing the direction of the magnetic field did not change the sign of the magnetostriction (table S7), which was fully consistent with the expected quadratic behavior. This large magnetostriction was comparable to those observed in ytterbium-based paramagnets. This phenomenon primarily had a single-ion character, and the related deformation can be equivalent in magnitude with that characteristic of magnetically long-range ordered systems (*51*). Notably, the association of magnetostriction and ferroelectricity engenders a pronounced ME coupling, as observed in inorganic multiphase ME materials (*3*).

Thus, we propose that the ME interaction in our Yb^{3+}-based ferroelectric complex originates from magnetoelastic coupling that corresponds to the magnetic field–induced deformation of the crystal lattice in the paramagnetic phase. Because *R*,*R*-**1** exhibited magnetostriction and ferroelectricity simultaneously, applying a magnetic field induced a mechanical strain via spin-lattice coupling that in turn influenced the polarization by affecting the overall dipole configuration. To support this, we made a comparative analysis of the crystal structures obtained under two directions of the magnetic field with respect to the zero-field one. Differences in the metal-ligand distances (tables S9 and S10) for both Yb^{3+} and Zn^{2+} ions could be discerned, which in turn affect the dipole order. Hence, the polarization values we calculated were found to be up to 10% greater or smaller (tables S3 and S11), depending on the orientation of the magnetic field, with respect to the zero-magnetic field value. Such results are in line with those obtained by PFM.

We have demonstrated room-temperature magnetoelectric control of ferroelectric domains in a molecule-based material. Thus, in the Yb^{3+}-based chiral compound *R*,*R*-**1**, the combination of ferroelectric behavior with a magnetostrictive effect generates a strong ME coupling we observed at room temperature and with a relatively low magnetic field. These properties are useful for practical device application, including nonvolatile memory where information would be stored as electrically detectable and controllable by Yb^{3+} paramagnetism. More generally, such features appear particularly distinctive in single-phase materials and confirm that the genuine chemical design of multifunctional molecular materials may provide an alternative strategy to usual solid-state compounds for engineering ME devices.

REFERENCES AND NOTES

1. S.-T. Han, Y. Zhou, V. A. L. Roy, *Adv. Mater.* **25**, 5425–5449 (2013).
2. S. Hong, O. Auciello, D. Wouters, *Emerging Non-Volatile Memories* (Springer, 2014).
3. W. Eerenstein, N. D. Mathur, J. F. Scott, *Nature* **442**, 759–765 (2006).
4. K. F. Wang, J. M. Liu, Z. F. Ren, *Adv. Phys.* **58**, 321–448 (2009).
5. J. F. Scott, *Nat. Mater.* **6**, 256–257 (2007).
6. P. Mandal *et al*., *Nature* **525**, 363–366 (2015).
7. M. Fiebig, T. Lottermoser, D. Meier, M. Trassin, *Nat. Rev. Mater.* **1**, 16046 (2016).
8. J. F. Scott, R. Blinc, *J. Phys. Condens. Matter* **23**, 113202 (2011).
9. S.-W. Cheong, M. Mostovoy, *Nat. Mater.* **6**, 13–20 (2007).
10. M. J. Pitcher *et al*., *Science* **347**, 420–424 (2015).
11. Y. Kitagawa *et al*., *Nat. Mater.* **9**, 797–802 (2010).
12. D. W. Bruce, D. O'Hare, R. I. Walton, Eds., *Molecular Materials* (Wiley, 2011).
13. T. Hang, W. Zhang, H.-Y. Ye, R.-G. Xiong, *Chem. Soc. Rev.* **40**, 3577–3598 (2011).
14. W. Zhang, R.-G. Xiong, *Chem. Rev.* **112**, 1163–1195 (2012).
15. S. Horiuchi *et al*., *Nature* **463**, 789–792 (2010).
16. S. Horiuchi, Y. Tokura, *Nat. Mater.* **7**, 357–366 (2008).
17. A. K. Boudalis, J. Robert, P. Turek, *Chemistry* **24**, 14896–14900 (2018).
18. M. Fittipaldi *et al*., *Nat. Mater.* **18**, 329–334 (2019).
19. P. Jain *et al*., *J. Am. Chem. Soc.* **131**, 13625–13627 (2009).
20. F. Kagawa, S. Horiuchi, M. Tokunaga, J. Fujioka, Y. Tokura, *Nat. Phys.* **6**, 169–172 (2010).
21. G.-C. Xu *et al*., *J. Am. Chem. Soc.* **133**, 14948–14951 (2011).
22. H.-L. Cai *et al*., *J. Am. Chem. Soc.* **134**, 18487–18490 (2012).
23. W. Wang *et al*., *Sci. Rep.* **3**, 2024 (2013).
24. J. Alberto Rodríguez-Velamazán *et al*., *Sci. Rep.* **5**, 14475 (2015).
25. M. Naka, S. Ishihara, *Sci. Rep.* **6**, 20781 (2016).
26. H. Ueda, T. Akita, Y. Uchida, T. Kimura, *Appl. Phys. Lett.* **111**, 262901 (2017).
27. D. M. Evans *et al*., *Nat. Commun.* **4**, 1534 (2013).
28. J. Long *et al*., *Angew. Chem. Int. Ed.* **54**, 2236–2240 (2015).
29. P.-F. Li *et al*., *Nat. Commun.* **7**, 13635 (2016).
30. Y.-M. You *et al*., *Nat. Commun.* **8**, 14934 (2017).
31. C.-K. Yang *et al*., *J. Am. Chem. Soc.* **141**, 1781–1787 (2019).
32. Materials and methods are available as supplementary materials.
33. X. L. Li *et al*., *Angew. Chem. Int. Ed.* **46**, 6820–6823 (2007).
34. Y. Sui *et al*., *Inorg. Chem.* **49**, 1286–1288 (2010).
35. E. Soergel, *J. Phys. D Appl. Phys.* **44**, 464003 (2011).
36. M. S. Ivanov *et al*., *Mater. Des.* **142**, 149–157 (2018).
37. R. K. Vasudevan, N. Balke, P. Maksymovych, S. Jesse, S. V. Kalinin, *Appl. Phys. Rev.* **4**, 021302 (2017).
38. N. Balke *et al*., *ACS Nano* **9**, 6484–6492 (2015).
39. Y.-M. You *et al*., *Science* **357**, 306–309 (2017).
40. D.-W. Fu *et al*., *Science* **339**, 425–428 (2013).
41. H.-Y. Ye *et al*., *Science* **361**, 151–155 (2018).
42. K. Aizu, *Phys. Rev. B* **2**, 754–772 (1970).
43. P.-P. Shi *et al*., *Chem. Soc. Rev.* **45**, 3811–3827 (2016).
44. Y.-Y. Tang *et al*., *J. Am. Chem. Soc.* **140**, 8051–8059 (2018).
45. S. Xie, F. Ma, Y. Liu, J. Li, *Nanoscale* **3**, 3152–3158 (2011).
46. H. Miao, X. Zhou, S. Dong, H. Luo, F. Li, *Nanoscale* **6**, 8515–8520 (2014).
47. L. F. Henrichs *et al*., *Adv. Funct. Mater.* **26**, 2111–2121 (2016).
48. J. M. Caicedo, J. A. Zapata, M. E. Gómez, P. Prieto, *J. Appl. Phys.* **103**, 07E306 (2008).
49. C. A. F. Vaz, J. Hoffman, C. H. Ahn, R. Ramesh, *Adv. Mater.* **22**, 2900–2918 (2010).
50. D. Lee *et al*., *Adv. Mater.* **24**, 402–406 (2012).
51. L. Bumagina, V. Krotov, B. Malkin, A. K. Khasanov, *Zh. Eksp. Teor. Fiz* **80**, 1543–1553 (1981).

ACKNOWLEDGMENTS

We thank J. Haines for fruitful discussions on crystallography. F. Salles is acknowledged for discussion on the point charge model. **Funding:** Financial support was provided by the University of Montpellier (UM), Centre National de la Recherche Scientifique (CNRS), Plateforme d'Analyze et de Caractérisation (PAC) et Institut Charles Gerhardt de Montpellier (ICGM), Fundação para a Ciência e a Tecnologia (FCT) Portugal (R&D project PDTC/QUI-QUI/098098/2008-FCOMP-01-0124-FEDER-010785), and NoE FAME. J.Lo. acknowledges the EMERGENCE@INC2019 funding. M.S.I. is grateful to FCT for financial support through the project MATIS–Materiais e Tecnologias Industriais Sustentáveis (CENTRO-01-0145-FEDER-000014). V.A.K. is grateful to FCT for financial support through the FCT Investigator Programme (project IF/00819/2014/CP1223/CT0011). This work was partly supported by funds from FEDER (Programa Operacional Factores de Competitividade COMPETE) and from FCT under the projects CICECO–Aveiro Institute of Materials (UIDB/50011/2020 and UIDP/50011/2020) and UID/FIS/04564/2019. Access to TAIL-UC facility funded under QREN-Mais Centro project ICT_2009_02_012_1890 is gratefully acknowledged as well. **Author contributions:** All authors contributed equally to this work. M.S.I. supervised, conceived of, and planned the SPM experiments. V.A.K. conducted the PFM and ME discussions. M.S.C.H. and J.A.P. performed the single-crystal XRD characterization. L.D.C. and R.A.S.F. measured the photoluminescence. B.D. resolved the crystal structures. E.M. and J.-M.T. performed the synthesis of the materials and standard characterizations. J.R. and M.B. measured the macroscopic dielectric and ferroelectric properties. D.G. and J.R. performed the single-crystal XRD characterization under magnetic field. J.La. and Y.G. provided critical feedback and helped with the analysis and writing process of the manuscript. J.Lo. conceived of the study, performed the magnetic characterization, and wrote the manuscript with input from all authors. **Competing interests:** All authors declare that they have no competing interests. **Data and materials availability:** All data are available in the main text or the supplementary materials.

SUPPLEMENTARY MATERIALS

science.sciencemag.org/content/367/6478/671/suppl/DC1
Materials and Methods
Figs. S1 to S32
Tables S1 to S11
References (*52*–*78*)
Crystallographic Information Files

3 September 2019; accepted 20 December 2019
10.1126/science.aaz2795

ORGANIC CHEMISTRY

Total synthesis of the complex taxane diterpene canataxpropellane

Fabian Schneider, Konstantin Samarin, Simone Zanella, Tanja Gaich*

Canataxpropellane belongs to the medicinally important taxane diterpene family. The most prominent congener, Taxol, is one of the most commonly used anticancer agent in clinics today. Canataxpropellane exhibits a taxane skeleton with three additional transannular C–C bonds, resulting in a total of six contiguous quaternary carbons, of which four are located on a cyclobutane ring. Unfortunately, isolation of canataxpropellane from natural sources is inefficient. Here, we report a total synthesis of (–)-canataxpropellane in 26 steps and 0.5% overall yield from a known intermediate corresponding to 29 steps from commercial material. The core structure of the (–)-canataxpropellane (2) was assembled in two steps using a Diels–Alder/*ortho*-alkene-arene photocycloaddition sequence. Enantioselectivity was introduced by designing chiral siloxanes to serve as auxiliaries in the Diels–Alder reaction.

Taxane diterpenes (*1*–*3*) are a medicinally vital family of natural products exhibiting potent anticancer activity (*4*–*6*) that were originally isolated from slow-growing evergreen shrubs in the genus *Taxus*, commonly known as yews. In 1994, major synthetic efforts (*7*–*15*) culminated in the first total syntheses of the most prominent anticancer drug, Taxol (**1**) (*4*–*6*) (Fig. 1A), by Holton (*7*, *8*) and Nicolaou (*9*), which turned out to be one of the top-selling anticancer drugs (peak sales in 1999 of 1.5 billion USD) over the past three decades (*16*). Ever since, different *Taxus* species have been screened for their constituents and >500 taxanes have been isolated to date [for a comprehensive review, see (*3*)]. Their structures are classified into 11 groups on the basis of their carbon ring systems (*3*). Among them, (–)-canataxpropellane (**2**) was isolated from *Taxus canadensis* (*17*) and represents a member of the complex taxane group (Fig. 1B). This highly oxygenated diterpene is one of the most intricate and complex natural products that has ever been isolated. As in the case of its sibling, Taxol, and other taxane diterpenes, it suffers from extremely inefficient sourcing from its natural producer, thus preventing biological and pharmaceutical investigations to this day.

(–)-Canataxpropellane (**2**) comprises a heptacyclic [5,5,5,4,6,6,6] carbon framework (Fig. 1C). It is densely functionalized and highly oxidized (five hydroxyl groups; one ketone), containing only two CH_2 groups. Among the features distinguishing the compound's structural complexity are the following: (i) it is the only natural product harboring two propellanes (*18*) simultaneously {see the colored portions of the structures in Fig. 1C **I** (a [3.3.2]-propellane) and **II** (a [4.4.2]-propellane)}; (ii) it contains 12 contiguous stereocenters (Fig. 1C **III**) including five quaternary centers, four of which reside in a cyclobutane ring (Fig. 1C **IV**); and (iii) except for two carbon atoms (6 and 14), its backbone consists exclusively of neopentylic motifs (Fig. 1C **IV**). The retrosynthetic analysis of (–)-canataxpropellane (**2**) (Fig. 2) required a completely different design than those in any of the previous works (*7*–*15*) because of the distinctive and intricate structural features displayed by (**2**). Our analysis leads to dialdehyde **3** by disconnecting cyclopentane A in **2** through a pinacol-coupling reaction between C9 and C10. Dialdehyde **3** could be obtained by functionalization of the B-ring in **4**, including introduction of the quaternary stereocenter at C8 and stereoselective hydroxylation of C5 (marked blue in **4**). Disconnection of the cyclobutane ring in **4** would give aromatic compound **5**. This disconnection represented by far the biggest synthetic challenge in this synthesis, requiring a transformation capable of not only closing a cyclobutane ring, but at the same time establishing four quaternary stereocenters (C3, C4, C11, and C12) at once. For this purpose, an alkene-arene-*ortho*-photocycloaddition (*19*, *20*) of aromatic compound **5** was designed. This transformation would furthermore accomplish dearomatization of ring B in photoprecursor **5**. Compound **5** could be efficiently disconnected using an intermolecular Diels–Alder reaction to give **6** and **7**. The starting materials **6** and **7** of this [4+2] cycloaddition are simple and easily accessible building blocks.

We devised a racemic and an enantiopure synthesis of (**2**). Both syntheses started from known lactone **8** (see Fig. 3) prepared on decagram scale in three steps (90% overall, no chromatographic purifications; see the materials and methods). Deprotonation of **8** and trapping with tert-butyl trimethylsilyl chloride (TBS-Cl) gave isobenzofuran diene **6** in situ, to which dieneophile **7** (prepared in three steps) was added to afford Diels–Alder adduct **5** in 71% yield with excellent diastereoselectivity (*endo*/*exo* = 100:1). This *endo*-selectivity was prerequisite for the application of the alkene-arene-*ortho*-photocycloaddition in the next step. The *cis* relation of the oxygen bridge and protons in the endo-Diels–Alder product (Fig. 3, blue) brings the olefin ring (C11–C12) and the aromatic ring (C3–C4) in close proximity, thus enabling the photoreaction. By contrast, in the minor *exo*-Diels–Alder product, the olefin and aromatic rings (Fig. 3, red) are blocked from reacting with each other in [2+2] fashion. Irradiation of **5**-(*endo*) (λ = 254 nm) in acetonitrile yielded 50% of the cage-like compound **4**. To push the photoequilibrium, **5** was separated from **4** and resubmitted to the photoreaction twice to give overall 73% of photoadduct **4**. The alkene-arene-*ortho*-photocycloaddition proved to be scalable and produced decagrams of the cage-like compound **4**. Photo-adduct **4** was thus accessed in only two steps (from known compounds **7** and **8**) and already contained the [4.4.2]-propellane, all four quaternary stereocenters of the cyclobutane, and the de-aromatized B-ring. The next task was a framework functionalization (Fig. 3), which first required opening of the lactol in **4**. However, after extensive experimentation, we were not able to selectively open the bridgehead lactol at the O–C20 bond (Fig. 3, blue) under any conditions. Instead, compound **4** exclusively underwent fragmentation of the C14–C20 bond (retro-aldol reaction; Fig. 3, red) when treated with tetrabutylammonium fluoride in THF to give keto-lactone **9**. At this tipping point in the synthesis, we realized that this unwanted fragmentation of C14–C20 was potentially capable of opening the tenacious O–C20 bond by translactonization. For this purpose, the keto-group in **9** was reduced with complete stereoselectivity to the corresponding alcohol at C13 by calcium borohydride [$Ca(BH_4)_2$•2THF] (*21*) in dichloromethane. Fortunately, this alcohol underwent the desired translactonization in situ to afford hydroxyl-lactone **10**, thus opening the critical O–C20 bond.

In addition to cleaving the bridgehead O–C20 bond, this transformation also served to differentiate the C2 alcohol, which was subsequently protected with methoxymethylene chloride (MOMCl) to give compound **11** in 73% yield over three steps. Reduction of **11** with lithium aluminum hydride ($LiAlH_4$), followed by Swern oxidation, yielded *bis*-carbonyl **12**. When **12** was subjected to basic conditions (KO*t*Bu; 5:1 THF:*t*BuOH), an intramolecular aldol reaction reestablished the C14–C20 bond with complete diastereoselectivity and formed cage structure **13** in 53% isolated yields from **11**. Compound **13** was confirmed by single-crystal x-ray analysis to contain all functional groups and stereocenters of the cage motif correctly in place, matching canataxpropellane (**2**). With compound **13** in hand, we introduced

Department of Chemistry, University of Konstanz, 78467 Konstanz, Germany.
*Corresponding author. Email: tanja.gaich@uni-konstanz.de

the correct functionalization pattern to the B-ring (Fig. 3). This required hydroxylation of C5 and installation of the fifth quaternary stereocenter at C8. [4+2]-Photooxygenation of the diene system in the B-ring with singlet oxygen gave *endo*-peroxide **14** as a single diastereomer. The selectivity in the course of the [4+2] reaction from **13** to **14** originates from a preferred *exo*-attack (front face) of oxygen versus an *endo*-attack (back face), together with complete shielding of the *endo*-face by the Me-18-group (marked blue in **13**; Fig. 3). Cleavage of the *endo*-peroxide proved to be challenging: Kornblum–DeLaMare rearrangement (*22*) of the *endo*-peroxide resulted in poor yields even upon extensive screening of conditions, whereas reductive cleavage of the peroxide was accompanied by decomposition under a range of common conditions. After extensive experimentation, we found that treatment of **14** with 2,6-di-tert-butyl-4-methylphenol (BHT) reductively cleaved the *endo*-peroxide bond cleanly to yield 71% of hydroxyenone **15** (the proposed mechanism is discussed in the supplementary materials). Compound **15** required inversion of stereochemistry at C5 to match the configuration of the alcohol in canataxpropellane (**2**) at this position. For this purpose, selective allylic oxidation to the ketone at C5 was performed with 2-iodoxybenzoic acid (IBX) and subsequent directed reduction of this ketone with sodium triacetoxy borohydride [$NaBH(OAc)_3$] assisted by the neighboring hydroxyl group at C20 proceeded by intermediate **16** (Fig. 3) and established the correct configuration at C5 in compound **17**. However, additional 1,4-reduction of **16** to give **18** was observed under these conditions. In both compounds **17** and **18**, the stereocenter at C5 now matched the configuration in the natural product, as confirmed by single-crystal x-ray analysis of **17**. Compounds **17** and **18** were converged to **19** under the conditions described below (Fig. 4). Protection of the 1,3-diol of enone **17** as the benzylidene acetal followed by 1,4-reduction afforded **19** in 95% yield (Fig. 4). Ketone **18** was directly protected as the benzylidene acetal to afford **19**. Elaboration of the B-ring was accomplished by converting the ketone at C8 to the vinyl triflate with Comin's reagent (**A**) and subsequent palladium-catalyzed carboxymethylation, affording α,β-unsaturated ester **20** in 77% yield. Dissolving metal reduction with Mg in methanol gave the corresponding saturated ester, and subsequent α-alkyation with methyl iodide exclusively installed the desired configuration at the quaternary stereocenter of C8 to give **21** in 83% yield. The stereoselective introduction of this methyl group is attributed to an attack from the *exo*-side (see Fig. 3). Up to this point, 1 g of compound **21** was obtained based on 9 g of the dienone building block **7**. With the B-ring fully established, we turned our attention to the final C–C bond-forming event, pinacol coupling. Selectively forming the desired *trans*-pinacol (out of four possible diastereomers) while avoiding radical fragmentation of the cyclobutane system posed a substantial challenge. For this purpose, **21** was reduced with $LiAlH_4$ and the TBS group was removed with tetrabutylammonium fluoride to deliver diol **22**. Swern oxidation of **22** gave the corresponding dialdehyde. After extensive experimentation, we were pleased to find that the use of titanium tetrachloride ($TiCl_4$)/Zn (*23*) resulted in the formation of pinacol **23** as a single and desired

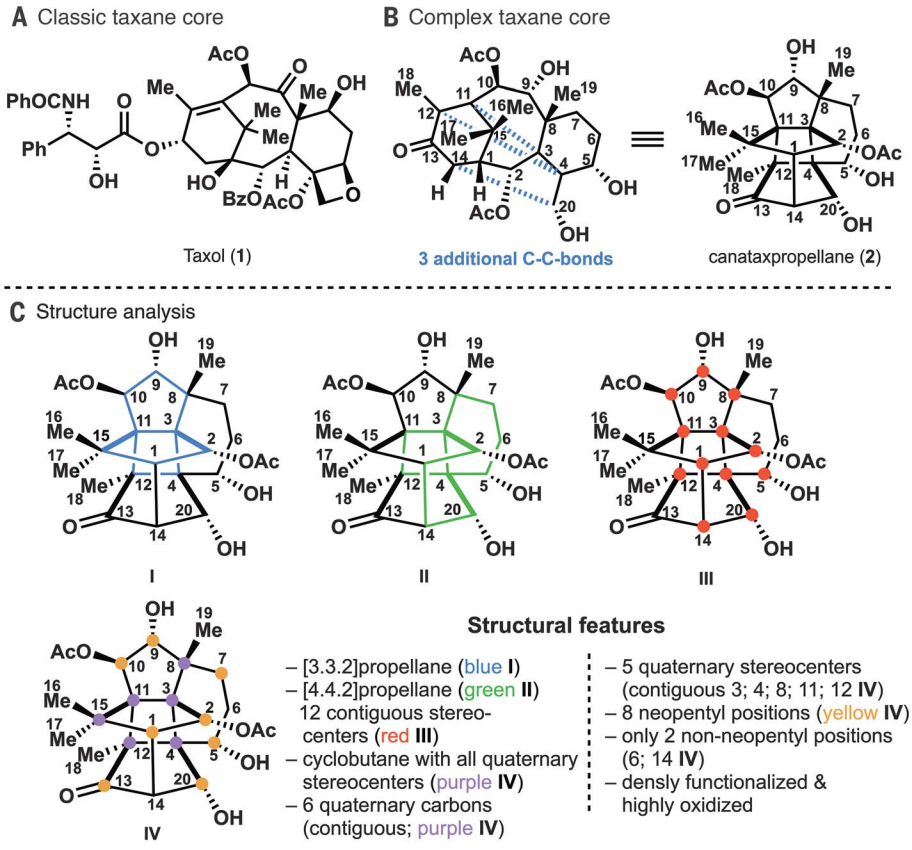

Fig. 1. Comparison of the Taxol core with the complex taxane core and key features of (–)-canataxpropellane (2).

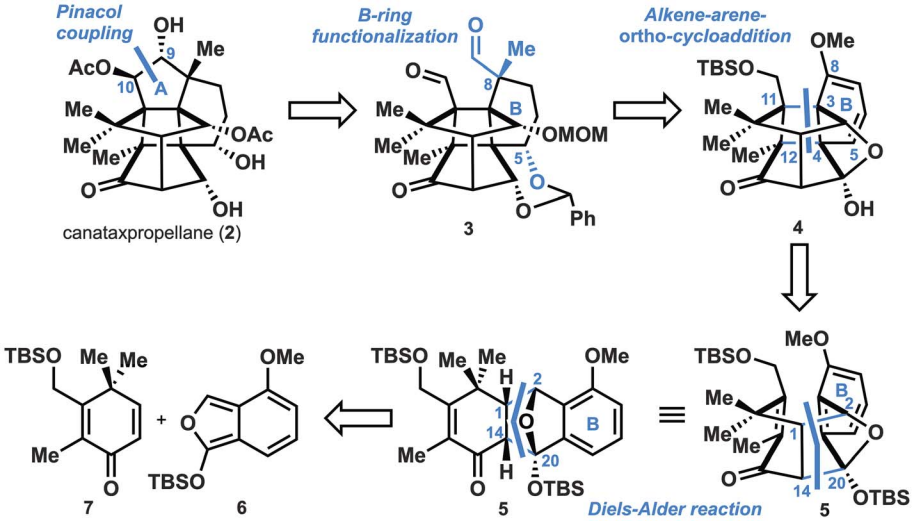

Fig. 2. Retrosynthetic analysis of (–)-canataxpropellane (2).

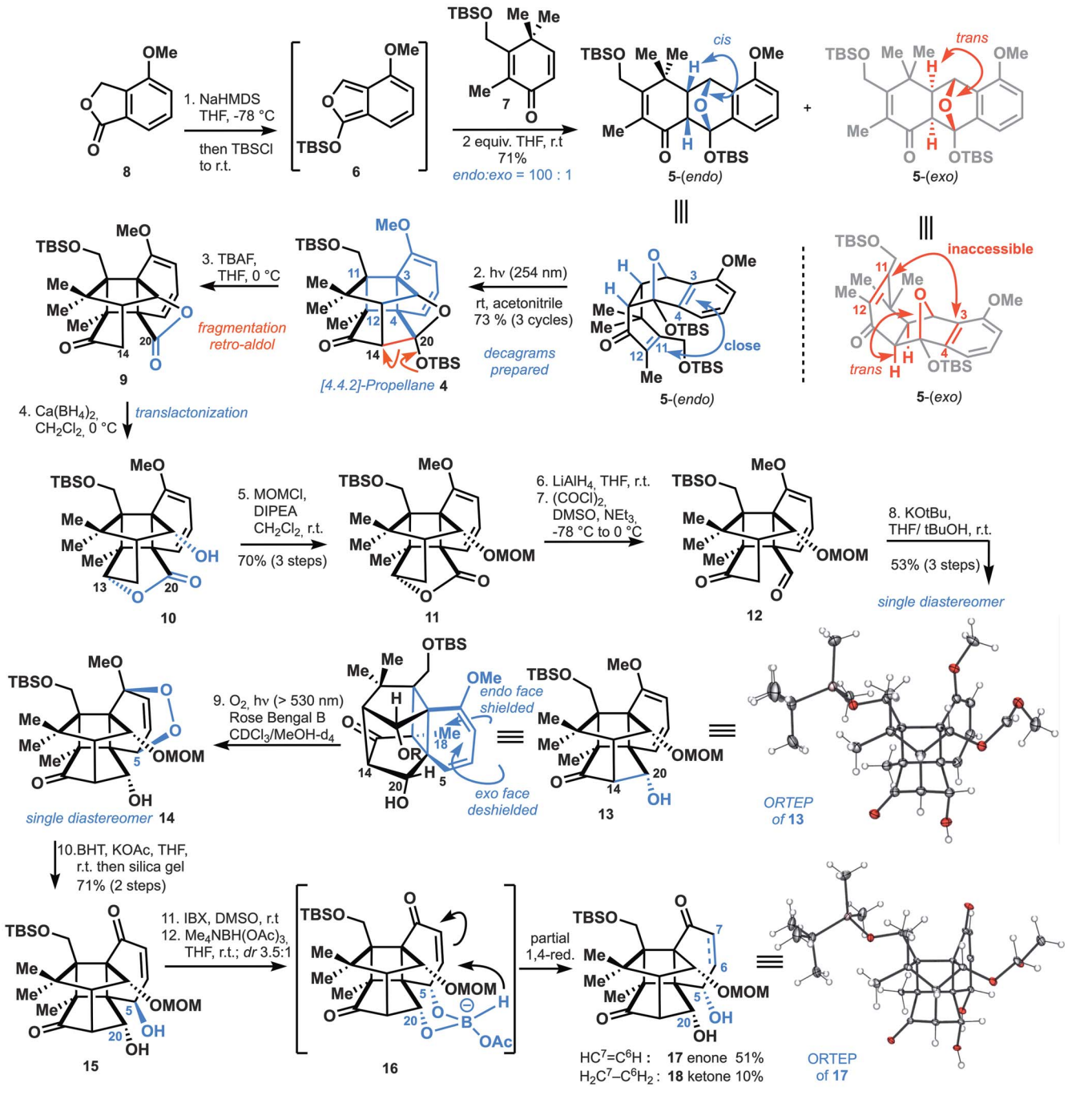

Fig. 3. Total synthesis of (−)-canataxpropellane (2) part I: Diels–Alder/ alkene-arene-ortho-photocycloaddition and photooxygenation. Reagents and conditions: 1. **8** 1.0 equivalents (equiv.), THF, −78°C, sodium hexamethyldisilazide (NaHMDS) (1.14 equiv.), then TBS-Cl (1.14 equiv.), to room temperature (r.t.), then **7** (2.0 equiv.), 71%. 2. hν (254 nm), r.t., acetonitrile 73%. 3. Tetrabutylammonium fluoride (1.05 equiv.), THF, 0°C. 4. $Ca(BH_4)_2$ (1.1 equiv.), 0°C, CH_2Cl_2. 5. MOMCl (5.0 equiv.), diisopropylethylamine (DIPEA) (5.0 equiv.), CH_2Cl_2 r.t. 70% (3 steps). 6. $LiAlH_4$ (3.0 equiv.), THF, 0°C. 7. Oxallylchloride (4.0 equiv.), dimethylsulfoxide (DMSO) (8.0 equiv.), trimethylamine (NEt_3) (12.0 equiv.), CH_2Cl_2, −78°C. 8. Potassium tert-butoxide (KOtBu) (1.2 equiv.), THF:tBuOH = 5:1, 53% (3 steps). 9. Rose Bengal (5 mol %), $CDCl_3$:MeOH-d_4 = 10:1, hν (>530 nm), then THF. 10. BHT (2.0 equiv.), potassium acetate (KOAc) (4.0 equiv.), 71%. 11. DMSO IBX (1.0 equiv.), r.t. 12. Acetonitrile (CH_3CN), AcOH (1 ml), $Me_4NHB(OAc)_3$ (3.0 equiv.), r.t.

trans-diastereomer (*24*). Single-crystal x-ray diffraction confirmed that pinacol **23** (0.2 g prepared) thus contained the [3.3.2]-propellane.

To complete the synthesis, we anticipated from our molecular models that the hydroxyl groups in **23** would rank from least sterically hindered at C10 to most hindered at C2. Therefore, we proceeded from pinacol product **23** with acetylation at both C10 and C9, followed by removal of the MOM group with bromocatechol borane to obtain alcohol **24** alongside triol **25** resulting from deprotection of the benzylidene acetal. Reprotection of **25** converged the synthetic material to **24**. Monodeprotection of the acetate at C9 proved feasible and delivered diol **26** in 67% yield. Selective acetylation of the hydroxyl group at C2 proceeded with 2.5:1 regioselectivity in

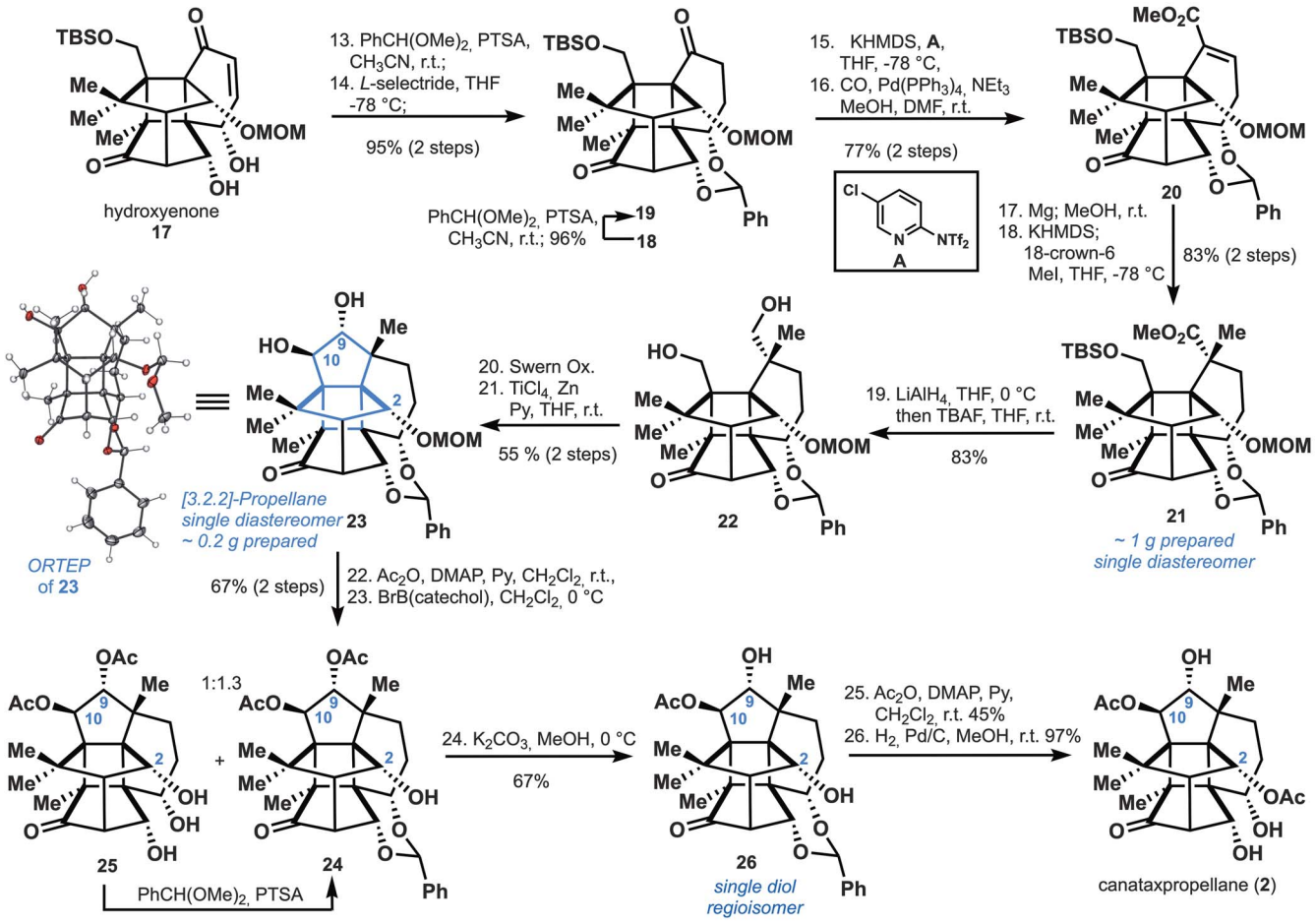

Fig. 4. Total synthesis of (–)-canataxpropellane (2) part II: B-ring elaboration, pinacol coupling, and end game to (2). Reagents and conditions: 13. Dimethoxybenzylidene [$PhCH(OMe)_2$] (5.0 equiv.), CH_3CN, para-toluenesulfonic acid (PTSA) (5 mol %), r.t., 96%. 14. Lithium tri-sec-butylborohydride (L-selectride) (1.1 equiv.), THF −78°C, 99%. 15. Potassium hexamethyldisilazide (KHMDS) (1.5 equiv.), Comin's reagent (A) (2.0 equiv.), −78°C, THF, 83%. 16. NEt_3 (3.0 equiv.), CO, palladium tetrakis triphenylphosphine [$Pd(PPh_3)_4$ (10 mol %)], *N*,*N*-dimethylformamide (DMF), MeOH, 89% r.t. 17. Magnesium turnings (Mg) (20.0 equiv.), MeOH, r.t., 88%. 18. KHMDS (1.5 equiv.), crown ether [18]-crown-6 (1.5 equiv.), THF −78°C, methyliodide (excess), 95%. 19. $LiAlH_4$ (2.0 equiv.), THF, 0°C, then tetrabutylammonium fluoride (TBAF) (1.5 equiv.), r.t., THF, 83%. 20. Oxalyl chloride (8.0 equiv.), DMSO (16.0 equiv.), NEt^3 (24.0 equiv.), CH_2Cl_2, −78°C. 21. $TiCl_4$ (20.0 equiv.), THF 0°C, zinc dust (Zn), (40.0 equiv.), pyridine (20.0 equiv.), 55%. 22. Pyridine, acetic anhydride (Ac_2O) (20.0 equiv.), *N*,*N*-dimethylaminopyridine (DMAP), (2,5 mol%), CH_2Cl_2, 79%. 23. 2-Bromo-1,3,2-benzodioxaborole [BrB(catechol)] (5.0 equiv.), CH_2Cl_2, 0°C, 56% and 44%. 24. MeOH r.t., potassium carbonate (K_2CO_3) (4.0 equiv.), 67%. 25. Pyridine, acetic anhydride (Ac_2O) (1.1 equiv.), DMAP, (2,5 mol %), 0°C, CH_2Cl_2, 45%. 26. Palladium on charcoal (Pd/C 10 wt %) (0.30 mol %), MeOH r.t., hydrogen (H_2), 97%.

favor of the desired and more reactive C2 position. Final hydrogenation of the benzylidene acetal delivered (±)-canataxpropellane (**2**). In the isolation report of (–)-canataxpropellane (**2**) from *T. canadensis* (*19*), an apparent conformational isomerism of the natural product, was described, with two compounds apparent in the ^{1}H-nuclear magnetic resonance (NMR) spectrum (major and minor). Our spectral data (^{1}H, ^{13}C, COSY, HSQC, HMBC, and NOESY) are in full accordance with the reported "major conformer" (see the supplementary materials) but we did not observe the second set of signals representing the "minor conformer." Given the rigidity of **2** and the fact that the dipropellane structure allows for very little conformational flexibility, we conclude that the second signal set observed in the isolation study likely corresponds to a naturally occurring, closely related derivative of (–)-canataxpropellane (**2**) that has yet to be identified. Having accomplished the racemic synthesis of the natural product, we performed its enantioselective synthesis. For this purpose, enantioselectivity needs to be introduced during the Diels–Alder reaction to product **5**. However, we found that **5** itself is extremely sensitive toward a wide range of Lewis and Brønsted acids even in catalytic amounts, leading to rapid degradation of the material. Therefore, many literature-reported methods of asymmetric Diels–Alder reactions, such as chiral Lewis acid catalysis (*25*) or iminium catalysis (*26*), were found to be impractical for our system. We therefore turned our attention toward chiral silyl chlorides to form a chiral isobenzofuran species as a chiral analog to **6** (Fig. 5). After screening a broad spectrum of chiral silyl groups, we found α,α,α′,α′-tetraaryl-1,3-dioxolan-4,5-dimethanol (TADDOL) (*27*)–based **27** to be the best choice, although the diastereoselectivity in the Diels–Alder reaction was modest (1.5:1 = **28:29**) for the desired stereoisomer **28**. The use of TADDOL **27** proved to be advantageous because the products **28** and **29** could be readily separated by column chromatography. Alkene-arene-*ortho*-photocycloaddition and retro-aldol reaction of **28** under the previously investigated conditions delivered the enantiopure intermediate (–)-**9**. The absolute configuration was assigned by determination of Flack

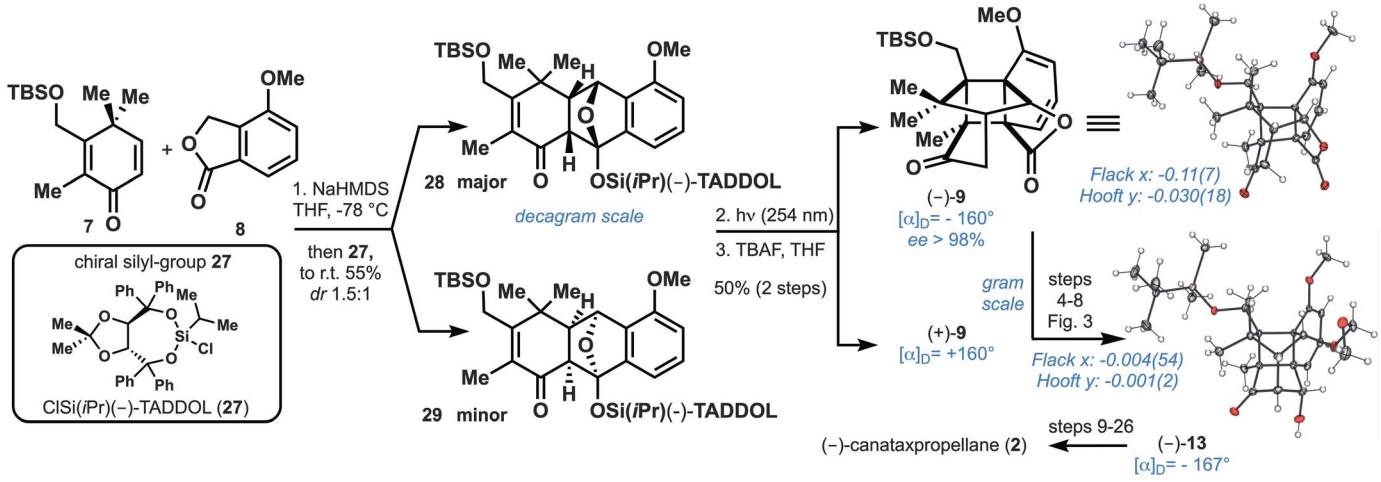

Fig. 5. Access to enantiopure key intermediate (−)-9 and (−)-13 for the enantiopure synthesis of (−)-(2).

factors on compounds (−)-**9** and (−)-**13** by Parsons' x-ray analysis (see the supplementary materials) (*28*). In addition, we determined the absolute configuration of (−)-**9** by circular dichroism (CD) spectroscopy and compared this with the simulated CD spectrum (see the supplementary materials). Both methods revealed that use of the (−)-TADDOL–based auxiliary gives the desired enantiomer (−)-**9** as the major product. With compound (−)-**13** in hand, we repeated the synthesis and obtained (−)-canataxpropellane (**2**). The optical rotation ($[\alpha]_D^{22}$ = −18.2) of our pure synthetic material was consistent with the literature ($[\alpha]_D^{22}$ = −39), the difference originating from the second species in the isolated material, as stated by the authors (*17*).

Our total synthesis of (−)-canataxpropellane (**2**) presents an efficient method for preparation of the complex taxane core on the multigram scale. The natural product itself was obtained in 0.5% yield. Our synthesis now renders (−)-canataxpropellane (**2**) available in amounts suitable for biological investigations, which have been hampered by the lack of materials. Our synthesis demonstrates the capability of photochemistry to rapidly assemble the most intricate and complex molecular scaffolds. We have furthermore demonstrated the robustness of our synthesis by carrying out 18 of 26 steps on decagram to gram scale. With enantiopure access to (−)-canataxpropellane (**2**), we established a previously unknown chiral siloxane as directing group Cl(*i*Pr)Si-TADDOL in the Diels–Alder reaction. The use of this chiral siloxane group was not only suitable on the multigram scale, but also enabled the facile separation of diastereomeric Diels–Alder products.

REFERENCES AND NOTES

1. E. Baloglu, D. G. I. Kingston, *J. Nat. Prod.* **62**, 1448–1472 (1999).
2. D. Schinzer, "Taxanes: An unusual class of natural products" in *Organic Synthesis Set*, H. Waldman, Ed. (Wiley, 2008), pp. 335–347.
3. Y.-F. Wang *et al.*, *Chem. Rev.* **111**, 7652–7709 (2011).
4. M. C. Wani, H. L. Taylor, M. E. Wall, P. Coggon, A. T. McPhail, *J. Am. Chem. Soc.* **93**, 2325–2327 (1971).
5. P. B. Schiff, J. Fant, S. B. Horwitz, *Nature* **277**, 665–667 (1979).
6. C. M. Spencer, D. Faulds, *Drugs* **48**, 794–847 (1994).
7. R. A. Holton *et al.*, *J. Am. Chem. Soc.* **116**, 1597–1598 (1994).
8. R. A. Holton *et al.*, *J. Am. Chem. Soc.* **116**, 1599–1600 (1994).
9. K. C. Nicolaou *et al.*, *Nature* **367**, 630–634 (1994).
10. S. J. Danishefsky *et al.*, *J. Am. Chem. Soc.* **118**, 2843–2859 (1996).
11. P. A. Wender *et al.*, *J. Am. Chem. Soc.* **119**, 2755–2756 (1997).
12. P. A. Wender *et al.*, *J. Am. Chem. Soc.* **119**, 2757–2758 (1997).
13. H. Kusama *et al.*, *J. Am. Chem. Soc.* **122**, 3811–3820 (2000).
14. T. Mukaiyama *et al.*, *Chemistry* **5**, 121–161 (1999).
15. A. Mendoza, Y. Ishihara, P. S. Baran, *Nat. Chem.* **4**, 21–25 (2011).
16. S. Malik *et al.*, *Process Biochem.* **46**, 23–34 (2011).
17. C.-H. Huo *et al.*, *Tetrahedron Lett.* **48**, 2721–2724 (2007).
18. A. M. Dilmaç, T. Wezeman, R. M. Bär, S. Bräse, *Nat. Prod. Rep.* (2019).
19. A. Gilbert, *Pure Appl. Chem.* **52**, 2669–2682 (1980).
20. For a review, see: R. Remy, C. G. Bochet, *Chem. Rev.* **116**, 9816–9849 (2016).
21. J. Kollonitsch, O. Fuchs, V. Gàbor, *Nature* **175**, 346 (1955).
22. N. Kornblum, H. E. DeLaMare, *J. Am. Chem. Soc.* **73**, 880–881 (1951).
23. T. Mukaiyama, T. Sato, J. Hanna, *Chem. Lett.* **2**, 1041–1044 (1973).
24. A. Chatterjee, N. N. Joshi, *Tetrahedron* **62**, 12137–12158 (2006).
25. K. Ishihara, A. Sakakura, "Intermolecular Diels–Alder reactions" in *Comprehensive Organic Synthesis II*, G. A. Molander, P. Knochel, Ed. (Elsevier, ed. 2, 2014), pp. 351–408.
26. P. Merino, E. Marqués-López, T. Tejero, R. P. Herrera, *Synthesis* **2010**, 1–26 (2010).
27. D. Seebach, A. K. Beck, R. Imwinkelzied, S. Roggo, A. Wonnacott, *Helv. Chim. Acta* **70**, 954–974 (1987).
28. S. Parsons, H. D. Flack, T. Wagner, *Acta Crystallogr. B Struct. Sci. Cryst. Eng. Mater.* **69**, 249–259 (2013).

ACKNOWLEDGMENTS

We thank Prof. Dr. R. W. Hoffmann from the University of Marburg (Germany) for continuous, very helpful, and interesting discussions during the project. We thank the NMR department of the University of Konstanz (A. Friemel and U. Haunz) for extensive analyses. We thank I. Göttker, M. Linseis, T. Huhn, and B. Weibert (Universität Konstanz) for x-ray analysis. **Funding:** Financial support was granted by the Landesgraduiertenförderung (LGFG stipend) by the state of Baden-Württemberg, Germany, and by the Georg Christoph Lichtenberg Stipendium by the state of Lower Saxony, Germany. **Author contributions:** F.S., K.S., and S.Z. contributed with experimental work and intellectual input; T.G. contributed with project planning/managing and intellectual input. **Competing interests:** The authors declare no competing interests. **Data and materials availability:** The x-ray data for compounds (−)-**13**, (−)-**9**, (±)-**13**, **17**, and **23** have been deposited at the Cambridge database and are available free of charge under CCDC numbers 1966216 for (−)-**13**, 1966215 for (−)-**9**, 1966212 for (±)-**13**, 1966213 for **17**, and 1966214 for **23**.

SUPPLEMENTARY MATERIALS

science.sciencemag.org/content/367/6478/676/suppl/DC1
Materials and Methods
Figs. S1 to S7
Tables S1 to S7
References (*29–45*)

29 July 2019; accepted 14 January 2020
10.1126/science.aay9173

MOSQUITO BIOLOGY

Mosquito heat seeking is driven by an ancestral cooling receptor

Chloe Greppi[1]*, Willem J. Laursen[1]*, Gonzalo Budelli[1], Elaine C. Chang[1], Abigail M. Daniels[1], Lena van Giesen[1], Andrea L. Smidler[2,3], Flaminia Catteruccia[2], Paul A. Garrity[1]†

Mosquitoes transmit pathogens that kill >700,000 people annually. These insects use body heat to locate and feed on warm-blooded hosts, but the molecular basis of such behavior is unknown. Here, we identify ionotropic receptor IR21a, a receptor conserved throughout insects, as a key mediator of heat seeking in the malaria vector *Anopheles gambiae*. Although *Ir21a* mediates heat avoidance in *Drosophila*, we find it drives heat seeking and heat-stimulated blood feeding in *Anopheles*. At a cellular level, *Ir21a* is essential for the detection of cooling, suggesting that during evolution mosquito heat seeking relied on cooling-mediated repulsion. Our data indicate that the evolution of blood feeding in *Anopheles* involves repurposing an ancestral thermoreceptor from non–blood-feeding Diptera.

Insect-borne diseases kill over 700,000 people annually, with >400,000 deaths resulting from malaria, a disease caused by protozoan *Plasmodium* spp. parasites that are transmitted by blood-feeding anopheline mosquitoes (*1*). Host seeking by mosquitoes and other pathogen-spreading insects relies on the detection of host-associated cues, including carbon dioxide (CO_2), odors, and body heat (*2*–*5*). Receptors for CO_2 and host odors have been characterized in mosquitoes (*6*–*9*), but receptors that promote heat seeking and heat-induced blood feeding have remained elusive (*4*, *10*–*12*). As vector mosquitoes are descendants of non–blood-feeding ancestors (*13*), it remains unknown whether the emergence of heat seeking and warming-induced blood feeding in mosquitoes involved the generation of novel thermoreceptors or the repurposing of existing thermoreceptors.

To date, mosquito orthologs of two *Drosophila* warmth receptors, TRPA1 (*14*) and GR28b (*15*), have been tested as candidate heat-seeking receptors in the yellow fever mosquito *Aedes aegypti* (*10*–*12*). However, neither is required for heat seeking in *Aedes* (*12*). Rather, TRPA1 promotes heat avoidance in both *Aedes* and *Drosophila* (*12*, *14*). Although efforts have focused on warmth receptors, insects also possess cooling-activated receptors, which should be equally capable of supporting heat seeking through cooling-mediated repulsion. In *Drosophila,* cooling detection is mediated by IR21a, IR25a, and IR93a (*16*–*18*), three members of the ionotropic receptor (IR) family, a group of invertebrate-specific sensory receptors related to ionotropic glutamate receptors (*19*). IR21a is specifically required for cooling detection in the fly and can confer cooling sensitivity when ectopically expressed (*16*, *18*), while IR25a and IR93a are more broadly acting co-receptors that support cooling detection and other IR-dependent sensory modalities (*17*, *19*, *20*). At the behavioral level in *Drosophila*, IR21a, IR25a, and IR93a help the fly achieve optimal body temperatures by supporting avoidance of excessively cool and warm temperatures (*16*, *18*). Beyond *Drosophila*, IR21a, Ir25a, and IR93a are each widely conserved from Diptera (flies and mosquitoes) to Isoptera (termites) (*19*), raising the possibility that their thermosensory functions may also be conserved. Using *Anopheles gambiae*, a major vector of malaria in sub-Saharan Africa, we first tested whether IR21a is required for detecting cooling in mosquitoes and subsequently whether it can drive heat attraction and heat-stimulated blood feeding.

Two mutant alleles of *A. gambiae Ir21a* were generated using CRISPR-Cas9 (see methods). $Ir21a^{+7bp}$ contains a 7-base pair (bp) insertion, introducing a frameshift positioned to disrupt IR21a's translation within the second of IR21a's three transmembrane domains; this lesion is predicted to generate a nonfunctional receptor (Fig. 1A). In $Ir21a^{EYFP}$, a disruption cassette containing an enhanced yellow fluorescent protein (EYFP) marker, was inserted into IR21a's fourth exon, a lesion also predicted to create a nonfunctional receptor (Fig. 1B). Both mutants lacked detectable IR21a protein expression (Fig. 1, C to E, and fig. S1), consistent with their acting as *Ir21a* null mutations.

Genome-wide analyses of *A. gambiae* sensory tissues suggest that *Ir21a* RNA is specifically expressed in the antenna (*21*). To visualize IR21a protein expression and localization with cellular resolution, anti-IR21a antisera were generated. The antenna's most distal segment (flagellomere 13) contains three coeloconic sensilla that house sensitive thermoreceptors (*22*–*24*) (Fig. 1C). In females, IR21a expression was detected in three sensory neurons in flagellomere 13, one innervating each of the coeloconic sensilla (Fig. 1D). Consistent with a role in thermosensory transduction, IR21a strongly localized to the sensory ending of each of these neurons (Fig. 1D). IR21a immunostaining was absent in *Ir21a* mutants, confirming antisera specificity (Fig. 1E and fig. S1A). The male antennal tip also contains thermoreceptors (*23*), and IR21a expression was detected in sensory endings there as well (fig. S1B).

Extracellular recordings were performed from the IR21a-positive coeloconic sensilla at the antennal tip (Fig. 2A). In wild-type mosquitoes, the activity of the Cooling Cell, a thermosensory neuron stimulated by cooling and inhibited by warming, was readily detected (Fig. 2B). On rare occasions of exceptional signal to noise, a smaller-amplitude spike was also detected, corresponding to a Heating Cell activated by warming and inhibited by cooling (fig. S2). Cooling Cell responses were highly thermosensitive: an ~0.5°C drop from ~30°C increased spiking by ~40%, and an ~0.5°C drop from ~37°C increased spiking by ~80% (Fig. 2C). Response adaptation initiated rapidly, followed by a slower decline to baseline (Fig. 2C and fig. S3). Heating inhibited spiking, in a similarly transient manner (Fig. 2C). Importantly, Cooling Cells remained highly active at warm temperatures (e.g., 37°C) and were neither more active nor more thermosensitive at colder temperatures (Fig. 2, C and D). Thus, while often referred to as Cold Cells in the classical literature, cooling and not cold is their activating stimulus. In addition, while often referred to as "phasic-tonic" receptors, their responses to temperature shifts adapted fully, albeit slowly, requiring sustained observation (>20 s) to fully appreciate (fig. S3). Therefore, although they fire robustly at constant temperature, Cooling Cells are phasic thermoreceptors. Their rate of baseline firing was relatively temperature insensitive with a fold change upon 10°C increase [Q10 of ~1.6, reflecting a slight increase with warmth], enabling the cell to respond to small temperature fluctuations over a wide range of absolute temperatures. [Physiologically similar Cooling and Heating Cells have been described in *A. aegypti* (*22*, *24*) and *Drosophila melanogaster* (*18*).] Taken together, these data indicate that Cooling Cells are phasic thermoreceptors that respond to temperature change rather than absolute temperature and that they are capable of responding to abrupt changes in temperature over the wide range of absolute temperatures relevant for host seeking (Fig. 2, C and D).

Cooling Cell thermosensitivity was eliminated in *A. gambiae Ir21a* mutants. The large-amplitude spike detected in *Ir21a* mutants was neither activated by cooling nor inhibited by warming (Fig. 2, B to D). Rather, its activity increased slightly upon warming, with a Q10

[1]Department of Biology and Volen Center for Complex Systems, Brandeis University, Waltham, MA 02453, USA. [2]Department of Immunology and Infectious Diseases, Harvard T. H. Chan School of Public Health, Boston, MA 02115, USA. [3]Wyss Institute for Biologically Inspired Engineering, Boston, MA 02115, USA.
*These authors contributed equally to this work.
†Corresponding author. Email: pgarrity@brandeis.edu

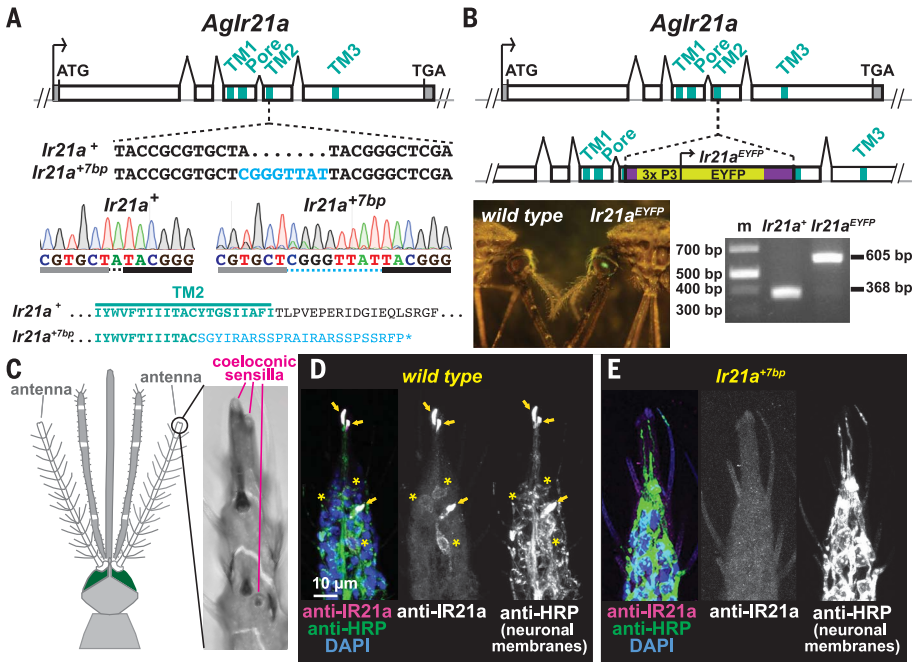

Fig. 1. IR21a is expressed in the antennal tip. (**A**, upper) *Ir21a* locus, with *Ir21a*$^{+7bp}$ mutations shown in blue. (Lower) Virtual translations, with 450 C-terminal amino acids of wild-type IR21a replaced by 24 novel amino acids (blue) and a premature stop in *Ir21a*$^{+7bp}$. (**B**) Targeted integration generating *Ir21a*^{EYFP}, a combined bright-field and fluorescent illumination image, and molecular genotyping results for *Ir21a*$^{+}$ and *Ir21a*^{EYFP} homozygotes. Lane m, DNA size markers. (**C**) Mosquito anterior [drawing based on (*27*)]. Inset, flagellomere 13. (**D** and **E**) Immunostaining of flagellomere 13 in wild-type (D) and *Ir21a*$^{+7bp}$ (E) females. (n = 13 wild type; n = 7 *Ir21a*$^{+7bp}$). Asterisks, IR21a-expressing cell bodies; arrows, sensory endings. HRP, horseradish peroxidase; DAPI, 4′,6-diamidino-2-phenylindole. Anti-HRP labels neuronal membrane proteins, and DAPI labels nuclei.

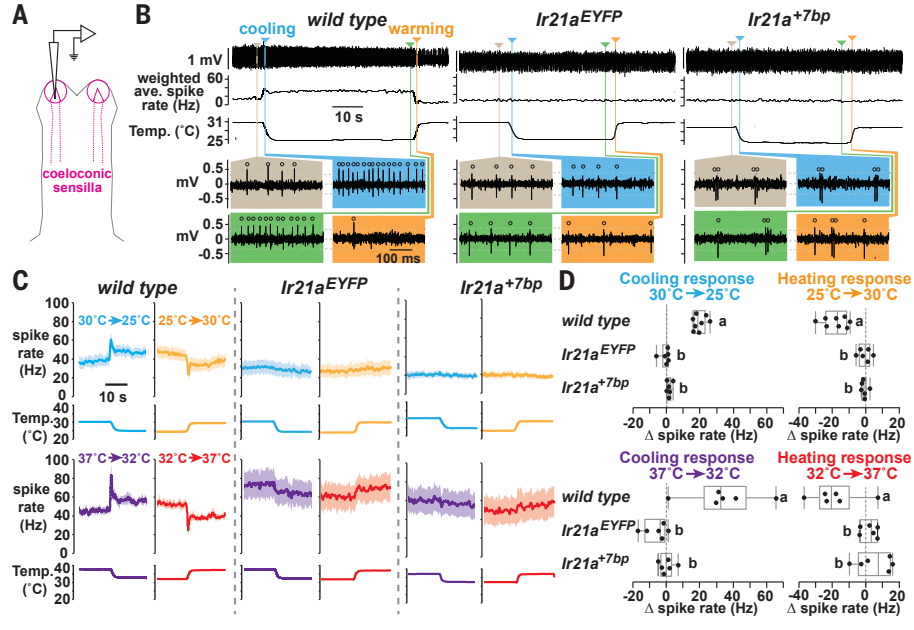

Fig. 2. *Ir21a* is required for thermosensing. (**A**) Recording electrode insertion site. (**B**) Representative recordings, with indicated regions displayed on an expanded time scale. Circles, spikes. The weighted average spike rate is the instantaneous spike frequency smoothed using a 1-s triangular window. Dotted lines, spike thresholds. (**C**) Peri-stimulus time histograms (averages ± SEM) for wild type (n = 8) and *Ir21a*^{EYFP} and *Ir21a*$^{+7bp}$ (n = 6) animals tested at 30°C and 25°C. One heating-cooling trial per animal. (**D**) Cooling response = (average frequency 0.2 to 0.7 s after cooling onset) − (average frequency 5 to 10 s precooling). Heating response = (average frequency 0.5 to 1.5 s after heating onset) − (average frequency 5 to 10 s preheating). Lowercase letters indicate distinct groups (Tukey's honest significant difference, α = 0.01, except 32°C→37°C, α = 0.05). Shapiro-Wilk test and analysis of variance values are provided in the statistics section of methods.

under 2, which is average for a biological process. Thus, *Ir21a* is essential for thermosensing by Cooling Cells in the mosquito, demonstrating that *A. gambiae* IR21a's molecular function is conserved with its *Drosophila* ortholog (*18*).

In female mosquitoes, heat seeking is part of a multimodal host-seeking program activated upon exposure to CO_2, with body heat serving as an important cue close to the host (within ~10 to 15 cm) (*3*, *8*, *12*). To assess heat seeking, female mosquitoes were provided a 20-s puff of 4% CO_2 and exposed to two targets, a control target at ambient temperature (~26°C) and a heated target at ~37°C (Fig. 3, A and B, and fig. S4A). Wild-type mosquitoes exhibited robust heat seeking, with 43 ± 3% of CO_2-activated mosquitoes landing on the 37°C target (average ± SEM) (Fig. 3, C and F; movie S1; and fig. S4B). The loss of *Ir21a* greatly reduced this behavior, with only 15 ± 4% of *Ir21a*^{EYFP} mutants and 14 ± 4% of *Ir21a*$^{+7bp}$ mutants landing on the 37°C target (Fig. 3, D to F; movie S2; and fig. S4B). In all cases, the control target was largely ignored, confirming temperature's importance in the assay (Fig. 3, C to F). While heat seeking was greatly reduced in *Ir21a* mutants, it was not entirely eliminated (Fig. 3, D to F). This residual activity likely reflects signaling from other as-yet-uncharacterized thermosensors. However, the strong reduction of heat seeking in *Ir21a* mutants (Fig. 3G) identifies this receptor as a major driver of mosquito attraction to warmth.

To test the specificity of the *Ir21a* mutant behavioral deficit for heat seeking, we examined their ability to perform an activation-dependent behavior less reliant on thermosensation. While body heat is a powerful short-range cue, a multimodal combination of longer-range chemosensory and visual cues mediates initial approach (*3*), suggesting that such behavior should be largely unaffected by a specific thermosensory

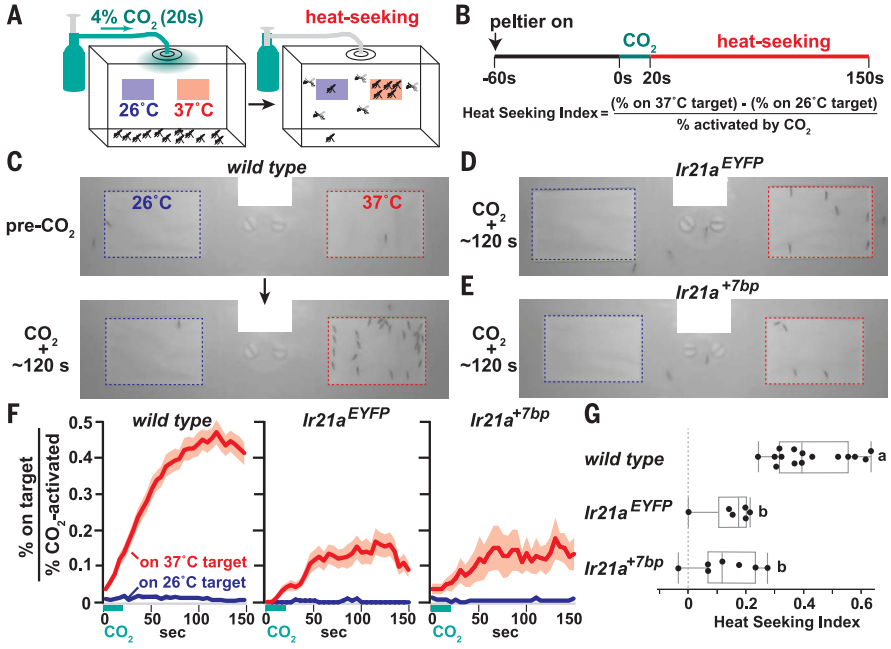

Fig. 3. *Ir21a* mediates heat seeking. (**A**) Heat seeking assay. Assay box is 28 cm deep, 40 cm long, and 16 cm tall. (**B**) The stimulus sequence and formula for the heat-seeking index. (**C**) Representative images of 26°C (blue) and 37°C (red) targets before and ~120 s after CO_2 pulse initiation in wild type. (**D** and **E**) Representative images from ~120 s after CO_2 pulse initiation in $Ir21a^{EYFP}$ (D) and $Ir21a^{+7bp}$ (E) mosquitoes. (**F**) Landing on 37°C and 26°C targets as the percentage of mosquitoes taking flight (averages ± SEM). Wild type, n = 15 independent groups; $Ir21a^{EYFP}$, n = 6; $Ir21a^{+7bp}$, n = 7. There were 42 to 52 females per group. (**G**) Heat seeking index (average from 105 to 135s). Letters denote distinct categories (Steel-Dwass test, $P < 0.01$). Shapiro-Wilk, Kruskal-Wallis, and Steel-Dwass test values are provided in the statistics section of methods.

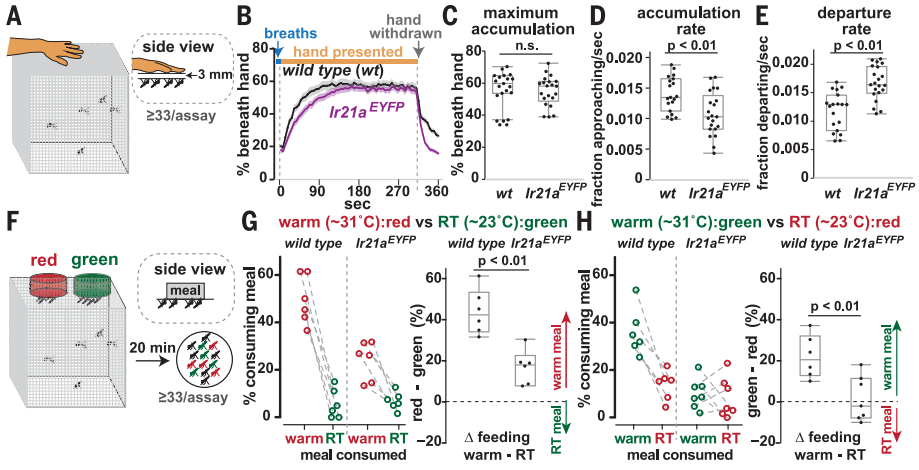

Fig. 4. *Ir21a* promotes warmth-stimulated blood feeding. (**A** to **E**) Host approach. (A) Mosquitoes were activated by five breaths and then presented a hand. (B) Mosquitoes landed (accumulated) on the cage roof below the hand. Values are averages ± SEM for 33 to 75 females per assay. Wild type (wt), n = 19 independent groups; $Ir21a^{EYFP}$, n = 21. (C) Average maximum accumulation, 180 s to 300s. (D) Accumulation rate, {[(accumulation at 45 s) − (accumulation pre–hand exposure)]/[(maximum accumulation) − (accumulation pre–hand exposure)]}/45 s. (E) Departure rate, 1 − [(accumulation at 340 s)/(accumulation at 300 s)]/40 s. (**F** to **H**) Blood feeding. (F) Two meals (one dyed green) were placed on the cage. (G) RT meal was dyed. (H) Warm meal was dyed. Dotted lines link pairs. Total of 33 to 75 females per assay. n = 6 independent groups per genotype, except in (H), where $Ir21a^{EYFP}$ n = 7. P values indicate t test results. The green tracking dye partially reduced relative consumption of meals to which it was added. Cages are 17.5-cm-sided cubes. Shapiro-Wilk test values are provided in the statistics section of methods.

deficit. To assess approach behavior, mosquitoes were activated by five human breaths and presented a human hand, positioned on a platform to prevent physical contact with the mosquitoes but otherwise providing host-associated cues (Fig. 4A). Hand approach was strong in the wild type, with 57 ± 2% of mosquitoes landing on the surface beneath the hand (Fig. 4, B and C). Hand-associated cues were critical, as hand withdrawal prompted rapid dispersal (Fig. 4B). $Ir21a^{EYFP}$ mutants remained robustly responsive, exhibiting maximum levels of approach (55 ± 2%) similar to wild-type levels (Fig. 4, B and C). Careful examination of response kinetics revealed that, compared to wild type, their initial accumulation rate decreased by ~25% (Fig. 4, B and D), and their dispersal rate upon hand removal increased by ~40% (Fig. 4, B and E), potentially reflecting subtle contributions of the warmth gradient created by the presence of the hand (fig. S4C) to the avidity of host approach. Similar results were obtained for $Ir21a^{+7bp}$ (fig. S4, D to G). Overall, these data demonstrate that the loss of *Ir21a* does not broadly disrupt orientation toward sensory cues and argue against the presence of global behavioral deficits in the mutants. These results are consistent with prior work indicating that the disruption of single sensory modalities is insufficient to completely eliminate host approach (*2*, *3*, *8*, *9*).

Heat strongly stimulates mosquito blood feeding (*8*, *9*). To assess the effect of warmth on blood feeding, artificial membrane feeders (*25*) were used to present human blood meals at different temperatures (Fig. 4F). One meal was held at room temperature (RT, ~23°C) and the other warmed to ~31°C, a temperature similar to the surface temperatures (~29°C to 33°C) of human torsos and extremities in a 23°C to 24°C room (*26*). In each trial, green food coloring was added to one meal so that the consumption of warm versus RT food could be distinguished (fig. S5). Each class of trial was assessed independently (RT meal dyed green in Fig. 4G and fig. S4H; warm meal dyed green in Fig. 4H and fig. S4I), and each yielded similar results. In wild type, elevated temperature robustly promoted feeding, as reflected in the greater percentages of mosquitoes consuming warm versus RT meals (Fig. 4, G and H, and fig. S4, H and I). For both $Ir21a^{EYFP}$ (Fig. 4, G and H) and $Ir21^{+7bp}$

(fig. S4, H and I) mosquitoes, this preference for warm blood was significantly reduced. Thus, similar to heat seeking, warmth-promoted blood feeding was reduced in the absence of *Ir21a*.

These data identify IR21a as a key mediator of heat-seeking behavior in *A. gambiae* mosquitoes. Although a cooling-activated receptor driving heat seeking is superficially counterintuitive, repulsion from cooling would yield a similar behavioral outcome as attraction to warming. Furthermore, Cooling Cells are bidirectional and are not only activated by cooling but also inhibited by heating (Fig. 2, D and E); each phase of the response could modulate downstream circuits to control behavior. Ultimately, the detection of temperature change by the Cooling Cells is critical, but is just one step in heat seeking, a response that involves the processing of multiple sensory inputs to generate a coherent response. Identification of a key molecular receptor for heat seeking provides a starting point for a deeper understanding of this complex behavior and its contribution to the multimodal process that culminates in mosquito blood feeding.

The conservation of IR21a's thermosensory function between *Drosophila* (*18*) and *Anopheles* (Fig. 2), whose last common ancestor lived ~250 million years ago, suggests thermosensing is an ancestral function of IR21a. As this ancestor predates the evolution of blood feeding (*13*), its IR21a would have regulated other behaviors, such as thermoregulation. Thus, our findings indicate that the evolution of blood feeding in *A. gambiae* mosquitoes involved repurposing an ancestral thermoreceptor to facilitate host seeking. Alterations in the connectivity or function of downstream circuits would likely have been crucial in this behavioral shift. Given the conservation of IR21a as well as IR25a and IR93a (IR21a's coreceptors in *Drosophila*) across insects (*19*), these IRs may be used in heat seeking not only by other mosquitoes but also across a range of hematophagous insect taxa.

In addition to *Ir21a*'s role in heat seeking, IR21a expression in the antennae of *A. gambiae* males suggests it continues to serve additional thermosensory functions. It will be interesting to assess whether IR21a mediates thermal preference in male and possibly female mosquitoes and the extent to which thermal preference and heat-seeking circuits overlap. Not all thermoreceptors appear to have been repurposed, as the TRPA1 warmth receptor has a similar role in flies and mosquitoes, mediating heat avoidance in both (*12*). At a practical level, exploiting and manipulating the sensory systems of vector insects offer an avenue for disease control strategies.

REFERENCES AND NOTES

1. World Health Organization, "A global brief on vector-borne diseases" (WHO, 2014).
2. A. W. A. Brown, *JAMA* **196**, 249–252 (1966).
3. R. T. Cardé, *Curr. Biol.* **25**, R793–R795 (2015).
4. C. R. Lazzari, *Curr. Opin. Insect Sci.* **34**, 112–116 (2019).
5. F. M. Howlett, *Parasitology* **3**, 479–484 (1910).
6. A. F. Carey, G. Wang, C. Y. Su, L. J. Zwiebel, J. R. Carlson, *Nature* **464**, 66–71 (2010).
7. M. DeGennaro *et al.*, *Nature* **498**, 487–491 (2013).
8. C. J. McMeniman, R. A. Corfas, B. J. Matthews, S. A. Ritchie, L. B. Vosshall, *Cell* **156**, 1060–1071 (2014).
9. J. I. Raji *et al.*, *Curr. Biol.* **29**, 1253–1262.e7 (2019).
10. G. Wang *et al.*, *Eur. J. Neurosci.* **30**, 967–974 (2009).
11. E. Maekawa *et al.*, *Parasites Vectors* **4**, 10 (2011).
12. R. A. Corfas, L. B. Vosshall, *eLife* **4**, e11750 (2015).
13. D. Grimaldi, M. S. Engel, *Evolution of the Insects* (Cambridge Univ. Press, 2005).
14. K. Kang *et al.*, *Nature* **481**, 76–80 (2011).
15. L. Ni *et al.*, *Nature* **500**, 580–584 (2013).
16. L. Ni *et al.*, *eLife* **5**, e13254 (2016).
17. Z. A. Knecht *et al.*, *eLife* **6**, e26654 (2017).
18. G. Budelli *et al.*, *Neuron* **101**, 738–747.e3 (2019).
19. R. Rytz, V. Croset, R. Benton, *Insect Biochem. Mol. Biol.* **43**, 888–897 (2013).
20. A. Enjin *et al.*, *Curr. Biol.* **26**, 1352–1358 (2016).
21. R. J. Pitts, D. C. Rinker, P. L. Jones, A. Rokas, L. J. Zwiebel, *BMC Genomics* **12**, 271 (2011).
22. E. E. Davis, P. G. Sokolove, *J. Comp. Physiol.* **96**, 223–236 (1975).
23. S. B. McIver, *J. Med. Entomol.* **19**, 489–535 (1982).
24. E. Gingl, A. Hinterwirth, H. Tichy, *J. Neurophysiol.* **94**, 176–185 (2005).
25. J. B. Cosgrove, R. J. Wood, D. Petrić, D. T. Evans, R. H. Abbott, *J. Am. Mosq. Control Assoc.* **10**, 434–436 (1994).
26. N. Zaproudina, V. Varmavuo, O. Airaksinen, M. Närhi, *Physiol. Meas.* **29**, 515–524 (2008).
27. K. S. Littig, C. J. Stovanovich, in "Pictorial keys to arthropods, reptiles, birds and mammals of public health significance". (Communicable Disease Center, U.S. Dept. Health, Education, and Welfare, 1966), p. 134.

ACKNOWLEDGMENTS

We thank A. Hammond, R. Harrell, T. Nolan, S. McIver, A. Crisanti, E. Marois, B. White, and L. Vosshall for reagents and advice, R. Albuquerque for assistance with data analysis, R. Gerber for assistance with mosquito husbandry and behavioral assays, and A. Lee, E. Marder, M. Rosbash, P. Sengupta, and C. Zhu for comments on the manuscript. **Funding:** This work was supported by grants from the National Institute of Allergy and Infectious Diseases (F31 AI133945 to C.G.; R01 AI122802 and R21 AI140018 to P.A.G. and F.C.), the National Institute of Neurological Disorders and Stroke (2T32NS007292-31) to W.J.L., the National Institute of General Medicine (F32 GM113318) to B.G., the Swiss National Science Foundation (P2FRP3_168480) to L.V.G., a Faculty Research Scholar Award by the Howard Hughes Medical Institute and the Bill & Melinda Gates Foundation (grant OPP1158190) to F.C., and the National Science Foundation (IOS 1557781) to P.A.G. **Author contributions:** C.G., W.J.L., G.B., L.V.G., A.L.S., F.C., and P.A.G. designed experiments. C.G., W.J.L., E.C.C., A.M.D., and L.V.G. performed husbandry, molecular genetics, and heat-seeking behavior experiments. C.G. performed NHEJ-based gene disruption. W.J.L. performed gene targeting. W.J.L. and E.C.C. performed hand approach and blood-feeding behavior analyses. L.V.G. and C.G. performed immunohistochemistry. G.B. and C.G. performed electrophysiology. A.L.S. performed transgenesis of gRNA expression vector. W.J.L. and P.A.G. performed data analysis. C.G., W.J.L., and P.A.G. wrote the paper with input from all authors. **Competing interests:** A.L.S. is a coinventor on patent WO2015105928A1 (WIPO PCT pending; inventors K. Esvelt and A. L. Smidler), "RNA-guided gene drives." The patent involves spreading desirable traits genetically through mosquito populations using Cas9-based gene drives. IR21a could potentially be used as a target for such a gene drive. P.A.G. is a coinventor on patent WO2017196861A1 (WIPO PCT pending; inventors Z. Knecht, P.Garrity, L. Ni) "Methods for modulating insect hygro- and/or thermosensation." This patent proposes using members of the ionotropic receptor family as targets for strategies to disrupt hygro- and thermo-sensation in insects. **Data and materials availability:** The datasets generated and analyzed during the current study are available at DRYAD (https://doi.org/10.5061/dryad.pzgmsbcg3).

SUPPLEMENTARY MATERIALS

science.sciencemag.org/content/367/6478/681/suppl/DC1
Materials and Methods
Figs. S1 to S5
References (*28*–*32*)
Movies S1 and S2

View/request a protocol for this paper from *Bio-protocol*.

4 August 2019; accepted 6 December 2019
10.1126/science.aay9847

POLLINATOR DECLINE

Climate change contributes to widespread declines among bumble bees across continents

Peter Soroye[1]*, Tim Newbold[2], Jeremy Kerr[1]

Climate change could increase species' extinction risk as temperatures and precipitation begin to exceed species' historically observed tolerances. Using long-term data for 66 bumble bee species across North America and Europe, we tested whether this mechanism altered likelihoods of bumble bee species' extinction or colonization. Increasing frequency of hotter temperatures predicts species' local extinction risk, chances of colonizing a new area, and changing species richness. Effects are independent of changing land uses. The method developed in this study permits spatially explicit predictions of climate change–related population extinction-colonization dynamics within species that explains observed patterns of geographical range loss and expansion across continents. Increasing frequencies of temperatures that exceed historically observed tolerances help explain widespread bumble bee species decline. This mechanism may also contribute to biodiversity loss more generally.

Recent climate changes have accelerated range losses among many species (*1*, *2*). Variation in species' extinction risk or chances of colonizing a new area determine whether species' ranges expand or decline as new climatic conditions emerge. Understanding how changing climatic conditions alter species' local extinction (extirpation) or colonization probabilities has proven exceptionally challenging, particularly in the presence of other environmental changes, such as habitat loss. Furthermore, identifying which species will most likely be at risk from climate change and where those risks will be greatest is critical to the development of conservation strategies (*3*, *4*).

Although many mechanisms could alter how species fare as climate changes, discovering processes that strongly affect species persistence remains among the foremost challenges in conservation (*5*). Climate change could pose risks to species in part by increasing the frequency of environmental conditions that exceed species' tolerances, causing population decline and potentially extirpation (*6*, *7*). Conversely, climate change may render marginal areas more suitable for a species, making colonization of that locale more likely (*1*). Understanding and predicting spatially explicit colonization and extinction likelihood could identify which species are vulnerable to climate change and where, identify which species may benefit, and suggest interventions to mitigate conservation risks. Colonization and extinction dynamics, in combination across a regional species assemblage, determine how species richness changes. Among taxa that contribute critically to ecosystem service provision, including pollinators such as bumble bees (*Bombus*), species richness decline could impair ecosystem services (*8*).

We evaluated changes in bumble bee species occupancy and regional richness across North America and Europe using a database of ~550,000 georeferenced occurrence records of 66 bumble bee species (figs. S1 and S2 and table S1) (*1*, *9*). We estimated species' distributions in quadrats that measured 100 km by 100 km, in a baseline (1901–1974) and recent period (2000–2014) (*9*). Climate across Europe and North America has changed greatly between these time periods (fig. S3). Although the baseline period was substantially longer, there were 49% more records in the recent period. Non–detection bias (difficulty distinguishing among true and false absences due to imperfect detection) in opportunistic occurrence records can reduce measurement accuracy of species distributions and overall richness (*10*). Consequently, we used detection-corrected occupancy models to estimate probability of occurrence for each species in quadrats in each time period (*9*). We calculated changes in species' probabilities of occupancy and generated detection-corrected estimates of species richness change between periods (fig. S4).

We predict greater declines in bumble bee species occupancy and species richness where changing climatic conditions more frequently exceed individual species' historically observed tolerances. Conversely, we predict greater occupancy and species richness in areas where climate changes more frequently cause local weather to fall within species' historically observed tolerances. Temperature and precipitation can affect bumble bee mortality and fecundity directly [e.g., (*11*)] and indirectly through changes to floral resources (*12*). For both periods, we calculated proximity of climatic conditions within quadrats across these continents to estimated thermal and precipitation limits of all 66 species. We averaged monthly temperatures and total precipitation in localities where species were observed and rescaled these measures relative to each species's historically observed climatic limits. Those limits were calculated from averages of the five highest monthly maximum and lowest monthly minimum temperatures, or five highest and lowest monthly total precipitation values, from among values for all location-year combinations where that species was observed during the baseline. Although climate limits inferred from observed distributions might not always identify actual physiological tolerances, they can suggest such limits and can prove useful in the absence of more mechanistic data (*1*). We calculated local changes in this new climatic position index between baseline and recent time periods and also averaged it across all species present per quadrat to calculate community-averaged climatic position index (Fig. 1 and fig. S5).

Our measurements of bumble bee species occupancy over time provide evidence of rapid and widespread declines across Europe and North America. The probability of site occupancy declined on average by 46% (±3.3% SE) in North America and 17% (±4.9% SE) in Europe relative to the baseline period (Fig. 2). Declines were robust to detection-correction methods (figs. S6A and S7) and consistent with reductions in detection-corrected species richness (fig. S6B) (*9*).

Declines among bumble bee species relate to the frequency and extent to which climatic conditions approach or exceed species' historically observed climatic limits, particularly for temperature. We modeled change in probability of site occupancy with phylogenetic generalized linear mixed models using thermal position variables (baseline, change since baseline, and the interaction between these), precipitation position variables (baseline, change since baseline, and the interaction between these), the interaction between baseline thermal and precipitation position terms, and the interaction between change in thermal position and change in precipitation position. We controlled for continent (*9*). The models support our predictions: Probability of occupancy decreases when temperatures rise above species' upper thermal limits (Fig. 3A, fig. S8A, and table S2), whereas warming in regions that were previously near species' cold limits is associated with increasing occupancy. Evidence for precipitation influencing site occupancy was mixed, but declines were more likely in sites that became drier (Fig. 3B, fig. S8B, and table S2). Our model's capacity to predict change in occupancy [marginal coefficient of determination (R^2) = 0.11] was comparable to the predictive ability of other macroecological models of the biological impacts of climate change (*2*), but our models predicted extirpation and colonization more capably [marginal R^2 = 0.53 to 0.87 (*9*)]. Whereas there was weak evidence for a phylogenetic signal in the response of occupancy (Pagel's λ = 0.12), modeling extirpation

[1]Department of Biology, University of Ottawa, Ottawa, ON K1N 6N5, Canada. [2]Centre for Biodiversity and Environment Research, Department of Genetics, Evolution and Environment, University College London, London WC1E 6BT, UK.
*Corresponding author. Email: peter.soroye@gmail.com

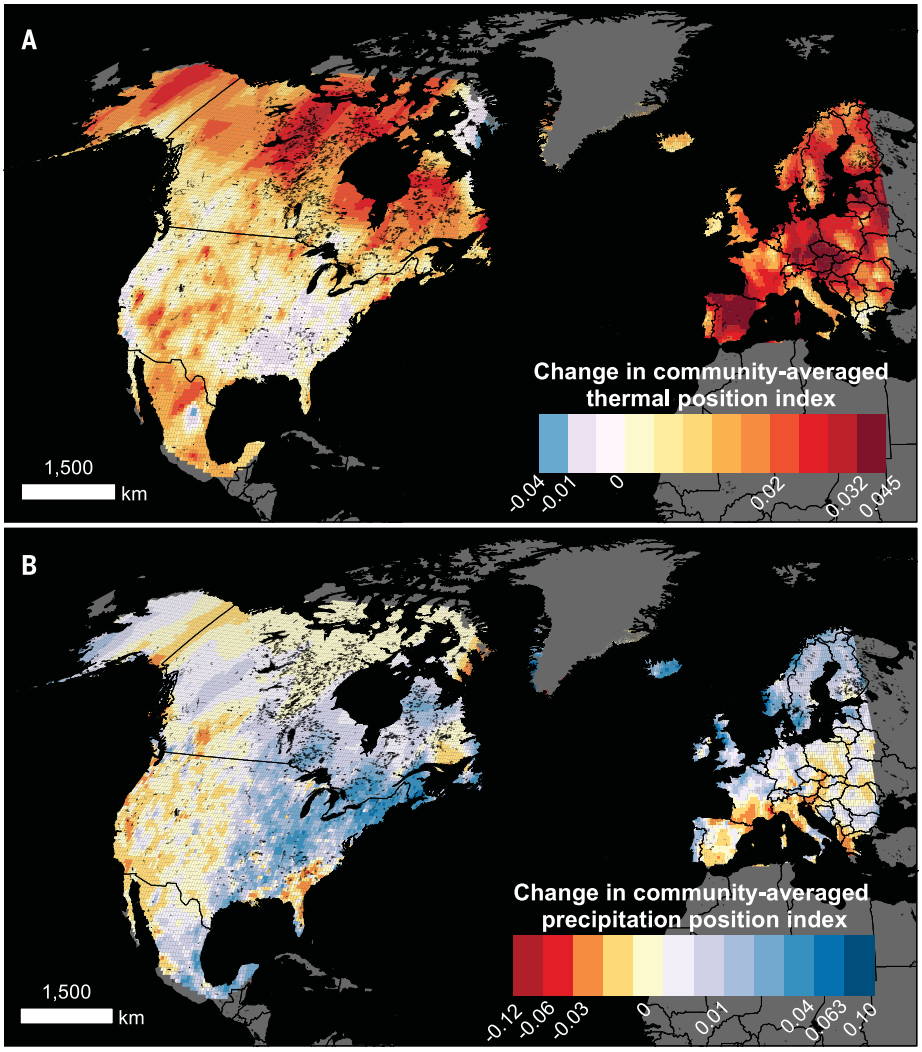

Fig. 1. Change in community-averaged measures from the baseline (1901–1974) to the recent period (2000–2015). Local changes in (**A**) thermal and (**B**) precipitation position indices are shown. Increases indicate warmer or wetter regions and that, on average, species in a given assemblage are closer to their hot or wet limits than they have been historically. Declines indicate cooling or drying regions and that, on average, species in a given assemblage are closer to their cold or wet limits than they have been historically.

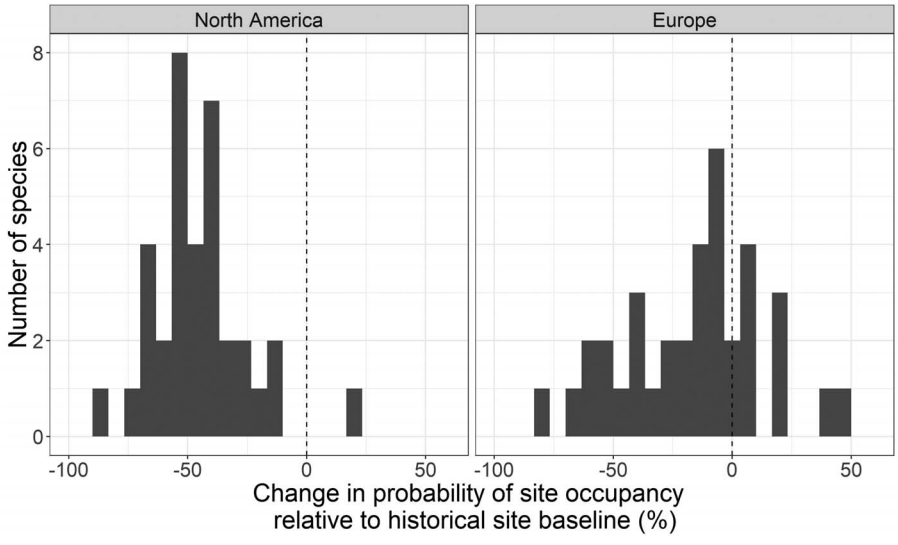

Fig. 2. Percent change in site occupancy since a baseline period (1901–1974) for 35 North American and 36 European bumble bee species.

and colonization separately yields a stronger signal (*9*). Results were robust to detection-correction method for measuring species' presences in quadrats, across spatial scales of analysis, and through a range of thresholds for inferring absences from occurrence data (*9*).

Bumble bee species richness declined in areas where increasing frequencies of climatic conditions exceed species' historically observed tolerances in both Europe and North America. An analysis of covariance that modeled the response of detection-corrected richness to community-averaged measures of climatic position revealed that, consistent with observed trends in species-specific occupancy change, richness was more likely to decline in regions experiencing warming, especially when species present were in the warmest parts of their historical ranges (table S2). These models accounted for potential spatial autocorrelation, and results were consistent regardless of method to correct for differences in species detection probabilities (*9*).

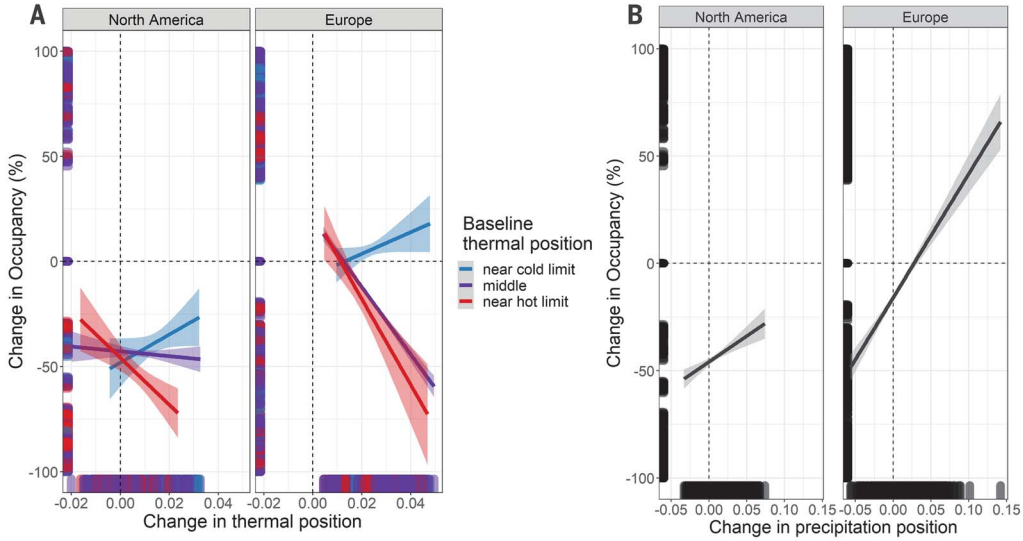

Fig. 3. Change in probability of occupancy in response to change in thermal and precipitation position from the baseline (1901–1974) to the recent period (2000–2014). Thermal (**A**) and precipitation (**B**) positions range from 0 to 1, with 1 indicating that conditions at a site are at a species's hot or wet limit for the entire year and 0 meaning that conditions are at a species's cold or dry limit for the entire year during the historic period. For ease of visualizing the significant interaction between baseline thermal position and change in thermal position, the continuous baseline thermal position variable has been split at the first and third quantile to show sites that were historically close to species' hot limits (red; n = 969 sites), cold limits (blue; n = 2244 sites), and the middle of their observed climatic limits (purple; n = 11,793 sites). Rug plots show the distribution of observations. Confidence intervals (±95%) are shown around linear trendlines.

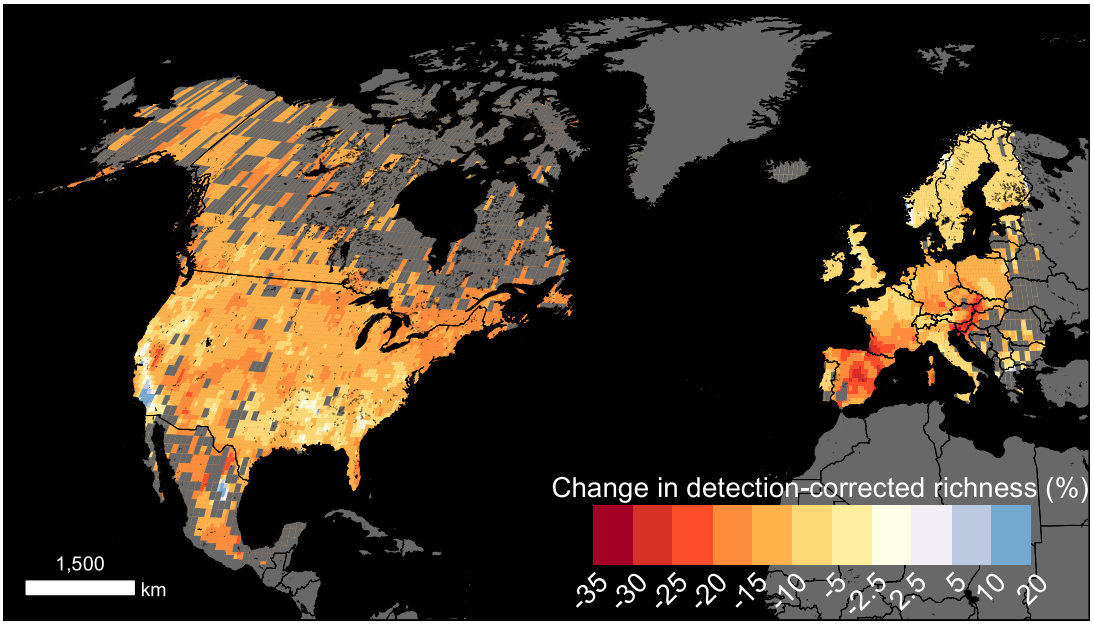

Fig. 4. Climate change–related change in bumble bee species richness from a baseline (1901–1974) to a recent period (2000–2014). Predictions are from a model projecting percent change in detection-corrected bumble bee species richness as a function of mean community-averaged thermal and precipitation position.

Projections suggest that recent climate change has driven stronger and more widespread bumble bee declines than have been reported previously, especially in Europe (Fig. 4). European estimates of observed richness rely particularly on observations from well-sampled regions that were cooler in the baseline period and that have experienced less warming subsequently (*9*), which may have contributed to underestimation of recent species richness decline across that continent (figs. S6B, S9, and S10). These findings contrast with those for other taxa that predict widespread range expansions and increasing species richness toward warming environments in the north (*13*, *14*).

Changes in climatic position index predict biologically important changes in bumble bee presence, colonization, extirpation, and richness across two continents. Species-specific changes in climatic position predict bumble bee diversity change as well as or better than mean, maximum, or minimum temperature or precipitation measures [models using climatic position index: marginal R^2 2.6% lower to 23% higher, change in deviance information criterion = 98.7 to 241.9 (*9*)]. Including land-use change in the models revealed a significant negative effect but did not influence results for climatic position variables (table S4) (*9*). At this scale, effects of climate change on bumble bees appear distinct from effects of land use. Other anthropogenic changes, such as agricultural intensification, pesticide use, and pathogens, can also affect occupancy and extirpation risk of bumble bees (*15*–*17*). Interactions between these factors are expected to accelerate biodiversity loss for bumble bees and other taxa over broad areas (*18*, *19*). Understanding how interactions between climate and land-use changes alter extinction risk is vital to conservation of pollinator species.

Climate is expected to warm rapidly in the future (*20*). Using a spatially explicit method of measuring climatic position and its change over time, we show that risks of bumble bee extirpation rise in areas where local temperatures more frequently exceed species' historical tolerances, whereas colonization probabilities in other areas rise as climate changes cause conditions to more frequently fall within species' thermal limits. Nevertheless, overall rates of climate change–related extirpation among species

greatly exceed those of colonization, contributing to pronounced bumble bee species declines across both Europe and North America with unknown consequences for the provision of ecosystem services. Mitigating climate change–driven extinction risk among bumble bees requires efforts to manage habitats to reduce exposure to the growing frequency of temperatures that are extreme relative to species' historical tolerances.

REFERENCES AND NOTES

1. J. T. Kerr *et al*., *Science* **349**, 177–180 (2015).
2. F. E. B. Spooner, R. G. Pearson, R. Freeman, *Glob. Change Biol.* **24**, 4521–4531 (2018).
3. S. D. Veloz *et al*., *Glob. Change Biol.* **18**, 1698–1713 (2012).
4. J. W. Williams, S. T. Jackson, *Front. Ecol. Environ.* **5**, 475–482 (2007).
5. M. C. Urban, *Science* **348**, 571–573 (2015).
6. K. D. T. Nguyen *et al*., *PLOS ONE* **6**, e29340 (2011).
7. J. M. Sunday *et al*., *Proc. Natl. Acad. Sci. U.S.A.* **111**, 5610–5615 (2014).
8. S. G. Potts *et al*., *Trends Ecol. Evol.* **25**, 345–353 (2010).
9. Materials and methods are available as supplementary materials.
10. G. Sadoti, B. Zuckerberg, M. A. Jarzyna, W. F. Porter, *Divers. Distrib.* **19**, 804–814 (2013).
11. S. H. Woodard, *Curr. Opin. Insect Sci.* **22**, 101–108 (2017).
12. J. E. Ogilvie *et al*., *Ecol. Lett.* **20**, 1507–1515 (2017).
13. C. A. Deutsch *et al*., *Proc. Natl. Acad. Sci. U.S.A.* **105**, 6668–6672 (2008).
14. C. Sirois-Delisle, J. T. Kerr, *Sci. Rep.* **8**, 14464 (2018).
15. B. A. Woodcock *et al*., *Science* **356**, 1393–1395 (2017).
16. R. J. Gill, O. Ramos-Rodriguez, N. E. Raine, *Nature* **491**, 105–108 (2012).
17. D. Goulson, E. Nicholls, C. Botías, E. L. Rotheray, *Science* **347**, 1255957 (2015).
18. T. Newbold, *Proc. R. Soc. B* **285**, 20180792 (2018).
19. C. S. Mantyka-Pringle *et al*., *Biol. Conserv.* **187**, 103–111 (2015).
20. IPCC, "Climate Change 2014: Synthesis Report. Contribution of Working Groups I, II and III to the Fifth Assessment Report of the Intergovernmental Panel on Climate Change" (IPCC, 2014); www.ipcc.ch/report/ar5/syr/.
21. P. Soroye, T. Newbold, J. T. Kerr, Climate change contributes to widespread declines among bumble bees across continents - DATA REPOSITORY, figshare (2020); doi: 10.6084/m9.figshare.9956471.

ACKNOWLEDGMENTS

The authors thank all data contributors for contributions to knowledge of bumble bee distributions, especially A. Pindar, P. Galpern, L. Packer, S. G. Potts, S. M. Roberts, P. Rasmont, O. Schweiger, S. R. Colla, L. L. Richardson, D. L. Wagner, L. F. Gall, D. S. Sikes, and A. Pantoja. See the supplementary materials for the full list of data contributors. **Funding:** J.K. is grateful for Discovery Grant and Discovery Accelerator Supplement from the Natural Sciences and Engineering Research Council of Canada (NSERC) and funds from his University Research Chair in Macroecology and Conservation at the University of Ottawa. J.K. is also supported through infrastructure funds from the Canada Foundation for Innovation. This collaboration was funded by a Royal Society grant to T.N. and J.K. and an NSERC Postgraduate Scholarship award to P.S. to work with J.K. T.N. was supported by a Royal Society University Research Fellowship and a grant from the UK Natural Environment Research Council (NE/R010811/1). **Author contributions:** P.S., T.N., and J.K. created techniques and designed the research. P.S. conducted analyses and, with J.K., wrote the manuscript. All authors contributed to editing the manuscript. **Competing interests:** None declared. **Data and materials availability:** Bumble bee observations, gridded environmental observations, and R scripts used to process data and generate all results are freely available through figshare (*21*).

SUPPLEMENTARY MATERIALS

science.sciencemag.org/content/367/6478/685/suppl/DC1
Materials and Methods
Supplementary Text
Supplementary Acknowledgments
Figs. S1 to S13
Tables S1 to S8
References (*22*–*59*)

1 May 2019; accepted 13 December 2019
10.1126/science.aax8591

NEUROSCIENCE

Microglia mediate forgetting via complement-dependent synaptic elimination

Chao Wang[1,2]*, Huimin Yue[1,2]*, Zhechun Hu[1,2], Yuwen Shen[1,2], Jiao Ma[3], Jie Li[1,2], Xiao-Dong Wang[4,5], Liang Wang[6], Binggui Sun[7], Peng Shi[8], Lang Wang[3]†, Yan Gu[1,2,9]†

Synapses between engram cells are believed to be substrates for memory storage, and the weakening or loss of these synapses leads to the forgetting of related memories. We found engulfment of synaptic components by microglia in the hippocampi of healthy adult mice. Depletion of microglia or inhibition of microglial phagocytosis prevented forgetting and the dissociation of engram cells. By introducing CD55 to inhibit complement pathways, specifically in engram cells, we further demonstrated that microglia regulated forgetting in a complement- and activity-dependent manner. Additionally, microglia were involved in both neurogenesis-related and neurogenesis-unrelated memory degradation. Together, our findings revealed complement-dependent synapse elimination by microglia as a mechanism underlying the forgetting of remote memories.

Memory is coded and allocated to engrams within related brain regions (*1*, *2*). Reactivation of engram cells is essential for memory recall, whereas failure in reactivation of engram cells leads to the forgetting of related memories (*3*). Synaptic connections between engram cells are believed to be substrates for memory storage (*4*, *5*). Circuit rewiring and synaptic reorganization may lead to loss or weakening of synaptic connections between engram cells, resulting in the forgetting of previously existing memories. For example, massive synaptic reorganization takes place in the dentate gyrus (DG) as continuously generated newborn neurons integrate into the hippocampal neural circuit, which leads to the forgetting of hippocampus-dependent memories (*6*–*8*). Even in mature neurons, experience- and learning-dependent, dynamic remodeling of synapses occurs constantly throughout life (*9*–*13*), providing a potential mechanism for the erasure of stored memories in the synaptic connections of these cells. Microglia are not only important for pruning excessive synapses during postnatal brain development but are also involved in the dynamics of synapses in the adult brain (*14*–*17*). Because they survey the brain and play crucial roles in monitoring synapses and determining the wiring of the brain (*15*, *18*, *19*), microglia may affect the stability of synaptic connections within the neural circuits where memories are allocated.

First, we used contextual fear conditioning (CFC) to assess the memory retention in C57BL/6 mice. We measured the freezing behavior of the animals during a test performed 5 or 35 days after three training sessions, each training session consisting of three weak foot shocks (Fig. 1A). We observed a significant decrease in the freezing of animals at 35 days compared with 5 days after training (Fig. 1B). We then carried out CFC training using CD11b-DTR mice, in which diphtheria toxin receptor (DTR) is specifically expressed in CD11b-expressing myeloid cells, including microglia in the brain (*20*). By intracerebroventricularly administering diphtheria toxin (DT) daily after training, we depleted microglia in these CD11b-DTR mice until the test (fig. S1). Thirty-five days later, CD11b-DTR mice treated with DT showed significantly higher freezing levels than those in the saline group (fig. S1). To avoid the effect of daily injection on animal behaviors, we depleted microglia in C57BL/6 mice with PLX3397 (PLX), a CSF1R/c-kit antagonist (*21*), via mouse diet after CFC training (Fig. 1C). Thirty-five days later, PLX treatment significantly increased freezing of the animals (Fig. 1D), with microglia depleted in the brain (Fig. 1, E and F), consistent with the results obtained from CD11b-DTR mice.

To exclude the possibility that depleting microglia may affect formation or retrieval of memories, we tested the freezing of mice a short time (5 days) after training (fig. S2A). We found that PLX treatment did not alter the freezing of animals (fig. S2B). Furthermore, we started administration of PLX to deplete microglia before the training and tested 24 hours later (fig. S2C). No significant difference was observed between control and PLX-treated animals (fig. S2D). Further behavioral tests showed that PLX treatment for 35 days did not significantly change the behavior of animals in an elevated plus maze or an open field (fig. S3).

Memory retrieval requires reactivation of engram cells (*3*), whereas dissociation of engram cells—i.e., engram cells being unable to reactivate at the same time—leads to forgetting. To test whether the microglia-mediated forgetting of already-formed memory correlates with dissociation of engram cells, we used a FosTRAP strategy for tagging activated neurons during CFC training (*22*). We trained c-Fos-Cre^{ERT2}::Ai14 mice for contextual fear memory and administered tamoxifen (TAM) before the last training session to induce permanent expression of dTomato in activated engram neurons. Immunofluorescent staining for c-Fos was performed after the test, and the reactivation rate of engram cells was assessed by analyzing c-Fos$^+$dTomato$^+$ colocalization in the DG (Fig. 1, G and H). Under physiological conditions, the reactivation rate of engram cells 35 days after training significantly decreased compared with that measured at 5 days, which correlates with the forgetting of related memory (Fig. 1I). Thirty-five days but not 5 days after training, PLX treatment significantly increased the reactivation rate of the engram cells (Fig. 1I), without altering the number of dTomato$^+$ engram cells in the DG (fig. S4). The freezing of animals during the test positively correlates with the reactivation rate of engram cells (Fig. 1J).

During postnatal development, microglia are involved in synaptic reorganization and circuitry refinement by synaptic pruning (*15*). We imaged microglia in the DG of adult CX3CR1$^{GFP/+}$ mice, in which microglia were labeled with green fluorescent protein (GFP). When costained with synaptophysin or PSD95, markers for pre- or postsynaptic components, we found synaptophysin$^+$ and PSD95$^+$ puncta were present in GFP$^+$ microglia, colocalizing with lysosome marker Lamp1 (Fig. 2, A and B, and movies S1 and S2).

To test whether synaptic elimination by microglial phagocytosis may mediate forgetting, we systematically administered minocycline (Mino)—which has been shown to inhibit microglial engulfment of synapses in vitro and in vivo (*15*, *23*)—after CFC training until the test (fig. S5A). Thirty-five days later, Mino-treated animals showed significantly longer freezing time (fig. S5B). Immunostaining showed that microglia in Mino-treated CX3CR1$^{GFP/+}$ animals

[1]Institute of Neuroscience and Department of Neurology of the Second Affiliated Hospital, NHC and CAMS Key Laboratory of Medical Neurobiology, Zhejiang University School of Medicine, Hangzhou 310058, China. [2]Center for Stem Cell and Regenerative Medicine, Zhejiang University School of Medicine, Hangzhou 310058, China. [3]Department of Neurology of the First Affiliated Hospital, Interdisciplinary Institute of Neuroscience and Technology, Zhejiang University School of Medicine, Hangzhou 310029, China. [4]Department of Neurobiology, Institute of Neuroscience, NHC and CAMS Key Laboratory of Medical Neurobiology, Zhejiang University School of Medicine, Hangzhou 310058, China. [5]Department of Psychiatry, Sir Run Run Shaw Hospital, Zhejiang University School of Medicine, Hangzhou 310016, China. [6]Institute of Neuroscience and Department of Neurology of the Second Affiliated Hospital, Mental Health Center, NHC and CAMS Key Laboratory of Medical Neurobiology, Zhejiang University School of Medicine, Hangzhou 310058, China. [7]Center for Neuroscience and Department of Neurology of the First Affiliated Hospital, NHC and CAMS Key Laboratory of Medical Neurobiology, Zhejiang University School of Medicine, Hangzhou 310058, China. [8]Department of Cardiology of the Second Affiliated Hospital, Zhejiang University School of Medicine, Hangzhou 310058, China. [9]Zhejiang Provincial Key Laboratory of Tissue Engineering and Regenerative Medicine, Hangzhou 310058, China.
*These authors contributed equally to this work.
†Corresponding author. Email: wanglang@zju.edu.cn (L.W.); guyan2015@zju.edu.cn (Y.G.)

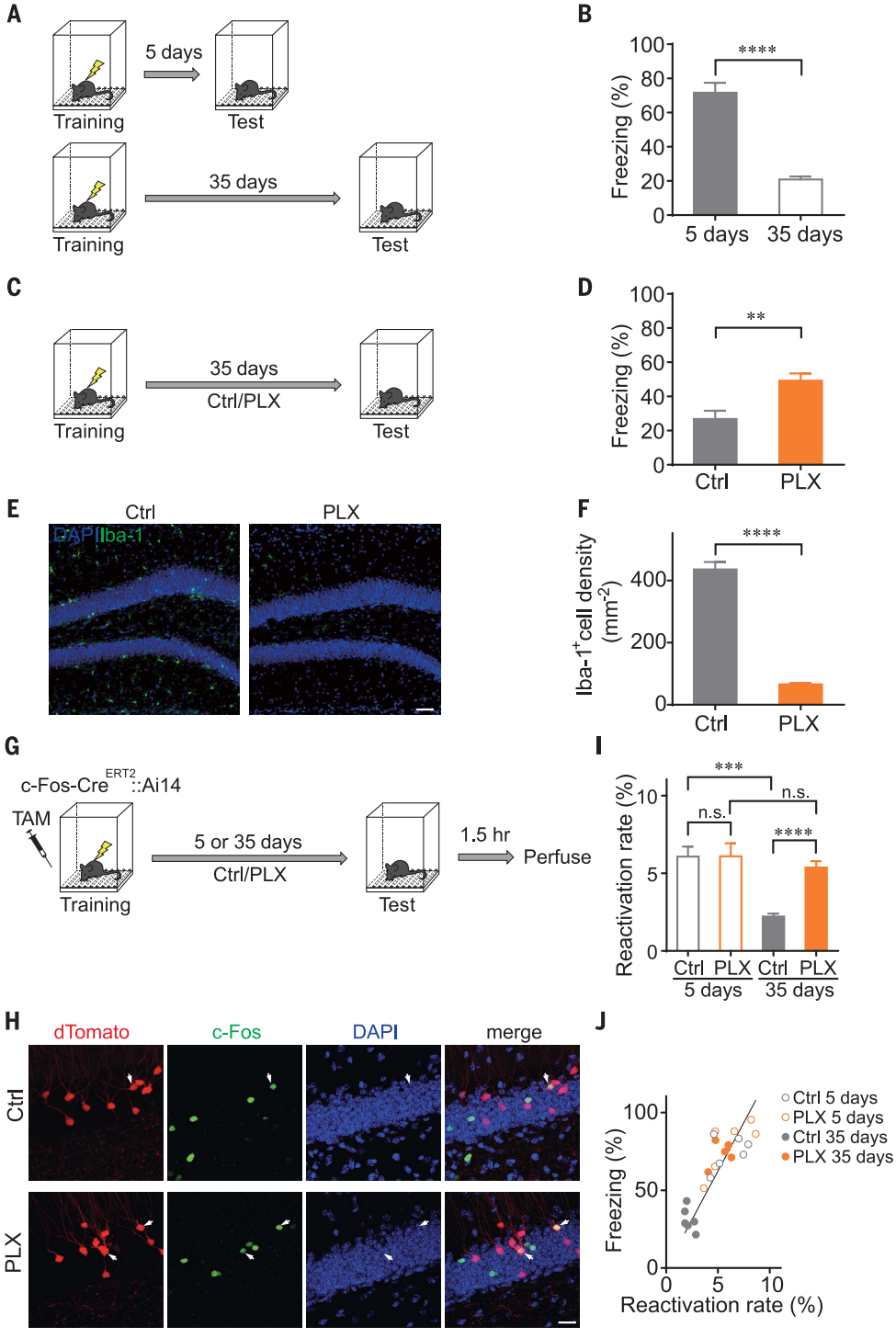

Fig. 1. Depletion of microglia prevents memory forgetting and engram dissociation. (**A**) Adult mice received CFC training and were tested 5 or 35 days later. (**B**) Animals showed significantly reduced freezing 35 days after training compared with 5 days after training. n = 9 mice per group; t = 8.316, df = 16; ****P < 0.0001. Error bars indicate standard error of the mean (SEM). (**C**) After CFC training, mice received normal food [control (Ctrl)] or food containing PLX before the test 35 days after training. (**D**) PLX treatment decreased forgetting. Ctrl n = 19 mice, PLX n = 17 mice; t = 3.443, df = 34, **P = 0.0015. (**E**) Confocal images showing decreased number of microglia (Iba1$^+$) in the DG of PLX-treated animals. Scale bar, 50 μm; DAPI, 4′,6-diamidino-2-phenylindole. (**F**) PLX significantly decreased the density of microglia in the DG. Ctrl n = 4 mice, PLX n = 7 mice; t = 20.39, df = 9, ****P < 0.0001. (**G**) c-Fos-Cre^{ERT2}::Ai14 mice were treated with TAM before the last training and then received Ctrl or PLX food until the test 5 or 35 days after training. (**H**) Confocal images showing the reactivation of engram cells in the DG of c-Fos-Cre^{ERT2}::Ai14 mice. White arrows indicate reactivated engram cells (c-Fos$^+$dTomato$^+$) during test. Scale bar, 20 μm. (**I**) Reactivation rate of engram cells (c-Fos$^+$dTomato$^+$/dTomato$^+$) decreased from 5 days to 35 days after training (Ctrl 5 days, n = 6 mice, versus Ctrl 35 days, n = 6 mice, t = 5.750, df = 10, ***P = 0.0002), whereas PLX3397 treatment prevented the decrease of reactivation rate over time (PLX 5 days, n = 6 mice, versus PLX 35 days, n = 5 mice, t = 0.7272, df = 9, P = 0.4856). PLX3397 treatment increased the reactivation rate of engram cells 35 days after training (Ctrl 35 days versus PLX 35 days, t = 7.340, df = 9, ****P < 0.0001), but not 5 days (Ctrl 5 days versus PLX 5 days, t = 0.01618, df = 10, P = 0.9874). n.s., not significant. (**J**) The reactivation rate of DG engram cells is positively correlated with freezing of animals. Ctrl 5 days, gray open circles, n = 6 mice; PLX 5 days, orange open circles, n = 6 mice; Ctrl 35 days, gray solid circles, n = 6 mice; PLX 35 days, orange solid circles, n = 5 mice. Solid line indicates linear fitting of all points; R^2 = 0.5998, where R^2 is the coefficient of determination.

contained smaller synaptophysin$^+$ puncta (fig. S5, C and D) or PSD95$^+$ puncta (fig. S5, E and F).

Complement cascades are important for tagging synapses to be eliminated by microglia during brain development. C1q, the initiating protein of the classical complement cascade, localizes to synapses during developmental circuit refinement (*24*). C1q-tagging of the synapses leads to deposition of C3, which activates C3 receptors on microglia and triggers synaptic elimination by microglial phagocytosis (*15*, *24*). We found that C1q was present within microglia, colocalizing with PSD95 and CD68, a microglial lysosomal marker (Fig. 2C and movie S3). Furthermore, using brain sections from c-Fos-Cre^{ERT2}::Ai14 mice, in which engram cells were labeled with dTomato, we found colocalization of C1q with ~1.193 ± 0.335% of the dendritic spines of engram cells (Fig. 2, D and E, and movie S4) as well as colocalization of dTomato, PSD95, and CD68 within microglia (Fig. 2F and movie. S5). Correspondingly, engram cells showed higher spine density in PLX-treated animals (fig. S6).

To test whether complement pathways are responsible for microglia-mediated engram dissociation and forgetting, we constructed a Cre-dependent adeno-associated virus (AAV) vector expressing CD55 (also known as decay-accelerating factor, or DAF), which is a

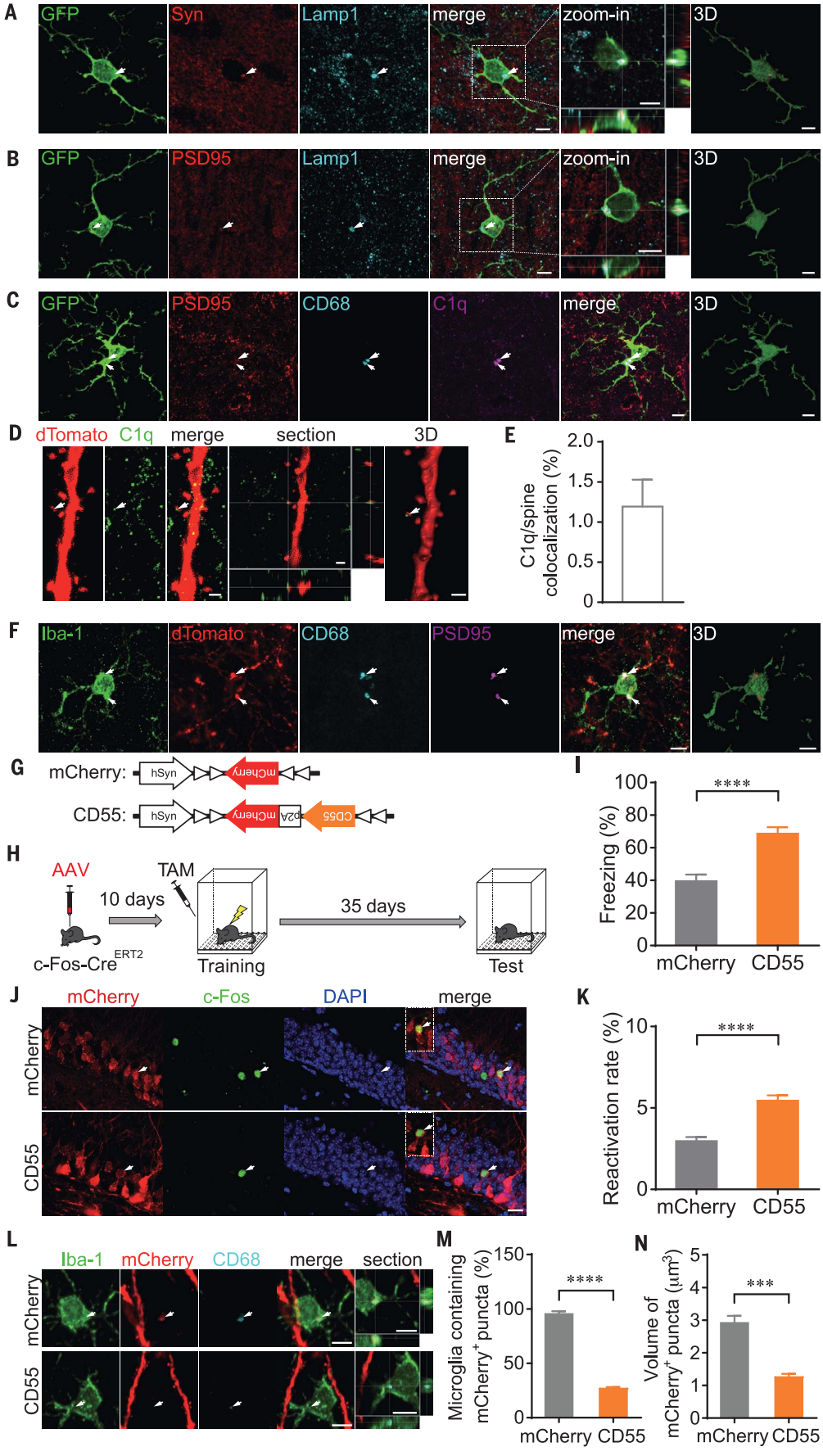

Fig. 2. Microglia mediate forgetting through complement system. (**A** and **B**) Superresolution microscopy images and three-dimensional (3D) reconstructions showing the presence of synaptophysin (Syn) or PSD95 in microglia (GFP^+), colocalizing with Lamp1, in the DG of $CX3CR1^{GFP/+}$ mice. Scale bars, 5 μm; white arrows indicate Syn^+Lamp1^+ (A) or $PSD95^+Lamp1^+$ (B) puncta within microglia. (**C**) Images and 3D reconstruction showing the presence of C1q and PSD95 in microglia, colocalizing with CD68. Scale bars, 5 μm; white arrows indicate $PSD95^+CD68^+C1q^+$ puncta within microglia. (**D**) Images and 3D reconstruction showing colocalization of C1q with a dendritic spine of an engram cell ($dTomato^+$) in the DG. Scale bars, 1 μm; white arrows indicate colocalization of C1q with a dendritic spine of an engram cell. (**E**) Percentage of engram cell dendritic spines showing colocalization with C1q. n = 3 mice, N = 76 dendritic segments. (**F**) Images and 3D reconstruction showing the presence of engram cell components ($dTomato^+$) in the microglia ($Iba\text{-}1^+$), colocalizing with PSD95 and CD68. Scale bars, 5 μm; white arrows indicate dTomato $^+CD68^+PSD95^+$ puncta within microglia. (**G**) Diagram of AAV vectors. (**H**) Experimental scheme for expressing CD55 in engram cells in the DG of c-Fos-Cre^{ERT2} mice. (**I**) CD55 animals showed higher freezing level. mCherry n = 21 mice, CD55 n = 17 mice; t = 5.033, df = 36, $^{****}P < 0.0001$. (**J**) Images showing engram cells labeled by mCherry or CD55 AAV vectors (red) in the DG and neurons activated during the test expressed by c-Fos (green). White arrows indicate reactivated engram cells ($mCherry^+c\text{-}Fos^+$). Insets show the colocalization of mCherry and c-Fos. Scale bar, 20 μm. (**K**) Reactivation rate of engram cells ($c\text{-}Fos^+mCherry^+/mCherry^+$) showed an increase in CD55 animals. n = 8 mice, CD55 n = 9 mice; t = 5.916, df = 15, $^{****}P < 0.0001$. (**L**) Images showing engram cell components ($mCherry^+$) colocalizing with CD68 in microglia ($Iba\text{-}1^+$) in mCherry mice, but not in CD55 animals. White arrows indicate $mCherry^+/CD68^+$ puncta in microglia. Scale bars, 5 μm; white arrows indicate $mCherry^+CD68^+$ (mCherry) puncta or $mCherry^-CD68^+$ (CD55) puncta in microglia. (**M**) Percentage of microglia containing $mCherry^+$ puncta decreased in CD55 mice. mCherry n = 3 mice, N = 36 cells; CD55 n = 4 mice, N = 34 cells; t = 24.16, df = 5, $^{****}P < 0.0001$. (**N**) CD55 expression in engram cells decreased the volume of $mCherry^+$ puncta in microglia containing $mCherry^+$ signals. mCherry n = 3 mice, N = 34 cells; CD55 n = 4 mice, N = 9 cells; t = 3.755, df = 41, $^{***}P = 0.0005$.

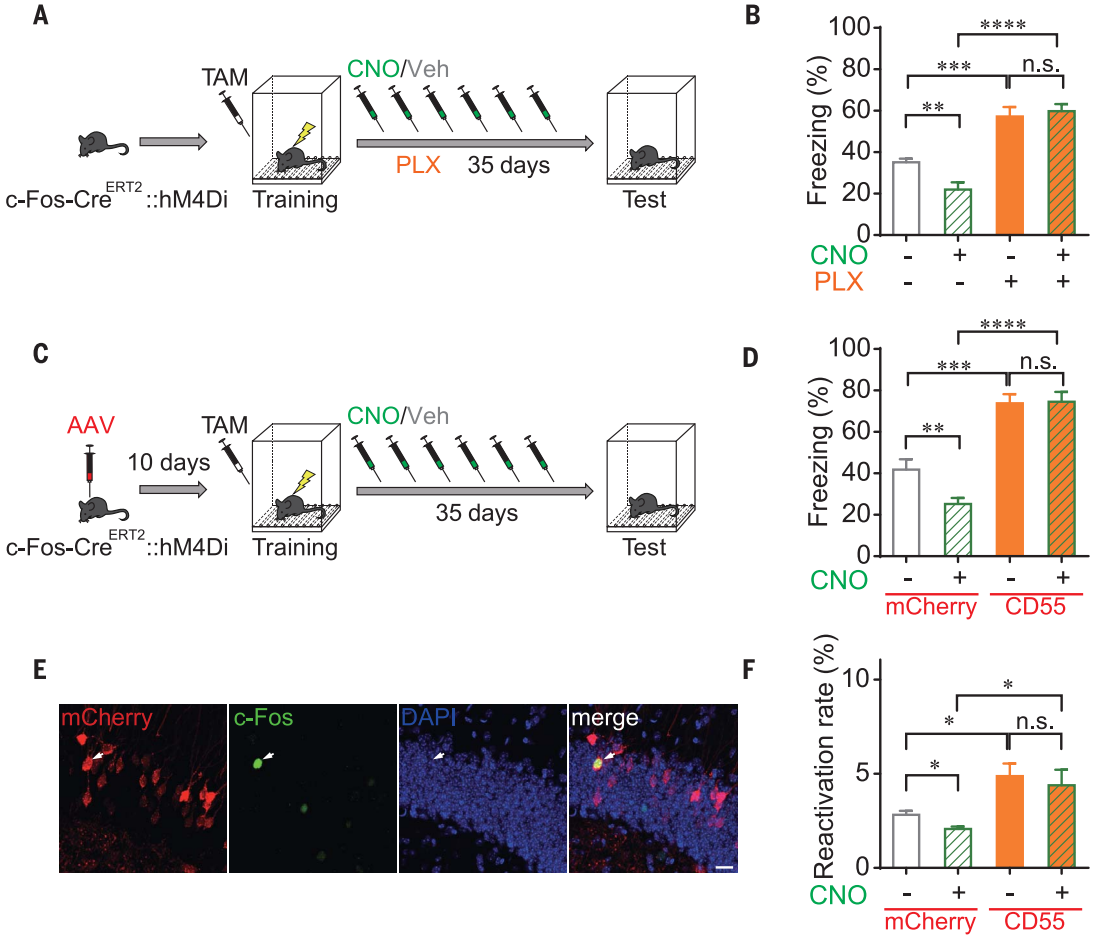

Fig. 3. Microglia mediate forgetting and dissociation of engram cells in an activity-dependent manner. (**A**) TAM was administered to c-Fos-Cre^{ERT2}::hM4Di mice before the last training. After training, animals were given food containing PLX and received daily injection of CNO or vehicle (Veh). (**B**) Freezing of animals during the test 35 days after training. CNO$^-$PLX$^-$ n = 10 mice, CNO$^+$PLX$^-$ n = 8 mice, CNO$^-$PLX$^+$ n = 7 mice, CNO$^+$PLX$^+$ n = 10 mice; CNO$^-$PLX$^-$ versus CNO$^+$PLX$^-$ t = 3.571, df = 16, $^{**}P$ = 0.0026; CNO$^-$PLX$^-$ versus CNO$^-$PLX$^+$ t = 5.068, df = 15, $^{***}P$ = 0.0001; CNO$^+$PLX$^-$ versus CNO$^+$PLX$^+$ t = 7.649, df = 16, $^{****}P$ < 0.0001; CNO$^-$PLX$^+$ versus CNO$^+$PLX$^+$ t = 0.4716, df = 15, P = 0.6440. (**C**) 10 days before CFC training, AAV vectors (mCherry: AAV-hSyn-DIO-mCherry; CD55: AAV-hSyn-DIO-CD55-p2A-mCherry) were injected into the DG of c-Fos-Cre^{ERT2}::hM4Di mice, and TAM was administered to the animals before the last training. After training, animals received injection of CNO or Veh every other day. (**D**) Freezing of animals during the test 35 days later. CNO$^-$mCherry n = 9 mice, CNO$^+$mCherry n = 12 mice, CNO$^-$CD55 n = 10 mice, CNO$^+$CD55 n = 12 mice; CNO$^-$mCherry versus CNO$^+$mCherry t = 3.035, df = 19, $^{**}P$ = 0.0068; CNO$^-$mCherry versus CNO$^-$CD55 t = 4.843, df = 17, $^{***}P$ = 0.0002; CNO$^+$mCherry versus CNO$^+$CD55 t = 8.823, df = 22, $^{****}P$ < 0.0001; CNO$^-$CD55 versus CNO$^+$CD55 t = 0.1057, df = 20, P = 0.9169. (**E**) Confocal images showing reactivated (c-Fos$^+$) engram cells (mCherry$^+$) in the DG during test. White arrows indicate an mCherry$^+$c-Fos$^+$ cell. Scale bar, 20 μm; white arrows indicate a reactivated engram cell in the DG (mCherry$^+$c-Fos$^+$). (**F**) CNO treatment decreased the reactivation rate of engram cells, (CNO$^-$mCherry n = 4 mice, CNO$^+$mCherry n = 4 mice, CNO$^-$CD55 n = 4 mice, CNO$^+$CD55 n = 5 mice; CNO$^-$mCherry versus CNO$^+$mCherry t = 2.937, df = 6, $^*P$ = 0.0260), whereas expression of CD55 in engram cells prevented the decrease of reactivation rate (CNO$^-$mCherry versus CNO$^-$CD55 t = 2.895, df = 6, $^*P$ = 0.0275; CNO$^+$mCherry versus CNO$^+$CD55 t = 2.435, df = 7, $^*P$ = 0.0451; CNO$^-$CD55 versus CNO$^+$CD55 t = 0.4375, df = 7, P = 0.6749).

known inhibitor of both classical and alternative complement pathways (*25*). We injected AAV-hSyn-DIO-CD55-p2A-mCherry (CD55) or AAV-hSyn-DIO-mCherry (mCherry) viruses into the DG of c-Fos-Cre^{ERT2} mice 10 days before CFC training, and TAM was administered before the last training to induce the expression of CD55 or mCherry only in DG engram neurons (Fig. 2, G and H, and fig. S7). Thirty-five days after training, mice in the CD55 group showed higher freezing (Fig. 2I) and a higher reactivation rate of engram cells (Fig. 2, J and K). Post hoc staining showed significantly fewer microglia containing mCherry$^+$ puncta (Fig. 2, L and M) and smaller mCherry$^+$ puncta within Iba-1$^+$ microglia in the CD55 group of animals (Fig. 2N).

Connectivity between engram cells is essential for memories (*26*), whereas microglia-dependent synaptic elimination preferentially targets weak or less-active synapses (*15*). We next examined whether microglia-mediated forgetting depends on the activity of engram neurons. We trained c-Fos-Cre^{ERT2}::hM4Di mice for contextual fear memory and administered TAM to induce the expression of inhibitory DREADD (designer receptors exclusively activated by designer drugs) receptor hM4Di in tagged engram cells. DREADD ligand clozapine-*N*-oxide (CNO) was administered every other day after CFC training to repetitively suppress the activity of tagged engram cells (Fig. 3A). Thirty-five days later, the animals treated with CNO alone exhibited significantly decreased freezing (Fig. 3B), whereas administration of PLX after training prevented the facilitated forgetting in CNO-treated animals (Fig. 3B).

To confirm this result, we injected AAV-hSyn-DIO-CD55-mCherry or AAV-hSyn-DIO-mCherry into the DG of c-Fos-Cre^{ERT2}::hM4Di mice and trained them for conditioned contextual fear memory. TAM was administered to express both hM4Di and CD55/mCherry in the engram cells (Fig. 3C). The animals treated with CNO alone showed reduced freezing (Fig. 3D) and decreased reactivation rate of labeled engram cells (Fig. 3, E and F). Expression of CD55 prevented the accelerated forgetting (Fig. 3D) and the decreased reactivation rate of engram cells induced by CNO-mediated DREADD inhibition of these cells (Fig. 3F).

In the hippocampal DG, newborn neurons are continuously generated and integrate into the hippocampal neural circuits. This leads to drastic synaptic reorganization and circuit rewiring (*7*, *27*, *28*) and the forgetting of hippocampus-dependent memories, especially during infanthood when massive neurogenesis is occurring within the DG (*6*). To investigate the relationship between microglia-mediated memory loss and neurogenesis-mediated forgetting, we enhanced neurogenesis in the DG of CX3CR1$^{GFP/+}$ mice by treating them with memantine (MEM), a pro-neurogenic drug

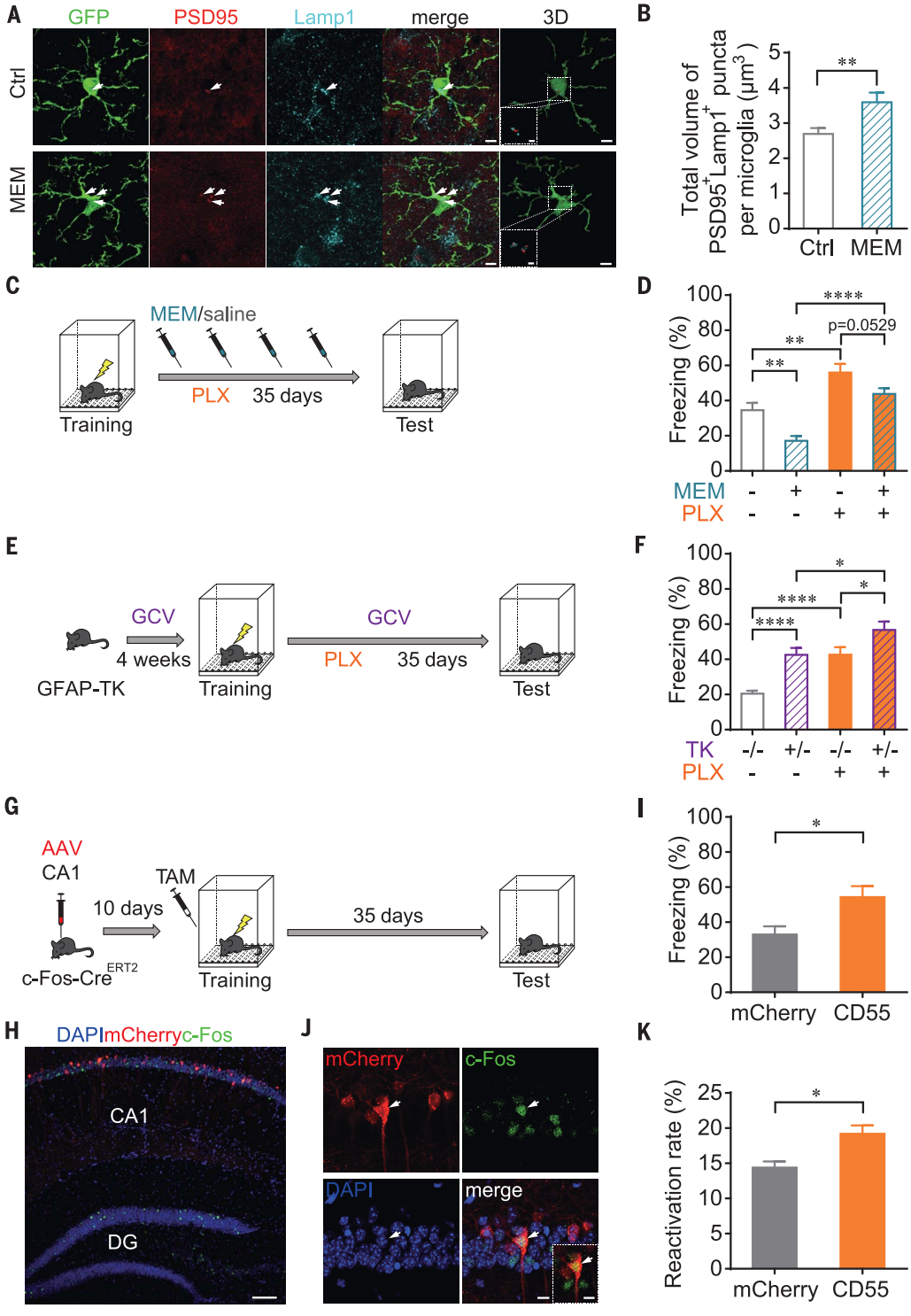

Fig. 4. Microglia contribute to both neurogenesis-mediated and non–neurogenesis-mediated forgetting. (**A**) Superresolution images and 3D reconstruction showing the PSD95^{+}Lamp1^{+} puncta in microglia in Ctrl and MEM-treated CX3CR1$^{GFP/+}$ mice. Scale bars, 5 μm; white arrows indicate PSD95^{+}Lamp1^{+} puncta in microglia. Insets are enlarged 3D reconstructions of PSD95^{+}Lamp1^{+} puncta in microglia. Scale bars, 2 μm. (**B**) MEM-treatment increased the volume of PSD95^{+}Lamp1^{+} puncta in each microglia. Ctrl n = 3 mice, N = 29 cells; MEM n = 3 mice, N = 30 cells; t = 2.774, df = 57, $^{**}P$ = 0.0075. (**C**) PLX and MEM treatment administered to mice. (**D**) Freezing of animals during the test 35 days after training. MEM^{-}PLX^{-} n = 10 mice, versus MEM^{+}PLX^{-} n = 10 mice, t = 3.511, df = 18, $^{**}P$ = 0.0025; MEM^{-}PLX^{-} versus MEM^{-}PLX^{+} n = 10 mice, t = 3.341, df = 18, $^{**}P$ = 0.0036; MEM^{+}PLX^{-} versus MEM^{+}PLX^{+} n = 10 mice, t = 6.277, df = 18, $^{****}P < 0.0001$; MEM^{-}PLX^{+} versus MEM^{+}PLX^{+} t = 2.072, df = 18, P = 0.0529. (**E**) GCV and PLX treatment administered to GFAP-TK$^{+/-}$ or GFAP-TK$^{-/-}$ mice. (**F**) Freezing during the test 35 days after training. TK$^{-/-}$PLX^{-} n = 14 mice versus TK$^{+/-}$PLX^{-} n = 14 mice, t = 5.181, df = 26, $^{****}P < 0.0001$; TK$^{-/-}$PLX^{-} versus TK$^{-/-}$PLX^{+} n = 14 mice, t = 4.895, df = 26, $^{****}P < 0.0001$; TK$^{+/-}$PLX^{-} versus TK$^{+/-}$PLX^{+} n = 13 mice, t = 2.333, df = 25, $^{*}P$ = 0.0280; TK$^{-/-}$PLX^{+} versus TK$^{+/-}$PLX^{+} t = 2.2426, df = 25, $^{*}P$ = 0.0341. (**G**) c-Fos-Cre^{ERT2} mice received AAV injection into CA1 and recovered for 10 days before CFC training. TAM was administered before the last training, and freezing was tested 35 days later. (**H**) Confocal image showing engram cells (mCherry^{+}) in CA1 but not in the DG. Scale bar, 100 μm. (**I**) CD55 animals showed higher freezing level. mCherry n = 11 mice, CD55 n = 11 mice; t = 2.728, df = 20, $^{*}P$ = 0.0130. (**J**) Confocal images showing the reactivation of engram cells in CA1. White arrows indicate a reactivated engram cell (mCherry^{+}c-Fos^{+}) in CA1. Inset shows the colocalization of mCherry and c-Fos; Scale bars, 20 μm. (**K**) Reactivation rate of engram cells in CA1 was increased in CD55 animals. mCherry n = 5 mice, CD55 n = 5 mice; t = 3.268, df = 8, $^{*}P$ = 0.0114.

(*6*), for 4 weeks. MEM-treatment significantly increased the number of DCX^{+} cells in the DG, indicating enhanced neurogenesis (fig. S8). We found significantly larger volumes of PSD95^{+}Lamp1^{+} puncta within microglia in MEM-treated animals (Fig. 4, A and B). Additionally, MEM treatment facilitated forgetting after CFC training (Fig. 4, C and D), whereas administering PLX blocked MEM-facilitated forgetting (Fig. 4D) without altering the enhanced neurogenesis by MEM (fig. S8).

To further investigate whether microglia also contribute to neurogenesis-unrelated forgetting, we used a GFAP-TK transgenic mouse line, which expresses herpes simplex virus thymidine kinase (TK) under the control of the glial fibrillary acidic protein (GFAP) promoter. Administration of the antiviral drug ganciclovir (GCV) ablates only mitotic GFAP^{+} cells that express TK, thus depleting neurogenesis (*29*). To completely deplete integration of new neurons, we started treating TK$^{+/-}$ mice and their wild-type littermates (TK$^{-/-}$) with GCV 4 weeks before CFC training and

continued until the test (Fig. 4E and fig. S9). PLX was administered after training to deplete microglia. GCV treatment in $TK^{+/-}$ mice prevented forgetting, whereas $TK^{+/-}$ mice treated with both PLX and GCV showed significantly higher levels of memory retention than $TK^{+/-}$ mice treated with GCV only (Fig. 4F).

To confirm that microglia-mediated forgetting contributes to neurogenesis-unrelated forgetting, we injected AAV-DIO-CD55-mCherry or AAV-DIO-mCherry into c-Fos-Cre^{ERT2} mice to label engram cells in hippocampal CA1 (Fig. 4, G and H), which is not a neurogenic region. We found that expression of CD55 in CA1 engram cells also prevented forgetting (Fig. 4I) and dissociation of engram cells (Fig. 4, J and K).

Synaptic connections in the brain are highly dynamic and variable in strength and connectivity (*14*). Our study shows that microglia eliminate synaptic components in the adult hippocampus, whereas depleting microglia or inhibiting phagocytosis of microglia prevents forgetting. This suggests that synapse elimination by microglia leads to dissociation of engrams and the forgetting of previously learned contextual fear memory. In the developing brain, microglial engulfment of synapses depends on the classical complement cascade (*15*). Disruption of the microglia-specific phagocytic pathway by knocking out complement components, such as C1q, C3, or CR3, results in sustained deficits in synaptic connectivity (*15*, *24*). C1q levels in the brain increase during aging, whereas C1q-deficient mice exhibit enhanced synaptic plasticity and less cognitive and memory decline when aged (*30*). Notably, our study showed that the C1q-dependent complement pathway is actively involved in synapse elimination by microglia in the healthy adult hippocampus. CD55 is a known inhibitor of complement pathways in the immune system and is expressed in neurons in response to chronic inflammation (*31*). We overexpressed CD55 to inhibit the complement pathways, specifically in engram cells, without affecting microglia or other neurons in the circuits, and we found that forgetting was prevented. This indicates that the elimination of synaptic structures by microglia in the DG of the healthy adult brain occurs in a complement-dependent manner. Moreover, inhibiting the activity of engram cells facilitates the forgetting of related memory, which could be blocked by depleting microglia or inhibiting complement pathways in engram cells. This indicates that synapse elimination by microglia is also activity-dependent, following similar rules in the developing brain (*15*), thus resulting in the erasure of less-active memories. Besides eliminating synapses, microglia have also been reported to be able to trigger long-term synaptic depression via AMPA receptor internalization, through activation of CR3 (*32*), which may also contribute to forgetting.

New neurons are continuously generated in the DG, providing a substrate for massive synaptic reorganization and circuit rewiring in this region. Newborn dentate granule neurons integrate into hippocampal neural circuits by competitively replacing existing synaptic connections formed by mature granule neurons (*7*, *27*), thus leading to the forgetting of hippocampal-dependent contextual fear memory (*6*). Our study shows that MEM-induced enhanced neurogenesis leads to increased synaptic engulfment by microglia, whereas depletion of microglia blocks facilitated memory forgetting induced by enhanced neurogenesis, suggesting that microglia contribute to neurogenesis-induced synaptic reorganization. Besides the rewiring of neural circuits caused by the continuous integration of newborn neurons, mature neurons are also able to reorganize their connectivity. We found that depletion of microglia in the DG without neurogenesis or inhibition of complement pathways in CA1 engram cells prevents forgetting. This indicates that microglia-mediated synaptic reorganization is also happening in mature hippocampal neurons, thus leading to weakening or loss of connections between engram cells and the forgetting of encoded memories. This also suggests that, in species lacking adult neurogenesis, or in non-neurogenic brain regions such as the cortex, microglia could be one major force contributing to synapse loss and forgetting.

REFERENCES AND NOTES

1. J. H. Han *et al*., *Science* **316**, 457–460 (2007).
2. S. A. Josselyn, S. Köhler, P. W. Frankland, *Nat. Rev. Neurosci.* **16**, 521–534 (2015).
3. S. Tonegawa, M. Pignatelli, D. S. Roy, T. J. Ryan, *Curr. Opin. Neurobiol.* **35**, 101–109 (2015).
4. S. B. Hofer, T. D. Mrsic-Flogel, T. Bonhoeffer, M. Hübener, *Nature* **457**, 313–317 (2009).
5. G. Yang, F. Pan, W. B. Gan, *Nature* **462**, 920–924 (2009).
6. K. G. Akers *et al*., *Science* **344**, 598–602 (2014).
7. N. Toni, A. F. Schinder, *Cold Spring Harb. Perspect. Biol.* **8**, a018903 (2015).
8. P. W. Frankland, S. Köhler, S. A. Josselyn, *Trends Neurosci.* **36**, 497–503 (2013).
9. M. Fu, Y. Zuo, *Trends Neurosci.* **34**, 177–187 (2011).
10. D. Tropea, A. K. Majewska, R. Garcia, M. Sur, *J. Neurosci.* **30**, 11086–11095 (2010).
11. J. T. Trachtenberg *et al*., *Nature* **420**, 788–794 (2002).
12. J. E. Coleman *et al*., *J. Neurosci.* **30**, 9670–9682 (2010).
13. A. Attardo, J. E. Fitzgerald, M. J. Schnitzer, *Nature* **523**, 592–596 (2015).
14. Y. Wu, L. Dissing-Olesen, B. A. MacVicar, B. Stevens, *Trends Immunol.* **36**, 605–613 (2015).
15. D. P. Schafer *et al*., *Neuron* **74**, 691–705 (2012).
16. R. C. Paolicelli *et al*., *Science* **333**, 1456–1458 (2011).
17. M. E. Tremblay, R. L. Lowery, A. K. Majewska, *PLOS Biol.* **8**, e1000527 (2010).
18. C. Madry *et al*., *Neuron.* **97**, 299–312.e6 (2018).
19. H. Wake, A. J. Moorhouse, S. Jinno, S. Kohsaka, J. Nabekura, *J. Neurosci.* **29**, 3974–3980 (2009).
20. M. Prinz, J. Priller, S. S. Sisodia, R. M. Ransohoff, *Nat. Neurosci.* **14**, 1227–1235 (2011).
21. R. A. Rice *et al*., *J. Neurosci.* **35**, 9977–9989 (2015).
22. C. J. Guenthner, K. Miyamichi, H. H. Yang, H. C. Heller, L. Luo, *Neuron* **78**, 773–784 (2013).
23. C. M. Sellgren *et al*., *Nat. Neurosci.* **22**, 374–385 (2019).
24. B. Stevens *et al*., *Cell* **131**, 1164–1178 (2007).
25. A. Nicholson-Weller, C. E. Wang, *J. Lab. Clin. Med.* **123**, 485–491 (1994).
26. M. M. Poo *et al*., *BMC Biol.* **14**, 40 (2016).
27. N. Toni *et al*., *Nat. Neurosci.* **10**, 727–734 (2007).
28. N. Toni *et al*., *Nat. Neurosci.* **11**, 901–907 (2008).
29. J. S. Snyder, A. Soumier, M. Brewer, J. Pickel, H. A. Cameron, *Nature* **476**, 458–461 (2011).
30. A. H. Stephan *et al*., *J. Neurosci.* **33**, 13460–13474 (2013).
31. J. van Beek *et al*., *J. Immunol.* **174**, 2353–2365 (2005).
32. J. Zhang *et al*., *Neuron* **82**, 195–207 (2014).

ACKNOWLEDGMENTS

We thank all the members of the Y.G. and La.W. laboratories for the discussion and constructive suggestions for this project. We thank P. Frankland for his critical comments. We are grateful to the Core Facilities of Zhejiang University School of Medicine for technical assistance. **Funding:** This work was supported by grants from the National Key R&D Program of China (2017YFA0104200), the Zhejiang Provincial Natural Science Foundation of China (LR17C090001) to Y.G., the National Natural Science Foundation of China (31700888) to La.W., and the Natural Science Foundation of Zhejiang Province (LZ19C090001) to B.S. **Author contributions:** C.W., H.Y., La.W., and Y.G. designed all of the experiments; C.W. performed all behavior tests, imaging, and most of the analysis; H.Y. performed vector constructions, viral injections, and some imaging; Z.H. and Y.S. performed some image analysis; J.M. and J.L. helped in genotyping some animals; X.-D.W. provided c-Fos-Cre^{ERT2} and hM4Di mice; Li.W. provided Ai14 mice; B.S. provided GFAP-TK mice; P.S. provided $CX3CR1^{GFP/+}$ and CD11b-DTR mice; C.W., H.Y., La.W., and Y.G. discussed the results and wrote the manuscript; and all authors discussed the manuscript. **Competing interests:** The authors declare no competing interests. **Data and materials availability:** All data needed to understand and assess the conclusions of this study are included in the text, figures, and the supplementary materials.

SUPPLEMENTARY MATERIALS

science.sciencemag.org/content/367/6478/688/suppl/DC1
Materials and Methods
Figs. S1 to S9
References (*33*, *34*)
Movies S1 to S5

View/request a protocol for this paper from *Bio-protocol*.

27 August 2019; accepted 6 January 2020
10.1126/science.aaz2288

PHASE SEPARATION

Valence and patterning of aromatic residues determine the phase behavior of prion-like domains

Erik W. Martin[1]*, Alex S. Holehouse[2,3]*, Ivan Peran[1]*, Mina Farag[2,3], J. Jeremias Incicco[4], Anne Bremer[1], Christy R. Grace[1], Andrea Soranno[3,4], Rohit V. Pappu[2,3]†, Tanja Mittag[1]†

Prion-like domains (PLDs) can drive liquid-liquid phase separation (LLPS) in cells. Using an integrative biophysical approach that includes nuclear magnetic resonance spectroscopy, small-angle x-ray scattering, and multiscale simulations, we have uncovered sequence features that determine the overall phase behavior of PLDs. We show that the numbers (valence) of aromatic residues in PLDs determine the extent of temperature-dependent compaction of individual molecules in dilute solutions. The valence of aromatic residues also determines full binodals that quantify concentrations of PLDs within coexisting dilute and dense phases as a function of temperature. We also show that uniform patterning of aromatic residues is a sequence feature that promotes LLPS while inhibiting aggregation. Our findings lead to the development of a numerical stickers-and-spacers model that enables predictions of full binodals of PLDs from their sequences.

Membraneless biomolecular condensates coordinate a variety of cellular processes such as stress responses (*1*–*3*), RNA splicing (*4*), mitosis (*5*), chromatin organization (*6*, *7*), and the clustering of receptors at membranes (*8*). Several condensates form through reversible phase transitions that are driven by key protein and RNA molecules (*9*, *10*). Multivalence (i.e., the number) of interaction domains or motifs is a defining hallmark of proteins that drive phase transitions (*9*). Many of these proteins encompass intrinsically disordered prion-like domains (PLDs) that are often necessary and sufficient for driving intracellular phase transitions (*3*, *11*). PLDs have distinctive amino acid compositions: They are enriched in polar amino acids and are often punctuated by aromatic residues (*12*). There have been various explanations for how aromatic residues and other polar moieties contribute to phase transitions of PLDs (*13*, *14*). Models based on high-resolution structural studies of hydrogels formed by PLDs suggest that the formation of β-sheeted structural motifs is obligatory for driving phase transitions in PLDs (*15*–*17*), whereas other experiments do not detect ordered structures in dense phases (*18*, *19*).

PLDs can be described using a stickers-and-spacers framework adapted from the field of associative polymers (*20*, *21*). These systems are characterized by noncovalent, intra- and intermolecular cross-links between stickers, whereas spacers either enable or suppress the formation of these cross-links (*20*, *22*, *23*). Above a threshold concentration known as the percolation threshold, the formation of a criticial number of intermolecular cross-links leads to the emergence of system-spanning networks (*22*, *24*). The percolation threshold can be predicted from knowledge of the number of complementary stickers (*21*). If percolation is a cooperative process, then it is driven by a density transition known as phase separation (*23*). In this scenario, the percolation threshold becomes a suitable proxy for the saturation concentration, defined as the threshold concentration for phase separation (*21*). The cooperativity of percolation and phase separation gives rise to dense-phase condensates that are akin to viscoelastic network fluids (*25*) in which individual molecules are incorporated into condensate-spanning networks within dense phases that coexist with non-percolated dilute solutions (*23*). In the interest of brevity, we shall refer to the combination of percolation and phase separation as liquid-liquid phase separation (LLPS).

Stickers can be patches on folded domains or sequence motifs within disordered regions that can be as small as individual residues (*23*). Spacers are residues that are interspersed between stickers (*25*). Previous studies identified arginine and tyrosine as stickers in FUS and other FET family proteins. An analytical model shows that the saturation concentrations of these proteins are inversely proportional to the product of the numbers of arginine and tyrosine residues in a given sequence (*21*). Although this is useful, a complete characterization of sequence-encoded driving forces for phase transitions requires knowledge of coexistence curves (binodals) of PLDs. Binodals quantify the dilute and dense phase concentrations as a function of temperature or other control variables. This allows us to predict how condensates spontaneously form and dissolve in response to changes to protein concentrations and solution conditions. In this work, we combined a multipronged experimental and computational approach to develop a predictive stickers-and-spacers model for constructing sequence-specific binodals. In doing so, we developed a protocol to identify stickers in an unbiased manner. Furthermore, we quantified how the sticker valence (number), patterning (relative positions along the sequence), and interaction strengths contribute to sequence-specific binodals with a numerical stickers-and-spacers model. Our work is focused on the archetypal PLD or low-complexity domain (LCD) from heterogeneous nuclear ribonucleoprotein A1 (hnRNPA1) (A1-LCD) (Fig. 1A and fig. S1), which shares sequence features with PLDs from an assortment of RNA-binding proteins (*21*).

Analysis of conformational ensembles in dilute solutions allowed us to identify putative stickers within the A1-LCD. First, we used nuclear magnetic resonance (NMR) spectroscopy to interrogate the conformational ensembles of monomeric forms of A1-LCD. To minimize artifacts due to aggregation, we used an A1-LCD construct from which a hexapeptide that acts as a steric zipper (residues 259 to 264) was removed (*26*). The ^{1}H-^{15}N heteronuclear single-quantum coherence (HSQC) spectrum of this A1-LCD construct displays the characteristic narrow proton chemical shift dispersion of disordered proteins (Fig. 1B). Resonance assignment (fig. S2A) and the experimental C^{α} and C^{β} chemical shifts demonstrate that the A1-LCD does not form a persistent secondary structure (fig. S2B).

Next, we used size exclusion chromatography–coupled small-angle x-ray scattering (SEC-SAXS) measurements to quantify the dimensions of monomeric A1-LCD in dilute solutions. We also used all-atom simulations based on the ABSINTH implicit solvation model and forcefield paradigm (*27*) to generate ensembles of conformations of the A1-LCD. For flexible polymers in the long-chain limit, the radii of gyration (R_g) may be quantified as: $R_g(T) = R_0(T)N^{\nu(T)}$, where N is the number of repeating units and the prefactor, $R_0(T)$, is determined by the temperature (T)–dependent excluded volume per residue, the average size of each residue, and the thickness of the chain (*28*). The temperature-dependent solvent quality is characterized by the exponent ν, which takes on limiting values of 0.33 and 0.59 well below and well above the theta temperature T_θ, where ν = 0.5 because polymer-solvent and intrapolymer interactions counterbalance one another. Polymer-solvent interactions are favored above T_θ, whereas intrapolymer interactions are favored below T_θ (*12*). For systems that undergo continuous globule-to-coil transitions, ν takes on values between 0.33 and 0.5 corresponding to the crossover regime between the poor and theta solvent limits (*29*).

[1]Department of Structural Biology, St. Jude Children's Research Hospital, 262 Danny Thomas Place, Memphis, TN 38105, USA. [2]Department of Biomedical Engineering, Washington University in St. Louis, St. Louis, MO 63130, USA. [3]Center for Science & Engineering of Living Systems (CSELS), Washington University in St. Louis, St. Louis, MO 63130, USA. [4]Department of Biochemistry and Molecular Biophysics, Washington University School of Medicine, St. Louis, MO 63110, USA.
*These authors contributed equally to this work.
†Corresponding author. Email: pappu@wustl.edu (R.V.P.); tanja.mittag@stjude.org (T.M.)

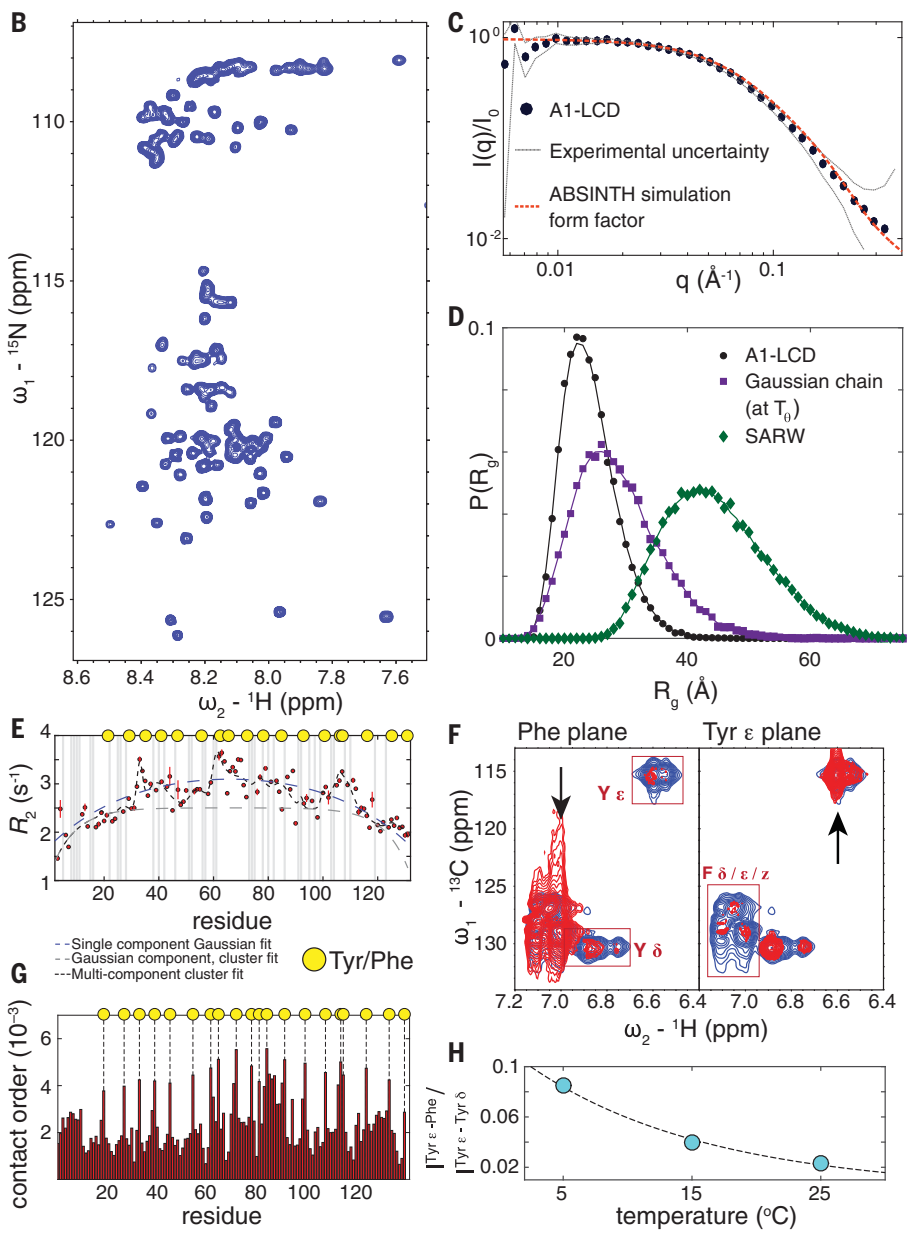

Fig. 1. Aromatic residues are the stickers in the PLD derived from hnRNPA1. (**A**) The sequence of the PLD or LCD from hnRNPA1 (A1-LCD); aromatic residues are indicated in orange. (**B**) ^{1}H-^{15}N HSQC spectrum recorded at 800 MHz and 25°C in pH 6 MES buffer. For assignments see fig. S2A. ω, chemical shift; ppm, parts per million. (**C**) SEC-SAXS data for A1-LCD. Calculated scattering profiles from simulated ensembles are overlaid in red. $I(q)/I_0$, scattering intensity normalized by zero-angle scattering; q, the momentum transfer vector, which is related to scattering angle. (**D**) R_g distribution from all-atom simulations of A1-LCD (black) versus Gaussian chain (violet) and self-avoiding random walk (SARW, green) reference states. P(R_g), probability density distribution of R_g. (**E**) ^{15}N amide transverse (R_2) relaxation rates recorded at 800 MHz and 25°C. Overlaid are fits to the data assuming a pure Gaussian-like profile (blue dashed line) or multiple regions of enhanced relaxation centered at aromatic residues (black dashed line) and the underlying Gaussian-like profile from this fit (gray dashed line) with a persistence length of 7.8 amino acid residues. The yellow circles indicate the positions of the aromatic residues. Gray bars indicate positions for which data were not analyzed owing to unresolvable overlap in 2D spectra. Monte Carlo sampling of the location of group centers shows a clear positive correlation between the quality of fit and positions of aromatic amino acids within the sequence (fig. S5A). (**F**) ^{13}C-^{1}H planes from the aromatic-edited 3D NOESY (red) recorded at 800 MHz and 25°C. Planes correspond to the Phe ^{1}Hδ/ε/ζ (left) and Tyr ^{1}Hε (right) frequencies and their corresponding diagonal signals are indicated by arrows. In both planes, red boxes show signals at Tyr ^{1}Hδ/^{1}Hε (left) and Phe (right), which exist in this plane only because of NOE transfer. The ^{1}H,^{13}C-HSQC aromatic region is shown superimposed in blue. [For NOEs in a A1-LCD variant with uniformly spaced aromatic residues (Aro^{Perfect}), see fig. S5, E and F.] (**G**) Contact order from simulations. The dashed lines and yellow circles indicate the positions of all aromatic amino acids. (**H**) Normalized intensity of Tyr-Phe NOEs as a function of temperature. The Tyr ^{1}Hε–Phe NOE is displayed normalized to the Tyr ^{1}Hδ–^{1}Hε NOE of fixed distance at 5°, 15°, and 25°C. The dashed line is a power-law fit. Single-letter abbreviations for the amino acid residues are as follows: A, Ala; D, Asp; F, Phe; G, Gly; K, Lys; M, Met; N, Asn; P, Pro; Q, Gln; R, Arg; S, Ser; and Y, Tyr.

SEC-SAXS experiments provided a direct measurement of the global dimensions of the A1-LCD (Fig. 1C). Guinier transformation of the SAXS data yields an ensemble-averaged R_g value of 26.1 ± 1.1 Å (fig. S3). We extracted an apparent scaling exponent of ν^{app} = 0.45 from the experimental scattering data by fitting to an empirically derived molecular form factor (MFF) (*30*) (fig. S3). Results from all-atom simulations agree with data from SEC-SAXS experiments (Fig. 1C and fig. S4). The distribution of R_g values obtained for the A1-LCD from all-atom simulations (movie S1) is biased toward compact conformations when compared with those of self-avoiding random walks and polymers at their theta temperatures (Fig. 1D). These analyses lead us to conclude that the A1-LCD adopts ensembles that lie in the crossover regime between poor and theta solvents.

We used NMR spectroscopy to uncover the putative stickers that determine the features of the conformational ensembles of the A1-LCD. NMR transverse relaxation rates (R_2) are sensitive to internal motions slower than the rotational correlation time and can be used to identify regions of restricted motion. Fitting the experimentally measured R_2 rates as a function of sequence position within the A1-LCD to a simple Gaussian chain model requires the use of unrealistic values for the persistence length (Fig. 1E). This suggests that groups of residues have enhanced relaxation. Allowing groups of enhanced R_2 rates along the sequence gave good agreement with the experimental data using values for the persistence length that are in line with those reported previously for denatured proteins (*31*). Fixing the group centers at aromatic residues results

in a qualitatively good fit to the R_2 profile. The R_2 profiles are largely concentration-independent (fig. S5B), suggesting that the observed R_2 rates are dominated by intramolecular interactions. Such interactions were directly observed as nuclear Overhauser effects (NOEs) between phenylalanine and tyrosine side chains in a three-dimensional (3D) aromatic-edited NOESY (NOE spectroscopy) spectrum (Fig. 1F and fig. S5, C to F). These types of long-range NOEs are not typically observed in disordered regions in the absence of well-defined secondary and tertiary structures (*32*, *33*). Given the absence of a persistent secondary or tertiary structure, we interpreted the NOEs to be evidence of transient clustering among aromatic residues, identifying them as the putative stickers in this sequence.

Next, we analyzed the simulated conformational ensembles to quantify the patterns of intramolecular interactions. In accordance with the NMR data (fig. S2B), the ensembles show weak preferences for persistent secondary structure (fig. S6A) and are characterized by interactions among networks of aromatic residues that are distributed along the chain (fig. S6B). Analysis of the contact order shows that many spikes are found at the positions coincident with aromatic residues (Fig. 1G). In addition, we calculated normalized distance maps, which quantify the average distance between pairs of residues normalized by the distance expected in a Gaussian chain. The distance map displays a checkerboard pattern, with pronounced spatial clustering of residues at the C terminus (fig. S6C). The observed pattern of distances indicates that the intramolecular contacts primarily involve aromatic residues, and these are indeed the stickers along the A1-LCD. Charged and polar residues interspersed between stickers do not display strong interaction patterns but instead act as spacers that mediate the contacts among stickers.

The A1-LCD undergoes phase separation with an upper critical solution temperature (*3*). Given the well-known coupling between the driving forces for phase separation and the determinants of single-chain dimensions (*34*), we inferred that the contraction of individual A1-LCD molecules in dilute solutions should be temperature dependent. Indeed, NOEs between aromatic residues measured as a function of temperature increased in magnitude when the temperature was lowered (Fig. 1H and fig. S5F). The increase in intensity is clearly visualized when the intensity of the NOE between Tyr ^{1}Hε and Phe protons (which have distinct resonance frequencies) is normalized by the ^{1}Hε-^{1}Hδ NOE within Tyr residues. This is suggestive of the intersticker interactions becoming stronger as temperature decreases, and this in turn promotes compaction as temperature is lowered. The temperature dependence of the interaction strength and protein size is also manifest in the R_2 relaxation profiles (fig. S7A) and in the translational diffusion coefficients determined from pulsed field gradient NMR diffusion experiments (fig. S7B).

Our results identify aromatic residues that are distributed along the sequence of A1-LCD as the stickers. To test the accuracy of our inferences regarding the identities of the stickers, we designed variants to quantify how R_g changes with changes to the number (valence) of aromatic residues (Fig. 2A). All-atom simulations indicate a systematic chain expansion that accompanies a decrease in the valence of aromatic residues (variants Aro$^-$ and Aro^{--}) and further compaction when the valence of aromatic residues increases beyond the wild-type (WT) A1-LCD (variant Aro$^+$) (Fig. 2B). SEC-SAXS measurements of the three variants confirm the simulation results (fig. S8); the dependence of the mean R_g and ν^{app} values on the valence of aromatic residues shows that they provide the cohesive interactions that drive chain contraction (Fig. 2C). Similarly, comparing normalized Kratky plots confirms the dependence of chain contraction and expansion on the valence of aromatic residues (stickers) (Fig. 2D).

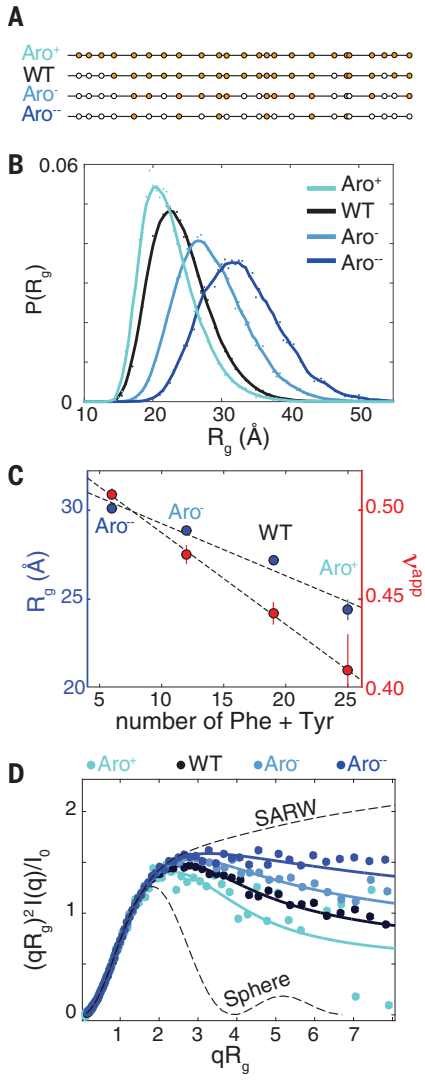

Fig. 2. Sticker valence directly determines the single-chain behavior of the A1-LCD. (**A**) Schematic showing the position of aromatic residues indicated as circles, where orange and white reflect the presence and absence of aromatic residues, respectively. (**B**) The R_g distributions from all-atom simulations of A1-LCD variants. (**C**) Values of R_g (blue) and ν^{app} (red) derived from the MFF fits in (D). Dashed lines are the lines of best fit through the four points. (**D**) Raw SEC-SAXS data in normalized Kratky representation (logarithmically smoothed into 60 bins). Solid lines are fits to an empirical MFF (*30*). The MFFs for a SARW and a solid sphere are overlaid as dashed lines.

Guided by our observations at the single-chain level, we developed a model for the phase behavior of A1-LCD using a lattice-based coarse-grained description that uses a single bead per residue. In this model, the sticker beads correspond to the aromatic residues, whereas the spacer beads correspond to the nonaromatic residues (Fig. 3A). We generated a single model by parameterizing the strengths of the sticker-sticker, sticker-spacer, and spacer-spacer interactions to reproduce the average R_g values from SEC-SAXS measurements and the R_g distributions obtained from all-atom simulations for the WT and three variant A1-LCD sequences. Simulations using a single, parameterized stickers-and-spacers lattice model reproduced the results obtained from all-atom simulations and SAXS experiments (Fig. 3B).

We used the parameterized stickers-and-spacers lattice model to perform Monte Carlo simulations of hundreds of polymers to quantify phase behavior as a function of simulation temperature that modulates the sticker-sticker, sticker-spacer, and spacer-spacer interaction strengths that are referenced to k_BT, where k_B is the Boltzmann constant and T is temperature. Interaction strengths are inversely proportional to simulation temperature. Simulations of different variants reveal that phase separation occurs in a sequence-, concentration-, and temperature-dependent manner (fig. S9 and movies S2 to S4; note that no phase separation was observed for Aro^{--} at this simulation temperature). Computed binodals are shown in terms of simulation temperatures (in units of k_BT) and volume fractions for the WT A1-LCD, Aro$^-$, Aro^{--}, and Aro$^+$ variants in fig. S10. As the valence of stickers decreases, the location of the low-concentration arm of the binodals shifts to the right, lowering the critical temperature and reducing the overall width of the two-phase regime. By contrast, if the valence of aromatic residues is increased, the opposite changes occur. Accordingly, calculated binodals directly link the valence of aromatic stickers to the phase behavior of A1-LCD and its designed variants.

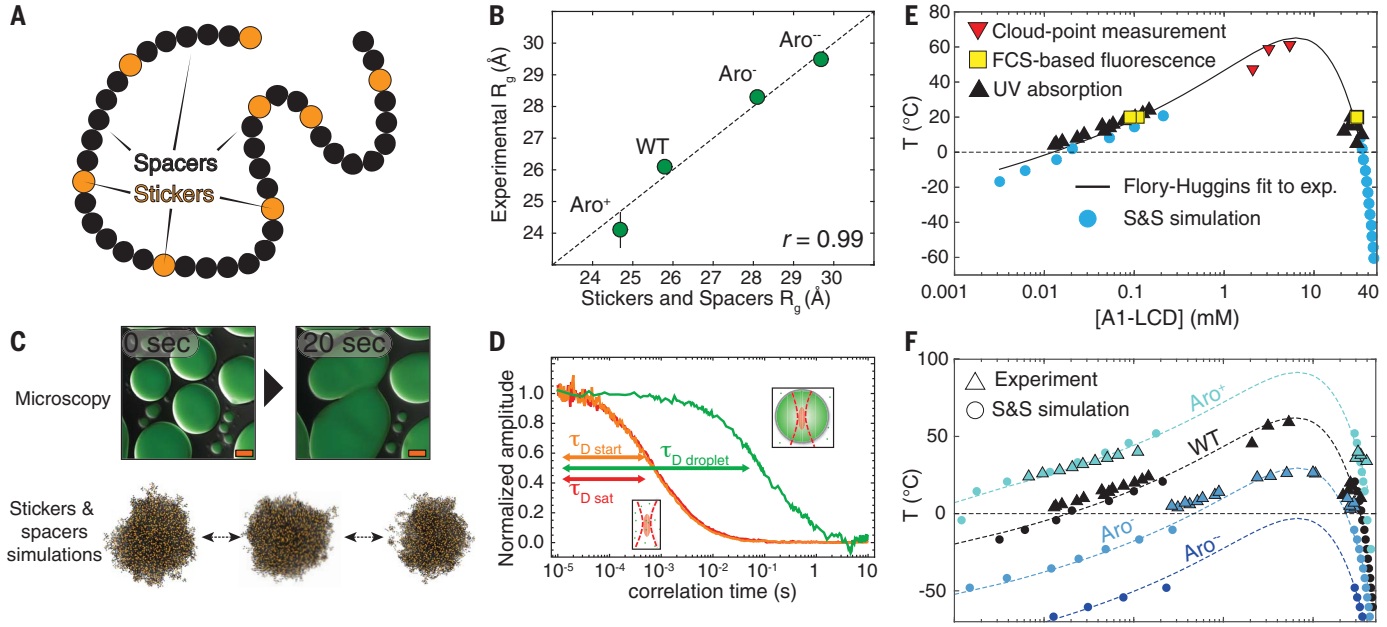

Fig. 3. Sticker valence directly determines the phase behavior of the A1-LCD. (**A**) Schematic representation of the stickers-and-spacers model. (**B**) Correlation between R_g from coarse-grained stickers-and-spacers simulations with values obtained from SEC-SAXS. Error bars, which indicate the quality of fit to the MFF (Fig. 2D), are shown if greater than marker size. (**C**) Overlaid differential interference contrast (DIC) and fluorescence images of LCD droplets fusing over the course of 20 s (see movie S5) (top). The scale bar represents 50 μm. Snapshots from lattice-based stickers-and-spacers simulations (bottom) are shown. (**D**) Amplitude-normalized FCS curves for WT A1-LCD before phase separation (orange) and in the dilute (red) and dense (green) phases. τ_D, the fluorescence decorrelation time. (**E**) Complete binodal for the WT A1-LCD computed from the lattice-based stickers-and-spacers (S&S) simulations (circles) and three different types of experiments: centrifugation followed by ultraviolet (UV) absorbance (triangles), cloud point (inverted triangles), and FCS or fluorescence intensity (squares) (see figs. S11, B and C, and S12). The solid line is a fit from Flory-Huggins theory to the experimental UV absorbance data. (**F**) Complete binodals as presented in (E) for the Aro^+, WT [shown in (E)], and Aro^- variants. For Aro^{--}, the binodal is from simulations that use the lattice-based stickers-and-spacers model (solid circles) and fits based on Flory-Huggins theory to simulation results. (**G**) The correlation between the experimentally reported saturation concentrations and those calculated by stickers-and-spacers simulations for WT and three FUS variants with deleted RACs. (*37*). *r*, Pearson correlation coefficient.

To test the predictions from the lattice-based stickers-and-spacers model, we performed in vitro experiments to quantify the temperature-dependent phase behavior of the A1-LCD and designed variants. Monitoring the temperature-dependent, reversible phase separation of the A1-LCD (fig. S11A) provided the basis for accurate mapping of full binodals. Fluorescence microscopy of a small proportion of labeled A1-LCD in the presence of unlabeled A1-LCD showed droplets that diffuse and fuse to form larger droplets (Fig. 3C and movie S5), providing evidence for LLPS. We used fluorescence correlation spectroscopy (FCS) to probe the mobility of protein molecules inside and outside the droplets (Fig. 3D). The increase in the correlation time of the protein molecules reflects the viscosity increase due to the concentration (fig. S11B). Amplitudes of the correlation curve, as well as the fluorescence intensities, allowed us to determine the concentrations and the molecular brightness of the diffusing species in the coexisting dilute and dense phases (Fig. 3E and fig. S11, C to F). The concentration of A1-LCD in its dense phase is approximately three orders of magnitude larger than its concentration in the dilute phase (Fig. 3E and table S1). Analysis of the brightness of the diffusing species indicates that A1-LCD molecules within the droplet are freely diffusing monomers.

Next, we obtained experimentally derived binodals, achieved for only a small number of disordered LCDs (*18*, *35*), by measuring the concentrations (c) within coexisting dilute and dense phases as a function of temperature (Fig. 3, E and F). For WT, Aro^-, and Aro^+ variants, coexistence points in the (T,c) space were mapped to quantify the locations of the dilute and dense phase arms of binodals (Fig. 3F and fig. S12A). To locate the critical point, we fit the measured binodals using a modified Flory-Huggins model for phase separation that includes two- and three-body interaction coefficients (*36*) to estimate the critical temperatures (T_c) for each system. The quality of the fits shown in Fig. 3E for the WT A1-LCD and in Fig. 3F for Aro^- and Aro^+ suggest that the PLDs can be approximated as effective homopolymers. Using the predicted values for T_c as a guide, we measured coexistence points close to the predicted critical temperatures using a cloud-point assay (see fig. S12, B and C) and found the predicted values (for WT A1-LCD and Aro^-) to be within a few degrees of the measured values (Fig. 3, E and F).

The measured binodals of WT A1-LCD were also fit to data from simulations that use the lattice-based stickers-and-spacers model (Fig. 3, E and F). Fits to the experimental data for the WT A1-LCD were used to rescale the simulation temperature to units of degrees Celsius (Fig. 3E) and to convert concentrations from volume fractions into molar units. This allowed us to compare calculated binodals for the WT, Aro^-, and Aro^+ sequences to the binodals extracted from experiments (Fig. 3F). These comparisons highlight the phenomenological accuracy of the stickers-and-spacers model. We also calculated the binodal for Aro^{--}, and these

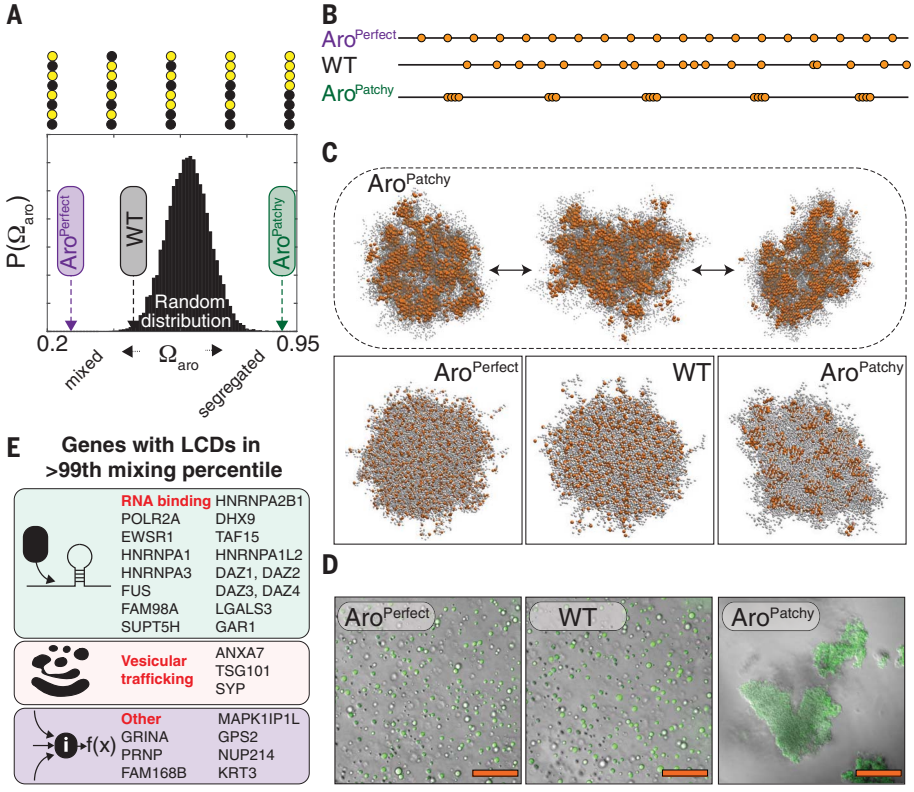

Fig. 4. Linear patterning of stickers versus spacers determines the ability of LCDs to undergo LLPS versus aggregation. (**A**) The aromatic residues in the WT A1-LCD are more uniformly distributed than 99.99% of sequence variants with the same composition as quantified by a mixing parameter Ω_{aro}. The positions of the Aro^{Perfect}, WT, and Aro^{Patchy} LCDs are indicated by arrows on the distribution. (**B**) A schematic showing the positions of aromatic amino acids as orange circles in the Aro^{Perfect}, WT, and Aro^{Patchy} LCDs. (**C**) Snapshots from stickers-and-spacers simulations of Aro^{Perfect}, WT, and Aro^{Patchy} LCDs. The Aro^{Patchy} LCD forms amorphous structures (top), whereas Aro^{Perfect} and WT both form spherical droplets (bottom). Stickers are orange, and spacers are either gray (bottom) or transparent (top). (**D**) Overlaid DIC and fluorescence images of Aro^{Perfect}, WT, and Aro^{Patchy} LCDs at identical concentrations and solution conditions. The scale bar represents 50 μm. (**E**) Functional annotation of proteins with PLDs that have similarly well-mixed distributions of aromatic residues.

calculations predict T_c for Aro^{--} to be below the freezing point of water. This explains why Aro^{--} does not undergo LLPS over all temperature and concentration ranges that were titrated ($T > 5$°C; $c < 0.8$ mM).

We next asked if the stickers-and-spacers model was generalizable to PLDs from other proteins. Short motifs known as low-complexity aromatic rich kinked segments (LARKS) and/or reversible amyloid cores (RACs) have been proposed to drive phase separation of the FUS-LCD (*16*, *37*). The removal of RACs leads to measurable changes in the driving forces for phase separation of the FUS-LCD (*37*). We used our lattice-based stickers-and-spacers model, parameterized using simulation results and experimental data for the A1-LCD, and simulated the phase behavior for four sequence variants of the FUS-LCD (WT, ΔRAC1, ΔRAC2, and ΔRAC1+ΔRAC2) (fig. S13). The nomenclature ΔRAC1 and ΔRAC2 reflects the deletion of RACs 1 and 2 that were identified in the FUS-LCD by Luo *et al.* (*37*). For each of the four constructs, previous measurements quantified the cloud point temperatures at a concentration of ~150 μM. The phase behavior of FUS$^{1\text{-}163}$ has been studied extensively in published work (*19*, *38*, *39*). In our simulations, all constructs formed well-defined, spherical, liquid-like assemblies, and we back-calculated the cloud point at ~150 μM. We observed a 1:1 correlation between experimentally measured cloud points and those estimated using simulation results rescaled to be in absolute temperature units and molar concentrations (Fig. 3G). The simulations do not use any specific information regarding the FUS-LCD other than the relative positions of the aromatic stickers nor do they invoke β sheet–dependent interactions. Accordingly, these results point to the transferability of our model to other PLDs with similar compositional biases.

The quality of the fits of measured binodals to a simple Flory-Huggins model indicate that the sequences studied here can be reduced to effective homopolymers. Accordingly, we asked if there was a general sequence pattern that characterizes PLDs and LCDs with aromatic stickers. Using a patterning parameter Ω_{aro} ($0 \le \Omega_{aro} \le 1$) (see methods), we performed a statistical analysis to determine how likely it would be for the evenly spaced aromatic residues observed in the A1-LCD to occur by random chance. This analysis was motivated by previous studies that connected sequence patterns to changes in conformational features of disordered regions and driving forces for phase separation (*14*, *40*–*42*). We found that aromatic residues are more uniformly spaced than 99.99% of randomly generated sequences (Fig. 4A). This suggests a clear bias toward a uniform, nonrandom patterning of aromatic stickers within the A1-LCD sequence.

To test the impact of the apparent preference for uniform distribution of stickers along the linear sequence, we used the parameterized version of the stickers-and-spacers model and performed simulations for two variants, Aro^{Perfect} and Aro^{Patchy} (Fig. 4B). These sequences are of identical composition when compared with the A1-LCD; they are distinguished by the patterning of stickers and hence values of Ω_{aro}. The simulations show that increased linear clustering of stickers in Aro^{Patchy} leads to the formation of micellar substructures within the droplet (Fig. 4C and movie S6). Theories predict that these micelles can aggregate to form amorphous precipitates as opposed to liquid-like droplets (*43*) because the increased linear clustering of stickers increases the apparent intersticker interaction strengths. In contrast to Aro^{Patchy}, Aro^{Perfect} forms spherical droplets that are indistinguishable from WT (Fig. 4C).

Our results suggest that increasing Ω_{aro} by clustering stickers together along the linear sequence will affect the interplay between LLPS and aggregation, with the latter becoming prominent as Ω_{aro} increases. We tested this prediction by performing fluorescence microscopy measurements using a small proportion of labeled molecules in the presence of unlabeled versions for the two designed variants. Whereas Aro^{Perfect} formed spherical droplets (Fig. 4D), Aro^{Patchy} formed large amorphous aggregates (Fig. 4D). Importantly, we observed aggregation of Aro^{Patchy} even under conditions in which the WT A1-LCD remains in the one-phase regime (fig. S14). In accordance with predictions, the experiments indicate that the uniform distribution of aromatic residues along LCDs favors solubility and LLPS over aggregation.

The preceding analysis suggests that there may be selection pressure against the linear clustering of aromatic stickers along the sequences of PLDs or a selection for uniformly distributed aromatic stickers along PLD sequences. To test this conjecture, we quantified the patterning of aromatic residues within PLDs

from different proteins that are known drivers of LLPS. We identified a strong bias toward uniform distribution of aromatic stickers along linear sequences for the PLDs of RNA-binding proteins such as FUS, TAF15, EWSR1, hnRNPA2B1, and hnRNPA3 (Fig. 4E) in which the patterning of aromatic residues is highly conserved despite very low levels of sequence conservation (fig. S15, A to C). A proteome-wide analysis of the patterning of aromatic residues within disordered PLDs showed a similar bias toward nonrandom, uniform patterning of aromatic stickers in PLDs from an assortment of dissimilar proteins that are known drivers of LLPS (*3*, *21*) (Fig. 4E and fig. S15, D and E). We also identified disordered regions from proteins involved in vesicular trafficking and signal transduction that have a similar nonrandom bias toward uniform patterning of aromatic residues (Fig. 4E). Intriguingly, the PLD of Xvelo, a protein that drives the formation of solid-like Balbiani bodies (*44*), is a prominent outlier in terms of its large value of Ω_{aro}.

We propose that the uniform spacing of aromatic stickers along the linear sequences of LCDs ensures that strong interactions among aromatic residues are weakened by the favorable solvation of the spacers. The preferential solvation of spacers likely dilutes the effects of aromatic stickers. Similar considerations are likely to apply to other nonaromatic stickers, such as hydrophobic motifs or those that contribute to cation-π interactions and/or complementary electrostatic interactions (*41*). Our findings point to interactions encoded in PLDs that are strong enough to drive LLPS and yet weak enough to suppress aggregation—a balance that is likely disrupted through mutations that (i) increase the valence of aromatic or other stickers; (ii) disrupt the nonrandom, well-mixed patterning of aromatic stickers; and/or (iii) add other cohesive interactions through mutations to spacers that weaken their preference for being well solvated.

We have demonstrated the applicability of the stickers-and-spacers framework for quantitative descriptions of sequence-binodal relationships of archetypal PLDs. We have converged on a transferable protocol (fig. S16) for identifying stickers; quantifying the relative strengths of sticker-sticker, sticker-spacer, and spacer-spacer interactions as a function of temperature or other equivalent control parameters; and using this information to generate sequence-to-binodal relationships. These methods will help in mapping cellular concentrations for PLDs to positions relative to their measured or calculated binodals, thus allowing the prediction of how condensates spontaneously form and dissolve in response to changes in protein concentration and cellular conditions (*1*).

REFERENCES AND NOTES

1. T. M. Franzmann *et al.*, *Science* **359**, eaao5654 (2018).
2. J. A. Riback *et al.*, *Cell* **168**, 1028–1040.e19 (2017).
3. A. Molliex *et al.*, *Cell* **163**, 123–133 (2015).
4. A. Wang *et al.*, *EMBO J.* **37**, e97452133 (2018).
5. J. B. Woodruff, *J. Mol. Biol.* **430**, 4762–4772 (2018).
6. A. G. Larson *et al.*, *Nature* **547**, 236–240 (2017).
7. A. R. Strom *et al.*, *Nature* **547**, 241–245 (2017).
8. S. Banjade, M. K. Rosen, *eLife* **3**, e04123 (2014).
9. S. F. Banani, H. O. Lee, A. A. Hyman, M. K. Rosen, *Nat. Rev. Mol. Cell Biol.* **18**, 285–298 (2017).
10. Y. Shin, C. P. Brangwynne, *Science* **357**, eaaf4382 (2017).
11. A. Patel *et al.*, *Cell* **162**, 1066–1077 (2015).
12. C. P. Brangwynne, P. S. Tompa, R. V. Pappu, *Nat. Phys.* **11**, 899–904 (2015).
13. R. M. Vernon, J. D. Forman-Kay, *Curr. Opin. Struct. Biol.* **58**, 88–96 (2019).
14. T. J. Nott *et al.*, *Mol. Cell* **57**, 936–947 (2015).
15. X. Gui *et al.*, *Nat. Commun.* **10**, 2006 (2019).
16. M. P. Hughes *et al.*, *Science* **359**, 698–701 (2018).
17. M. Kato *et al.*, *Cell* **149**, 753–767 (2012).
18. J. P. Brady *et al.*, *Proc. Natl. Acad. Sci. U.S.A.* **114**, E8194–E8203 (2017).
19. K. A. Burke, A. M. Janke, C. L. Rhine, N. L. Fawzi, *Mol. Cell* **60**, 231–241 (2015).
20. M. Rubinstein, A. V. Dobrynin, *Trends Polym. Sci.* **5**, 181–186 (1997).
21. J. Wang *et al.*, *Cell* **174**, 688–699.e16 (2018).
22. A. N. Semenov, M. Rubinstein, *Macromolecules* **31**, 1373–1385 (1998).
23. T. S. Harmon, A. S. Holehouse, M. K. Rosen, R. V. Pappu, *eLife* **6**, e30294 (2017).
24. P. J. Flory, *J. Am. Chem. Soc.* **63**, 3083–3090 (1941).
25. A. E. Posey, A. S. Holehouse, R. V. Pappu, in *Methods in Enzymology*, E. Rhoades, Ed. (Academic Press, 2018), vol. 611, pp. 1–30.
26. H. J. Kim *et al.*, *Nature* **495**, 467–473 (2013).
27. A. Vitalis, R. V. Pappu, *J. Comput. Chem.* **30**, 673–699 (2009).
28. A. S. Holehouse, R. V. Pappu, *Annu. Rev. Biophys.* **47**, 19–39 (2018).
29. G. Raos, G. Allegra, *J. Chem. Phys.* **107**, 6479–6490 (1997).
30. J. A. Riback *et al.*, *Science* **358**, 238–241 (2017).
31. J. Klein-Seetharaman *et al.*, *Science* **295**, 1719–1722 (2002).
32. P. A. Evans, K. D. Topping, D. N. Woolfson, C. M. Dobson, *Proteins* **9**, 248–266 (1991).
33. D. Neri, M. Billeter, G. Wider, K. Wüthrich, *Science* **257**, 1559–1563 (1992).
34. G. L. Dignon, W. Zheng, R. B. Best, Y. C. Kim, J. Mittal, *Proc. Natl. Acad. Sci. U.S.A.* **115**, 9929–9934 (2018).
35. M. T. Wei *et al.*, *Nat. Chem.* **9**, 1118–1125 (2017).
36. M. Rubinstein, R. H. Colby, *Polymer Physics* (Oxford Univ. Press, 2003).
37. F. Luo *et al.*, *Nat. Struct. Mol. Biol.* **25**, 341–346 (2018).
38. Z. Monahan *et al.*, *EMBO J.* **36**, 2951–2967 (2017).
39. A. E. Conicella, G. H. Zerze, J. Mittal, N. L. Fawzi, *Structure* **24**, 1537–1549 (2016).
40. R. K. Das, R. V. Pappu, *Proc. Natl. Acad. Sci. U.S.A.* **110**, 13392–13397 (2013).
41. C. W. Pak *et al.*, *Mol. Cell* **63**, 72–85 (2016).
42. E. W. Martin *et al.*, *J. Am. Chem. Soc.* **138**, 15323–15335 (2016).
43. F. Tanaka, M. Ishida, *Macromolecules* **30**, 1836–1844 (1997).
44. E. Boke *et al.*, *Cell* **166**, 637–650 (2016).
45. A. Holehouse, R. V. Pappu, PIMMS (0.24 pre-beta), Zenodo (2019); doi:10.5281/zenodo.3588456

ACKNOWLEDGMENTS

We thank J.-M. Choi, A. A. Hyman, and J. P. Taylor for insightful discussions; M. Stuchell-Brereton and N. Milkovic for technical help; S. Chakravarthy, J. Hopkins, and all BioCAT beamline staff at the Advanced Photon Source for assistance with SAXS measurements; C. Liu for providing the raw data associated with the FUS measurements; and anonymous reviewers for constructive criticisms that helped us immensely with our narrative. Microscopy images were acquired at the Cell & Tissue Imaging Center, which is supported by SJCRH and NCI (grant P30 CA021765). NMR assignments are available from the BMRB at accession code ID 50017. **Funding:** This work was funded by the St. Jude Children's Research Hospital Research Collaborative on Membrane-less Organelles in Health and Disease (to T.M. and R.V.P.), the U.S. National Science Foundation (MCB1614766 to R.V.P.), the Human Frontier Science Program (RGP0034/2017 to R.V.P), the American Federation for Aging Research (to A.S.), and the American Lebanese Syrian Associated Charities (to T.M.). Use of the Advanced Photon Source was supported by the U.S. Department of Energy under contract DE-AC02-06CH11357. **Author contributions:** Conceptualization: E.W.M., A.S.H., R.V.P., and T.M.; Methodology: E.W.M., I.P., A.S.H., A.S., R.V.P., and T.M.; Investigation: E.W.M., I.P., A.S.H., M.F., J.J.I., A.B., C.R.G., A.S., R.V.P., and T.M.; Resources: A.S., R.V.P., and T.M.; Writing – original draft: E.W.M., A.S.H., R.V.P., and T.M.; Writing – reviewing and editing: all authors; Visualization: E.W.M., I.P., A.S.H., and A.S.; Funding acquisition: R.V.P. and T.M. **Competing interests:** R.V.P. is a member of the scientific advisory board of DewpointX. This work was not funded or influenced in any way by this affiliation. The remaining authors declare no competing interests. **Data and materials availability:** Code needed to reproduce the results is available at Zenodo (*45*). All other data are available in the manuscript or the supplementary materials. All expression plasmids are available from T.M. under a material transfer agreement with St. Jude Children's Hospital.

SUPPLEMENTARY MATERIALS

science.sciencemag.org/content/367/6478/694/suppl/DC1
Materials and Methods
Figs. S1 to S16
Tables S1 to S3
References (*46*–*70*)
Movies S1 to S6

View/request a protocol for this paper from *Bio-protocol*.

16 February 2019; resubmitted 30 August 2019
Accepted 6 January 2020
10.1126/science.aaw8653

STRUCTURAL BIOLOGY

Structure of an active human histone pre-mRNA 3′-end processing machinery

Yadong Sun[1]*, Yixiao Zhang[2]*, Wei Shen Aik[1]†, Xiao-Cui Yang[3], William F. Marzluff[3,4], Thomas Walz[2]‡, Zbigniew Dominski[3,4]‡, Liang Tong[1]‡

The 3′-end processing machinery for metazoan replication-dependent histone precursor messenger RNAs (pre-mRNAs) contains the U7 small nuclear ribonucleoprotein and shares the key cleavage module with the canonical cleavage and polyadenylation machinery. We reconstituted an active human histone pre-mRNA processing machinery using 13 recombinant proteins and two RNAs and determined its structure by cryo–electron microscopy. The overall structure is highly asymmetrical and resembles an amphora with one long handle. We captured the pre-mRNA in the active site of the endonuclease, the 73-kilodalton subunit of the cleavage and polyadenylation specificity factor, poised for cleavage. The endonuclease and the entire cleavage module undergo extensive rearrangements for activation, triggered through the recognition of the duplex between the authentic pre-mRNA and U7 small nuclear RNA (snRNA). Our study also has notable implications for understanding canonical and snRNA 3′-end processing.

The 3′-end processing machineries for polyadenylated (*1*, *2*) and histone precursor mRNAs (pre-mRNAs) (*3*, *4*) both use the 73-kDa subunit of the cleavage and polyadenylation specificity factor (CPSF73) to cleave pre-mRNA (*5*, *6*), but the molecular mechanism for their functions is still poorly understood. CPSF73, CPSF100, symplekin, and the 64-kDa subunit of the cleavage stimulation factor (CstF64) compose the histone pre-mRNA cleavage complex (HCC) (Fig. 1, A and B, and table S1), which is equivalent to the mammalian cleavage factor (mCF) for polyadenylated pre-mRNAs (*7*, *8*). The cleavage site in histone pre-mRNAs is located between a conserved stem-loop (SL) that is recognized by SL binding protein (SLBP) and a histone downstream element (HDE) that forms base pairs with the 5′ end of U7 small nuclear RNA (snRNA), forming an HDE-U7 duplex (Fig. 1A). The U7 small nuclear ribonucleoprotein (snRNP) is critical for this processing, and the Lsm11-FLASH complex recruits the HCC to the machinery (*9*–*12*) (see supplementary text in the supplementary materials).

To prepare a fully recombinant machinery, we reconstituted human U7 snRNP (*13*) and mixed it with purified human HCC, FLASH (*14*), and SLBP (*15*). Using a modified mouse histone H2a pre-mRNA (H2a*) (fig. S1) as substrate, we observed robust cleavage activity generating the authentic product (supplementary text and figs. S2 and S3). Notably, the N-terminal domain (NTD) of symplekin was essential for processing, and its binding partner Ssu72 (*16*) inhibited the cleavage reaction. A mutation in the active site of CPSF73 abolished the cleavage.

We purified the active machinery (fig. S3F) and obtained a cryo–electron microscopy (cryo-EM) reconstruction at 3.2-Å resolution for its core (Fig. 1, C and D) and a reconstruction at 4.1-Å resolution for the entire machinery (tables S2 and S3 and figs. S4 to S6). The overall structure of the machinery resembles an amphora with one long handle (Fig. 1E, fig. S6B, and movie S1). The machinery core constitutes the body of the amphora, with the U7 snRNA 3′-end SL and the Sm ring at the base and the CTDs of CPSF73 and CPSF100 and the first few helical repeats of the symplekin CTD forming the mouth. CPSF73 and symplekin NTD are positioned opposite each other on the Sm ring (Fig. 1D and fig. S6A). CPSF100 interacts with both CPSF73 and symplekin but does not directly contact the Sm ring (Fig. 1C). The symplekin CTD, FLASH dimer (*14*), SLBP, pre-mRNA SL, and residues 20 to 65 of Lsm11 form the handle of the amphora (Fig. 1E). The FLASH dimer makes an 80-Å-long connection from the symplekin CTD to the SLBP-SL complex. CstF64 was not observed in the EM density and is not required for cleavage in vitro (supplementary text and fig. S2F).

Twelve consecutive Watson-Crick base pairs in the HDE-U7 duplex were observed in the center of the amphora (Fig. 1D and fig. S1). The metallo-β-lactamase domain of CPSF73, the β-CASP domain of CPSF100, and the concave face of the symplekin NTD (fig. S6C) surround the duplex on three sides (Figs. 1, D and E, and 2A). The interactions are ionic and hydrophilic in nature but involve none of the bases in the duplex (Fig. 2B), which explains earlier observations that base pairing rather than sequence is important for processing (*3*, *4*, *13*). The structure revealed an extra, U-U base pair at the bottom of the duplex (Fig. 2C and fig. S1), and analysis of histone pre-mRNA sequences suggested that U-U base pairs are common in HDE-U7 duplexes (fig. S7).

The structure also revealed a Watson-Crick base pair between C28 and G31 of the CUAG sequence at the 3′ end of the U7 Sm site (Fig. 2D and fig. S1). It is flanked by residues from Lsm10 and Lsm11 and assumes a different backbone conformation compared with other Sm sites (Fig. 2D and fig. S8A). In addition, G26 is hydrogen-bonded with C33 of H2a*, providing a direct connection between the Sm site and the pre-mRNA (figs. S1 and S8B). The recognition of the first five Sm site nucleotides (21-AAUUU-25) and U27 is similar to that in spliceosomal Sm rings (figs. S1 and S8B) (*17*, *18*), although there are substantial differences in the extensions of the Sm proteins and the positions of the RNA outside the Sm ring (fig. S8, C to E).

The pre-mRNA substrate (Fig. 3A) is bound in the active site of CPSF73. The correct scissile phosphate, after A26 (fig. S1), is coordinated to the two zinc ions in the active site (Fig. 3B). The A26 base has hydrogen-bonding interactions to its N1 and N6 atoms, which is consistent with the preference for an adenine at the cleavage site (*3*, *4*) (fig. S9, A to C). C25 has weak density (Fig. 3A) and is not recognized by CPSF73. This binding mode of the pre-mRNA clearly illuminates the molecular mechanism for the cleavage reaction. The hydroxide ion that is a bridging ligand between the two zinc ions (*6*) is the nucleophile that initiates the cleavage reaction (Fig. 3B), and the 3′ oxyanion of A26, the leaving group, is protonated by His^{396}, which is activated by Glu^{204}. Glu^{204}, His^{396}, and the ligands to the zinc ions are conserved among CPSF73 homologs (*19*, *20*), including integrator complex subunit 11 (IntS11), the endonuclease for snRNA cleavage (*21*). Therefore, the conformation of the machinery observed here is likely poised for the cleavage reaction. Except for the brief moment during EM grid preparation, the sample was kept at 4°C or on ice, which slowed the reaction (*12*) and allowed us to observe the pre-mRNA in the CPSF73 active site. There are substantial differences in the orientation of the β-CASP domain compared with the orientation in ribonuclease J (*22*, *23*) (fig. S9D) and especially in the binding modes of the RNA substrate (fig. S9E).

The reported structures of CPSF73 (*6*) and its yeast homolog Ysh1 (*24*) are in a closed, inactive conformation. We observed in this study an open, active conformation of CPSF73. A large rearrangement of its β-CASP domain relative to the metallo-β-lactamase domain, corresponding to a rotation of ~17° (Fig. 3C and fig. S9F), is necessary to create a narrow, deep canyon that is only large enough to accommodate

[1]Department of Biological Sciences, Columbia University, New York, NY 10027, USA. [2]Laboratory of Molecular Electron Microscopy, Rockefeller University, New York, NY 10065, USA. [3]Integrative Program for Biological and Genome Sciences, University of North Carolina at Chapel Hill, Chapel Hill, NC 27599, USA. [4]Department of Biochemistry and Biophysics, University of North Carolina at Chapel Hill, Chapel Hill, NC 27599, USA.
*These authors contributed equally to this work.
†Present address: Department of Chemistry, Hong Kong Baptist University, Kowloon Tong, Kowloon, Hong Kong SAR.
‡Corresponding author. Email: ltong@columbia.edu (L.T.); zbigniew_dominski@med.unc.edu (Z.D.); twalz@rockefeller.edu (T.W.)

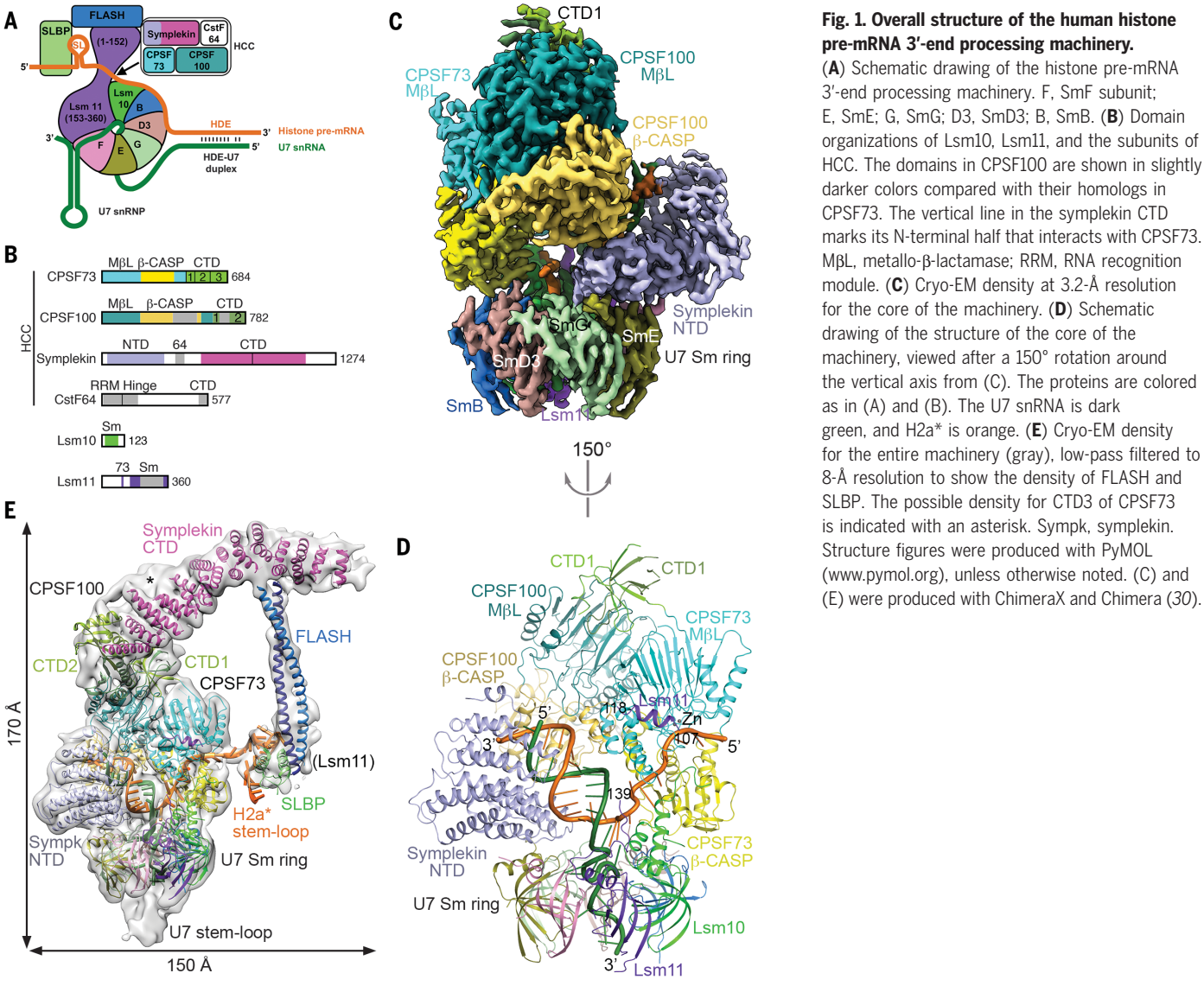

Fig. 1. Overall structure of the human histone pre-mRNA 3′-end processing machinery. (**A**) Schematic drawing of the histone pre-mRNA 3′-end processing machinery. F, SmF subunit; E, SmE; G, SmG; D3, SmD3; B, SmB. (**B**) Domain organizations of Lsm10, Lsm11, and the subunits of HCC. The domains in CPSF100 are shown in slightly darker colors compared with their homologs in CPSF73. The vertical line in the symplekin CTD marks its N-terminal half that interacts with CPSF73. MβL, metallo-β-lactamase; RRM, RNA recognition module. (**C**) Cryo-EM density at 3.2-Å resolution for the core of the machinery. (**D**) Schematic drawing of the structure of the core of the machinery, viewed after a 150° rotation around the vertical axis from (C). The proteins are colored as in (A) and (B). The U7 snRNA is dark green, and H2a* is orange. (**E**) Cryo-EM density for the entire machinery (gray), low-pass filtered to 8-Å resolution to show the density of FLASH and SLBP. The possible density for CTD3 of CPSF73 is indicated with an asterisk. Sympk, symplekin. Structure figures were produced with PyMOL (www.pymol.org), unless otherwise noted. (C) and (E) were produced with ChimeraX and Chimera (*30*).

single-stranded RNA (Fig. 3D and fig. S9, A, F, and G).

The N- and C-terminal extensions of Lsm10, highly conserved among vertebrate homologs (fig. S10A), play a crucial role in this conformational change for CPSF73. These extensions are placed directly against the β-CASP domain (fig. S11A) and have extensive steric clashes with its closed conformation (Fig. 3C and fig. S9F), likely helping to trigger the activation of CPSF73. In addition, a segment in the C-terminal extension of Lsm10 (residues 107 to 110) is positioned at the rim of the canyon (fig. S9A) and forms a part of the binding site for the 3′ portion of the substrate (Fig. 3D).

The recognition of the HDE-U7 duplex may be the critical event to initiate the conformational rearrangement in CPSF73, which is consistent with the requirement of symplekin NTD for cleavage. On the other hand, the NTD-Ssu72 complex is incompatible with the structure observed here, as Ssu72 would clash with the duplex as well as with CPSF73 (fig. S6D), explaining the inhibitory effect of Ssu72 (supplementary text).

Besides the rearrangement in CPSF73, an extensive change in the architecture of HCC is required for activation. We recently showed that mCF (or HCC) in an inactive state has a trilobal structure and is highly dynamic (*25*). In contrast, the HCC structure observed in this study in the active state shows drastic differences compared with the inactive state (Fig. 4A). There are intimate contacts between CPSF73 and CPSF100 in the current structure, and in fact they form a pseudo-dimer (fig. S11, B and C). These may be hallmarks of the active state for HCC (or mCF).

The conformational dynamics of HCC (mCF) is due to flexibility in its core, formed by the CTDs of CPSF73, CPSF100, and symplekin (*10*–*12*, *26*, *27*) (Figs. 1E and 4B). The CTD of CPSF73 likely has three subdomains (CTD1 to 3), and that of CPSF100 has two subdomains (Fig. 1, B and E, and fig. S12A). The CTD1 subdomains of CPSF73 and CPSF100 form a six-stranded β barrel–like structure (fig. S12B). The CTD2 subdomains form a separate complex, which makes only limited contact with the CTD1 complex, contributing to the flexibility in HCC (mCF). The overall structure of the CTD2 complex is similar to that of IntS11 and IntS9 (*28*). The first two helices of the symplekin CTD pack against the helices in the CTD2 complex (Fig. 4B) in the core of HCC (mCF).

The structure showed that HCC is recruited to the machinery directly by both FLASH and Lsm11 through two tethering contacts. Residues in FLASH N-terminal to the coiled-coil domain, including the LDLY motif (*10*), interact with the symplekin CTD (fig. S10C), and residues 107 to 118 of Lsm11 interact with CPSF73 (figs. S10B and S11D and supplementary text). These

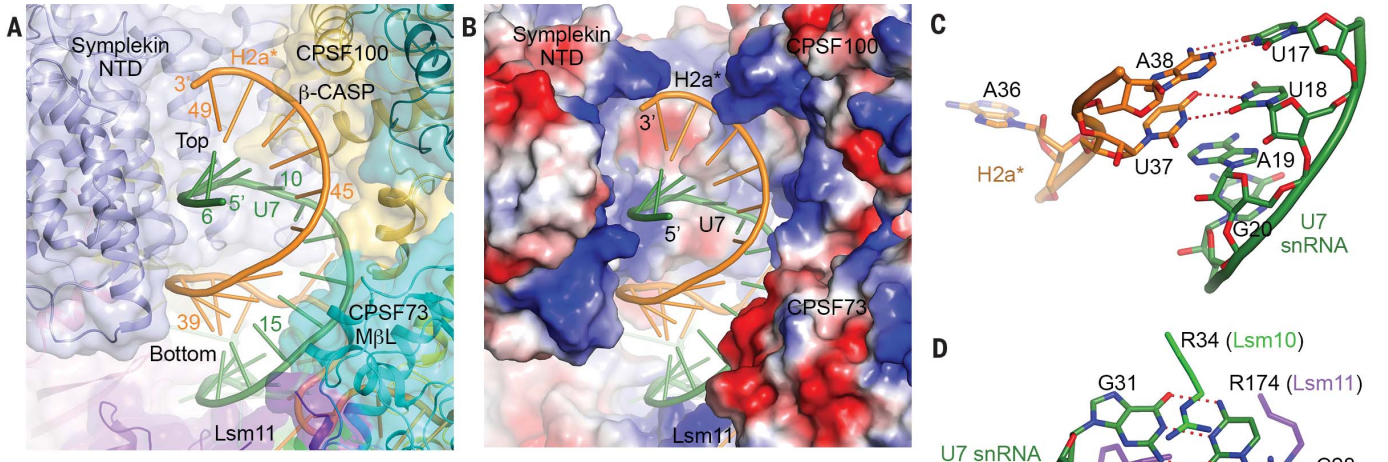

Fig. 2. Recognition of the HDE-U7 duplex and the U7 Sm site. (**A**) The HDE-U7 duplex is surrounded by CPSF73, CPSF100, and symplekin NTD, shown as a transparent surface. Lsm11 has interactions with the bottom of the duplex. (**B**) Electrostatic surface of the proteins in the duplex binding site, showing charged interactions with the backbone of the duplex. (**C**) A U-U base pair at the bottom of the duplex, flanked on the other face by A19 of U7 snRNA. (**D**) A C-G base pair in the 3′ CUAG sequence of the U7 Sm site. The base pair is flanked on one side by Arg^{34} of Lsm10 and on the other by Arg^{174} of Lsm11. Single-letter abbreviations for the amino acid residues are as follows: F, Phe; K, Lys; R, Arg.

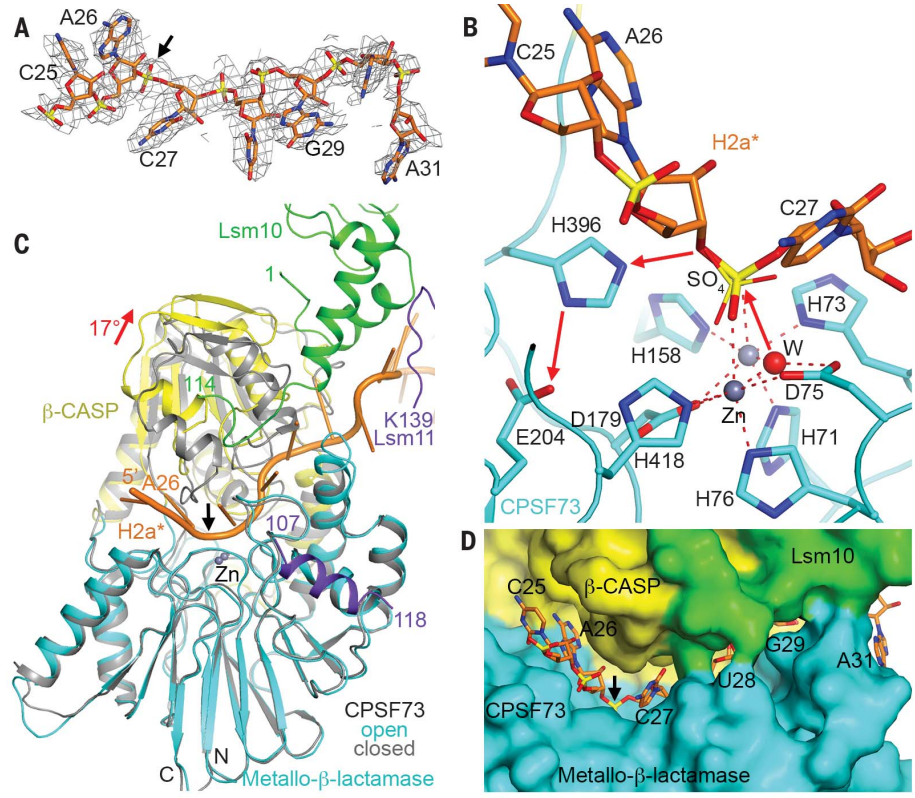

Fig. 3. CPSF73 is in an active state, poised for the cleavage reaction. (**A**) Cryo-EM density for H2a* nucleotides bound in the CPSF73 active site. The scissile phosphate is indicated with a black arrow. (**B**) The endonuclease mechanism of CPSF73. The positions of the zinc ions (gray spheres) and the bridging hydroxide (red sphere) are based on the crystal structure of CPSF73 alone (*6*) (Protein Data Bank ID 2I7V), and EM density is observed for the two zinc ions. The position of the sulfate ion observed in the earlier structure is shown using thin sticks. D, Asp; E, Glu; H, His. (**C**) Overlay of the structure of CPSF73 in the active state observed here (in color) with the inactive, closed state reported earlier (gray) (*6*). The metallo-β-lactamase domain was used for the overlay. The rearrangement of the β-CASP domain is indicated with a red arrow, corresponding to a rotation of 17°. (**D**) Molecular surface of the active site region of CPSF73, colored according to the domains. Lsm10 is located at the rim of the canyon, contacting nucleotides downstream of the cleavage site.

observations explain earlier data showing the importance of the LDLY motif in FLASH and residues 65 to 130 in Lsm11 for HCC recruitment (*10*, *11*, *29*).

Mutagenesis and biochemical experiments supported the structural observations (supplementary text). HCC recruitment was abolished by mutating the FLASH LDLY motif or symplekin CTD (fig. S13A). Removing the N- and C-terminal extensions of Lsm10 greatly reduced the cleavage activity without affecting U7 snRNP or machinery assembly (fig. S13, B to D). Moreover, the Lsm10 mutants showed misprocessing of the pre-mRNA. Therefore, these extensions may also play a crucial role in correctly positioning CPSF73 for the cleavage reaction. Mutating as few as two symplekin NTD residues that interact with the HDE-U7 duplex (fig. S6C) greatly reduced the cleavage activity (fig. S13E). Finally, the experiments also provided evidence for an Lsm11-FLASH-SLBP-SL quaternary complex (Fig. 1E and fig. S13F).

The structure of the machinery suggests how it may be assembled for processing (Fig. 4C, movie S2, and supplementary text) and provides a molecular foundation to understand and explain the large body of biochemical and functional data on histone pre-mRNA 3′-end processing (*3*, *4*). The structure also has important implications for understanding canonical pre-mRNA and snRNA 3′-end processing. The binding mode of the histone pre-mRNA in CPSF73 is likely similar for canonical pre-mRNAs and snRNAs, and the active conformation of mCF for canonical pre-mRNAs is likely to be the same as that of HCC observed in this study. The comparison to the structure of mCF in an inactive state suggests that the correct architecture of this

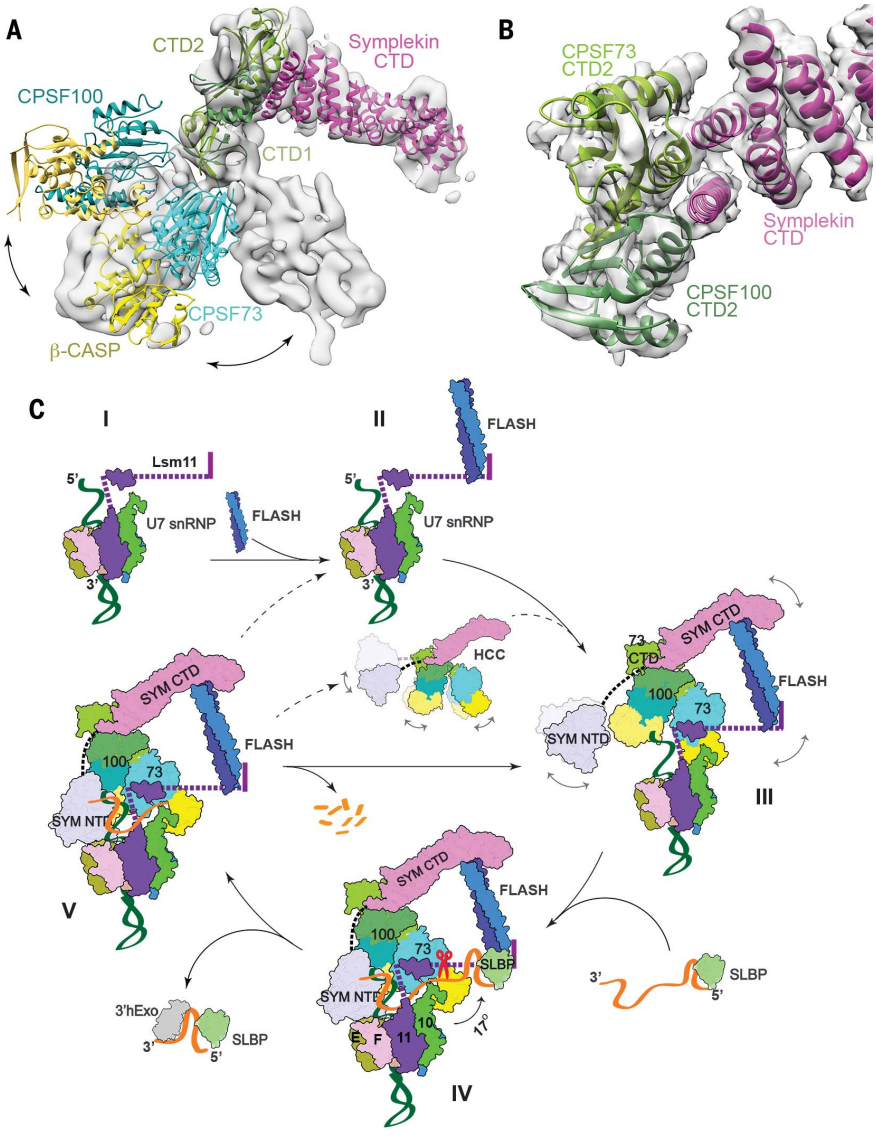

Fig. 4. Schematic of histone pre-mRNA 3′-end processing cycle. (**A**) Notable structural differences of HCC in an active state compared with an inactive state. The structure of HCC observed here is docked into the EM density for mCF (gray surface) (*25*), using the symplekin CTD as the reference. (**B**) Schematic drawing of the CTD2 domain complex of CPSF73 (light green) and CPSF100 (darker green) and the N-terminal segment of the symplekin CTD (magenta). The CTD complex of IntS9 and IntS11 (*28*) was docked into the EM density at 4.1-Å resolution (transparent surface) using Chimera. (A) and (B) were produced with Chimera. (**C**) A putative model for histone pre-mRNA 3′-end processing cycle. The machinery is assembled from the U7 snRNP (state I) with the recruitment of the FLASH dimer (state II) and HCC (state III), followed by the recognition of the pre-mRNA for CPSF73 and HCC activation and pre-mRNA cleavage (state IV). The machinery is likely highly dynamic before the binding of the authentic pre-mRNA, and the possible flexible regions are indicated with curved arrows and dashed lines. After cleavage (state V), the downstream product is degraded by an exonuclease activity, and the machinery can be recycled directly (solid arrow), or possibly disassembled and then reassembled (dashed arrows). State IV corresponds to the structure reported here, with the scissors indicating cleavage by CPSF73, and the other states are models.

cleavage module is another critical requirement for the activation of the processing machineries.

REFERENCES AND NOTES

1. J. Zhao, L. Hyman, C. Moore, *Microbiol. Mol. Biol. Rev.* **63**, 405–445 (1999).
2. Q. Yang, S. Doublié, *Wiley Interdiscip. Rev. RNA* **2**, 732–747 (2011).
3. Z. Dominski, W. F. Marzluff, *Gene* **396**, 373–390 (2007).
4. V. Romeo, D. Schümperli, *Curr. Opin. Cell Biol.* **40**, 23–31 (2016).
5. Z. Dominski, X.-C. Yang, W. F. Marzluff, *Cell* **123**, 37–48 (2005).
6. C. R. Mandel *et al.*, *Nature* **444**, 953–956 (2006).
7. L. Schönemann *et al.*, *Genes Dev.* **28**, 2381–2393 (2014).
8. S. L. Chan *et al.*, *Genes Dev.* **28**, 2370–2380 (2014).
9. X.-C. Yang, B. D. Burch, Y. Yan, W. F. Marzluff, Z. Dominski, *Mol. Cell* **36**, 267–278 (2009).
10. X.-C. Yang *et al.*, *Mol. Cell. Biol.* **33**, 28–37 (2013).
11. I. Sabath *et al.*, *RNA* **19**, 1726–1744 (2013).
12. A. Skrajna, X.-C. Yang, M. Dadlez, W. F. Marzluff, Z. Dominski, *Nucleic Acids Res.* **46**, 4752–4770 (2018).
13. K. Bucholc *et al.*, *Nucleic Acids Res.* 10.1093/nar/gkz1148 (2019).
14. W. S. Aik *et al.*, *PLOS ONE* **12**, e0186034 (2017).
15. D. Tan, W. F. Marzluff, Z. Dominski, L. Tong, *Science* **339**, 318–321 (2013).
16. K. Xiang *et al.*, *Nature* **467**, 729–733 (2010).
17. Y. Kondo, C. Oubridge, A. M. M. van Roon, K. Nagai, *eLife* **4**, e04986 (2015).
18. J. Li, A. K. W. Leung, Y. Kondo, C. Oubridge, K. Nagai, *Acta Crystallogr. D* **72**, 131–146 (2016).
19. I. Callebaut, D. Moshous, J.-P. Mornon, J.-P. de Villartay, *Nucleic Acids Res.* **30**, 3592–3601 (2002).
20. Z. Dominski, A. J. Carpousis, B. Clouet-d'Orval, *Biochim. Biophys. Acta* **1829**, 532–551 (2013).
21. D. Baillat, E. J. Wagner, *Trends Biochem. Sci.* **40**, 257–264 (2015).
22. A. Dorléans *et al.*, *Structure* **19**, 1252–1261 (2011).
23. Y. Zhao *et al.*, *Nucleic Acids Res.* **43**, 5550–5559 (2015).
24. C. H. Hill *et al.*, *Mol. Cell* **73**, 1217–1231.e11 (2019).
25. Y. Zhang, Y. Sun, Y. Shi, T. Walz, L. Tong, *Mol. Cell* 10.1016/j.molcel.2019.11.005 (2019).
26. K. D. Sullivan, M. Steiniger, W. F. Marzluff, *Mol. Cell* **34**, 322–332 (2009).
27. D. Michalski, M. Steiniger, *RNA* **21**, 1404–1418 (2015).
28. Y. Wu, T. R. Albrecht, D. Baillat, E. J. Wagner, L. Tong, *Proc. Natl. Acad. Sci. U.S.A.* **114**, 4394–4399 (2017).
29. A. Skrajna *et al.*, *J. Mol. Biol.* **428**, 1180–1196 (2016).
30. E. F. Pettersen *et al.*, *J. Comput. Chem.* **25**, 1605–1612 (2004).

ACKNOWLEDGMENTS

We thank L. Yen, D. Bobe, E. Eng, and R. Grassucci for data collection at the New York Structural Biology Center; M. Ebrahim and J. Sotiris for grids screening at the Evelyn Gruss Lipper Cryo-Electron Microscopy Resource Center at The Rockefeller University; and K. Xiang and D. Tan for initial studies for this project. **Funding:** This research was supported by NIH grants R35GM118093 (to L.T.) and R01GM029832 (to W.F.M. and Z.D.). W.S.A. was also supported by a fellowship from the Raymond and Beverley Sackler Center for Research at Convergence of Disciplines at Columbia University Medical Center. The Simons Electron Microscopy Center at the New York Structural Biology Center is supported by grants from the Simons Foundation (349247), NYSTAR, NIH (GM103310, S10 OD019994), and Agouron Institute (F00316). **Author contributions:** Y.S. produced the HCC and prepared all the samples for the EM analysis, carried out the mixing experiments, and performed model building and structure refinement. Y.Z. carried out EM data collection and analysis, EM reconstruction, and model building and refinement. W.S.A. developed the protocols for reconstituting the U7 snRNP and its complex with FLASH-SLBP-H2a*. Z.D. and X.-C.Y. carried out the cleavage assays. L.T., Z.D., T.W., and W.F.M. supervised the research and analyzed the data. L.T. wrote the paper, with substantial contributions from Z.D., Y.S., Y.Z., and W.F.M. All authors commented on the paper. **Competing interests:** The authors declare no competing interests. **Data and materials availability:** The atomic coordinates and the EM maps can be accessed in the Protein Data Bank (ID 6V4X).

SUPPLEMENTARY MATERIALS

science.sciencemag.org/content/367/6478/700/suppl/DC1
Materials and Methods
Supplementary Text
Figs. S1 to S13
Tables S1 to S3
References (*31*–*73*)
Movies S1 and S2

View/request a protocol for this paper from *Bio-protocol*.

8 October 2019; accepted 31 December 2019
10.1126/science.aaz7758

Perfusion-Based Dendritic Cell Culture Platform

The Corning MicroDEN automated perfusion system enables the efficient generation of dendritic cells from monocytes. It delivers reproducible results in less time while reducing contamination risk, as compared to the current "Gold Standard" manual approach to manufacturing dendritic cells. The system is programmed to perform the generation, washing, and harvesting steps with Corning single-use, closed-system technology. The technician loads peripheral blood mononuclear cells (PBMCs) or enriched monocytes with the preferred differentiation media, and places the MicroDEN system into the incubator.

Corning
For info: 800-492-1110
www.corning.com/lifesciences

Cell Line for Recombinant Antibody Production

ProteoGenix decided to overcome the cost and timeline issues associated with the production of monoclonal antibodies for preclinical trials. Our solution? XtenCHO, a high-performance cell line combining high-productivity yields with inexpensive reagents. As proven in our comparative study, this new Chinese hamster ovary (CHO) transient gene expression system outperforms most of the solutions currently available. For pembrolizumab, utolimumab, and claudiximab production, XtenCHO's production yields are 1.2–1.9 times higher than ExpiCHO and 3.0–8.5 times higher than CHO-S (with each system measured in their optimal conditions). In ideal conditions, XtenCHO achieves a maximum yield of 1.28 g/L for claudiximab. Its high efficiency was also validated for chimeric (0.5 g/L) and bispecific antibodies (CrossMab, DuoBody, and Fab-Fab; yields around 200 mg/L). At ProteoGenix we strive for the success of every antibody production project. XtenCHO is our solution for decreasing the production costs of therapeutic antibodies and accelerating your way to the clinic.

ProteoGenix
For info: +33-(0)-390-20-54-70
www.proteogenix.science

Incubation Monitoring System

The OLYMPUS Provi CM20 monitoring system provides quantitative data about the health of cell cultures while they are in the incubator. The system periodically scans the cultures, counts the number of cells without the need of staining or peeling, determines confluency, and wirelessly communicates the data to a tablet or PC. It has a thin, compact design, and can be installed in confined spaces. Using the CM20 system, you can acquire data that will improve the reproducibility and stability of your cell culture process. Cultivating cell cultures can be costly, complicated, and time consuming, since it involves multiple steps and careful timing; the CM20 improves quality management and reduces the amount of labor involved. With proven experience in regenerative medicine and expertise in optics, image analysis, and data management, Olympus is uniquely positioned to empower users to push the boundaries of regenerative medicine.

Olympus
For info: 609-820-5176
www.olympus-lifescience.com/en/cell_culture_solution/cm20

18-Well Slides

With its thin ibidi Polymer Coverslip Bottom, the µ-Slide 18 Well allows for excellent cell adhesion onto the tissue culture–treated surface. In addition, it has the highest optical quality and is ideally suited for a variety of microscopic techniques, such as widefield fluorescence, confocal microscopy, and differential interference contrast. For scientists who perform special microscopic applications, such as total internal reflection fluorescence and superresolution microscopy, ibidi provides the µ-Slide 18 Well Glass Bottom with a #1.5H D 263 M Schott glass. It is also available as a sticky-Slide 18 Well without any bottom, which enables the researcher to mount any chosen substrate. The entire µ-Slide 18 Well family is ideal for experiments with small cell numbers and low reagent volumes. The spaces between the individual well walls minimize any well-to-well crosstalk and contamination. Scientists who would like to test one of the µ-Slide 18 Well variations with their own experiments can request free samples at ibidi.com.

ibidi
For info: 844-276-6363
ibidi.com

Automated Cell Culture Analyzer

BioProfile FLEX2 combines Nova's groundbreaking MicroSensor Card technology with optical measurement and freezing point osmometry for an automated, comprehensive cell culture analyzer that eliminates chemistry sensor maintenance, increases analyzer speed, and reduces sample volume. The full 16-cell-culture test menu includes glucose, lactate, glutamine, glutamate, ammonium, sodium, potassium, calcium, pH, PCO_2, PO_2, total cell density, viable cell density, viability, cell diameter, and osmolality. Compared to the previous generation BioProfile FLEX, there is no maintenance for any of the 11 chemistry and gas sensors, sample volume for the full test menu is reduced by 75% to 275 µL, and testing time is reduced to just 4.5 min. Automated sampling from 96-well plates, syringes, or a 24-position external "load-and-go" sample tray provides maximum workflow flexibility and efficiency for cell culture monitoring.

Nova Biomedical
For info: 781-894-0800
www.novabio.us/flex-2/index.php

Inductive Charging Stand

An inductive charging stand is now available for the BRAND HandyStep touch and HandyStep touch S repeating pipettes. The stand allows for easy charging of the instrument without a plug connection. A blue light indicates when the instrument is charging and goes out when charging is completed. A tip can be inserted, and the instrument can be used simultaneously while charging. The stand is available separately or in an attractively priced bundle with either pipette.

BrandTech Scientific
For info: 888-522-2726
www.brandtech.com

Electronically submit your new product description or product literature information! Go to www.sciencemag.org/about/new-products-section for more information.

Newly offered instrumentation, apparatus, and laboratory materials of interest to researchers in all disciplines in academic, industrial, and governmental organizations are featured in this space. Emphasis is given to purpose, chief characteristics, and availability of products and materials. Endorsement by *Science* or AAAS of any products or materials mentioned is not implied. Additional information may be obtained from the manufacturer or supplier.

THE UNIVERSITY OF CHICAGO

Academic Gastroenterologist
Inflammatory Bowel Disease #MED125
The University of Chicago: Biological Sciences Division: Department of Medicine

Position Description

The University of Chicago's Department of Medicine, Section of Gastroenterology, Hepatology and Nutrition, is searching for an assistanat professor with interests in the area of Inflammatory Bowel Disease (IBD). The appointee will have a mix of outpatient and inpatient endoscopy, IBD and general GI clinic, inpatient IBD service and consultation. The appointee will be able to staff clinics at multiple sites including Chicagoland suburbs and Northwest Indiana. We especially welcome applicants with advanced training in IBD and experience managing a clinical practice of IBD and general GI patients. Other duties will include teaching and supervision of trainees and students. Compensation (including a generous package of fringe benefits) is dependent upon qualifications.

Prior to the start of employment, qualified applicants must: (1) have an medical doctorate or equivalent, (2) hold or be eligible for medical licensure in the State of Illinois, and (3) be BC/BE in Gastroenterology.

To be considered, those interested must apply through The University of Chicago's Academic Recruitment job board, which uses Interfolio to accept applications: **http://apply.interfolio.com/70800**. Applicants must upload: CV including bibliography. Review of applications ends when the position is filled.

For instructions on the Interfolio application process, please visit http://tiny.cc/InterfolioHelp.

Equal Employment Opportunity Statement

The University of Chicago is an Affirmative Action/Equal Opportunity/Disabled/Veterans Employer and does not discriminate on the basis of race, color, religion, sex, sexual orientation, gender identity, national or ethnic origin, age, status as an individual with a disability, protected veteran status, genetic information, or other protected classes under the law. For additional information please see the University's Notice of Nondiscrimination.

Job seekers in need of a reasonable accommodation to complete the application process should call 773-702-1032 or email equalopportunity@uchicago.edu with their request.

THE UNIVERSITY OF CHICAGO

Academic Interventional Endoscopist

The University of Chicago's Department of Medicine, Center for Endoscopic Research and Therapeutics (CERT) and Section of Gastroenterology, are searching for an assistant professor to join our rapidly growing interventional endoscopy and metabolic endoscopy practice. The appointee will have a mix of outpatient and inpatient clinical responsibilities, including advanced endoscopic esophageal and bariatric procedures, and provide consultation and procedures at multiple sites in the Chicago area. Other duties will include teaching and supervision of trainees and students, and scholarly activity. Compensation (including a generous package of fringe benefits) is dependent upon qualifications.

Prior to the start of employment, qualified applicants must: (1) have a medical doctorate or equivalent, (2) hold or be eligible for medical licensure in the State of Illinois, (3) be Board Certified or Eligible in Gastroenterology.

To be considered, those interested must apply through The University of Chicago's Academic Recruitment job board, which uses Interfolio to accept applications: **http://apply.interfolio.com/73574**. Applicants must upload: a CV including bibliography and cover letter. Review of applications ends when the position is filled.

Equal Employment Opportunity Statement

We seek a diverse pool of applicants who wish to join an academic community that places the highest value on rigorous inquiry and encourages diverse perspectives, experiences, groups of individuals, and ideas to inform and stimulate intellectual challenge, engagement, and exchange.

The University of Chicago is an Affirmative Action/Equal Opportunity/Disabled/Veterans Employer and does not discriminate on the basis of race, color, religion, sex, sexual orientation, gender identity, national or ethnic origin, age, status as an individual with a disability, protected veteran status, genetic information, or other protected classes under the law. For additional information please see the University's Notice of Nondiscrimination.

Job seekers in need of a reasonable accommodation to complete the application process should call 773-702-1032 or email equalopportunity@uchicago.edu with their request.

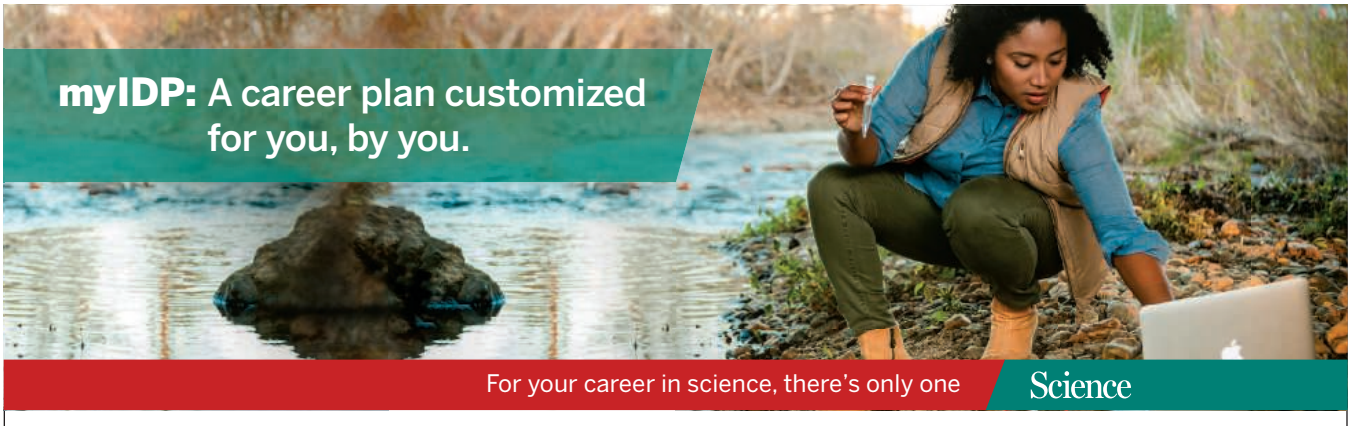

Features in myIDP include:

- Exercises to help you examine your skills, interests, and values.
- A list of 20 scientific career paths with a prediction of which ones best fit your skills and interests.

myIDP

Visit the website and start planning today!
myIDP.sciencecareers.org

ScienceCareers | AAAS In partnership with:

FASEB Federation of American Societies for Experimental Biology
University of Massachusetts Medical School UMASS
UCSF University of California San Francisco
UIC
BURROUGHS WELLCOME FUND

ScienceCareers online @sciencecareers.org
FOCUS ON DIVERSITY AND INCLUSION

ICYS Research Fellow at ICYS, NIMS, Japan

International Center for Young Scientists (ICYS) of National Institute for Materials Science (NIMS) is now seeking a few research fellows who have passion to conduct innovative materials research based on their original idea. ICYS research fellows are expected to pursue high quality research with their initiatives using the most advanced facilities in NIMS.

ICYS offers a "Melting Pot" environment mixing different materials research fields and cultures. Common language in ICYS is English. Clerical and technical support in English will be given by the ICYS staffs. An annual salary of approximately 5.35 million yen will be offered, which may depend on the qualification and performance of the research fellow. Additional research grant of 2 million yen per year will be supplied to each research fellow. The initial contract term is two years and may be extended by another year depending on one's performance.

All applicants must have obtained a PhD degree within the last ten years. Applicants should submit an **application form** including a research proposal to be conducted during the ICYS term, **CV Header**, **CV** with a list of publications and patents (be sure to attach the header), **a list of DOI of journal publications** following our instruction, **PDF files of three significant publications** to ICYS Recruitment Desk by **March 31, 2020 JST**. The format for **application form** and **CV header** can be downloaded from **our website**. Please visit our website for more details.

ICYS Recruitment Desk,
National Institute for Materials Science
http://www.nims.go.jp/icys/recruitment/index.html

Who's the Top Employer for 2019?

Science Careers' annual survey reveals the top companies in biotech & pharma voted on by *Science* readers.

Read the article and employer profiles and listen to podcasts at sciencecareers.org/topemployers

SPECIAL JOB FOCUS:

Biology

Issue date: March 20
Book ad by March 5

Ads accepted until March 13 if space allows

To book your ad, contact:
advertise@sciencecareers.org

The Americas
202 326 6577
Europe
+44 (0) 1223 326527
Japan
+81 3 6459 4174
China/Korea/Singapore/Taiwan
+86 131 4114 0012

Produced by the *Science*/AAAS Custom Publishing Office.

Why choose this job focus for your advertisement?

- Relevant ads lead off the career section with a special biology banner
- Bonus distribution: Experimental Biology, April 4–7, San Diego, CA.

Science Careers
AAAS
SCIENCECAREERS.ORG

FOR RECRUITMENT IN SCIENCE, THERE'S ONLY ONE *SCIENCE*.

Overseas Chinese Scholars' Visit to Top Chinese Universities

Check the Details from www.edu.cn/zgx

- 10,000+ academic job vacancies in China
- Free one-to-one consultation service

Send your CV to consultant@acabridge.edu.cn

烟台大学
YANTAI UNIVERSITY

上海立信会计金融学院
SHANGHAI LIXIN UNIVERSITY OF ACCOUNTING AND FINANCE

西安交通大学
XI'AN JIAOTONG UNIVERSITY

学术桥
AcaBridge.edu.cn

ScienceCareers online @sciencecareers.org

ScienceCareers
FROM THE JOURNAL SCIENCE AAAS

Confused about your next career move?

Download Free Career Advice Booklets!

ScienceCareers.org/booklets

CityU
香港城市大學
City University of Hong Kong

52nd World University
4th World's top 50 Universities under age 50
1st Engineering/Technology/Computer Sciences in Hong Kong
2nd Business School in Asia

Worldwide Search for Talent

City University of Hong Kong is a dynamic, fast-growing university that is pursuing excellence in research and professional education. As a publicly-funded institution, the University is committed to nurturing and developing students' talents and creating applicable knowledge to support social and economic advancement. The University has nine Colleges/Schools. As part of its pursuit of excellence, the University aims to recruit **outstanding scholars** from all over the world in various disciplines, including **business, creative media, data science, energy and environment, engineering, humanities and social sciences, law, science, veterinary medicine and life sciences.**

The University welcomes applications and nominations for all faculty positions of Chair Professor, Professor, Associate Professor and Assistant Professor. The remuneration package will be highly competitive, commensurate with qualifications and experience. Interested parties are invited to submit an online application with current curriculum vitae to apply for current openings at http://go.cityu.hk/hrojobus or by email to "hrojob@cityu.edu.hk".

City University of Hong Kong is an equal opportunity employer and we are committed to the principle of diversity. Personal data provided by applicants will be used for recruitment and other employment-related purposes.

Worldwide recognition ranking 52nd, and 4th among top 50 universities under age 50 (QS survey 2020); 1st in Engineering/Technology/Computer Sciences in Hong Kong (ARWU survey 2016); and 2nd Business School in Asia-Pacific region (UT Dallas survey 2017).

By **Bill D. Roebuck**

Just for fun

About 10 years ago, I sat in my office, struggling to muster up the motivation to write an annual progress report for my dean. I enjoy writing grant applications and scientific papers—tasks that engage my creativity and further my research. But report writing doesn't come with any reward apart from the momentary satisfaction of crossing something off my to-do list. Like other routine paperwork, I find it hard to get through. So that day, I offered myself a reward: When I finished the report, I'd give myself 2 hours to examine slides under the microscope—a task I've always loved but never had much time for as a faculty member.

Over my 40-year academic career, I have learned that I need to give myself special projects as a reward for completing onerous paperwork. I retired from my faculty position 3 years ago, so thankfully I don't face much paperwork anymore. But I still break out this reward system every so often. It's a strategy I call "just for fun."

The strategy was born out of challenges I experienced in grad school. I could handle failed experiments, equipment malfunctions, and other hiccups. Bureaucratic busywork was a bigger hurdle. I usually delayed putting together reports for grant agencies and university administrators until threatening letters arrived—or the deadline was so close that I became gripped with panic. I never felt that paperwork was advancing my science, but rather sapping my energy and time for research.

"I ... give myself special projects as a reward for completing onerous paperwork."

One of my committee members recognized and understood my difficulties. He asked, "If a day is going badly, what might you like to do at work—just for fun?" I must have looked confused, because I didn't see how his question was relevant to the problem at hand. Then he told me about his strategy of rewarding himself with a fun project when he completed a task that he didn't particularly enjoy. He advised me to think about doing something similar. I immediately liked the idea, but it took me a few years to fully implement my own system. It also evolved over the course of my career.

As a Ph.D. student, I did not see labwork as a special reward because I already spent most of my time in the lab. So, I devised a different kind of reward: I'd let myself attend seminars on topics I was curious about but that lay outside of my immediate field. For example, one day I remember telling myself, "If I get this report submitted on time, I am going to that seminar on pathology." I got better at meeting deadlines—and I had some fun in the process.

When I became a faculty member with a lab of my own, my "just for fun" strategy began to shift. I was at my microscope less and less, and I started to miss it. At the same time, my need for fun rewards multiplied because bureaucratic tasks started to clog up my to-do list.

So, as my laboratory grew, I started to jealously guard some small projects—such as microscope tasks, simple experiments, and data analyses—that I could complete myself. Sometimes I even sought out those projects. For example, a collaborator told me that he was having problems staining liver tumors, so I told him: "Send me the slides; I can do that!" At that point in my career, my role in research mostly took the form of advising students and technicians. The research didn't feel like my own anymore, and when it was done, I certainly could not say, "Look what I discovered!" But with the "just for fun" projects, I had full ownership. I felt as though I'd done real science.

Over the course of my career, this strategy helped me complete and move past the parts of my job that I didn't particularly enjoy. The rewards I gave myself provided a way to relax and reminded me why I love being a scientist.

As for that annual report, I spent an uninspiring morning on it—but got it done. Then I hurried over to the microscope, eager to inspect a series of slides that my collaborators had sent a couple weeks earlier.

To others, it may have looked like work. But to me, it was just for fun. ■

Bill D. Roebuck is a professor emeritus at Dartmouth College in Hanover, New Hampshire. Do you have an interesting career story to share? Send it to SciCareerEditor@aaas.org.

ILLUSTRATION: ROBERT NEUBECKER

Published by AAAS